

Mechanisms and Machine Science

Volume 8

Series Editor

Marco Ceccarelli

For further volumes:
<http://www.springer.com/series/8779>

Jaroslav Beran · Martin Bílek
Monika Hejnova · Petr Zabka
Editors

Advances in Mechanisms Design

Proceedings of TMM 2012

Editors

Jaroslav Beran
Textile Machine Design Department
Technical University of Liberec
Liberec
Czech Republic

Monika Hejnova
Textile Machine Design Department
Technical University of Liberec
Liberec
Czech Republic

Martin Břlek
Textile Machine Design Department
Technical University of Liberec
Liberec
Czech Republic

Petr Zabka
Textile Machine Design Department
Technical University of Liberec
Liberec
Czech Republic

ISSN 2211-0984

ISBN 978-94-007-5124-8

DOI 10.1007/978-94-007-5125-5

Springer Dordrecht Heidelberg New York London

ISSN 2211-0992 (electronic)

ISBN 978-94-007-5125-5 (eBook)

Library of Congress Control Number: 2012943369

© Springer Science+Business Media Dordrecht 2012

This work is subject to copyright. All rights are reserved by the Publisher, whether the whole or part of the material is concerned, specifically the rights of translation, reprinting, reuse of illustrations, recitation, broadcasting, reproduction on microfilms or in any other physical way, and transmission or information storage and retrieval, electronic adaptation, computer software, or by similar or dissimilar methodology now known or hereafter developed. Exempted from this legal reservation are brief excerpts in connection with reviews or scholarly analysis or material supplied specifically for the purpose of being entered and executed on a computer system, for exclusive use by the purchaser of the work. Duplication of this publication or parts thereof is permitted only under the provisions of the Copyright Law of the Publisher's location, in its current version, and permission for use must always be obtained from Springer. Permissions for use may be obtained through RightsLink at the Copyright Clearance Center. Violations are liable to prosecution under the respective Copyright Law.

The use of general descriptive names, registered names, trademarks, service marks, etc. in this publication does not imply, even in the absence of a specific statement, that such names are exempt from the relevant protective laws and regulations and therefore free for general use.

While the advice and information in this book are believed to be true and accurate at the date of publication, neither the authors nor the editors nor the publisher can accept any legal responsibility for any errors or omissions that may be made. The publisher makes no warranty, express or implied, with respect to the material contained herein.

Printed on acid-free paper

Springer is part of Springer Science+Business Media (www.springer.com)



Technical University of Liberec
Studentská 1402/2
461 17 Liberec 1
Czech Republic
<http://www.tul.cz>



Czech Society of Mechanics
Dolejšková 5
182 00 Praha 8
Czech Republic
<http://www.csm.cz>



IFTToMM
International Federation for the Promotion
of Mechanism and Machine Science
<http://www.iftomm.org>
Czech National Committee of IFTToMM
Institute of Thermomechanics AS CR, v. v. i.,
Dolejšková 5
182 00 Praha 8
Czech Republic
<http://www.it.cas.cz/IFTToMM-TC-NO/>



VÚTS, a.s.
U Jezu 525/4
461 19 Liberec 1
Czech Republic
<http://www.vuts.cz>

Scientific Committee

J. Beran—Chairman, Czech Republic
M. Bílek—Secretary, Czech Republic
V. Arakelyan, France
T. Březina, Czech Republic
M. Ceccarelli, Italy
B. Corves, Germany
L. Frýba, Czech Republic
J.C. Garcia-Prada, Spain
V. Goldfarb, Russia
A. Gronowicz, Poland
J. Horáček, Czech Republic
C. Kratochvíl, Czech Republic
T. Leinonen, Finland
M. Lima, Portugal
E.CH. Lovasz, Romania
K. Luck, Germany
E. Macha, Poland
K.H. Molder, Germany
V. Natarajan, India
L. Pešek, Czech Republic
L. Půst, Czech Republic
Š. Segľa, Slovakia
B. Shchokin, Ukraine
J. Stadnicki, Poland
I. Tempea, Romania
D. Tesar, USA
M. Václavík, Czech Republic
M. Valášek, Czech Republic
J. Zapoměl, Czech Republic
V. Zeman, Czech Republic

Preface

The international conference on the theory of machines and mechanisms has been held since 1973 in regular 4-year intervals. The expert agenda of the conference focuses on a wide range of problems including theoretical and practical findings related to theories pertaining to machines and mechanisms. The person involved in the creation of this conference was an important personality and leading expert in mechanics and mechanism theories—Prof. Jaroslav Charvát. He was not only a renowned expert regarding mechanism theories, but he was also an excellent teacher and promoter of mechanics for the professional and lay public.

The 11th International Conference on the Theory of Machines and Mechanisms was held from 4 to 6 September 2012 at the Liberec Technical University, Liberec, Czech Republic. The conference was organized under the auspices of the Czech National Committee for Theories of Machines and Mechanisms IFToMM, the Czech Society for Mechanics, and the Textile Machines Research Institute Liberec. The lectures focused particularly on the areas of analysis, synthesis of articulated, cam, planar, and spatial mechanisms.

A major part included a focus on problems related to the dynamics of machines and mechanisms as well as mechatronic and biomechanical systems. Robotic systems were another major focus of the conference.

During the conference, the Meeting of the Technical Committee for Linkages and Mechanical Controls of IFToMM and the Meeting of the Czech Society for Mechanics took place.

In this book contributions from the conference have been included in seven main sections:

- General Theory of Machines and Mechanisms
- Analysis and Synthesis of Planar and Spatial Mechanisms, Linkages, and Cams
- Dynamics of Machines and Mechanisms, Rotor Dynamics, Vibration and Noise in Machines, Computational Mechanics
- Robots and Manipulators

- Biomechanics
- Optimization of Mechanisms and Machines, The Mechanisms of Textile Machines
- Mechatronics, Control and Monitoring Systems of Machines

As it has for more than 39 years, this volume of proceedings offers both a broad perspective on the state of the art in the field as well as an in-depth look at its leading edge research. It is our privilege to be able to offer this collection and we express our sincere thanks to the contributing authors for making this series a continuing success.

We appreciate the interest in this conference and believe it will bring many suggestions for further extension of knowledge in the field of machines and mechanisms theory and will provide new ideas for international cooperation in this field.

Jaroslav Beran

Contents

Part I General Theory of Machines and Mechanisms

Mobile Wheel-Legged Robot: Researching of Suspension Leveling System	3
J. Bałchanowski	
Comparison of Alternative Equivalent Circuits of Induction Motor with Real Machine Data	13
J. Bradna, J. Bauer, S. Fligl and V. Hlinovsky	
Band Mechanism with Nonlinear Gear Ratio for Gravity Force Balance: Design and Analysis in Total System Network	21
F. Ebert and M. Berger	
Application of the Research Environment e-Kinematix in Mechanism Development	27
G. Lonij, B. Corves, M. Reeßing and M. Razum	
Advanced Digitization Techniques in Retrieval of Mechanism and Machine Science Resources	35
E-Ch. Lovasz, C. M. Gruescu, V. Ciupe, I. Carabas, D. Margineanu, I. Maniu and N. Dehelean	
Trends in Development of Positioning Mechanisms	43
F. Palčák	
New Models of Mechanisms for the Motion Transformation	49
Tomislav Petrović and Ivan Ivanov	

Structural Synthesis of a Class of the Parallel Mechanisms Providing Plane-Parallel Displacement of a Mobile Platform.	57
L. Rybak, A. Chichvarin, R. Sidorenko and J. Šklíba	
Development of a Wearable Assist Robot for Walk Rehabilitation After Knee Arthroplasty Surgery.	65
H. Terada, Y. Zhu, K. Horiguchi, M. Nakamura and R. Takahashi	
Modeling of Lifting Equipment with Backlash Consideration	73
J. Vondrich and E. Thöndel	
Analysis of Automatic Automotive Gear Boxes by Means of Versatile Graph-Based Methods.	81
J. Drewniak, J. Kopeć and S. Zawiślak	
 Part II Analysis and Synthesis of Planar and Spatial Mechanisms, Linkages and Cams	
Direct and Inverse Kinematic of 3DOF Parallel Mechanism with Singularity Analysis.	89
J. Bałchanowski	
Measuring of Radial Cams Contours	97
V. Crhak	
High-Speed Parallel Shaft Indexing Drive	105
P. Dostrašil, F. Hartig, M. Václavík and P. Jirásko	
A Simplified Design with a Toothed Belt and Non-circular Pulleys to Separate Parts from a Magazine File.	113
U. Hanke, K.-H. Modler, R. Neumann and C. Fischer	
Path Generation of Regular Polygon Using a Geared-Parallelogram Mechanism	121
S. Lin, Y. Fan, Z. Ren and U. Hanke	
MOCAD: A Tool for Graphical and Interactive Calculation and Optimization of Cam Mechanisms and Motion Control Systems. . .	129
A. Heine and M. Berger	
Efficiency of Integrated Anti-Backlash Designed Planetary Gearbox	137
V. Klouček	

Numerical Method for Determination of Base Circle Radius of Cam Mechanisms with Oscillating Flat-Face Follower	143
E.-C. Lovasz, D. Perju, C. M. Gruescu, K.-H. Modler, Cărbăș I and E. S. Zăbavă	
Analytical Displacement and Velocity Modeling of the RSSR-SS Linkage	151
Q. Shen, K. Russell and R. S. Sodhi	
 Part III Dynamics of Machines and Mechanisms, Rotor Dynamics, Vibration and Noise in Machines, Computational Mechanics	
Shaking Force Minimization of High-Speed Robots via Optimal Trajectory Planning	159
S. Briot, V. Arakelian and J.-P. Le Baron	
Nonlinear Antiresonance Vibrating Screen	167
V. N. Belovodskiy, S. L. Bukin and M. Y. Sukhorukov	
Modeling and Simulation of a Slider Crank Mechanism with a Flexible Extensible Link	175
M. Dupac and S. Noroozi	
Multipoint Contact Approach to the Analysis of Interacting Flexible Bodies Vibration	181
M. Hajžman and D. Rychecký	
Dynamic Analysis of Resonance: Bifurcation Characteristics of Non-linear Parametric Systems	187
M. Hortel, A. Škuderová, C. Kratochvíl and M. Houfek	
Control of Compliant Mechanisms with Large Deflections	193
D. Kern, J. Bauer and W. Seemann	
About Problems of Nonlinear Dynamics of the Elastic Rod Elements in Practice of Chisel Works	201
L. Khajiyeva	
Dynamic Analysis of Hammer Mechanism “Twin Hammer” of Impact Wrench	209
M. Konečný and J. Slavík	

Forces and Moments Acting on the Fluttering Profile	217
J. Kozánek, V. Vlcek and I. Zolotarev	
Rotor-Liquid-Fundament System's Oscillation	223
A. Kydyrbekuly	
Simulations of Radiation Heat Transfer in Design of Alternative Infrared Emitters	231
J. Loufek	
Creating a Mathematical Model for Solving Chatter and Dealing the Problems Concerning the Maximum Allowable Size of a Machining Chip	237
J. Ondrášek	
Impact of Thermal Stresses on Micro-Fabricated Devices Used for Optical Applications	245
K. Malinauskas, V. Ostasevicius and R. Dauksevicius	
Exponential Damping as an Approach to Internal Hysteretic Damping of Rotor Systems: FEM Model of Timoshenko Rotating Beam with Maxwell-Weichert Damping Model	253
Antonín Skarolek	
Contribution to Numerical Analysis of Uncertain Mechanical Systems Using Probability and Possibility Theory	263
M. Vaško, M. Sága and V. Dekýš	
Reducing the Steady State Vibrations of Flexible Rotors by Squeezing Thin Layers of Normal and Magneto Rheological Oils	271
J. Zapoměl and P. Ferfecki	
 Part IV Robots and Manipulators	
Development of an Upper Limb Motorized Assistive-Rehabilitative Robot	281
Masoud Amiri and Federico Casolo	
Workspace Evaluation for Analysis and Synthesis of Manipulators . . .	289
M. Ceccarelli	

The Force Reaction Control of the Wheel-Legged Robot's Limb Prototype.	303
A. Gronowicz, J. Szrek and S. Wudarczyk	
Method for Planning the Finger's Movement in the Anthropomorphic Manipulator Hand-K3, Using a Tactile Sensors Network, with the Aim of Optimal Grasping.	309
A. Handke and W. Twaróg	
Development of Spherical Ultrasonic Motor as a Camera Actuator for Pipe Inspection Robot	317
M. Hoshina and S. Toyama	
Research on Multi-Directional Pose Accuracy Variation to a Welding Robot	323
V. Vacaescu, E. Ch. Lovasz and C. F. Buciuman	
 Part V Biomechanics	
Inverse Dynamics Model for the Ankle Joint with Applications in Tibia Malleolus Fracture	331
E. Budescu, E. Merticaru and M. Chirazi	
Dynamic Characteristics of Prosthetic Feet: A Comparison Between Modal Parameters of Walking, Running and Sprinting Foot.	339
S. Noroozi, A. G. A. Rahman, M. Dupac and J. E. Vinney	
Biomechanical Solutions in Tibial Malleolus Fracture.	345
C. Oprisan, E. Budescu and V. Cotoros	
Validation of Human Body Model VIRTHUMAN and its Implementation in Crash Scenarios	351
Ing. Jaroslav Mañas, Ing. Luděk Kovář, Ing. Jan Petřík, Ing. Hana Čechová and Ing. Stanislav Špírk	
Numerical Simulation of the Self-Oscillations of the Vocal Folds and of the Resulting Acoustic Phenomena in the Vocal Tract	357
P. Švancara, J. Horáček and J. G. Švec	

Part VI Optimization of Mechanisms and Machines, The Mechanisms of Textile Machines

Analysis of Heald Motion During of Weaving Process	367
M. Bilek	
Kinematic Design and Ideal Dimensioning of New Highly Dynamic Drive Assemblies for Knitting and Braiding Machines	375
D. Denninger, M. Berger and A. Heine	
Analysis of the Loop Spinning System	383
J. Beran and M. Hejnova	
Adjusting the Chain Gear	393
Z. Koloc, J. Korf and P. Kavan	
Modification of Upper Thread Tensioner of Sewing Machine	401
P. Klouček and P. Škop	
Optimization of Car Seats in the Interaction of Sitting Man on the Size of the Contact Pressure	407
R. Martonka and V. Fliegel	
Trajectories of Dop Points on a Machining Wheel During Grinding of High Quality Plane Surfaces	413
I. Petrikova, R. Vrzala and J. Kafka	
A Design and Optimization of the Fully Automatic Shunting Mechanism	421
A. Sapietova and V. Dekys	
Modelling and Optimization of the Half Model of a Passenger Car with Magnetorheological Suspension System	429
S. Segla	
Optimization of Industrial Sewing Machine Balancing Using Adams and Mathematica Software	437
P. Šidlof and J. Ondrášek	
Application of the Impact-Free Lift Dependence in Small-Diameter Knitting Machines.	445
J. Skřivánek and M. Bilek	

The Optimal Design of an Auxiliary Switch for an Internal Combustion Engine Starter	451
J. Stropnik	
Construction for High Pressure Application on 3D Nanofibers	459
L. Ševčík and D. Vejrych	
Dynamic Properties of Traversing Rod	469
P. Žabka, J. Valtera and J. Beran	
Flexible Elements in the Mechanisms of Weaving Machines	475
J. Žák	
 Part VII Mechatronics, Control and Monitoring Systems of Machines	
 New Conception of Waving Machine CamEl Drive.	483
A. Bílkovský, O. Marek, P. Jirásko and Z. Volanský	
Application of Motion API for Input Production Data in a Single-Purpose Machine Tool with Control System by YASKAWA	489
P. Bureš	
The Conception of the Control System of Radial Cam Grinder.	495
P. Jirásko, V. Crhák and P. Bureš	
An Analysis of Planetary Gearboxes for Their Use With Electronic Cam.	501
P. Dostrašil, P. Jirásko and M. Bušek	
DC/DC Power Converter for Super-Capacitor Supplied by Electric Power Splitter	509
T. Haubert and P. Mindl	
Traction Control System for Formula Student Electric.	517
Z. Houf, Z. Čeřovský and V. Hlinovský	
Electro Dermal Quantification of Some Dental Treatment's Efficiency.	523
M. Mateas and E. Ianosi	

Servo Control Using Wave-Based Method	531
O. Marek	
Drives Dynamic Models Implementation with Regard to Real-Time Simulation	537
J. Opálka	
High Performance Real-Time Simulation for Control Systems Development on Fast but Ordinary PC	543
J. Rameš	
Function Properties of Electronic Cam with Great Unevenness of Angular Speed	549
P. Šidlof and P. Klouček	
Index	557

Contributors

M. Amiri Politecnico di Milano, Milan, Italy

V. Arakelian Institut National des Sciences Appliquées de Rennes, Rennes, France

J. Balchanowski Wroclaw University of Technology, Wroclaw, Poland

J. Bauer Czech Technical University in Prague, Faculty of Electrical Engineering, Technicka 2, Prague 6, 166 27 Prague, Czech Republic

V. Belovodskiy Donetsk National Technical University, Donetsk, Ukraine

J. Beran Technical University of Liberec, Liberec, Czech Republic

M. Berger Technical University Chemnitz, Chemnitz, Germany

M. Bílek Technical University of Liberec, Liberec, Czech Republic

A. Bílkovský VÚTS, a.s., Liberec, Czech Republic

J. Bradna Czech Technical University in Prague, Faculty of Electrical Engineering, Technicka 2, Prague 6, 166 27 Prague, Czech Republic

S. Briot Institut de Recherches en Communications et Cybernétique de Nantes (IRCCyN), Nantes, France

C.F. Buciuman Politehnica University of Timisoara, Timisoara, Romania

E. Budescu Gh. Asachi Technical University, Iasi, Romania

S.L. Bukin Donetsk National Technical University, Donetsk, Ukraine

P. Bureš VÚTS, a.s., Liberec, Czech Republic

M. Bušek VÚTS, a.s., Liberec, Czech Republic

I. Cărbăș Politehnica University of Timisoara, Timisoara, Romania

F. Casolo Politecnico di Milano, Milan, Italy

- M. Ceccarelli** University of Cassino and South Latium, Cassino, Italy
- Z. Čerovský** Department of Electrical Drives and Traction, Faculty of Electrical Engineering, Czech Technical University in Prague, Prague, Czech Republic
- A. Chichvarin** Stary Oskol Technological Institute of National University of Science and Technology «MISIS», Stary Oskol, Russia
- M. Ciupe** Universitatea Politehnica din Timisoara, Timisoara, Romania
- B. Corves** RWTH Aachen University, Aachen, Germany
- V. Cotoros** Municipal Hospital Medgidia, Medgidia, Romania
- V. Crhák** VÚTS, a.s., Liberec, Czech Republic
- R. Dauksevicius** Kaunas University of Technology, Kaunas, Lithuania
- N. Dehelean** Universitatea Politehnica din Timisoara, Timisoara, Romania
- V. Dekýš** University of Žilina, Žilina, Slovakia
- D. Denninger** Chemnitz University of Technology, Chemnitz, Germany
- P. Dostrašil** VÚTS, a.s., Liberec, Czech Republic
- J. Drewniak** University of Bielsko-Biała, Bielsko-Biała, Poland
- M. Dupac** Bournemouth University, Poole, UK
- F. Ebert** Technical University Chemnitz, Chemnitz, Germany
- Y. Fan** Tongji University, Shanghai, China
- P. Ferfecki** VSB-Technical University of Ostrava, Ostrava, Czech Republic
- C. Fischer** Technische Universität Dresden, Dresden, Germany
- V. Fliegel** Technical University of Liberec, Liberec, Czech Republic
- S. Fligl** Czech Technical University in Prague, Faculty of Electrical Engineering, Technicka 2, Prague 6, 166 27 Prague, Czech Republic
- A. Gronowicz** Wroclaw University of Technology, Wroclaw, Poland
- C.M. Gruescu** Universitatea Politehnica din Timisoara, Timisoara, Romania
- M. Hajžman** University of West Bohemia, Plzeň, Czech Republic
- H. Čechová** University of West Bohemia, Plzeň, Czech Republic
- A. Handke** Wroclaw University of Technology, Wroclaw, Poland
- U. Hanke** Technical University of Dresden, Dresden, Germany
- F. Hartig** VÚTS, a.s., Liberec, Czech Republic

T. Haubert Czech Technical University in Prague, Faculty of Electrical Engineering, Technická 2, Prague 6, 166 27 Prague, Czech Republic

A. Heine Chemnitz University of Technology, Chemnitz, Germany

M. Hejnova Technical University of Liberec, Liberec, Czech Republic

V. Hlinovsky Czech Technical University in Prague, Faculty of Electrical Engineering, Technická 2, Prague 6, 166 27 Prague, Czech Republic

J. Horáček Institute of Thermomechanics, Academy of Sciences of the Czech Republic, Prague, Czech Republic

K. Horiguchi Graduate School of Medical and Engineering Science, University of Yamanashi, Tokyo, Japan

M. Hortel Institute of Thermomechanics ASCR, v.v.i., Prague, Czech Republic

M. Hoshina Tokyo University of Agriculture and Technology, Tokyo Noko Daigaku, 3-8-1 Harumi-cho, Fuchu-shi, Tokyo 183-8538, Japan

Z. Houf Czech Technical University in Prague, Faculty of Electrical Engineering, Technická 2, Prague 6, 166 27 Prague, Czech Republic

M. Houfek Institute of Thermomechanics ASCR, v.v.i., Prague, Czech Republic

E. Ianoi University Politehnica of Timisoara, Timisoara, Romania

I. Ivanov Faculty of Mechanical Engineering, University of Niš, Medvedeva 14, 18000 Niš, Serbia

J. Mañas MECAS ESI s.r.o, Plzen, Czech Republic

P. Jirásko VÚTS, a.s., Liberec, Czech Republic

J. Kafka Technical University of Liberec, Liberec, Czech Republic

P. Kavan VÚTS, a.s., Liberec, Czech Republic

D. Kern Karlsruhe Institute of Technology, Karlsruhe, Germany

L. Khajiyeva Kazakh National University al-Farabi, Almaty, Kazakhstan

P. Klouček VÚTS, a.s., Liberec, Czech Republic

V. Klouček VÚTS, a.s., Liberec, Czech Republic

Z. Koloc VÚTS, a.s., Liberec, Czech Republic

M. Konečný Technical University of Liberec, Liberec, Czech Republic

J. Kopeć University of Bielsko-Biała, Bielsko-Biała, Poland

J. Korf VÚTS, a.s., Liberec, Czech Republic

J. Kozanek Institute of Thermomechanics ASCR, v.v.i., Prague, Czech Republic

C. Kratochvíl Institute of Thermomechanics ASCR, v.v.i., Prague, Czech Republic

A. Kydyrbekuly Kazakh National University, Almaty, Kazakhstan

J.-P. Le Baron Institut National des Sciences Appliquées de Rennes, Rennes, France

S. Lin Tongji University, Shanghai, China

G. Lonij RWTH Aachen University, Aachen, Germany

J. Loufek Technical University of Liberec, Liberec, Czech Republic

E.CH. Lovasz University Politehnica of Timisoara, Timisoara, Romania

L. Kovář MECAS ESI s.r.o, Plzen, Czech Republic

K. Malinauskas Kaunas University of Technology, Kaunas, Lithuania

I. Maniu Universitatea Politehnica din Timisoara, Timisoara, Romania

O. Marek VÚTS, a.s., Liberec, Czech Republic

D. Margineanu Universitatea Politehnica din Timisoara, Timisoara, Romania

R. Martonka Technical University of Liberec, Liberec, Czech Republic

M. Mateas Politehnica University of Timisoara, Timisoara, Romania

E. Merticaru Technical University of Iasi, Iasi, Romania

P. Mindl Czech Technical University, Prague, Czech Republic

K.-H. Modler Technische Universität Dresden, Dresden, Germany

M. Nakamura Kofu Municipal Hospital, Yamanashi, Japan

R. Neumann Technische Universität Dresden, Dresden, Germany

S. Noroozi Bournemouth University, Poole, UK

J. Ondrášek VÚTS, a.s., Liberec, Czech Republic

J. Opálka VÚTS, a.s., Liberec, Czech Republic

C. Oprisan Gh. Asachi Technical University, Iasi, Romania

V. Ostasevicius Kaunas University, Kaunas, Lithuania

F. Palčák Slovenska Technical University, Bratislava, Slovakia

D. Perju Politehnica University of Timisoara, Timisoara, Romania

I. Petrikova Technical University of Liberec, Liberec, Czech Republic

T. Petrovic University of Nis, Nis, Serbia

- J. Petřík** Technical University of Liberec, Liberec, Czech Republic
- A.G.A. Rahman** University Malaysia Pahang, Pahang, Malaysia
- J. Rameš** VÚTS, a.s., Liberec, Czech Republic
- M. Razum** FIZ Karlsruhe, Karlsruhe, Germany
- M. Reeßing** Ilmenau University of Technology, Ilmenau, Germany
- Z. Ren** China Tobacco Machinery Technology Center Co., Ltd (CTMTC), Shanghai, China
- K. Russell** New Jersey Institute of Technology, Newark, NJ, USA
- L. Rybak** Belgorod State Technological University named after V.G. Shoukhov, Belgorod, Russia
- D. Rycheký** University of West Bohemia, Plzeň, Czech Republic
- M. Sága** University of Žilina, Žilina, Slovakia
- A. Sapietová** Žilinská University, Žilina, Slovakia
- W. Seemann**
- S. Segla** Technical University of Liberec, Liberec, Czech Republic
- L. Ševčík** Technická Univerzita v Liberci, Liberec, Czech Republic
- Q. Shen** Emerson Network Power, Columbus, USA
- P. Šidlof** VÚTS, a.s., Liberec, Czech Republic
- R. Sidorenko** Stary Oskol Technological Institute of National University of Science and Technology «MISIS», Stary Oskol, Russia
- A. Skarolek** VÚTS, a.s., Liberec, Czech Republic
- J. Šklíba** Technical University of Liberec, Liberec, Czech Republic
- P. Škop** VUTS Liberec, a.s., Measuring Department, Liberec, Czech Republic
- J. Skřivánek** Technical University of Liberec, Liberec, Czech Republic
- A. Škuderová** Institute of Thermomechanics ASCR, v.v.i., Prague, Czech Republic
- J. Slavík** Technical University of Liberec, Liberec, Czech Republic
- R.S. Sodhi** New Jersey Institute of Technology, Newark, NJ, USA
- S. Špírk** University of West Bohemia, Plzeň, Czech Republic
- J. Stropnik** University of Ljubljana, Ljubljana, Slovenia
- M.Y. Sukhorukov** Donetsk National Technical University, Donetsk, Ukraine

- P. Švancara** Brno University of Technology, Brno, Czech Republic
- J. G. Švec** Department of Biophysics, Faculty of Science, Palacky University Olomouc, Olomouc, Czech Republic
- J. Szrek** Wroclaw University of Technology, Wroclaw, Poland
- R. Takahashi** Suncall Engineering Corporation, Kyoto, Japan
- H. Terada** University of Yamanashi, Yamanashi, Japan
- E. Thöndel** Czech Technical University in Prague, Prague, Czech Republic
- S. Toyama** Tokyo University of Agriculture and Technology, Tokyo Noko Daigaku, 3-8-1 Harumi-cho, Fuchu-shi, Tokyo 183-8538, Japan
- W. Twaróg** Wroclaw University of Technology, Wroclaw, Poland
- V. Vacarescu** University Politehnica of Timisoara, Timisoara, Romania
- M. Václavík** VÚTS, a.s., Liberec, Czech Republic
- J. Valtera** Technical University of Liberec, Liberec, Czech Republic
- M. Vaško** Žilinská University, Žilina, Slovakia
- D. Vejrych** Technical University of Liberec, Liberec, Czech Republic
- J. E. Vinney** Bournemouth University, Bournemouth, UK
- V. Vlček** Institute of Thermomechanics ASCR, v.v.i., Prague, Czech Republic
- Z. Volanský** VÚTS, a.s., Liberec, Czech Republic
- J. Vondřich** Czech Technical University in Prague, Prague, Czech Republic
- R. Vrzala** Technical University of Liberec, Liberec, Czech Republic
- S. Wudarczyk** Wroclaw University of Technology, Wroclaw, Poland
- E.S. Zăbavă** Politehnica University of Timisoara, Timisoara, Romania
- P. Žabka** Technical University of Liberec, Liberec, Czech Republic
- J. Žák** VÚTS, a.s., Liberec, Czech Republic
- J. Zapoměl** VŠB-Technical University of Ostrava, Ostrava, Czech Republic
- S. Zawislak** University of Bielsko-Biala, Bielsko-Biala, Poland
- Y. Zhu** Graduate School of Medical and Engineering Science, University of Yamanashi, Tokyo, Japan
- I. Zolotarev** Institute of Thermomechanics ASCR, v.v.i., Prague, Czech Republic

Part I
General Theory of Machines
and Mechanisms

Mobile Wheel-Legged Robot: Researching of Suspension Leveling System

J. Bałchanowski

Abstract As part of this research a computational model of a wheel-legged robot wheel suspension was created and simulation studies of the dynamics of the suspension were carried out. The research focused on the development of a model of the robot's suspension and control system maintaining the robot chassis at a constant elevation relative to the ground and on simulation studies aimed at determining the basic dynamic and kinematic properties.

Keywords Mobile robots • Wheel-legged robots • Design • Computer simulation

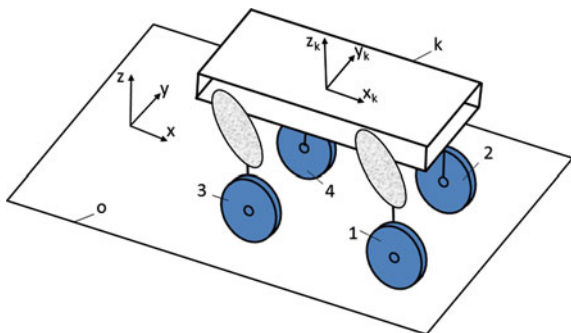
1 Introduction

The research on mobile robots has intensified in recent years, especially to meet the demand for mobile robots for the inspection of (chemically or biologically) contaminated areas and explosion or fire hazard areas [3].

Mobile wheel-legged robots are hybrid systems combining efficient travel on wheels on flat terrain with the capability of surmounting obstacles by walking. A major challenge in designing a wheel-legged robot is the design of its wheel suspension enabling the robot to both move on wheels and walk, and automatically levelling its chassis (keeping it at a constant height from the ground) during travel on a bumpy surface [5, 6].

J. Bałchanowski (✉)
Wrocław University of Technology, Wrocław, Poland
e-mail: Jacek.Balchanowski@pwr.wroc.pl

Fig. 1 Schematic of mobile wheel-legged robot (k —robot chassis, $1 \div 4$ —wheel suspensions, o —ground)



The aims of this research were: to create computational models of the wheel suspension and a model the control system for the levelling system and to carry out simulation studies of the robot suspension system.

2 Synthesis of Wheel-Legged Robot

The wheel-legged robot being designed is a four-wheel system with a rigid chassis (Fig. 1). The synthesis of such a system comes down to the selection of the wheel steering-suspension mechanism structure. The robot's wheel suspension system is a spatial mechanism with four degrees of freedom: the wheel can roll and turn (2 DOF) and move horizontally and vertically (2 DOF), executing respectively protrusion and lifting.

Its function is to move the wheel relative to the robot chassis in order to enable both driving (rolling and turn) and walking so that the robot can negotiate obstacles on its way as well as to enable the levelling of its chassis when the robot travels on a bumpy surface. The way in which walking and chassis levelling (keeping the chassis at a constant elevation from the ground) are executed is schematically shown in Fig. 2.

The robot suspension structure was designed as part of a wheel-legged robot construction project being carried out in Wrocław University of Technology. A kinematic scheme of the wheel suspension is shown in Fig. 3. The basic dimensions of the wheel suspension, shown in Table 1, were matched using a special method of geometrical synthesis and a genetic algorithm [4, 6].

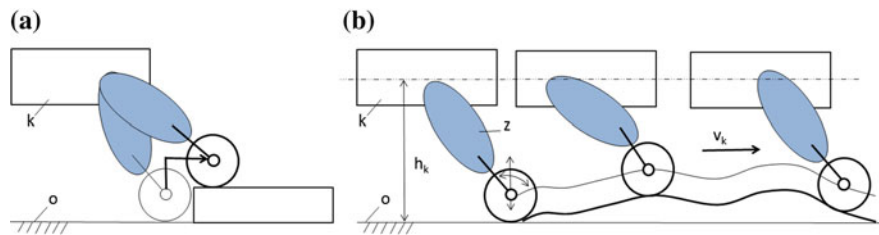


Fig. 2 Schematic showing execution of suspension motions: **a** walking, **b** maintaining constant chassis elevation h_k (levelling)

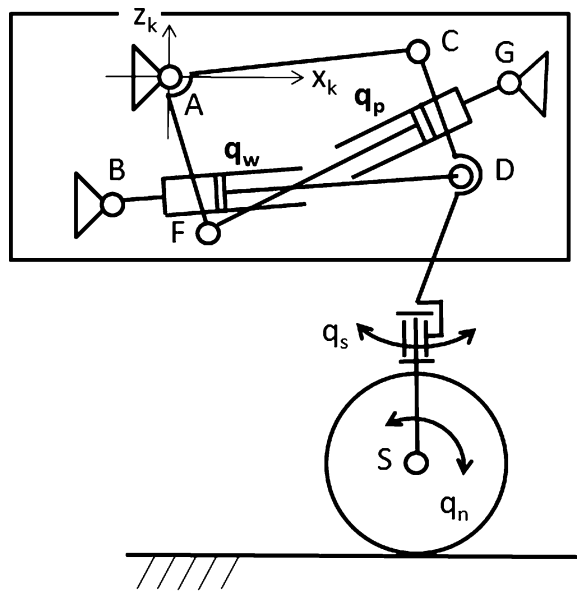
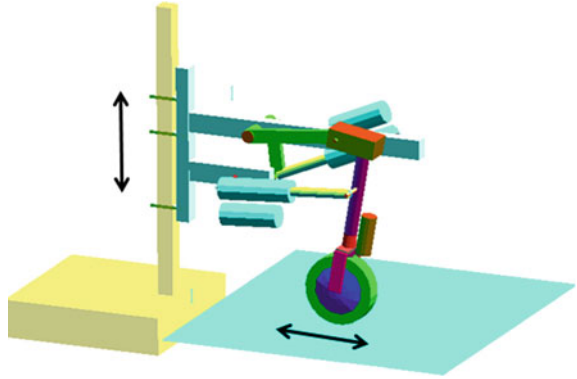


Fig. 3 Kinematic scheme of wheel-legged robot suspension

Table 1 Parameters of suspension (Fig. 3)

Name	Value (m)	Name	Value (m)
x_B	-0.07	AC	0.303
z_B	-0.152	AF	0.17
x_G	0.408	CD	0.162
z_G	0.005	CS	0.5
q_p, q_w	$0.35 \div 0.5$	DS	0.35

Fig. 4 Model of wheel-legged robot suspension



3 Computational Model of Wheel-Legged Robot Wheel Suspension

During travel the mobile robot chassis moves vertically and horizontally relative to the travel path. In the suspension model the vertical movement of the chassis was obtained by placing the chassis on linear guides mounted on a base [1].

In order to run simulations a computational model of the suspension, shown in Figs. 4 and 5 was created in the LMS DADS dynamic analysis system [2]. Kinematic excitations: rotational excitations q_n and q_s (wheel rolling and turn) and linear excitation q_p and q_w (wheel lifting and protrude ing) were defined for the 4 DOF.

The interaction between the wheel and the running track was modelled using the tyre force/ground model (TIRE).

The suspension model will be used in dynamic and kinematic computer simulation studies of the levelling motions of the robot suspension system. The aim of the studies is to design a suitable control system ensuring the automatic maintenance of a constant elevation of the chassis above the ground while travelling on a bumpy surface. In the case of the computational robot model, the levelling function boils down to keeping a constant elevation of the robot chassis above the ground according to the schematic shown in Fig. 2b. This function can be effected solely by lifting the chassis by means of lift actuator q_p (Fig. 3) while the other drives (protrusion, turn and rolling) remain fixed.

First, simulation studies of chassis lifting were carried out. A schematic of the simulation is shown in Fig. 4. The aim of the studies was to determine the dependence between chassis elevation h_k above the ground and lifting actuator extension q_p . Location z_A of suspension rotational couple A (Fig. 3) was assumed as chassis elevation h_k . Figure 7 shows the obtained graphs of chassis elevation h_k and the change in active force F_p in the lifting actuator versus lifting actuator extension q_p . The range of change in actuator extension q_p is determined by the basic suspension specifications shown in Table 1. For such a actuator its chassis elevation h_k was found to range from 0.44 to 0.7 m.

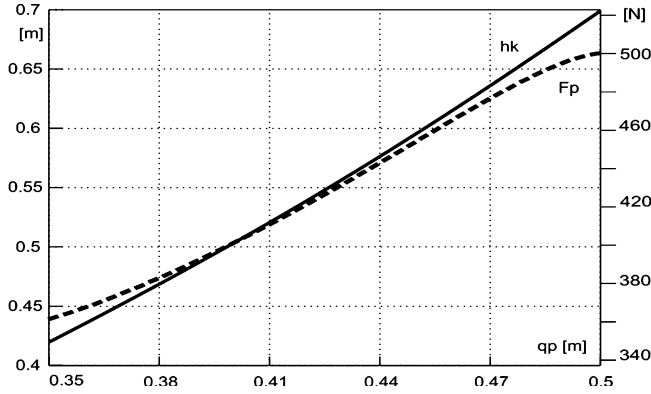
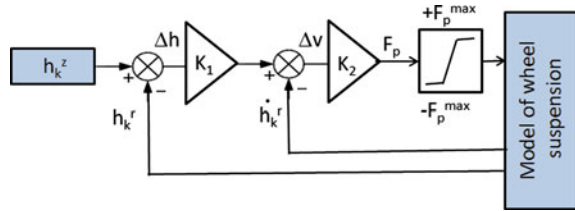


Fig. 5 Robot chassis elevation h_k and force F_p in lifting actuator versus extension of lifting actuator q_p

Fig. 6 Block diagram of mechanism control system



4 Design of Control System for Robot Chassis Levelling Mechanism

Only one lifting actuator q_p is used to level the robot chassis (keep it at specified constant elevation h_k^z) during travel on a bumpy surface, which requires such excitation force F_p of the actuator which results in prescribed elevation h_k^z with the required accuracy.

The proposed control system has a closed structure with a feedback loop controlling elevation h_k . Figure 6 shows a block diagram of the control system. In this system an external control loop computes the difference between prescribed robot chassis elevation h_k^z and actual chassis elevation h_k^r read from the chassis location. The computed elevation deviation Δh passes through a proportional controller with a constant (K_1). In the internal control loop the determined required speed is compared with actual speed \dot{h}_k^r read off the system. The speed deviation passes through another proportional controller with a constant (K_2), generating a signal specifying the required demand for active lifting force F_p , which is applied to the driving member of the mechanism. The control system incorporates limiter blocks limiting the generated value of force F_p to the maximum values ($-F_p^{max} < F_p < F_p^{max} = 950 \text{ N}$) which the lifting actuator is capable of generating. Besides the suspension model, a

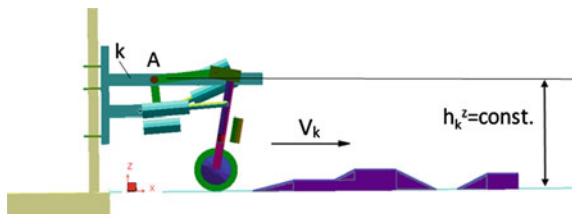


Fig. 7 Schematic of simulation of suspension travel on bumpy surface

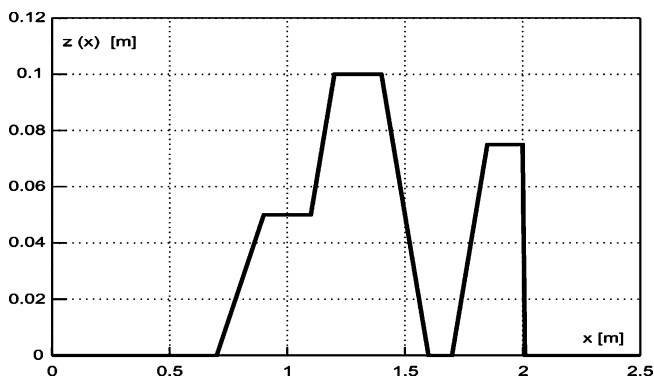


Fig. 8 Variation in ground bump height z along travel axis x

computational model of the designed control system was created in LMS DADS in order to study its dynamics.

The control parameters, i.e. constants K_1 , K_2 of the controllers in the control loops, of the control system shown in Fig. 10 need to be defined and matched. The parameters depend on the character of the object (the controlled mechanism). In control theory there are many methods of matching such parameters. In this research work, a numerical parameter matching procedure based on the Ziegler-Nichols method was carried out. The simulations were run in LMS DADS. The results of the controller parameter matching are: $K_1 = 5,300$, $K_2 = 3,100$.

4.1 Simulation Studies of Suspension with Positioning System

In order to determine the basic dynamical properties of the mechanism and to verify the control system matching, the travel of the system on a bumpy surface was simulated. A schematic of the simulation is shown in Fig. 7. The surface bumps were built from wedge-shaped obstacle drive-ons to drive-offs. One obstacle had a sharp dip. The variation in the route height along the travel direction is shown in Fig. 8.

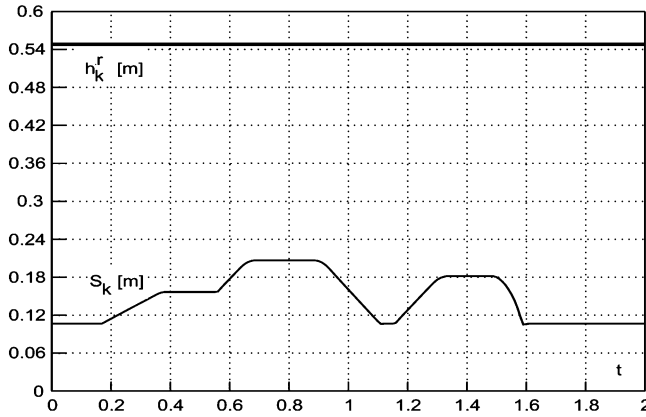


Fig. 9 Variation in robot chassis real elevation h_k^r and in wheel centre z_s during travel

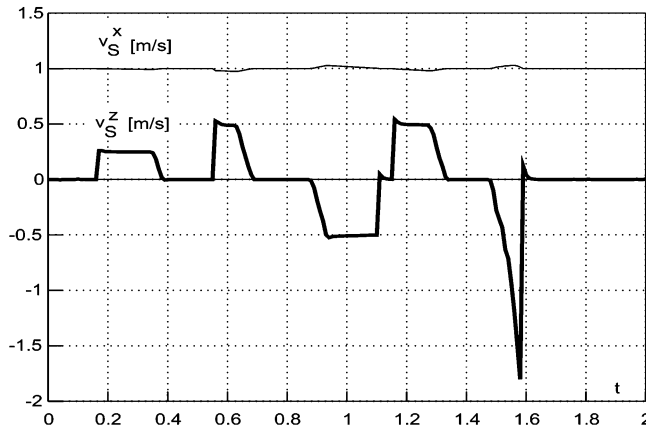


Fig. 10 Diagrams of vertical velocity v_s^z and horizontal velocity v_s^x of wheel centre S

The control system set value is robot chassis elevation $h_k^z = 0.545$ m above the ground, which is constant during travel. It was assumed that the system would move at constant speed $v_k = 1$ m/s (3.6 km/h). One of the aims of the simulations was to determine the control system response for the adopted motion excitations, in particular the accuracy with which setting h_k^z was executed, as well as the active forces and the load.

The diagrams below (Figs. 9, 10, 11, 12 and 13) show the results of the simulations of the system in LMS DADS. Figure 9 shows the variation in robot chassis real elevation h_k^r and wheel centre z_s during travel while the variation in vertical velocity v_s^z and horizontal velocity v_s^x of wheel centre S is shown in Fig. 10. The quality of the control is illustrated in the next diagram where errors $\Delta h_k = h_k^r - h_k^z$ in executing setting h_k^z are shown (Fig. 11). A chassis elevation h_k^z setting accuracy below 0.05 mm was achieved. The control system quickly

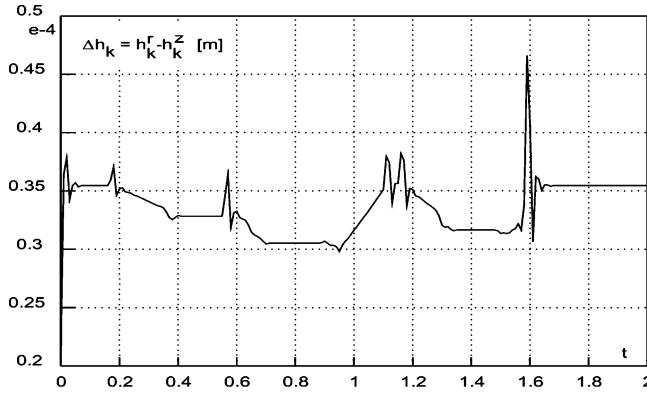


Fig. 11 Diagrams of errors $\Delta h_k = h_k^r - h_k^z$ in executing robot chassis elevation setting h_k^z

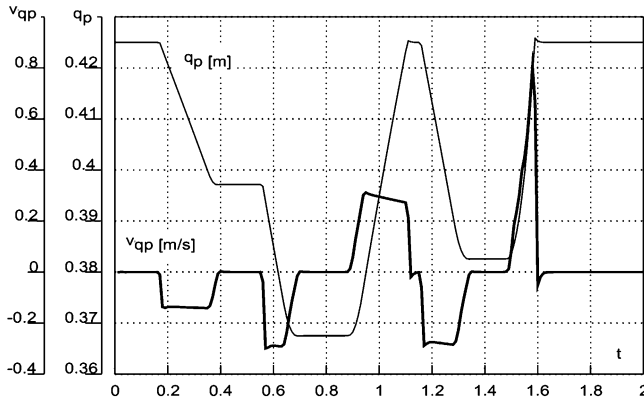


Fig. 12 Variation in extension q_p and velocity v_{qp} of lifting actuator

reacts to disturbances in the form of surface bumps (points for $t = 0.17, 0.4, 0.5, 0.9, 1.1, 1.3$ s in figures). The control system handled well the dip in the ground, quickly stabilizing the robot (for time $t = 1.6$ s in Fig. 10). The next figures show the determined operating parameters of the lifting actuator. Figure 12 shows the variation in length q_p and velocity v_{qp} of the lifting actuator while Fig. 13 shows the diagrams of computed active force F_p in this actuator.

An analysis of the levelling system reveals that the performance of the latter mainly depends on the height of the obstacle to be negotiated and on robot travelling speed v_k . These quantities determine vertical wheel velocity component v_s^z (Fig. 10) which must be cancelled out by the opposite vertical motion of the chassis effected by lifting actuator q_p moving with appropriate velocity v_{qp} (Fig. 12) and generating appropriate active force F_p (Fig. 13). The choice of a proper lifting actuator whose dynamics ensure that the required operating parameters can be exceeded is a guarantee of the correct operation of the robot's levelling system.

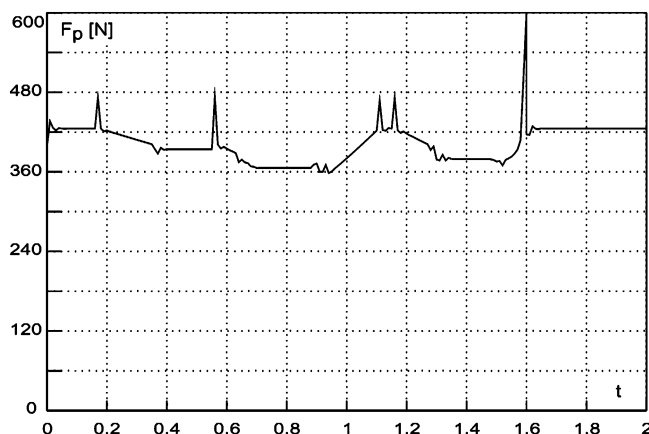


Fig. 13 Diagrams of active force F_p in actuator q_p , determined by control system

5 Conclusions

The dynamic and kinematic parameters of the wheel-legged robot wheel suspension were determined as a result of the simulation studies. Mechanisms of this kind are subject to considerable loads generated during travel on a bumpy surface. In order to build an efficient and reliable suspension system one needs to identify the state of loading in the robot. The research concentrated on the modelling of the levelling system maintaining a constant elevation of the robot chassis during travel on a bumpy terrain.

The simulations validated the structure of the control system adopted for levelling the robot chassis and showed the controller parameter values to be correct. The numerical results can be used to design and build the wheel suspension (with properly matched drives) for the wheel-legged robot being constructed.

Acknowledgments This research, carried out under project no. N N502 271037, was funded from the resources for science in Poland in the years 2009–2012.

References

1. Bałchanowski, J., Gronowicz, A.: Budowa i badania symulacyjne zawieszenia koła robota kołowo-kroczącego, XI International Science Conference of CAE, Szklarska Poręba, Poland, 2012.
2. Haug, E. J.: Computer Aided Kinematics and Dynamics of Mechanical Systems. Allyn and Bacon, Boston (1989)
3. Hołdanowicz, G.: PIAP Robots eyes combat role, Jane's International Defence Review, July 2008

4. Sperzyński, P., Szrek, J., Gronowicz, A.: Synteza geometryczna mechanizmu realizującego trajektorię prostoliniową odcelowaną. *Acta Mech. Automatica*. **4**, nr 2 (2010)
5. Tchoń, K., Mazur, A., Dulęba, I., Hossa, R., Muszyński, R.: *Manipulatory i Roboty Mobilne*. Akademicka Oficyna Wydawnicza, Warszawa (2000)
6. Wójtowicz, P., Szrek, J.: Idea of wheel-legged robot and its control system design. In: *Bulletin of the Polish Academy of Sciences. Technical Sciences*. vol. 58, nr 1 (2010)

Comparison of Alternative Equivalent Circuits of Induction Motor with Real Machine Data

J. Bradna, J. Bauer, S. Fligl and V. Hlinovsky

Abstract The algorithms based on separated control of the motor flux and torque is used in order to gain the maximum performance from the induction machine. To push the efficiency and dynamics limits of the IM to its limits mostly FOC or DTC control strategies are used. Both are based on the knowledge of the hardly measurable variable-machine flux. To obtain the information about inner machine flux models based on the machine equivalent circuit are mostly used. Therefore the accuracy of the equivalent circuits has direct influence on the accuracy of the machine control. To reduce the complexity of the mathematical model the resistances and inductances are concentrated to one component and three phase winding is assumed to be symmetrical. In order to design control strategy for the induction motor, system equations and equivalent circuit must be established at first. This paper examines and compares some of the issues of adequate machine modeling and attempts to provide a firmer basis for selection of an appropriate model and to confirm or disprove the equivalence of different approaches. The results of the IM model run up are then compared to the results obtained from the measurements on the real machine and the equivalency is discussed..

Keywords Induction motor • Equivalent circuit • IM model

J. Bradna · J. Bauer (✉) · S. Fligl · V. Hlinovsky
Czech Technical University in Prague, Faculty of Electrical Engineering,
Technicka 2, Prague 6, 166 27, Prague, Czech Republic
e-mail: bauerja2@fel.cvut.cz

J. Bradna
e-mail: bradnaj@fel.cvut.cz

S. Fligl
e-mail: xfligl@fel.cvut.cz

V. Hlinovsky
e-mail: hlinovsk@fel.cvut.cz

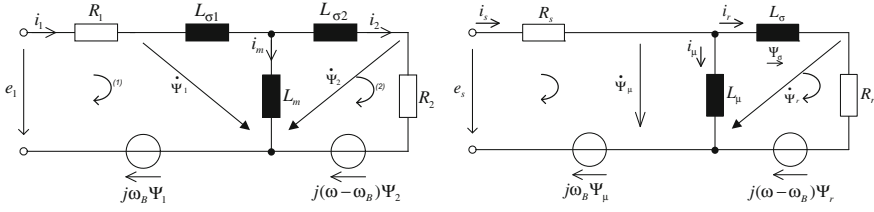


Fig. 1 Equivalent T-circuit of an IM Γ -circuit of the IM

1 Introduction

Induction machines (IM) are widely used as electro-mechanics changers in variable speed drives [1]. For describing the electromagnetic processes in induction machines different equivalent circuits can be used. To reduce the complexity of the mathematical model, resistances and inductances are represented as concentrated components and the 3-phase winding system is assumed to be symmetrical [2]. These equivalent circuits are also used as a starting point for the design of a drive controller [1]. Moreover for the function of a regulation algorithm of the drive or model of a machine, designed on the basis of the machine's equivalent circuit, the parameters of the equivalent circuit must be known with sufficient accuracy.

In IM drive controllers the representations based on an equivalent T-formed circuit are used, because they serve as a solid basis for an advanced motor control. However, other authors tend to use gamma models instead [3–5].

2 Equivalent Circuit in T-form

In the equivalent IM circuit in T-form (Fig. 1) can be established two Kirchhoff loops and (1), (2) for the derivation of the fluxes can be written

$$\dot{\underline{\Psi}}_1(t) - \underline{e}_1 + R_1 \dot{I}_1(t) + \omega_B j \underline{\Psi}_1(t) = 0 \quad (1)$$

$$-\dot{\underline{\Psi}}_2(t) + R_2 \dot{I}_2(t) + j \underline{\Psi}_2(t)(\omega - \omega_B) = 0, \quad (2)$$

where: $\underline{\Psi}_1$ —stator flux complex space vector, $\underline{\Psi}_2$ —rotor flux complex space vector, \underline{e} —supplying voltage complex space vector, ω_B —angular speed of the reference frame.

Then (1) and (2) can be rewritten in a standard vector form (3)

$$\dot{\underline{\Psi}}(t) = A_T \underline{\Psi}(t) + \underline{g}(t) \quad (3)$$

where \mathbf{A}_T is the state space matrix (4) and \mathbf{g} respects the influence of the supplying voltage.

$$\mathbf{A}_T = \begin{pmatrix} -\frac{R_1(L_m+L_{\sigma 2})}{c} & \omega_B & \frac{L_m R_1}{c} & 0 \\ -\omega_B & -\frac{R_1(L_m+L_{\sigma 2})}{c} & 0 & \frac{L_m R_1}{c} \\ \frac{L_m R_2}{c} & 0 & -\frac{R_2(L_m+L_{\sigma 1})}{c} & \omega_B - \omega \\ 0 & \frac{L_m R_2}{c} & \omega - \omega_B & -\frac{R_2(L_m+L_{\sigma 1})}{c} \end{pmatrix} \mathbf{g} = \begin{pmatrix} e_{1a}(t) \\ e_{1b}(t) \\ 0 \\ 0 \end{pmatrix} \quad (4)$$

where $c = L_{\sigma 1} + L_{\sigma 2} + L_m L_{\sigma 1} + L_m L_{\sigma 2}$

3 Equivalent Circuit in Γ -form

The Γ -equivalent circuit is second equivalent circuit used in electric drives. The advantage of this circuit is a simplification consisting in fusion of the rotor and stator inductances into one inductance on the rotor side without loss of information. The two loops for the stator resp. rotor flux (5) and (6) can be established too

$$\underline{\dot{\Psi}}_{\mu}(t) - e_s(t) + R_s \underline{i}_s(t) + \omega_B j \underline{\Psi}_{\mu}(t) = 0 \quad (5)$$

$$-\underline{\dot{\Psi}}_r(t) + R_r \underline{i}_r(t) + j \underline{\Psi}_r(t)(\omega - \omega_B) = 0 \quad (6)$$

where: \underline{i}_s —stator current complex space vector, \underline{i}_r —rotor current complex space vector, L_{σ} —leakage inductance, L_{μ} —magnetizing inductance. When we use similar labeling to that for a T-circuit (5), (6) can be rewritten into standard vector form (7) again.

$$\underline{\Psi}(t) = \mathbf{A}_{\Gamma} \Psi(t) + \mathbf{b}(t) \quad (7)$$

where \mathbf{A}_{Γ} is the system state space matrix.

$$\mathbf{A}_{\Gamma} = \begin{pmatrix} -\frac{R_s}{L_{\mu}} - \frac{R_s}{L_{\sigma}} & \omega_B & \frac{R_2}{L_{\sigma}} & 0 \\ -\omega_B & -\frac{R_s}{L_{\mu}} - \frac{R_s}{L_{\sigma}} & 0 & \frac{R_3}{L_{\sigma}} \\ \frac{R_r}{L_{\sigma}} & 0 & -\frac{R_r}{L_{\sigma}} & \omega_B - \omega \\ 0 & \frac{R_r}{L_{\sigma}} & \omega - \omega_B & -\frac{R_r}{L_{\sigma}} \end{pmatrix}; \mathbf{b} = \begin{pmatrix} e_{sa}(t) \\ e_{sb}(t) \\ 0 \\ 0 \end{pmatrix} \quad (8)$$

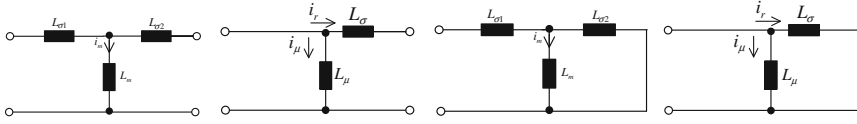


Fig. 2 Equivalency of the impedances

4 Recalculation Formulas Between T and G Circuit

We must express the recalculation relations between the variables in the circuits in order to compare them. Let us to follow the most widespread approach in text books—impedance equivalency and time constant comparison [2–3].

Firstly, let us suppose the input voltage and the stator resistance to be the same for both circuits. Secondly we can substitute the fluxes under the assumption that in a similar way as the fluxes the rotor currents have a certain recounting as follows:

$$e_s = e_1, R_s = R_1, i_s = i_1, i_r = \frac{L_m i_2}{L_m + L_{\sigma 1}} \quad (9)$$

Next we assume that inductance circuits have the same behaviour when the right-hand sides of the circuits are opened or short-circuited. From the principle of the superposition it then follows that for the opened right-hand side the same current will flow through the primary circuit (left-hand side) (10). The same behaviour shall be guaranteed in the case of the short-circuit on the right-hand side (11) Fig. 2.

For the impedance can be then written

$$Z_T = \omega j (L_m + L_{\sigma 1}), Z_{\Gamma} = \omega j L_{\mu} \Rightarrow L_{\mu} = L_m + L_{\sigma 1} \quad (10)$$

$$\begin{aligned} Z_T &= \omega j \left(L_{\sigma 1} + \frac{L_m L_{\sigma 2}}{L_m + L_{\sigma 2}} \right), Z_{\Gamma} = \frac{\omega j L_{\mu} L_{\sigma}}{L_{\mu} + L_{\sigma}} \Rightarrow L_{\sigma} \\ &= \left(\frac{L_{\sigma 1}}{L_m} + 1 \right) L_{\sigma 1} + \left(\frac{L_{\sigma 1}}{L_m} + 1 \right)^2 L_{\sigma 2} \end{aligned} \quad (11)$$

Finally, the very last assumption is the equality of the rotor and stator time constants: $T_1 = T_s$ and $T_2 = T_r$

The stator time constants can be expressed as (12). Because of (9) the equivalency is obvious.

$$T_1 = \frac{L_m + L_{\sigma 1}}{R_1}, T_s = \frac{L_{\mu}}{R_s} \quad (12)$$

In the case of the rotor time constant the situation is depicted in Fig 3. This can be described by (13).

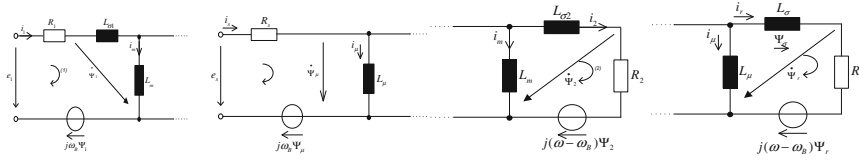


Fig. 3 Equivalency of the time constants

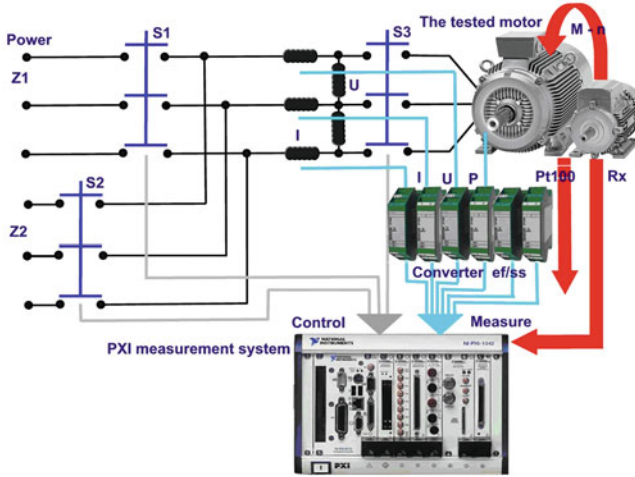


Fig. 4 System “OMEGA 2011”

$$T_2 = \frac{L_m + L_{\sigma 2}}{R_2}, T_r = \frac{L_\mu + L_\sigma}{R_r} \Rightarrow R_r = \frac{R_2(L_m + L_{\sigma 1})^2}{L_m^2} \quad (13)$$

5 Induction Motor Parameter Test Bed

Measuring system is based on components from National Instruments—PXI device. Whole system is managed by interactive programme “Omega 2011”, which was created in program Lab Windows CVI in language “C++”. Whole system is placed in chassis with eight positions, which protects system from disturbance and outer damage. The efficient power supply and fast data bus PCI are placed in the base unit for direct processing measured data in the memory of control computer (Fig. 4).

Nominal parameters of the IM are summarized in (Table 1), the parameters for the T-equivalent circuit calculated from the measurements are in (Table 2). These parameters were recalculated according to (10–13) to obtain the parameters for the

Table 1 Nominal values of the IM

Nominal values of the IM–R623 + 4 + Db + H02			
P_n (kW)	5,5	I_{In} (A)	11,8
f_n (Hz)	50	n_n (min ^{−1})	1430
U_{In} (V)	380	J (kg m ²)	0,14

Table 2 Equivalent circuit parameters

T-Circuit		Γ -Circuit	
R_1 (Ω)	3,300	R_S (Ω)	3,300
$L_{\sigma 1}$ (H)	0,026	R_R (Ω)	2,690
R_2 (Ω)	2,300	L_{σ} (H)	0,052
$L_{\sigma 2}$ (H)	0,200	L_{μ} (H)	0,3499
L_m (H)	0,3235		

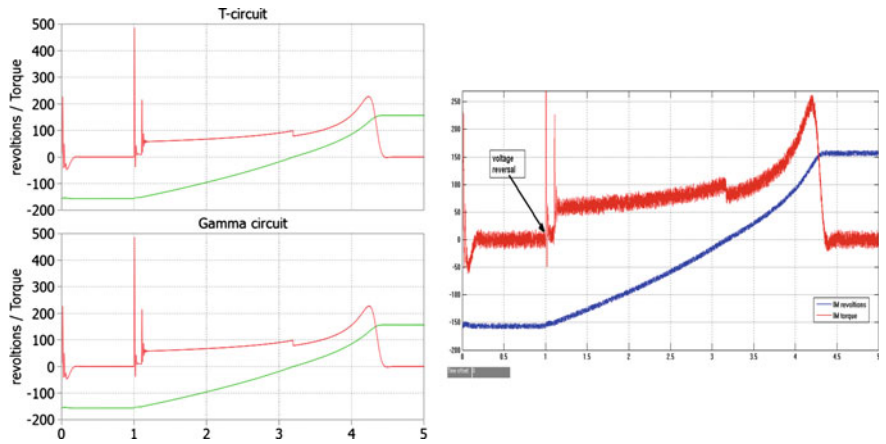


Fig. 5 Simulation results—IM reversal measured reversal of IM

Γ -circuit. Based on these parameters were established two models in Matlab/ Simulink.

The Fig. 5 (left) show the simulation of reversal of the IM from negative nominal speed to positive. Figure 5 (right) shows measured results by system Omega 2011.

6 Conclusions

Simulation results show that both equivalent circuits are equal. Also the recal-culation equations for transformation from T-circuit to Γ -circuit are correct. This is proof for the full equivalence of both circuits. However, size adjustment for rotor state variables must be undertaken if those are to be exchanged directly between

the Gamma and the T model running in parallel. Also measured and simulated reversal of the IM show same behavior of IM and same variable scales.

Acknowledgments the research was supported by the Grant Agency of the Czech Technical University, Prague, grant No. SGS11/119/OHK3/2T/13.

References

1. D.W. Novotny and T.A. Lipo, *Vector Control and Dynamics of AC Drive*, 1.edn. Oxford, Oxford University Press, 1996.
2. Fitzgerald, A E., Kingsley, Ch, Jr., Umans, S.D.: “Electric machinery,” McGraw-Hill Book Company, Japan, ISBN 0-07-066286-X (1983)
3. Barnes, M.L., Gross, C.A., Comparison of induction machine equivalent circuit models, in system theory, Proceedings of the twenty-seventh southeastern symposium on, 1995, pp. 14–17 (1995)
4. Boglietti, A., Cavagnino, A., Ferraris, L., Lazzari, M.: Induction motor equivalent circuit including the stray load losses in the machine power balance, in Industrial electronics society. IECON 2007. 33rd annual conference of the IEEE, 2007, pp. 1250–1255 (2007)
5. Ergene, L.T., Salon, S.J.: Determining the equivalent circuit parameters of canned solid-rotor induction motors, *Magnetics, IEEE Trans*, **41**(7), 2281–2286 (2005)

Band Mechanism with Nonlinear Gear Ratio for Gravity Force Balance: Design and Analysis in Total System Network

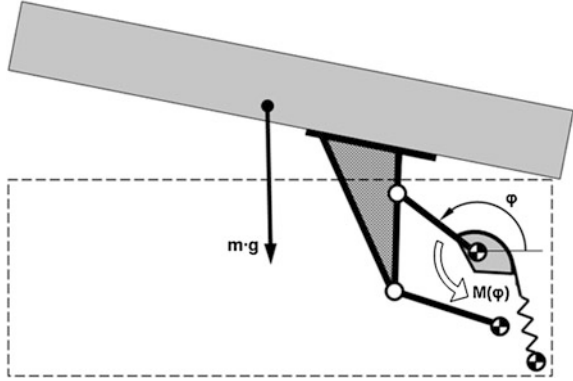
F. Ebert and M. Berger

Abstract The application of band mechanisms offers a wide range of possibilities in designing concepts of modern guide mechanisms. The applied belt pulleys are designed as continuous convex cam disks and allow the application of different transmission functions. A large number of transmission functions can be generated with convex curve shapes. It takes a great deal of effort to determine the correct pulley curve and is difficult for engineers without special knowledge to calculate. The syntheses process of a nonlinear band mechanism is based on the relationships between the evolute and involute [1]. The evolute corresponds to the pulley curve and the involute corresponds, for example, to the curve of the fix point of a rocker arm. By applying this method in relation with the reverse kinematics and the maintenance of total band length, allowing to generate band mechanism with required curve of transmission ratio. Beside the comments of band mechanism construction and the mathematical method of resolution—the first part of the article explains a simple four bar mechanism of couch chest the total gravity force balance with band mechanism. Therefore, the essential computing steps and limits of the solving process will be explained. With this it is possible to calculate the nonlinear transmission ratio of band mechanism with consideration of elastic band properties and inertia of bodies.

Keywords Band mechanism • Reverse kinematics • Nonlinear transmission ratio • System network

F. Ebert (✉) · M. Berger
Technical University, Chemnitz, Germany
e-mail: falk.ebert@mb.tu-chemnitz.de

Fig. 1 Nonlinear four bar mechanism with band mechanism to balance couch mattress in every demand opening position



1 Introduction

This paper concerns the calculation for a gravity balance mechanism with simple designed nonlinear band structure “Rotate Band Spring Rotate”. Gravity force balance allows only compensating the static Forces. Figure 1 shows a couch mechanism with four bar linkage to lead the mattress in required positions. The demand balance torque on the upper lever arm can easily be calculated by a multi body system.

2 Synthesis of Band Mechanism

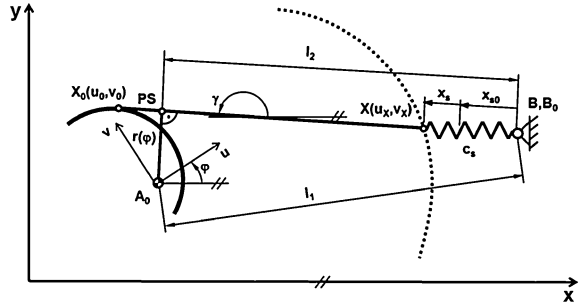
2.1 Effective Lever Arm for Transmission Function

This chapter shows the kinematical design of a simple band mechanism consisting of a variable band drum with an elastic band and a chassis mounted spring, Fig. 1. For a total force balance, the spring force on the effective lever arm must keep in equilibrium with the static linkage torque in every angle position. The free design parameters for the band mechanism are the spring stiffness c_s the preload x_{s0} and requested function of the effective lever arm $r(\varphi)$. Equation (1) describes the differential function of this mechanical problem with one inertial condition (2). This formula can only be solved by iterative steps.

$$M(\varphi) = r(\varphi)c_s \left(x_{s0} + \int_{\varphi_0}^{\varphi} \sqrt{r(\varphi)^2 + r'(\varphi)^2} d\varphi \right) \quad (1)$$

$$r_0(\varphi_0) = \frac{M(\varphi_0)}{c_s \cdot x_{s0}} \quad (2)$$

Fig. 2 Kinematics for band structure: rotate band spring rotate



2.2 Kinematics for Rotate Band Spring Rotate Structures

After the computation of the effective lever arm function $r(\varphi)$ and the definition of the mounting points A_0 and B_0 the evolvente curve can be determined with the following calculating procedure (compare Fig. 2):

$$H_1 = B_{0x} - A_{0x} \quad (3)$$

$$H_2 = B_{0y} - A_{0y} \quad (4)$$

$$H_3 = H_1^2 + H_2^2 \quad (5)$$

$$l_1 = \sqrt{H_1^2 + H_2^2} \text{ (Chassis distance between } A_0 \text{ and } B_0) \quad (6)$$

$$l_2(\varphi) = \sqrt{l_1^2 - r(\varphi)^2} \text{ (Distance between Points } PS \text{ and } B_0) \quad (7)$$

$$H_4(\varphi) = l_1^2 - l_2(\varphi)^2 + H_3 \quad (8)$$

$$H_5(\varphi) = K \sqrt{4H_3 r(\varphi) - H_4(\varphi)} \quad (9)$$

The variables H_1 to H_7 are equivalent to the regularly of DDD double link module for linkage calculation of VDI 2729. It computes the brake-even point of two cycles.

Parameter K describes the position of point PS on the rectilinear connection of point A_0 to B_0 . If the parameter $K = +1$ the point PS is placed left from $\overline{A_0 B_0}$ and if $K = -1$ the geometric solution of the point is placed right.

$$H_6(\varphi) = \frac{H_1 H_4(\varphi) - H_2 H_5(\varphi)}{2H_3} \quad (10)$$

$$H_7(\varphi) = \frac{H_2 H_4(\varphi) - H_1 H_5(\varphi)}{2H_3} \quad (11)$$

$$PS_x(\varphi) = A_{0x} + H_6(\varphi) \quad (12)$$

$$PS_y(\varphi) = A_{0y} + H_7(\varphi) \quad (13)$$

By means of the band angle $\gamma(\varphi)$ (14) the Eqs. (15) and (16) show the coordinates of the band/spring fixation point P . This point is also the moving point for the development the evolvente.

$$\gamma(\varphi) = \arctan \frac{H_7(\varphi) - H_2}{H_6(\varphi) - H_1} \quad (14)$$

$$P_x(\varphi) = B_{0x} + x_s(\varphi) \cos(\gamma(\varphi)) \quad (15)$$

$$P_y(\varphi) = B_{0y} + x_s(\varphi) \sin(\gamma(\varphi)) \quad (16)$$

The reverse kinematics of point P follows from the coordinate transformation. In (17) and (18) point P will turn back with $-\varphi$ on axis A_0 and create the evolvente in this way.

$$u_x(\varphi) = (P_x - A_{0x}) \cos(-\varphi) - (P_y - A_{0y}) \sin(-\varphi) \quad (17)$$

$$v_x(\varphi) = (P_x - A_{0x}) \sin(-\varphi) + (P_y - A_{0y}) \cos(-\varphi) \quad (18)$$

2.3 Relationship Between Evolvente and Eevolute Curve

As shown in Fig. 3 the band curve is equal with the evolute and the evolvente is the curve of a fix point of the band. The calculation of the band curve follows the differential equations (19) and (20) [4]. The variables x' , y' and x'' , y'' are angle derivatives of a function.

$$u_0(\varphi) = u_x(\varphi) - v_x'(\varphi) \cdot \frac{u_x'(\varphi)^2 + v_x'(\varphi)^2}{u_x'(\varphi) \cdot v_x''(\varphi) - v_x'(\varphi) \cdot u_x''(\varphi)} \quad (19)$$

$$v_0(\varphi) = v_x(\varphi) + u_x'(\varphi) \cdot \frac{u_x'(\varphi)^2 + v_x'(\varphi)^2}{u_x'(\varphi) \cdot v_x''(\varphi) - v_x'(\varphi) \cdot u_x''(\varphi)} \quad (20)$$

3 System Simulation

Figure 4 shows the recalculation of a complete balance mechanism with nonlinear curve drum on the linkage crank arm in ITI SimulationX. Simple bidirectional working connections and interfaces allow to model and solve complex dynamic

Fig. 3 Condition between the evolvente and the evolute for simple band mechanism [4]

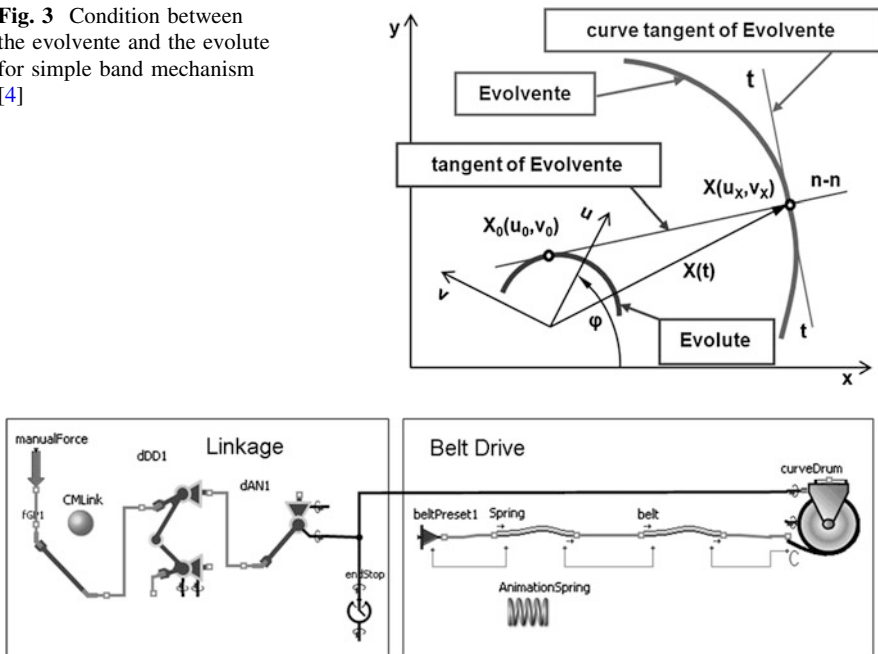


Fig. 4 Model of complete recalculation of gravity balance mechanism with linkage gear in SimulationX [4]

systems with many physical domains like 1D, 2D or 3D mechanics or pneumatics, hydraulics and controls.

The working principle of the new developed belt drive and linkage library is written on user manual of SimulationX and is also published [2, 3].

4 Conclusions

Due to the beneficial properties of band mechanisms, like low weight, fewer components and variable design of transmission ratio band mechanism are adequate solutions for static force balance systems. This article shows the computing steps of synthesis for a “Rotate Band Spring Rotate” mechanism. The calculation starts with the analysis of the effective lever and ends after the derivation of specific band mechanism kinematics with the computation of the nonlinear band curve. In conclusion, the dynamic behavior of the complete system, consisting of nonlinear linkage gear and belt drive, can be easily simulated by the new belt drive and linkage library in SimulationX.

References

1. Lovasz, E. C.: Synthese der Übertragungsgetriebe mit Anwendung in der Feinmechanik. Dissertation, Dresden (1989)
2. Berger, M., Ebert, F.: Effiziente Werkzeuge zur ganzheitlichen Systemsimulation komplexer nichtlinearer Antriebssysteme mit Koppel- und Bandgetrieben, VVD 20112, Selbstverlag der Technischen Universität Dresden, 99 (2012)
3. Ebert, F., Berger, M.: Ganzheitliche Systemsimulation komplexer Antriebssysteme mit nichtlinearer Charakteristik, 9. Kolloquium Getriebetechnik, Chemnitz (2011)
4. Ebert, F.; Berger, M., Rodionow, P.; Schreiber, U.: Development of a library to analysis belt drives on SimulationX, 12. ITI Symposium, Dresden (2009)

Application of the Research Environment e-Kinematix in Mechanism Development

G. Lonij, B. Corves, M. Reeßing and M. Razum

Abstract Research and development (R&D) projects require a structured approach for the creation of sound results. Particularly, complex problems benefit from information and data management and clear organizational structures to increase process efficiency. With the creation of a virtual research environment to organize, enhance, link and publish data, the cooperation between project partners, documentation and re-use of research and development results are supported. The aim of the e-Kinematix Project has been the creation of such a virtual research environment for the research and development of mechanisms.

Keywords R&D process • Web based support tools • Interactive design

G. Lonij (✉) · B. Corves
RWTH Aachen University, Aachen, Germany
e-mail: lonij@igm.rwth-aachen.de

B. Corves
e-mail: corves@igm.rwth-aachen.de

M. Reeßing
Ilmenau University of Technology, Ilmenau, Germany
e-mail: michael.reessing@tu-ilmenau.de

M. Razum
FIZ Karlsruhe, Karlsruhe, Germany
e-mail: matthias.razum@fiz-karlsruhe.de

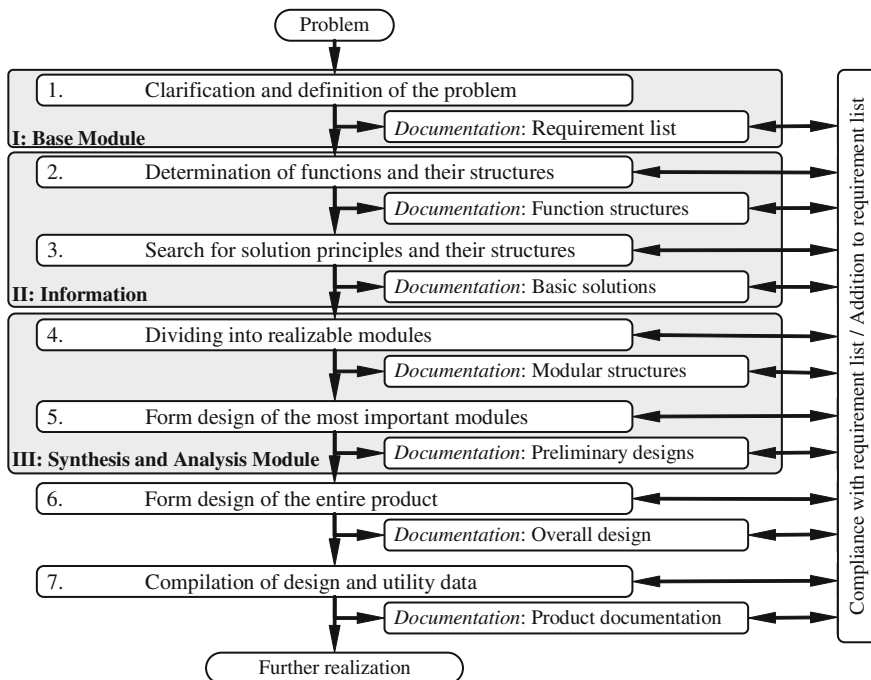


Fig. 1 R&D Process structure and underlying e-Kinematix Research environment modules

1 Introduction

The e-Kinematix research environment is based on a modular architecture using the e-Research environment eSciDoc [1], the mechanism and gear library DMG-Lib [2] and the application Gecko [3]. The combination establishes an integral instrument for the support of mechanism research and development. For this purpose technologies are provided for project organization, execution and documentation. Individual modules have been created for the administration, inquiry, synthesis and analysis.

To increase acceptance of the e-Research environment, the optional use of modules does not cause limitations or increased effort for the user. In addition, the modules resemble a typical R&D process [4, 5] shown in Fig. 1. The aim of this process structure is to help systemize and plan the R&D process without restricting the creative freedom during its execution. A key issue within the process is a continuous documentation.

Within the process as a whole and each individual step the following activities are performed numerous times in succession.

- gathering information
- solving problems
- analyzing results

- evaluating solutions.

Each activity produces data based on prior steps [6]. Only organizing, enhancing and linking the data lead to verifiable results and the continuity of the documentation.

2 Modules

The base module (I, Fig. 1), formed by the open source eSciDoc infrastructure, provides features for project, user, access, data and document management. Using a loosely coupled set of services, data and accompanying xml files for metadata are stored in a Fedora commons repository [1]. To avoid restricting the type of data, which can be stored in the repository, only a few basic types of objects such as items (actual data or documents), containers (collection of items), context (root of project structure), organizational units (human resources) and content models (definition of contents for container and items) are defined to manage the data.

The information module (II, Fig. 1) provides access to numerous sources of information, particularly the digital mechanism and gear library DMG-Lib, in which digital versions of books, images, models, drawings etc. pertaining to mechanism theory are gathered, preserved, systemized and appropriately presented. In addition several web based search engines are referenced inside the information module in order to preserve search queries, results and data, which can be saved for future use.

The analysis and synthesis module (III, Fig. 1) are combined into the application Gecko providing interactive design capabilities to quickly create and analyze mechanism models. The application is built up around a 3D Open-GL design view, in which simple elements such as points, lines, circles, planes and spheres can be created to form mechanical models. The elements are defined by geometric constraints and are updated constantly in order to adapt the model to changes automatically. To enable fast creation of models the level of detail is kept relatively low. In addition, the import of existing model files into the new model allows the creation of a catalogue, containing re-usable standard models for instance regarding synthesis procedures.

The base and information module are web based whereas the analysis-synthesis module is an application or fat client [7]. The communication between the modules is also based using HTML get and post requests. To incorporate the base and information module in the application a browser is included in its user interface.

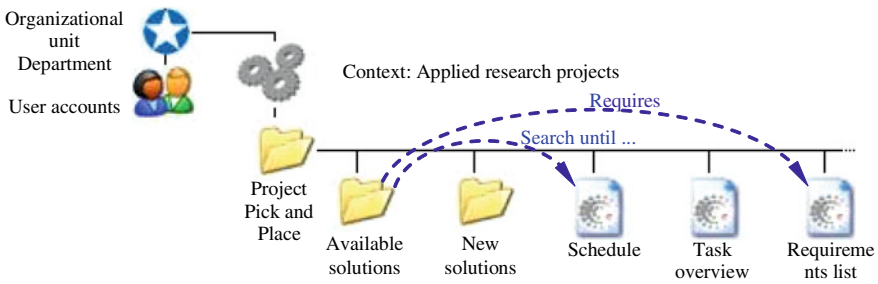


Fig. 2 Use of base module in project organization

3 Use Case

The R&D process steps and the use of the research environment to execute these will be described with the aid of a use case, in particular a repeating pick and place operation.

In step 1 of the R&D process (Fig. 1), details about the operation e.g. weight of the transported object, desired motion etc. are gathered. This results in technical requirements and an overview of tasks concerning unresolved questions, which form the foundation for the project definition. Using the base module, container objects are created inside a context for a project folder and task folders Fig. 2.

Depending on the task overview and available human resources, either from a preexisting organizational unit or newly created users, the project planning as well as user rights and access are defined. Metadata with regard to creator and submission date are automatically generated. The Project folder contains the item objects for documentation regarding the technical requirement list and the task overview, which are linked to folders to define references.

The first task defined in the overview (Fig. 2), the search for available solutions, leads to the steps 2 and 3 in the R&D process (II, Fig. 1). Initially, the search carried out with the information module is focused on the complete pick and place operation and leads to robotic, pneumatic and cam driven systems. Technical requirements are used to evaluate the available solutions, Fig. 3.

The overall result of the search is documented using the evaluations in a separate document. Summarized, the robotic and pneumatic solutions offer high flexibility at the expense of high complexity and high costs. Cam systems are less flexible but allow high speed and accuracy at moderate costs. The technical requirements regarding flexibility or speed of the available systems exceed the demands for the current pick and place operation and warrant the creation of a new simpler solution. By splitting the pick and place operation into moving the object and gripping it, solutions can be found more efficiently. From the search for available solutions' information regarding the gripping function it is clear that creating a new solution is not required and the vacuum technology mainly applied in the pneumatic systems is adequate. Finding a new solution is therefore only

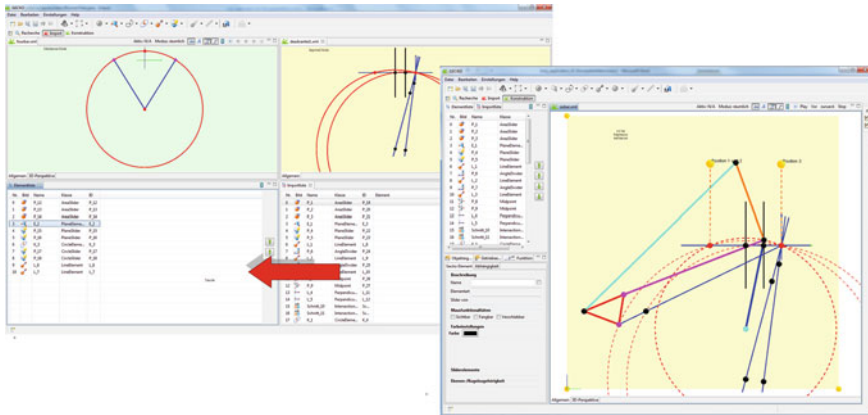


Fig. 5 Gecko **a** import view showing dead center synthesis, **b** six bar Stephenson mechanism

The application of the synthesis procedures to find the kinematic dimensions of the mechanism is realized in steps 4 and 5 of the R&D process using the analysis and synthesis module of the research environment or rather the application Gecko. Two mechanism models are created. A four bar crank rocker mechanism and a six bar Stephenson mechanism. In both models an existing model file containing the dead centre synthesis procedure is imported, Fig. 5a.

The kinematic parameters of the four bar crank rocker mechanism are completed with this procedure, the six bar Stephenson mechanism requires two more parameters which result from an imported position synthesis procedure, Fig. 5b.

The mechanism models show that the six bar Stephenson mechanism is best suited for the pick and place operation due to its adjustability of the orientation of the coupler the gripper system is attached to. To further finalize the mechanism a professional 3D CAD system will be used.

4 Conclusions

Using the e-Kinematix virtual research environment, research and development engineers are supported in tasks regarding project, user, access, data and document management. In addition it offers web based tools and application support. Current development of the research environment is aimed at viewing analysis results in interactive diagrams, which adapt to changes in the mechanism view. In addition efforts regarding automatic metadata creation are conceived to enhance re-use of the mechanism models in future projects.

References

1. Razum, M., Schwichtenberg, F., Wagner, S., Hoppe, M.: eSciDoc infrastructure: a fedora-based e-research framework. *Research and Advanced Technology for Digital Libraries ECDL*, pp. 227–238. Springer, Berlin (2009)
2. Corves, B., Kloppenburg, J., Modler, K.H., Brix, T.: Methodical design using DMG-Lib, X. *International Conference on the Theory of Machines and Mechanisms*, Liberec: Technical University, Department of Textiles Machines Design, (2008)
3. Lonij, G., Hüsing, M., Choi, S.W., Corves, B.: Development of a spherical linkage mechanism with the aid of the dynamic spatial geometry program GECKO. *Proceedings of the 2nd European Conference on Mechanism Science*. Springer, Berlin (2009)
4. VDI Guideline 2221: Systematic approach to the development and design of technical systems and products. Beuth, Berlin (1993)
5. VDI Guideline 2223: Systematic embodiment design of technical products. Beuth, Berlin (2004)
6. Pahl, G., Beitz, W., Feldhusen, J., Grote, K.H.: *Konstruktionslehre*. (2003)
7. McAffer, J., Lemieux, J.-M.: *Eclipse Rich Client*, Pearson Education Inc., New Jersey (2005)
8. VDI Guideline 2727: Mechanisms for motion transfer; fundamentals, Catalogues for machine design. Beuth, Berlin (1991)
9. Kerle, H., Corves, B., Hüsing, M.: *Getriebetechnik*. Wiesbaden, Vieweg Teubner (2011)

Advanced Digitization Techniques in Retrieval of Mechanism and Machine Science Resources

E-Ch. Lovasz, C. M. Gruescu, V. Ciupe, I. Carabas, D. Margineanu,
I. Maniu and N. Dehelean

Abstract The European project thinkMOTION works on the purpose of retrieving all-times content regarding mechanisms and machine science by means of creating a digital library, accessible to a broad public through the portal Europeana. DMG-Lib is intended to display the development in the field, from its very beginning up to now days. There is a large range of significant objects available, physically very heterogeneous and needing all to be digitized. The paper presents the workflow, the equipments and specific techniques used in digitization of documents featuring very different characteristics (size, texture, color, degree of preservation, resolution and so on). Once the workflow established on very detailed steps, the development of the workstation is treated. Special equipments designed and assembled at Universitatea “Politehnica” Timisoara are presented. A large series of software applications, including original programs, work for digitization itself, processing of images,

E-Ch.Lovasz (✉) · C. M. Gruescu · V. Ciupe · I. Carabas · D. Margineanu
I. Maniu · N. Dehelean
Universitatea “Politehnica” din Timisoara, Timisoara, Romania
e-mail: erwin.lovasz@mec.upt.ro

C. M. Gruescu
e-mail: corina.gruescu@mec.upt.ro

V. Ciupe
e-mail: valentin.ciupe@mec.upt.ro

I. Carabas
e-mail: iosif.carabas@mec.upt.ro

D. Margineanu
e-mail: dan.margineanu@mec.upt.ro

I. Maniu
e-mail: inocentiu.maniu@mec.upt.ro

N. Dehelean
e-mail: nicolae.dehelean@mec.upt.ro

management of files, automatic optoelectronic control of capture, storage of information in different stages of processing. An illustrating example is explained, showing the steps followed in order to obtain a clear, high-resolution image from an old original document (very valuable as a historical proof but very poor in quality regarding clarity, contrast and resolution).

Keywords Development of Mechanism Science • Digitization • Advanced image processing

1 Introduction

The European project thinkMOTION [1] is intended to offer knowledge in the field of mechanisms and machine science through the portal Europeana [2] on a specialized site called DMG-Lib [3]—Fig. 1. DMG-Lib is a digital library, which provides content originating from a large range of sources (universities, technical libraries, museums, patent offices, individual owners etc.).

The content posted on DMG-Lib presents information in more categories: books, articles, proceedings, Ph.D thesis, contributions, journals, reports, biographies, images, interactive animations, software and so on. One of the main goals of the project is the retrieval of mechanism science in its history [4–7]. Almost all content before 1990 exists in analogue form, written, printed or drawn on paper support. Getting back and gathering national historical treasures in a well-organized collection requires digitization of a large amount of documents. The digital library offers a novel way of describing the history of development in mechanism science field, from antiquity up to now-days.

The partners in the project are Ilmenau University of Technology (Germany), University of Basque Country (Spain), University “Politehnica” of Timisoara (Romania), RWTH Aachen University (Germany), French Institute of Advanced Mechanics (France) and University of Cassino (Italy). The partners put together content from national sources and from providers in the neighborhood areas, willing to collaborate. No matter what the original source is, it requires digitization and preparation of high-quality web-compliant files to be posted online.

2 Workflow

Digitization of heterogeneous support-type documents at high quality of online items is resource consuming from both technical and duration point of view.

The processing of an item starting with an analogue document and ending up to having a high-quality online information was planned to follow the workflow presented in Fig. 2.

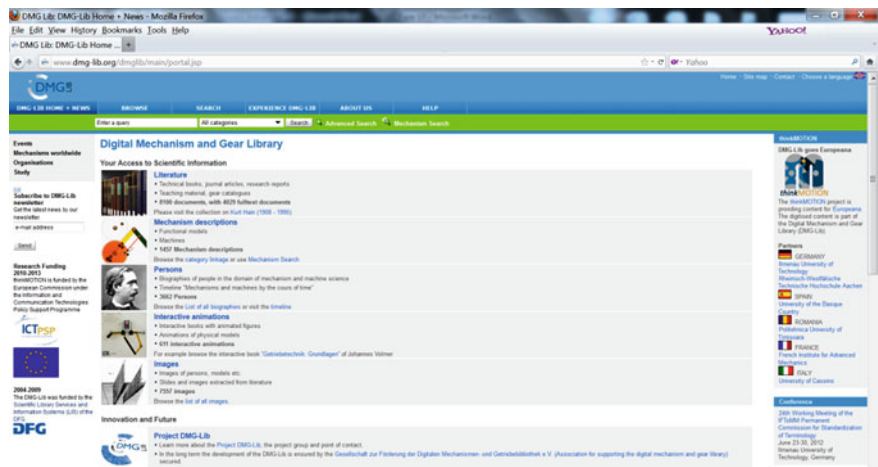


Fig. 1 The web-site of DMG-Lib

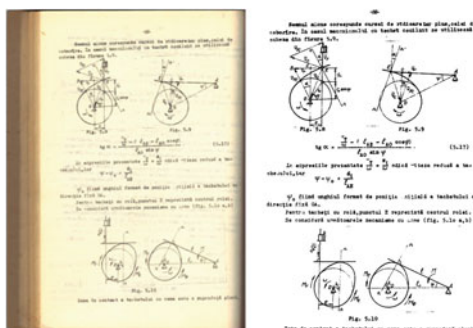


Fig. 2 Workflow of the digitization process

- The workflow consists of the following steps:
- locating of potential content providers, having the rights of use granted by the owner of intellectual property and getting the physical support carrying content
 - performing the primary digitization by means of specially designed equipment, in order to obtain raw scanned images of the original document
 - processing the raw images with appropriate software so that the quality of images matches an imposed standard and the final files are web-compliant
 - posting the items online.

Figure 3 illustrates the input and the output of digitization, quality improvement and web-compliant conversion.

Fig. 3 Raw scanned image of a page book (*left*) and its final digitized look online (*right*)



Physical support carrying content is very heterogeneous regarding dimensions, degree of preservation, resolution, clarity etc. The equipment which achieves the primary digitization (scanning) should be very adaptable, as scanning is necessary for single sheets, mid thickness journals, very thick books, which feature very different dimensions, flatness degree, background and foreground color, texture etc.

The equipment assembled at the University “Politehnica” Timisoara was designed considering the following requirements:

- capacity to scan any type of source document without damaging in any way the original paper (bending, folding, scratching, heating etc.). This totally non-destructive feature is very important especially for old documents, with fragile pages, which exist in a small number of copies or even may be one of a kind
- maximum scanning area $\sim 400 \times 260$ mm (standard A4 plus a safety range of 50 mm extension on each edge)
- high degree of similarity of the scanned copy in respect with the original document and high optical resolution (at 300 dpi, at least) [8, 9]
- high speed scanning. The large amount of analogue documents imposes a high-speed work. The equipment delivers up to 600 copies per hour
- software facilities regarding management of image taking process, stocking of digital copies and insurance of compatibility with advanced processing programs
- the mechanical design must ensure flatness of active surfaces, quick placement and removal of the original document, mechanical raw focusing facilities, adjustment regarding the thickness of the original document.

Figure 4 presents an overview of the equipment used for scanning at the University “Politehnica” Timisoara.

Raw images got by scanning require professional processing, which take a lot of operations:

- splitting of pages (Fig. 5)
- deskew of pages (Fig. 6)
- selection of content (Fig. 7)

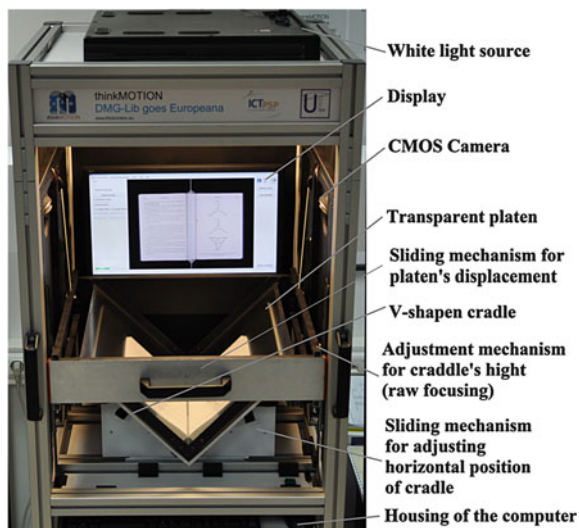
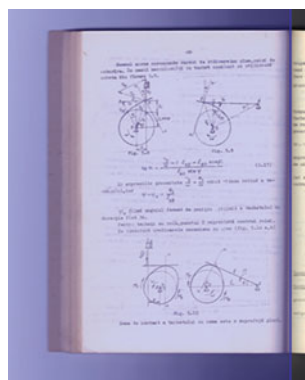


Fig. 4 Scanning equipment developed at the University “Politehnica” Timisoara

Fig. 5 Splitting of pages



- setting margins of page (Fig. 8)
- despeckling and setting color mode (color/gray scale/black and white) and setting final resolution.

All processing operations, briefly defined above were performed using the software Scan Tailor [10].

The images in graphic format require processing for conversion to searchable PDF files. Multi-page searchable PDF files were got by means of software Abbyy Fine Reader [11]. The image of a page posted online was presented in Fig. 1 (right). Software used for the management of image taking process, the stocking of digital copies and the assurance of compatibility with further advanced processing programs were developed by members of the thinkMOTION team of Timisoara.

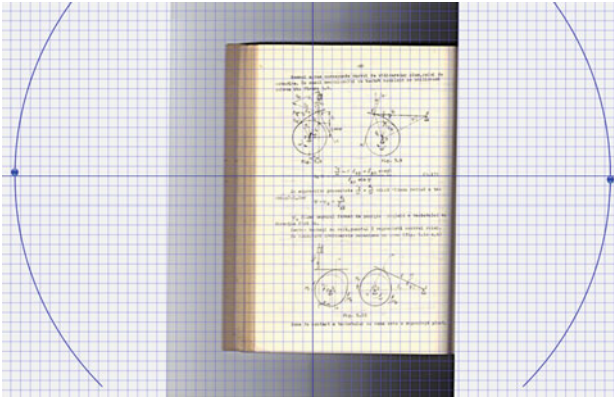


Fig. 6 Deskew of the page

Fig. 7 Selection of content

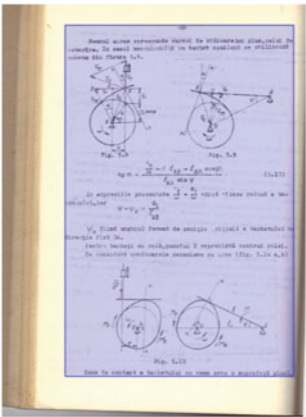
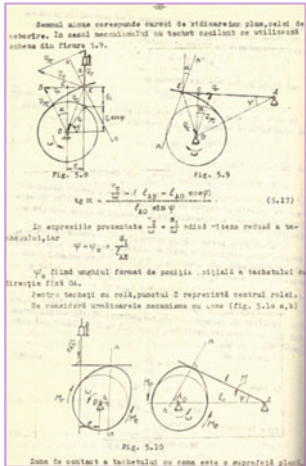


Fig. 8 Setting margins of page



3 Conclusions

Digitization of analogue documents requires special resources regarding equipment and software. The team from the University “Politehnica” Timisoara, as partner in the thinkMOTION project, developed a workstation specialized in digitization of all-type documents. Design and assembling of the scanning equipment as well as the capturing, stocking and managing raw image files software were developed as original contributions of the team. Thousands of high quality pages are now available online for a large range of users (academic staff, students, Ph.D. students, engineers, historians etc.). Digitization techniques are used on the purpose of retrieving the history of mechanism science and of creating a coherent description of its development since early ages until present days.

Acknowledgments The work reported here was made possible through the project thinkMOTION, which is funded under the Information and Communication Technologies Policy Support Programme, CIP ICT PSP 2009 2.3—Digital Libraries: European Digital Library Digitizing content for Europeana.

References

1. <http://www.thinkmotion.eu/>
2. <http://www.europeana.eu/portal/>
3. <http://www.dmg-lib.org/dmglib/main/portal.jsp>
4. Döring, U., Brecht, R., Brix, T.: thinkMOTION—DMG-Lib Goes Europeana. Mech., Transm. Appl. p. 37, Springer, Heidelberg (2011)
5. Kerle, H., Mauersberger, K., Ceccarelli, M.: Some Historical Remarks on Past Model Collections of Machines and Mechanisms in Europe, 13th world congress in mechanism and machine science, Guanajuato, México (2011)
6. Brix, T., Döring U., Reeßing, M.: Creating present-day solutions from historical knowledge, 13th World congress in mechanism and machine science, Guanajuato, México (2011)
7. Brecht, R., Henkel, V.: thinkMOTION: DMG-Lib goes Europeana—Portal für Europas Ingenieurwissen, Universität Ilmenau (UNI). Jahrgang **54**(1):34–35 (2011)
8. Smith, W. J.: Modern optical engineering, MacGraw Hill, New York, (1995)
9. Luther, A., Inglis, A.: Video Engineering, 3rd edn. McGraw-Hill, New York (1999)
10. <http://scantailor.sourceforge.net>
11. <http://www.abbyy.ro>

Trends in Development of Positioning Mechanisms

F. Palčák

Abstract The role and position of analysis and synthesis of mechanisms in the current education and research. Task categories in the synthesis of mechanisms depending on the mission that mechanisms perform. The historical transition from scalar, vector, matrix, and quaternion formalism to the subgroup formalism. Application of the objective laws derived from development of technical systems in the case of development of positioning mechanisms. The parameterization, optimization and robust design. The evolution of technical systems by balancing of two opposite contradictory directions.

Keywords Analysis • Synthesis • Positioning mechanisms • Evolution

1 Introduction

In today's multi-disciplinary product development the industry expects from graduates the knowledge from diverse areas. Contradictory they are forced to do more in less time, therefore it is worth to search procedures how manage the growing demands in spite of restricted physical and mental capabilities. The paper will point to the potential of new approach for improving existing and invent new positioning mechanisms by transition from existing local deterministic methods to the systematic global creative methods.

F. Palčák (✉)

Slovak University of Technology of Bratislava, Bratislava, Slovakia

e-mail: frantisek.palcak@stuba.sk

2 The Role and Position of Analysis and Synthesis of Mechanisms in the Current Education and Research

The lower levels of classification of learning objectives within education and research (knowledge, comprehension and application) help us learn to replicate what has already been done elsewhere, while the higher levels (analysis, synthesis and evaluation) drive innovation [1].

In teaching and also in the research of mechanisms performance, the methods of analysis predominates within universities of technology. It has its justification in terms of the need to build the knowledge base as well as in the historical background, because the analysis is the starting point for synthesis. Methods of analysis are algorithmizable what was of a great advantage for the extensive development of computer support in comparison with the methods of synthesis.

In generally, the synthesis is compilation of information together in a different way by combining elements in a new pattern or proposing alternative solutions. The synthesis of mechanisms in development of new products for the industry has much more important mission than analysis. The goal of topology synthesis is to identify the optimum number and connectivity of structural elements to achieve specified motion requirements. Therefore the topology synthesis is a critical stage of the design process, due to the fact that the main performance of a complex system is determined by its structure configuration. Dimensional synthesis finalizes the design so that the mechanism satisfies the given specifications and with optimum performance such as energy efficiency [2].

A great variety of mechanisms are used in machines and devices. Even though these applications are quite different, all mechanisms can be classified into three task categories depending on the mission that mechanisms perform: Function generation (positioning of output link local coordination system-LCS axes), Path generation (positioning of output link LCS origin), and Motion generation (positioning of output link LCS origin and axes, too. It is simultaneous combination of positioning of output link LCS origin and orientation of output link LCS).

Development of mathematical formalism in mechanics is associated with the increasing complexity of an inspected object. In describing the motion of objects (point, body, system of bodies) the hierarchy of complexity graduates: motion of a point (along straight line, curve in the plane, in space), translational motion of a body (straightforward, curvilinear), rotational motion of a body, general body motion in plane (the method of Cauchy, Poisson), the simultaneous motions of bodies (resulting, carrying, local relative), spherical motion (Euler method, Cardan,...), and spatial motion of the body (method of Cauchy, Poisson), (method of Mozzi, Chasles).

From the algebraic equations with scalar quantities, sufficient to study the static properties, it was necessary to transit to the vector algebra for planar tasks, and to the matrix calculus for spatial tasks while studying the movement of bodies. For description of the inertial properties of bodies the tensors are used, and for

nonsingular description of position of spherical body motion the quaternions appear as suitable formalism.

In the methods of synthesis of new topology for parallel mechanisms that have practical use, as a suitable formalism were used Lie subgroup of the displacement Lie group [3].

To achieve high computational efficiency of numerical methods (speed, convergence, accuracy) it was necessary to convert complex mixed system of differential equations of motion and binding algebraic equations (DAE), which represent the mathematical model of the mechatronic product (MBS), to the more numerically stable system of ordinary differential equations (ODE). But solving (ODE) requires expensive evaluations of Jacobean, therefore it was more suitable to convert (ODE) to the system of nonlinear algebraic equations (NAE). In order to employ the fastest numerical methods (Calahan) it was necessary linearize (NAE) by the Newton–Raphson approximation using Taylor series to a system of linear algebraic equations (LAE) [4].

3 The Parameterization, Optimization and Robust Design

Trial and error approach has its place only if the solution does not require a lot of combinations, so a compromise is often the way to an agreement with opposing requirements.

Optimization of parameterized models with the estimated range of tolerances is only the application of more advanced form of compromise in the development of new products. Nature, which is and remains a model for us, reminds us that the optimization of the properties of its elements is not its aim. The random changes in the intrinsic properties and external influences, which were used as starting point for the optimization, may cause the failure of optimized element.

Robust design based on techniques of Monte Carlo methods can be achieved when the designer understands the potential sources of random changes and take steps to numb the product to fulfill its mission even if these changes occur [5].

The complexity and engineering seem at odds: complex systems are about adaptation, whereas engineering is about purpose. However, it is robustness and failure where both camps merge [6].

4 Directions of Evolution of Technical Systems

The paper Psychology of innovative technology, [7] was the first step in creating TRIZ, the new science dedicated for study of evolution of technical systems with new instruments derived from idea of mutual interaction of nature, human and technology.

Laws of evolution of technical systems belong to the most important, informational instruments of TRIZ. The main idea of TRIZ refers to the observation that our world evolves according to objective laws, which can be explored and implemented in practice [8].

Any system develops in two opposite directions, therefore, each law of system development should be considered in two opposite directions. Including opposing pathways for system development complements the existing system of laws and enables forecasting system development more accurately [9].

Development of positioning mechanisms can be also observed in the two opposite directions. The first direction of development the weight of positioned objects is increasing, which requires more and more massive devices for assembly of vehicles, for transport of containers, large-sized products (containers, turbines), and sometimes for relocation of the whole buildings. Opposite direction we see in the positioning of increasingly smaller objects in biomedicine, microelectronics, and it is up to the level of positioning of molecules in nanotechnology. Development of technical systems theory is therefore to be understood as one of the possible theories that arise depending on how we define the requirements.

The example of application of TRIZ tools in the development of numerical methods proved the assumption that knowledge is also fractal as everything in nature. Adopting fractality allows to impart knowledge in compact systematic form and therefore considerably to improve efficiency of study, experimentation and creation [10].

The applied scientific General Theory of Powerful Thinking (OTSM) could be used for the study of existing theories and for developing new ones [11].

5 Application of the Objective Laws Derived from Development of Technical Systems in the Case of Development of Positioning Mechanisms

The main requirements for the operational characteristics of the mechanisms for mutual positioning of the tool head and the work piece is high accuracy, speed, static and dynamic stiffness, homogeneity of the workspace, machined surface quality, high natural frequencies, the possibility of multiaxial machining, a small number of re-clamping of work piece, low weight and price.

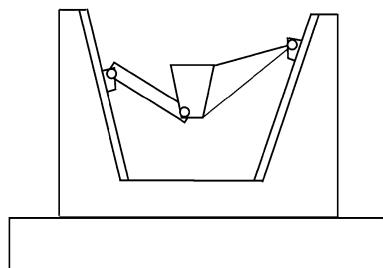
Most from positioning mechanisms in industrial robots have articulated structures of the serial type where each axis is in line relative to the preceding one. This technology has the advantage of being able to move the mechanics in all directions giving the required dexterity and envelope however, without acceptable accuracy and stiffness.

On the other hand, parallel robots have three or more prismatic or rotary axes which function parallel to one another. The result of the parallel architecture is a robot that has increased stability and arm rigidity, with faster cycle times than

Fig. 1 The parallel kinematical structure of a Tricept



Fig. 2 The parallel kinematical structure of a Trijoint



serial robots technology. The first Parallel Kinematics Machine (PKM) in the industry which already performed real work was Tricept, (Fig. 1), [12]. The new design of the hybrid PKM Exechon utilize the flexibility and cost benefits of articulated arm robots, the performance of CNC machines, as well as the efficiency of special machines [13].

Current development is focused on the combined (hybrid) structures with a scissor mechanism for positioning of the tool head and with open mechanism for positioning of the work piece on the separate clamping plate as it has Trijoint, (Fig. 2). The parallel kinematical structure of a Trijoint offer acceptable accuracy of positioning of the output body as a machine tool [14].

If we apply the laws of evolution of technical systems for positioning mechanisms of synthesis, we find that efforts should focus on the transition from planar to dexterous spatial mechanisms that allow to achieve comparable outcomes with fewer elements, with fewer demands on the operating space during working regimes, as well with fewer inputs, which is advantageous in terms of production, assembly and maintenance but also from design of control system point of view.

6 Conclusions

All we are looking for hidden reserves for further improving ourselves and the world. Products that are more secure, efficient and environmentally friendly prove that a combination of real experiments with simulations have not said the last word. A much greater potential than upgrading existing things by prevailing methods of analysis mainly in one area of knowledge, have nonalgorithmizable methods of synthesis with a systematic approach of creating new things. For this we have a method of multidisciplinary approach, patterns of development of technical and non-technical systems with methods of overcoming of contradictions and constantly emerging new approaches. New thinking technology: General Theory of Powerful Thinking (OTSM) for non typical problem solving process and dynamic self evolving mind is required to survive in the world of accelerated rapid changes.

References

1. Bloom, B.S., Engelhart, M.D., Furst, E.J., Hill, W.H., Krathwohl, D.R.: *Taxonomy of Educational Objectives: The Classification of Educational Goals; Handbook I: Cognitive Domain*. Longmans Green, New York (1956)
2. Erdman, A.G., Sandor, G.N., Kota, S.: *Mechanism Design, Analysis and Synthesis*. Prentice Hall, New Jersey (2001)
3. Huynh, P., and Hervé, J.M.: Equivalent kinematic chains with planar-spherical bonds application to the development of 3-DOF 3-RPS parallel mechanism. In: *Proceedings RAAD'03, Cassino, 2003*
4. Orlandea, N., Chace, M.A., Calahan, D.A.: A sparsity oriented approach to the dynamic analysis and design of mechanical systems. Part I. and II. *J. Eng. Ind.* **99**, 773–784 (1976)
5. Marczyk, J.: Stochastic Simulation: New Challenges and Perspectives for CAE in the 21st Century. *Alpha Magazine*, vol. 1, p. 8–11. Winter (2003)
6. Ottino, J.M.: Engineering complex system. *Nature* **427**, 29 (2004)
7. Altshuller, G.S., Shapiro, R.B.: On psychology of inventive creativity. *Probl. Psychol.* **6**, 37–49, (1956)
8. Altshuller, G.S.: *40 Principles: TRIZ Keys to Technical Innovation*. Translated by Lev Shulyak, Technical Innovation Center, Worcester (1998)
9. Petrov, V.: Law–Antilaw. ETRIA TRIZ futures conference 2006. In: *5th ETRIA. Kortrijk, Belgium*, pp. 133–140, 2006
10. Berdonosov, V., Redkolis, E.: TRIZ fractality for Mathematics, TIZ future conference 2007. *Procedia Eng.* **9**, 461–472, (2011)
11. Khomenko, N., Ashtiani, M.: Classical TRIZ and OTSM as a scientific theoretical background for no typical problem solving instruments. ETRIA TRIZ futures conference, Frankfurt am Main, Germany, 2007
12. Neuman, K.E.: Robot, US Patent 4,732,525, 1988
13. IEEE International Conference on Robotics and Automation (ICRA 2011). Shanghai (2011)
14. Valášek, M., Šika, Z., Hamrle, V.: From dexterity to calibrability of parallel kinematical structures. In: *12th IFToMM World Congress, Besançon (France), 2007*

New Models of Mechanisms for the Motion Transformation

Tomislav Petrović and Ivan Ivanov

Abstract In this paper two new mechanisms for the motion transformations are presented: screw mechanism for the transformation of one-way circular into two-way linear motion with impulse control and worm-planetary gear train with extremely height gear ratio. Both mechanisms represent new models of construction solutions for which patent protection has been achieved. These mechanisms are based on the application of the differential gearbox with two degrees of freedom. They are characterized by series of kinematic impacts at motion transformation and the possibility of temporary or permanent changes in the structure by subtracting the redundant degree of freedom. Thus the desired characteristic of the motion transformation is achieved. For each mechanism separately the principles of motion and transformation are described and the basic equations that describe the interdependence of geometric and kinematic and kinetic parameters of the system dynamics are given. The basic principles of controlling new mechanisms for motion transformation have been pointed to and the basic constructional performances which may find practical application have been given. The physical models of new systems of motion transformation have been designed and their operation has been presented. Performed experimental researches confirmed the theoretical results and very favorable kinematic characteristics of the mechanisms.

Keywords New mechanisms • Motion transformation • Experimental research

T. Petrović (✉) · I. Ivanov

Faculty of Mechanical Engineering, University of Niš, Medvedeva 14,
18000 Niš, Serbia
e-mail: tpetrovic@mehatronika.co.rs

I. Ivanov

e-mail: ivani@masfak.ni.ac.rs

1 Introduction

This paper presents newly developed mechanisms for the transformation of different motion types.

- (a) The new principles and structures of mechanisms with two degrees of freedom of movement had been developed as follows:
 - new principle of transformation of motion and structures of mechanism for transforming of circular into two-way rectilinear motion with impulse control.
- (b) The new structures of mechanisms with one degree of freedom of movement had been developed as follows:
 - reducer with extremely high transmission ratio for the transformation of rotation into rotation motion was shown.

2 Mechanism for the Transformation of One-Way Circular into a Two-way Linear Motion with Impulse Control

In the theory of machines a great number of mechanisms by which circular motion of drive element can be transformed into a linear motion of driven element are known. Requirements of contemporary machines and units in accomplishing principle motion, energy balance and control are increasingly stringent, so it is very difficult to find a mechanism that can fulfill all the requirements. Goal is to indicate the possibilities which new mechanism for transformation of one-way circular into a two-way linear motion provides.

Primary goal is for the mechanism to transform one-way rotary motion into linear with the possibility of stopping and simple change of direction of driven elements. In order to ensure use of the mechanisms for transmission of motion and energy, screw mechanism as a basic mechanism was used. The basis kinematic parameters can be seen on Fig. 1 [1].

To facilitate consideration of working principle of mechanism it is given that screw nut is the driven component which performs as rectilinear motion. Since the same direction movement of spindle is needed to ensure both directions motion of screw nut on the lead screw (a) both left and right chock are threaded, and screw nut (b and c) with appropriate thread are set (Fig. 2).

If the screw nut can rotate about its own axis while the lead screw is rotating, due to mutual friction the screw nuts would also be rotated. If we take away the possibility of rotation from any of the screw nuts, then each screw nut will change its distance. Then the problem remains: installation of such additional mechanism (m) between the screw nuts, that will be in constant contact with them, and with moving one of the screw nut along the lead screw would enable relative rotation of second screw nut over the lead screw in opposite direction. That rotation should be

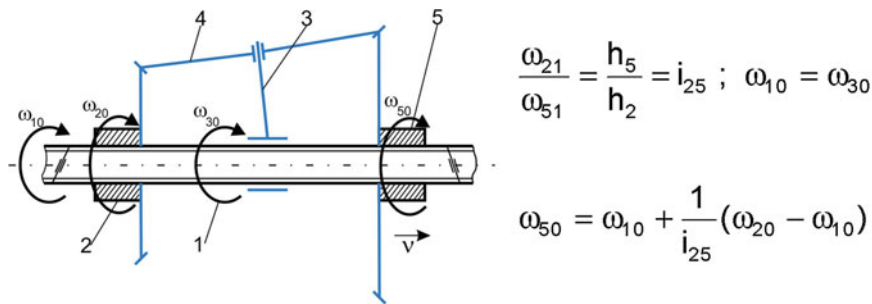


Fig. 1 Kinematics parameters of mechanism

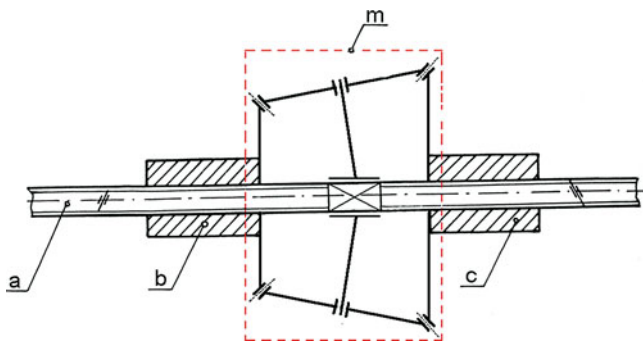


Fig. 2 Structure of mechanism

the right size to provide the same axial movement of screw nut as the move of the screw nut which is deprived the opportunity to rotate around its own axis [2]. Thus with one-way rotation of the lead screw by alternately depriving the opportunity to rotate around its own axis from the screw nut, two-way linear motion is achieved.

Additional mechanism is differential sprocket gear with negative transfer ratio whose standing gears are tightly connected to screw nuts (b) and (c) loose gears are driven by the lead screw directly or by gear.

Mechanism for the transformation of one-way circular into two-way linear motion represents the combination of the screw mechanism and the differential gear with negative transfer ratio. During inaction mechanism has two degrees of freedom of movement. By the alternate prevention of rotation of screw nut about its own axis or by defining their angular velocity (by subtracting another degree of freedom of movement) two-way rectilinear motion is achieved. Throughout stationary motion characteristics of mechanism in terms of achieving force and kinematic legality are identical to thread mechanism (Fig. 3a), while the differential gear enables quick stop and easy change of the direction of linear motion (Fig. 3b). Minor losses at the change of direction of movement represent the biggest advantage of these mechanisms compared to mechanisms applied to tool machines. All elements of the mechanism are always in conjunction, so that

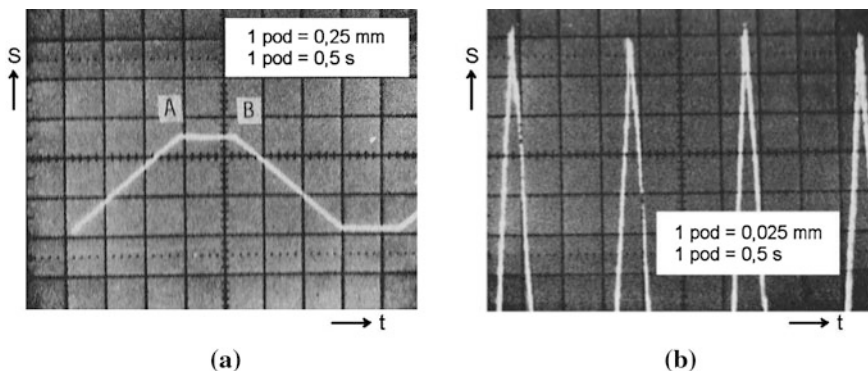


Fig. 3 Research results

transitional processes that would incurred in plugging or disconnecting the drive are avoided.

3 Special Structure of Combined Worm-Planetary Gear Trains Enabling Realization of High Transmission Ratios

An analysis of the possibility of high transmission ratios ($i > 100$) and very high transmission ratios ($i > 1,000$) being realized by gear trains confirms that there is no ideal gear train type enabling the realization of such transmission ratios without limitations.

Combined gear trains, produce marked improvements. Because of the transmission ratios being rather limited, very high transmission ratios can be achieved, only when a combined gear train is composed of several serially connected transmission stages.

However, in that case, such design can hardly remain compact. For these reasons a new combined gear train, which eliminates problems caused by limited transmission ratios, has been developed (Fig. 4).

The suggested structure of the new combined worm-planetary gear train represents the combination of a worm gearing and planetary gear trains of the type A + A (German is transmitted from a worm (1) (Fig. 3a) to a worm wheel (2) (Fig. 3b)). The worm wheel is at the same time a carrier of doubled planet gears ($4 = 4'$) and rotates on an output shaft. A stationary sun gear ($3 \equiv 0$) is in mesh with planet gears (4) while a sun gear (5), which is fastened to the output shaft, is in mesh with planet gears ($4'$). The planet gears (4) and ($4'$) are attached to each other by planet axles. The output shaft rotates with the rotation speed n_5 (Fig. 1).

The expression for the total efficiency η_{15} of the new worm-planetary gear train is obtained [3] (Fig. 5).

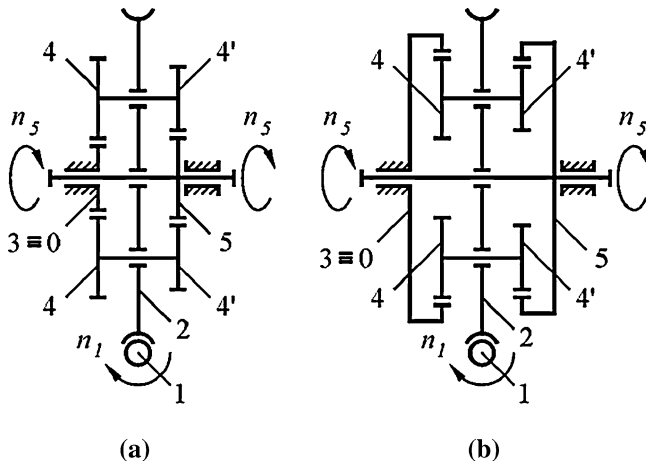


Fig. 4 Structure of new worm-planetary gear train

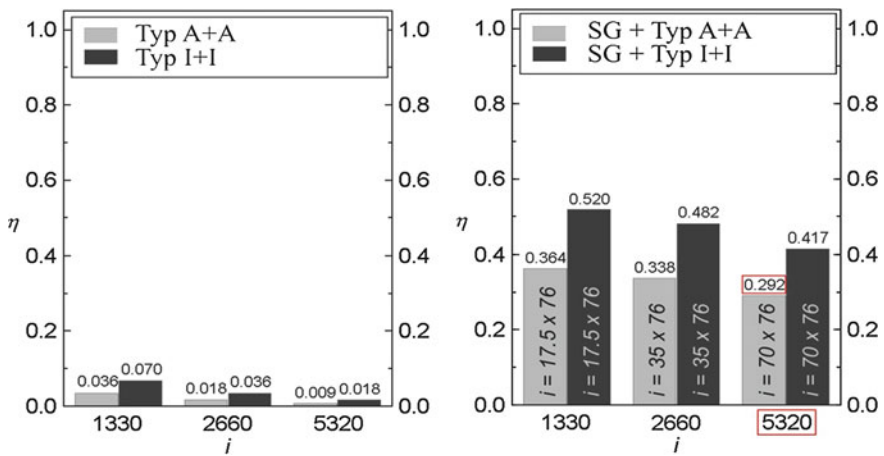
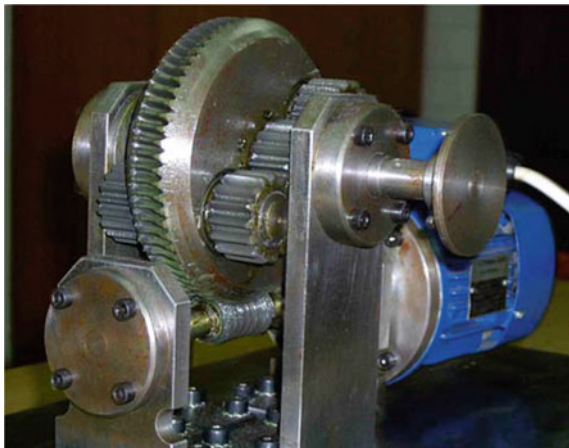


Fig. 5 Comparative values of theoretical efficiency

$$\eta_{15} = \eta_{12} \cdot \eta_{25} = \eta_{12} \cdot \frac{1}{i_{25} + (1 - i_{25}) \cdot k} \quad (1)$$

As a result of the development of the new worm-planetary gear train [3, 4] a corresponding prototype (Fig. 6) were made for the structure with the planetary gear train of the type A + A. On these prototypes the functionality of the new type of combined gear train was proved successfully for the extremely high transmission ratio: $i_{15} = 5320$.

Because rather high transmission ratios can be realized by a one-stage worm gearing, the suggested structure of the worm-planetary gear train has a high or very high total transmission ratio, even with the relatively low transmission ratio of the

Fig. 6 Prototype model

planetary gear train. The total efficiency is then quite good and nearly equal to the total efficiency of the combination of a worm gearing and a spur gearing or the ordinary combination of a worm gearing and a simple planetary gear train, by which only limited high transmission ratios can be achieved. Thereby, the total efficiency of the suggested structure is much better than the efficiency of separate planetary gear trains of the type $A + A$ or the type $I + I$ [4]. In that case this worm-planetary gear train can be used both for high power transmission and realization of very high transmission ratios. In the case of increasing of the transmission ratio of the planetary gear train, the total efficiency rather decreases, so then the suggested structure of the worm-planetary gear train can be used a priori for motion transmission, namely for transferring low powers by very high transmission rates. In this way extremely high transmission ratios can be achieved, for which very complicated structures of combined worm gearings will be necessary, with a very poor total efficiency as well. So high transmission rates could also be obtained by independent planetary gear trains with double planet gears of the type $A + A$ and the type $I + I$, but also with extremely low efficiencies.

Acknowledgments Parts of this research were supported by the Ministry of Education and Sciences Republic of Serbia through Mathematical Institute SANU Belgrade Grant ON174001 Dynamics of hybrid systems with complex structures. Mechanics of materials and Faculty of Mechanical Engineering University of Niš.

References

1. Petrović, T.: Zavojni mehanizam za transformaciju jednosmernog kružnog u dvosmerno pravolinijsko kretanje sa impulsnim upravljanjem, Doktorska disertacija, Niš (1981)
2. Petrović, P., Živković, Ž., Bögelsack, G.: Impulsgesteuerte Positioniereinrichtung mit kombiniertem Schrauben-Umlaufräder-Getriebe, 28. International Wiss. Koll. TH Ilmenau p. 165 (1983)

3. Ivanov, I.: Sinteza kombinovanog prenosnika velikog prenosnog odnosa, magistarska teza, Mašinski fakultet, Niš (2004)
4. Petrović, T., Ivanov, I.: A contribution to the development of gear trains with high transmission ratios. Proceedings of the 11th world congress in mechanism and machine science, China Machine Press, Tianjin, pp. 695–698 (2004)

Structural Synthesis of a Class of the Parallel Mechanisms Providing Plane-Parallel Displacement of a Mobile Platform

L. Rybak, A. Chichvarin, R. Sidorenko and J. Šklíba

Abstract In this article the structural synthesis method of a class of the parallel mechanisms providing plane-parallel displacement of a mobile platform is considered. The considered method is based on application of the screw theory and the concept of virtual chains. The structures of all parallel mechanisms containing three legs are received.

Keywords Parallel mechanism • Kinematic chain • Screw theory • Virtual chain

1 Introduction

Consider the class of parallel mechanisms with a mobile platform which makes a plane-parallel moving, e.g. linear motion in plane and turns relating axis of perpendicular to this plane.

L. Rybak (✉)
Belgorod State Technological University named after V.G. Shoukhov,
Belgorod, Russia
e-mail: rl_bgtu@intbel.ru

A. Chichvarin · R. Sidorenko
Staryy Oskol Technological Institute of National University of Science
and Technology «MISIS», Moscow, Russia
e-mail: ch_alex79@rambler.ru

J. Šklíba
Technical University of Liberec, Liberec, Czech Republic
e-mail: jan.skliba@tul.cz

In any general configuration, the wrench system [1] of the parallel kinematic chain (PKC) correspond this mechanism consists of all wrenches with an infinite parameter ζ_∞ which are located in the plane of motion and all wrenches with zero parameter ζ_0 , that perpendicular to this plane that is $2-\zeta_\infty - 1-\zeta_0$ - system. This PKC can be put under the virtual serial chain which later will denote as—E, and kinematic chain—E = PKC.

Functioning of the PKC doesn't changes if the connection to the base and moving platform using the virtual chain E. Any of its legs and virtual chain E will form a 3 DOF single loop kinematic chain. If the order of the leg wrench system is greater than 0, the single loop kinematic chain constructed must be an over constrained kinematic chain. [2]

From these considerations, we can make a structural synthesis of parallel mechanisms class.

2 Decomposition of the Wrench System 3-DOF E = PKC

As the wrench system of a PKC is the linear combination of those of all its legs in a general configuration, any leg-wrench system in a E = PKC is a sub-system of its wrench system. It then follows that any leg-wrench system of a E = PKC is either a $1 - \zeta_0$ - system, a $1 - \zeta_\infty$ - system, a $2 - \zeta_\infty$ - system, a $1 - \zeta_\infty - 1 - \zeta_0$ - system, or a $2 - \zeta_\infty - 1 - \zeta_0$ - system).

The combinations of the leg-wrench subsystems of leg-wrench systems have been determined by solving equation

$$\sum_m c^i = 6 + F + \Delta \quad (1)$$

where m —leg-wrench system quantity which equals number of leg, in real event $2 \leq m \leq 4$; c —order of leg-wrench subsystem, $0 \leq c^i \leq c$; c —order of leg-wrench system, in real event $c = 3$; F —number of degree of freedom of PKC, in real case $F = 3$; Δ —number of over constraints.

All solutions of this equation for the case of three legs are presented in Table 1.

3 Type Synthesis of Legs

3.1 Type Synthesis of 3-DOF Single-Loop Kinematic Chains That Involve an E Virtual Chain and Have a Specified Leg-Wrench System

Number of joints in single-loop kinematic chain f can be defined by the equation

$$f = F + 6 - c. \quad (2)$$

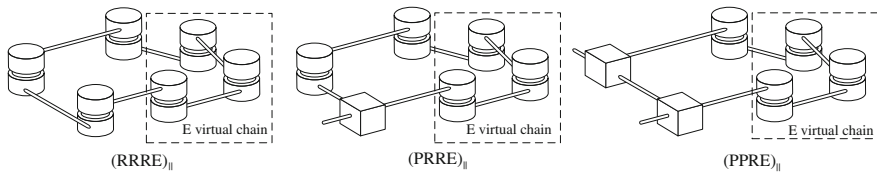


Fig. 1 Some 3-DOF single-loop KCs involving a E virtual chain and having a $2 - \zeta_{\infty} - 1 - \zeta_0$ - system

In the further will consider kinematic chain which consist only from rotation (R) and prismatic (P) joints to ease the task.

From the synthesized legs, we must to discard the supports in which the twists of all joints linearly dependent except that which included in the virtual chain.

For that need and enough compliance of the next terms:

- There are no coaxial R joints.
- There are no P joints along the same direction.
- The direction of at most one P joint is parallel to the axis of an R joints.
- At most three R joints have parallel axes.
- The axes of at most three R joints pass through the same point.
- The directions of at most two P joints are parallel to the same plane.
- The sum of the number of R joints with parallel axes and the number of P joints is not greater than four.
- If the directions of n_P P joints are perpendicular to the axes of n_R R joints with parallel axes, then $n_P + n_R \leq 3$.

Case with the $2 - \zeta_{\infty} - 1 - \zeta_0$ - system. In that case number of joints equals 6. It kinematic chain consists from six R and/or P joints. The axes of the all R joints are parallel to the ζ_0 axes and directions of the all P joints are parallel to the plane which perpendicular ζ_0 .

After the linear independent check of the screws to remain a three kinematic chain $(RRRE)_{||}$, $(PRRE)_{||}$, $(PPRE)_{||}$, where by $()_{||}$ we denote successive joints that are arranged such that all the links move along parallel planes (Fig. 1).

Case with the $1 - \zeta_{\infty} - 1 - \zeta_0$ - system. In that case number of joints equals 7. It is formed by reduction of one coaxial R joint into one kinematic chain which makes a parallel-plane moving. It is the same chain like we analyzed early. From conditions of the linear independent follow that number of the coaxial R joints must be no more than two. In the result we get a following kinematic chains: $\tilde{R}(RRRE)_{||}$, $\tilde{R}(PRRE)_{||}$, $\tilde{R}(PPRE)_{||}$, where by \tilde{R} we denote R joint is coaxial to the any other joint of kinematic chain (Fig. 2).

Case with the $2 - \zeta_{\infty}$ - system. In that case number of joints equals 7. That kinematic chain consist as minimum from one R joint and as minimum from one P joint where all axes of R joints are parallel and directions of not all P joints are perpendicular to the axes of R joints.

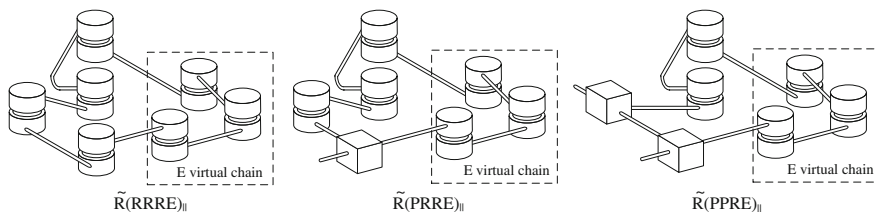


Fig. 2 Some 3-DOF single-loop KCs involving a E virtual chain and having a $1 - \zeta_{\infty} - 1 - \zeta_0$ - system

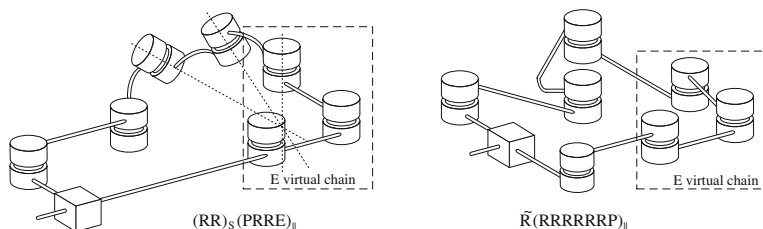


Fig. 3 Some 3-DOF single-loop KCs involving a E virtual chain and having a $1 - \zeta_0$ - system

After the linear independent check of the screws remain a four kinematic chain: $P(RRRE)_{II}$, $P(PRRE)_{II}$, $P(PPRE)_{II}$.

Case with the $1 - \zeta_{\infty}$ - system. In that case number of joints equals 8. Get a kinematic chain which consist as minimum from one R joint and as minimum from one P joint (where all axes of the R joints are parallel and directions of motion not all R joints are perpendicular to the axes of R joints) and from one or more R joints which have a consist axes. Get a follow kinematic chain: $PPPPRE$, $PPPR(RE)_{II}$, $PPR(RRE)_{II}$, $PPR(RRRE)_{II}$.

Case with the $1 - \zeta_0$ - system. In that case number of joints equals 8. In that case there is a two variants structure of the kinematic chain.

Firstly, the kinematic chain which consist from combination of the minimal from two R and/or P joints (it has one R joint; and all joints moving in parallel plane) and from two ore more R joints with crosscut axes. Get a follow kinematic chain: $(RR)_S(RRRE)_{II}$, $(RRR)_S(RRE)_{II}$, $(RR)_S(PRRE)_{II}$, $(RRR)_S(PRE)_{II}$, where by $()_S$ we denote successive joints that are arranged such that all the links move along concurrent spherical surfaces (Fig. 3).

Secondly, kinematic chain which consist from union of two R joints at least and/or P joints (contains at minimum one R joint in which all links are motion in parallel planes) and from two or more R joints whose axes coincide. Have only one kinematic chain: $(RRRRRRP)_{II}\tilde{R}$ (Fig. 3).

Table 2 Legs for $E = \text{PKCs}$

C^i	Class	No.	Structure
3	$2_{minus}; \zeta_\infty - 1 - \zeta_0$	1	$(XXX)_E$
2	$1 - \zeta_\infty - 1 - \zeta_0$	2	$\tilde{R}(XXX)_E$
		3	$(XXX)_E \tilde{R}$
	$2 - \zeta_\infty$	4	$(XXXX)_E$
1	$1 - \zeta_0$	5	$(RR)_S(RRR)_E$
		6	$(RRR)_S(RR)_E$
		7	$(RR)_S(PRR)_E$
		8	$(RRR)_S(PR)_E$
		9	$(RRRRRRP)_E \tilde{R}$
	$1 - \zeta_\infty$	10	PPPPR
		11	PPPR(R) _E
		12	PPR(RR) _E
		13	PPR(RRR) _E

3.2 Generation of Types of Legs

The types of legs can be readily obtained from the 3-DOF single-loop kinematic chains obtained above, by removing the E virtual chain. The results are in Table 2.

4 Assembly of legs

$E = \text{PKCs}$ can be generated by assembling a set of legs for $E = \text{PKCs}$ shown in Table 2 selected according to the combinations of the leg-wrench systems shown in Table 1. In assembling $E = \text{PKCs}$, the following condition should be met: the linear combination of the leg-wrench systems forms a $2 - \zeta_0 - 1 - \zeta_0$ - system.

Let's consider for example $E = \text{PRC}$ of family 3 (Table 1). $E = \text{PKC}$ of this family consist of two legs with $1 - \zeta_\infty - 1 - \zeta_0$ - system and one leg with $2 - -\zeta_\infty - -$ system. By selecting from Table 2 for example two legs of type $(XXX)_E \tilde{R}$ and one leg of type $(XXXX)_E$, we have $2 - (XXX)_E \tilde{R} - (XXXX)_E = \text{PKC}$.

5 Selection of Actuated Joints

Selection of actuated joints consists from found utmost combination of actuated joints that from it which not performs follow terms:

- actuated joints must be standing on all the legs as evenly as possible;
- actuated joints on the base or as close as possible for it;
- no unactuated active P joint should exist.

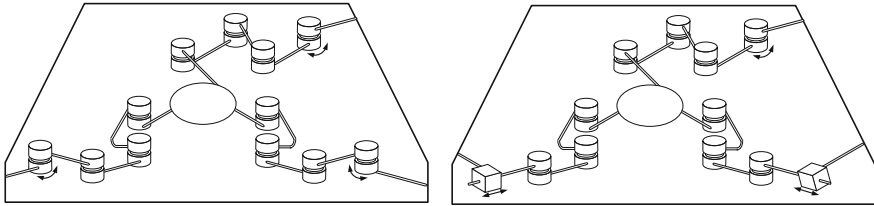


Fig. 4 Some E = PM of type $2-\tilde{R}(XXX)_{||}-(XXXX)_{||}$: $(\underline{RRR})_{||}\tilde{R}-(\underline{RRRR})_{||}$ and $2-(\underline{PRR})_{||}\tilde{R}-(\underline{RRRR})_{||}$

We can make a follow term of selection of actuated joints: for an F-DOF parallel mechanism a set of F actuated joints is valid if and only if, in a general configuration, all the actuation wrenches of the F actuated joints together with a set of basis wrenches of the wrench system of the PKC constitute a 6-system.

In particular, for this terms satisfy a mechanism which shown on Fig. 4, actuated kinematic joints identified of the arrows.

Thus, in the result of the method which based on screw theory and virtual chain conception we obtained a big parallel mechanism group which provides a plane-parallel motion of the output platform.

Acknowledgments The research work reported here was made possible by Ministry of Education and Science of Russian Federation, state contract No. 14.740.11.0325.

References

1. Dimentberg, F. M. : Screw calculation and its appendices to mechanics, Nauka (1965)
2. Kong, X., Gosselin, C.M. : Type synthesis of parallel mechanisms, series: springer tracts in advanced robotics, Springer, Heidelberg (2007)

Development of a Wearable Assist Robot for Walk Rehabilitation After Knee Arthroplasty Surgery

H. Terada, Y. Zhu, K. Horiguchi, M. Nakamura and R. Takahashi

Abstract In Japan, it is popular that the disease knee joints will be replaced to artificial joints by surgery. And we have to assist so many patients for walk rehabilitation. So, the wearable assist robot has been developed. This robot includes the knee motion assist mechanism and the hip joint support mechanism. Especially, the knee motion assist mechanism consists of a non-circular gear and grooved cams. This mechanism rotates and slides simultaneously, which has two degree-of-freedom. Also, the hip joint support mechanism consists of a hip brace and a ball-joint. This mechanism can avoid motion constraints which are the internal or external rotation and the adduction or abduction. Then, the control algorithm, which considers an assisting timing for the walk rehabilitation, has been proposed. A sensing system of a walk state for this control system uses a heel contacts sensor and knee and hip joint rotation angle sensors. Also, the prototype robot has been tested. And it is confirmed that the assisting system is useful.

Keywords Robot • Wearable • Walk assist • Grooved cam • Non-circular gear

H. Terada (✉) · Y. Zhu · K. Horiguchi
Graduate School of Medical and Engineering Science, University of Yamanashi, Tokyo,
Japan
e-mail: terada@yamanashi.ac.jp

M. Nakamura
Kofu Municipal Hospital, Yamanashi, Japan
e-mail: MXE02560@nifty.com

R. Takahashi
Suncall Engineering Corporation, Kyoto, Japan
e-mail: rei_takahashi@suncall-eng.co.jp

1 Introduction

An Osteoarthritis (OA) is mechanical abnormalities of human body involving degradation of joints. Especially, in Japan, patients of knee-OA increase abruptly. This is the most popular joint disease which is caused by aging. This disease prevents to walk with pain. At this disease, the knee/hip joint transformation turns worse slowly, and finally a patient will be not able to walk. Therefore, there are many cases that the disease joints will be replaced to artificial joints. This surgery is called as “Total Knee Arthroplasty (TKA)” which is about forty-thousand times per every year in Japan. However, the abnormal walk habits caused by knee-OA remain, even if they relieved gonalgia. Therefore, it is difficult to recover walk status to normalize for knee-OA patients without rehabilitation. So, we have to assist so many patients for rehabilitation. In general, continuous passive motion (CPM) device [1] will be often used to the rehabilitation. However, there still is substantial debate about the usefulness of CPM applications [2]. It is the main reason that operating condition of CPM device is different from walk state. So, the walking type wearable knee assist robot is required. In this report, a structure of wearable assist robot with a knee assist mechanism and a hip joint support mechanism is proposed. And the motion algorithm for the walk rehabilitation is shown. Also the prototype robot is tested to verify the proposed approach.

2 Structure of a Wearable Assist Robot

The proposed wearable assist robot consists of a knee joint assist mechanism, a hip joint support mechanism with braces, shoes with foot sensors to detect a heel contacts, rotation sensors to detect hip/knee joint rotation and a CPU control unit with Li-ion battery as shown in Fig. 1. Especially, in a TKA surgery, it is popular that a patient operates for unilateral knee. Therefore, for walk rehabilitation, it is sufficient to assist the unilateral knee. And this proposed assist robot has a knee motion assist mechanism for unilateral knee. Also, for the opposite side knee, to adjust a weight balance, control unit and battery are attached on the un-assist side brace.

In general, the knee joint rotates within 0 to about 130° at the walking on flat and slope. And, during the $15\text{--}90^\circ$, knee joint rotates with gliding to the back direction [3]. So, this motion is defined as the “roll-back” motion. And the hip joint which has a spherical joint structure rotates with the flexion, extension, internal rotation, external rotation, abduction and adduction. Nevertheless, conventional assist robots haven’t almost considered these motions. Therefore, when the equipped person walks for rehabilitation, it has been difficult that person walks smoothly using those robots. To solve these problems, we have developed the knee joint assist mechanism with grooved cams and a non-circular gear, and the hip joint support mechanism, as follows.

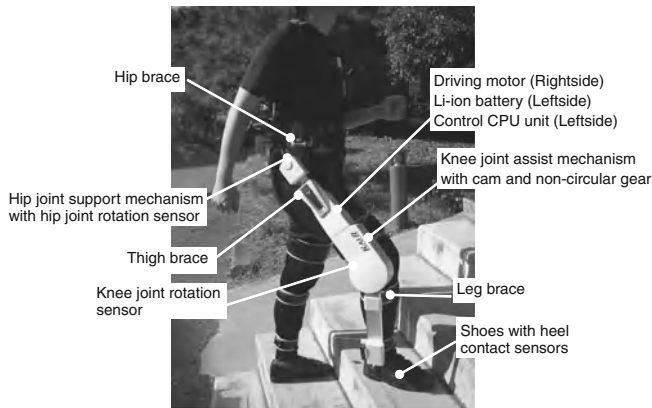


Fig. 1 Wearable assist robot for walk type rehabilitation (*Right leg version*)

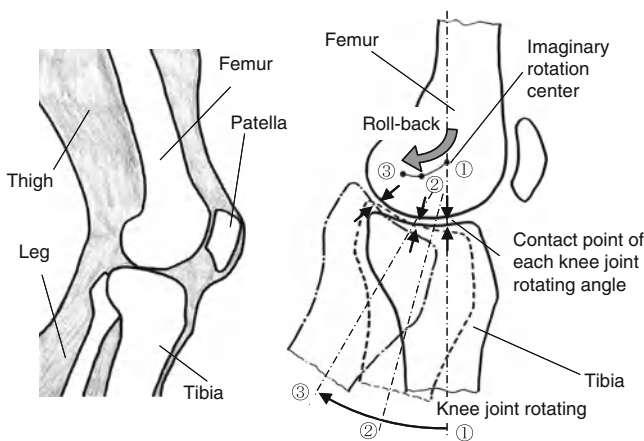


Fig. 2 Motion of a knee joint at the bones contacts section (*Right leg; x-y view*)

3 Knee Joint Assist Mechanism

The roll-back motion is defined as the knee joint rotation with gliding motion to the back direction as shown in Fig. 2. Especially, this roll-back motion length on the outside of leg is extended from that length at the bone center section, which is caused by a medial rotation. Therefore, a conventional mechanism which has 1-DOF rotation joint is insufficient. Considering this point, a knee joint driving mechanism which is attached on the outside of leg has been newly developed [4].

This mechanism consists of two grooved cams and one non-circular gear [5]. Especially, the profiles of these cams and a non-circular gear are generated which are calculated using an-symmetrical modified trapezoid motion curves [6]. And a grooved cam at the mechanism center is the imaginary rotation center on the leg

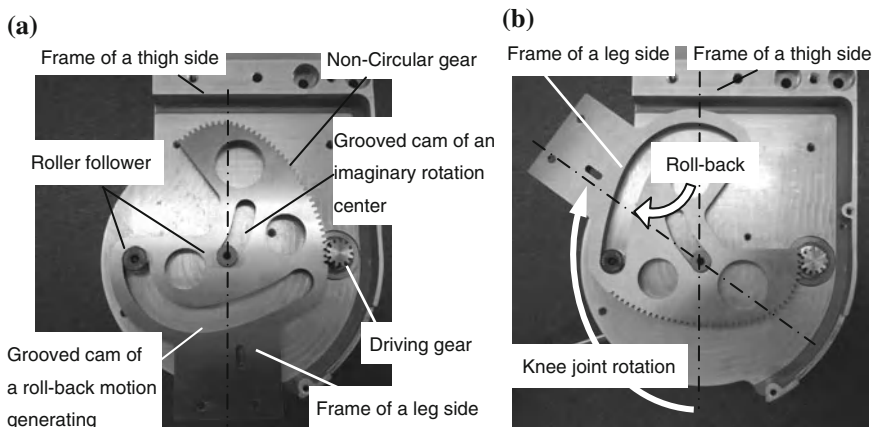


Fig. 3 Prototype of a knee joint driving mechanism **a** Before the roll-back motion **b** After roll-back motion

side. The prototype of a knee joint driving mechanism is made using a wire-cut electrical discharge machining, as shown in Fig. 3.

4 Hip Joint Support Mechanism

When the patients make rehabilitations with wearable robot, it is important to eliminate an influence of assist robot weight. In general, the assist robot connects on the hip joint. On the other hand, a hip joint rotates around the 3 axes, and these rotations are called as the “flexion”, “extension”, “internal rotation”, “external rotation”, “adduction” and “abduction” [7]. At walking, the main motion are “flexion” and “extension”, however, other motion are needed to walk smoothly. However, almost conventional wearable robots connect on the hip joint using a 1-DOF rotation joint. And, that joint gives constraints which are the internal or external rotation and the adduction or abduction.

So, to rotate smoothly, we have developed the hip joint support mechanism. For this mechanism a hip brace is attached on the pelvic girdle. And the ball-joint is attached on the frame which extends from this brace to an outside of the hip joint as shown in Fig. 4. This mechanism can transmit the up/down motion caused by the lumbar lateral bending around the cardinal frontal plane. Also, the shoulder-belt distributes the assist robot weight to the shoulder.

Fig. 4 Hip joint support mechanism

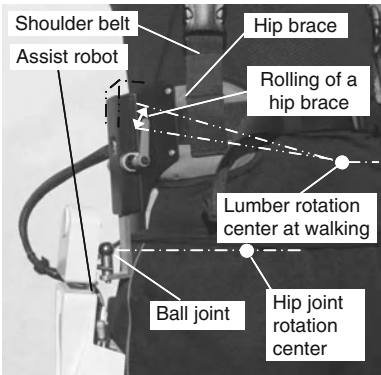
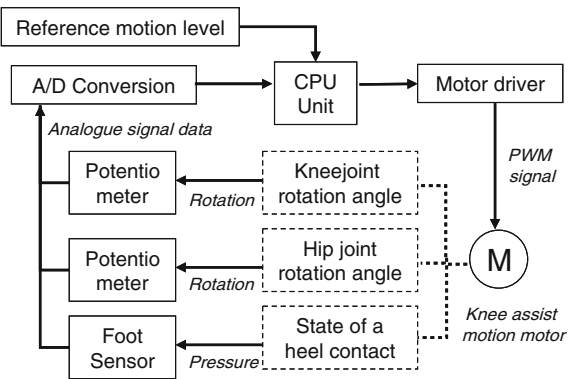


Fig. 5 Block diagram of a control system



5 Control Systems and Motion Verification

At this robot system, the main purpose is to correct the walk state and not to assist simple walk. Therefore, this robot system doesn't use the simple feedback control with servomotors.

A DC motor is driven by the PWM control in which a heel contact, a knee joint rotation angle and a hip joint rotation angle are feedback signals as shown in Fig. 5. The PWM duties can be changed according to the conditions of the patients or the kinds of rehabilitation. At the real-time, these signal data calculate using the threshold level signals which can command the arbitrary value. These levels can be changed according to the conditions of the patients or the kinds of rehabilitation, too.

Also, the Fig. 6 shows a timing chart of the PWM duty ratio and the threshold levels of each walk state detection sensor, which are the knee flexion, hip joint flexion and the heel contacts. Especially for walk rehabilitation, the extension timing of the hip joint gives large influence on the foot bottom height. At this system, it is possible to set the required hip joint flexion angle which prevent drop.

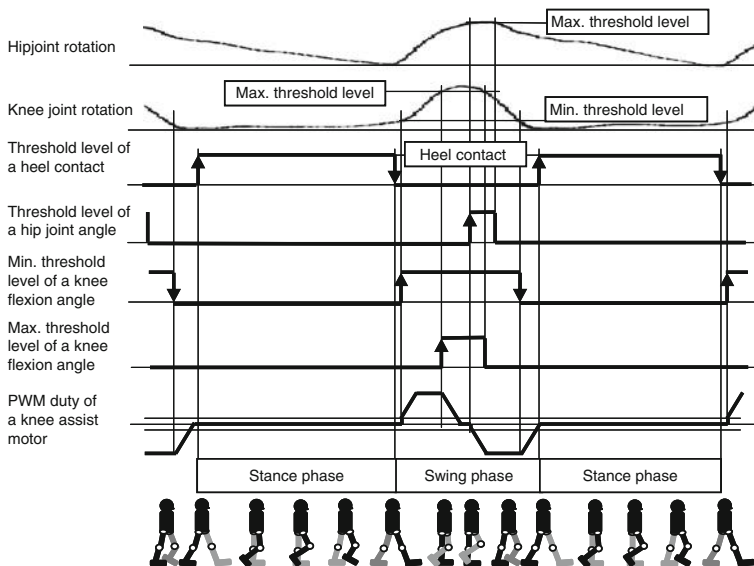


Fig. 6 Gait cycle and motion timings of an assist robot

Based on a proposed control algorithm, the prototype of an assist-robot system has been verified to the usefulness for the walk rehabilitation. Using this system, it is confirmed that the maximum hip joint and knee joint angles are improved. Especially, at the rehabilitation after the surgery, it is very important to enlarge the knee flexion angle. At this prototype, the maximum knee flexion angle enlarges from 73 to 103° . In addition, it is confirmed that the normal persons can go up and down steps which are 200 mm height easily by use of this system.

6 Conclusions

For many patients for walk rehabilitation after the total knee arthroplasty surgery, the wearable assist robot which includes a knee assist mechanism and a hip joint support mechanism has been developed. Especially, the knee joint assist mechanism has grooved cams and a non-circular gear, and it is easy to flex the knee joint and the hip joint support mechanism. And the motion control algorithm which assists knee flexion/extension timing has been proposed. So, it is confirmed that has been easy to walk smoothly using this robot. In future work, to realize the optimization of assist timing, we have to investigate the gait analysis and the clinical test for many patients.

References

1. Salter, R.B.: The biological effects of continuous passive motion on the healing of full-thickness defects in articular cartilage: an experimental investigation in the rabbit, *J Bone Joint Surgery*. **62A**, 1232 (1980)
2. Milne S., et al.: Continuous passive motion following total knee arthroplasty, *Cochrane. Database Syst Rev*. **2**, CD004260 (2003)
3. The Japanese Orthopaedic Association: *Check Point of the Prosthetist and Orthotist*, Igakushoin, 262 (1978)
4. Terada H., et al.: Developments of a knee motion assist mechanism for wearable robot with a non-circular gear and grooved cams, *Mechanisms. Transmissions and applications: mechanism and machine science*, 3, p. 69 Springer, (2012)
5. Katori H., et al.: A simplified synthetic design method of pitch curves based on motion specifications for noncircular gears. *Trans Jpn Soc Mech Engi-neers. Part C*. **60**(570), 668 (1994)
6. Makino H.: *Automatic assembly machine kinematics*, Nikkan Kogyo Shimbun Ltd, p. 29 (1976)
7. Sato K.: *Practical kinematics for co-medical*, Medical-friend Co, p. 16 (1993)

Modeling of Lifting Equipment with Backlash Consideration

J. Vondrich and E. Thöndel

Abstract This paper looks at the impact of backlash between the worm and worm gear in an electric-driven machine the vibrations of the propelled section of the machine. The assessment is carried out for a lift machine, in which the resulting vibrations will affect the lift cab due to backlash. Eventual backlash in the worm gear will result in cage vibrations, which cause problems with ride smoothness and imprecision in stopping in desired stations. The lift has been chosen to analyze the matter in hand; in this kind of machine, excessive backlash between the worm and worm gear results in vibration of the lift cab. Equations of motion have been prepared for the lift model and worm drive backlash which can be solved in the Matlab application for different lift parameters. The equations provide cab velocity and acceleration data which can be subsequently compared with the desired values as defined in the applicable technical standards.

Keywords Lift • Gear • Backlash • Vibration • Matlab

1 Introduction

When designing a machine tool, it is necessary to start from desired machine output parameters. It is advisable to check the dynamic behaviour of the machine tool before making constructional design, which is combined with dimensional and strength calculation of individual machine parts. By dynamic behaviour of the machine, we mean determining the time flow of trajectories, velocities, or

J. Vondrich (✉) · E. Thöndel
Czech Technical University in Prague, Prague, Czech Republic
e-mail: vondrich@fel.cvut.cz

accelerations, and arisen forces and torques of individual output working parts of the machine tool. We assume that dynamic behaviour will be assessed using a suitably built machine tool model, which describes the machine tool itself as closely as possible.

The model then can be described by system of motion equations, which we solve numerically using Matlab. Based on the results calculated, we used the most often generated inappropriate vibrations of individual machine parts. By simulating input parameters, or respectively, by change of structure, we try to minimize such vibrations. The described procedure is demonstrated by an example of lift drive with backlash consideration design. After considering carefully all the parameters the electrical kind of drive is selected, with worm gear unit.

2 Device Model

The lift is comprised of several sections: mechanical, electric, control and safety. The mechanical section consists of the worm drive, traction wheel, counterweight, hoist cables and lift cab guiding elements. The asynchronous motor driving the lift can be controlled by position sensors, control buttons and additional electric devices and equipment, such as lift control switches etc. Lift type and the control and safety equipment to be used always have to be selected based on the intended purpose and required cab speed and acceleration. General requirements on lift operation include, in particular, smooth motion, stopping accuracy, reliability, minimum movement time and economical operation. Lifts are designed to move goods and persons vertically between two and more locations at different levels.

The motion of a lift cab is usually intermittent, as it has to stop in different floors. The nominal speed of a lift cab normally ranges from 0.63 ms^{-1} to 6.3 ms^{-1} ; however, speeds up to 10 ms^{-1} are allowed in tower blocks. In order to ensure passenger comfort during transportation, acceleration values should not exceed $1.8\text{--}2.0 \text{ ms}^{-2}$.

The electric motor used to drive the lift should be able to work in both directions of rotation in motor or generator mode, having, at the same time, suitable torque characteristics and generating minimum noise levels and vibration. However, excessive backlash between the worm and worm gear cogs can cause lift cab vibration and result in jerky motion or prevent the lift from achieving the desired stopping accuracy.

Figure 1 shows a model of the lift, comprising of an electric motor (1), worm drive (2), rope wheel and worm (3), hoist ropes (4), flywheel (5) and brake (6). Q_Z is the load mass, Q_{vz} the counterweight mass.

The equations of motion of the lift model (Fig. 1) can be written as follows:

$$\begin{aligned} I_1 \ddot{\varphi}_1 &= -k_1 (\varphi_1 - \bar{\varphi}_1) + M, \\ I_2 \ddot{\varphi}_2 &= -k_{21} (\varphi_2 - \bar{\varphi}_2) + Q_{vz} \frac{D}{2} - Q_z \frac{D}{2}. \end{aligned} \quad (1)$$

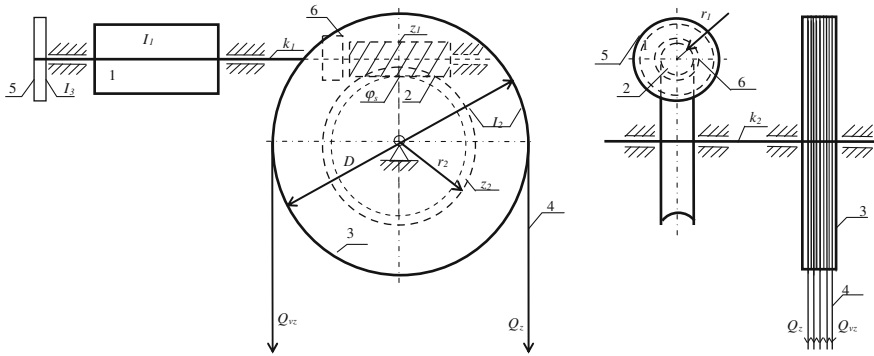
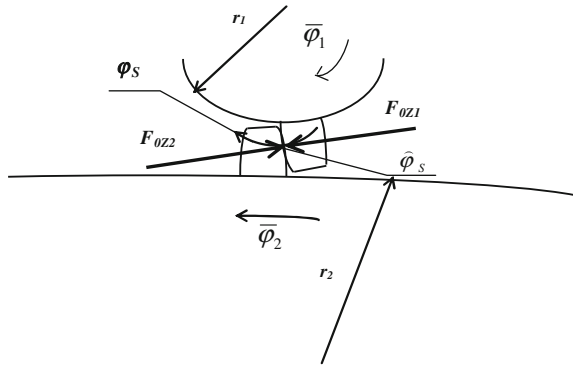


Fig. 1 Design of the mechanical section of the lift (1—electric motor, 2—worm drive, 3—rope wheel and worm, 4—hoist ropes, 5—flywheel, 6—brake, Q_z —lift cab mass, Q_{vz} —counterweight mass)

Fig. 2 Forces acting between the worm and worm gear cogs— F_{OZ1} , F_{OZ2}



In addition, the model includes shaft stiffness (k_1 and k_2) and backlash between the cogs determined by the angle $\hat{\varphi}_s$ (see Fig. 2) [1].

The forces between the worm and worm gear cogs F_{OZ1} , F_{OZ2} (see Fig. 2) can be expressed using the following two equations:

$$\begin{aligned} F_{OZ1}r_1 - k_1(\varphi_1 - \bar{\varphi}_1) &= 0, \\ F_{OZ2}r_2 + k_2(\varphi_2 - \bar{\varphi}_2) &= 0. \end{aligned} \quad (2)$$

The system is subject to the usual principles of forces acting between cogs (i.e. $F_{OZ1} = F_{OZ2}$) and gear transmission rules, i.e. $i = r_2/r_1 = z_2/z_1$, where z_1 , z_2 is the number of cogs of the worm and worm gear (Fig. 1). The gear mesh frequency ω_z can be expressed as:

$$\omega_z = z_1 \dot{\varphi}_1. \quad (3)$$

As a result of the backlash $\widehat{\varphi}_s$ between the worm and worm gear cogs the worm drive is expected to vibrate: $\varphi_s = \widehat{\varphi}_s \sin \omega_z t$. During worm gear engagement phases the angular displacement of the worm gear $\bar{\varphi}_2$ changes as a result of the backlash between the cogs:

$$\bar{\varphi}_2 = \varphi_2^* + \varphi_s = \varphi_2^* + \widehat{\varphi}_s \sin \omega_z t, \quad (4)$$

where the following relationship applies to the angle φ_2^* :

$$r_1 \bar{\varphi}_1 = r_2 \varphi_2^*. \quad (5)$$

3 Numerical Solutions

Numerical solution of eq. (1) using Simulink [2] was calculated for the following parameters lifts:

$I_1 = 0.018 \text{ kgm}^2$	$I_2 = 0.385 \text{ kgm}^2$	$k_1 = 2.06 \cdot 10^5 \text{ Nm}^{-1}$	$k_2 = 5.49 \cdot 10^6 \text{ Nm}^{-1}$
$z_1 = 4$	$z_2 = 160$	$\widehat{\varphi}_s = (10^{-2} \div 10^{-4}) \text{ rad}$	$D = 0.51 \text{ m}$
$r_1 = 0.016 \text{ m}$	$r_2 = 0.64 \text{ m}$		

The type of the motor to be used is chosen with respect to the required nominal speed and maximum load of the lift. Typically, a three-phase induction motor with a squirrel cage rotor is used for the envisaged speeds of $0.63\text{--}2.5 \text{ ms}^{-1}$. Assuming certain simplified conditions, the behavior of the induction motor driving the lift shows that motor torque decreases with respect to the square of voltage. The behavior of the induction motor's torque can be described using the Kloss formula:

$$M = M_0 \frac{2s_z \left(1 - \frac{\phi_1}{\omega_{SYN}}\right)}{s_z^2 + \left(1 - \frac{\phi_1}{\omega_{SYN}}\right)^2}, \quad (6)$$

where the motor's maximum torque $M_0 = 80 \text{ Nm}$, maximum torque slip, $s_z = 0.25$ and $\omega_{SYN} = 157 \text{ s}^{-1}$.

4 Solution Results

Figure 3 shows the behavior of the velocity and position of the lift cabin case of a small backlash between the worm and worm gear cogs, $\widehat{\varphi}_s = 10^{-4} \text{ rad}$, with the bottom chart showing the development of motor torque.

Figure 4 below shows the behavior of the velocity and position of the lift cab in case of a large backlash between the worm and worm gear cogs: $\widehat{\varphi}_s = 10^{-2} \text{rad}$. Again, the bottom part shows the development of motor torque.

5 Conclusions

This paper presents a numerical model of the propulsion of a worm gear cable-drum lift, respecting the backlash between the worm and worm gear cogs. The drive unit has to provide sufficient peripheral force to lift the frame, cab and load. During downward motion the drive unit has to exert sufficient braking power to stop the same mass. The motor is controlled by a variable-frequency drive to increase control efficacy and ensure smooth operation. The propulsion unit has to be rather robust, providing at least twice the required power. The mass of the counterweight corresponds to the mass of the frame and lift cab plus a half the maximum load. As one of the main operating risks, cab vibrations can have a deteriorating effect on stopping accuracy. The extent of this phenomenon is closely related to the backlash of the slide surfaces, in order to minimize torque losses and wear and tear of the worm and worm gear cogs. The backlash between the worm and worm gear generates vibration which has a negative influence on lift operation. Simulation results show that when the thickness of the protective oily layer between the worm and worm gear cogs $\widehat{\varphi}_s = 10^{-4} \text{rad}$ (Fig. 3) lift cab velocity amounts to 1 ms^{-1} with a velocity amplitude of 0.16 ms^{-1} , the cab moves smoothly and without significant vibration, and the torque during stabilized cab motion amounts to 36.1 Nm. These results comply with the applicable technical standards for these parameters. Larger backlash between the worm and worm gear, caused for instance by excessive wear and tear, has a significant impact on operation quality. With $\widehat{\varphi}_s = 10^{-2} \text{rad}$ (Fig. 4), cab speed amounts to 1 ms^{-1} with an amplitude of 1.4 ms^{-1} ; however, the movement is not smooth and the cab vibrates (amplitude 0.06 m). Torque during stabilized cab motion amounts to 36.1 Nm and vibrations are transferred to the motor (amplitude 10 Nm). The results prove that even a minute increase in the backlash between the worm and worm gear cogs (Fig. 4) can result in dangerous cab vibration, which can be eliminated only by replacing the worm and worm gear. Further research on this matter will be carried out both with a physical model and an enhanced numerical model respecting passive resistances.

This work was supported by grant of Czech Technology Agency TACR, TA01030651 “Safety Improvement of Flight, Crew and Other Participants of Flight Transport in Normal and Emergency Situations by Assistive Technologies”.

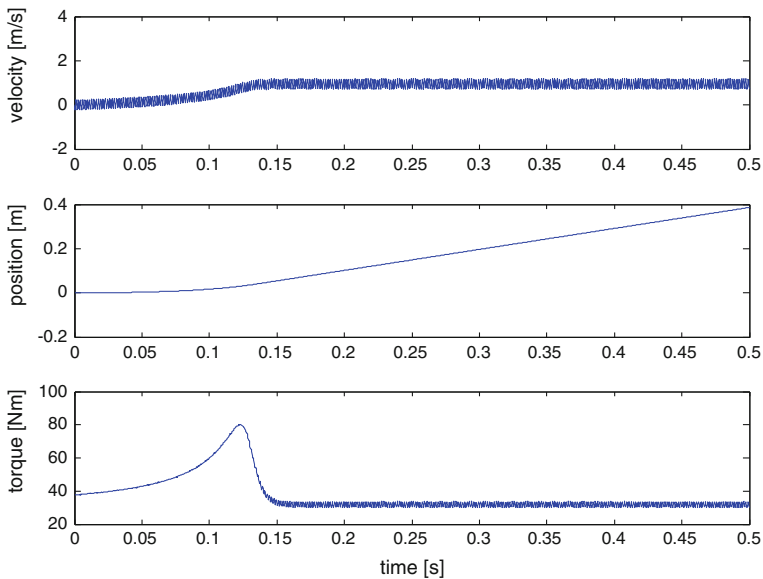


Fig. 3 Simulation results—backlash between the worm and worm gear cogs: $\hat{\varphi}_s = 10^{-4} \text{ rad}$

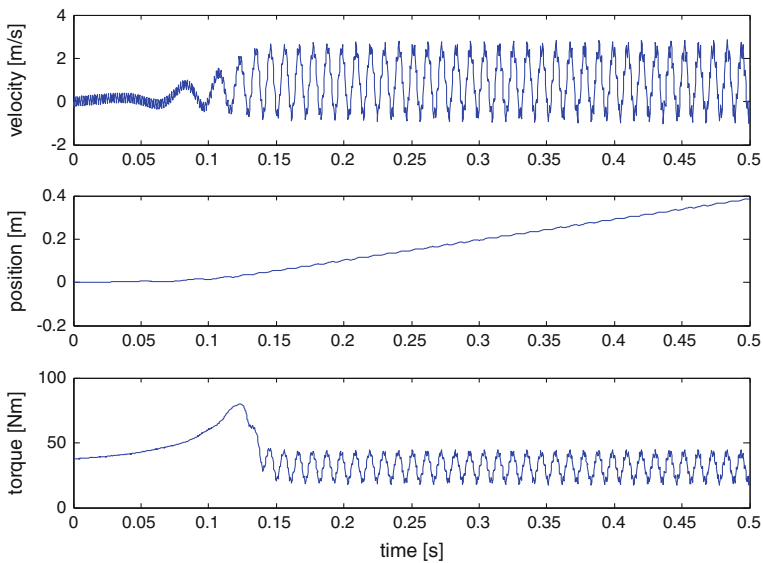


Fig. 4 Simulation results—backlash between the worm and worm gear cogs: $\hat{\varphi}_s = 10^{-2} \text{ rad}$

References

1. Dresig, H., Rockhausen, L.: Aufgabensammlung Maschinendynamik. *Fachbuchverlag Leipzig-Köln* (1994)
2. Kocarnik, P., Jirku, S.: The model of oscillating system with coil its validation. *Res. Agric. Eng.* 53(4), p. 182–187 (2007) (Prague)

Analysis of Automatic Automotive Gear Boxes by Means of Versatile Graph-Based Methods

J. Drewniak, J. Kopeć and S. Zawiślak

Abstract Automotive gear boxes are special mechanisms which are created based upon some planetary gears and additionally equipped in control systems. The control system allows for an activation of particular drives. In the present paper, some graph based models of these boxes are considered i.e. contour, bond and mixed graphs. An exemplary automatic gear box is considered. Based upon the introduced models, ratios for some drives have been calculated. Advantages of the proposed method of modeling are: algorithmic approach and simplicity.

Keywords Mixed • Bond • Contour graph • Planetary gear • Drive ratios

1 Introduction

Automatic gear boxes are very important parts of vehicle drive systems. They are designed based upon unification of several elementary planetary gears in such a way that particular drive is switched on via a dedicated control system. The control system usually consists of clutches, brakes and mechatronic activation system.

Graph models of mechanical systems especially gears are very useful and relatively simply. There are several different graph approaches to modeling (of

J. Drewniak · J. Kopeć · S. Zawiślak (✉)
University of Bielsko-Biała, Bielsko-Biała, Poland
e-mail: szawislak@ath.bielsko.pl

J. Drewniak
e-mail: jdrewniak@ath.bielsko.pl

J. Kopeć
e-mail: jkopec@ath.bielsko.pl

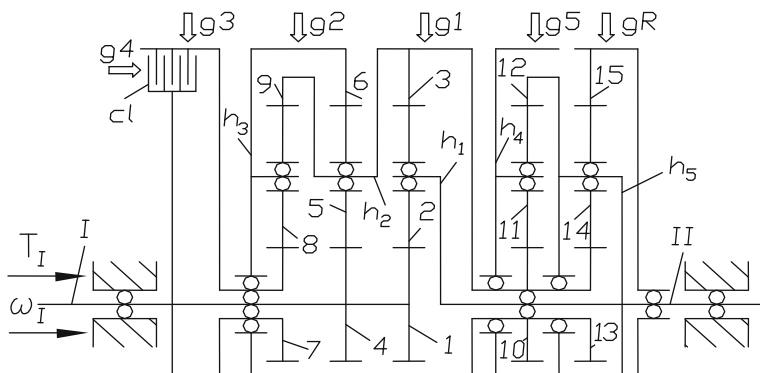


Fig. 1 Functional scheme of an exemplary gear

mechanical systems) which in general can be divided into the following steps/phases: graph assignment, distinguishing of some subgraph and/or their algebraic representations, derivation of some codes of these structures, creation of system of equations and solution. The mentioned subgraphs, codes and equations are adequate for a particular mechanical problem e.g.: kinematics. The advantage is—that several phases of modeling can be computerized but all of them are algorithmic. The following problems—connected with gear boxes—were modeled and considered by means of graph methods: efficiency analysis and optimization [1], generation and detection of gear isomorphism [2], computer-aided sketching [3], analysis [4, 5], synthesis [6] and design [7] but also many others. Several different graphs were assigned to the automatic gear boxes: simple graphs [1–3], bond graphs [7], Hsu graphs [6] as well as modified Hsu graphs [4, 5] which here will be named as mixed graphs. So called contour graphs were also utilized [4, 5, 8, 9].

In the papers [4, 5] single planetary gears were analyzed by means of bond, contour and mixed graphs by the authors. In the present paper these methods will be applied for modeling of automatic gear boxes. An exemplary gear box is analyzed but it is done only to show the methods and their usefulness. Similar gear was analyzed in [8, 9]. So, this paper closes the series. Here only one drive is analyzed in details, however other drives are considered in the last mentioned papers.

2 Exemplary Gear and its Graphs

In the present paper, an exemplary gear is considered which simplified functional scheme is presented in Fig. 1. The gear has five planet wheels: 8, 5, 2, 11 and 14, five arms/carriers: h_1, h_2, \dots, h_5 , sun wheels 1 and 4 as well as several wheels with internal teeth e.g. 3, 6 and 9. Moreover some parts are stiffly coupled e.g. sun wheels 1 and 4 are fixed on the same shaft as well as carriers: h_1 and h_5 are connected to the other same shaft. So, some parts have the equal rotational speeds.

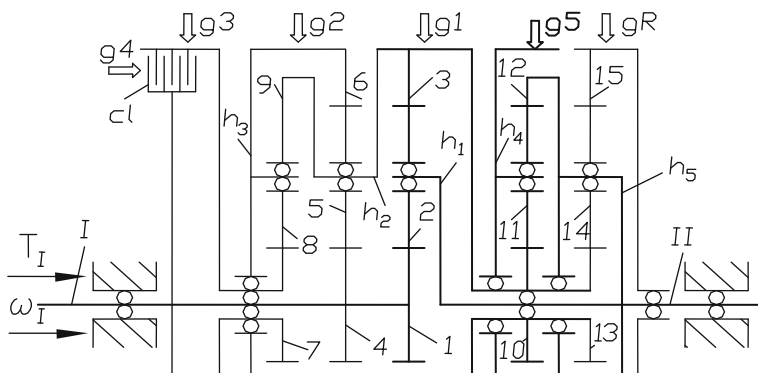


Fig. 2 Functional scheme of the considered gear box—fifth drive duty state; the active elements are marked by means of bold lines, redundant elements are drawn by means of thin line

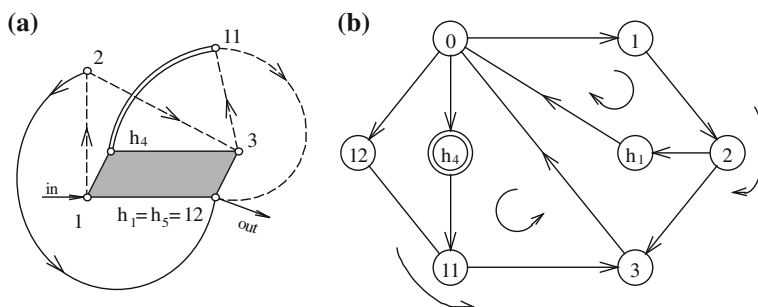


Fig. 3 Transformed graphs of the fifth drive gear working mode: **a** mixed graph. **b** contour graph

The particular drives are triggered via activation of particular control elements. Namely: drive “i” is achieved by an action of control element “ g_i ”, where there are brakes ($i = 1, 2, 3$ and 5) and a clutch ($i = 4$). A brake for the reverse drive is depicted as: “ g_R ”. In Fig. 2, the fifth drive mode is presented i.e. gear parts which are active in passing rotational movement from an input to an output are marked by bold lines. Other parts (drawn by thin lines) are temporarily redundant, but they are utilized. The teeth numbers are as follows: $z_2 = z_5 = z_8 = z_{11} = z_{14} = 30$; $z_3 = z_6 = z_9 = z_{12} = z_{15} = 84$ and $z_1 = z_4 = z_7 = z_{10} = z_3, \text{ ext} = 24$.

In Fig. 3, graph models of the gear box adequate for the 5th drive are presented. We named previously the 1st graph as modified Hsu graph [4, 5] but here it is called as mixed graph.

A mixed graph has edges and arcs simultaneously. It is worth to highlight that the shaded polygon (according to Hsu’s idea) is an adequate subgraph creating a clique. The clique edges symbolize the relations among the gear element (represented by vertices of the clique)—“rotation around the main symmetry axis of a planetary gear”. The introduced path (created of arcs) represents passing of rotational

movement and power from an input to an output. Only the transformed graph [10] relevant to fifth drive is shown. Complete graph of similar gear box is given in [8]. Additionally, so called contour graphs were also utilized [4, 5, 8, 9]. In this case, two (or even more) equations are assigning to every contour. Double lines for mixed graphs or double circles for contour graphs symbolize the braked parts.

3 Drive Ratios Calculations by Mixed and Contour Graphs

In the present chapter, kinematical analysis of gear boxes via graph methods is discussed based upon the exemplary gear. Like was described above calculation routine for the mixed graph is as follows: distinguishing of f-cycles and creation of their codes i.e.: (1, 2) h_1 , (2, 3) h_1 , (3, 11) h_4 and (11, 12) h_4 , where a description outside the brackets represents a carrier. Based on these cycle codes a system of kinematical equations can be written:

$$\begin{cases} \omega_1 - \omega_{h1} = -N_{2,1}(\omega_2 - \omega_{h1}) \\ \omega_2 - \omega_{h1} = +N_{3,2}(\omega_3 - \omega_{h1}) \\ \omega_3 - \omega_{h4} = -N_{11,3}(\omega_{11} - \omega_{h4}) \\ \omega_{11} - \omega_{h4} = +N_{12,11}(\omega_{12} - \omega_{h4}) \\ \omega_{h4} = 0 \end{cases} \quad (1)$$

Solution of the system is as follows:

$$\frac{\omega_1}{\omega_{h1}} = 1 + \frac{z_3}{z_1} \left(\frac{z_{12}}{z_{3,ext}} + 1 \right) = 16,75 \quad (2)$$

In case of contour graphs, the codes of contours have to be created. Every code yields two kinematic equations. The equations are vector-type but the vector values can be turned into scalar ones due to co-linearity of the considered vectors and the fact that the vectors of rotational velocities and radiuses are perpendicular ($\sin 90^\circ = 0$). The following relations among the radiuses can be established; where A—is for the lower engagements point, B—for planet axels and C—for internal engagements—tangential point of the adequate pitch diameters:

$$\begin{cases} r_A = r_1 = r_4 = r_{3,ext} \\ r_B = r_1 + r_2 \\ r_C = r_1 + 2 \cdot r_2 \end{cases} \quad (3)$$

The codes of contours are: $0 \rightarrow 1 \rightarrow 2 \rightarrow 3 \rightarrow 0$; $0 \rightarrow 1 \rightarrow 2 \rightarrow 3 \rightarrow 0$; $0 \rightarrow 12 \rightarrow 11 \rightarrow 3 \rightarrow 0$ and $0 \rightarrow h_4 \rightarrow 11 \rightarrow 3 \rightarrow 0$. Therefore the following system of equations can be written:

$$\begin{cases} \omega_{10} + \omega_{21} + \omega_{32} + \omega_{03} = 0 & \omega_{21} \cdot r_A + \omega_{32} \cdot r_C = 0 \\ \omega_{10} + \omega_{21} + \omega_{h1,2} + \omega_{0,h1} = 0 & \omega_{21} \cdot r_A + \omega_{h1,2} \cdot r_B = 0 \\ \omega_{12,0} + \omega_{11,12} + \omega_{3,11} + \omega_{03} = 0 & \omega_{11,12} \cdot r_C + \omega_{3,11} \cdot r_A = 0 \\ \omega_{h4,0} + \omega_{11,h4} + \omega_{3,11} + \omega_{03} = 0 & \omega_{11,h4} \cdot r_B + \omega_{3,11} \cdot r_A = 0 \end{cases} \quad (4)$$

Additionally, $\omega_{h4,0} = 0$. The solution consists in elimination of relative rotational velocities: ω_{ij} i.e. velocity of part “i” in relation to part “j”. We tend to leave only the velocities in relation to the support system marked by 0. Then ω_{i0} is just equal to ω_i . It was assumed that we consider cylindrical geared wheel as well as that the module is the same for all wheels. Therefore appropriate radiuses can be replaced by adequate tooth numbers.

Solution of the system (4) gives the same result as previously despite the fact that the set of different notions is considered.

Other drives can be analyzed in the same way—for every drive a transformed graph should be considered which is obtain from the general graph of the gear. The transformation rules consists in representation of gear elements which are drawn by bold line in Fig. 2. It simplifies the analysis. The following ratios for the consecutive drives (gears) where obtained: 4.5; 2.5312; 1.58; 1.0; 16.75; −11.25 (reverse drive).

4 Bond Graphs Approach

The analysis of toothed gears is possible using power flow graphs (bond graphs). However, this method gives insight into dynamical processes within engineering systems [11] and moreover enables synthesis of mechatronic systems [12], we use bond graphs methodology only to find out kinematical dependencies of the gearbox. We consider here the first drive. The bond graph is shown in Fig. 4a. This bond graph depicts the kinematics of the planetary gear for the first drive. All kinematical pairs for the first drive have assigned corresponding nodes (called transformers) **TF** with weights n_i . These weights are equal to local kinematical ratios of all consecutives pairs. Since, angular velocity $\omega_3 = 0$ (braked part 3), the graph has simplified form shown in Fig. 4b. The simplification was performed according to the general rules for bond graphs transformations.

The weight of the transformer **TF** : n is equal to product of n_1 and n_2 (Fig. 4b):

$$n = \frac{1}{3} r_A \frac{1}{r_B} = \frac{1}{2} \frac{z_1}{z_1 + z_2} = \frac{1}{4.5} = 0,22 = \frac{\omega_{h1}}{\omega_1} \quad (4)$$

Note that it is the inverse of ratio coefficient for the first drive.

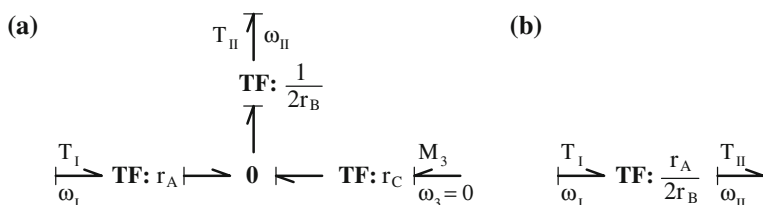


Fig. 4 Bondgraphs for the first drive of the gear: **a** general case. **b** simplified graph

5 Conclusions

In the present paper, three graph methods were applied for a kinematical analysis of an exemplary gear box. The five fore-drives (and reverse drive) automatic gear box has been considered. Kinematical analyzes were performed. Only two drives were considered in details but are only due to paper length rules. The methods allow for comparison of calculations within the conceptual phase of design.

References

1. Zhao, N., Jia, Q.: The efficiency analysis and optimization of gear trains. *Adv. Manuf. Technol.* **156–157**, pp. 1000–1005 (2010)
2. Srinath, A., Singh, S., Jagadeesh, A.: Computerized generation and detection of isomorphism in kinematic linkages/planetary gear trains, *Int. J. Adv. Sci. Technol.* 2(5), 19–28 (2011)
3. Chatterjee, G., Tsai, L.W.: Computer aided-sketching of epicyclic-type automatic of transmission gear trains. University of Maryland, ISR, TR 1995–92
4. Drewniak, J., Kopeć, J., Zawiślak, S.: Graph based analysis of planetary gears. *ACC J.* XVII, 1/2011, pp. 15–23
5. Drewniak, J., Zawiślak, S.: Analysis and modification of planetary gears based upon graph-theoretical models. *Trans. Univ. Košice.* **2**, pp. 84–87 (2009)
6. Hsu, C.-H., Hsu, J.-J.: Epicyclic gear trains for automotive automatic transmissions., *J. Automobile Eng.* **214**(5), pp. 523–532 (2000)
7. Coudert, N. Dauphin-Tanguy, G.: Mechatronic design of an automatic gear box using bond graphs., *Conference Proceedings 'Systems, Man and Cybernetics'*, **2**, pp. 216–221(1993)
8. Drewniak, J., Zawiślak, S.: An analysis of multi-speed epicyclic gears by means of graph-theoretical methods. *Int. J. Appl. Mech. Eng.* (accepted for printing in March 2012)
9. Drewniak, J. Zawiślak, S.: Graph-based models of compound planetary gears. *Solid State Phenom.* (submitted for printing in March 2012)
10. Zawiślak, S. et al.: Some application of graph transformations in modeling of mechanical systems. *International Workshop on Graph Transformations and Visual Modeling Technique*, Budapest, pp. 332–345 (2008)
11. Brown, F.T.: *Engineering System Dynamics: A Unified Graph-Centered Approach*, Marcel Dekker, New York, Basel, (2001)
12. Kopeć, J., Applying bondgraphs for modeling and analysis of discrete mechanical systems, manuscript of Ph.D. Thesis, University of Bielsko-Biała, in Polish (2009)

Part II
Analysis and Synthesis of Planar
and Spatial Mechanisms, Linkages
and Cams

Direct and Inverse Kinematic of 3DOF Parallel Mechanism with Singularity Analysis

J. Bałchanowski

Abstract This paper presents the structure and geometry of a new translational parallel mechanism. Relations for the analysis of the direct and inverse kinematics problems are derived. An analytical procedure for determining the system's singular positions is presented and illustrated with examples.

Keywords Parallel mechanisms • Direct and inverse kinematic • Singularity

1 Introduction

In translational parallel mechanisms the follower, i.e. the platform, can perform only three translational motions relative to the base at a constant orientation. Such systems are used mainly in three-axis milling machines, assembling or packing manipulators (e.g. ABB 340, Fanuc M-1iA, M-3iA) or translational positioners. Parallel mechanisms owe their peculiar translational properties to the well-matched topology and structure, the form of the kinematic pairs and the geometry of the members [1, 2].

This paper describes the geometry and kinematics of a new translational parallel mechanism MT3100 with linear drives, developed as part of the research on parallel mechanisms conducted in the Mechanical Engineering Faculty at Wrocław University of Technology [3]. Also an analysis of the mechanism's singular positions is presented.

J. Bałchanowski (✉)
Wrocław University of Technology, Wrocław, Poland
e-mail: Jacek.Balchanowski@pwr.wroc.pl

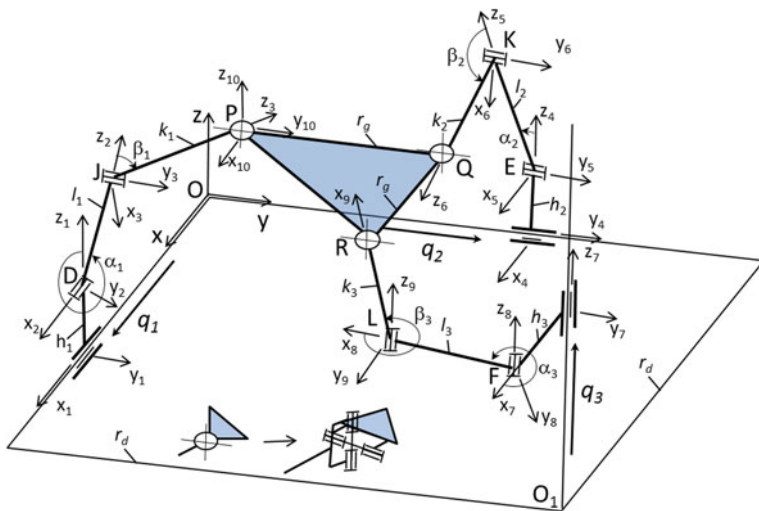


Fig. 1 The translational parallel mechanism mt3100—kinematic scheme

2 Design and Geometry of Parallel Mechanism mt3100

A translational parallel mechanism with three degrees of freedom, denoted as mt3310, is considered [3]. Its structure and kinematic diagram are shown in Fig. 1.

The mechanism consists of base and 10 moving members connected by 3 translational pairs (at the base), 6 rotational pairs and 3 universal (Cardan) joints. In order to ensure that the mechanism's follower 10 (the platform) performs only translational motions relative to the base while maintaining a constant orientation for any movement of linear drives q_1 , q_2 , q_3 , a peculiar geometry of the position of the rotation axes of the pairs relative to each other (shown in Fig. 1) needs to be determined [3].

3 Kinematic Analysis of Parallel Mechanism mt3100

Basic relations for the kinematic analysis of the parallel translational mechanism are derived below. The formulas are used to describe the kinematics direct and inverse problems and form the basis for determining singular configurations.

Equations for the mechanism constraints are derived using the vector notation method [4]. Accordingly, the kinematic chain is replaced by an appropriate vector chain. In the considered case, three closed contours (each for a different branch of the mechanism) were obtained and the closing vector is the vector describing the position of the follower.

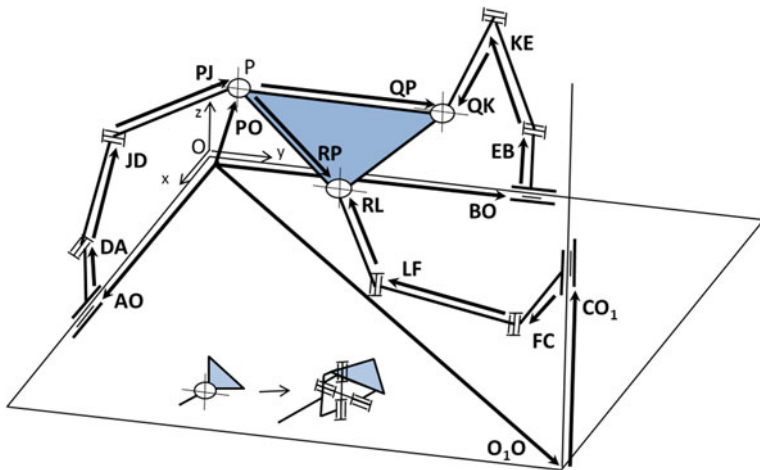


Fig. 2 Vector contours against parallel mechanism mt3100

A global system of coordinates xyz was located on base (Fig. 1). Local systems of coordinates $x_i y_i z_i$ ($i = 1 \div 10$) were defined on the mechanism members. Dimensions $h_1, h_2, h_3, l_1, l_2, l_3, k_1, k_2, k_3$ describe the basic dimensions of respectively members $1 \div 9$ while r_d, r_g define the arrangement of the pairs on base and on platform 10 (Fig. 1). The position of follower 10 (the platform) is described by vector \mathbf{PO} . The orientation of the follower is constant, the latter being parallel to base 0. Under the above assumptions, for each of the branches one can write the vector equation (Fig. 2):

$$\mathbf{AO} + \mathbf{DA} + \mathbf{JD} + \mathbf{PJ} = \mathbf{PO} \quad (1)$$

$$\mathbf{BO} + \mathbf{EB} + \mathbf{KE} + \mathbf{QK} = \mathbf{PO} + \mathbf{QP} \quad (2)$$

$$\mathbf{O_1O} + \mathbf{CO_1} + \mathbf{FC} + \mathbf{LF} + \mathbf{RL} = \mathbf{PO} + \mathbf{RP} \quad (3)$$

The left side of Eq. (4) describing contour DJP can be presented in the form of the product of the transformation matrices:

$$\mathbf{AO} + \mathbf{DO} + \mathbf{JD} + \mathbf{PJ} = \mathbf{A}_{01} \mathbf{A}_{12} \mathbf{A}_{23} \mathbf{r}_P^3 \quad (4)$$

where: \mathbf{A}_{ji} —matrices of transformation from the i -th member to the j -th member,

$$\mathbf{A}_{01} = \begin{bmatrix} 1 & 0 & 0 & q_1 \\ 0 & 1 & 0 & 0 \\ 0 & 0 & 1 & 0 \\ 0 & 0 & 0 & 1 \end{bmatrix}; \mathbf{A}_{12} = \begin{bmatrix} 1 & 0 & 0 & 0 \\ 0 & \cos \alpha_1 & -\sin \alpha_1 & 0 \\ 0 & \sin \alpha_1 & \cos \alpha_1 & h_1 \\ 0 & 0 & 0 & 1 \end{bmatrix}; \mathbf{A}_{23} \\ = \begin{bmatrix} \cos \beta_1 & 0 & \sin \beta_1 & 0 \\ 0 & 1 & 0 & 0 \\ -\sin \beta_1 & 0 & \cos \beta_1 & l_1 \\ 0 & 0 & 0 & 1 \end{bmatrix}$$

α_1, β_1 —rotation angles in rotational pairs D, J ;

$\mathbf{r}_P^3 = [0 \ 0 \ k_1 \ 1]^T$ —the vector of the location of point P on member 3

The right side of Eq. (4) is defined by the vector of the location of point P on the platform relative to the base:

$$\mathbf{PO} = [x_P \ y_P \ z_P \ 1]^T \quad (5)$$

Equating (4) and (5) and performing transformations, three equations describing the position of contour DJP were obtained. They have the form of the following constraints equations:

$$\Phi_1^P = \begin{bmatrix} q_1 - x_P + k_1 \sin(\beta_1) \\ -y_P - l_1 \sin(\alpha_1) - k_1 \cos(\beta_1) \sin(\alpha_1) \\ h_1 - z_P - l_1 \cos(\alpha_1) + k_1 \cos(\alpha_1) \cos(\beta_1) \end{bmatrix} = 0 \quad (6)$$

Transforming similarly contour Eqs. (5) and (6) for contours EKQ and FLR , using appropriate transformation matrices, the following constraints equations for EKQ were obtained:

$$\Phi_2^P = \begin{bmatrix} k_2 \sin(\alpha_2 + \beta_2) - x_P + l_2 \sin(\alpha_2) \\ q_2 - y_P - r_g \\ h_2 - z_P - k_2 \cos(\alpha_2 + \beta_2) + l_2 \cos(\alpha_2) \end{bmatrix} = 0 \quad (7)$$

For contour FLR the constraints assume the following form:

$$\Phi_3^P = \begin{bmatrix} h_3 - x_P - r_g + r_d + k_3 \cos(\alpha_3 + \beta_3) + l_3 \cos(\alpha_3) \\ r_d - r_g - y_P + k_3 \sin(\alpha_3 + \beta_3) + l_3 \sin(\alpha_3) \\ q_3 - z_P \end{bmatrix} = 0 \quad (8)$$

where: $\alpha_2, \beta_2, \alpha_3, \beta_3$ —the angles of rotation in pairs E, K, F, L .

Equations (6), (7) and (8) form a system of constraints for the considered parallel mechanism mt310.

3.1 Direct and Inverse Kinematics of *mt3100* Mechanism

The simple kinematics problem consists in determining the position of follower **PO** for prescribed kinematic excitations q_1, q_2, q_3 (Figs. 1,2). Mechanism constraints matrix Φ^P is defined on the basis of constraints Eqs. (6), (7) and (8) for the particular branches:

$$\Phi^P = [\Phi_1^P \Phi_2^P \Phi_3^P]^T \quad (9)$$

By solving the above system of nine nonlinear equations with regard to prescribed q_1, q_2, q_3 one gets the unknown configuration (the position of follower 10), i.e. vector $\mathbf{PO} = [x_P \ y_P \ z_P]^T$ and the orientation angles $\alpha_1, \beta_1, \alpha_2, \beta_2, \alpha_3, \beta_3$ of the other members of the mechanism.

The velocity equation for the simple kinematics problem was obtained by differentiating Eq. (9) over time. After basic algebraic transformations and ordering the velocity equation assumes the form:

$$\Phi_q^d [\dot{\alpha}_1 \ \dot{\alpha}_2 \ \dot{\alpha}_3 \ \dot{\beta}_1 \ \dot{\beta}_2 \ \dot{\beta}_3 \ \dot{x}_P \ \dot{y}_P \ \dot{z}_P]^T = \mathbf{F}_q \quad (10)$$

where: $\mathbf{F}_q = [\dot{q}_1 \ 0 \ 0 \ 0 \ \dot{q}_2 \ 0 \ 0 \ 0 \ \dot{q}_3]^T$ is the velocity vector of actuators q_1, q_2, q_3 .

Matrix Φ_q^d can also be presented in the form:

$$\Phi_q^d = [A, B_q] \quad (11)$$

where:

$$A = \begin{bmatrix} 0 & 0 & 0 & k_1 \cos \beta_1 & 0 & 0 \\ \begin{pmatrix} -\cos \alpha_1 \\ (l_1 + k_1 \cos \alpha_1) \\ -\sin \alpha_1 \end{pmatrix} & 0 & 0 & k_1 \sin \alpha_1 \sin \beta_1 & 0 & 0 \\ 0 & 0 & 0 & k_1 \cos \alpha_1 \sin \beta_1 & 0 & 0 \\ 0 & \begin{pmatrix} k_2 \cos(\alpha_2 + \beta_2) + \\ + l_2 \cos \alpha_2 \end{pmatrix} & 0 & 0 & -k_2 \cos(\alpha_2 + \beta_2) & 0 \\ 0 & 0 & 0 & 0 & 0 & 0 \\ 0 & \begin{pmatrix} -k_2 \sin(\alpha_2 + \beta_2) + \\ -l_2 \sin \alpha_2 \end{pmatrix} & 0 & 0 & -k_2 \sin(\alpha_2 + \beta_2) & 0 \\ 0 & 0 & \begin{pmatrix} -k_3 \sin(\alpha_3 + \beta_3) + \\ -l_3 \sin \alpha_3 \end{pmatrix} & 0 & 0 & -k_3 \sin(\alpha_3 + \beta_3) \\ 0 & 0 & \begin{pmatrix} k_3 \cos(\alpha_3 + \beta_3) + \\ + l_3 \cos \alpha_3 \end{pmatrix} & 0 & 0 & k_3 \cos(\alpha_3 + \beta_3) \\ 0 & 0 & 0 & 0 & 0 & 0 \end{bmatrix}$$

$$\mathbf{B}_q = \begin{bmatrix} -1 & 0 & 0 & -1 & 0 & 0 & -1 & 0 & 0 \\ 0 & -1 & 0 & 0 & -1 & 0 & 0 & -1 & 0 \\ 0 & 0 & -1 & 0 & 0 & -1 & 0 & 0 & -1 \end{bmatrix}^T$$

The inverse problem of the parallel mechanism kinematics consists in determining kinematic excitations q_1, q_2, q_3 from the platform 10 position defined by vectors $\mathbf{PO} = [x_P \ y_P \ z_P]^T$ (Figs. 1,2).

Constraints matrix Φ^P has the same form (9) as for the direct problem. Solving this system of nonlinear equations with regard to the follower 10 position defined by vector \mathbf{PO} prescribed by coordinates x_P, y_P, z_P one gets the unknown inverse kinematics problem configuration in the form kinematic excitations q_1, q_2, q_3 and the orientation angles in pairs $\alpha_1, \beta_1, \alpha_2, \beta_2, \alpha_3, \beta_3$.

Having *differentiated* the constraints equation, one gets a velocity equation for the inverse kinematics problem, which after algebraic transformations and ordering assumes the form:

$$\Phi_q^i \begin{bmatrix} \dot{\alpha}_1 & \dot{\alpha}_2 & \dot{\alpha}_3 & \dot{\beta}_1 & \dot{\beta}_2 & \dot{\beta}_3 & \dot{q}_1 & \dot{q}_2 & \dot{q}_3 \end{bmatrix}^T = \mathbf{F}_P \quad (12)$$

where: $\mathbf{F}_P = [\dot{x}_P \ \dot{y}_P \ \dot{z}_P \ \dot{x}_P \ \dot{y}_P \ \dot{z}_P \ \dot{x}_P \ \dot{y}_P \ \dot{z}_P]^T$ is the vector of platform velocity.

Matrix Φ_q^i is expressed by the formula:

$$\Phi_q^i = [\mathbf{A}, \mathbf{B}_P] \quad (13)$$

where: $\mathbf{B}_P = \begin{bmatrix} 1 & 0 & 0 & 0 & 0 & 0 & 0 & 0 & 0 \\ 0 & 0 & 0 & 0 & 1 & 0 & 0 & 0 & 0 \\ 0 & 0 & 0 & 0 & 0 & 0 & 0 & 0 & 1 \end{bmatrix}^T$

4 Analysis of Singular Positions of Mechanism

A singular position (configuration) of a system occurs when the latter is kinematically indeterminate. Such positions of the mechanism are commonly referred to as singular or dead positions. When the system is brought into a singular position, its kinematic and dynamic properties change. The values of some of its parameters (forces, velocities and accelerations) become indeterminate or approach infinity. In some cases, the occupation of singular positions by the members of the mechanism may result in the destruction of or damage to the mechanism [4, 5].

For the considered mechanism's direct and inverse kinematics problems singular *configurations* occur when matrices Φ_q^d and Φ_q^i from velocity Eqs. (10) and (12) are singular, i.e. when

$$\det(\Phi_q^d) = 0 \quad \det(\Phi_q^i) = 0 \quad (14)$$

After determinants (14) are determined and algebraic transformations are performed, singular positions for the direct and inverse kinematics problems will occur provided that the following equation is equal to zero:

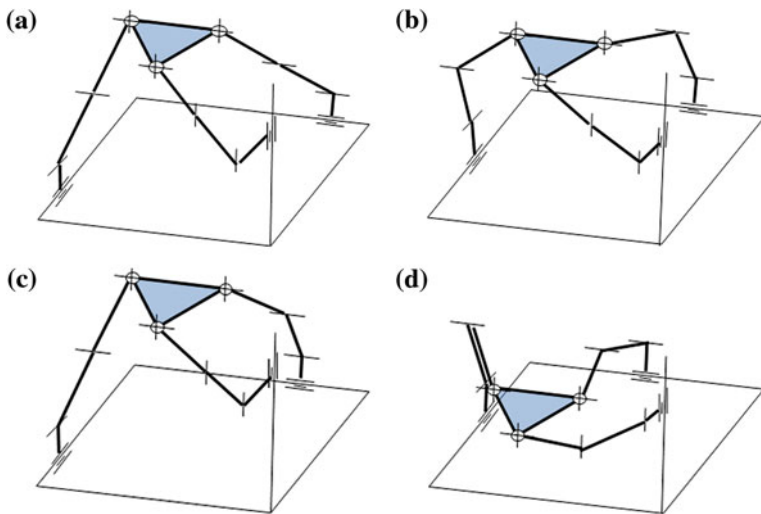


Fig. 3 Examples of singular configurations of mechanism mt3100 for direct and inverse kinematics problem: **a** for $\beta_1, \beta_2, \beta_3 = 0$; **b** for $\beta_3 = 0$; **c** for $\beta_1 = 0$ and $\beta_3 = 0$; **d** for $l_1 = k_1$ and $\beta_1 = \pi$

$$\det(\Phi_q^d) = \det(\Phi_q^i) = -k_1 k_2 k_3 l_2 l_3 \sin(\beta_1) \sin(\beta_2) \sin(\beta_3) (l_1 + k_1 \cos(\beta_1)) = 0 \quad (15)$$

It follows from the above equation that the singular configurations for the direct problem and the inverse problem are the same. The equation holds true when any of the elements of the product in Eq. (15) is equal to zero. This occurs in the cases:

$$(\beta_1 = 0) \text{ or } (\beta_2 = 0) \text{ or } (\beta_3 = 0) \text{ or } (l_1 = k_1 \text{ and } \beta_1 = \pi)$$

The first three conditions mean that members 2 and 3, 5 and 6, 8 and 9 are straightened. The fourth condition is satisfied for members 2 and 3 ($l_1 = k_1$) arranged along each other. The next Figs. 3 show the considered mechanism in its singular positions.

5 Conclusions

The geometry and kinematics of a translational parallel mechanism with linear drives, with three degrees of freedom was analysed and the singular positions of the mechanism were determined. The geometric conditions which the dimensions of the members and of the kinematic pairs must satisfy in order for the considered mechanism to be able to perform its translational motions were determined.

The occurrence of singular positions in the work zone of parallel mechanisms is one of the drawbacks of such systems. Therefore analyses aimed at determining

their *singular* configurations should not be neglected in the design process. If such a mechanism is to be used, it should be so designed as to prevent it from getting into a singular position while performing tasks.

References

1. Tsai Lung-Wen: Robot Analysis. The Mechanics and Parallel Manipulators. Wiley, New York (1999)
2. Merlet, J-P.: Parallel Robots, Kluwer Academic Publishers, London (2000)
3. Bałchanowski, J.: Topology, geometry and kinematics selected translational parallel mechanisms (in Polish). Przegląd Mechaniczny. 2008 R. 67, nr 10.
4. Bałchanowski, J., Prucnal-Wiesztort, M.: Translational parallel mechanisms. Elements of kinematics with singularity analysis. X. International conference on the theory of machines and mechanisms. Liberec, Czech Republic, 2008
5. Merlet, J-P.: Singular configurations of parallel manipulators and grassmann geometry. Int. J. Robot. Res. **8**, (1992)

Measuring of Radial Cams Contours

V. Crhak

Abstract Measurements of radial contours on a single-purpose cam grinding machine to speed up and refine their production. Measurement methods were described in terms of accuracy and integration into the machine structure. It is mentioned the suitability of selected principles of measurement and results of lasers and touch probe tests. Transfer of measured data from the measuring device to the PLC with their evaluation and modification.

Keywords Radial cam • Contour measurement • Measurement methods • Accuracy • Data transmission and processing

1 Introduction

The aim is to find a suitable inspection system for measuring the radial cam contours, which can be implemented into the construction of a single-purpose grinding machine, Fig. 1. Measuring equipment must meet the conditions for the ability to measure distances with accuracy up to 0.01 mm in the relatively severe operating conditions and with respect to the place for location in the machine.

V. Crhak (✉)

VÚTS, a.s., Technical University of Liberec, Liberec, Czech Republic
e-mail: v.crhak@vuts.cz

Fig. 1 Radial cam grinding machine



1.1 Theory

Measuring of radial cams contours can theoretically be performed in two ways. The first is the rotating workpiece measurement without moving of another machine axis. Gauge follows the contour and must cover the entire cam stroke in the range up to tens of millimeters. The result is a displacement diagram [1].

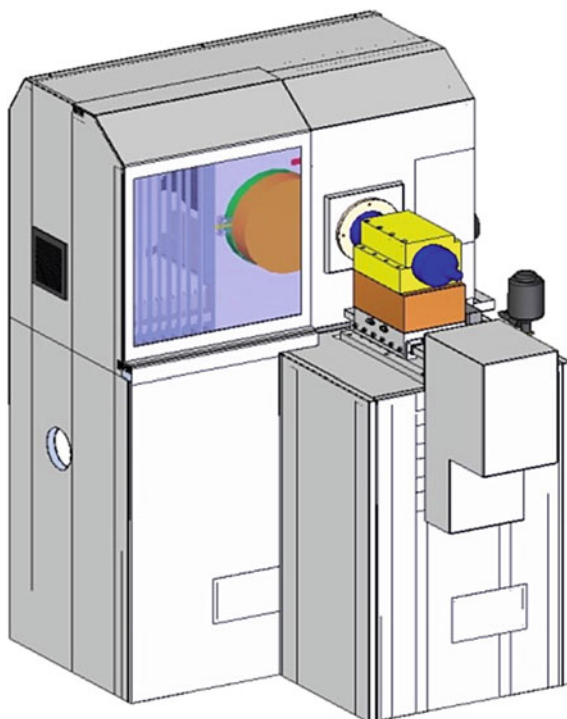
The second method of measurement is called “grinding simulation” when the machine is running according to the interpolation data as it would be working. If the cam surface was grinded with no deviations, the gauge would show zero displacement. This method allows directly get the difference between the calculated data and the real cam dimensions. With regard to touch measurement method come on force an application of linear sensor or swinging roller follower in conjunction with the rotary encoder. Contactless method suitable for the said purposes is based on using of laser.

Testing: Two cams were measured by external 3D measuring center with an accuracy of 3 μm and output data were set as reference values. Then both types of cams of the same profile, but with a normal surface and polished surface, Fig. 2 were measured with linear touch probe and laser sensor and data compared with reference input.

2 Position of Sensor, Geometric Measurement Errors

The cam profile must be measured at the exact point, which corresponds to a certain angle according to the calculated theoretical data in polar coordinates from the synthesis of cam [1]. It must therefore be guaranteed mutual position of the workpiece and gauge. The best way is to orient the gauge in a linear direction to the true center of the workpiece.

The correctness of measurement is ensured when the cam is clamped and exactly centered on the rotary table and zero angle point of the contour lies in a straight line between the center point of the cam and the measurement probe.

Fig. 2 Tested cam ST2

Geometric measurement errors depend on the measuring principle and construction of the measuring elements. These errors are suppressed when the beam has theoretically infinitely small projection area in case of laser or mechanical gauge has infinitely small element of the contact area. Such claims cannot be ensured in practice and errors must be eliminated by suitable selection of components and the results must be mathematically corrected.

3 Linear Touch Sensor

Linear mechanical sensor appears to be a relatively simple measurement method. With regard to control system hardware, which includes a digital card LIO-02 (Yaskawa) containing counter TTL level module, it is advantageous to use sensor with incremental pulses. Important is the measurement range and the associated measurement accuracy because the gauge nonlinearity is usually expressed as a percentage of full scale.

An error occurs at the cam profile where the normal line n is not parallel to the sensor axis x . The gauge actually measures at a point M instead of considered measuring at point M' , Fig. 3. The difference between correct angle of cam

Fig. 3 Geometric measurement error

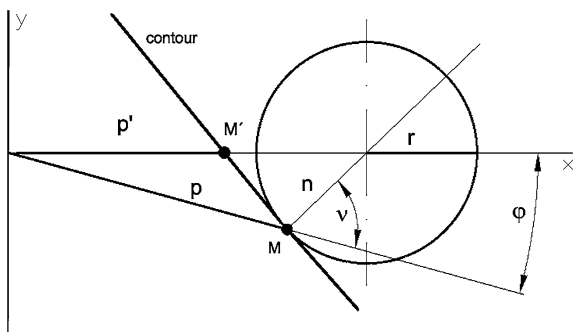
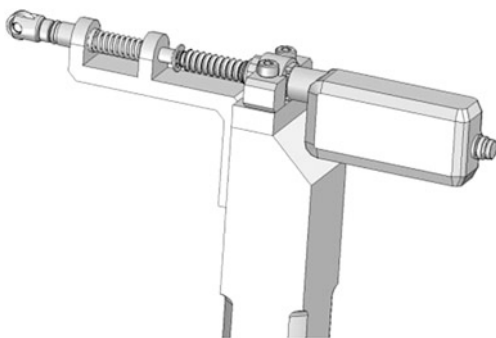


Fig. 4 Sensor with an auxiliary frame



rotation is equal to φ and length vector is p instead of p' . Quality of sensor manufacturing and its components has a large influence on the measurement accuracy, especially for general telescopic element with ruby or metal ball. Sliding rod is misaligned by action of frictional forces. Due to this problem it is appropriate to use a roller with an auxiliary structure, Fig. 4, to reduce friction forces and the forces acting in the radial direction. There were chosen two renowned manufacturers of measuring devices, probe Larm MSL50 [4] and probe Keyence GT2-H12. The first one is used for measuring straight coordinates in the measuring range of 50 mm. GT2-H12K [2] sensor is an optical sensor system, providing resolution $0.1 \mu\text{m}$, accuracy $1.0 \mu\text{m}$ and measurement range 12 mm. It has high resistance against mechanical damage and ingress of water and dust (IP67 protection class) [3]. Disadvantage compared to MSL50 is necessity of using amplifiers for processing output signals. The advantage is the possibility of digital data transmission in case of using relevant hardware.

4 Laser Sensor

Laser measuring device with high-quality scanning heads for detecting the reflected beam in negative angles of reflection are available on the market. But success of measuring always depends on the concrete material, its color and

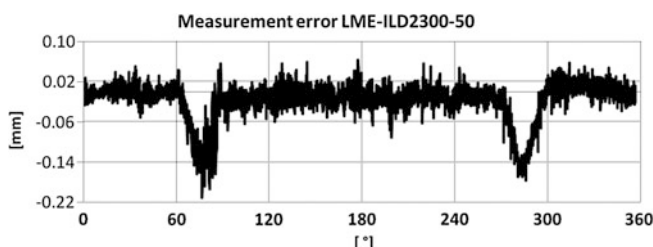


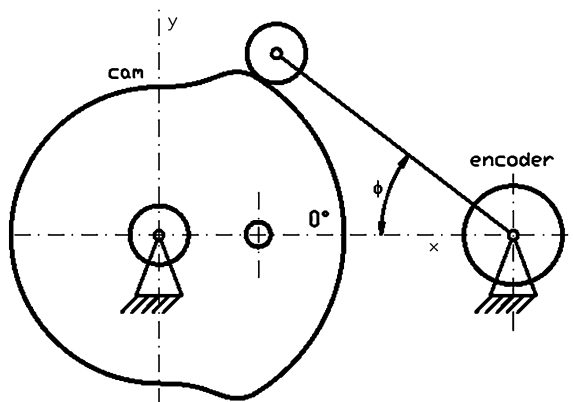
Fig. 5 Measurement protocol of micro-epsilon laser sensor

surface roughness. Software is an integral part of advanced types of sensors and correct setting plays a significant role. Beam emission setting, its intensity and frequency of measurement can considerably affect the results. Different products are more or less able to measure with the required accuracy, depending on the capabilities of the optimal automatic or manual settings. Incorrect setting has a direct impact on measurement accuracy and in extreme cases may result in inability to detect the reflected beam. Another factor that contributes to a successful measurement is the sensor position in relation to the measured workpiece, especially when rotating parts are measured, because the sensor is in principle designed for measuring in the expected direction of a beam reflected from the measured material. Laser devices differ in shape and surface projection of the emitted beam. Bar lasers with few millimeters wide oval shape beam are usually designed for shiny reflective surfaces. Insufficient reflection is compensated by sensing light returned from a larger area. The average distance from the whole illuminated area is calculated according to the used evaluating principles. Therefore, it is necessary to ensure the location of the probe in a purely perpendicular direction to the measured object. Minimum projection of transmitted laser beam is in the reference measurement distance. With change of this distance are also changed measurement errors due to increasing surface reflection.

Optical measurement techniques are disadvantageous in relation to finely polished or machined metal products because of the problematic ray reflectivity. The problem arises especially in the cam contours, where the gradient exceeds a certain level and the beam after reflection is not returned in sufficient intensity back to the sensor.

For testing the suitability of using a laser measurement was borrowed following measuring devices:

- 1) Keyence LK-H157: A special type of measuring head for measuring shiny surfaces with bar projection of laser light at the measurement point. The smallest attained measurement error at surface of a glossy cam was 0.3 mm. LK-H082: A more accurate variant of measuring head for the price of a smaller measuring range, shape of emitted light is point—allows greater measurement variability in areas with little surface. This sensor is designed for general surfaces [3]. It is able to detect the cam shiny material, but with less precision than the LK-H157. The maximum error reaches 0.47 mm.

Fig. 6 Rocker with follower

- 2) Best results were achieved using Micro-Epsilon ILD2300-50 under same circumstances. Maximum error of measurement is 0.15 mm in cam strokes. The difference between reference values and measured data is shown in Fig. 5. Laser Micro-Epsilon is a compact measuring head contains the sensor and controller in one.

5 Swinging Roller Follower

One of the variants determining real dimensions of the workpiece can be combination of a rotary encoder attached to the roller, Fig. 6. Measured values can be transformed into the real shape of tested cam and compared with the theoretical profile, because geometry of individual elements, such as the radius of the follower, the length of the roller and the distance of swinging axes from the workpiece center is known.

This set of parts can be simply designed as a passive mechanical measuring device where roller and follower operate only with a gravitational force. Rotary encoder is mounted on a rotary axis and measures the roller angle φ .

Another way is based on a rotary servomotor and its own encoder. Roller is directly mounted on the motor shaft. This axis is incorporated into the control system as another fully controlled axis with all possibilities it offers. It can be controlled in torque mode, so the measurement is performed with defined pressure of follower to the surface. Casual “bounce” of follower is suppressed and roller may be automatically positioned without physical intervention of operator and mutual location of the roller and workpiece is arbitrary.

6 Data Transmission and Modification

The aim is to obtain an output protocol, which contains the actual cam data. Results can be transferred to the PLC through the analog channel ± 10 V, serial transmission RS-232 or Ethernet network. Data are compared with the desired profile of the cam and modified using conversion algorithms. The difference between the real and the desired profile decrease in later grinding stages. The process of measuring and grinding operation is controlled individually according to the required parameters.

7 Conclusions

In order to verify the accuracy of radial cams grinding was analyzed suitable measuring equipment. When laser micrometer is used, problems arise at a very shiny surface of cam strokes, where the beam is reflected at an acute angle (congestion amount of reflected light directly returned to the receiver), or at an obtuse angle, where most of the reflected light from the object goes out of receiver. There was created program in Microsoft Excel for results evaluation and to ensure an objective comparison by graphical analysis. None of the tested laser gauge meets requirements completely for measuring cam surface with a roughness of $R_a = 0.5 \mu\text{m}$.

There were also tested touch probes. Problems with deflection of telescopic parts in radial direction were detected and resulted in a measurement error of approximately $\pm 20 \mu\text{m}$ in case of Larm MSL50. Probe cannot operate with the prescribed properties without an auxiliary mechanism, Fig. 4, which eliminates radial forces.

Based on comparing the final cost, speed of implementation and measurement accuracy was selected measurement touch probe Keyence GT-H12K.

The benefit of mentioned cam profile verification is more accurate workpiece control and speed up the production of radial cams.

References

1. Koloc, Z.; Václavík, M., Vačkové mechanismy, Praha: SNTL, 1988. 384 s
2. MICRO-EPSILON, katalog *Přehled výrobků*, s. 8–9 [Y9760185-010096MLO]
3. KEYENCE, catalogue high-precision contact digital senso, p. 28 [GT2-WW-C-E 0019-2]
4. Katalog, Larm, Optoelektronické snímače, XX. upravené vydání—IX. (2008)

High-Speed Parallel Shaft Indexing Drive

P. Dostrašil, F. Hartig, M. Václavík and P. Jirásko

Abstract VÚTS, a.s., has been involved in the design and manufacture of parallel shaft indexing drive for many years. Market requirements are placed on the ever increasing numbers of steps in time or high input speed, which brings special demands on the structure and materials of the gearbox components. The paper analyzes the issues of high-speed of those mechanisms. The computational methodology of the important lightweight of cam contours is depicted. Other problems concerning high speed are outlined in the paper.

Keywords Radial cam • Double cam • Displacement diagram • Lightweight of cam contour • Indexing drive

1 Introduction

At present, an intensive defining of the scope of application of conventional and electronic cams is being carried out. Electronic cams are growing considerably in economic importance due to their re-programming of displacement diagrams.

P. Dostrašil (✉) · F. Hartig · M. Václavík · P. Jirásko
VÚTS, a.s, Liberec, Czech Republic
e-mail: pavel.dostrasil@vuts.cz

F. Hartig
e-mail: fillip.hartig@vuts.cz

M. Václavík
e-mail: miroslav.vaclavik@vuts.cz

P. Jirásko
e-mail: petr.jirasko@vuts.cz

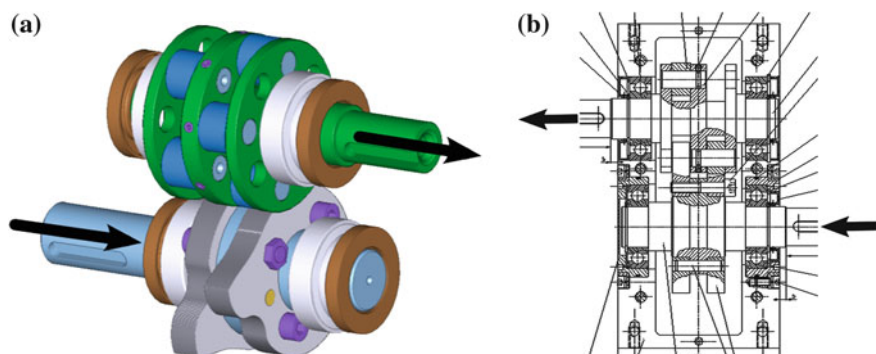


Fig. 1 Indexing drive and gearbox with radial cams

However, conventional cam mechanisms will not long be replaced by electronic cams in dynamically demanding applications [1]. For example, such applications are high-speed mechanisms with periodic or non-periodic displacement diagrams. In this paper, we will be dealing with indexing drive.

2 Parallel Shaft Indexing Drive

Indexing drives are manufactured with radial, axial and globoid cams. With regard to a high dynamic load from the inertia masses and working technological forces, the mechanisms with radial cams are the most advantageous according to Fig. 1 (the arrows indicate uniform rotary input and step rotary output). The advantage is their relatively easy production and especially in two-sides mounted rollers in the carousel (output link with step motion).

VÚTS, a.s., has been engaged in the indexing drives or gearboxes with radial cams for many years [2]. It manufactures gearboxes in a standard size range of 65, 80, 105 and 120 mm of the axial distance of cam and carousel rotation (Fig. 1).

3 The Issues of High-Speed Indexing Drives

High-speed requirements depend on the production technology. For example, the manufacturers of forming machines for the production of nails require revolutions above $1200 \text{ [min}^{-1}]$. In order to meet those requirements on high speed, it means to address a number of design, material and computational problems. For example, the dimensional accuracy of cam contours, mounting and lubricating the carousel rollers, cam and roller material, cam manufacture are the fundamental problems. The calculation of cams and the design of displacement diagrams require special

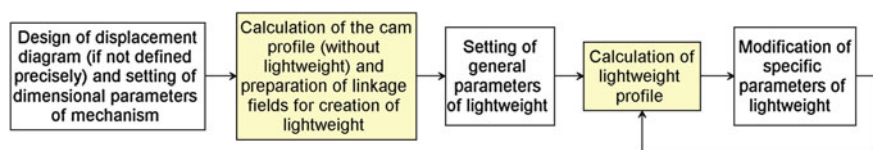


Fig. 2 Description of the cam profile synthesis with highlighting the parts for the calculation of lightweight

computer software that solves all geometric parameters of the cam mechanism in a productive manner [3].

4 Lightweight of the Contours of Radial Double Cams

The requirement for dimensional accuracy of the cam contours is essential. The tolerance of the cam active surface should not exceed the values of ± 0.01 mm. The most important, however, is the creation of the so-called cam contour lightweight which ensures that only two rollers are always in contact with the cam contours.

The process of lightweight the cam profile can be divided into two parts. The first part consists in the preparation of auxiliary fields that store information about the link between the individual roller contacts on both cams. By using those fields, for a specific profile point of one of the cams it is possible to determine the points where other rollers contact the cam profiles.

Based on the user-defined parameters and the amount of calculated auxiliary fields, in the second part of the process there will be defined the intervals of cam profile where lightweight will occur. In those intervals, there will be then carried out the superposition of cam profile (its radius) with the chosen displacement diagram (Fig. 2).

4.1 Preparation of Linkage Fields

The preparation of linkage fields already proceeds during the synthesis of the profile because it can be advantageous to use also the auxiliary data being generated during the synthesis. Moreover, the change of the parameters of lightweight will not influence those linkage fields so that it is not necessary to adjust them when modifying parameters in any way. The cam profile is defined by a radius vector which consists of angle φ and radius u . At first, a function defining the dependence of rotating (displacing) master shaft τ on angle φ will be created (i.e., the reverse process takes place than that in the synthesis). Then, the resulting function has the jumps due to the change of the active roller. For better handling,

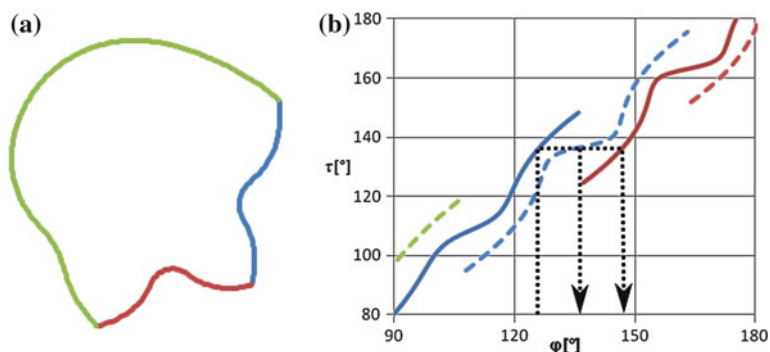


Fig. 3 Cam division into sections and a detail of the graphical solution of finding the points of contact (the dashed line indicates the second cam)

this field is off-rotated and divided into several smaller ones according to these jumps.

The following Figures demonstrate this division and the subsequent graphic solution. For a particular angle ϕ , it can be unambiguously determined the angle of rotation of shaft τ . If we will lead through this point a parallel to axis x , we will always find (a minimum of one, a maximum of three) other intersections with functions $\tau(\phi)$. After re-subtracting the values in the horizontal axis, we will get other contact points of the rollers with the cam. In the numerical solution, it is necessary to take into account many other factors, for their analysis there is not enough place here, so I will mention them only in brief. It is not possible to predict how many more contact points will be assigned to a specific angle ϕ . In addition to the situation that is shown in the Figures below, a cam can have only one point of discontinuity. These two situations require the significantly different way of finding points of contact then.

The output of this section are two fields (one for each cam) with three columns. The index of the row corresponds to the index of the point of contact of the first roller and the remaining three columns contain indices to other points of contact (minimally one, maximally three). The calculation of those fields is a quite complex and time-consuming problem. On the other hand, the calculation of a particular lightweight is a very quick matter then (Fig. 3).

4.2 The Implementation of Lightweight

The main objective of lightweight is to avoid the over-determining of a mechanism, thus eliminating redundant links (it is necessary to ensure that just two rollers are in contact with the cams). It is necessary to find in the cam profile the intervals of the values of angle ϕ for which the value of radius u will be diminished in a specific way so that the touching of the roller and the cam can be

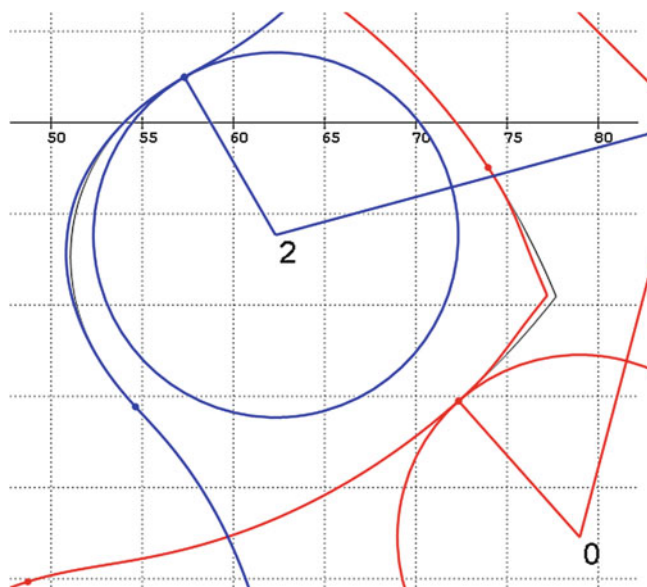


Fig. 4 Detail of the mechanism in its marginal position from Fig. 4

avoided. At the beginning of the lightweight section, it is necessary to ensure a smooth change of the radius (i.e., the continuity of zero, the first and ideally also the second derivative of radius u), for an impact-free running of the roller. Therefore, a displacement diagram will be applied that will be extended to the length of the selected interval and subtracted from it. The interval part where the roller is in a safe distance from the cam can be replaced by a circular arc to reduce the total maximum radius of the cam.

The first step is to choose the intervals where lightweight will be realized. The selection of the interval depends on many factors, from the dimensional parameters up to loading, etc. Therefore, at first, the algorithm will enable the user to specify the general parameters of lightweight for all intervals, i.e., the angle size and the depth of lightweight in the pit and on the top. Using the linkage fields, an automatic calculation of lightweight will be subsequently carried out, as shown in the Figure below. Then, the user can perform the adjustments of particular intervals according to specific requirements and immediately observe their influence on the kinetostatic parameters of the cam. For example, the maximum angle of pressure into the required limits can be easily adjusted.

To create the final lightweight profile, the superposition of the cam radius with a specific function is applied then. The specific shape of this function is important for two reasons. First and foremost, it must ensure an impact-free incidence (running) of the roller to the cam. If the cam is made by grinding, it is important to prevent such profile adjustment that would be too complicated for the manufacture. A significant parameter is the radius of curvature of the profile that has a

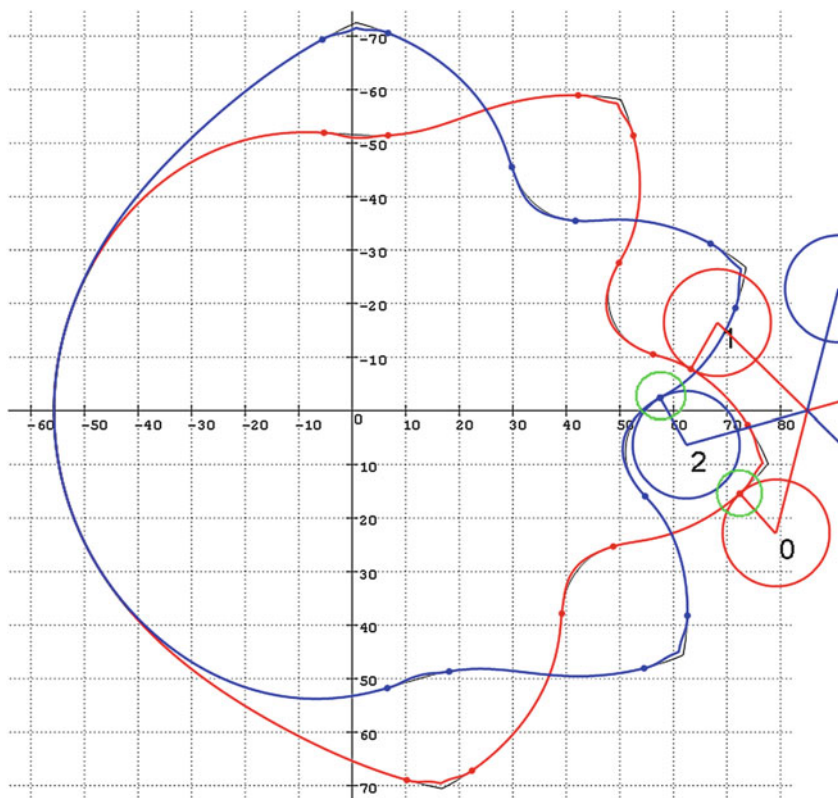


Fig. 5 Detail of the mechanism in its marginal position from Fig. 4

direct impact on the size of the grinding tool. It can be significantly smaller than it is the carousel roller radius when choosing lightweight inconveniently (Fig. 5).

5 Conclusions

The limited extent of the paper does not allow us to deal with other important factors such as the impact of asymmetric displacement diagrams or asymmetric initial positions of the cam carousel [3]. The automatic creation of cam contour lightweight (as part of computing software) is a highly productive tool for determining the optimal geometry of the cam contours of step cam mechanisms intended for the dynamically demanding applications.

References

1. Tesar, D., Ashok, P., Krishnamoorthy, G.: Preliminary design results for reprogrammable servocams, X. International Conference IFToMM, Liberec (CZ), 2–4 (2008)
2. Jirásko, P.: Methodology of electronic cam applications in drives of working links of mechanisms of processing machines, Dissertation, TU Liberec CZ, (2010)
3. Dostrašil, P., Jirásko, P.: Productive design and calculation of intermittent mechanisms with radial parallel cams. In world academy of science, engineering and technology. Issue 59. Part XV. Venice (Italy) : [s.n.], 2011. 1909–1913. Contribution to the conference ICAMME 2011. Available from WWW: <<http://www.waset.org/journals/waset/v59/v59-360.pdf>>. pISSN 2010-376X. eISSN 2010-3778

A Simplified Design with a Toothed Belt and Non-circular Pulleys to Separate Parts from a Magazine File

U. Hanke, K.-H. Modler, R. Neumann and C. Fischer

Abstract The objective of this paper is to simplify a very complex guidance mechanism, currently used for lid separating issues in a packaging-machine. The task of this machine is to pick up a lid from a magazine file, rotate it around 180° and place it on tins. The developed mechanism works successfully but with a very complex construction. It consists of a planetary cam mechanism, combined with a toothed gear (with a constant transmission ratio) and a guiding mechanism with a toothed belt and circular pulleys. Such complex constructions are very common in industrial solutions. The idea of the authors is to show a much simpler design in solving the same problem. They developed a guidance mechanism realizing the same function, consisting only of a toothed belt with non-circular pulleys. The used parts are common trade articles.

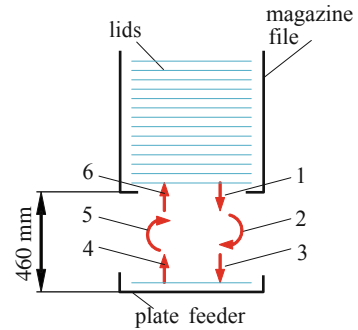
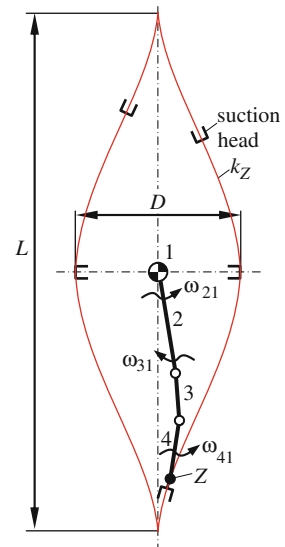
Keywords Guidance mechanism · Non-uniform belt-drive · Synthesis · Packaging-machine

1 Introduction

In [1, 2], a construction to separate lids from a magazine file in a packaging-machine was presented. The task of this device was to pick up a lid with a suction head from a magazine file (see Fig. 1) and place it after a half turn on a plate-

This report has the permission of the creators of the practical used separating device [1, 2].

U. Hanke (✉) · K.-H. Modler · R. Neumann · C. Fischer
Technische Universität Dresden, Dresden, Germany
e-mail: Uwe.Hanke@tu-dresden.de

Fig. 1 Motion problem**Fig. 2** Suction-head-trajectory

feeder, which runs in a step motion. Thereby the suction-head has to run through the following partial-tasks:

1. take off the lid from the magazine file,
2. turn the lid around 180° ,
3. place the lid on the tin,
4. move the suction head backwards without the lid,
5. turn back the suction head around 180° ,
6. towards the magazine file and the steps are repeated all over again.

This cycle follow two suction heads. For a collision free guidance, they have to follow the trajectory k_Z (see Fig. 2). The design parameter L and D of k_Z determine the overall machine-construction. The practical solution of the guidance-mechanism for moving the suction head is shown in Figs. 3 and 4, which has been built by HEINZ Automations-Systeme GmbH in the year 2006. It consists of three

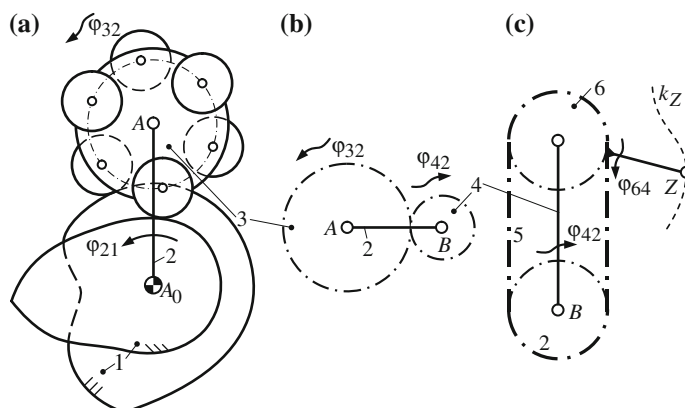


Fig. 3 Separating device-components of a packaging-machine for separating issues. **a** planetary cam-mechanisms, **b** spur gear ($i = 2 = \text{constant}$), **c** belt-drive ($i = 1 = \text{constant}$)



Fig. 4 Arrangement of the separating mechanism

device-components and has been working reliably ever since. But according to the authors of this paper this design is too complex. Since two non-uniform motions are needed for the suction head (ω_{64} , ω_{42} —Fig. 3). So we looked for a simpler solution.

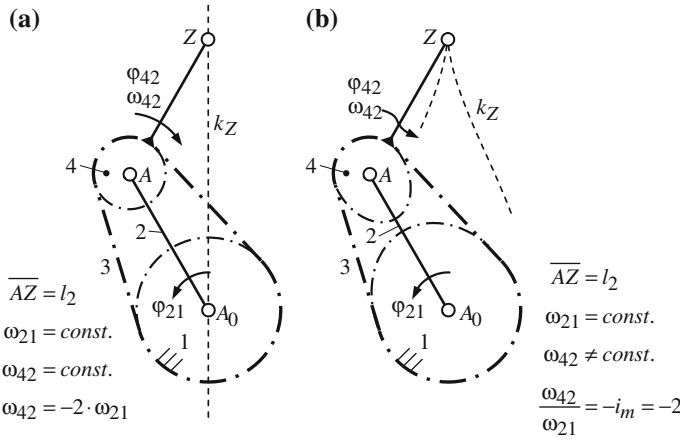
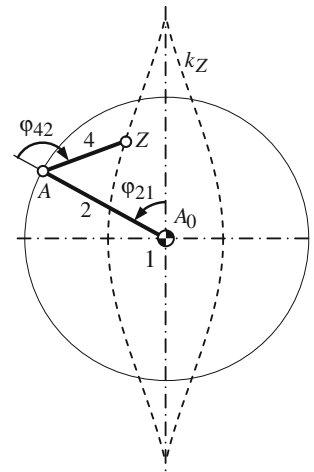


Fig. 5 Belt-drives for a trajectory k_Z . **a** with circular gears/straight line = k_Z , **b** with non-circular gears

Fig. 6 Trace the given trajectory k_Z , to get the non-uniform motion of φ_{42}



2 The Simpler Solution

The trajectory shown in Fig. 2 looks like a modified cycloid, especially a modified cardanic-trajectory. Taking a belt-drive with $i = 2$ and circular gears/pulleys you get a straight line k_Z , here the motions of the links 2 and 4 are constant, as seen in Fig. 5a. Having only one of the links, namely \overline{AZ} a non-uniform motion, we get a trajectory of the required form (Fig. 5b). The non-uniform transfer-function φ_{42} (φ_{21}) can be obtained through the given trajectory k_Z with the dyad A_0AZ . The link lengths of this dyad are defined by k_Z with the design parameters L and D (Fig. 2), with $\overline{A_0A} = \frac{1}{2} \cdot (L + D)$ and $\overline{AZ} = \frac{1}{2} \cdot (L - D)$. Tracing the trajectory k_Z (see Fig. 6)

Fig. 7 Transfer-function $\varphi_{42}(\varphi_{21})$ and $\varphi'_{42}(\varphi_{21})$ for the motion of the suction-head

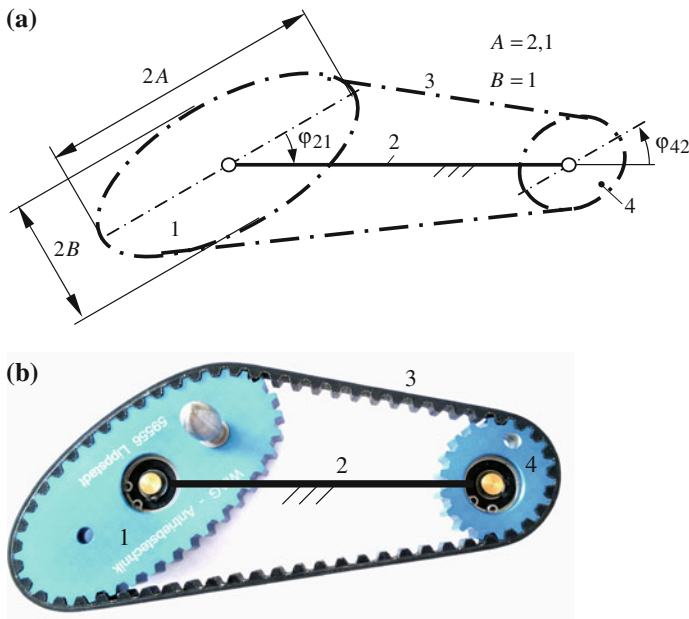
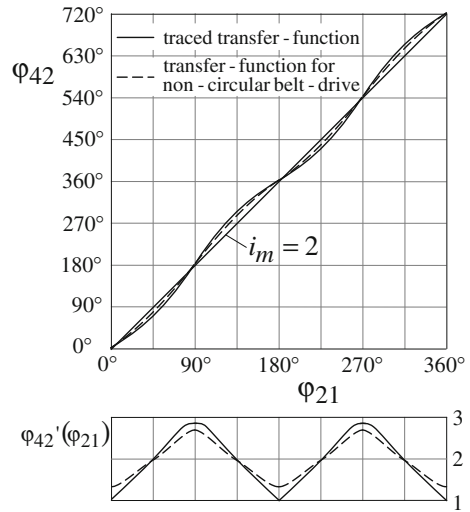


Fig. 8 Belt-drive ($i_m = 2$) with elliptical pulleys with the non-uniform transfer-function in Fig. 7. **a** mechanism scheme, **b** common trade article [3]

leads to the transfer-function $\varphi_{42}(\varphi_{21})$, see Fig. 7. The non-uniformity of $\varphi_{42}(\varphi_{21})$ can be better analysed by its first order transfer-function $\varphi'_{42}(\varphi_{21})$. Here we see that the cusps in the trajectory k_Z are cusps in the first order transfer-function. This cusp point causes a jump in the second order transfer-function. Beside this

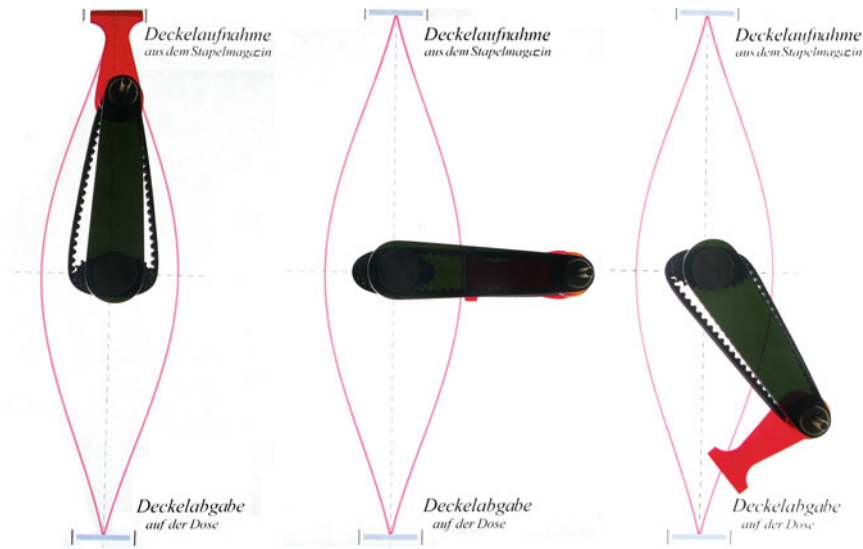


Fig. 9 Overhead-model shown in three positions of the suction-head

critical property the general character of the transfer-function endorse the structure synthesis. In this case the traced transfer-function is similar to the transfer-function of a belt-drive with non-circular pulleys as seen in Fig. 8. These are used as function generating mechanisms, with fixed link 2 and input pulley 1. To use this mechanism for link guidance, we have to change the frame and input pulley 1 as fixed and the arm 2 as input. These drives are available by company [3, 4], for theory see [5].

The solution of the given problem is shown in Fig. 9a as a moveable model for an overhead projector.

For a synthesis one has to take in account the conditions: $L/2 = l_2 + l_4$ and $D/2 = l_2 - l_4$, that means: $D/L = (l_2 - l_4)/(l_2 + l_4)$. Further on, there are limitations to this non-uniformity or i_m [5].

3 Conclusions

In a packaging-machine a very complex and expensive separation device is used for the lid guidance out off a magazine file for placing on this [1–4].

The suction head (a belt-drive) runs along a special trajectory, and needs 2 non-uniform inputs.

For the same task we found, based a simple solution, one belt-drive with elliptical pulleys and only one non-constant motion.

This belt-drive is marketable, and need only about one third of the construction-expense.

References

1. Seemann, U., Enderlein, L.: Planeten-Kurvengetriebe zur Teilevereinzelnung aus Stapelmagazin. VDI-Berichte Nr. 1966, pp. 335–349 (2006)
2. Seemann, U., Enderlein, L.: Planeten-Kurvengetriebe zur Teilevereinzelnung aus Stapelmagazin. Antriebstechnik, pp. 20–24 (7/2007)
3. Prospekt: Ungleichförmig übersetzende Zahnriemengetriebe. Firma WIAG-Antriebstechnik/Lippstadt, Benninghausen/Germany (2010)
4. Prospekt: Elliptical Pulleys. Firma Nanni Ingranaggi, Bologna/Italy (2009)
5. Frenken, E., Ungleichförmig übersetzende Zahnriemengetriebe. VDI-Berichte, Reihe 1/Nr. 272 (1996)

Path Generation of Regular Polygon Using a Geared-Parallelogram Mechanism

S. Lin, Y. Fan, Z. Ren and U. Hanke

Abstract The paper proposes a geared-parallelogram mechanism (GPM) for path generation of regular polygon. The model presents the structural features of the mechanism as shown in Fig. 1 which forms the basis for the guiding features of its path and also for the guiding function in its kinematic parameters and dimensions. It is shown from the analysis results that length l_2 has an effect on the size of the path, the initial phase θ on path direction and transmission ratio k on number of polygon sides. More important is that length ratio λ plays a crucial role in path curvature and defines indirectly the straightness for the regular polygon of path generation. In order to generate the path of regular polygon, some available value ranges of each parameter have been suggested. An example to solve path generation task with such mechanism using the method presented in this paper is given, through which a practical procedure to develop a synthesis tool for generating a regular polygon path will be provided.

Keywords Geared-parallelogram mechanism • Path generation • Regular polygon • Mechanism synthesis

S. Lin (✉) · Y. Fan
Tongji University, Shanghai, China
e-mail: slin@tongji.edu.cn

Z. Ren
China Tobacco Machinery Technology Center Co., Ltd (CTMTC), Shanghai, China
e-mail: ren_zw@ctmtc.net

U. Hanke
Technische Universität Dresden, Dresden, Germany
e-mail: Uwe.Hanke@tu-dresden.de

1 Introduction

A common geared four-bar mechanism (GFBM) is a combined mechanism consisting of a single DOF gear-chain and a four-bar mechanism which can be hinge four-bar mechanism, slider-crank mechanism, Scotch-Yoke mechanism and crank-and-rocker mechanism [1]. In order to meet a given motion task, a special form of four-bar mechanism can be conditionally used to build a GFBM.

The kinematic parameters can be simplified by using parallel-crank mechanism as baseline mechanism [2–5]. Although the complexity of the output path will be theoretically decreased by the simplification of kinematic parameters, it can still meet the requirements of the different design conditions on the path [6]. Moreover, GPM will simplify the mechanism synthesis task and will also be helpful to maintain kinematic accuracy [7].

2 Structural Features of GPM

Figure 1 shows a GPM positioned in a plane. Four-bar mechanism A_0ABB_0 is a parallel-crank mechanism. The external meshing gears mechanism (EMGM) $4'$ and $5'$ is in connection with link 3 at joints A and B. The relation of the two pitch circles (with the centers at A and B) can be written as $l_3 = R + r$ where l_3 is the length of the link 3, R and r are the pitch circle radii of gears $4'$ and $5'$. Gear $4'$ is fixed to link 4 at B, and gear $5'$ is connected to link 3 (or link 2 or link 5) at A, and let k ($k = R/r$) be the transmission ratio of the two gears. Link 5 is fixed to gear $5'$ and M is the guiding point of the GPM. The parameter λ ($\theta = l_5/l_2$) is used to define the length ratio of link 2 and 5, where l_2 is the length of link 2 and l_5 is the length of link 5. The DOF for the GPM shown in Fig. 1 is 1 using the formula of DOF for a planar mechanism. The driver link 2 makes an angle φ with the horizontal axis Ox .

3 Guiding Features of GPM

The guiding features of a mechanism can be defined by using parametric equation of path guiding point. To further study the influence of the kinematic parameters on the guiding path of GPM, the parametric equation of guiding point M is needed. If the absolute motion of guiding point M is considered as a resultant motion consisting of the relative motion of M (the rotation of M with respect to link AB) and the motion of link AB (the parallel translation of link AB with respect to the fixed link A_0B_0), the path equation of guiding point M can be parameterized by using the theory of motion resolution and synthesis. Let fixed reference frame xOy be the fixed link A_0B_0 (as shown in Fig. 1 and moving reference frame $x_1O_1y_1$ be link AB (as shown in Fig. 2 which rotates with respect to A_0B_0).

Fig. 1 Structural diagram of GPM

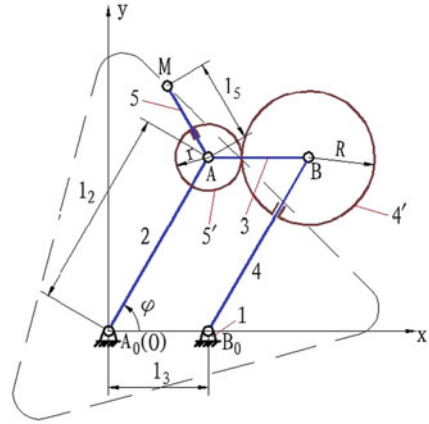
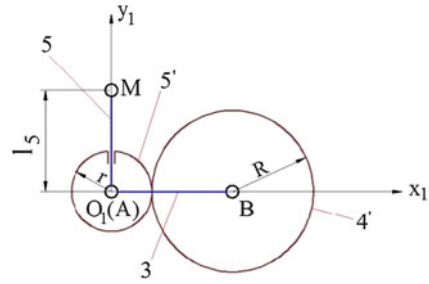


Fig. 2 Relative motion of M



Then the parametric equation of the absolute path of M can be written:

$$\begin{cases} M_x(l_2, k, \theta, \lambda\varphi) = l_2[\cos\varphi + \lambda\cos(k\varphi - \theta)] \\ M_y(l_2, k, \theta, \lambda\varphi) = l_2[\sin\varphi - \lambda\sin(k\varphi - \theta)] \end{cases} \quad (1)$$

where M_x is the x-coordinate of M with the reference frame xOy , M_y is the y-coordinate of M with the same reference frame, and θ is the initial angle of link 5 with the reference frame $x_1O_1y_1$.

4 Influences of Kinematic Parameters on Guiding Path

From Eq. (1), the path of guiding point M can be influenced by the length of link 2 (l_2), length ratio λ , transmission ratio k , initial angel θ and driver angle φ . The length of coupler 3 will not change the path because Eq. (1) possesses no parameter l_3 . The influence of each parameter on the guiding path is studied as follows.

Fig. 3 Path curves with various l_2 values

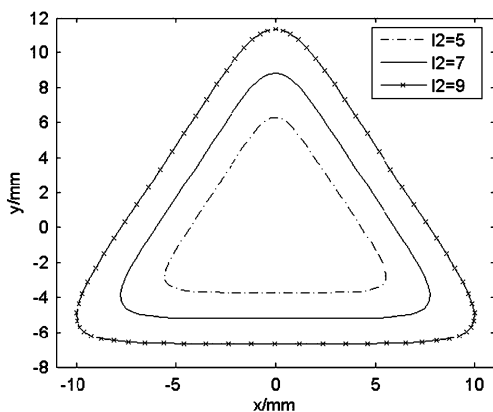
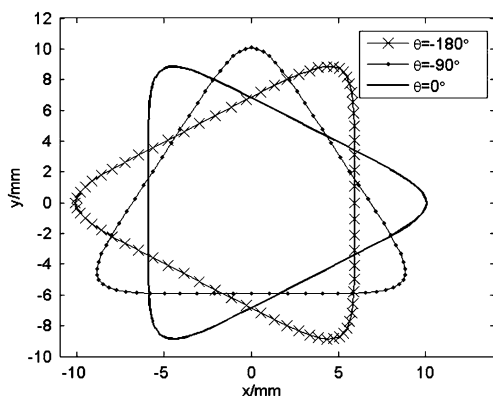


Fig. 4 Path curves with various θ values



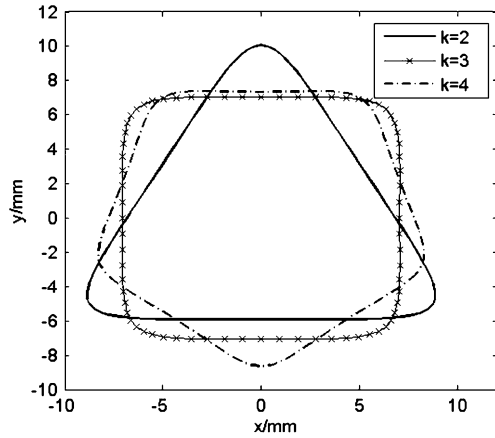
4.1 Influence of l_2 on Guiding Path

To analyze the influence of l_2 on the guiding path, the path curves of the point M with different l_2 values are needed to plot (as shown in Fig. 3) according to Eq. (1), in which parameters λ , k and θ remains unchanged (e.g. $\lambda = 0.25$, $k = 2$ and $\theta = -90^\circ$). Figure 3 illustrates that l_2 determines the size of the guiding path which grows similarly with the increase of l_2 , but in this case the shape of the path has no observable change.

4.2 Influence of θ on Guiding Path

To study the influence of θ on the guiding path, the path curves of the point M with different θ values need to be plotted (as shown in Fig. 4 according to Eq. (1), in which parameters λ , k and l_2 remains unchanged (e.g. $\lambda = 0.25$, $k = 2$ and

Fig. 5 Path curves with various k values



$l_2 = 8$ mm). Figure 4 shows that θ determines the path direction which rotates with the change of θ with the fixed reference frame xOy , but in this case the shape of the path remains the same.

4.3 Influence of k on Guiding Path

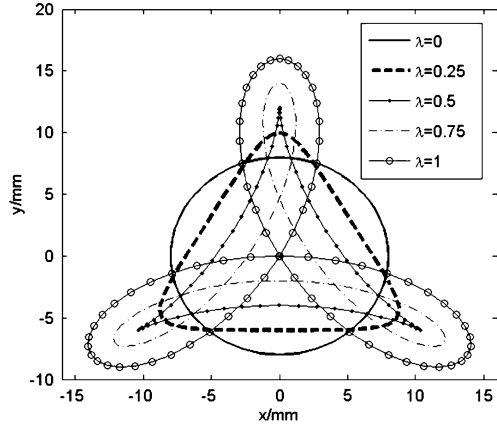
In order to find the influence of k on the guiding path, the path curves of the point M with different k values are needed to plot (as shown in Fig. 5 according to Eq. (1), in which parameters λ , θ and l_2 remains unchanged. Figure 5 shows that k determines the number of polygon sides n ($n = k + 1$). If k is a positive integer, guiding point M will travel along a closed polygon path (e.g. if $k = 2$, it will travel along an approximate triangle path, and if $k = 3$ an approximate quadrilateral, and if $k = 4$ an approximate pentagon).

4.4 Influence of λ on Guiding Path

Similarly, the influence of λ on the guiding path can be represented with the path curves of the point M shown in Fig. 6 with different λ values using Eq. (1) where parameters θ , k and l_2 remains unchanged (e.g. $\theta = -90^\circ$, $k = 2$ and $l_2 = 8$ mm). From Fig. 6, length ratio θ determines the path curvature and defines indirectly the straightness for the regular polygon of the path. The shape of the path varies from an outward curve to a relatively inward one with the increase of λ .

In engineering, because curvature of curves is used to define the straightness in case of a line, the optimal length ratio λ ($\lambda = \lambda_0$) can be determined by using the path curvature computed from the Eq. (1). Then the path curvature can be written:

Fig. 6 Path curves with different λ values



$$C = \frac{|1 + (k^2\lambda - k\lambda)\cos[(k+1)\varphi - \theta] - k^3\lambda^2|}{l_2[1 + k^2\lambda^2 - 2k\lambda\cos[(k+1)\varphi - \theta]]^{3/2}} \triangleq C(\varphi, \lambda) \quad (2)$$

Equation (2) can be viewed as a binary function which takes two inputs φ and λ using the fact that parameters l_2 , k and θ have no influence on the path curvature. The length ratio λ can be defined as the optimal value λ_0 when curvature C takes its minimum C_{\min} at a point, namely if $\lambda = \lambda_0$ and $C = C_{\min} = C(\varphi_0, \lambda_0)$ each side of the regular polygon path can be approximated to a straight line.

5 Path Synthesis of GPM

The regular polygon path has great practical value in engineering. The execution of the path synthesis task for a GPM requires the number of regular polygon sides, path direction, the optimal length ratio λ_0 and an acceptable error range for path curvature C which can determine the length of the regular polygon side (Table 1).

Example: Generate a path of an approximate equilateral triangle using a GPM (i.e. $k = 2$). The path direction has the requirement that the link 5 makes an initial angle $\theta = -90^\circ$. The unknown mechanism has the dimension: $l_2 = 8$ mm. Determine the optimal length ratio λ_0 , l_5 and the length of regular polygon side.

Solution: Using $k = 2$, $\theta = -90^\circ$ and $l_2 = 8$ mm Eq. (2) can be written:

$$C = \frac{|1 - 8\lambda^2 - 2\lambda\sin(3\varphi)|}{8[1 + 4\lambda^2 + 4\lambda\sin(3\varphi)]^{3/2}} \quad (3)$$

The minimum of curvature C is: if $\varphi = 150.80^\circ$, $\lambda = \lambda_0 = 0.25$ and therefore $C = C_{\min} = 7.31e-7$. Figure 7 shows that curvature C is directly proportional to

Fig. 7 Contour lines of λ of variables φ and C

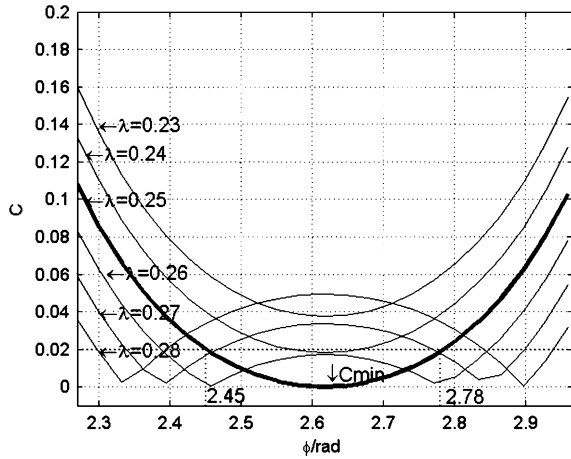


Table 1 Recommended values of k and λ_0 when $n = 2, 3$ and 4

n	k	λ_0
2	1	1
3	2	0.25
4	3	0.13

driver angle increment $\Delta\varphi$. The length of regular polygon side will diminish with the increase in straightness of regular polygon path. In this case, if $C \leq 0.02$, the driver angle increment $\Delta\varphi = (2.78 - 2.45) \text{ rad} = 0.33 \text{ rad} = 159.28 - 140.37^\circ = 18.91^\circ$ can be accepted.

Knowing the accepted driver angle increment $\Delta\varphi_{\text{accepted}} = 159.28 - 140.37^\circ = 18.91^\circ$, the positions of the points P ($\varphi = 159.28^\circ$) and Q ($\varphi = 140.37^\circ$) can be computed using Eq. (1):

$$\begin{cases} M_x|_P = -6.159 \\ M_y|_P = 1.331 \end{cases} \begin{cases} M_x|_Q = -4.196 \\ M_y|_Q = 4.730 \end{cases} \quad (4)$$

Then the length of line PQ = 3.925 mm and $l_5 = \lambda \cdots l_2 = 2 \text{ mm}$.

6 Conclusions

The structural features of GPM are presented, which are fundamental to the analysis of the guiding features and the influence of each kinematic parameter on the guiding path. The length ratio λ among all parameters is of special significance to the straightness of the regular polygon path. Thus, the definition of the optimal

length ratio λ which makes the path an approximate regular polygon has been framed. The approach to the path synthesis for the GPM has been introduced by giving an example of generating an approximate equilateral triangle path.

References

1. Lv, Y., Shen, A.: Design and Innovation of Combined Mechanism. Mechanical Industry Press, Beijing (2008)
2. Ge, W., Jiang, A., Zhang, G.: Study on fully parametric character of the link curves of geared five-bar linkage. *Mach. Des. Res.* **20**(3), 61–64 (2004)
3. Jiang, J., Xie, J., Chen, Y.: On the design of geared five-bar mechanism to produce curves of figure eight type. *Mach Des. Manuf.* **2**, 115–116 (2008)
4. Zhang, Y., Wu, X.: Study on track dimensional synthesis of connecting rod in geared four-bar linkage. *J. Mach. Des.* **20**(3), 41–43 (2003)
5. AWF und VDMA: Getriebeblätter, Beuth-Verlag (1930)
6. Bock, L.: Arbeitsblätter für die Konstruktion von Mechanismen, Beuth-Verlag (1997)
7. VDI-Richtlinie: VDI-Handbuch Getriebetechnik I und II, Beuth-Verlag GmbH (1971)

MOCAD: A Tool for Graphical and Interactive Calculation and Optimization of Cam Mechanisms and Motion Control Systems

A. Heine and M. Berger

Abstract The classical meaning of motion design is the usage of laws of motion with convenient characteristic values. Whereas the software MOCAD supports a graphical and interactive mode of operation, among others by using an automatic polynomial interpolation. Besides a direct coupling for motion control systems, different file formats for data export are offered. The calculation of plane and spatial cam mechanisms is also based on the data, generated in the motion design module. Drawing on an example of an intermittent cam mechanism with an inside cam profile used as a new drive concept for indexing tables, the influence of motion design on the transmission properties is shown. Another example gives an insight into the calculation and export of envelope curves for cylindrical cam mechanisms. The gained geometry data can be used for generating realistic 3D-models in the CAD-system Pro/ENGINEER, using a special data exchange format.

Keywords Cam mechanism • Motion control systems • Software • Motion design

1 Introduction

Cam mechanisms and so called motion control systems are used as drive concept, especially when high demands are made on any path of motion concerning motion quality. Definite indexed positions of positioning tasks, exact target speed for

A. Heine (✉) · M. Berger
Chemnitz University of Technology, Chemnitz, Germany
e-mail: andreas.heine@mb.tu-chemnitz.de

M. Berger
e-mail: maik.berger@mb.tu-chemnitz.de

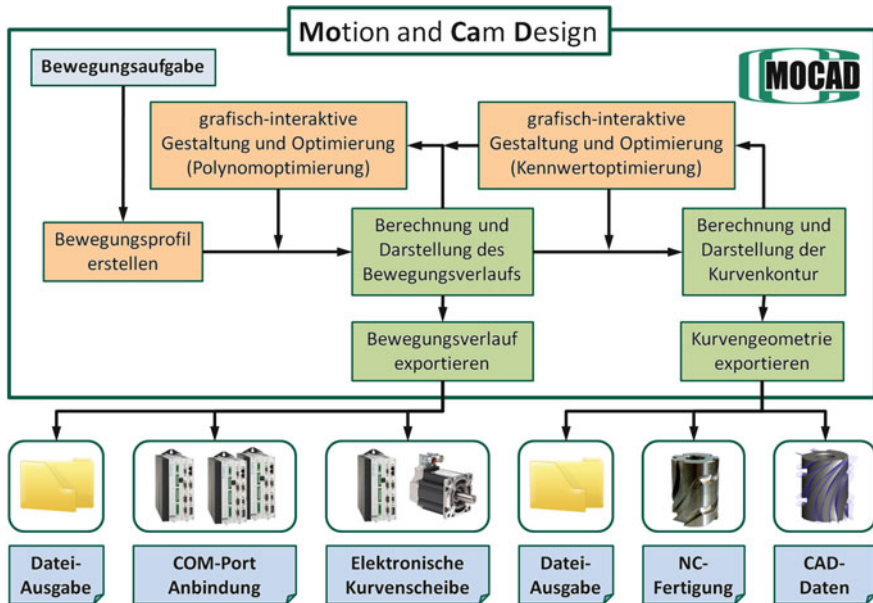


Fig. 1 Systematical Overview of MOCAD (in German)

synchronization of multiple axes, as well as cycle time reduction are examples for the necessity of specific optimization of motion.

In general, motion tasks are defined just in certain sections and therefore provide an opportunity of free structuring of transition areas. Using the typical calculation approach according to VDI 2143, a transition zone is deemed by the use of a transfer function considering different mathematical functions and preset marginal values. If the design of movement is a result of graphic-interactive movement methods, it is often called motion design. While the classical approach of optimization is often effected by the best possible selection of a law of movement, according to its convenient parameters, for each transition section, the use of MOCAD (Motion and Cam Design) institutes additional possibilities for interactive and possibly intuitively guided variations of basic values.

2 Overview of MOCAD

MOCAD is modular application software for characterizing and free structuring of movement tasks as well as dimensioning of plane and spatial cam mechanisms and electronic cam profiles. The graphic-interactive user interface offers a

dynamic engagement in the development process with an automatic adjustment of all calculation steps in real time. Figure 1 shows an overview of the software concept.

The plan of motion is an essential component during the construction phase and processing of a movement profile. It is possible to define and delete supporting points within the diagram intuitively, as well as the free manipulation of the transfer function and the marginal values up to the 6th order.

For the characterization of each section between the points of movement, a multiplicity of predefined laws of movement can be used. The implemented function library refers partly to the VDI Guidelines 2143, but beyond that, provides further specific polynomials and functions from [1] and [2]. In addition to the standardized laws of movement, the user is offered an automatic interpolation of higher polynomial, whose characteristics can easily be manipulated by directed setting of the marginal values. With increasing polynomial degree, higher derivations are considered.

If a comparison of movements is required, any number of motion plans can be edited simultaneously and diagramed. Aside from the coordination of motions, these motion plans enable the generation of a cam mechanism with different transfer functions and the comparison of kinematic and kinetostatic parameters of modified cam profiles. If identical or similar motion tasks need to be applied repeatedly, user-defined templates can be used.

The use of limiting functions can lead to a minimization of speed- and acceleration peaks, in certain cases to an optimization of cycle time. The program offers, next to this functionality, the containment of the function of motion up to 3rd order in sections and prevents user input automatically, which overruns or under runs these limits. The results of this design process can be used in different ways. The software provides different export formats, for example an ASCII-based text file or an exposition as Fourier coefficient. The immediate transfer of data to motion control systems is possible as well.

Another focus of the software is the calculation of plane and spatial cam mechanisms, based on motion design settings. For different motion plans, the required curve shape and the kinetostatic analysis can be calculated simultaneously. User-defined diagrams enable an ideal comparison of the different dimensional parameter specifications and can be dynamically updated by the connection to the motion plan.

The cam mechanism module possesses different export functions as well. Therefore especially for spatial cam mechanisms the envelope curves can be calculated. The use of a specific data format allows for the simple and regenerative replacement of calculation results with the CAD system Pro/ENGINEER. The possibility to calculate the NC-data for all curve shapes exists in order to cover the complete process with MOCAD, from dimensional parameter specifications to the assembly.

3 Dimensioning of a Plane Indexing Cam Mechanism

Within the limits of a research project at the professorship Assembly and Handling Technology, a new structural form for rotary indexing tables was designed, which constitutes an alternative mechanic solution to the cylindrical cam mechanisms that is currently customary in the market. It is based on so far little-known plane indexing cam mechanisms with an internal cam disk. The slight mass moment of inertia of the curve, the flat structural form and the beneficial cam roller contact with the work curve provide a so far incomprehensive explored potential in the area of indexing mechanisms, in spite of evidently inappropriate transmission properties [3]. Another specialty of this structural form is the possible use of multiple parallel drive mechanisms, which are arranged beneath the shift ring. By the even partition of the driving torque onto multiple cam disks, the durability of the components and the stiffness of the system are increased. The principle of load distribution as used in [4] was rarely deployed on structural forms with cylindrical curves so far.

Unfortunately, mostly stepping gears of this structural form possess a poor transmission angle at the beginning and at the end of the transmission motion. Especially for this reason, the selection or rather the design of a suitable transfer function is a challenge and of great importance for the course of the drive torques as well as the joint forces [5].

In case of an indexing mechanism with an internal cam disk, a maximized center distance provides the best minimal transmission angle and has therefore an immediate influence on the loading in the mechanism. If the ratio between the radius of the follower and the center distance is selected too small, undercut appears at the work curve. The generation of profile peaks and undercut is verified at this point by the calculation of the curvature radius and if necessary denoted by a warning message.

A first estimation, if the mechanism is qualified, is already possible at this point, considering the major analysis values, Fig. 2. Another quick check of the transmission function was affected by the modification of the selected motion profile and the comparison of the resulting kinetostatic values. A more accurate estimation was possible via diagrams.

4 Generation of Envelope Curve and Analysis in CAD

As previously discussed, the program offers the possibility to calculate envelope curves for spatial cam mechanisms for visualization and analysis of the resultant sidewall geometry. The proceeding of the creation of the geometric data, the

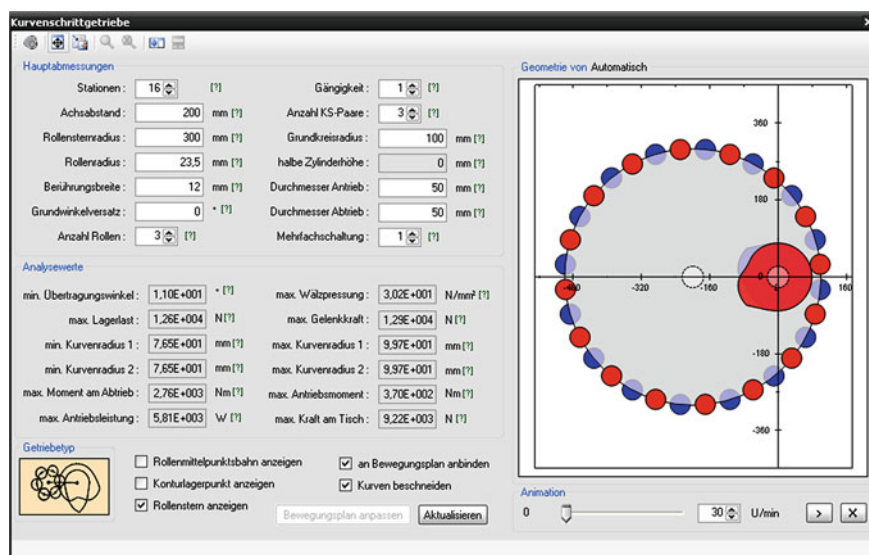


Fig. 2 Definition of major dimensions and visualization of the cam mechanism

export of its data as well as the subsequent processing in the CAD-system Pro/ENGINEER is demonstrated using the example of a swivel mechanism.

After the definition of the movement points and the selection of the adequate law of movements for the transition section, the dialog call up for defining cam mechanisms occurred. At this point, it has to be distinguished between two- and three-dimensional mechanisms and cam- and cam step mechanisms. During the input of the parameters, such as number of steps, center distance and roller diameter, an automatic inspection of the data regarding obviousness and if necessary the output of an error message takes place.

For further estimation of performance of the originated cam profile, such as the three-dimensional curvature an export to the data format IBL (Index By Location) occurred by setting the values "Number of curves". An IBL-file is a text file in an ASCII-format, which contains all coordinates of points besides predefined topline, Fig. 3. If a cam profile is imported via this format in the CAD-system Pro/ENGINEER, a linkage to the source data is preserved by using the so called Associative Topology Bus (ATP). If a modification of the parameters in MOCAD and another export is carried out, the import geometry in Pro/ENGINEER can be updated automatically.

The first step of modeling a cylindrical cam is the generation of a raw part with adequate dimensions. By the use of the imported IBL data it was possible to generate the sidewalls and the track ground of the curves. After the fusion of these

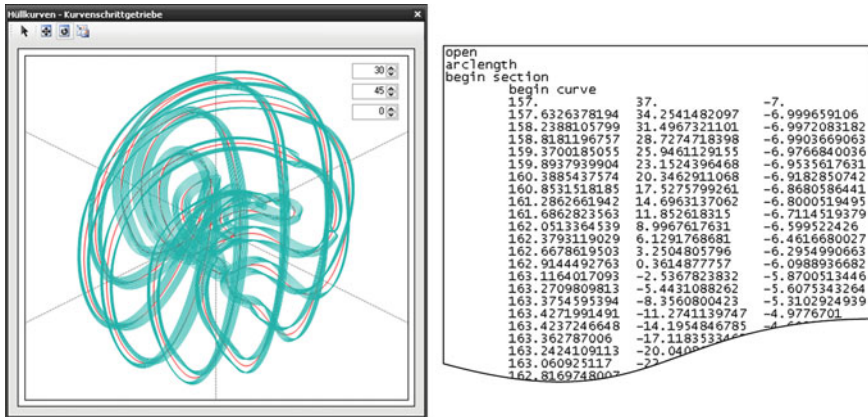


Fig. 3 3D visualization of envelope curves in MOCAD and an extract from an IBL-File

areas into a collection surface, once per track, a volume was generated, in which the grooves were arranged as negative volume. Using the originated geometry, there was a possibility of a kinematic simulation of the mechanism, a global penetration study as well as a three-dimensional curvature analysis.

5 Conclusions

Facing the problem to describe sections of a motion plan, you can use classical transmission functions with the demand of characteristic values. Furthermore the software MOCAD offers the possibility to describe these segments with higher polynomials and to shape them by manipulating the characteristic values.

Besides the generation of electronic cams for servo-systems, which can be interlinked by specifically implemented interfaces, the calculation of planar and spatial cams and intermittent cam mechanisms is another core competency of the program. With the connection of the mechanism design and the motion design module, a visual clarification of the influences of the movement function with simultaneously calculated kinetostatic values is enabled. Hence MOCAD is an optimal tool for motion design, but it is also reliant to the user's knowledge and experience.

References

1. Volmer, J.: Getriebetechnik—Kurvengetriebe, Berlin: Verlag Technik, (1989)
2. Berger, M.; Matthes, J., Kitzig, P.: Kennwertkreis und normierte Bewegungsgestaltung - Möglichkeiten zur optimalen Auslegung von Servoantriebssystemen, VDI-Berichte 2050, Düsseldorf: VDI-Verlag, pp. 17 (2008)

3. Berger, M.; Heine, A.; Matthes, J. and Schulz, R.: Realisierung von taktzeitoptimalen Schritt- und Schwenkbewegungen für Prozessabläufe in der Automobilindustrie, *Proc. of the 9 Magdeburger Maschinenbautage*, 2009.
4. Patent: DE102007021681B3: Konen, W.: Schrittschaltdrehtisch (2008)
5. Berger, M., Heine, A., Matthes, J., Schulz, R.: Der optimale Schritt—Bewegungsdesign, Berechnung und Gestaltung von Schrittgetrieben für Rundschalttische, *Proceedings of the 8. Kolloquium Getriebetechnik*, Aachen (2009)

Efficiency of Integrated Anti-Backlash Designed Planetary Gearbox

V. Klouček

Abstract The paper contains description of the anti-backlash designed planetary gearbox with Oldham couplings, which is integrated into the chassis of the electric motor. The solution results of kinematics and dynamics of components, which held a general planar motion, are presented. The following explains the power flow branching through transmission mechanism and the overall efficiency of mechanism is solved. The mechanism design is subject to a patent protection.

Keywords Planetary gears • Oldham coupling • Preload • Backlash

1 Introduction

In engineering practice are very large and varied issue electric drives and motors. Because the standard electric motors (except for so called torque motors) operate at higher speeds and lower torques than often require their technical applications, it is usually necessary between the electric motor and driven mechanism inserts the appropriate transmission mechanism.

According to various aspects, there are diverse requirements on the transmission mechanisms. They are especially high efficiency, high loading capacity and durability, low noise emission, precise repeatability of the output shaft angular position, small space requirements, low cost, etc. The purpose of this paper is

V. Klouček (✉)
VÚTS Liberec, a.s., Czech Republic
e-mail: vojtech.kloucek@vuts.cz

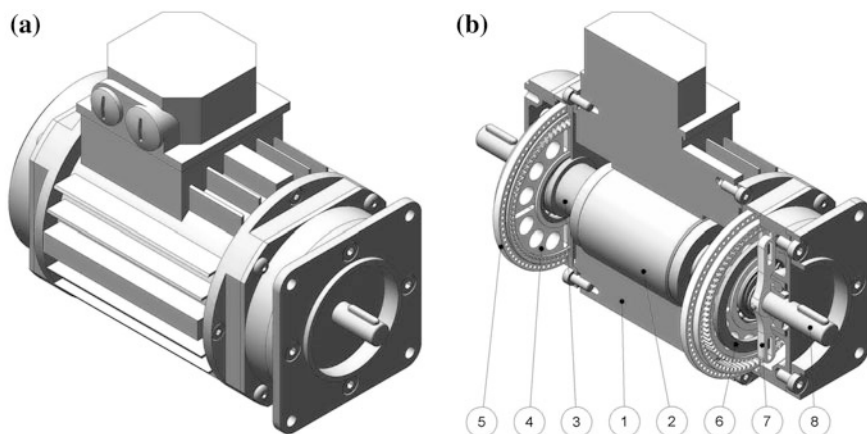


Fig. 1 **a** electric motor with integrated gearbox. **b** internal structure: 1—stator with stator winding, 2—rotor, 3—eccentric cam, 4—planet wheel, 5—central gear with internal teeth, 6—Oldham coupling, 7—output shaft carrier, 8—continuous output shaft

design of a special gear mechanism, which is integrated into chassis of the electric motor.

The gear mechanism is an anti-backlash designed, thus ensures a well defined dependence of the output shaft rotation angle to the input shaft. Another advantage of this concept is extremely compact design that makes the whole device can be called “low-speed motor” (Fig. 1).

The article aim is publication of principle and properties of new gear mechanism concept, which is patent protected. There is the design description in the article, outcomes of the transmission mechanism kinematics and dynamics and will be determine overall efficiency.

2 Design of Integrated Gearbox

2.1 Internal Structure

The design of the “low-speed motor” so arranged that to the three-phase asynchronous motor chassis with a squirrel cage is integrated gear mechanism with internal teeth (Fig. 1). In order to eliminate all the backlashes in the gearing and bearings, is branched into two identical gears, between which is inserted the flexible component [1, 2].

The paths of transmission are located symmetrically around the plane of symmetry of the motor. The rotor is equipped at the ends of eccentric cams on which are stored by rolling bearings toothed wheels (satellites). These are in mesh with the central wheels with internal teeth, which are rigid supported in the chassis

of the motor. From the satellites is converted rotary motion to output shaft through an annular Oldham couplings and carriers.

Output shaft rotation is opposite to the rotor rotation. Overall transmission ratio is given by Eq. (1), where z_k is number of teeth of central wheel with internal teeth and z_s is number of teeth of satellite.

$$i = - \frac{z_k}{z_k - z_s} \quad (1)$$

2.2 The Backlash Elimination

The backlash elimination in the gear mechanism is achieved by turning the central wheels and fixation of their positions in the base frame. Because the exact location of the wheels, in which are all backlashes just eliminated, is not known before assemble, it is necessary connection between the central wheels and the frame to be solved that it is possible to fix the wheel in any angular position. This property has connections with force contact, such as compression joints. At the same time in the long-term use must not cause self rotation central wheels, which would result in loss of anti-backlash effect. This property has connections with shaped contact, such as grooved joints.

For correct function of the transmission mechanism described construction, it was necessary to resolve this contradiction. It was designed joint with shaped contact and continuous adjustment angular position as follows: Central wheel has number of teeth z_k and on its circuit is drilled $(z_k + 1)$ holes for pin. The basic frame has drilled along the circuit $(z_k + 2)$ holes for pin, thus creating a vernier (Fig. 2).

The correct angular position is ensured by one pin that is inserted into a pair of holes, which lie against each other. Number n_p of mutual angular positions of central wheels are not infinite, but is very high. The number is given by (2).

$$n_p = z_k(z_k + 1)(z_k + 2) \quad (2)$$

For $z_k = 80$, as in the already made prototype, is $n_p = 531360$, which corresponds to an angular accuracy of approximately $\pm 2,5''$. Such accuracy can be within tolerances of standard engineering practise considered as a continuous adjustment of angular position.

An important feature of this mechanism is its static indeterminacy. From the indeterminacy results output shaft torsional preload M_{Tk} in the area between carriers. It must be considered in assessing the load capacity and durability of individual components and in determining overall efficiency.

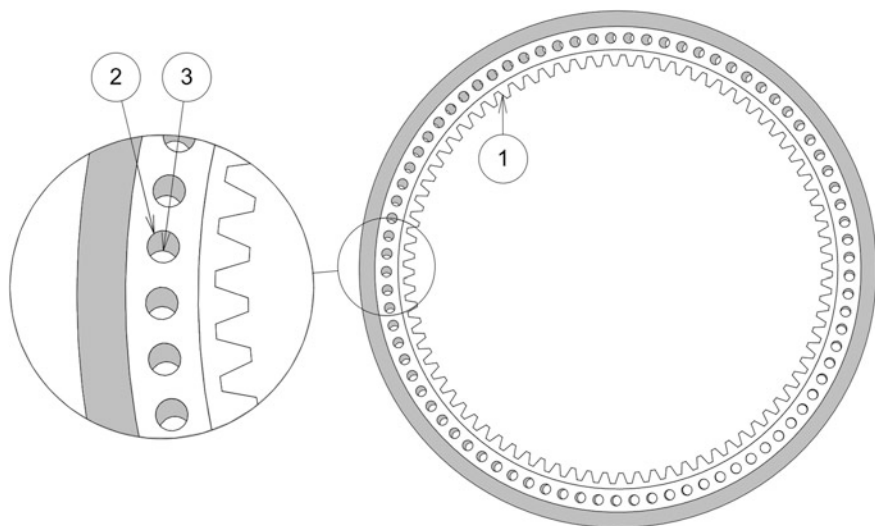


Fig. 2 Vernier for backlash elimination in gear mechanism: 1—number of teeth of central wheel z_k , 2—number of holes for pin on central wheel ($z_k + 1$), 3—number of holes for pin on basic frame ($z_k + 2$)

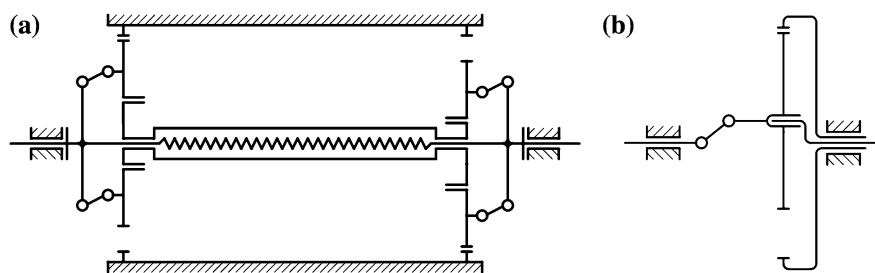


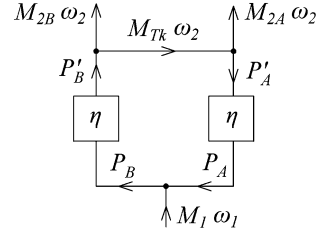
Fig. 3 **a** kinematics scheme of integrated gearbox. **b** kinematics scheme of equivalent planetary differential gear

3 Kinematics and Dynamics

Figure 3a shows the kinematic diagram of the integrated gearbox. Figure 3b shows the equivalent planetary differential gear. By using Willis method is possible to determine the kinematics of mechanism and gear ratio (1). The integrated gearbox corresponds to the two differential gears (Fig. 3b), with joined output shafts and fixed central wheels.

Rotor with excentric cams and output shaft with carriers held rotary motion, satellites and Oldham couplings held general plane motion. In terms of dynamics is important motion of Oldham couplings.

Fig. 4 The power flow scheme of integrated gearbox mechanism



Because some mechanism components held rotary motion, in which their centers of mass lies off the axis of rotation, it is necessary to solve dynamic balancing of mechanism. The subassembly consisting of rotor, excentric cams and satellites with bearings can be designed so that the resulting dynamic forces were zero. This subassembly is possible to balance on balancing machine.

The only mechanism components, the dynamic forces cannot simply eliminate, are the Oldham couplings. They held the same general plane motion, which are mutually turned by 180° . During operation thus causes dynamic reaction moment that is transmitted through the bearings to the base frame, which is the main disadvantage of the described integrated gearbox design. Its time dependence is harmonic at constant rotor speed. Detailed solution of force conditions resulting to the outcome (3), where $M_{R,\max}$ is amplitude of the reaction moment, m_{oc} mass of Oldham coupling, e excentricity of excentric cam, ω_1 rotor angular speed, i gear ratio, ζ_s distance of satellites and f_R the reaction moment frequency.

$$M_{R,\max} = m_{oc} \frac{e \omega_1^2}{i^2} \left[(1+i)^2 + 1 \right] \zeta_s, \quad f_R = \frac{\omega_1 (1+i)}{2\pi i} \quad (3)$$

4 Efficiency of Gear Mechanism

Because the integrated gearbox mechanism includes two parallel identical planetary gears, there will be branching of power flow. The output shaft power can be taken at both ends. Schematic of power flow through gear mechanism is on Fig. 4.

As mentioned above, the torque M_{Tk} is the output shaft torque preload, that arises due to the static indeterminate assembly. Due to this preload, occurs power circulation. Through each path of the mechanism flow powers P_A and P_B . Power which is applied to the rotor is given by $P_1 = M_1 \omega_1$, power piped by output shaft is $P_2 = (M_{2A} + M_{2B}) \omega_2$. Overall efficiency of mechanism η_v is given by (4).

$$\eta_v = \frac{M_{2A} + M_{2B}}{\frac{M_{Tk} + M_{2B}}{\eta} - \eta(M_{Tk} - M_{2A})} \quad (4)$$

From Eq. (4) implies that the overall efficiency depends on the gearbox load and torsional preload of output shaft.

The value η is the efficiency of the planetary gear, which includes each path of the transmission. The mechanism consists of a spur gear with internal teeth and annular Oldham coupling. For the efficiency applies (5), where η_g is efficiency of the spur gear and η_{oc} is efficiency of Oldham coupling.

$$\eta = \eta_g \eta_{oc} \quad (5)$$

There occurs a sliding friction on the Oldham coupling. The principle of the calculation of its efficiency is based on the determination of mechanical work of friction forces. The efficiency is given by (6), where f is the slide friction coefficient, e eccentricity of excentric cams, i gear ratio and d diameter of Oldham coupling.

$$\eta_{oc} = 1 - \frac{8fe(1+i)}{\pi d} \quad (6)$$

Spur gear efficiency depends on many parameters and its numerical determination is not simple. This efficiency is usually determined experimentally, e.g [3].

5 Conclusions

Aim of the article was publication of principle and properties of atypical designed gear mechanism.

Acknowledgments The research work was made possible by VÚTS Liberec, a.s. and research project TIP FR-TII/594.

References

1. Hale, L.C., Slocum, A.H.: Design of anti-backlash transmissions for precision position control systems. *Precis. Eng.* 16(4), 244–258 (1994)
2. Klouček, V.: Dynamics of the anti-backlash designed gearings with elastic elements. *International conference on vibration problems*, Praha (2011)
3. Petry-Johnson, T. T., Kahraman, A., Anderson, N. E., Chase, D. R.: Experimental investigation of spur gear efficiency. *Proceedings of the ASME* (2007)

Numerical Method for Determination of Base Circle Radius of Cam Mechanisms with Oscillating Flat-Face Follower

E.-C. Lovasz, D. Perju, C. M. Gruescu, K.-H. Modler, Cărbăș I
and E. S. Zăbavă

Abstract The paper proposes an original numerical method for computation of the base circle radius of the cam mechanism with oscillating flat-face follower. The base circle radius is a parameter in order to optimise the design of the cam profile. The synthesized cam profile should be continuously convex without inflection or singularity points. The numerical method uses the conditions to avoid the singularities and to achieve a strictly positive curvature radius.

Keywords Cam mechanisms • Oscillating flat-face follower • Cam mechanism • Base circle radius • Singularities

E.-C. Lovasz (✉) · D. Perju · C. M. Gruescu · C. I · E. S. Zăbavă
Politehnica University of Timisoara, Timisoara, Romania
e-mail: erwin.lovasz@mec.upt.ro

D. Perju
e-mail: dan.perju@mec.upt.ro

C. M. Gruescu
e-mail: corina.gruescu@mec.upt.ro

C. I
e-mail: iosif.carabas@mec.upt.ro

E. S. Zăbavă
e-mail: eugen.zabava@mec.upt.ro

K.-H. Modler
Technische Universität Dresden, Dresden, Germany
e-mail: karl-heinz.modler@tu-dresden.de

1 Introduction

In order to minimize the size of the cam mechanism with oscillating flat-face follower it is necessary to design the minimum size of the cam, which implies the computing of the base circle radius.

The already-developed graphic-analytical and analytical methods for the calculation of the base circle radius are mostly restricted for the cam mechanisms with translating or oscillating roller follower, respectively for cam mechanism with translating flat-face follower [1–8]. Wunderlich [9] proposed a method to compute the cam profile of the cam mechanism with oscillating flat-face follower based on its “support function” relating the distance from the centre to the profile tangent with its angle direction. Angeles [10] obtained the optimum parameters of the cam mechanism with oscillating flat-face follower through cam-disk area minimization. Yu [11] designed the cam mechanism with flat-face follower considering an optimized proper motion and the requirement to have a curvature radius of the cam profile greater than a minimum limit.

The authors proposed in [12–14] some variants of numerical methods for computing the base circle radius for the cam mechanism with oscillating flat-face follower, which uses the conditions to avoid the inflection or singularity points and to achieve a strictly positive curvature radius.

2 Synthesis Equation of the Cam Profile

The cam profile equation used in synthesis can be calculated in inverse movement as envelope of the relative positions of the follower in respect with the cam [1–6].

The transmission function $\psi = \psi(\varphi)$, the follower arm offset e , the frame length a and the base circle radius r_b are known according to the technical application (Fig. 1). The initial flat-face follower angle in respect with the frame line $A_0B_0^1$ is:

$$\psi_0 = \arcsin((r_b + e)/a) \quad (1)$$

In respect with the cam co-ordinate system (Fig. 1), the co-ordinates of the follower oscillating axis B_0 are:

$$x_{B_0} = a \times \sin(\psi_0 + \varphi), \quad y_{B_0} = -a \times \cos(\psi_0 + \varphi). \quad (2)$$

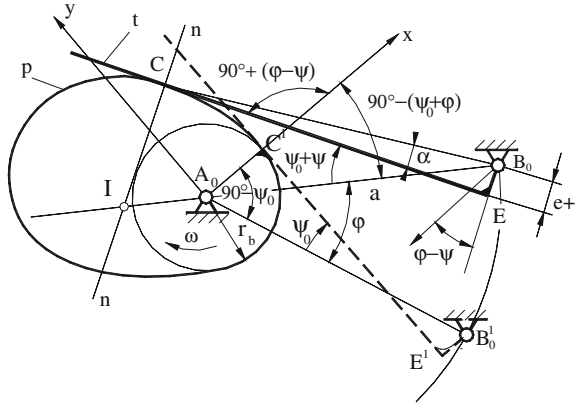
The co-ordinates of the point E of the follower are:

$$\begin{aligned} x_E &= a \times \sin(\psi_0 + \varphi) - e \times \cos[\varphi - \psi(\varphi)], \quad y_E \\ &= -a \times \cos(\psi_0 + \varphi) - e \times \sin[\varphi - \psi(\varphi)] \end{aligned} \quad (3)$$

The equation of the follower line (t) in inverse motion is:

$$t(x, y, \varphi) : (x - x_E) + (y - y_E) \cdot \tan(\varphi - \psi(\varphi)) = 0 \quad (4)$$

Fig. 1 Synthesis method of the cam mechanism with flat oscillating follower



The parametric equation of the cam profile is determined by considering the equations system:

$$\begin{cases} t(x, y, \varphi) = 0, \\ \frac{\partial t(x, y, \varphi)}{\partial \varphi} = 0. \end{cases} \quad (5)$$

from which yields:

$$\begin{aligned} x(\varphi) &= a \times \sin(\psi_0 + \varphi) - e \times \cos[\varphi - \psi(\varphi)] - \frac{a}{1 - \psi'(\varphi)} \cos[\psi_0 + \psi(\varphi)] \cdot \sin[\varphi - \psi(\varphi)], \\ y(\varphi) &= -a \times \cos(\psi_0 + \varphi) - e \times \sin[\varphi - \psi(\varphi)] + \frac{a}{1 - \psi'(\varphi)} \cos[\psi_0 + \psi(\varphi)] \cdot \cos[\varphi - \psi(\varphi)], \end{aligned} \quad (6)$$

with the current angle of the cam φ as parameter and $\psi'(\varphi) = d\psi/d\varphi$ the first derivative of the transmission function.

3 Numerical Method for Computing the Base Circle Radius

The sizing of the base circle radius of the cam mechanism with oscillating flat-face follower through a numerical method is based on the condition to avoid the cam profiles singularities:

$$\frac{dx(\varphi)}{d\varphi} \neq 0 \text{ and } \frac{dy(\varphi)}{d\varphi} \neq 0 \quad (\forall) \varphi \in [0, 2\pi], \quad (7)$$

which means the derivatives of the parametric cam profile coordinates (6) should avoid being simultaneously zero.

The derivatives of the cam profile coordinates can be written in the form:

$$\begin{aligned}\frac{dx(\varphi)}{d\varphi} &= A_1(\varphi)\cos\psi_0 + B_1(\varphi)\sin\psi_0 + C_1(\varphi), \\ \frac{dy(\varphi)}{d\varphi} &= A_2(\varphi)\cos\psi_0 + B_2(\varphi)\sin\psi_0 + C_2(\varphi)\end{aligned}\quad (8)$$

where:

$$\begin{aligned}A_1(\varphi) &= a \cdot \cos \varphi - a \cdot \cos[\varphi - \psi(\varphi)] \cdot \cos \psi(\varphi) + \\ &+ \frac{a \cdot \psi'(\varphi)}{1 - \psi'(\varphi)} \cdot \sin[\varphi - \psi(\varphi)] \sin \psi(\varphi) - \frac{a \cdot \psi''(\varphi)}{(1 - \psi'(\varphi))^2} \sin[\varphi - \psi(\varphi)] \cos \psi(\varphi), \\ B_1(\varphi) &= -a \cdot \sin \varphi + a \cdot \cos[\varphi - \psi(\varphi)] \cdot \sin \psi(\varphi) + \\ &+ \frac{a \cdot \psi'(\varphi)}{1 - \psi'(\varphi)} \cdot \sin[\varphi - \psi(\varphi)] \cos \psi(\varphi) + \frac{a \cdot \psi''(\varphi)}{(1 - \psi'(\varphi))^2} \sin[\varphi - \psi(\varphi)] \sin \psi(\varphi), \\ C_1(\varphi) &= e \cdot (1 - \psi'(\varphi)) \cdot \sin(\varphi - \psi(\varphi)),\end{aligned}\quad (9)$$

$$\begin{aligned}A_2(\varphi) &= a \cdot \sin \varphi - a \cdot \sin[\varphi - \psi(\varphi)] \cdot \cos \psi(\varphi) - \\ &- \frac{a \cdot \psi'(\varphi)}{1 - \psi'(\varphi)} \cdot \cos[\varphi - \psi(\varphi)] \sin \psi(\varphi) + \frac{a \cdot \psi''(\varphi)}{(1 - \psi'(\varphi))^2} \cos[\varphi - \psi(\varphi)] \cos \psi(\varphi), \\ B_2(\varphi) &= -a \cdot \cos \varphi + a \cdot \sin[\varphi - \psi(\varphi)] \cdot \sin \psi(\varphi) - \\ &- \frac{a \cdot \psi'(\varphi)}{1 - \psi'(\varphi)} \cdot \cos[\varphi - \psi(\varphi)] \cos \psi(\varphi) - \frac{a \cdot \psi''(\varphi)}{(1 - \psi'(\varphi))^2} \cos[\varphi - \psi(\varphi)] \sin \psi(\varphi), \\ C_2(\varphi) &= -e \cdot (1 - \psi'(\varphi)) \cdot \cos(\varphi - \psi(\varphi)),\end{aligned}\quad (10)$$

A base circle radius function will be defined according to the relationships (7) and (1):

$$f(\varphi, r_b) = -e + a \cdot \frac{2 \cdot \operatorname{tg}(\psi_0(\varphi)/2)}{1 + \operatorname{tg}^2(\psi_0(\varphi)/2)}. \quad (11)$$

The first derivatives of the cam profile coordinates (8) ensure the conditions (7), if the relationship:

$$r_b - f(\varphi, r_b) \neq 0 \quad (\forall) \quad \varphi \in [0, 2\pi] \quad (12)$$

is satisfied.

The cam base circle radius r_b of cam mechanism with oscillating flat-face follower is necessary to be strictly positive ($r_b > 0$) and the base circle radius function $f(\varphi, r_b)$ should be within the range $[\min\{f(\varphi, r_b)\}, \max\{f(\varphi, r_b)\}]$, where:

$$\min\{f(\varphi, r_b)\} < 0 \quad \text{and} \quad \max\{f(\varphi, r_b)\} > 0 \quad (13)$$

The cam base circle radius of the cam mechanism with oscillating flat-face follower satisfying the conditions (12), (13) and ($r_b > 0$) results as:

$$r_b > \max\{f(\varphi, r_b); \varphi \in [0, 2\pi]\} \quad (14)$$

Table 1 Geometrical and kinematical parameters

Inferior dwell 1	$\varphi_1 = 30^\circ$	Inferior dwell 2	$\varphi_5 = 30^\circ$
Rise	$\varphi_2 = 120^\circ$	Angular stroke	$\psi_{\max} = 15^\circ$
Superior dwell	$\varphi_3 = 60^\circ$	Frame length	$a = 100\text{ mm}$
Return	$\varphi_4 = 120^\circ$	Follower arm offset	$e = 0\text{ mm}$

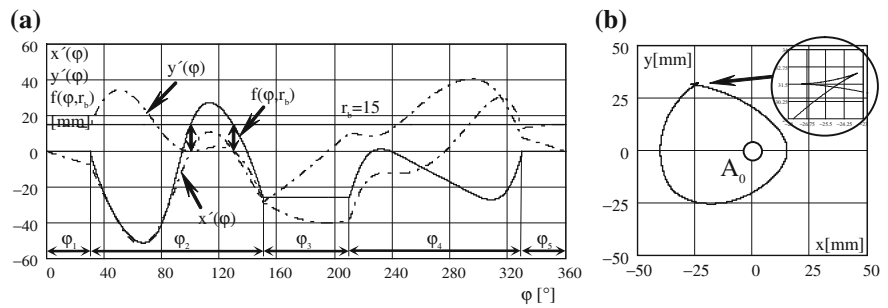


Fig. 2 Identification of the cam profile singularities by means of first derivative of the parametric equations and the base circle radius function (a) and cam profile (b) for $r_b = 15\text{ mm}$

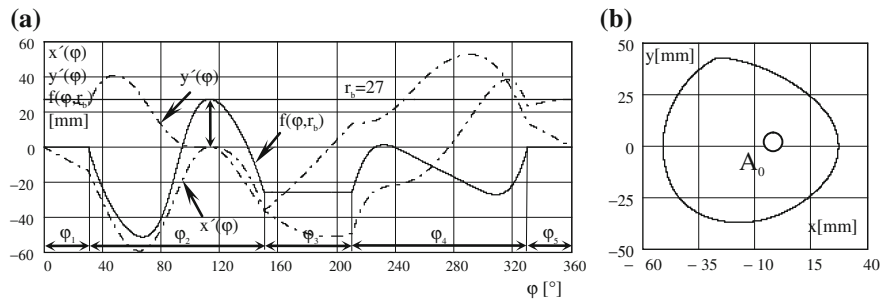


Fig. 3 Identification of the cam profile singularities by means of first derivative of the parametric equations and the base circle radius function (a) and cam profile (b) for $r_b = 27\text{ mm}$

It is recommended to use a numerical iterative method for computing the cam base circle radius out of the condition (14).

4 Numerical Examples

An example problem will be calculated through the proposed numerical method with chosen geometrical and kinematic values for the cam mechanism with oscillating flat-face follower, as given in Table 1. For the rise and return angular strokes (φ_2 and φ_4), the polynomial 3-4-5 motion functions are chosen.

In Figs. 2a and 3a is shown the variation of the first derivatives $x'(\varphi)$ and $y'(\varphi)$ and the base circle radius function $f(\varphi, r_b)$ for two chosen values of the base circle radius $r_b = 15$ mm and $r_b = 27$ mm. Figure 2a shows that for the two intersection points between the chosen value for the base circle radius and the base circle radius function both first derivatives are simultaneous null. In this case, which does not satisfy the condition (14) the cam profile contains singularity points (Fig. 2b). The base circle radius function does not intersect the value of the given base circle radius $r_b = 27$ mm and the consequence is the cam profile without singularities (Fig. 3b). The numerical solution of the associated equation to relationship (8) is $r_b = 26.705$ mm.

5 Conclusions

The proposed method allows the establishing of cam's base circle radius of the cam mechanism with oscillating flat-face follower, in order to avoid the cam's profile singularities through a numerical method.

The example problem confirms the theoretical hypothesis of the numerical iterative method conceived to avoid the profile singularities through defining the base circle radius function and imposing the base circle radius bigger than the maximum value of the base circle radius function.

References

1. Artobolevski I.I.: Mechanism theory (Theory mehanizmov). Izdatelsvo Nauka, Moskva (1965)
2. Manolescu, N., Kovacs, F. and Orănescu, A.: Mechanisms and Machine Theory (Teoria mecanismelor și a mașinilor). ed. Didactică și Pedagogică, București, (1972)
3. Perju, D.: Mechanism for Precision Mechanics (Mecanisme de mecanică fină). Lito. UPT, Timișoara, (1986/1990)
4. Angeles, J. and Lopez-Cajun, C.S.: Optimization of Cam. Mechanisms. Kluwer Academic Publishers, Dordrecht (1991)
5. Duca, C.: Basics in Cam Mechanisms Design (Bazele proiectării mecanismelor cu came). ed. Gh.Asachi, Iasi, (1999)
6. Lovasz, E.-C. and Cărăbaș I.: Synthesis Principles of Gears and Cam Mechanisms (Principii de sinteză a mecanismelor cu roți dințate și came). Ed. Politehnica Timișoara (2004)
7. Antonescu, P., Antonescu O.: A Unitary Method for Analytical Synthesis of Mechanisms with Rotary Disc-Cam. Proceedings of a 3rd International Conference on Manufacturing Engineering (ICMEN), Chalkidiki, Greece, 01–03 October, pp. 599–609 (2008)
8. Moise, V., Ene, M., Tabara, I.A., Dugășescu, I.: Determination of the minimum size of the disk cam with translating flat-face follower. Proceedings of 13th World congress in mechanism and machine science, Guanajuato, México, 19–25 June, A11_554, (2011)
9. Wunderlich, W.: Contributions to the geometry of cam mechanisms with oscillating followers, J. Mech. 6, pp. 01–20 (1971)

10. Angeles, J., Lopez-Cajun C.: Optimal synthesis of cam mechanism with oscillating flat-face followers. *Mechanisms and machine theory*, 23(1), pp. 1–6 (1988)
11. Yu, Q., Lee H.P.: Optimum design of cam mechanisms with flat-face followers. *Mech. Res. Commun.* 23(2), pp. 181–187 (1996)
12. Lovasz E.-C., Perju D., Cărbăș I., Zăbavă E.S., Modler K.-H.: On the synthesis of the cam mechanisms with tangential oscillating follower, *Proceedings of the IX-th international symposium SYROM05*, ed. Printech, Bucharest, vol. 2, pp. 81–86 (2005)
13. Lovasz E.-C., Perju D., Cărbăș I., Modler K.-H., Zăbavă E.: Basic circle radius of the cam mechanism with flat oscillating follower, *Bulletin of Politehnic Institut of Iași*, ed. Politehnia, Iași, Tom LVI(LX) Fasc. 4A, pp. 255–262 (2010)
14. Lovasz, E.-C., Perju, D., Duca, C., Modler, K.-H., Cărbăș, I., Zăbavă, E.S.: Numerical method for determination of the basic circle radius of the cam mechanism with flat oscillating follower. *scientific bulletin of the “Politehnica” University of Timisoara, Transactions on Mechanics*, 55(69)/1, pp. 21–26 (2010)

Analytical Displacement and Velocity Modeling of the RSSR-SS Linkage

Q. Shen, K. Russell and R. S. Sodhi

Abstract This work presents two fundamental contributions to RSSR-SS linkage kinematics: fully analytical RSSR-SS displacement and velocity models. These models are extensions of the analytical RSSR and RRSS linkage displacement and velocity models by Suh and Radcliffe [1]. The models formulated in this work provide an analytical benchmark in RSSR-SS displacement and velocity analyses.

Keywords Kinematics • RSSR-SS linkage • Displacement analysis • Velocity analysis

1 Introduction

The Revolute-Spherical-Spherical-Revolute or RSSR linkage is a spatial four-bar linkage having two degrees of freedom. The rotation of the coupler link about its own axis of symmetry is called a *passive degree of freedom*. This passive DOF makes the RSSR linkage ineffective for spatial rigid-body guidance. The RSSR linkage is often utilized in function generation applications.

Q. Shen (✉)

Emerson Network Power, Columbus, USA

e-mail: john.shen@emerson.com

K. Russell

U.S. Army ARDEC, Newark, USA

e-mail: kevin.russell1@us.army.mil

R. S. Sodhi

New Jersey Institute of Technology, Newark, USA

e-mail: rajpal.s.sodhi@adm.njit.edu

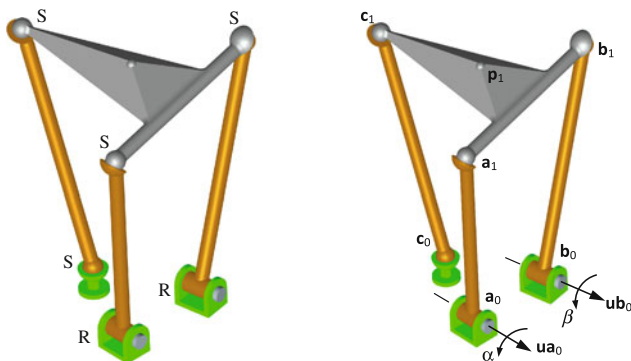


Fig. 1 (left) RSSR-SS linkage and (right) RSSR-SS linkage with design variables

Extending the coupler of the RSSR linkage and affixing a Spherical–Spherical dyad to the extended coupler produces the Revolute–Spherical–Spherical–Revolute–Spherical–Spherical or RSSR-SS linkage (Fig. 1). Unlike the RSSR linkage, the coupler of the RSSR-SS linkage has no passive DOF and is therefore suitable for rigid-body guidance. The RSSR-SS linkage is a particular type of *spatial multi-loop mechanism* [1–4].

In this work, analytical displacement and velocity models are formulated for the RSSR-SS linkage. Analytical kinematic modeling offer the advantage of a zero calculation error and the analytical RSSR-SS displacement and velocity models to be presented in this work can be codified for computational efficiency.

2 RSSR-SS Displacement and Velocity Models

2.1 RSSR-SS Displacement Model

From the RSSR displacement model by Suh and Radcliffe [1], the displacements of RSSR-SS moving pivots \mathbf{a}_1 and \mathbf{b}_1 (Fig. 1) are calculated. For a complete RSSR-SS displacement model however, equations to calculate the displacements of follower moving pivot \mathbf{c}_1 and rigid-body point \mathbf{p}_1 (Fig. 1) are also required.

The displacement of the RSSR-SS rigid-body can be divided into three distinct rotations. The first rotation is about the fixed pivot joint axis \mathbf{ua}_0 by rotation angle α . The second rotation is about a vector that includes the displaced moving pivot \mathbf{a} (vector \mathbf{w}) by rotation angle ω . The third and final rotation is about the displaced RSSR coupler unit vector \mathbf{ua} (where $\mathbf{ua} = (\mathbf{b} - \mathbf{a})/|\mathbf{b} - \mathbf{a}|$) by rotation angle γ .

For the first rotation (Fig. 2 left), RSSR-SS dyad \mathbf{a}_0 – \mathbf{a}_1 – \mathbf{c}_1 is treated as the RRSS linkage driving link dyad where $\mathbf{ua}_1 = (\mathbf{b}_1 - \mathbf{a}_1)/|\mathbf{b}_1 - \mathbf{a}_1|$. Based on the RRSS displacement model, the first rotations of \mathbf{c}_1 , \mathbf{p}_1 and \mathbf{ua}_1 become

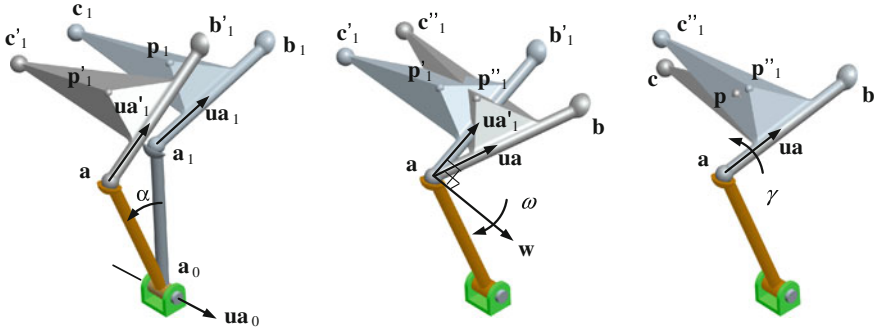


Fig. 2 (left) First, (middle) second and (right) third RSSR-SS rigid-body rotations

$$\mathbf{c}'_1 = [\mathbf{R}_{\alpha, \mathbf{ua}_0}](\mathbf{c}_1 - \mathbf{a}_0) + \mathbf{a}_0 \quad (1)$$

$$\mathbf{p}'_1 = [\mathbf{R}_{\alpha, \mathbf{ua}_0}](\mathbf{p}_1 - \mathbf{a}_0) + \mathbf{a}_0 \quad (2)$$

$$\mathbf{ua}'_1 = [\mathbf{R}_{\alpha, \mathbf{ua}_0}]\mathbf{ua}_1 \quad (3)$$

For the second rotation (Fig. 2 middle), unit vector \mathbf{ua}_1 is rotated to unit vector \mathbf{ua} (about vector \mathbf{w} by rotation angle ω). Vector \mathbf{w} is defined as

$$\mathbf{w} = \frac{\mathbf{ua}'_1 \times \mathbf{ua}}{|\mathbf{ua}'_1 \times \mathbf{ua}|} \quad (4)$$

and the cosine and sine of rotation angle ω are

$$\cos \omega = \frac{\mathbf{ua}'_1 \cdot \mathbf{ua}}{|\mathbf{ua}'_1| \cdot |\mathbf{ua}|} \quad \sin \omega = \frac{|\mathbf{ua}'_1 \times \mathbf{ua}|}{|\mathbf{ua}'_1| \cdot |\mathbf{ua}|} \quad (5)$$

Based on the RRSS displacement model, the second rotations of \mathbf{c}_1 and \mathbf{p}_1 become

$$\mathbf{c}''_1 = [\mathbf{R}_{\omega, \mathbf{w}}](\mathbf{c}'_1 - \mathbf{a}) + \mathbf{a} \quad (6)$$

$$\mathbf{p}''_1 = [\mathbf{R}_{\omega, \mathbf{w}}](\mathbf{p}'_1 - \mathbf{a}) + \mathbf{a} \quad (7)$$

For the third and final rotation (Fig. 2 right), moving pivot \mathbf{c}''_1 and coupler point \mathbf{p}''_1 are rotated about unit vector \mathbf{ua} by rotation angle γ . Based on the RRSS displacement model, the final rotations of \mathbf{c}_1 and \mathbf{p}_1 become

$$\mathbf{c} = [\mathbf{R}_{\gamma, \mathbf{ua}}](\mathbf{c}''_1 - \mathbf{a}) + \mathbf{a} \quad (8)$$

$$\mathbf{p} = [\mathbf{R}_{\gamma, \mathbf{ua}}](\mathbf{p}''_1 - \mathbf{a}) + \mathbf{a} \quad (9)$$

where

$$\gamma_{1,2} = 2 \tan^{-1} \frac{-X \pm \sqrt{W^2 + X^2 - Y^2}}{Y - W} \quad (10)$$

and

$$\begin{aligned} W &= (\mathbf{a} - \mathbf{c}_0)^T \{[\mathbf{I} - \mathbf{Q}_{\mathbf{ua}}](\mathbf{c}''_1 - \mathbf{a})\} \\ X &= (\mathbf{a} - \mathbf{c}_0)^T \{[\mathbf{P}_{\mathbf{ua}}](\mathbf{c}''_1 - \mathbf{a})\} \\ Y &= (\mathbf{a} - \mathbf{c}_0)^T \{[\mathbf{Q}_{\mathbf{ua}}](\mathbf{c}''_1 - \mathbf{a})\} + \frac{1}{2} \left\{ \begin{aligned} &(\mathbf{c}''_1 - \mathbf{a})^T (\mathbf{c}''_1 - \mathbf{a}) + (\mathbf{a} - \mathbf{c}_0)^T (\mathbf{a} - \mathbf{c}_0) \\ &-(\mathbf{c}_1 - \mathbf{c}_0)^T (\mathbf{c}_1 - \mathbf{c}_0) \end{aligned} \right\} \end{aligned}$$

Equations (8) and (9) calculate the displacements of RSSR-SS follower moving pivot \mathbf{c}_1 and rigid-body point \mathbf{p}_1 respectively and complete the RSSR-SS displacement model.

2.2 RSSR-SS Velocity Model

From the RSSR velocity model by Suh and Radcliffe [1], the velocities of RSSR-SS moving pivots \mathbf{a}_1 and \mathbf{b}_1 are calculated. For a complete RSSR-SS velocity model however, equations to calculate the velocities of follower moving pivot \mathbf{c}_1 and rigid-body point \mathbf{p}_1 (Fig. 1) are also required.

Incorporating the $\dot{\mathbf{a}}$ equation into the $\dot{\beta}$ equation (both from the RSSR velocity model [1]) produces an expanded formulation for $\dot{\beta}$ and incorporating it into the $\dot{\mathbf{b}}$ equation (from the RSSR velocity model [1]) produces the expanded $\dot{\mathbf{b}}$ formulation

$$\dot{\mathbf{b}} = \dot{\alpha} \frac{(\mathbf{a} - \mathbf{a}_0)^T [\mathbf{P}_{\mathbf{ua}_0}](\mathbf{a} - \mathbf{b})}{(\mathbf{a} - \mathbf{b})^T [\mathbf{P}_{\mathbf{ub}_0}](\mathbf{b} - \mathbf{b}_0)} [\mathbf{P}_{\mathbf{ub}_0}](\mathbf{b} - \mathbf{b}_0) \quad (11)$$

By treating dyad $\mathbf{a}_0\text{-}\mathbf{a}_1\text{-}\mathbf{b}_1$ of the RSSR-SS linkage as the R-R dyad of an RRSS linkage and adopting the $\dot{\mathbf{b}}$ equation (from the RRSS velocity model [1]) produces the $\dot{\mathbf{b}}$ formulation

$$\dot{\mathbf{b}} = \dot{\omega} [\mathbf{P}_{\mathbf{w}}](\mathbf{b} - \mathbf{a}) + \dot{\alpha} [\mathbf{P}_{\mathbf{ua}_0}](\mathbf{b} - \mathbf{a}_0) \quad (12)$$

where combining Eqs. (11) and (12) produces the $\dot{\omega}$ formulation

$$\dot{\omega} = \dot{\alpha} \frac{(\mathbf{b} - \mathbf{b}_0)^T \left\{ \frac{(\mathbf{a} - \mathbf{a}_0)^T [\mathbf{P}_{\mathbf{ua}_0}](\mathbf{a} - \mathbf{b})}{(\mathbf{a} - \mathbf{b})^T [\mathbf{P}_{\mathbf{ub}_0}](\mathbf{b} - \mathbf{b}_0)} [\mathbf{P}_{\mathbf{ub}_0}](\mathbf{b} - \mathbf{b}_0) - [\mathbf{P}_{\mathbf{ua}_0}](\mathbf{b} - \mathbf{a}_0) \right\}}{(\mathbf{b} - \mathbf{b}_0)^T [\mathbf{P}_{\mathbf{w}}](\mathbf{b} - \mathbf{a})}. \quad (13)$$

Treating the RSSR-SS loop $\mathbf{a}_0\text{-}\mathbf{a}_1\text{-}\mathbf{c}_1\text{-}\mathbf{c}_0$ as an RRSS linkage, the RRSS velocity constraint becomes

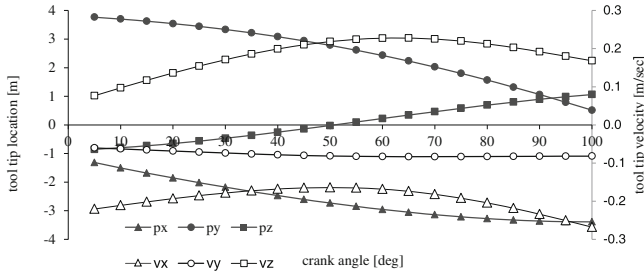


Fig. 3 Tool tip displacement and velocity profiles vs. driving link displacement angle

$$(\underline{\mathbf{c}})^T(\mathbf{c} - \mathbf{c}_0) = 0 = 0 \quad (14)$$

Adopting the \mathbf{b} and \mathbf{p} equations (from the RRSS velocity model [1]), the velocities of RSSR-SS follower moving pivot \mathbf{c}_1 and rigid-body point \mathbf{p}_1 become

$$\underline{\mathbf{c}} = \dot{\gamma}[\mathbf{P}_{\mathbf{ua}}](\mathbf{c} - \mathbf{a}) + \dot{\omega}[\mathbf{P}_{\mathbf{w}}](\mathbf{c} - \mathbf{a}) + \dot{\alpha}[\mathbf{P}_{\mathbf{ua}_0}](\mathbf{c} - \mathbf{a}_0) \quad (15)$$

$$\mathbf{p} = \dot{\gamma}[\mathbf{P}_{\mathbf{ua}}](\mathbf{p} - \mathbf{a}) + \dot{\omega}[\mathbf{P}_{\mathbf{w}}](\mathbf{p} - \mathbf{a}) + \dot{\alpha}[\mathbf{P}_{\mathbf{ua}_0}](\mathbf{p} - \mathbf{a}_0) \quad (16)$$

where combining Eqs. (14) and (15) produces the $\dot{\gamma}$ formulation

$$\dot{\gamma} = \frac{-\dot{\omega}(\mathbf{c} - \mathbf{c}_0)^T[\mathbf{P}_{\mathbf{w}}](\mathbf{c} - \mathbf{a}) - \dot{\alpha}(\mathbf{c} - \mathbf{c}_0)^T[\mathbf{P}_{\mathbf{ua}_0}](\mathbf{c} - \mathbf{a}_0)}{(\mathbf{c} - \mathbf{c}_0)^T[\mathbf{P}_{\mathbf{ua}}](\mathbf{c} - \mathbf{a})} \quad (17)$$

Equations (15) and (16) calculate the velocities of RSSR-SS moving pivot \mathbf{c}_1 and rigid-body point \mathbf{p}_1 and complete the RSSR-SS velocity model.

3 Example

The fixed and moving pivot coordinates (in meters) for an RSSR-SS linkage used to guide a milling tool are $\mathbf{a}_0 = (0, 0.0230, -0.0791)$, $\mathbf{a}_1 = (-0.4508, 1.9500, -0.1127)$, $\mathbf{ua}_0 = (0.2705, 0.0800, 0.9594)$, $\mathbf{b}_0 = (0.8236, 0.2848, -0.2711)$, $\mathbf{b}_1 = (0.8097, 2.6941, -0.7919)$, $\mathbf{ub}_0 = (0.5965, 0.1729, 0.7838)$, $\mathbf{c}_0 = (0, 0, -1)$ and $\mathbf{c}_1 = (-0.4655, 1.7992, -1.3256)$. The coordinates for the tool tip (\mathbf{p}_1) are $\mathbf{p}_1 = (-1.1176, 3.8219, -0.9088)$. In this example, the analytical RSSR-SS displacement and velocity models were used to calculate the path and velocity of the milling tool tip.

The tool tip position and velocity components are plotted in Fig. 3 (using a constant driving link velocity of $\dot{\alpha} = 1.0 \text{ rad/sec}$). These results are in precise agreement with those measured from an identical RSSR-SS linkage modeled in the mechanical simulation software *Sim Mechanics*.

4 Conclusions

The analytical RSSR-SS displacement and velocity models formulated in this work were used to calculate the tool tip path and velocity profiles of an RSSR-SS linkage used as a milling tool manipulator. In this example, the analytically-calculated tool tip path and velocity profiles are in precise agreement with those measured in the mechanical modeling software package *SimMechanics*.

References

1. Suh, C.H., Radcliffe, C.W.: Kinematics and Mechanism Design. Wiley, New York (1978)
2. Sandor, G.N., Xu L.J., Yang, S.P.: Computer-aided synthesis of two-closed-loopRSSR-SS spatial motion generator with branching and sequence constraints. Mech. Mach. Theory **21**, 345–350 (1986)
3. Russell, K., Sodhi, R.S.: Kinematic synthesis of adjustable RSSR-SS mechanisms for multi-phase finite and multiply-separated positions. ASME J. Mech. Des. **125**, 847–853 (2003)
4. Russell, K., Sodhi, R.S.: On displacement analysis of the RSSR-SS mechanism. Mech. Based Des. Struct. Mach. **31**, 281–296 (2003)

Part III
Dynamics of Machines and Mechanisms,
Rotor Dynamics, Vibration and Noise
in Machines, Computational Mechanics

Shaking Force Minimization of High-Speed Robots via Optimal Trajectory Planning

S. Briot, V. Arakelian and J.-P. Le Baron

Abstract The shaking force balancing is mostly obtained via an optimal redistribution of movable masses. Therefore, the full or partial cancellation of the shaking force is a complicated task, which leads to a significant increase in mass and assembly complexity. In this paper an innovative solution is developed which is based on the optimal control of the robot links centre of masses. Such a solution allows the reduction of the acceleration of the total mass centre of moving links and, consequently, the considerable reduction in the shaking forces. The efficiency of the suggested method is illustrated by the numerical simulations carried out for the three links serial manipulator. This approach is also a more appealing alternative to conventional balancing methods because it allows the reduction of the shaking force without counterweights. As a result, the input torques are also decreased, which is shown via mentioned numerical simulations.

Keywords Shaking force · Balancing · High-speed robots and optimal control

S. Briot (✉)

Institut de Recherches en Communications et Cybernétique
de Nantes (IRCCyN), Nantes, France
e-mail: Sebastien.Briot@irccyn.ec-nantes.fr

V. Arakelian · J.-P. Le Baron

Institut National des Sciences Appliquées (INSA) de Rennes,
Rennes, France
e-mail: vigen.arakelyan@insa-rennes.fr

J.-P. Le Baron

e-mail: jean-paul.le-baron@insa-rennes.fr

1 Introduction

Different approaches and solutions devoted to the problem of mechanism balancing have been developed and documented for one degree of freedom mechanisms [1, 2]. A new field for their applications is the design of mechanical systems for fast manipulation, which is a typical problem in advanced robotics.

The balancing of a mechanism is generally carried out by two steps: (1) the cancellation (or reduction) of the shaking force and (2) the cancellation (or reduction) of the shaking moment. Traditionally, the cancellation of the shaking force transmitted to the manipulator frame can be achieved via adding counterweights in order to keep the total centre of mass of moving links stationary [1], via additional structures [2] or by elastic components [3].

With regard to the shaking moment balancing of manipulators, the following approaches were developed: (1) balancing by counter-rotations [4], (2) balancing by adding four-bar linkages [5], (3) balancing by creating redundant mechanism which generates optimal trajectories of moving links [6], (4) balancing by prescribed rotation of the end-effector [7, 8] and (5) balancing by adding an inertia flywheel rotating with a prescribed angular velocity [9].

In the present paper we consider a simple and effective balancing method, which allows the considerable reduction of the shaking force of non-redundant manipulators without adding counterweights. It is based on the optimal motion planning of the acceleration of the total mass centre of moving links.

2 Minimization of the Shaking Forces Via an Optimal Motion Planning of the Total Mass Centre of Moving Links

The shaking forces \mathbf{f}^{sh} of a manipulator can be written in the form:

$$\mathbf{f}^{\text{sh}} = m\ddot{\mathbf{x}}_S \quad (1)$$

where m is the total mass of the moving links of the manipulator and $\ddot{\mathbf{x}}_S$ is the acceleration of the total mass centre. The classical balancing approach consists in adding counterweights in order to keep the total mass centre of moving links stationary. However, it leads to the increase of the total mass of the manipulator. Thus, in order to avoid this drawback, in the present study, a new approach is proposed, which consists of the optimal motion planning of the total mass centre of moving links.

Classically, manipulator displacements are defined considering either articular coordinates \mathbf{q} or Cartesian variables \mathbf{x} . Knowing the initial and final manipulator configurations at time t_0 and t_f , denoted as $\mathbf{q}_0 = \mathbf{q}(t_0)$ and $\mathbf{q}_f = \mathbf{q}(t_f)$, or $\mathbf{x}_0 = \mathbf{x}(t_0)$ and $\mathbf{x}_f = \mathbf{x}(t_f)$, in the case of the control of the Cartesian variables, the classical displacement law may be written in the form:

$$\mathbf{q}(t) = s_q(t) (\mathbf{q}_f - \mathbf{q}_0) + \mathbf{q}_0 \quad (2a)$$

or

$$\mathbf{x}(t) = s_x(t) (\mathbf{x}_f - \mathbf{x}_0) + \mathbf{x}_0 \quad (2b)$$

where $s_q(t)$ and $s_x(t)$ may be polynomial (of orders 3, 5 and higher), sinusoidal, bang–bang, etc. laws.

From expression (1), we can see that the shaking force, in terms of norm, is minimized if the norm $\|\ddot{\mathbf{x}}_S\|$ of the masses centre acceleration is minimized along the trajectory. This means that if the displacement \mathbf{x}_S of the manipulator centre of masses is optimally defined, the shaking force will be minimized. As a result, the first problem is to define the optimal trajectory for the displacement \mathbf{x}_S of the manipulator centre of masses.

For this purpose, let us consider the displacement \mathbf{x}_S of a point S in the Cartesian space. First, in order to minimize the masses centre acceleration, the length of the path followed by S should be minimized, i.e. point S should move along a straight line passing through its initial and final positions, denoted as \mathbf{x}_{S0} and \mathbf{x}_{Sf} , respectively.

Then, the temporal law used on this path should be optimized. It is assumed that, at any moment during the displacement, the norm of the maximal admissible acceleration the point S can reach is constant and denoted as \ddot{x}_S^{\max} . Taking this maximal value for the acceleration into consideration, it is known that the displacement law that minimize the time interval (t_0, t_f) for going from position $\mathbf{x}_{S0} = \mathbf{x}_S(t_0)$ to position $\mathbf{x}_{Sf} = \mathbf{x}_S(t_f)$ is the “bang–bang” law:

$$\begin{cases} \mathbf{x}_S(t) = s(t) (\mathbf{x}_{Sf} - \mathbf{x}_{S0}) + \mathbf{x}_{S0} \\ \dot{\mathbf{x}}_S(t) = \dot{s}(t) (\mathbf{x}_{Sf} - \mathbf{x}_{S0}) \\ \ddot{\mathbf{x}}_S(t) = \ddot{s}(t) (\mathbf{x}_{Sf} - \mathbf{x}_{S0}) \end{cases} \quad (3)$$

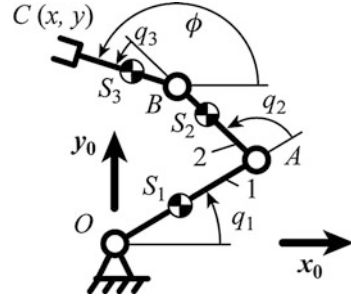
with

$$\ddot{s}(t) = \frac{1}{\|\mathbf{x}_{Sf} - \mathbf{x}_{S0}\|} \begin{cases} \ddot{x}_S^{\max} & \text{for } t \leq (t_f - t_0)/2 \\ -\ddot{x}_S^{\max} & \text{for } t \geq (t_f - t_0)/2 \end{cases} \quad (4)$$

Consequently, if the time interval (t_0, t_f) for the displacement between positions \mathbf{x}_{S0} and \mathbf{x}_{Sf} is fixed, the “bang–bang” law is the trajectory that minimizes the value of the maximal acceleration \ddot{x}_S^{\max} . Thus, in order to minimize $\|\ddot{\mathbf{x}}_S\|$ for a displacement during the fixed time interval (t_0, t_f) , the “bang–bang” law has to be applied on the displacement \mathbf{x}_S on the manipulator total mass centre.

Once the displacement of the manipulator centre of masses is defined, the second problem is to find the articular (or Cartesian) coordinates corresponding to this displacement. For this purpose, let us consider a manipulator composed of n links. The mass of the link i is denoted as m_i ($i = 1, \dots, n$) and the position of its centre of masses as \mathbf{x}_{Si} . Once the articular coordinates \mathbf{q} or Cartesian variables

Fig. 1 The 3R serial manipulator



\mathbf{x} are known, the values of \mathbf{x}_{Si} may easily be obtained using the manipulator kinematics relationships. As a result, the position of the manipulator centre of masses, defined as

$$\mathbf{x}_S = \frac{1}{m} \sum_{i=1}^n m_i \mathbf{x}_{Si} \quad (7)$$

may be expressed as a function of \mathbf{x} or \mathbf{q} . But, in order to control the manipulator, the inverse problem should be solved, i.e. it is necessary to express variables \mathbf{q} or \mathbf{x} as a function of \mathbf{x}_S . Here, two cases should be distinguished:

1. $\dim(\mathbf{x}_S) = \dim(\mathbf{q})$, i.e. the manipulator has got as many actuators as controlled variables for the displacements \mathbf{x}_S of the centre of masses (two variables for planar cases, three variables for spatial problems). In such case, the variables \mathbf{q} or \mathbf{x} can be directly expressed as a function of \mathbf{x}_S using (7), i.e. $\mathbf{q} = \mathbf{f}(\mathbf{x}_S)$.
2. $\dim(\mathbf{x}_S) < \dim(\mathbf{q})$, i.e. the manipulator has got more actuators than controlled variables. In this case, the some of parameters will be used for ensuring the necessity conditions of the optimal displacement of the manipulator centre of masses and the other parameters can be used in order to minimize some other performance criteria, by example, such as the shaking moment.

3 Illustrative Example

The end-effector pose (x, y, ϕ) of the planar 3R serial manipulator (Fig. 1) is controlled using three input parameters q_1 , q_2 and q_3 . The manipulator parameters are the following: the lengths of links: $l_{OA} = 0.5$ m, $l_{AB} = 0.3$ m and $l_{BC} = 0.1$ m, the dispositions of the mass centres: $l_{OS1} = r_1 = 0.289$ m, $l_{AS2} = r_2 = 0.098$ m, $l_{BS3} = r_3 = 0.05$ m. The masses and the axial inertia parameters are: $m_1 = 24.4$ kg, $m_2 = 8.3$ kg, $m_3 = 2$ kg, $I_1 = 1.246$ kg.m², $I_2 = 0.057$ kg.m², $I_3 = 0.025$ kg.m². The payload: $m_p = 5$ kg.

In the relationship $\mathbf{x}_S = [x_S, y_S]^T = f(q_1, q_2, q_3)$, there are three unknowns q_1, q_2, q_3 for two fixed parameters x_S and y_S . Therefore, as mentioned above, a way to solve this problem is to consider that one parameter, for example ϕ , is used to minimize some other objective function. In the present study, the angle ϕ is used for minimisation of the shaking moment m^{sh} . However, it should be noted that the same parameter can be used for minimisation, by example, the torques or another chosen objective function.

The angles q_1, q_2 and q_3 , which are functions of x_S, y_S and ϕ , are determined from $\mathbf{x}_S = f(q_1, q_2, q_3)$:

$$q_1 = 2 \tan^{-1} \left(\frac{-b \pm \sqrt{b^2 - c^2 + a^2}}{c - a} \right) \quad (8)$$

where

$$a = -2l_{eq1}(x_S - l_{eq3} \cos \phi), \quad b = -2l_{eq1}(y_S - l_{eq3} \sin \phi), \quad c = (x_S - l_{eq3} \cos \phi)^2 + (y_S - l_{eq3} \sin \phi)^2 + l_{eq1}^2 - l_{eq2}^2, \quad l_{eq1} = (m_1 r_1 + m_2 + m_3 + m_p)l_{OA}/m, \\ l_{eq2} = (m_2 r_2 + m_3 + m_p)l_{AB}/m \text{ and } l_{eq3} = (m_3 r_3 + m_p)l_{BC}/m.$$

In expression (8), the sign \pm stands for the two possible working modes of the manipulator (for simulations, the working mode with the “+” sign is used).

$$q_2 = \tan^{-1} \left(\frac{(y_S - l_{eq3} \sin \phi) - l_{eq1} \sin q_1}{(x_S - l_{eq3} \cos \phi) - l_{eq1} \cos q_1} \right) - q_1 \quad (9)$$

$$q_3 = \phi - q_1 - q_2 \quad (10)$$

Let us now test the proposed approach. The tested trajectories are defined as follows. First, the maximal inscribed square inside of the workspace, for any end-effector orientation, is found (Fig. 2). For this manipulator, it is a square of length 0.375 m, of which centre E is located at $x = 0$ m and $y = 0.487$ m. Then, in order to avoid problems due to the proximity of singular configuration, the tested zone is restricted to a square centered in E of edge length equal to 0.3 m (in grey on Fig. 2). Finally, each edge is discretized into four segments delimited by the points P_i ($i = 1-16$). The tested trajectories are the segments P_1P_{13} , P_2P_{12} , P_3P_{11} , P_4P_{10} , P_5P_9 , $P_{15}P_7$, $P_{14}P_8$ and $P_{13}P_9$. For numerical simulations, the independent parameter ϕ is chosen to begin the tested trajectories with an end-effector orientation $\phi_0 = 0$ deg and to finish it at $\phi_f = 120$ deg.

The simultaneous minimization of the shaking force and the shaking moment cannot be done without using an optimization algorithm. Several laws for ϕ were tested. Our observation showed that the polynomial function that makes it possible to obtain optimal results is of degree 8.

For each trajectory three different kinds of law are applied: (1) a fifth order polynomial law is applied on the displacement (translation and rotation) of the manipulator end-effector; (2) a “bang–bang” law is applied on the displacement of

Fig. 2 The tested trajectories

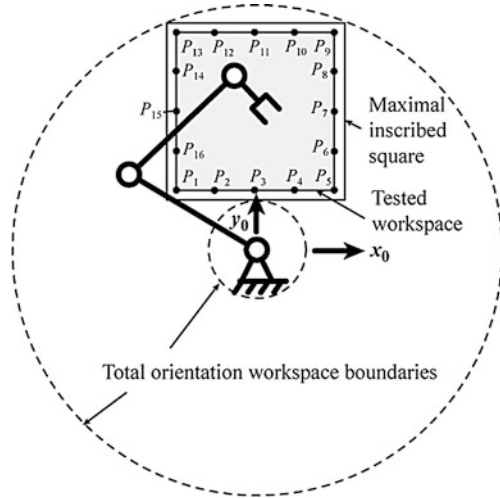
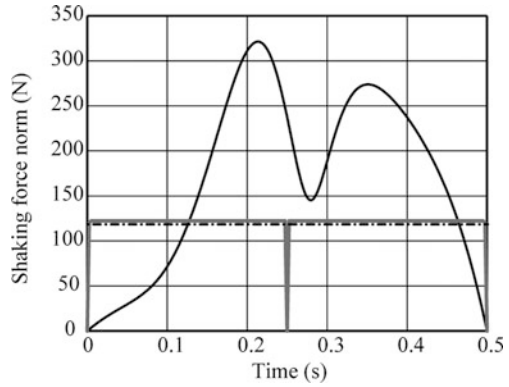


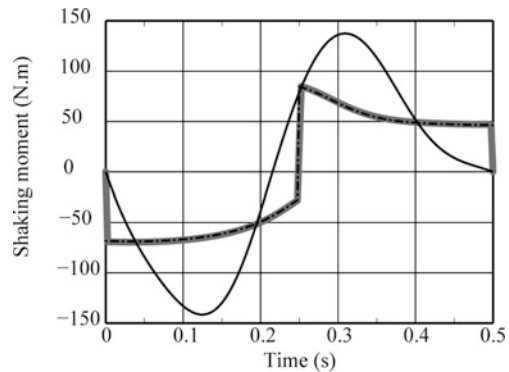
Fig. 3 Variations of the shaking forces: case 1 (*black full line*), case 2 (*black dashed line*) and case 3 (*grey full line*)



the manipulator centre of masses and the angle ϕ is optimized in order to minimize the shaking moment; (3) a trapeze acceleration profile is applied on the displacement of the manipulator centre of masses, taking into account that, for each actuator, the input effort variation is limited by $3 \cdot 10^4$ Nm/s; the trajectory for angle ϕ optimized in the previous case is used in order to compute the actuator displacements.

The obtained results showed that the optimal trajectory planning by bang–bang law allows the reduction of the shaking forces from 48 % up to 62.2 %. Moreover, with a simultaneous optimal definition of angle ϕ , the shaking moment can be reduced from 37.2 % up to 61 %. The obtained profit depends on the design parameters of the manipulator, as well as the given trajectory. It is clear that it will be variable. However, it is obvious, that the shaking force and shaking moment for any manipulator shall be decreased. Figures 3 and 4 show the variations of the

Fig. 4 Variations of the shaking moment: case 1 (black full line), case 2 (black dashed line) and case 3 (grey full line)



shaking force and the shaking moment of the manipulator for the trajectory $P_{15}P_7$ (see Fig. 2). The software simulations showed that in comparison with mass balanced manipulator a significant reduction in input torque has been achieved.

4 Conclusions

In this paper, we have presented a new approach, based on an optimal trajectory planning, which allows the considerable reduction of the shaking force. This simple and effective balancing method is based on the optimal motion planning of the acceleration of the manipulator centre of masses. For this purpose, the “bang–bang” displacement law has been used. The aim of the suggested method consists in the fact that the manipulator is controlled not by applying end-effector trajectories but by planning the displacements of the total mass centre of moving links. Such an approach allows the reduction of the maximum value of the centre of mass acceleration and, consequently, the reduction in the shaking force. It should be mentioned that such a solution is also very favourable for reduction of input torques because it is carried out without adding counterweights. The proposed balancing method has been illustrated via a numerical example.

References

1. Lowen, G.G., Tepper, F.R., Berkof, R.S.: Balancing of linkages—an update. *Mech. Mach. Theory* **18**(3), 213–230 (1983)
2. Arakelian, V., Smith, M.R.: Shaking force and shaking moment balancing of mechanisms: a historical review with new examples. *Trans. ASME, J. Mech. Des.* **127**, 334–339 (2005)
3. Alici, G., Shirinzadeh, B.: Optimum force balancing with mass distribution and a single elastic element for a five-bar parallel manipulator. In: *Proceedings of the 2003 IEEE International Conference on Robotics and Automation*, pp. 3366–3371. Taipei, Taiwan, 14–19 Sept 2003

4. Berkof, R.S.: Complete force and moment balancing of inline four-bar linkages. *Mech. Mach. Theory* **8**(3), 397–410 (1973)
5. Herder, J.L., Gosselin, C.M.: A counter-rotary counterweight for light-weight dynamic balancing. In: *Proceedings of ASME 2004 DETC/CIEC Conference*, pp. 659–667. Salt Lake City, Utah, USA, 28 Sept–2 Oct 2004
6. Papadopoulos, E., Abu-Abed, A.: Design and motion planning for a zero-reaction manipulator. In: *Proceedings of the IEEE International Conference on Robotics and Automation*, pp. 1554–1559. San Diego, CA (1994)
7. Fattah, A., Agrawal, S.K.: On the design of reactionless 3-DOF planar parallel mechanisms. *Mech. Mach. Theory* **41**(1), 70–82 (2006)
8. Arakelian, V., Briot, S.: Dynamic balancing of the SCARA robot. In: *Proceedings of the 17th CISM-IFTOMM Symposium on Robot Design, Dynamics, and Control (Romansy 2008)*, pp. 167–174. Tokyo, Japan, 5–9 July 2008
9. Arakelian, V., Smith, M.R.: Design of planar 3-DOF 3-RRR reactionless parallel manipulators. *Mechatronics* **18**, 601–606 (2008)

Nonlinear Antiresonance Vibrating Screen

V. N. Belovodskiy, S. L. Bukin and M. Y. Sukhorukov

Abstract A mathematical model of two masses vibrating screen with nonlinear elastic and dissipative ties working under ideal harmonic excitation is considered. The focus of the article is the study of the stationary movements in the “antiresonance” zone between the two natural frequencies. Using harmonic balance method the construction and analysis of bifurcation diagrams of this dynamical system are carried out, the stability factor of chosen regimes is appreciated with the help of their basins of attraction. The spectral and phase composition of the 2:1 superharmonic regimes is demonstrated, technological parameters of such machines are evaluated.

Keywords Vibromachine • Antiresonance • Polyharmonic vibration • Numerical analysis

1 Introduction

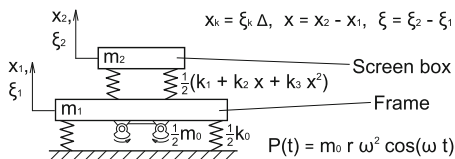
In comparison with hydraulic machines vibrating screens separate material on working surfaces, they are more effective and give an opportunity to improve quality of separation and simplify technological process [1]. For fine classification

V. N. Belovodskiy (✉) · S. L. Bukin · M. Y. Sukhorukov
Donetsk National Technical University, Donetsk, Ukraine
e-mail: belovodskiy@cs.dgtu.donetsk.ua

S. L. Bukin
e-mail: s.bukin08@gmail.com

M. Y. Sukhorukov
e-mail: max.sukhorukov@gmail.com

Fig. 1 The principal scheme of vibrating screen



of material small harmonic oscillations with high frequency are usually used. But for the last years the effectiveness of polyharmonic vibrations has been confirmed experimentally [2] and there are already some machines used for purpose of fine classification bi- and polyharmonic vibrations [3, 4]. There are different ways of forming polyharmonic vibrations [5], here we intend to do this with the help of combinational resonances [6]. Here the principal scheme of two masses vibrating screen with polynomial characteristic of elastic ties is considered and qualitative analysis of oscillations in the zone located between two natural frequencies is carried out. The general purpose of the investigation was to form polyharmonic vibrations of the required structure and to try to combine this effect with “anti-resonance properties” of that frequency domain.

2 Considered Model

The principal scheme of the screen is shown in Fig. 1.

In non-dimensional form the movement of the screen may be described by the following equations

$$\begin{cases} \frac{d^2 \xi_1}{d\tau^2} + b_{10} \frac{d\xi_1}{d\tau} + b_{11} \frac{d\xi}{d\tau} + b_{12} \xi \frac{d\xi}{d\tau} + b_{13} \xi^2 \frac{d\xi}{d\tau} \\ \quad + k_{10} \xi_1 + k_{11} \xi + k_{12} \xi^2 + k_{13} \xi^3 = P_1 \cos \eta \tau, \\ \frac{d^2 \xi}{d\tau^2} + b_{20} \frac{d\xi_1}{d\tau} + b_{21} \frac{d\xi}{d\tau} + b_{22} \xi \frac{d\xi}{d\tau} + b_{23} \xi^2 \frac{d\xi}{d\tau} \\ \quad + k_{20} \xi_1 + k_{21} \xi + k_{22} \xi^2 + k_{23} \xi^3 = P_2 \cos \eta \tau, \end{cases} \quad (1)$$

where

$$\begin{aligned} b_{10} &= \frac{\mu k_0}{m_1 \omega_1}, \quad b_{11} = -\frac{\mu k'_1}{m_1 \omega_1}, \quad b_{12} = -\frac{\mu k'_2 \Delta}{m_1 \omega_1}, \quad b_{13} = -\frac{\mu k'_3 \Delta^2}{m_1 \omega_1}, \\ b_{20} &= -\frac{\mu k_0}{m_1 \omega_1}, \quad b_{21} = \frac{\mu (m_1 + m_2) k'_1}{m_1 m_2 \omega_1}, \quad b_{22} = \frac{\mu (m_1 + m_2) k'_2 \Delta}{m_1 m_2 \omega_1}, \\ b_{23} &= \frac{\mu (m_1 + m_2) k'_3 \Delta^2}{m_1 m_2 \omega_1}, \quad k_{10} = \frac{k_0}{m_1 \omega_1^2}, \quad k_{11} = -\frac{k_1}{m_1 \omega_1^2}, \quad k_{12} = -\frac{k_2 \Delta}{m_1 \omega_1^2}, \\ k_{13} &= -\frac{k_3 \Delta^2}{m_1 \omega_1^2}, \quad k_{20} = -\frac{k_0}{m_1 \omega_1^2}, \quad k_{21} = \frac{k_1 (m_1 + m_2)}{m_1 m_2 \omega_1^2}, \quad k_{22} = \frac{k_2 (m_1 + m_2) \Delta}{m_1 m_2 \omega_1^2}, \\ k_{23} &= \frac{k_3 (m_1 + m_2) \Delta^2}{m_1 m_2 \omega_1^2}, \quad P_1 = \frac{m_0 r}{m_1 \Delta} \eta^2, \quad P_2 = -P_1, \quad \xi_1 = x_1 / \Delta, \quad \xi = x / \Delta, \end{aligned}$$

$x = x_2 - x_1$, x_1 —displacement of frame, x_2 —displacement of a working organ, $\Delta = 10^{-3} m$, m_0 —unbalanced mass, m_1 —mass of a frame, m_2 —mass of a screen box, k_0 —stiffness of isolators, k_1, k_2, k_3 —parameters of elastic ties and k'_1, k'_2, k'_3 —of dissipation, r —eccentricity of an exciter, μ —coefficient of dissipation, $\eta = \omega/\omega_1$, ω —frequency of an vibroexciter, ω_1 —the first natural frequency of a vibromachine, $\tau = \omega_1 t$. The exciter is supposed to be ideal.

3 Method of Investigation

Using harmonic balance method solution of the system (1) is found in a form

$$\xi_1(\tau) = \sum_{n=-N}^N c_n^{(1)} e^{in\eta\tau}, \quad \xi(\tau) = \sum_{n=-N}^N c_n e^{in\eta\tau}, \quad (2)$$

where N is a number of harmonics taken into consideration. Substituting (2) into (1) and equating the coefficients we get the system of polynomial equations with respect to $c_n^{(1)}$ and c_n

$$\left\{ \begin{array}{l} (k_{10} + b_{10} i \eta n - \eta^2 n^2) c_n^{(1)} + (k_{11} + b_{11} i \eta n) c_n + \\ + \sum_{j=-N}^N c_j c_{n-j} (k_{12} + b_{12} i \eta (n-j)) + \\ + \sum_{j=-N}^N \sum_{m=-N}^N c_j c_m c_{n-j-m} (k_{13} + b_{13} i \eta (n-j-m)) = \begin{cases} P_1/2, & n = \pm 1 \\ 0, & n \neq \pm 1 \end{cases}, \\ (k_{20} + b_{20} i \eta n) c_n^{(1)} + (k_{21} + b_{21} i \eta n - \eta^2 n^2) c_n + \\ + \sum_{j=-N}^N c_j c_{n-j} (k_{22} + b_{22} i \eta (n-j)) + \\ + \sum_{j=-N}^N \sum_{m=-N}^N c_j c_m c_{n-j-m} (k_{23} + b_{23} i \eta (n-j-m)) = \begin{cases} P_2/2, & n = \pm 1 \\ 0, & n \neq \pm 1 \end{cases}, \end{array} \right. \quad (3)$$

where $n, n-j, n-j-m \in [-N, N]$. Then, successively changing one of the parameters of the system (1) and solving the system (3) the bifurcation diagrams describing the dependence of the parameters of the motion with respect of the bifurcation parameter may be found. The points of bifurcation are discovered by control of change of sign of Jacobian of system (3), stability of the bifurcation branches is investigated by analyzing the multipliers of variation equations of system (1) [7]. The basins of attraction of periodic regimes are investigated with the help of special software programs. It is supposed that the trigonometric view of

the solutions of (1) is $\sum_{j=0}^N A_j \cos(j\eta\tau - \varphi_j)$, where $\varphi_j \in [-\pi, \pi)$.

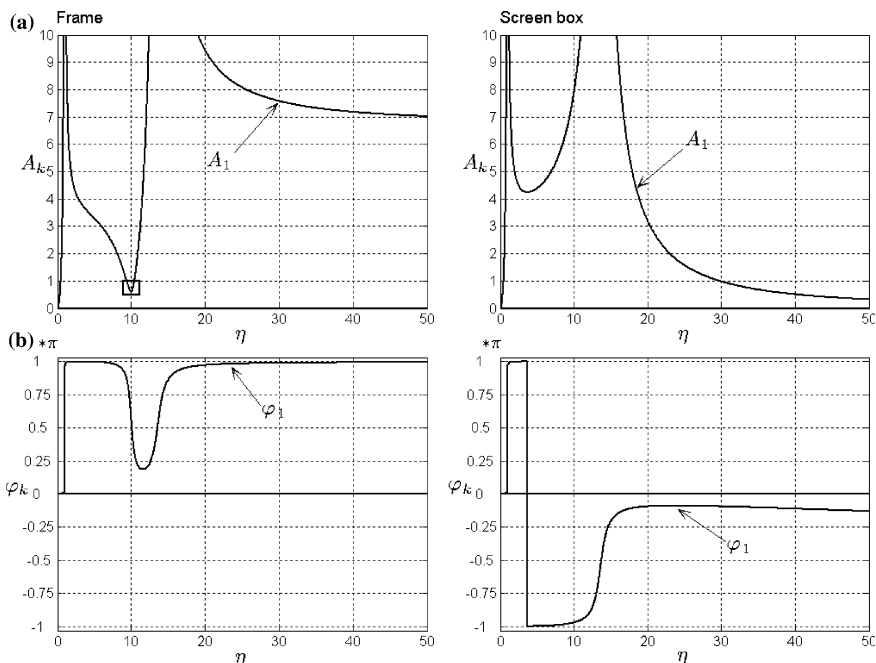


Fig. 2 AFC (a), PFC (b) of (1) for $k_2 = k_3 = 0$, where $A_n^{(m)}$, $\varphi_n^{(m)}$ —are the amplitude and initial phase of n -th harmonic of m -th regime

4 Results

The results of the investigation are presented in Figs. 2, 3, 4. They illustrate the appearance of nonlinearity in elastic ties and some results of changing of its certain parameters. Computations are fulfilled for vibration machine having the values of its main parameters: $m_1 = 650 \text{ kg}$, $m_2 = 550 \text{ kg}$, $k_0 = 0.12 \cdot 10^6 \text{ N/m}$, $k_1 = 5.5 \cdot 10^6 \text{ N/m}$, $m_0 = 50 \text{ kg}$, $r = 0.088 \text{ m}$, $\mu = 0.0008 \text{ sec}$. and five harmonic components in (2) were taken into account, i.e. $N = 5$. It is supposed here $k'_1 = k_1$, $k'_2 = k'_3 = 0$.

The nonlinear dissipation ($k'_2 = k_2$, $k'_3 = k_3$) causes changes in absolute values of the harmonics and preserve their relative correlations. One may also note that a decrease of the main stiffness k_1 causes the decreasing of natural frequencies and contracts the frequency domain of the existence of superharmonic resonance. It is necessary to say that our attempts to get superharmonic regimes in vicinity of antiresonance frequency by varying of values k_3/k_1 , k_2/k_1 and remaining among elastic characteristics with one potential well have been unsuccessful yet. Based on the experience of exploitation of the vibrating machines, one can predict improvement in technological parameters and increase of productivity of vibrating screens for fine materials at the expense of polyharmonic vibrations by 25–30 %.

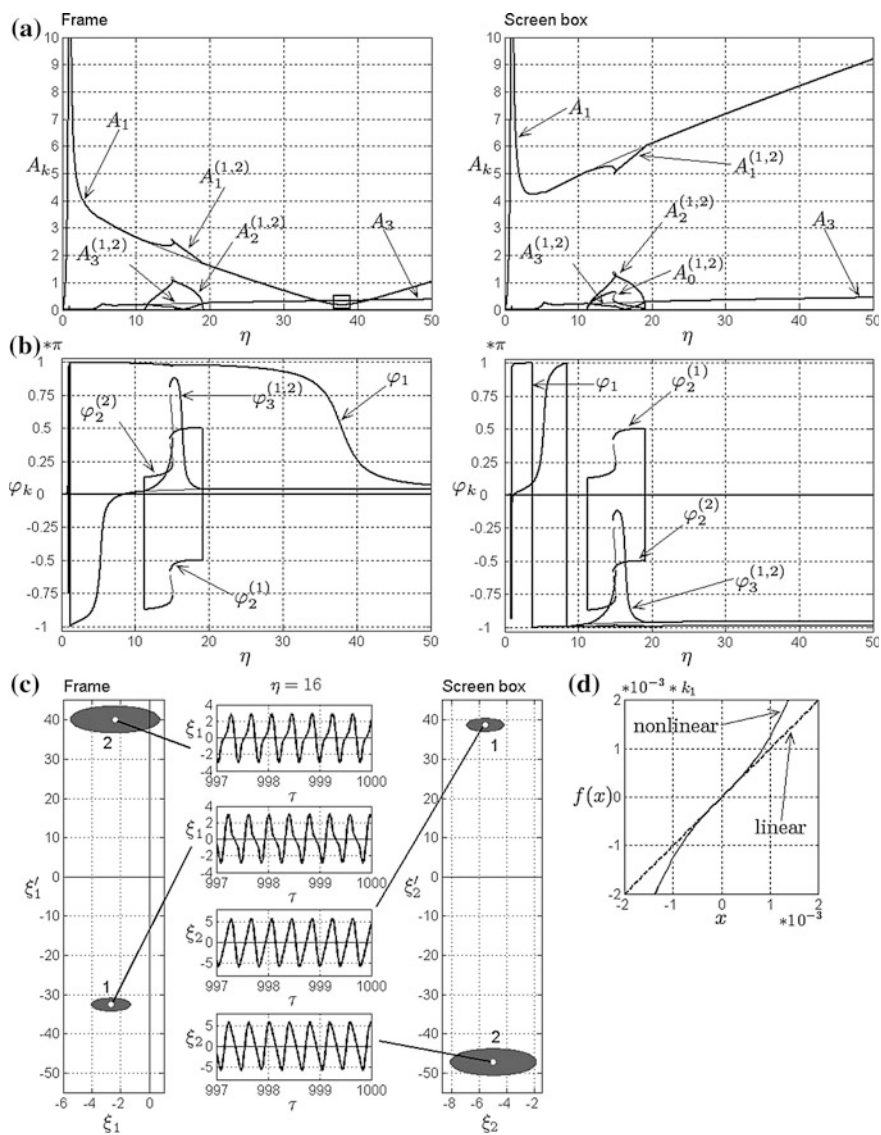


Fig. 3 AFC (a), PFC (b), section $\tau = 0$ of cores of BOA (c) and form of characteristic of elastic ties (d) for $k_2 = 0$, $k_3/k_1 = 0.25/\Delta^2$

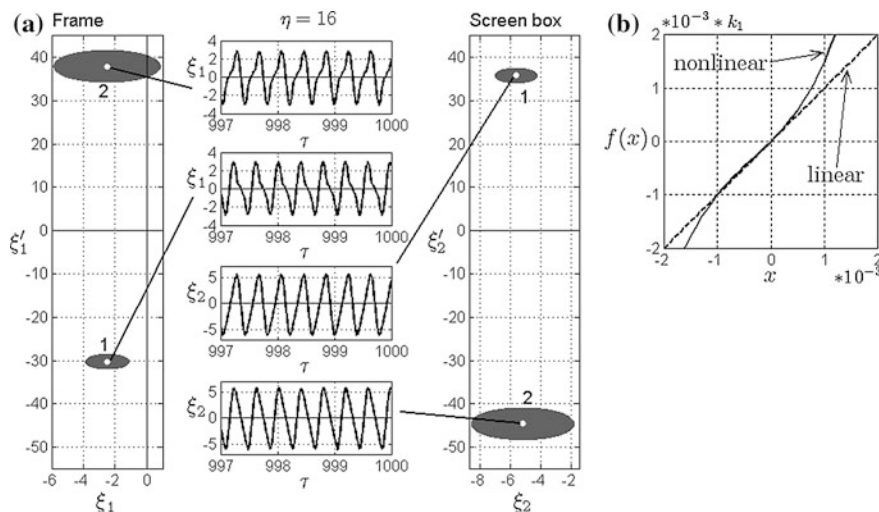


Fig. 4 Section $\tau = 0$ of cores of BOA (a) and form of characteristic of elastic ties (b) for $k_2/k_1 = 0.25/\Delta$, $k_3/k_1 = 0.25/\Delta^2$

5 Conclusions

The performed analysis discovers the principal possibility of forming practically meaningful biharmonic vibrations in two masses nonlinear vibrating machine with monoharmonic excitation and necessity of accepting compromised decisions concerning the worsening of its isolation properties. The next topical problems to deal with are the design of the elastic system having the required characteristic and the study of the running at the chosen superharmonic regime under limited capacity of source of energy.

References

1. Vaisberg, L.A., Korovnikov, A.N.: Fine screening as alternative of hydraulic classification by size Concentration **3**, 23–34, (In Russian) (2004)
2. Goncharevich, I.F.: Increase of productivity and profitability of industrial nanotechnologies. Moscow: RIA, Section “Mining”, 2010, Available via, <http://www.engineeracademy.ru/otrasli/mining>, (In Russian) (2010)
3. Multi-frequency vibromachines. Materials of the site “Kroosh Technologies Ltd.”, 2010, <http://www.kroosh.ru> (In Russian) (2010)
4. Bukin, S.L., Maslov, S.G., Luity, A.P., Reznichenko, G.L.: Intensification of technological processes of vibrating machines by realization of biharmonic working regimes. Concentration Miner.: Sci. Tech. Collect. **36**(77), **37**(78), 81–89, (In Ukrainian) (2009)
5. Vibrations in engineering: Handbook in 6 volumes. Vol. 4. Vibration processes and machines. In: Lavendel, E.E. (ed.) Moscow: Mashinostroenie, p. 509, (In Russian) (1981)

6. Belovodskiy, V.N., Sukhorukov, M.Y.: Combination resonances and their bifurcations in the nonlinear vibromachines with a polynomial characteristic of restoring force and periodic excitation, vibration Problems ICOVP 2011. The 10th International Conference on Vibration Problems, Series: Springer Proceedings in Physics, Vol. 139, Springer Science + Business Media, pp. 235–240 (2011)
7. Jakubovich, V.A., Starjinskiy, V.M.: Linear differential equations with periodic coefficients and their applications. Moscow: Nauka, p. 720, (In Russian) (1972)

Modeling and Simulation of a Slider Crank Mechanism with a Flexible Extensible Link

M. Dupac and S. Noroozi

Abstract In this paper the modelling of a slider-crank mechanism with an extensible flexible link is presented and its dynamical behaviour analyzed. The link flexibility is modelled using extensible rigid links and rotational springs. The equations of motion with and without slider clearance are written. Accurate simulation of the extensible mechanism is performed to study its possible performance and behaviour under the combined effect of different parameters. A dynamic analysis is carried out in order to understand its behaviour under motion reconfiguration.

Keywords Dynamics • Extensible links • Clearance • Impact

1 Introduction

The design of complex mechanical systems usually means the testing of the physical prototypes to evaluate their functionality. To avoid time-consuming and high costs, engineering simulations are used to study parameters effect on the mechanical system dynamical behaviour. Novel studies shown that simple flexible systems [1] with clearances [2] can exhibit complex dynamic behaviour such as particular vibration modes, and many times may exhibit sub harmonic and chaotic vibrations. The mentioned parameters (clearance, changing velocity, impacts, etc.)

M. Dupac (✉) · S. Noroozi
Bournemouth University, Bournemouth, UK
e-mail: mdupac@bournemouth.ac.uk

S. Noroozi
e-mail: snoroozi@bournemouth.ac.uk

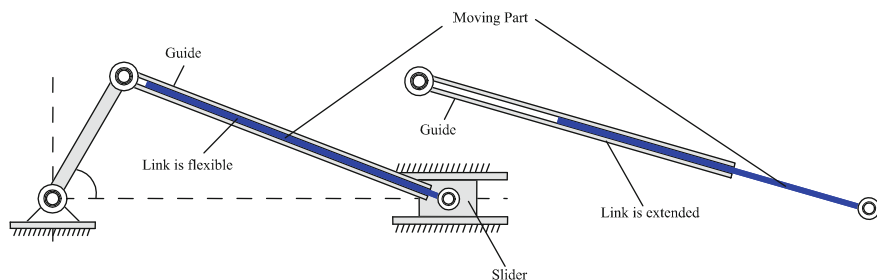


Fig. 1 The flexible extensible mechanism

may affect the mechanical system performance and/or life, having a long term effect on their precision.

The impact response of a multi-body system with consistent and lumped mass was studied in [3]. The impact dynamics of elastic mechanical joints with clearance and their response under various conditions have been studied experimentally and analytically in [4]. Dynamic analysis of planar mechanisms with rotating slider joint and clearance and the prismatic joint inertia on the dynamics of kinematic chains was studied in [5, 6]. The modelling and analysis of planar rigid mechanism with translational clearance joints studied in [2].

The design and dynamics of some impact systems with lumped masses was studied in [3, 7–9]. The influence of clearance on the mechanical behaviour of different systems has been considered in [4, 8, 10, 11]. Friction constraints and contact have been used in [12–14] to study the stick slip phenomena and different impact lows, while frictionless impact models in [15]. The impact equations using Newton's law when only single collisions have been considered have been discussed in [16]. Rigid body impacts have been described in [17].

The aim of this study is a better understanding of system dynamics when an extensible link and clearance is considered. Other aim includes an optimal design of such mechanisms. For the proposed system periodic motion was observed for both systems with and without clearance. Simulation tests have been performed for medium to high crank speeds.

2 System Model

The slider-crank mechanism system with a flexible extensible rod (guide and moving part) is shown in Fig. 1.

To illustrate the geometry of the slider-crank mechanism, the translational flexible link was modelled using successive extensible rigid rods (4 successive extensible rigid rods have been used for this study) connected with torsional springs. The spring constant was defined for this study as in [18]. Each one of the extensible rods are equal (Fig. 2). $d_{AB} = L_2 = L$, $d_{BC} = L_3 = L$, $d_{CD} = L_3 = L$ and can

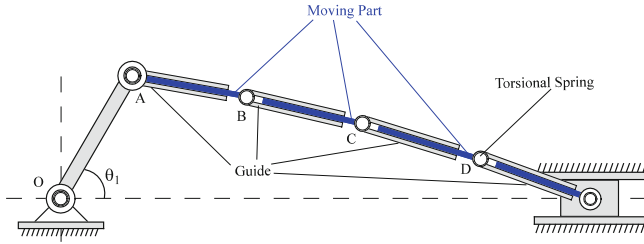


Fig. 2 The flexible extensible mechanism modeled as a system of 4 extensible links with clearance and torsional springs

extend (change length) based on the physical law $L_i = L + L_e^* \cos(\theta_1)$ where θ_1 is the crank angle and $d_{OA} = L_1$ is the crank length. A variable motor torque defined as $M = M_0(1 - \omega_1/\omega_0)$ is acting on the crank.

3 Equations of Motion

3.1 Equations of Motion with no Clearance

For the model with no clearance shown in Fig. 2, the moving part of each extensible link translate parallel to its support (the guide) called the line of translation. The centre of the mass C_i of the links $i = \overline{1, 6}$ (crank, 4 extensible links and the slider) is given by the position vector $\mathbf{r}_{Ci} = x_{Ci}\mathbf{i} + y_{Ci}\mathbf{j}$. The velocity vector is the derivative with respect to time of the position vector $\mathbf{v}_{Ci} = \dot{\mathbf{r}}_{Ci} = \dot{x}_{Ci}\mathbf{i} + \dot{y}_{Ci}\mathbf{j}$, and the acceleration vector is the double derivative with respect to time, that is $\mathbf{a}_{Ci} = \ddot{\mathbf{r}}_{Ci} = \ddot{x}_{Ci}\mathbf{i} + \ddot{y}_{Ci}\mathbf{j}$. The Lagrange differential equation of motion is

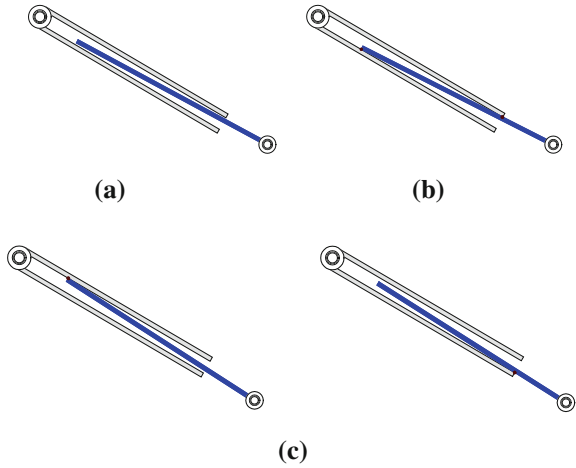
$$\frac{d}{dt} \left(\frac{\partial T}{\partial \dot{q}_i} \right) - \frac{\partial T}{\partial q_i} = Q. \quad (1)$$

where T is the total kinetic energy of the system, Q is the generalized force and q_i are the generalized coordinates. The total kinetic energy is $T = \sum_{i=1}^n T_i$ where $\omega_i = \theta_i \mathbf{k}$ and $T_i = \frac{1}{2} m v_{Ci}^2 + \frac{1}{2} I_{Ci} \omega_i^2$ is the angular velocity and respectively the kinetic energy of the i th component. The generalized forces can be written as

$$Q_i = \sum_{j=1}^n \frac{\partial \mathbf{r}_{Cj}}{\partial \theta_i} \cdot \mathbf{G}_j + \frac{\partial \omega_i}{\partial \dot{\theta}_i} \cdot \mathbf{M}_i \quad (2)$$

where $\mathbf{G}_i = -m_i g \mathbf{j}$ is the force acting on the i -th component.

Fig. 3 A flexible extensible link component with clearance model, **a** no impact, **b** impact on two points, and, **c** impact on one point



3.2 Equations of Motion with Clearance

For the clearance model, the moving part of each extensible link can translate and rotate about its support (perpendicular to the axis of translation). To illustrate the geometry of each extensible link with clearance the guide was made with a very large backlash in order to make the clearance clearly visible as shown in Fig. 3.

The cases shown in Fig. 3 illustrates the possible clearance model for each extensible link, that is: (a) no impact between the moving link and the guide as shown in Fig. 3a, (b) impact on two points as shown in Fig. 3b, and, (c) impact on a single point as shown in Fig. 3c.

The condition for switching from one case to another depends on the initial conditions, system dynamic response as well as material properties. The simultaneous impact on two points in not considered in this study. The equation of motion with impact on a single point is written as in [5, 6, 12, 18, 19]

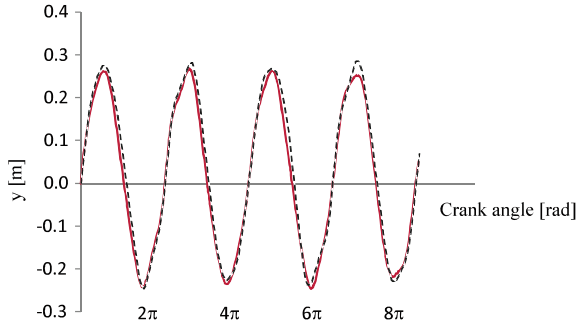
$$\left. \frac{\partial T}{\partial \dot{q}_i} \right|_{t_s} - \left. \frac{\partial T}{\partial \dot{q}_i} \right|_{t_a} = P_i, \quad (3)$$

where T is the kinetic energy, \dot{q}_i is the velocity associated, P_i is the generalized impulse and t_a and t_s represents the moments of time before (time of approach) and after (time of separation) the impact. The generalized impulses [right-hand sides of Eq. (3)] can be written as

$$P_i = \frac{\partial v_P}{\partial \dot{q}_i} \cdot (F_n \mathbf{e}_n + F_t \mathbf{e}_t), \quad (4)$$

where \mathbf{e}_n and \mathbf{e}_t are the unit vectors normal and tangential to contact, and F_n and F_t are the normal and the tangential components of the impulse momentum. The velocity of the impacting point P of the moving part of an extensible link can be

Fig. 4 Trajectory of the middle of the extensible flexible rod vs. crank angle for **a** mechanical system without clearance (*dotted line*), and **b** mechanical system with clearance (*continuous line*)



expressed as $\mathbf{v}_P = \mathbf{v}_C + \omega \times \mathbf{r}_P$. The velocity of approach and separation can be written as $\mathbf{v}_a = \mathbf{v}_P|_{t_a}$, $\mathbf{v}_s = \mathbf{v}_P|_{t_s}$ where \mathbf{v}_a is the velocity at time t_a , and \mathbf{v}_s is the velocity at time t_s . The relation

$$e\mathbf{v}_a \cdot \mathbf{e}_n = \mathbf{v}_s \cdot \mathbf{e}_n \quad (5)$$

have been written using the definition of the coefficient of restitution e .

4 Results and Conclusions

In this section, the results of the simulations are presented and discussed. For the simulation, a flexible link with 4 equal rigid rods was considered. The extensible rod was assumed to have a uniform cross section of 0.06 m, crank length 0.044 m, an initial length of each flexible extensible link of 0.04 m and mass density $\rho = 7.85 \text{ g/cm}^3$. Each extensible link i is extended based on the equation $L_i = L + L_e^* \cos(\theta_1)$, $L = 0.04$ and $L_e = 0.007$. The torque of the motor is calculated using $M_0 = 1 \text{ Nm}$. The flexural response at the middle of the extensible rod was considered and its trajectory plotted vs. the crank angle.

The flexural response at a relatively low angular velocity of the extensible rod with clearance vs. extensible rod without clearance can be observed in Fig. 4. At high angular velocities and high clearance a chaotic response was observed.

References

1. Chu, S.C., Pan, K.C.: Dynamic response of a high-speed slider-crank mechanism with an elastic connecting rod. *ASME J. Eng. Ind. Trans.* **97**, 542–550 (1975)
2. Flores, P., Leine, R., Glocker, C.: Modelling and analysis of planar rigid multibody systems with translational clearance joints based on the non-smooth dynamics approach. *Multibody Sys. Dyn.* **23**, 165–190 (2010)
3. Khulief, Y.A., Shabana, A.A.: Impact responses of multibody system with consistent and lumped masses. *J. Sound Vib.* **104**(2), 187–207 (1986)

4. Dubowsky, S., Moening, M.: An experimental and analytical study of impact forces in elastic mechanical system with clearances. *Mech. Mach. Theory*, **64**, 89–95 (1978)
5. Stoenescu, E.D., Marghitu, D.B.: Dynamic analysis of a planar rigid-link mechanism with rotating slider joint and clearance. *J. Sound Vib.* **266**, 394–404 (2003)
6. Stoenescu, E.D., Marghitu, D.B.: Effect of prismatic joint inertia on dynamics of kinematic chains. *Mech. Mach. Theory* **39**, 431–443 (2004)
7. Dupac, M., Beale, D.G., Marghitu, D.B.: Lumped mass modelling and chaotic behaviour of an elastic levitated droplet. *Nonlinear Dyn.* **27**, 311–326 (2002)
8. Dupac, M., Beale, D.G.: Dynamic analysis of a flexible linkage mechanism with cracks and clearance. *Mech. Mach. Theory* **45**(12), 1909–1923 (2010)
9. Rubinstein, D.: Dynamics of a flexible beam and a system of rigid rods, with fully inverse (one-sided) boundary conditions. *Comput. Methods Appl. Mech. Eng.* **175**, 87–97 (1999)
10. Farahanchi, F., Shaw, S.W.: Chaotic and periodic dynamics of a slider-crank mechanism with slider clearance. *J. Sound Vib.* **177**(3), 307–324 (1994)
11. Gilmore, B.J., Cipra, R.J.: Simulation of planar dynamic mechanical systems with changing topologies: part I and part II, American society of mechanical engineers. *J. Mech. Design*, **113**, 70–83 (1991)
12. Marghitu, D.B., Hurmuzlu, Y.: Nonlinear dynamics of an elastic rod with frictional impact. *Int. J. Nonlinear Dyn.* **10**, 187–201 (1996)
13. Pfeiffer, F.: Complimentarily problems of stick-slip vibrations, American society of mechanical engineers. *Dyn. Vibr. Time-Varying Sys. Struct.* **56**, 43–50 (1993)
14. Payr, M., Glocker, C.: Oblique frictional impact of a bar: analysis and comparison of different impact laws. *Nonlinear Dyn.* **41**(4), 361–383 (2005)
15. Glocker, C.: On frictionless impact models in rigid-body systems, *Philos. Trans. R. Soc. Lond., Ser. A* **359**(1789), 2385–2404 (2001)
16. Brach, R.M.: *Mechanical impact dynamics*, Wiley, New York (1991)
17. Brach, R.M.: Rigid body collisions, American society of mechanical engineers. *J. Appl. Mech.* **56**, 133–138 (1989)
18. Mitiguy, P., Banerjee, A.K.: Determination of spring constants for modelling flexible beams. Working Model Technical Paper (2000)
19. Dupac, M., Marghitu, D.B.: Nonlinear dynamics of a flexible mechanism with impact. *J. Sound Vib.* **289**(4–5), 952–966 (2006)

Multipoint Contact Approach to the Analysis of Interacting Flexible Bodies Vibration

M. Hajžman and D. Rychecký

Abstract The efficient method usable for the vibrational analysis of interacting flexible bodies is presented in this paper. It is motivated by the research of blades interaction in the framework of turbine bladed disks. The approach is based on the decomposition of a contact surface into a set of elementary areas and on the expression of contact and friction forces between these areas. The methodology is implemented in the MATLAB system and obtained results for the chosen test case are compared with the results obtained by the ANSYS software.

Keywords Dynamics • Contact • Friction • Blade • Vibration

1 Introduction

Lots of real industrial problems of flexible bodies vibration are characterized by effects of contact and friction forces. Problems of contact dynamics are studied very intensively and various approaches for their solution exist (e.g. [1–4]). The method presented in this paper is motivated by the research of blades interaction in the framework of turbine bladed disks [5]. One of the possible approaches for the reducing of blade vibrations is the usage of the friction phenomenon for energy dissipation and successive vibration suppression [6].

M. Hajžman (✉) · D. Rychecký
University of West Bohemia, Plzeň, Czech Republic
e-mail: mhajzman@kme.zcu.cz

D. Rychecký
e-mail: rychecky@kme.zcu.cz

The most common contact treatment employs the finite element analysis and is a suitable way to the solution of blade dynamics. It is possible to solve complex problems related to the blades interaction during their operation, which is characterized by mutual contacts and friction forces. However the utilization of commercial codes (e.g. ANSYS, NASTRAN, ...) can be inefficient for large and long contact problems due to high computational costs. On the other hand different approaches were developed in the framework of multibody dynamics, but they can be very general for analysis of rotating bodies vibration and it can bring higher computational times or too complex model creation.

The methodology presented in this paper is based on the combination of the finite element method with discrete elements and on the derivation of expressions for contact and friction forces using several contact geometry simplifications. Obtained results in case of a simple mechanical system are compared with the solution by ANSYS system.

2 Modelling of Flexible Bodies Vibration and Their Mutual Contact

Suitable mathematical description of a vibrating body should be created for sake of a contact analysis performance. Especially in case of blade modelling the most convenient way is the usage of special blade 1D finite elements of undeformable cross-section (e.g. [7]) combined with rigid bodies and discrete elastic elements. The finite element model of one rotating flexible blade includes all effects of stationary rotation (constant angular velocity ω) and can be of the form

$$\mathbf{M}_B \ddot{\mathbf{q}}_B + (\mathbf{B}_B + \omega \mathbf{G}_B) \dot{\mathbf{q}}_B + (\mathbf{K}_B - \omega^2 \mathbf{K}_{dB} + \omega^2 \mathbf{K}_{\omega B}) \mathbf{q}_B = \omega^2 \mathbf{f}_{\omega B}, \quad (1)$$

where symmetric matrices \mathbf{M}_B , \mathbf{B}_B , \mathbf{K}_B , $\omega^2 \mathbf{K}_{dB}$, $\omega^2 \mathbf{K}_{\omega B}$ are mass, material damping, stiffness, spin softening and centrifugal stiffening matrices. Matrix $\omega \mathbf{G}_B$ is skew symmetric matrix of gyroscopic effects. Constant centrifugal forces are expressed by vector $\omega^2 \mathbf{f}_{\omega B}$. The generalized coordinate vector of nodal displacements of i -th node is composed of three translations and three rotations

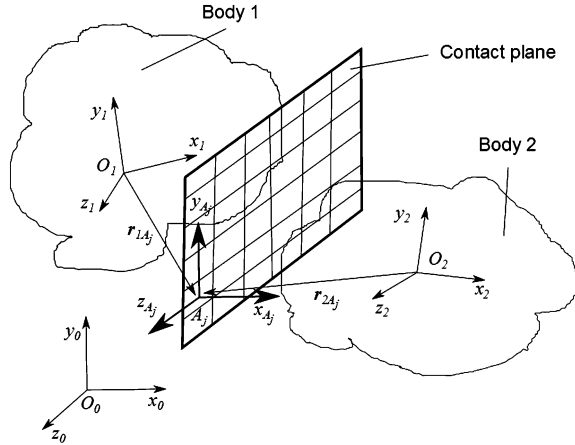
$$\mathbf{q}_i = [u_i, v_i, w_i, \varphi_i, \vartheta_i, \psi_i]^T. \quad (2)$$

The form of the whole generalized coordinate vector \mathbf{q}_B , which is usually composed of nodal vectors (2), and the meaning of its particular elements are important characteristics related to the contact and friction forces derivation.

Although the presented model of a flexible rotating blade is based on 1D finite elements and generalized coordinate vector (2), possible generalization for 3D finite elements with another nodal variables is straightforward.

Particular models of two or more flexible bodies are considered in form (1) and the next step of the presented methodology is the derivation of an interaction

Fig. 1 Scheme of a contact plane for the definition of an interaction between two bodies



model between chosen bodies. The most simple case and computationally the most efficient is the consideration of a single contact point presented e.g. in [7]. Two flexible bodies are defined in global coordinate system $O_0x_0y_0z_0$ and each body s has one coordinate system $O_sx_sy_szs$, $s = 1, 2$ in the chosen node of the finite element mesh, which is related to the contact surface. The more comprehensive method, presented in this paper, is based on the division of the whole contact surface into a set of smaller elementary contact areas defined by their positions and dimensions (see Fig. 1). Six generalized coordinates (three translations and three rotations in \mathbf{q}_{0s} , $s = 1, 2$) can be used for the particular node according to (2) and together with vectors \mathbf{r}_{sAj} they determine the motion of the contact surface. In case of a solid finite element mesh the situation is more complex, several nodes with only three translational coordinates should be used for the definition of $O_sx_sy_szs$ ($s = 1, 2$) coordinate system.

The potential (strain) energy E_{Aj} of normal elastic contact forces and dynamic deformation \mathbf{d}_{Aj} of the contact point can be written as

$$E_{Aj} = \frac{1}{2} \mathbf{d}_{Aj}^T \mathbf{K}_{Aj} \mathbf{d}_{Aj}, \quad \mathbf{d}_{Aj} = \mathbf{T}_{1,Aj} \mathbf{q}_{01} - \mathbf{T}_{2,Aj} \mathbf{q}_{02}, \quad (3)$$

where \mathbf{q}_{01} , \mathbf{q}_{02} are generalized coordinate vectors of nodes on body 1 and body 2, $\mathbf{T}_{1,Aj}$ and $\mathbf{T}_{2,Aj}$ are transformation matrices from the body coordinate systems ($O_sx_sy_szs$, $s = 1, 2$) to the elementary contact area coordinate system ($A_jx_{Aj}y_{Aj}z_{Aj}$) and \mathbf{K}_{Aj} is the local diagonal contact stiffness matrix created using the normal stiffness [8] calculated by Hertzian law (see e.g. [7] for more detail on the contact stiffness calculation). Strain energy E_{Aj} is used for the calculation of global contact stiffness matrix \mathbf{K}_C . Global proportional damping matrix of the contact $\mathbf{B}_C = \beta \mathbf{K}_C$ should be employed analogously (β is the proportional damping coefficient).

The calculation of the friction effects is based also on the transformation of generalized nodal velocities $\dot{\mathbf{q}}_{01}$, $\dot{\mathbf{q}}_{02}$ by $\mathbf{T}_{1,Aj}$ and $\mathbf{T}_{2,Aj}$ and expression of relative slip velocities in $A_jx_{Aj}y_{Aj}z_{Aj}$ coordinate system. Friction forces T_{Ajy} and T_{Ajz} in y

Fig. 2 Two interacting blades through shrouds with contact plane

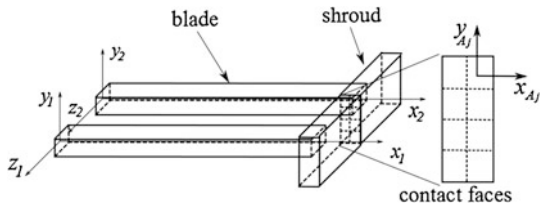
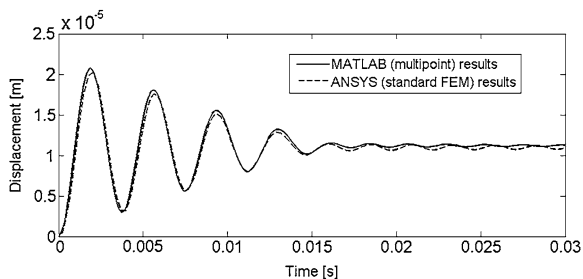


Fig. 3 Comparison of the tip displacement of the loaded blade (in z direction) obtained by the new multipoint methodology and by the ANSYS FEM approach



and z directions are the components of the total friction force vector, whose value T_{A_j} can be expressed as

$$T_{A_j} = N_{A_j}(d_n)f(\dot{d}_\tau), \quad (4)$$

where N_{A_j} is the normal contact force dependent on total normal contact deformation d_n and $f(\dot{d}_\tau)$ is the nonlinear friction coefficient dependent on relative slip velocity \dot{d}_τ , which lies in a contact tangent plane. Friction forces for all basic contact areas should be arranged in generalized force vector $\mathbf{f}_F(\mathbf{q}, \dot{\mathbf{q}})$.

The advantage of the presented approach is in the fact that the overall normal deformation can be evaluated in each integration step for each basic contact surface. If the value of a normal deformation is negative it means, that the contact does not occur and the contribution of the particular contact surface into the normal and tangential effects is not considered. The overall model of the vibrating bodies considering rotation and mutual contact effects is of the form

$$\mathbf{M}\ddot{\mathbf{q}} + (\mathbf{B} + \omega\mathbf{G} + \mathbf{B}_C)\dot{\mathbf{q}} + (\mathbf{K} - \omega^2\mathbf{K}_d + \omega^2\mathbf{K}_\omega + \mathbf{K}_C)\mathbf{q} = \omega^2\mathbf{f}_\omega + \mathbf{f}_0 + \mathbf{f}_F, \quad (5)$$

where the global matrices and vectors are composed of previously explained variables in (1) and \mathbf{f}_0 defines external excitation force vector. The whole model should be solved by numerical integration of motions equations in most cases.

3 Results of a Test Example of Two Blades Vibration

A system of two clamped blades (see Fig. 2) with mutual contacts was chosen as a test example and was modelled and analyzed using the commercial ANSYS software and original in-house tool created in MATLAB system on the basis of the

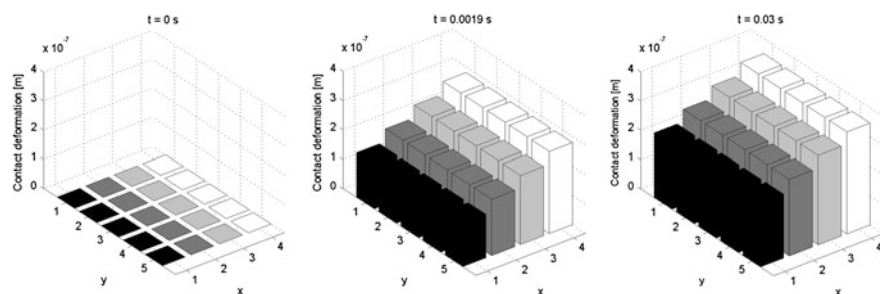


Fig. 4 Contact deformation for particular elementary areas of the discretized contact plane in chosen times (for the multipoint approach implemented in MATLAB)

presented methodology. The blades were discretized using 3D solid finite elements in ANSYS, where a standard FE contact procedure was used. The MATLAB model was characterized by using 1D blade elements with rectangular cross-section and by the shrouds considered as rigid bodies. The loading was applied as a force in z direction on the shroud of one blade in order to push the blade against the second blade. The force amplitude has a step character. It was initially zero (at time 0 s) and then non-zero constant (10 N) in the course of the solution. The equations of motion were solved by the numerical integration. The comparison of the results obtained by the ANSYS standard approach and by the created in-house MATLAB tool is shown in Fig. 3. It can be seen that the loaded blade displacements calculated using standard and newly proposed multipoint method are comparable.

The normal forces were calculated as linear functions of contact normal deformations and the friction forces were considered with exponentially decreasing coefficient of friction from its static to dynamic value. The illustration of contact deformations for particular elementary contact areas is shown in Fig. 4 for chosen simulation times. It is obvious that the deformations are uniformly distributed across the whole contact surface according to Fig. 2.

4 Conclusions

The modelling of flexible bodies vibrations influenced by mutual contact and friction forces is briefly described in this paper. The effort is motivated by the need to solve the problems of contact dynamic analyses of interacting blades. The motivation for development of this method for the solution of contact dynamics arises from high computational costs when using the commercial finite element software tools. Without suitable solution methodologies it is not possible to design, optimize and to tune proper and effective structural elements for sake of undesirable vibration suppression.

The presented multipoint contact modelling approach is based on the division of the whole contact surface to a set of several elementary contact areas. The calculation of normal and friction forces can be modified with respect to studied application. Relatively fast computational times compared to the standard FEM approaches allow to use the multipoint contact approach for optimization tasks.

Acknowledgments This work was supported by the European Regional Development Fund (ERDF), project “NTIS—New Technologies for Information Society”, European Centre of Excellence, CZ.1.05/1.1.00/02.0090, and by project SGS-2010-046.

References

1. Pfeiffer, F., Glocker, C.: *Multibody dynamics with unilateral contacts*, Wiley, New York (2004)
2. Pfeiffer, F.: On non-smooth dynamics. *Meccanica*, vol. 43, p. 533 (2008)
3. Popov, V.L.: *Contact mechanics and friction: physical principles and applications*, Springer, Berlin (2010)
4. Wriggers, P., Nackenhorst, U. (eds.): *IUTAM Symposium on computational methods in contact mechanics*, Springer, Berlin (2007)
5. Půst, L., Pešek, L.: Non-proportional nonlinear damping in experimental bladed disk. *Eng. Mech.* vol. 17, pp. 237 (2010)
6. Petrov, E.P., Ewins, D.J.: Effects of damping and varying contact area at blade-disk joints in forced response analysis of bladed disk assemblies. *J. Turbomach.* vol. 128, pp. 403 (2006)
7. Zeman, V., Byrtus, M., Hajžman, M.: Harmonic forced vibration of two rotating blades with friction damping. *Eng. Mech.* vol. 17, pp. 187 (2010)
8. Rivin, E.I.: *Stiffness and damping in mechanical design*, Marcel Dekker (1989)

Dynamic Analysis of Resonance: Bifurcation Characteristics of Non-linear Parametric Systems

M. Hortel, A. Škuderová, C. Kratochvíl and M. Houfek

Abstract The dynamic analysis is an important part of basic research of complex planetary transmission systems with split power flow. The bifurcation characteristics of the resonance courses especially for high-speed weakly and strongly non-linear parametric and in the damping time-heteronymous systems are highly sensitive to their parameters, i.e. to the quality and quantity of their bifurcation features and ambiguities. In the case of mass discretization, their analytical—numerical solution leads to complex integro-differential equations with solving kernels in the form of Green's resolventes and complex simulation models in MATLAB/Simulink. The case of one branch of the planetary transmission system with six degrees of freedom is analysed in terms of internal dynamics in this paper, i.e. the causes of the quantity and quality of resonance bifurcation curves and formation of ambiguity characteristics of relative motion in gear meshes.

Keywords Nonlinear dynamics • Time-heteronymous systems • Damping • Gears

1 Introduction

The analysis of the internal dynamics of time heteronymous weakly and strongly non-linear, in general, planetary gear differential systems with kinematic couplings (gears) and split power flows is a complex analysis of mathematical functional systems of equations. The design of disc shapes of gears with lightening holes can be characterized by time variable nature of the material damping in gear meshes

M. Hortel (✉) · A. Škuderová · C. Kratochvíl · M. Houfek
Institute of Thermomechanics, AS CR, v. v. i, Prague, Czech Republic
e-mail: hortel@it.cas.cz

and may have a still-unknown complex functional dependences. Therefore, it is necessary to determine the damping characteristics experimentally and they must be then expressed, for example, by means of Fourier's series.

Such a time-dependent function of cogwheel disc damping $k_D(t) = k_D(t + T)$ with the period $T = 2\pi/\omega$ in the interval $\langle 0; T \rangle$, which fulfils the conditions of uniqueness and finiteness, and with a finite number of maximums and minimums and discreteness (Dirichlet's conditions), can be expanded into a convergent series as follows

$$\begin{aligned}
 k_D(t) = k_D(t + T) &= \frac{1}{2T} \int_v^{2T} k_D(t) dt \\
 &+ \sum_{m=1}^{\infty} \left\{ \left[\frac{2}{T} \int_0^T k_D(t) \cos(p m \omega t) dt \right] \cos(p m \omega t) \right. \\
 &\left. + \left[\frac{2}{T} \int_0^T k_D(t) \sin(p m \omega t) dt \right] \sin(p m \omega t) \right\}, \quad (1)
 \end{aligned}$$

where $\omega = \pi n/30$ is angular velocity of the cogwheel ($n = n_2 = n_3$, if the ratio of transmission between the sun gear 2 and the satellite 3 is $i = 1$), n is the number of wheel revolutions, p is the number of lightening holes in the cogwheel disc or, more generally, the number of damping periods caused by non-homogeneity of the wheel disc.

2 Mathematical-Physical Model of System

By introducing the time heteronomous function (1) into the system of motion equations of the substitutive mathematical-physical model of *one* branch of power flow of the pseudoplanetary system from Fig. 1, i.e. the sun gear 2 and one satellite 3 with spur gear with straight teeth, we obtain a system of ordinary differential equations with time-variable coefficients in the following form [1]

$$\begin{aligned}
 \mathbf{M}\mathbf{v}'' + [{}_1\mathbf{K}(\beta, \delta_i, H) + {}_1\mathbf{k}_D(t)]\mathbf{v}' + \sum_{K_1 > 1} [{}_{K_1}\mathbf{K}(D, D_i, H) + {}_{K_1}\mathbf{k}_D(t)] \\
 \times |\mathbf{w}'(\mathbf{v}')|^{K_1} \text{sgn}(\mathbf{w}'(\mathbf{v}')) + {}_1\mathbf{C}(\varepsilon, \kappa, Y_n, U_n, V_n, H, t)\mathbf{v} \\
 + \sum_{K > 1} {}_K\mathbf{C}(\varepsilon, \kappa, I_n, H, t)\mathbf{w}^K(\mathbf{v}) = \mathbf{F}(a_n, b_n, \bar{\varphi}, H, t), \quad (2)
 \end{aligned}$$

where \mathbf{v} generally denotes the 6-dimensional vector of displacement of system vibration, $\mathbf{w}^K(\mathbf{v})$ is the K -th power of vector \mathbf{v} defined by expression $\mathbf{w}^K(\mathbf{v}) = \mathbf{D}(\mathbf{w}(\mathbf{v})\mathbf{w}^{K-1}(\mathbf{v}))$. The term $\mathbf{D}(\mathbf{w}(\mathbf{v}))$ denotes the diagonal matrix, whose

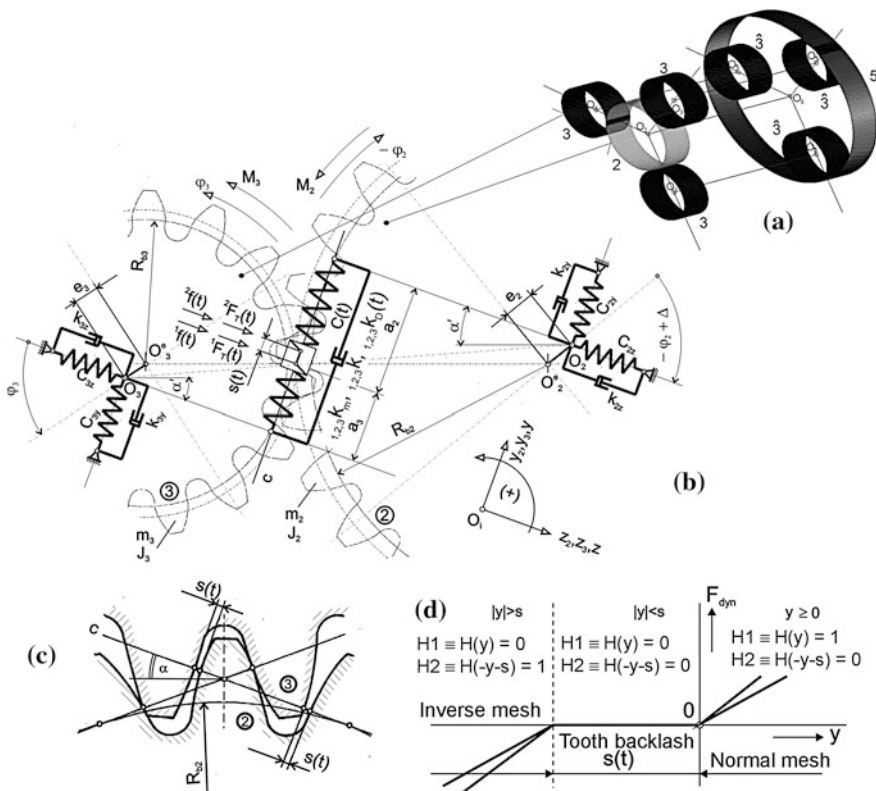


Fig. 1 Substitutive mathematical-physical model of kinematic pair of gears (b) of pseudoplanetary gear system with double planet wheels (a), the technological tooth backlash $s(t)$ (c) and the values of Heaviside's function H in the area of gear mesh with backlash (d)

elements at the main diagonal are comprised by the elements of vector $\mathbf{w}(\mathbf{v}) \equiv \mathbf{v}$. \mathbf{M} is the matrix of mass and inertia forces, ${}_1\mathbf{K}$, ${}_1\mathbf{k}_D(t)$ and ${}_K\mathbf{K}$, ${}_K\mathbf{k}_D(t)$ are matrices of linear and non-linear (index $K_1 = 2; 3$) constant and time-variable damping forces, respectively, ${}_1\mathbf{C}$ and ${}_K\mathbf{C}$ are matrices of linear and non-linear reversible forces, respectively, etc., see [1].

Because the functional damping relations $k_D(t)$ are not yet known from experiment, we will replace Eq. (1) for whole range of relative motion $y(t) \geq 0$ and $y(t) < 0$ in gear mesh (i.e. for the normal mesh, the phase of contact bounces of tooth profiles—impact effects and the inverse mesh) by the following simplified function for the resulting linear, non-linear (quadratic and cubic) time-variable damping ${}_{1,2,3}k_v(t)$ in our “zero” approximation

$${}_{1,2,3}k_v(t) = [{}_{1,2,3}k + R({}_{1,2,3}k_{d0} + {}_{1,2,3}k_d \sin p\omega t)](H1 + H2) + {}_{1,2,3}k_m[1 - (H1 + H2)], \quad (3)$$

Fig. 2 Resonance bifurcation characteristics $\{v_{s,\max,\min}; y(t)_{\max,\min}\}$ of extremes of relative motion $y(t)$ in gear mesh for frequency tuning $v_s \in \langle 0.2; 2.2 \rangle$ with constant (for $p = 0$) linear damping ${}_1k$ and variant $b(x_1)$, see Table 1 [1], in one branch of power flow of transmission between sun gear 2 and satellite 3 of pseudoplanetary system

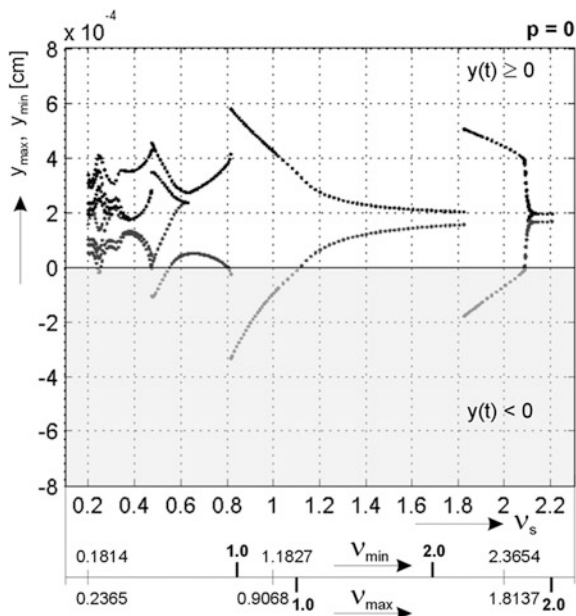
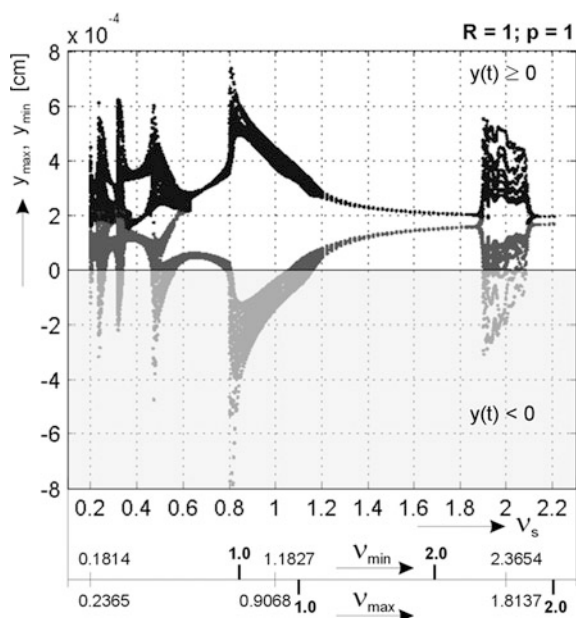


Fig. 3 Resonance bifurcation characteristics $\{v_{s,\max,\min}; y(t)_{\max,\min}\}$ of extremes of relative motion $y(t)$ in gear mesh for frequency tuning $v_s \in \langle 0.2; 2.2 \rangle$ for time-variable—heteronomous (for $p = 1$) linear damping ${}_1k_v(t)$ with order coefficient of quantitative appraisal $R = 1$ and variant $b(x_1)$, see Table 1 [1], in one branch of power flow of transmission between sun gear 2 and satellite 3 of pseudoplanetary system



where are $H1 = H[y(t)]$, $H2 = H[-y(t) - s(t)]$, see Fig. 1d, ${}_{1,2,3}k \dots$ constant material damping in gearing, ${}_{1,2,3}k_m \dots$ damping of lubricating medium in tooth backlash, ${}_{1,2,3}k_{d0} \dots$ mean coefficient of variable damping ${}_{1,2,3}k_D(t)$, ${}_{1,2,3}k_d \dots$

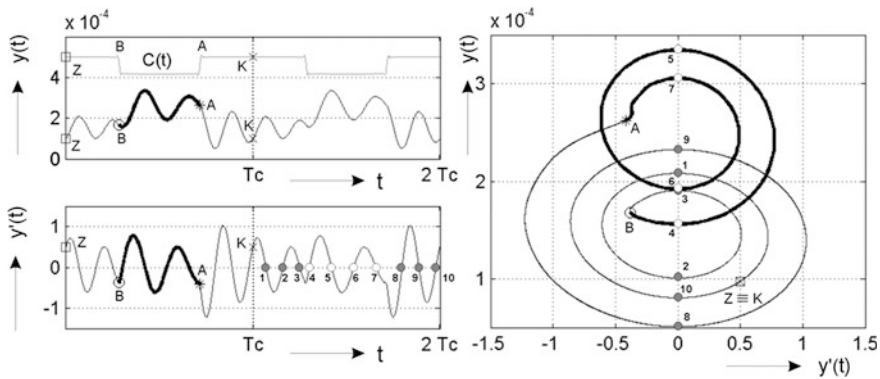


Fig. 4 In the *left part* of figure are given two periods T_c (corresponding with meshing frequency of gearing ω_c) of resulting stiffness $C(t)$ in gear mesh and of time courses of relative motion $y(t)$ and of its velocity $y'(t)$ in gear mesh with designation of jump places A,B including the beginning Z, and end K, \times of period. In the right part, the phase plane $\{y'(t); y(t)\}$ with highlight of solution ambiguity (bifurcation) is plotted for frequency tuning $v_s = 0.200$ and for purely parametrically excited system (Fig. 1) with linear constant damping in gear mesh

amplitude of variable damping, (index 1—linear, 2—quadratic, 3—cubic) and R is order coefficient of quantitative appraisal of time heteronomous damping. The resulting stiffness function of gearing in mesh $C(t, \varepsilon, \kappa, \dots) \equiv C(t)$, see Fig. 1b, is the parametric exciting term.

3 Analysis of Bifurcation Characteristics

We will now shortly analyse the dynamic bifurcation characteristics of non-linear parametric system from Fig. 1 with full ($p = 0$) and lightening ($p = 1$) cogwheel discs, i.e. with constant (Fig. 2) and variable (time-heteronomous) damping (Fig. 3) in gear mesh. The characteristics depending on tuning $v_{s, \max, \min}$ show areas with smooth simple and more complex ambiguous bifurcations with jumps and with dispersion both in areas of normal gear mesh ($y(t) \geq 0$) and in areas of impact effects ($y(t) < 0$).

The origin of bifurcation ambiguity is a complex function of given stiffness function $C(t)$, i.e. the coefficient of mesh duration ε and the amplitude modulation κ including linear, non-linear, constant and time-heteronomous damping $_{1,2,3}k_v(t)$. The damping forces cause displacements of relative motion $y(t)$ against $C(t)$.

The quality and quantity of bifurcation is also influenced by impact effects due to existence of tooth backlash $s(t)$. The illustration of such ambiguity is evident from the example of Fig. 4, which shows the loop courses of phase plane and they have for $y'(t) = 0$ a tenfold solution—bifurcation.

4 Conclusions

The study shows that changing the values of the meshing frequency of gearing ω_c , of the resulting stiffness function in gear mesh $C(t)$, of the time-variable damping $_{1,2,3}k_v(t)$ in gear mesh, etc. there are significant qualitative and quantitative changes in bifurcation characteristics of relative motion $y(t)$ in gear mesh of weakly and strongly non-linear transmission systems. It is associated with subsequent necessary deep research of stability solution.

Acknowledgments This work was supported by the research project AVOZ 20760514 of the Institute of Thermomechanics AS CR, v. v. i. Prague, Czech Republic.

Reference

1. Hortel, M., Škuderová, A.: Time heteronomous non-linear—cubic damping in internal dynamics of high-speed parametric transmission systems. Monograph deterioration, dependability, diagnostics, University of defence Brno, pp. 65–78 (2011)

Control of Compliant Mechanisms with Large Deflections

D. Kern, J. Bauer and W. Seemann

Abstract Very often elastic joints are used in high precision applications. In the case of rotational joints flexure hinges do have some advantages compared to conventional ones. However, the most important disadvantages are the complicated and complex kinematics and kinetics. As consequence, the control of mechanisms comprised of flexure hinges gets more difficult. The strategy pursued here is to reduce flexure hinges to pseudo rigid-body systems that fit into the elaborated framework of multi-body dynamics, in particular pre-control in combination with a feedback controller. The inherent deviations of these reduced models are described as uncertainties. Methods from robust control are used to synthesize controllers for such systems with uncertainty. The procedure is illustrated by examining an example of a single flexure hinge (leaf spring type).

Keywords Compliant mechanism • Elastica • Robust control

D. Kern (✉) · J. Bauer · W. Seemann
Karlsruhe Institute of Technology (KIT), Kaiserstraße 10, 76131 Karlsruhe, Germany
e-mail: kern@kit.edu

J. Bauer
e-mail: bauer@kit.edu

W. Seemann
e-mail: wolfgang.seemann@kit.edu

1 Introduction

Compliant mechanisms are systems, which consist of flexure hinges. These hinges have many advantages, such as absence of backlash, no need for lubrication, no frictional contacts (stick–slip) and no acoustical noise. On the other hand their disadvantages are the limited stroke, the storage of elastic energy that may cause oscillations and the complex kinematics and kinetics. Thus they are typically utilized for high precision applications with a small workspace. The extension to larger workspaces is in the focus of current research. The entailed large deflections require the description of flexure hinges in form of a continuum model, e.g. as bars, beams or elastica. In the controller design for a compliant mechanism the flexure hinges have to be reduced from the continuum description to a lower order model. Nevertheless, due to the deformation during operation the parameters of the lower order model are position dependent. In addition only a limited number of modes are considered, so that higher order modes may cause spillover.

The control problem was approached by different methods, such as sliding control [1] or feedback linearization [2]. In this work the reduction of flexure hinges to pseudo rigid-body systems (PRBS) [3] is used as basis. These models are intuitive and fit well into the classical framework of multi-body systems. In addition their evaluation is computationally much less expensive than for continuum models. The inherent deviations of this simplified modeling are taken into account as uncertainties in the description of the system. Methods from robust control enable the design of a controller, which fulfills the design goals in the presence of uncertainty. Once the controller is found, it can be reduced and applied to the system with little computational efforts.

For simplicity the explanations refer to flexure hinges of leaf spring type, i.e. to planar bending of slender beams with constant cross section. In terms of mechanics they can be modeled by the theory of elastica [4]. For notched hinges the same strategy applies with the difference that the characteristic load–deflection curves must be computed with more efforts, e.g. by finite element methods (FEM).

2 Reduction of a Flexure Hinge to a Pseudo Rigid-Body System

PRBS contain only few degrees of freedom, a fact which makes them suitable for application of a controller. Furthermore, rigid-body systems are well-known from the field of multi-body dynamics. Thus there exist many textbooks about trajectory planning and control, e.g. [5, 6] which give a basis for these topics.

As proposed by Kimball and Tsai [7] or Howell and Midha [8] such a PRBS approximation can be derived from elastica by optimization methods. First a parametric approximation of the beam deflection path is found in order to determine the link lengths of the PRBS that match best with the elastica solutions and

secondly the load–deflection curves of the joints (rotational springs) are determined once more by optimization. Analytic solutions may be found in terms of elliptic integrals for specific cases, however, in the general case numerical solutions are preferable to compute point-wise the load–deflection curves (static solutions). Here the problem is solved as a boundary value problem using the collocation method [9].

In addition to the highly geometrically nonlinear static solution (large deflection) modal analysis is done for selected positions, in order to obtain information about higher order modes that are neglected by the PRBS model. The methodology of this modal analysis follows Virgin [10] assuming small oscillations around the large deflection static solution.

The results of the model order reduction are geometric parameters (link lengths), dynamic parameters (spring stiffnesses) and upper bounds for the higher order dynamics. This model will be the basis for the controller design. The deviations of the parameters enter the system description as parametric uncertainties and the higher order dynamics as uncertain dynamics.

3 Controller Design for a Compliant Mechanism

The task of the controller is to move the tool center point (TCP) along a desired trajectory $x(t)$, $y(t)$, referred to as nominal trajectory. As usual in multi-body dynamics the design is a two stage process [11]. In the first stage, also known as pre-control, the nominal actuation forces are calculated (offline) and in the second stage corrections are made by a feedback controller comparing the actual value with the nominal value (online). Thus, the system is decomposed into its nominal motion and deviations, i.e. $\mathbf{f} = \mathbf{f}_n + \mathbf{f}_d$ and $\mathbf{q} = \mathbf{q}_n + \mathbf{q}_d$ for forces and coordinates, respectively.

The trajectory is usually defined as an interpolated curve in the space-fixed coordinate system and then converted into generalized coordinates by using inverse kinematics. These coordinates are convenient for the formulation of the equations of motion. Since in the control problem only the driving forces are of interest and not the constraint forces, it is sufficient to apply Lagrange's Equations of second kind

$$\frac{d}{dt} \frac{\partial(T - V)}{\partial \dot{q}_i} + \frac{\partial V}{\partial q_i} = f_i \quad \rightarrow \quad \mathbf{M} \ddot{\mathbf{q}} + h(\dot{\mathbf{q}}, \mathbf{q}) = \mathbf{f} \quad (1)$$

where T denotes kinetic energy, V potential energy, q_i the generalized coordinates and f_i the generalized forces. Inserting the nominal trajectory $\mathbf{q}_n(t)$ in the left hand side of Eq. (1) gives nominal generalized forces $\mathbf{f}_n(t)$. Similar to the inverse kinematics they must be converted into the actuation forces $\mathbf{f}_a(\mathbf{f})$. Linearization around the nominal trajectory $\mathbf{q}_n(t)$

$$\mathbf{D} = \frac{\partial \mathbf{h}}{\partial \dot{\mathbf{q}}}, \quad \mathbf{K} = \frac{\partial \mathbf{h}}{\partial \mathbf{q}}, \quad \rightarrow \quad \mathbf{M}(t)\ddot{\mathbf{q}}_d + \mathbf{D}(t)\dot{\mathbf{q}}_d + \mathbf{K}(t)\mathbf{q}_d = \mathbf{f}_d(t) \quad (2)$$

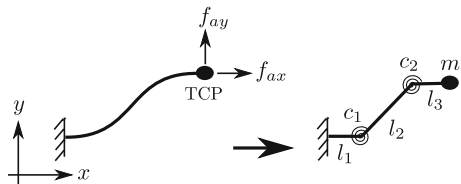
gives a linear equation of motion with variable coefficient matrices for the deviations \mathbf{q}_d from the nominal trajectory. The controller only regulates the control forces $\mathbf{f}_d(t)$ to minimize the deviations \mathbf{q}_d . Further on, the working point for the controller design is assumed to be in the central position, which introduces further deviations into the system description. This is permissible as long as the systematic relations are not distorted during operation. This is approximately the case, since flexure hinges are limited in their operating range, e.g. bending flexure hinges as rotatory joints allow angles about $-20 \dots +20$ [12]. To conclude, there are different sources of parametric uncertainties in modeling the system as a PRBS:

- As usual in multi-body dynamics the position dependent matrices \mathbf{M} , \mathbf{D} , \mathbf{K} , and additionally for flexure hinges the corresponding spring stiffnesses and link lengths lead to deviations from the nominal plant defined at the working point.
- The eigenfrequencies are position dependent with further variations in the case of flexure hinges.
- The modeling itself causes deviations in the dynamics of the nominal trajectory.

The most distinctive feature of the flexure hinges in comparison with rigid body models are the neglected higher modes that may cause spillover, a well-known effect in the theory of active damping on continua [13–15]. This is included in the system description as uncertain dynamics. It is sufficient to find a weighting function that is an upper bound for all higher modes, which are known via modal analysis for selected positions. With this the system description is complete covering all deviations as uncertainties.

The theory for the design of controllers in the presence of uncertainty is robust control [16]. In this context robust means that large variations of the system parameters result in small variations of the output. The controller is obtained by the μ -synthesis [17]. The performance goals are formulated by weighting functions in the frequency domain. Typically, the tracking error is desired to be small in the low frequency range while larger deviations in the high frequency range can be tolerated. The weighting functions for the control efforts are set in a way to avoid actuator saturation. Further on disturbances and noise can be included in the design. Therefore, their frequency characteristics must also be defined as weighting functions. The synthesized controller is usually of high order. It can be reduced without degrading its performance by balanced model truncation based on Hankel singular values [18]. The application of robust control will be illustrated by the example of a single flexure hinge in Sect. 4.

Fig. 1 Approximation of the flexure hinge as pseudo rigid-body system



4 Design of a Controller for a Simple Example

In the following a flexure hinge of the leaf spring type is considered. Such a hinge may be used in biglide mechanisms, parallel spring translators and other mechanisms. It is modeled in such a way that it is clamped on one end and carrying a concentrated mass at the other end. This mass is assumed to be located in the TCP. For simplicity, the actuation forces f_{ax} , f_{ay} apply at the same location. As illustrated in Fig. 1 it is modeled as PRBS with two rotational joints (angles γ_1 and γ_2). Its total length is divided into three links of length l_1 , l_2 and l_3 connected by rotational joints with spring stiffnesses c_1 and c_2 respectively. Their values were obtained by optimization. The links are assumed massless carrying the concentrated mass m at the right end. The equations of motion in terms of joint angles are derived using Lagrange's equations of second kind starting from the energy expressions

$$T = \frac{1}{2} m ((\dot{x}_{tcp}(\gamma_1, \gamma_2, \dot{\gamma}_1, \dot{\gamma}_2))^2 + \dot{y}_{tcp}(\gamma_1, \gamma_2, \dot{\gamma}_1, \dot{\gamma}_2)^2) \quad (3)$$

$$V = \int_0^{\gamma_1} \int_0^{\gamma_1^*} c_1 (\gamma_1^{**}) d\gamma_1^{**} d\gamma_1^* + \int_0^{\gamma_2} \int_0^{\gamma_2^*} c_2 (\gamma_2^{**}) d\gamma_2^{**} d\gamma_2^* \quad (4)$$

The forward kinematics assuming the unstressed state of the rotational springs being γ_{01} and γ_{02} , respectively

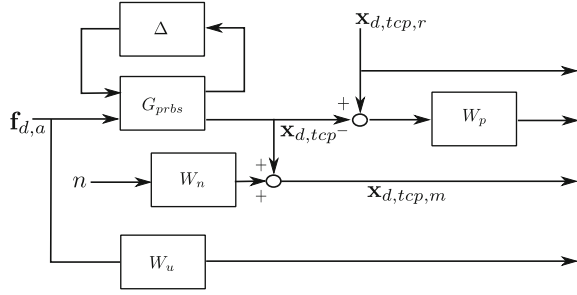
$$x_{tcp} = l_1 + l_2 \cos(\gamma_{01} + \gamma_1(t)) + l_3 \cos(\gamma_{02} + \gamma_2(t)) \quad (5)$$

$$y_{tcp} = l_2 \sin(\gamma_{01} + \gamma_1(t)) + l_3 \sin(\gamma_{02} + \gamma_2(t)) \quad (6)$$

can be inverted geometrically as intersection of two circles, one of radius $R = l_3$ around the TCP and the other of radius $R = l_2$ around $[l_1, 0]$. Note, there are two intersections but only one is relevant, which minimizes the deformation of the flexure. Since the actuation forces apply at the TCP, the transformation between actuation forces and generalized forces is given by the Jacobian

$$\left. \begin{aligned} f_1 &= f_{ax} \frac{\partial x}{\partial \gamma_1} + f_{ay} \frac{\partial y}{\partial \gamma_1} \\ f_2 &= f_{ax} \frac{\partial x}{\partial \gamma_2} + f_{ay} \frac{\partial y}{\partial \gamma_2} \end{aligned} \right\} \mathbf{f} = \mathbf{J} \mathbf{f}_a \quad (7)$$

Fig. 2 Block diagram of the weighted open loop system



The working space definition $\gamma_{1,\min} \leq \gamma_1 \leq \gamma_{1,\max}$ and $\gamma_{2,\min} \leq \gamma_2 \leq \gamma_{2,\max}$ yields the bounds of the parametric uncertainties $c_{1,\min} \leq c_1 \leq c_{1,\max}$ and $c_{2,\min} \leq c_2 \leq c_{2,\max}$ as well as the upper bounds of the frequency response functions $|F(j\omega)| < W_b$ for different TCP positions. The block diagram of the weighted open loop (augmented plant) is illustrated in Fig. 2. The uncertain plant in the center is described by the transfer matrix function G_{PRBS} . Its input are the additional actuation forces $\mathbf{f}_{d,a}$ and its output the TCP position deviation $\mathbf{x}_{d,tcp}$. The reference value $\mathbf{x}_{d,tcp,r}$ should be zero for ideal tracking. The measured signal $\mathbf{x}_{d,tcp,m}$ is corrupted by noise. The tracking error is penalized by the performance weighting function W_p keeping the error bound low in the low frequency range and moderate in the high frequency range. The actuation cost is weighted by W_u , setting high frequency actuation expensive. The noise n is assumed to be low amplitude white noise expressed by the weighting function W_n . The controller is found via D-K-Iterations [19]. As result, the synthesized controller outperforms conventional Linear-Quadratic Regulator (LQR) control in numerical simulations for several example trajectories and different sets of sample parameter values.

5 Conclusion and Outlook

A method is proposed to use the reduction of flexure hinges to pseudo rigid-body systems for the controller design of compliant mechanisms. The parameter deviations of the model and its higher dynamics are thereby included as uncertainty. The method works well for small and moderate deflections of the hinges. This coincides with the limitations of flexure hinges. Future work is related to the evaluation of the state dependent matrices in order to improve the control action further.

Acknowledgments Financial support from the German Research Foundation (DFG) Priority Programme 1476 Small machine tools for small work pieces is gratefully acknowledged.

References

1. Fite, K., Goldfarb, M.: Position control of a compliant mechanism based micromanipulator. In: *Proceedings IEEE International Conference on Robotics and Automation*, vol. 3, pp. 2122–2127, 1999
2. Speich, J., Goldfarb, M.: A compliant-mechanism-based three degree-of-freedom manipulator for small-scale manipulation. *Robotica* 18(01), 95–104 (2000).
3. Howell, L.: *Compliant mechanisms*. Wiley-Interscience, London (2001)
4. Love, A.: *A Treatise on the Mathematical Theory of Elasticity*. Dover Publications, New York (1944)
5. Shabana, A.: *Dynamics of Multibody Systems*. Cambridge University Press, Cambridge (2005)
6. Wittenburg, J.: *Dynamics of Multibody Systems*. Springer, Berlin (2008)
7. Kimball, C., Tsai, L.: Modeling of flexural beams subjected to arbitrary end loads. *J. Mech. Des.* **124**, 223 (2002)
8. Howell, L., Midha, A.: Parametric deflection approximations for end-loaded, large-deflection beams in compliant mechanisms. *J. Mech. Des.* **117**, 156 (1995)
9. Shampine, L., Kierzenka, J., Reichelt, M.: Solving boundary value problems for ordinary differential equations in matlab with bvp4c. *Tutorial Notes* (2000)
10. Santillan, S., Virgin, L., Plaut, R.: Equilibria and vibration of a heavy pinched loop. *J. sound vibr.* **288**(1–2), 81–90 (2005)
11. Heimann, B., Gerth, W., Popp, K.: *Mechatronik: Komponenten-Methoden-Beispielen*. Hanser Verlag, Germany (2006)
12. Raatz, A.: *Stoffschlüssige Gelenke aus pseudo-elastischen Formgedächtnislegierungen in Parallelrobotern*. Vulkan-Verlag GmbH, Essen (2006)
13. Fuller, C., Elliott, S., Nelson, P.: *Active control of vibration*. Chs VIII and IX (Academic, Loutou) (1996)
14. Kar, I., Miyakura, T., Seto, K.: Bending and torsional vibration control of a flexible plate structure using h-based robust control law. *IEEE Trans. Control Syst. Technol* **8**(3), 545–553 (2000)
15. Preumont, A., Seto, K.: *Active control of structures*. Wiley, London (2008)
16. Zhou, K., Doyle, J.: *Essentials of Robust Control*, vol. 104. Prentice Hall Upper Saddle River, New Jersey (1998)
17. Balas, G., Doyle, J., Glover, K., Packard, A., Smith, R.: *m-Analysis and Synthesis Toolbox*. MUSYN Inc. and The MathWorks, Natick (1993)
18. Safonov, M., Chiang, R., Limebeer, D.: Optimal hankel model reduction for nonminimal systems. *IEEE Trans. Autom. Control.* **35**(4), 496–502 (1990)
19. Chiang, R., Safonov, M., MathWorks, I.: *Robust Control Toolbox for Use with MATLAB®: User's Guide*. MathWorks Incorporated, Natick (1997)

About Problems of Nonlinear Dynamics of the Elastic Rod Elements in Practice of Chisel Works

L. Khajiyeva

Abstract The purpose of the paper is modeling of nonlinear vibrations and stability of movement of boring columns at various complicating factors taking into account finite deformations in particular. Movement of boring columns for shallow drilling (up to 500 m) applied in oil–gas extractive industry is considered. Various types of loading and deformations of rod elements are developed in the paper. Nonlinear models of movement of a compressed-torsion drill rod within the nonlinear theory of finite deformations of V.V. Novozhilov are constructed. A method for its analysis and criterion of dynamic stability are offered. The case of a flat curve of a rotating drill rod under the action of variable longitudinal force is investigated at an assumption of finiteness of elastic deformations. The numerical analysis of its elastic dislocations and instability zones of the basic resonance is carried out, which confirm the efficiency of the offered nonlinear dynamic model of rod elements and techniques for their calculation.

Keywords Dynamics • Nonlinear vibrations • Finite deformations • Boring column • Stability • Instability zone

1 Introduction

The paper is devoted to applied problems of dynamics of nonlinear deformable mediums. Practical application of models of nonlinear deformable mediums to the analysis of movement of drill rods is considered in the view of finite deformations.

L. Khajiyeva (✉)

Al-Farabi Kazakh National University, Almaty, Kazakhstan

e-mail: khadle@mail.ru

From boring practice it is known that up to 30 % of drill holes are rejected. Major factors for a borehole rejection are its curving and drill rods breakage [1, 2]. They can be caused by reasons of various natures—geological, technological and technical.

Many researchers consider that geological conditions for position of rock, distinction in their hardness and drilling are a principal cause of a borehole curvature.

Under another concept the principal cause of a borehole curvature is instability of the rectilinear form of the rod. It can arise under the action of such factors as dynamic cross-section influences; the big inertial forces arising at drilling; initial curvature of the rod; stress concentrators, etc. In the literature linear models of movement of drill rods are known, which basic restriction is the assumption of deformations by the small. The finite deformations of drill rods arising under the action of big axial loadings and twisting moments can complicate their dynamics essentially. They are poorly studied and represent scientific and practical interest.

The purpose of the work is modeling of movement of drill rods at various complicating factors in view of finite deformations in particular.

The solution of the given problem assumes: (1) development of nonlinear model of movement of a drill rod in view of finite deformations; (2) development of a technique of the dynamic analysis of a drill rod with definition of finite dislocations and stability of movement; (3) the numerical analysis of the dynamic model of a drill rod with application of the developed techniques.

2 Nonlinear Model of Movement of a Drill Rod

Movement of a drill rod for shallow drilling (up to 500 m) is considered, which is used in oil and gas extraction industry (Fig. 1). The admitted in work finiteness of deformations of a drill rod can be caused by changeability of axial forces $N(t)$ and twisting moments $M(t)$:

$$N(x, t) = N_0(x) + N_t(x)\Phi_N(t), \quad (1)$$

$$M(x, t) = M_0(x) + M_t(x)\Phi_M(t), \quad (2)$$

where $N_0(x)$ —is the longitudinal force, caused by the construction body weight mgx and by constant in time compression force N_1 :

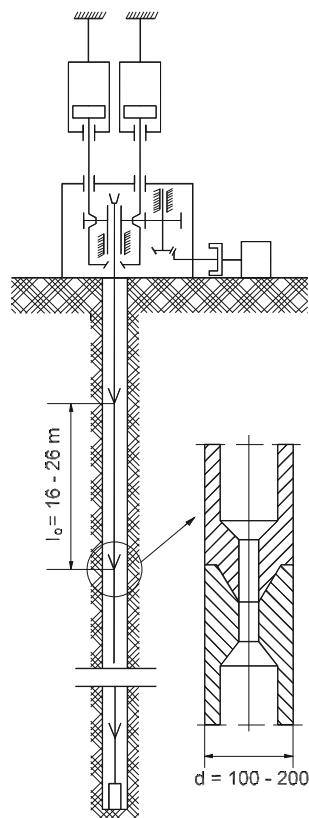
$$N_0(x) = N_1(x) + mgx, \quad (3)$$

G —gravity acceleration, x —distance from the top end of the rod, $\Phi(t)$ —the periodic function of time defining a weighting mode.

The elementary variant of function $\Phi(t)$ corresponds to harmonious influence:

$$\Phi_N(t) = \cos \omega t. \quad (4)$$

Fig. 1 The kinematic circuit of the boring machine



Similarly for twisting moment $M(t)$: M_0 —is the nominal moment, constant in time; M_t —defines contribution of a variable component; $\Phi_M(t)$ —is the periodic function. Within the framework of the nonlinear theory of deformations of V.V. Novozhilov [3], where components of tensor of deformations for the general three-dimensional case of deformation are defined as:

$$\varepsilon_{ij} = \frac{1}{2} \left(\frac{\partial u_i}{\partial x_j} + \frac{\partial u_j}{\partial x_i} + \frac{\partial u_k}{\partial x_i} \frac{\partial u_k}{\partial x_j} \right), \quad i, j = 1, 2, 3, \quad (5)$$

nonlinear model of rotation of a drill rod is constructed in view of finite deformations. For this purpose, accepting the second system of simplifications by V.V. Novozhilov, when in comparison with a unit not only extensions e_{ii} and shears e_{ij} , but also corners of turn ω_i are small, the elastic potential of volumetric deformation [4, 5] is received:

$$\begin{aligned}
\Phi = & G \left[\left(1 + \frac{v}{1-2v} \right) (\alpha + U_x \alpha_x + \alpha_x^2 + V_y \alpha_y + \alpha_y^2 + W_z \alpha_z + \alpha_z^2) \right. \\
& + \frac{2v}{1-2v} ((W_z + 0,5\alpha_z)(U_x + V_y + 0,5\alpha_x + 0,5\alpha_y) + (U_x + 0,5\alpha_x) \\
& \times (V_y + 0,5\alpha_y)) + \frac{1}{2} ((U_y \beta_x + V_x \beta_y + W_x W_y)^2 \\
& \left. + (V_z \beta_y + W_y \beta_z + U_y U_z)^2 + (W_x \beta_z + U_z \beta_x + V_x V_z)^2 \right],
\end{aligned} \quad (6)$$

where indexes at components of elastic dislocation $U(x, y, z, t)$, $V(x, y, z, t)$ and also $W(x, y, z, t)$ mean differentiation of these functions on the specified variables, and the following designations are entered:

$$\begin{aligned}
\alpha &= U_x^2 + V_y^2 + W_z^2; & \alpha_x &= U_x^2 + V_x^2 + W_x^2; & \alpha_y &= U_y^2 + V_y^2 + W_y^2; \\
\alpha_z &= U_z^2 + V_z^2 + W_z^2; & \beta_x &= 1 + U_x; & \beta_y &= 1 + V_y; & \beta_z &= 1 + W_z.
\end{aligned} \quad (7)$$

The potential (6), (7) has the general character and allows to pass to individual cases of deformation of elastic systems. So, for the considered case of a drill rod as rod element [6], with the circuit of deformation Fig. 2 and rotating at angular speed ω , the equations of its movement are received:

$$\begin{aligned}
EJ_v \frac{\partial^2}{\partial x^2} \left[\frac{\partial^2 V}{\partial x^2} \left(1 - \frac{3}{2} \left(\frac{\partial V}{\partial x} \right)^2 \right) \right] + \frac{\partial^2}{\partial x^2} \left[M(x, t) \frac{\partial U}{\partial x} \right] + \frac{\partial}{\partial x} \left[N(x, t) \frac{\partial V}{\partial x} \right] + K_1 V &= -\frac{\gamma F}{g} \frac{\partial^2 V}{\partial t^2}, \\
EJ_u \frac{\partial^2}{\partial x^2} \left[\frac{\partial^2 U}{\partial x^2} \left(1 - \frac{3}{2} \left(\frac{\partial U}{\partial x} \right)^2 \right) \right] + \frac{\partial^2}{\partial x^2} \left[M(x, t) \frac{\partial V}{\partial x} \right] + \frac{\partial}{\partial x} \left[N(x, t) \frac{\partial U}{\partial x} \right] + K_1 U &= -\frac{\gamma F}{g} \frac{\partial^2 U}{\partial t^2},
\end{aligned} \quad (8)$$

where $K_1 = \gamma F \omega^2 / g$.

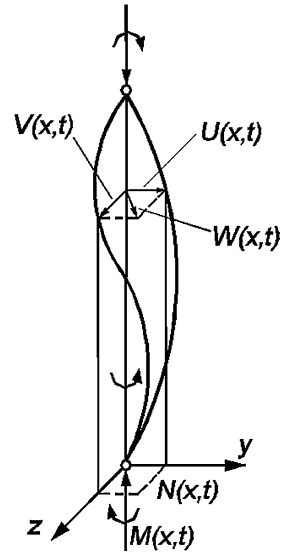
3 Analysis of Finite Dislocations of a Drill Rod and Stability of its Movement

A special case of a model (8) is considered—a case of a flat curving of the rod rotating at speed ω under the action of longitudinal force $N(t) = N_0 + N_t \Phi(t)$. Presuming the drill rod is highly supported on the ends, the boundary conditions are set:

$$V = EJ_v \frac{\partial^2 V}{\partial x^2} = 0, \quad U = EJ_u \frac{\partial^2 U}{\partial x^2} = 0, \quad (x = 0, x = l). \quad (9)$$

The following solution satisfies these conditions

Fig. 2 The form of the curved axis of a rod



$$U(x, t) = \sum_{k=1}^{\infty} f_k(t) \sin \frac{k\pi x}{l} \quad (10)$$

Substituting the solution (10) in the equation of the curved axis of a rod and applying direct variational method of Bubnov-Galyorkin, the latter leads to the nonlinear parametrical equations with one degree of freedom:

$$\ddot{f} + C_k^2(1 - 2v_k \cos \Omega t)f + \alpha f^2 = 0, \quad (11)$$

where

$$C_k = \frac{k^2 \pi^2}{l^2} \sqrt{\frac{EI}{m} \left(1 - \frac{N_2}{N_k}\right)} = \omega_0, \quad N_k = \frac{k^2 \pi^2 EI}{l^2}, \quad v_k = \frac{N_t}{2(N_k - N_0)}, \quad (12)$$

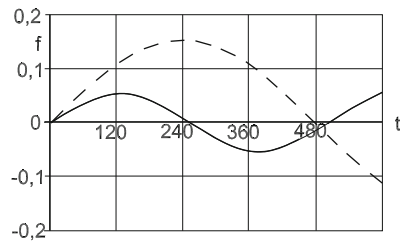
$$\alpha = \frac{3Ek^4 \pi^4}{8\rho l^4}.$$

Stability of the set modes of movement of a drill rod has basic value for maintenance of its trouble-free operation. Here steady movement of a drill rod will be understood as its movement in absence of dangerous resonant modes of fluctuations. For this purpose stability of the basic resonance is investigated:

$$f_0 = r_1 \cos(\Omega t - \varphi_1). \quad (13)$$

The technique of definition of instability zones of resonant vibrations of a drill rod with application of Flock theory is offered. According to it the solution of the equation of the perturbed condition of model (11):

Fig. 3 Amplitude of fluctuations of linear and nonlinear models (— for linear, — for nonlinear) at $E_A = 0,7 \cdot 10^5$ MPa, $\rho_A = 2698,9$ kg/m³, $l = 500$ m; $D_1 = 0,12$ m; $D_2 = 0,2$ m



$$\frac{d^2 \delta f}{dt^2} + \delta f (C_k^2 + 1,5 \alpha r_1^2 - 2C_k^2 v \cos \Omega t + 1,5 \alpha r_1^2 \cos 2\varphi_1 \cos 2\Omega t + 1,5 \alpha r_1^2 \sin 2\varphi_1 \sin 2\Omega t) = 0. \quad (14)$$

set as follows: $\delta f = e^{\mu t} P(t)$. The type of expression $P(t)$ defines the instability zone of fluctuations.

Having set $P(t) = b_1 \cos(\Omega t - \psi_1)$, the border of the first zone of instability of the basic resonance [7, 8] is received:

$$\Delta(\mu = 0) = \Omega^4 + \frac{27}{16} \alpha^2 r_4 + (3c_k^2 \alpha - 3\Omega^2 \alpha) - 2\Omega^2 c_k^2 + c_k^2 = 0. \quad (15)$$

The numerical analysis of dislocations of nonlinear fluctuations (11) and definition of an instability zone (15) represent no hard work. The given approach can be distributed for research of fluctuations on the maximum modes and with definition of their instability zones.

4 Numerical Example

The numerical analysis of nonlinear fluctuations and instability zones of the basic resonance of the rotating drill rod is carried out, undergone to a flat curving under the action of variable longitudinal force $N(t) = N_0 + N_t \Phi(t)$.

The numerical analysis of the Eqs. (11), (12) is carried out at entry conditions [9] $f_k(t=0) = 0$, $\frac{\partial f_k}{\partial t}(t=0) = 0,001$.

Steel and dural drill rods are considered. From the comparative analysis of the research results one can see that the amplitude of fluctuations of nonlinear model (11) in both cases is less than in linear position (Fig. 3). The influence of forms of a rod curving on amplitude of its fluctuations is investigated. It is established that at the basic form of a curving the amplitude of dislocations of a drill rod exceeds the amplitudes of the big forms. Thus, duralumin drill rod is subject to smaller deflections from the rectilinear form than the steel one at the same modes of drilling (Fig. 4).

In Figs. 5, 6 the results of the research of influence of forms of fluctuations of a rod, its length and properties of the material on the width of instability zones of the

Fig. 4 Influence of properties of the material of a rod (— steel, --- duralumin) at $E_c = 2,1 \cdot 10^5$ MPa; $\rho_s = 7,8 \cdot 10^3$ kg/m³; $E_d = 0,7 \cdot 10^5$ MPa; $\rho_d = 2698,9$ kg/m³; $l = 500$ m; $D_1 = 0,12$ m; $D_2 = 0,2$ m

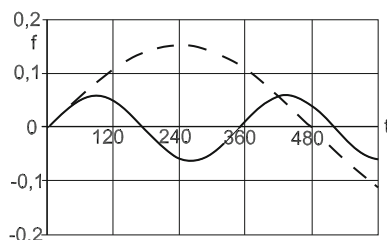


Fig. 5 Influence of the forms of fluctuations on the instability zone of a rod (— $k = 2$, --- $k = 1$) at $L = 300$ m, $N_0 = 500N$, $N_t = 2195,5$ kN, $d = 120$ mm, $D = 200$ mm, $E_{cm} = 2,1 \times 10^5$ MPa

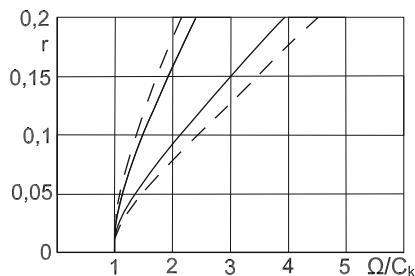
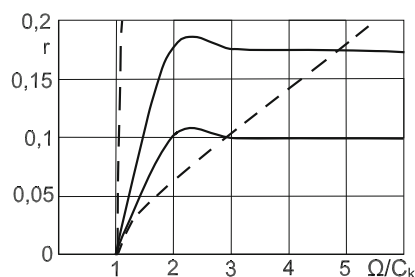


Fig. 6 Influence of the length of a rod on the instability zone of a rod (— $L = 500$ m, --- $L = 1000$ m) at $N_0 = 500N$, $N_t = 2195,5$ kN, $d = 120$ mm, $D = 200$ mm, $E_{cm} = 2,1 \times 10^5$ MPa



basic resonance are submitted. It is established that the first two forms of fluctuations influence the width of the instability zone (Fig. 5). The increase in length of a rod leads to the expansion of instability zone (Fig. 6). In all the considered cases instability zones for a duralumin rod are larger than for a steel one.

5 Conclusions

In the work practical application of the nonlinear model of elastic deformation of mediums developed by the author for the general spatial case is considered. The results of the numerical analysis of movement of compressed—torsioned drill rod without restrictions of the deformation sizes testify to the efficiency of a nonlinear model. It is established that the account of nonlinear factors leads to essential specification of the dynamic model of drill rods—to the downturn of fluctuation

amplitudes and displacement of basic resonance zones into the area of big frequencies. In spite of the fact that the suggested techniques were applied to the research of stability of the basic resonance of elastic dynamic systems, they can also be successfully applied to the analysis of resonances on the maximum frequencies.

References

1. Баграмов, Р.А.: Буровые машины и комплексы. Москва (1988)
2. Рабинович, Н.Р.: Инженерные задачи механики сплошной среды в бурении. Москва (1989)
3. Новожиллов, В.В.: Основы нелинейной теории упругости. Москва (1948)
4. Aytaliev, Sh.M., Masanov, J.K., Khajiyeva, L.A., Kydyrbekuly, A.B.: Dynamics of mechanisms with elastic links. In Proceedings 12 International Workshop on Computation Kinematic, Cassino, Italy, pp. 1–11 (2005)
5. Khajiyeva, L.A., Kydyrbekuly, A.B., Bayjigitov B.: Nonlinear oscillation of the multi-link mechanism with elastic links. International scientific conference, Ostrava, Czech Republic, pp. 123–126 (2005)
6. Филиппов, А.П.: Колебания деформируемых систем. Москва (1970)
7. Хаяси, Т.: Нелинейные колебания в физических системах. Москва (1968)
8. Тондл, А.: Нелинейные колебания механических систем. Москва (1973)
9. Хаджиева Л.А.: Об анализе нелинейных колебаний буровых штанг с конечными деформациями. *Известия НАН РК. Серия физ.-мат.*, №1, с. 38–43 (2012)

Dynamic Analysis of Hammer Mechanism “Twin Hammer” of Impact Wrench

M. Konečný and J. Slavík

Abstract This paper describes function of the hammer mechanism “Twin hammer” the impact wrench, calculation of dynamic forces exerted on the mechanism and determining the contact pressures between the parts of the mechanism. The modelling of parts was performed in system Pro ENGINEER—standard. The simulation and finding dynamic forces was performed in advanced module Pro ENGINEER—mechanism design and finding contacts pressures in modul Pro ENGINEER—mechanica.

Keywords Hammer mechanism • Impact wrench • Twin hammer • Dynamic analysis • Contact pressure

1 Introduction

Impact Wrench is a mechanical tool designed to provide high torque with minimal operator effort so that the drums for its internal mechanism uses the kinetic energy of rotating mass and subsequently transferred in the form of torque to the output spindle. Used mainly for tightening or loosening screws and nuts.

M. Konečný (✉) · J. Slavík
Technical University of Liberec, Liberec, Czech Republic
e-mail: martin.konecny@tul.cz

J. Slavík
e-mail: jakub.slavik@tul.cz

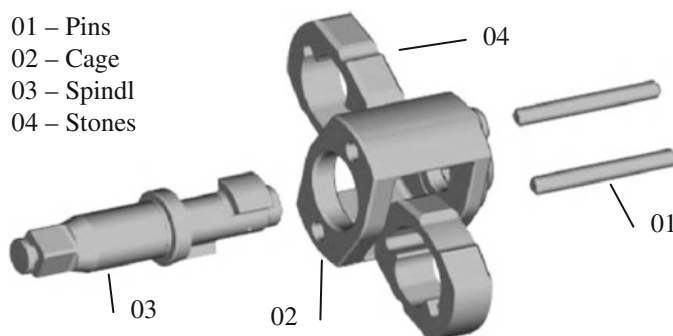
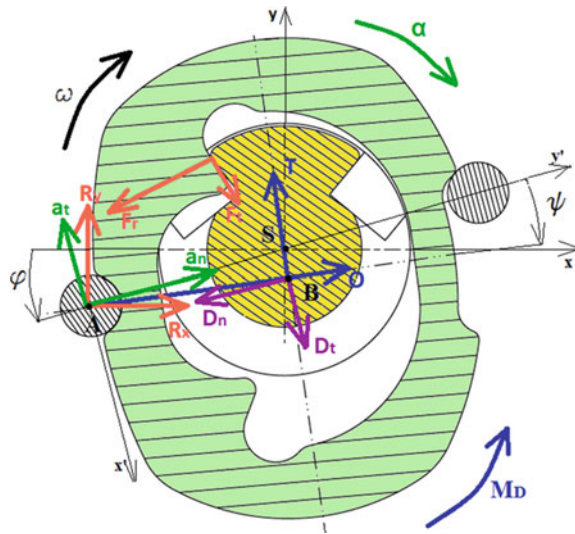


Fig. 1 Hammer mechanism “Twin hammer”.

2 Impact Wrench with Hammer Mechanism “Twin Hammer”

The principle of the “Twin hammer” function (Fig. 1) is based on the strike of two identical blocks. The cage of the striking mechanism is connected with the input shaft by means of involute spline, able to transmit better the high torque of the motor. Therefore, during the rotation of the motor there also starts rotating the cage housing two pins, which provide for fulfilment of two functions. They serve as drivers for the blocks of striking mechanism, which are pivoted on them, and moreover, they take up their slewing play. During the driving of the cage pins, the blocks are rotating round the spindle at the same time. The blocks perform an equal motion; however, they are displaced mutually through 180° . Therefore, both of them strike at the same time, but on opposite sides of the spindle. In this way, a balanced impact is produced, and the generated vibrations are lower. As the blocks allow striking both sides of the spindle at the same time, the “Twin hammer” is able to produce a high tightening torque since the first rotations of the rotor already. The transmission of a balanced impact also allows imparting a higher angular momentum at lower wearing. After the impact, the blocks slew slightly, namely through the play delimited by the pins. Next, the blocks rotate freely round the spindle again, and they set up to a position suitable for producing an impact. At a low tightening torque, the blocks wedge into the spindle, with fast tightening or releasing as a consequence. This type of mechanism has a long life and is convenient for long operating cycles in particular. Another advantage is the fact that it consists of a relatively small number of components, which makes its maintenance much easier. The mechanism is lubricated with grease. The “Twin hammer” is intended for demanding use in heavy industry, tire service shops or in construction works.

Fig. 2 Firing position of the hammer mechanism “Twin hammer”



2.1 Firing Position of the Hammer Mechanism

In order to be able to determine properly the forces acting on the block during operation, it was necessary to devise two co-ordinate systems, in which the movements of the block can be defined. Into the point S, which is the centre of rotation of the absolute motion, there was implemented a fixed global co-ordinate system (xy), and into the point A, which is the centre of relative motion, there was implemented a local co-ordinate system ($x'y'$), which rotates around the fixed co-ordinate system. The mutual position of these two systems is defined by the transformation angle φ , and the angle ψ defines the angular displacement of the block with respect to the relative system. Both the angles are dependent on time. The point A performs rotary driving motion. In the Fig. 2, we can see the forces acting on the block of the striking mechanism in its striking position, when there takes place absolute rotation round the axis of the spindle S only, at the angular velocity ω and with angular acceleration α . Against the sense of acceleration there acts the dynamic moment M_D . The point A, which performs the driving motion, is influenced in this moment by the normal acceleration a_n and the tangential acceleration a_t . These accelerations produce a reaction in the form of D'Alembert dynamic forces D_n and D_t , the directions of which are exactly opposite to the directions of accelerations and which operate in the centre of gravity of the block B. Since the rotation is eccentric, it generates in the block the centrifugal force O as well, which passes both through the point A and the centre of gravity B, and also a tangential force which operates in the centre of gravity and with respect to the centrifugal force, it is lagged by 90° in the sense of the rotation. Furthermore, the block produces reactions R_x and R_y , which also include the driving force [1].

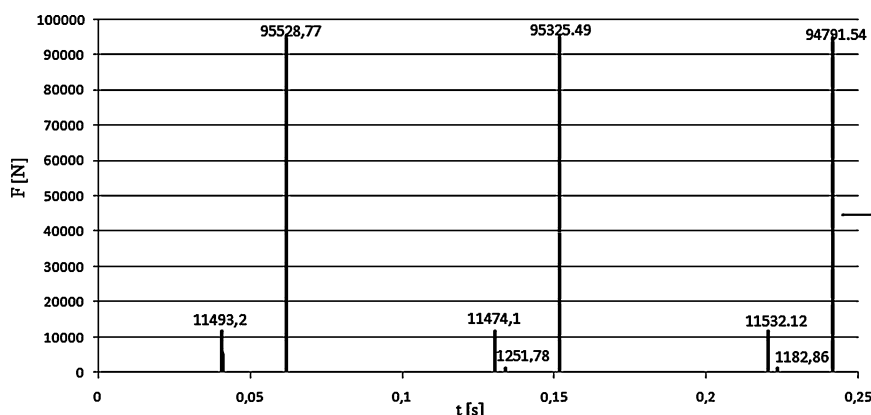


Fig. 3 Course of shock forces of the hammer mechanism

3 Determine the Size of the Major Impact Force

After establishing the rigidity of the system of components which are in mutual contact during the impact, there was carried out the calculation of the impact force. In order to be able to ascertain the magnitude of the impact force, the simulation had to include the rigidity of the system, too. However, the spindle was situated in such a way that it was able to rotate freely, in contrast to the spindle seating for the calculation of the rigidity. In order to provide for the respective rigidity, a torsional spring with rigidity value 1,490 Nm/deg was situated on its axle. On the cams there has been set up the co-efficient of restitution 0.75, the value of which had been determined experimentally, by evaluation of the record of behaviour of an actual striking mechanism obtained by a fast-speed camera. The course of impact forces is displayed in Fig. 3. The value of the principal impact attains 95,000 N approximately. A lower value of the impact force, ranging around 11,000 N, applies from second contact of the block with the spindle, which comes about during re-setting of the block for another stroke.

4 The Contact Pressures

For the contact analysis, we have availed ourselves of the already existing model for establishing the rigidity of the system. The model was subject to minor modifications only. The moment acting on each block was assigned by the value 1.367 Nm, which corresponds approximately to the impact force 95,000 N, acting on an arm of 0.014 m. Another modification referred to definition of contact areas. There has been employed the tool “component–component”, in which the software compares any two areas separately, whether they would not come into

Fig. 4 The computational model for finding the contact pressures

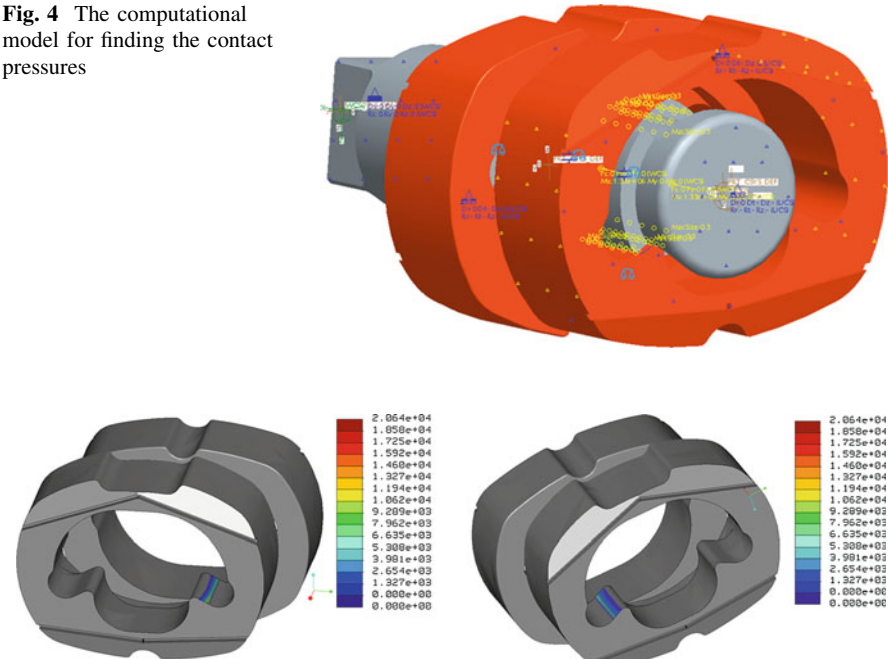


Fig. 5 Places of contact pressures on the stones

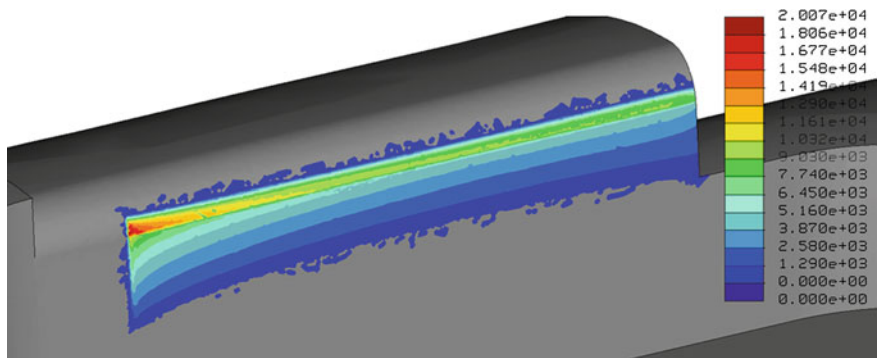


Fig. 6 Detailed distribution of pressures on the anvil in the middle section of the spindle

contact. However, on the areas where it was known they would come into contact, there was defined—like in the case of rigidity—a condensation of the network of finite elements. The magnitude of the element was set up to 0.3 mm. Here also, the analysis was carried out by means of the tool “single—pass adaptive”. The calculation model is visualized in the Fig. 4.

Places of contact pressures on the rocks and anvils are the pictures 5, 6 and 7.

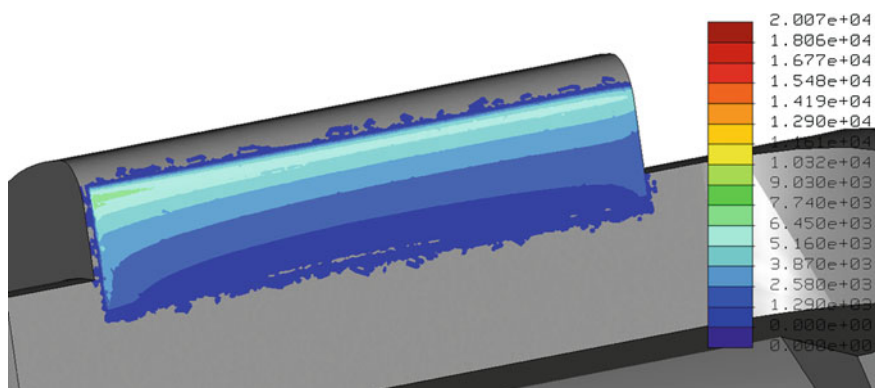


Fig. 7 Detailed distribution of pressures on the anvil in outside section of the spindle

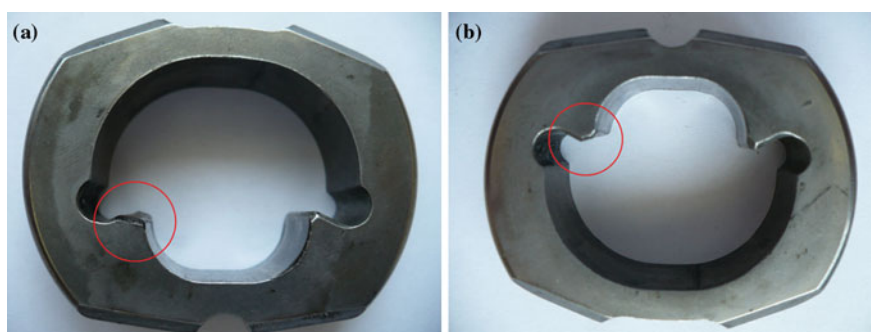


Fig. 8 Wear of blocks located in **a** the middle section, **b** outside section of the spindle

The anvil situated in the centre of the spindle (closer to the square—Fig. 6) is evidently exposed to higher pressures, mainly in the areas closer to the point of fixed support. In the critical place, the pressure attains 20,000 MPa. In the rest of the anvil, it ranges about 7,500 Mpa approximately. Therefore, it is exposed to considerably higher strain than the anvil in the front section of the spindle (farther from the square—Fig. 7). By comparison with the results of wear during several years (Fig. 8), we can see that the results come close to the real thing, even if maybe not concerning the value of the pressure, but concerning the proportion of distribution of operating pressures. The distribution of pressures is similar in both the blocks, too.

5 Conclusions

Because of limited extent of the paper, it is impossible to describe the concerned analysis in detail. Owing to high values of contact pressures acting on a relatively small area, the wear and tear will be fast in the beginning. However, it will result in an enlargement of contact areas; consequently, the force will be distributed to a larger area, and the contact pressure will drop down. The wear will also result in toughening of the material, too. The higher will be the wear of the components, the more slowly it will continue subsequently.

Acknowledgments The paper was supported in part by the Project OP VaVpI Centre for Nanomaterials, Advanced Technologies and Innovation CZ.1.05/2.1.00/01.0005.

Reference

1. Slavík, J.: Dynamic analysis of hammer mechanism “Twin Hammer” of impact wrench, Bachelor’s thesis, TUL (2011)

Forces and Moments Acting on the Fluttering Profile

J. Kozánek, V. Vlček and I. Zolotarev

Abstract A high speed camera NanoSense MK III-IDT was used for the interferometric visualization of the fluttering NACA0015 experimental profile during the several motion periods. The kinematics of this self-excited profile and the pressure amplitudes acting on the profile surface were computed from registered interferograms. Drag and lift forces and total moment acting on the profile are evaluated via numerical integration and regression methods.

Keywords Fluttering profile • Interferometry • Drag and lift forces • Moments

1 Introduction

The dynamic behavior of the elastically supported profile in subsonic air flow was studied in [1, 2]. Investigated profile—see Fig. 1—was situated in a special stand in the aerodynamic tunnel of the Institute of Thermomechanics AS CR.

The kinematics of the self-excited profile and the pressure amplitudes acting on the vibrating profile surface were computed from interferograms registered by the high-speed camera—[3]. The methodology of the evaluation of resulting forces in x and y directions and moments were proposed in [4]. Here, for one profile

J. Kozánek (✉) · V. Vlček · I. Zolotarev
Institute of Thermomechanics, AS CR, v.v.i, Prague, Czech Republic
e-mail: kozanek@it.cas.cz

V. Vlček
e-mail: vlcek@it.cas.cz

I. Zolotarev
e-mail: igor@it.cas.cz

Fig. 1 Schema of the vibrating airfoil in the experiment

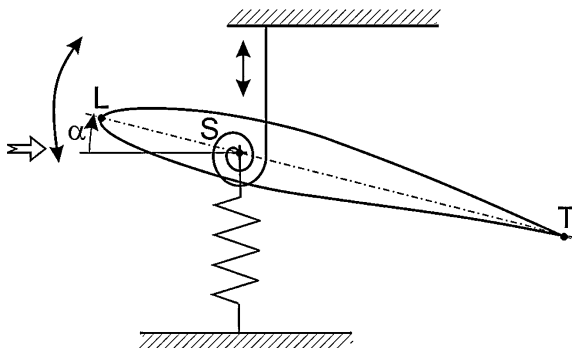
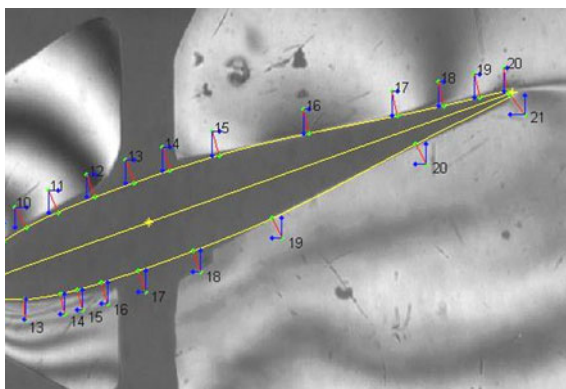


Fig. 2 Determined aerodynamic pressure acting on the profile, normal, x, y directions—detail



position were above quantities numerically evaluated as a continuous functions of the perimeter coordinate of the profile including resulting drag and lift forces and total moment acting on the profile. This research is important for post flutter vibrations of airplanes and for flow-induced vibrations of blades of turbines.

2 Experimental Setup

The investigated profile with a chord length of 65 mm was installed in the test section of the high-speed wind tunnel of the Institute of Thermomechanics AS CR, Laboratory at Nový Knín—[3]. Experiments in the flutter regime were performed for the inlet Mach number $M = 0.43$, the Reynolds number $Re = 0.52 \cdot 10^6$ and the flutter frequency was 27.8 Hz. The Mach-Zehnder's interferometer was used for the air flow visualization and the high-speed camera NanoSense MK III-IDT registered the flow field with the frequency 1000 frames/s.

Table 1 Normal aerodynamic pressure acting on the profile in discretized surface points

Upper profile surface				Lower profile surface			
No	s [mm]	i	p/p_0	No	s [mm]	i	p/p_0
1	0.1030	0.5	0.8695	1	0.0737	1	0.8566
2	0.1762	0	0.8824	2	0.1616	1.5	0.8437
3	0.2200	0.5	0.8695	3	0.2928	2	0.8309
4	0.4672	1	0.8566	4	0.3945	2.5	0.8182
5	0.7005	1.5	0.8437	5	0.5253	3	0.8055
6	1.1022	2	0.8309	6	0.5690	3.5	0.7929
7	1.5689	2.5	0.8182	7	0.7445	4	0.7803
8	4.1147	2.5	0.8182	8	0.8922	4.5	0.7678
9	5.9238	2	0.8309	9	1.1630	5	0.7553
10	9.0253	1.5	0.8437	10	1.3947	5.5	0.7429
11	13.0697	1	0.8566	11	1.8294	6	0.7306
12	17.6551	0.5	0.8695	12	2.3428	6.5	0.7183
13	22.4190	0	0.8824	13	5.9717	7	0.7061
14	26.7838	0.5	0.8695	14	10.1859	6.5	0.7183
15	32.6402	0	0.8824	15	12.1749	5.5	0.7429
16	43.1622	0.5	0.8695	16	15.0343	4.5	0.7678
17	53.5066	0	0.8824	17	19.5179	4	0.7803
18	58.9650	0.5	0.8695	18	26.1213	3.5	0.7929
19	63.2276	1	0.8566	19	36.0093	3	0.8055
20	66.3649	1.5	0.8437	20	54.4673	3	0.8055
				21	66.6409	2.5	0.8182

3 Pressure Acting on the Profile, Drag, Lift Forces and Moments

Precise zooming graphical procedure in Matlab was created for the evaluation of flow parameters of interferograms. From one interferogram was determined the pressure distribution on the upper and lower parts of the profile surfaces—Fig. 2.

The pressure amplitudes $p(s_j)$, $j = 1, 2, \dots, n$ are known in the perimeter coordinates s_j on the profile (from leading edge)—Table 1, where i are interferometric fringes numbers. Supposing isentropic flow, we have $p_0 = 98925 \text{ N/m}^2$.

These discrete pressure values were substituted by the continuous function $p(s)$ and decomposed into x , y components $p_x(s)$, $p_y(s)$, respectively—Figs. 3, 4. The x and y -components of the total force F_x and F_y acting on the profile were calculated by the integration of the above pressure functions around the perimeter s and profile width $w = 60 \text{ mm}$:

$$F_x = w \cdot \int_s p_x(s) \cdot ds, \quad F_y = w \cdot \int_s p_y(s) \cdot ds. \quad (1)$$

Fig. 3 Normal (solid line) and x (...), y (—) pressure components along the upper part of the profile as a continuous function of the perimeter coordinate s

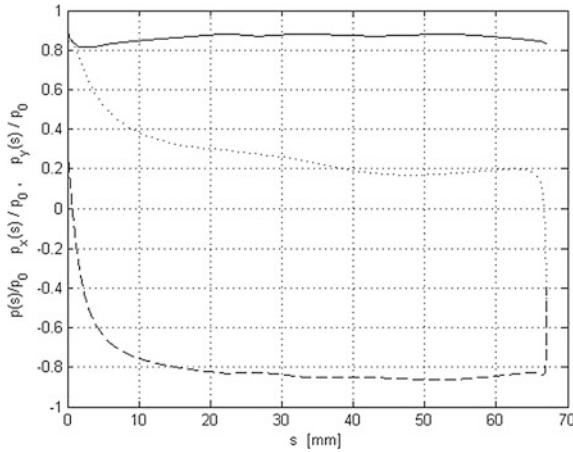


Fig. 4 Normal (solid line) and x (...), y (—) pressure components along the lower part of the profile as a continuous function of the perimeter coordinate s

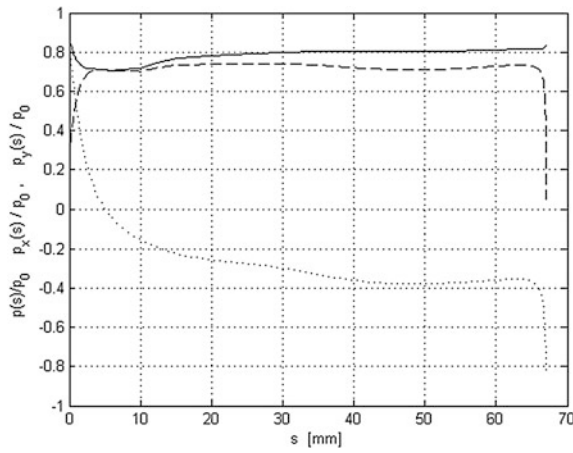


Fig. 5 Moment (area related) caused by the normal pressure acting on the upper part of the profile as a continuous function of the perimeter coordinate s

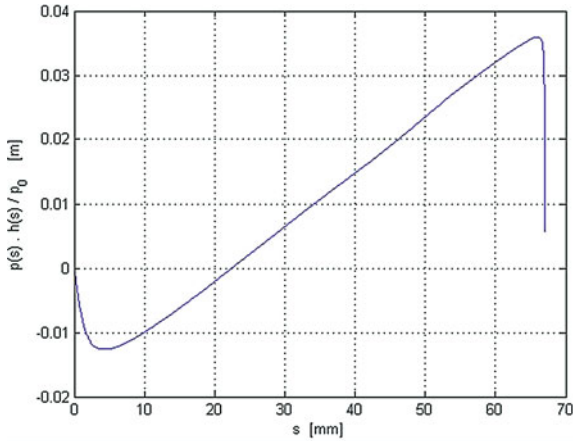


Fig. 6 Moment (area related) caused by the normal pressure acting on the lower part of the profile as a continuous function of the perimeter coordinate s

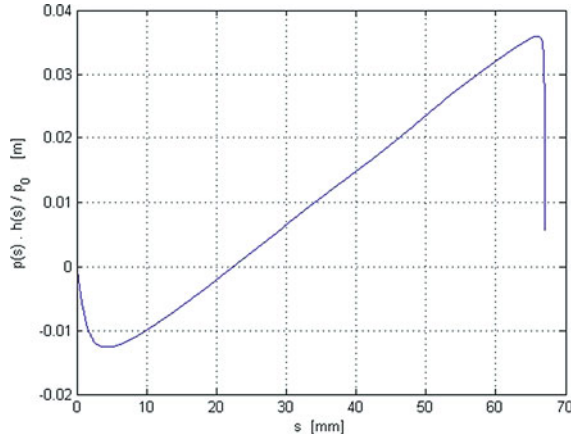


Table 2 Resulting forces and total moments acting on the investigated profile. The positive directions of the F_x , F_y , M is from left to the right, from the bottom to the upwards, clockwise, respectively—see Fig. 2

	F_x [N]	F_y [N]	M [N · m]
Upper profile surface	111.02	-314.99	3.98
Lower profile surface	-103.39	284.91	-3.75
Total	7.63	-30.08	0.23

The total moment acting on the profile is given as

$$M = w \cdot \int_s h(s) \cdot p(s) \cdot ds, \tag{2}$$

where the function $h(s)$ is corresponding force arm with appropriate sign, the area related moments $h(s) \cdot p(s)$ for upper and lower surfaces are in Figs. 5, 6

By numerical integration were calculated the above integrals (1) and (2), separately for upper and lower surfaces, resulting forces in x and y directions and total moment acting on the profile are in the Table 2.

4 Conclusion

Interferogram measurements of the dynamic experiments on elastically supported NACA0015 profile in subsonic wind tunnel were realized. The mathematical model of the profile was superimposed onto interferogram. The pressure acting on the profile, resulting drag, lift forces and total moment were evaluated by regression methods and numerical integration.

Acknowledgments The research work reported here was made possible by the Grant Agency of the Czech Republic under Grant No 101/09/1522 “Experimental investigation of unsteady flow patterns around vibrating airfoil with application in aeroelasticity”.

References

1. Vlček, V., Horáček, J., Luxa, M., Veselý, J.: Visualization of unsteady flow around a vibrating profile. Flow induced vibrations proceedings of the 9th international conference on flow-induced vibration, FIV2008, Prague, IT AS CR, 531–536 (2008)
2. Vlcek, V., Horáček, J., Luxa, M., Veselý, J., Bula, V.: Visualization of unsteady flow around a vibrating profile: experimental set-up and preliminary tests. Interaction and feedbacks proceedings, Prague, IT AS CR, 75–83 (2009)
3. Vlcek, V., Kozánek, J.: Preliminary interferometry measurements of a flow field around fluttering NACA0015 profile, *Acta Technica*, **56**, 379–387 (2011)
4. Kozánek, J., Vlcek, V., Zolotarev, I.: The flow field acting on the fluttering profile, measurements and evaluation. Proceedings of dynamical systems—analytical, numerical methods, stability, bifurcation and chaos, DSTA 2011, Lodz, Poland, pp. 283–288. (2011)

Rotor-Liquid-Fundament System's Oscillation

A. Kydyrbekuly

Abstract The work is devoted to research of oscillation and sustainability of stationary twirl of vertical flexible static dynamically out-of-balance rotor with cavity partly filled with liquid and set on relative frame fundament. The accounting of such factors like oscillation of fundament, liquid oscillation, influence of asymmetry of installation of a rotor on a shaft, anisotropism of shaft support and fundament, static and dynamic out-of-balance of a rotor, an external friction, an internal friction of a shaft, allows to settle an invoice more precisely kinematic and dynamic characteristics of system.

Keywords Rotor • Dynamics • Liquid oscillation • Oscillation of fundament • Dynamic out-of-balance of a rotor

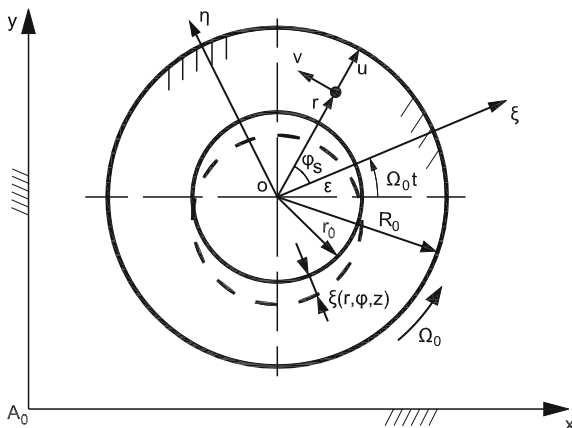
1 Introduction

In design and an assessment of vibrating characteristics of rotor cars it is necessary to consider case fluctuations, i.e. to consider dynamic system “rotor-corpus-fundament” as a whole [1, 2]. In many theoretical and practical researches on dynamics of the rotor systems containing liquid, rotor fluctuations with liquid are considered only and thus the bed (base) is considered motionless. Such assumption leads to essential errors at an assessment of dynamic and kinematic characteristics of rotor system as a whole [2–4]. Pilot studies of such dynamic systems as rotor systems, show importance of the accounting of vibration of the base and need of development of measures for their decrease [2, 5].

A. Kydyrbekuly (✉)

Institute of Mechanics and Machine Studies, Almaty, KAZAKHSTAN
e-mail: almatbek@list.ru

Fig. 1 Coordinates system definition



2 Putting Problems, Movement Equation System and Their Solution

The rotor cavity has a form of cylinder. The mass of liquid is considered a constant in time, and its quantity—sufficient completely to moisten cylindrical walls of a cavity even at big deviations of a rotor. Angular speed of shaft rotation Ω_0 is constant and it is rather great so that on a free surface of liquid gravitational acceleration appears negligible in comparison with centrifugal acceleration, and the free surface represents the cylinder concerning a rotation axis. The damped movement of system moves in the horizontal plane. Movement of liquid is described in the cylindrical system of coordinates connected with a rotating rotor. In a condition of dynamic balance the rotor and liquid rotate as a uniform firm body (Fig. 1).

Deflections of an axis of a shaft in the direction of axes x and y motionless system of coordinates are relied the small. Liquid deviations from position of balance, derivatives on time from all amplitudes of fluctuations also are accepted by the small. Thus, for an assessment of stability of the related system the system of the linearized differential equations as a whole is considered. The solution of this task becomes complicated that movement of a rotating rotor and liquid movement in his cavity are interconnected that causes change of frequency of the compelled fluctuations and instability emergence, and the solved system of the equations consists of the connected equations of movement of a firm body, the equations of the continuous environment and boundary conditions for liquid:

$$m\ddot{x} + (n_e + n_i)\dot{x} + p_1x + \Omega_0 n_i y - q_1\alpha + \sigma_1 x_k = m\epsilon\Omega_0^2 \cos \Omega_0 t + F_x, \quad (1)$$

$$m\ddot{y} + (n_e + n_i)\dot{y} + p_2y - \Omega_0 n_i x - q_2\beta + \sigma_2 y_k = m\epsilon\Omega_0^2 \sin \Omega_0 t + F_y, \quad (2)$$

$$\begin{aligned} A\ddot{\alpha} + C\Omega_0\dot{\beta} + (\mu_e + \mu_i)\dot{\alpha} - r_1x + \Omega_0\mu_i\beta + s_1\alpha + \sigma_3 x_k \\ = (C - A)\delta \Omega_0^2 \sin(\Omega_0 t - \chi) + M_\alpha, \end{aligned} \quad (3)$$

$$A\ddot{\beta} - C\Omega_0\dot{\alpha} + (\mu_e + \mu_i)\dot{\beta} - r_2y - \Omega_0\mu_i\alpha + s_2\beta + \sigma_4y_k = (A - C)\delta\Omega_0^2\cos(\Omega_0t - \chi) + M_\beta, \quad (4)$$

$$M\ddot{x}_k + p_3x_k + r_3x + s_3\alpha + n_1\dot{x}_k = 0, \quad (5)$$

$$M\ddot{y}_k + p_4y_k + r_4y + s_4\beta + n_2\dot{y}_k = 0, \quad (6)$$

$$\frac{\partial U}{\partial t} - 2\Omega_0v = -\frac{1}{\rho}\frac{\partial P}{\partial r} - \ddot{Q}e^{-i(\Omega_0t+\varphi)} + iz\ddot{\theta}e^{-i(\Omega_0t+\varphi)}, \quad (7)$$

$$\frac{\partial v}{\partial t} + 2\Omega_0U = -\frac{1}{\rho r}\frac{\partial P}{\partial \varphi} + \ddot{Q}e^{-i(\Omega_0t+\varphi)} + z\ddot{\theta}e^{-i(\Omega_0t+\varphi)}, \quad (8)$$

$$\frac{\partial W}{\partial t} = -\frac{1}{\rho}\frac{\partial P}{\partial z} - (i\ddot{\theta} + 2\Omega_0\dot{\theta})re^{-i(\Omega_0t+\varphi)}, \quad (9)$$

$$\frac{\partial(rU)}{\partial r} + \frac{\partial v}{\partial \varphi} + \frac{\partial W}{\partial z} = 0 \quad \text{under} \quad \rho = \text{const}, \quad (10)$$

with boundary conditions: on a wall, the top and bottom borders of the cylinder

$$U = W = 0, \quad (11)$$

on a free surface of liquid

$$\left(\frac{\partial P}{\partial t} - \rho\Omega_0^2r_0U\right)_{/r=r_0} = 0. \quad (12)$$

Here is $Q = x + iy$, $\theta = \alpha + i\beta$.

The equations of movement of rotor system and boundary conditions to them, linearized near stationary rotation, allow decisions proportional $\exp(i\Omega_0t)$ and $\exp(i\omega t)$ where ω is characteristic number

$$\left. \begin{aligned} x &= A_1e^{i\Omega_0t} + B_1e^{i\omega t}, \\ y &= A_2e^{i\Omega_0t} + B_2e^{i\omega t}, \end{aligned} \right\} \left. \begin{aligned} \alpha &= A_3e^{i\Omega_0t} + B_3e^{i\omega t}, \\ \beta &= A_4e^{i\Omega_0t} + B_4e^{i\omega t}, \end{aligned} \right\} \left. \begin{aligned} x_k &= A_5e^{i\Omega_0t} + B_5e^{i\omega t}, \\ y_k &= A_6e^{i\Omega_0t} + B_6e^{i\omega t}, \end{aligned} \right\} \quad (13)$$

where A_1, A_2 и A_3, A_4 are respectively linear and angular complex amplitudes of fluctuations of the rotor, caused by action of own unbalance; A_5, A_6 amplitudes of the compelled fluctuations of the base; $B_1, B_2, B_3, B_4, B_5, B_6$ are amplitudes of self-excited fluctuations of a rotor and base; required frequency of fluctuations of a rotor ω generally is the complex size which valid part defines frequency of self-oscillations, and the imaginary part characterizes degree of instability of system; the second members in the right parts of the equations (13) express the fluctuations of the rotor caused by indignant movement of liquid concerning the cylinder.

To exclude a time of arguments of trigonometrical and indicative functions at the solution of the main equations of movement, relative speed of a particle of liquid and function of pressure are accepted by the proportional $\exp i(\sigma t - \varphi)$ where σ is complex own meaning that results in expediency of creation of private decisions with the same dependence on time. Function of pressure and making speeds of a particle of liquid for any point of volume, and also expression for the hydrodynamic moment and force of reaction of liquid are as a result defined:

$$P' = \left[\sum_{k=1}^{\infty} Z_1 \left(\frac{\pi k}{H} \gamma_1 r \right) \cos \frac{\pi k}{H} (z - H) + A_0 r + \frac{B_0}{r} + i \rho r \omega z (\omega - 2\Omega_0) B_{34} \right] e^{i(\sigma t - \varphi)} \quad (14)$$

$$U = \left\{ \frac{1}{\rho a^2} \sum_{k=1}^{\infty} \left[\frac{2\Omega_0 i}{r} Z_1 \left(\frac{\pi k}{H} \gamma_1 r \right) - e Z_1' \left(\frac{\pi k}{H} \gamma_1 r \right) \right] \cos \frac{\pi k}{H} (z - H) + \right. \\ \left. - \frac{A_0}{\rho(2\Omega_0 i + e)} + \frac{B_0}{\rho r^2(e - 2\Omega_0 i)} + \frac{\omega^2 B_{12} - 2iz\Omega\sigma B_{34}}{2\Omega_0 i + e} \right\} e^{i(\sigma t - \varphi)}, \quad (15)$$

$$v = \left\{ \frac{1}{\rho a^2} \sum_{k=1}^{\infty} \left[2\Omega_0 Z_1' \left(\frac{\pi k}{H} \gamma_1 r \right) - \frac{ei}{r} Z_1 \left(\frac{\pi k}{H} \gamma_1 r \right) \right] \cos \frac{\pi k}{H} (z - H) + \right. \\ \left. + \frac{iA_0}{\rho(2\Omega_0 i + e)} + \frac{iB_0}{\rho r^2(e - 2\Omega_0 i)} - \frac{2z\omega\sigma B_{34}}{2\Omega_0 i + e} \right\} e^{i(\sigma t - \varphi)}, \quad (16)$$

$$W = \left\{ -\frac{1}{\rho\sigma H} \sum_{k=1}^{\infty} Z_1 \left(\frac{\pi k}{H} \gamma_1 r \right) \sin \frac{\pi k}{H} (z - H) \right\} e^{i(\sigma t - \varphi)}, \quad (17)$$

$$F = \Omega_0^2 m_L \left(A_{12} - \frac{1}{2} i H A_{34} \right) e^{i\Omega_0 t} + m_L \left(\frac{A_0}{\rho} + \frac{B_0}{\rho R^2} + i\omega(\omega - 2\Omega_0) \frac{H}{2} B_{34} \right) e^{i\omega t}, \quad (18)$$

$$M_\theta = \Omega_0^2 m_L \left\{ \frac{1}{2} i H A_{12} + E_1 A_{34} \right\} e^{i\Omega_0 t} + m_L \left\{ \frac{2H}{\pi\rho R} \sum_{k=1}^{\infty} \left[\frac{1}{k^2} Z_1 \left(\frac{\pi k}{H} \gamma_1 R \right) - \right. \right. \\ \left. \left. - \frac{2i}{\rho H} \sum_{k=1}^{\infty} \left[Z_2 \left(\frac{\pi k}{H} \gamma_1 R \right) - \frac{1}{q^2} Z_2 \left(\frac{\pi k}{H} \gamma_1 r_0 \right) \right] + \frac{iH}{2\rho} \left(A_0 + \frac{B_0}{R^2} \right) - E_1 \omega(\omega - 2\Omega_0) B_{34} \right\} e^{i\omega t}, \quad (19)$$

$$E_1 = \frac{H^2}{3} - \frac{R^2}{4} \left(1 - \frac{1}{q^4} \right), \quad Z_1 \left(\frac{\pi k}{H} \gamma_1 r \right) = C_{1k} J_1 \left(\frac{\pi k}{H} \gamma_1 r \right) \\ + C_{2k} N_1 \left(\frac{\pi k}{H} \gamma_1 r \right), \quad e = i\sigma,$$

J_1 and N_1 are Bessel and Neiman functions of 1st order real argument; k —axial wave number; $k = 0, 1, 2, 3, \dots$. The unknown constants A_0, B_0, C_{1K}, C_{2K} are defined by means of boundary conditions (11), (12).

The solution proportional $\exp(i\Omega_0 t)$ gives the chance calculation of the compelled fluctuations of the rotor caused by its own unbalance, and the compelled fluctuations of the base by means of system of the equations which in a matrix form looks like:

$$\bar{A} = (a)^{-1} \bar{b}, \quad (20)$$

where (a) is coefficients matrix, \bar{A} is vector column of unknown amplitudes of the compelled fluctuations, \bar{b} is vector column of free members. The equation for determination of critical speeds is deduced from an equality condition to zero of a determinant of a square matrix (a) in the absence of a friction also is a polynom of the 12th degree of an even order. Twelve critical speeds are in the case under consideration possible, from which six there correspond to the direct precession, six following are the return precession caused by a rotor unbalance.

3 Solution Results Analysis

For research of features of the compelled fluctuations of rotor system taking into account spatial movement of the ideal liquid filling a cavity of a rotor, system of the equations (20) without difficulties is solved analytically, for example, by Gauss method or number on the computer. Some results of the solution of the equation (20) are shown in Figs. (2), (3). At increase in the relation of weight of a rotor to mass of the base μ as the amplitude of the compelled fluctuations of a rotor and the base increases and moves to higher values of angular speed of system ($k_m = 0, 5$). At the smallest relation of weight of a rotor to mass of the base the amplitude of the compelled fluctuations of a rotor and the base essentially decreases

($A'_1 = \sqrt{|A_1|^2 + |A_2|^2}$, $A'_3 = \sqrt{|A_5|^2 + |A_6|^2}$, $A_1^* = A'_1/\varepsilon$, $k_m = c_1/c$, $A_3^* = A'_3/\varepsilon$, $\Omega_0^* = \Omega_0/\Omega_{kp}$, $\Omega_{kp} = \sqrt{(p_1 + p_2)/2m}$). Stability of stationary movement of system is determined by character of an imaginary part of complex roots of the characteristic equation. The mode of stationary rotation is unstable if possible values of the characteristic equation ω have a negative imaginary part.

The common numerical decision of the characteristic equation is inconvenient, as required values ω are included in arguments of Bessel functions. For of the confidant definition of a zone instability we will accept $k = 0$, i.e. when rotor raises waves only on a flat surface of liquid. In this case the axial component of speed of a particle of liquid is equal to zero ($W = 0$) and the characteristic equation after transformations becomes a polynom of the twentieth degree with complex factors. Roots of this polynom will serve as zero approach of roots of the transcendental characteristic equation where space movement of liquid is

Fig. 2 Amplitude A_1^* 's dependence on angular speed of rotor at a variation m

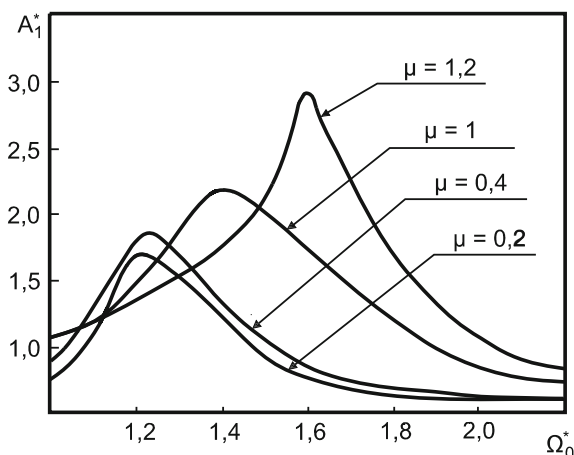
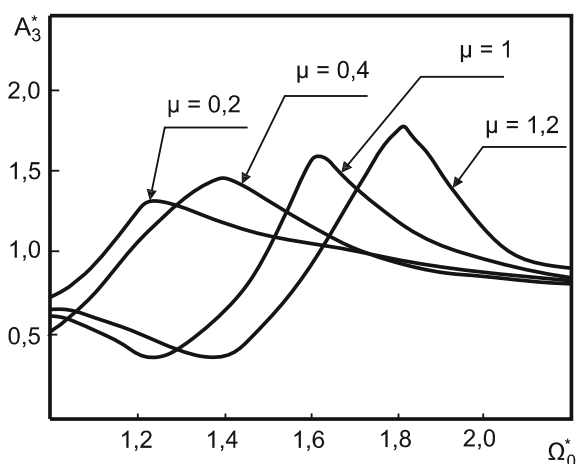
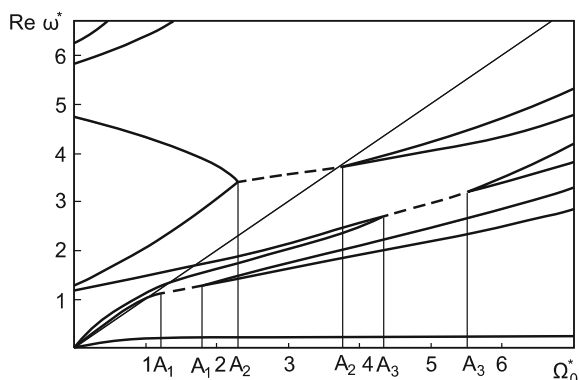


Fig. 3 Amplitude A_3^* 's dependence on



considered at $k > 0$. In a considered task, as well as in many problems of mechanics and equipment, research of stability of system at its not conservatism has paramount value. Stability of movement of a rotor is determined by character of roots of the characteristic equation of system, i.e. by Lyapunov's method. Some results of the solution of these equations, are presented in Fig. 4 where dependences of a material part are shown ω^* from angular speed of rotor Ω_0^* under filling $q = 1,5$ in case of anisotropic support $c'_1 = c''_1 \neq c'_2 = c''_2$. On speed intervals A_1A_1 , A_2A_2 и A_3A_3 among roots of the equation there are roots with a negative imaginary part. Therefore, intervals of speeds of a rotor A_1A_1 , A_2A_2 и A_3A_3 limit zones of system instability. Critical speed of system is defined graphically by line crossing $\omega^* = \Omega_0^*$ with schedules of frequencies $\omega^* = \omega^*(\Omega_0^*)$. Emergence of three zones of instability is a direct consequence of asymmetry of installation on shaft of rotor, oscillation of the fundament, anisotropism of support and internal resistance.

Fig. 4 Dependence of material part ω^* angular speed of rotor at variation μ angular speed at $q = 1, 5$; $\mu = 0, 4$



With extent growth of filling at the fixed values of other parameters, the width of all zones of instability at first extends, their borders move to higher speeds of rotor rotation then are narrowed. When the rotor is completely filled with liquid, zones of instability disappear.

4 Conclusions

Analytically generalized dynamic model of the Rotor-Liquid-Fundament system being generalized and for systems without liquid, and also without interrelation of a rotor and the base is solved. Exact solutions of the linearized equations of liquid movement, giving the chance studying and estimating effect of wave properties of a free surface of liquid on movement of rotor system are found. Elastic installation of the base allows enter the external damping necessary for obtaining of the best characteristics, than at its rigid installation.

References

1. Feng, N., Hahn, E.: Vibration analysis of rotor-bearing-pedestal system. In proceedings 5th international congress on sound and vibration, Adelaide, Australia, 2457–2464 (1997)
2. Gasch, R., Maurer, J., Sarfeld W.: Soil influence on unbalance response and stability of a simple rotor-foundation system. J. Sound Vib. 9(34), 549–566 (1984)
3. Тондл, А.: Автоколебания механических систем. М., 430 с (1979)
4. Rahimov, E.R., Rahmatullaev, A.Sh., Kydyrbekuly A.B.: Dynamics of unbalanced rotor in the interaction with the other physical fields. Transactions seventh world congress on the theory of machines and mechanisms. Sevilla, Spain, 532–539 (1987)
5. Рахимов, Е.Р.: Построение асимптотических приближений уравнений движения обобщённой динамической модели « ротор-фундамент » . *Теор-~~NA~~-я механ-~~NA~~-змов -~~NA~~- у-~~NA~~-равлен-~~NA~~-е маш-~~NA~~-нам-~~NA~~-*, Алма-Ата, с. 8–17 (1986)

Simulations of Radiation Heat Transfer in Design of Alternative Infrared Emitters

J. Loufek

Abstract The article presents a numerical model of radiation heat transfer. The model is designed to bring a support for innovation in heating shell moulds. Such shell moulds are used in the process of creating leather imitation by slush moulding method. The model description aims at the relevant radiation heat transfer processes. The contribution also provides comparison between model results and relevant measured values to outline that described model corresponds with real behaviour. One of the aims of the work is the use of the eventual simulation tool for a design such a shape of reflector that will be suitable for required criteria. According to that, the article describes the heat distribution and characteristics of considered infrared emitters. This implemented tool, along with the optimization algorithms, can be used to find out the best position or shape of emitters. After the particular model design, during the process of its calibration, the simulated values are needed to be compared with the real measured values. The article briefly demonstrates the mentioned procedure as a utility for practical usage.

Keywords Simulation • Optimization • Radiative heat transfer • Infrared emitters

1 Introduction

Heating shell moulds for artificial leather manufacturing process are realized in various ways. The forms can be heated for example by means of hot sand or oil. Such methods require significant demands on storage and transport heating

J. Loufek (✉)
Technical University of Liberec, Liberec, Czech republic
e-mail: Jan.Loufek@tul.cz

medium. The forms also can be heated by hot air. In this case, there is a problem with the size and noise of the equipment for handling heated air.

Another utilizable method of heating-up the form is based on the using a set of infrared heat emitters located above the shell. This heating method has several advantages. Heating using thermal radiation does not require any heating medium [1]. The equipment sizes are, in general, less space consuming than in the case of another above-mentioned methods. On the other hand, the main disadvantage of this approach is the difficulty in uniformly heating of shell moulds. The uniformity must be assured by the appropriate emitters' control. Then, the considerable outcome can provide the model of heating-up the form by particular set of emitters, which is based on the understanding of single emitter contribution to the warming. This paper concerns on the radiation of heat transfer model that simulates single emitter characteristics.

2 Radiation Heat Transfer Model

The presented model supposes two main parts of the whole system. There is a source or set of sources of heat on one side and a heated-up object or set of objects on the other side. We assume that there is not a physical contact between the source and object, so the heat transfer predominantly goes on by the radiation.

In general, every part of the system radiates continuously some electromagnetic energy. The magnitude of the energy depends on the temperature of the object and its surface properties. The amount of the radiated energy depends on the biquadrate of absolute temperature. In the case of "black body" i.e. a body, which absorbs/emits all the incident energy without any reflection, the amount of energy absorbed or emitted per square meter e_b (Wm^{-2}) is described by the Stefan-Boltzmann's law

$$e_b(T) = \sigma T^4, \quad (1)$$

where T (K) stands for absolute temperature and $\sigma = 5.670373 \times 10^{-8} \text{ Wm}^{-2}\text{K}^{-4}$ is Stefan-Boltzmann constant. In the case of a real body ("gray body") we deal with emissivity ε (—)

$$\varepsilon = \frac{e(T)}{e_b(T)} = \frac{\int_0^{\infty} e_{\lambda}(\lambda, T) d\lambda}{\sigma T^4}, \quad (2)$$

that expresses the rate of emitted energy against black body emission. In the term (2) λ (m) is wavelength of radiating energy.

Supposing all the parts of the system are in thermodynamic equilibrium state, according to the Kirchhoff's law [2] every body emits as much energy, at each direction and each wavelength, as it absorbs. In general, monochromatic emittance ε_{λ} (—) and monochromatic absorptance α_{λ} (—) depend on absolute temperature

T (K) and the direction of radiation. For non-black diffusive body is possible to simplified angle independent term

$$\varepsilon_\lambda(T) = \alpha_\lambda(T). \quad (3)$$

For more details see [2]. Amount of radiated energy (radiosity) B (Wm^{-2}) is determined as sum of reflected energy and energy emitted by self. It can be expressed by

$$B = \rho H + \varepsilon e_b, \quad (4)$$

where H (Wm^{-2}) stands for irradiance (i.e. flux of energy that irradiates the surface per square meter), ρ (–) stands for reflectivity of the surface of the considered body.

Next we perform partition of surface of all parts of the system into a set of particle surfaces A_i . For arbitrary two particle surfaces A_i, A_j ($A_i \neq A_j$) we introduce view factor F_{i-j} (–), which quantifies the fraction of energy that leaves surface A_i and reach the surface A_j , so way

$$F_{i-j} = \frac{1}{A_i} \iint \frac{\cos\beta_i \cos\beta_j}{\pi r^2} dA_i dA_j, \quad (5)$$

where r (m) stands for the join of particular points A_i and A_j and β_i (rad) is the angle between the join and outer normal of A_i in the particular point of A_i . The form (5) introduces a general term for view factor evaluation. Our model deals with 2D simplification, which has been presented in [2] as Hottel's crossed-string method. Eventually, heat flux Q_i (Wm^{-2}) of particular surface A_i in the direction of outer normal due to radiation can be expressed as

$$Q_i = \frac{e_b - B}{(1 - \varepsilon)(\varepsilon A_i)} \quad (6)$$

3 Numerical Model

Our model is designed to be able to figure heat flux distribution (6) over any surface in two-dimensional space. Model is composed of set of straight particle surfaces, whereas every particle surface has given particular properties (location, emittance and temperature). Model uses Hottel's crossed-strings rule to determine view factors between particle surfaces of the whole system [3].

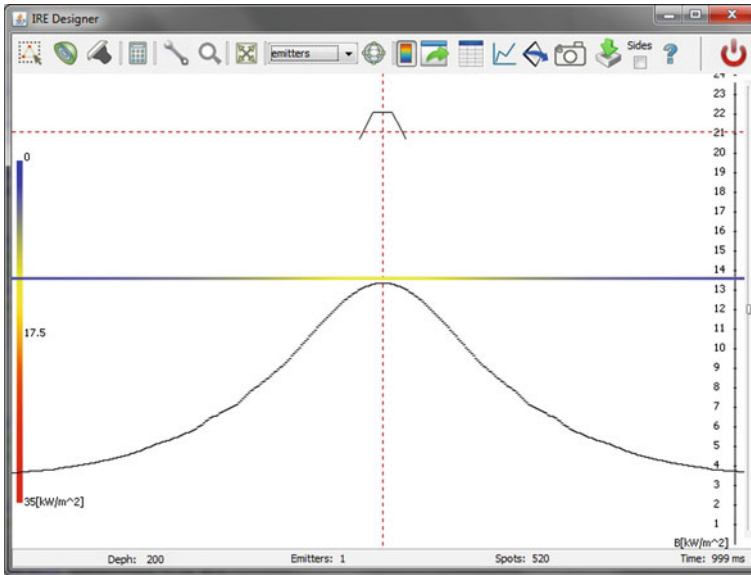


Fig. 1 Sample simulation in IRE Designer tool

3.1 IRE Designer

The model was implemented in simulation tool named IRE Designer. In this tool the concrete simulated system is divided into two logical parts. The first part is the irradiated surface. The second part supplies emitters functionality. As it was already mentioned, the numerical model supposes partition both these parts into a set of straight partial surfaces i.e. segments. Difference between irradiated surface and emitter segments is at access to those single surfaces. In case of irradiated surface segment, the main demand is to point out numerical outputs of particular simulation. Every emitter segment has implemented several functions, which supply the manipulation with shapes, position and other emitter properties. Figure 1 shows sample screen of IRE Designer user interface [4].

3.2 Calibration

To determine accuracy of values given by particular simulation, we need to compare values with real measured ones. The IRE Designer tool has implemented functionality for importing measured values in specific text format.

For testing, we selected the Phillips IRZ500 emitter. Figure 2 shows the side view of the emitter. Real measurement was realized by Hukseflux SBG01 heat flux sensor. The comparison between measured values and values obtained by the

Fig. 2 Side view of Phillips IRZ500

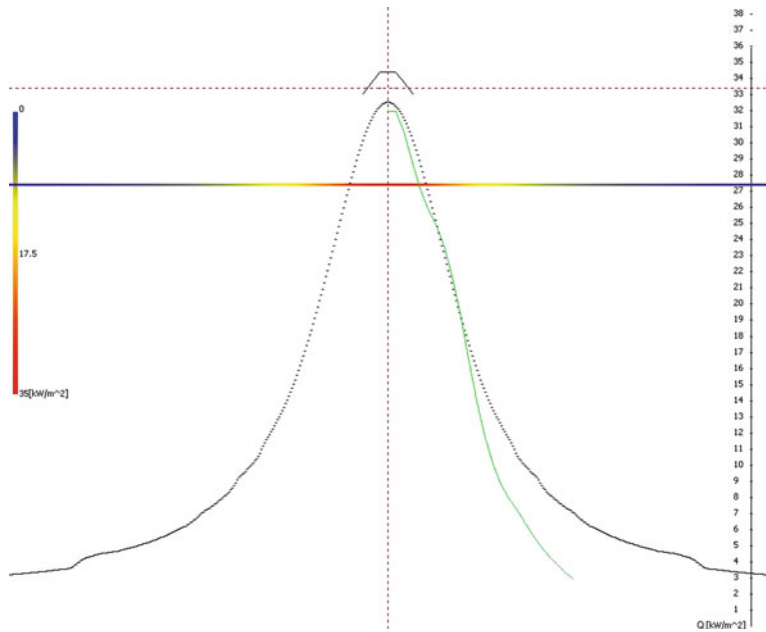
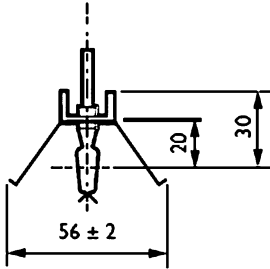


Fig. 3 Comparison of measured values and the simulated ones

numerical model is shown in Fig. 3. There, the gray line on the right half figures out the measured values, the black curve points out the numerical simulation results. Due to symmetry of heat flux trace, the measurement is performed under only a quarter of irradiated surface.

3.3 Optimization

Described numerical model is able to use for example for new emitter configuration design. In general, it is not possible to solve the problem analytically. So it

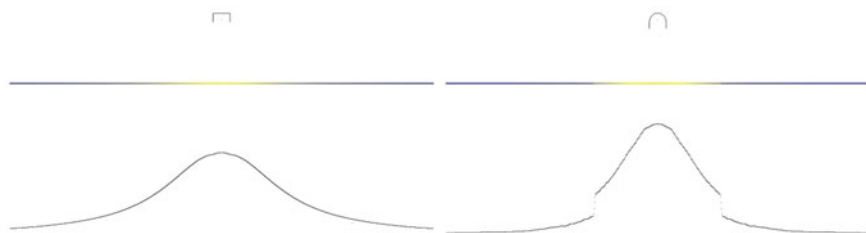


Fig. 4 Comparison of two different reflector shapes with the same properties

is appropriate to use automated optimization. For the purpose, the tool implements gradient descent algorithm. The algorithm supposes that there is specified required tracing. Then, the algorithm gradually manipulates the reflector points and compares the simulated results to the demanded track. The best partial result is the basis for the next step of the algorithm. Figure 4 shows two different model situations. The two presented cases differ only in reflector shape, the properties of all surfaces are the same for both configurations.

4 Conclusions

Represented numerical model is based on radiation heat transfer theory and its utilisation for two-dimensional case. Such model enables to use optimization algorithm, which finds alternative reflector shape. Actually, the model does not include dynamical processes such as heat transfer by conduction or gradual heating of model components. Numerical model implemented in IRE Designer tool can be used as tool for a design of demanded reflector configuration.

Acknowledgments This work is co-financed from the student grant SGS 2011/7821 Interactive Mechatronics Systems Using the Cybernetics Principles and the project Ministry of Industry and Trade number FR-TI1/266.

References

1. LIENHARD IV, John, H., John, H., LIENHARD V. A heat transfer textbook. 3rd ed. Cambridge, Mass: Phlogiston Press (2003) ISBN 09-713-8352-9
2. SIEGEL, Robert and John, R HOWELL. Thermal radiation heat transfer. 4th ed. New York, Taylor, (2002) 868 s. ISBN 15-603-2839-8
3. LOUFEK, Jan. *Simulace teplotních polí*. Liberec, 2012. Teze disertační práce. Technická univerzita v Liberci. In preparation. Only in Czech
4. LOUFEK, Jan. IRE Designer. Liberec 2012. User manual of IRE Designer software. Only in Czech

Creating a Mathematical Model for Solving Chatter and Dealing the Problems Concerning the Maximum Allowable Size of a Machining Chip

J. Ondrášek

Abstract The paper deals with the issues of self-excited vibration. Such vibration occurs in those systems in which an internal source continuously exists from which the system draws power to maintain or even increase the amplitude of vibration when this take-off is controlled by the oscillating motion of the system itself. Thus, this energy source considerably influences the dynamic and stability features of the system. An example of such a system is a machine tool during machining as well when a part of the energy of the cutting process in chip machining can be changed into energy that will be vibrating the machine as a whole. The vibrations are then shown with a strong machined surface waviness and are usually accompanied by noise. In general, it can be determined the range of cutting conditions in which, when applying them, no chatter will occur, i.e. the cutting process is stable. One of the ways of such a determining is a stability lobe diagram e.g. which expresses the dependence of chip thickness on the speed of a workpiece. The subject of this paper is a possible procedure and approach when creating stability lobe diagrams.

Keywords Chatter • Machine tool • Chip thickness • Lobe diagram

1 Introduction

One of the main causes of the generation of self-excited vibration in mechanic systems is dry friction between two mutually moving parts. Self-excited vibration is undesirable and we try to avoid it either by increasing positive damping or by

J. Ondrášek (✉)
VÚTS Liberec a.s., Liberec, Czech Republic
e-mail: jiri.ondrasek@vuts.cz

eliminating the causes of negative damping. The frequency of steady self-excited vibration is close to the natural frequency of mechanical systems.

The proper problems of investigating self-excited vibration (chatter) during machining present a creation of the following partial mathematical models: a model of the machining process itself, see [1], a model of mechanical system inclusive flexible links and real constraints, see [2] and a drive model that presents a model of electromotor itself and its control, see [3]. For their creation, there were used the NX I-DEAS, MSC-ADAMS and MSC-EASY5 program environment and data flow between them via MSC-ADAMS Flex and Controls modules.

2 Chatter

The next section provides some basic relations that are derived and explained in detail in [1], see Chap. 5, on those assumptions:

1. Cutting force F is proportional to width b and depth of cut y_N in the direction of the normal to the machined surface by the relation:

$$F = -C_0 b y_N, \quad (1)$$

where C_0 denotes specific cutting resistance.

2. Specific cutting resistance C_0 is independent of speed.
3. Cutting edge geometry does not affect the direct correlation between force F and chip depth y_N in the normal direction.
4. Angle β (an angle between cutting force F and the axis perpendicular to the normal of the machined surface) does not change with chip depth y_N .
5. Friction forces between tool, workpiece and leaving chip are neglected.

In Fig. 1, there is shown a block diagram of the continuous machining process in which the dynamic system can be described by the so-called oriented dynamic compliance $G_y(s)$. This is a transfer function between the Laplace transforms of cutting force $F(s)$ and the movement of the tool group $y(s)$:

$$G_y(s) = \frac{y(s)}{F(s)}, \quad (2)$$

where s is the complex variable.

If depth of chip $y_0(t) < 0$ is specified, cutting force F is generated which will cause the movement of tool group $y(t)$ that will be superimposed to the specified depth, so instantaneous chip depth $y_N(t)$ is given by an expression:

$$y_N(t) = y_0(t) + y(t). \quad (3)$$

The chip thickness is negative because chip cutting occurs in the opposite direction of the y -axis orientation. If there is a case of $y_N(t) > 0$, the cutting edge got out from engagement.

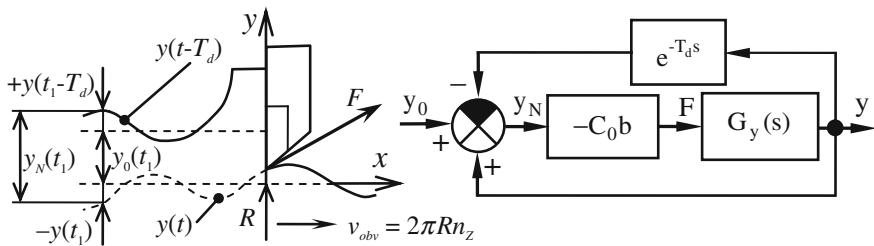


Fig. 1 Continuous machining and its block diagram

When working with a fixed time link between the cuts, the freshly machined surface will get again into contact with the tool after a defined time with the so-called transport time delay T_d . This fact can be expressed with a relation:

$$y_N(t) = y_0(t) + y(t) - y(t - T_d), \quad (4)$$

where $y_0(t)$ is the feed per one revolution, term $y(t)$ is valid for immediate waviness and term $y(t - T_d)$ applies for waviness from the previous cut which will come under the cutting edge of the tool over a time period T_d . Waviness $y(t - T_d)$ from the previous cut together with an immediate tool position $y(t)$ always affects the variation of chip depth $y_N(t)$, see Fig. 1, where the instantaneous chip depth y_N at time $t = t_1$ is shown. The Laplace image of Eq. (4) is:

$$y_N(s) = y_0(s) + y(s)(1 - e^{-T_d s}). \quad (5)$$

Using Eqs. (1), (2) and (5), the closed loop transfer as to Fig. 1 can be determined in the following form:

$$G_{\text{Cellk}}(s) = \frac{y(s)}{y_0(s)} = \frac{-C_0 b G_y(s)}{1 + C_0 b G_y(s)(1 - e^{-T_d s})} \quad (6)$$

To ensure the stability of the machining process it is necessary so that chip width b does not exceed the limit chip width b_{mez} at which the amplitude characteristic of the closed loop transfer (6) shall not exceed the unit level at any angular frequency ω . This condition is expressed by the relationship:

$$b < b_{mez} = -\frac{1}{2C_0(\text{Re}_{neg} G_y(j\omega))_{\min}} = \text{function 1}(\omega). \quad (7)$$

in which $\text{Re}_{neg} G_y$ represents negative values of the real component of dynamic compliance G_y , see [1].

The stability lobe diagram expresses the dependence of limit chip width b_{mez} on the speed of workpiece n_z . The speed equation, see [1], is given by the expression:

$$f = n_z \left(N + 1 - \frac{1}{\pi} \arctg \frac{\text{Re} G_y(j\omega)}{\text{Im} G_y(j\omega)} \right) = \text{function 2}(\omega), \quad (8)$$

where $f = \omega/2\pi$ is the frequency of self-excited vibrations on the limit of stability for each value of N individually. Number N indicates the number of whole waves of the workpiece surface ripple to be incurred over period $T_d = 1/n_Z$. The full version of the stability lobe diagram is generated in practice as follows:

1. To the theoretically or experimentally determined set of the values of dynamic compliance, there are completed arranged pairs $f \leftrightarrow b_{mez}$ as to (7).
2. By means of (8), there are created pairs $f \leftrightarrow n_Z$ repeatedly for values $N = 0, 1, 2, \dots$ which may be further displayed by a set of curves $f = f(n_Z)$.
3. From pairs $f \leftrightarrow n_Z$ and $f \leftrightarrow b_{mez}$, there are assembled pairs $n_Z \leftrightarrow b_{mez}$ which are shown as a set of curves—**lobs** for various values N again.
4. The individual „lobs“ may intersect each other and the area of the stable widths is under their lower envelope.

3 Effect of Feed Drives on the Chatter

Transfer functions in the preceding paragraph were investigated in a mechanical system only. In the same way it is possible to obtain transfer functions for the regulation drives in the feeds of machine tools because their behavior with regard to external forces is expressed by the dynamic flexibility of regulation, which is again a transfer function, having the shape of a quotient of two polynomials.

In computer simulations it is assumed that the drive of the feeds of machine tool will be implemented by a 3phase synchronous electromotor with permanent magnets with which an exciting magnetic rotor flow is produced. For the purposes of simulations, the model of this servomotor was replaced by a simplified model which is based on the description of a DC motor, see Fig. 2, in which the block *Mechanical system* is a motor rotor with mass moment of inertia J . The parameters of a single coil, i.e., inductance L_s , electrical resistance R_s and motor voltage constant K_E are substituted in this model. Only at torque constant K_T it is necessary to substitute the value:

$$K_{T_{Celk}} = \frac{3}{2} K_T, \quad (9)$$

whereby the common interaction of all three coils is taken into account, see [3]. Furthermore, in the scheme, there stands U for voltage, I electrical current, M electromagnetic torque, ω rotor angular velocity and φ rotor angular displacement. The above given parameters of the electromotor were substituted in its simulation model from the data sheet stated by the manufacturer.

In the vector control of this type of electric motor, it is almost exclusively used the cascade control circuit with three hierarchically arranged feedbacks: current, speed and position, see Fig. 3. Maintaining the required values of position,

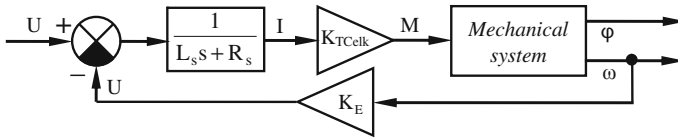


Fig. 2 A simplified block diagram of a synchronous motor

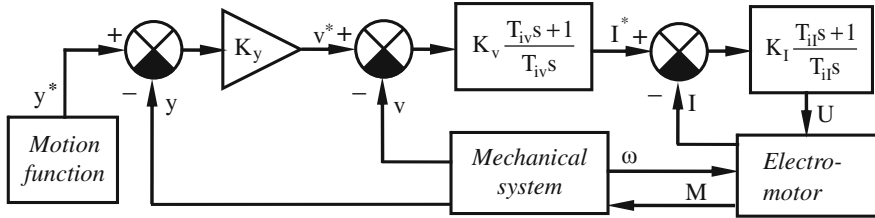


Fig. 3 A cascade control circuit with a current speed and position feedback

revolutions and current is ensured by PID linear controllers. Constant K is a proportional component of the controller, constant T_i expresses the integral time constant of the controller and T_d is a derivative time constant, $v = y, \dot{y}, \ddot{y}$. Index v reflects competence of the various constants to the position, velocity and current feedback. Those constants in the control structure according to Fig. 3 were debugged for the needs of the simulation model by the Ziegler-Nichols method, see [4]. In the diagram in Fig. 3, y expresses the position of the tool group, \dot{y} its velocity, and $*$ denotes the desired value of a particular variable.

4 Mathematical Model of the Cross-Slide Mechanical System

The aim of the calculations in the mathematical model of the chatter of the cross-slide was to calculate the limit chip width b_{mez} and to create the stability lobe diagram in the machining processes of recessing (machining in u -direction) and longitudinal turning (machining in w -direction) while both operations do not occur simultaneously. To establish them, it is necessary to determine the appropriate dynamic compliance $G_y(s)$, $y = u, w$, in the given direction depending on the method of machining. Those transfer functions between the acting forces and the mass deviations of the controlled mechanical system with discretely distributed mass and stiffness parameters are determined generally by the appropriate matrix elements:

$$\mathbf{G}(s) = (\mathbf{M}s^2 + \mathbf{B}s + \mathbf{K})^{-1}. \quad (10)$$

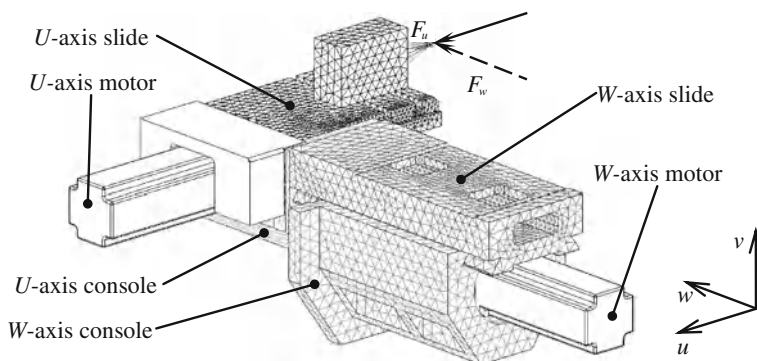


Fig. 4 Cross slide model

However, in this case, the dynamical compliances were determined by a numerical solution of the equations of motion made up through the MSC-ADAMS and MSC-EASY5 expert systems.

In the case of a mathematical model of the cross slide, which was created in the MSC-ADAMS program environment, see Fig. 4, it is a spatial system of 24 perfectly rigid bodies and 4 flexible bodies, a console of U and W axes and the slide of U and W axes. Between the bodies, kinematic pairs were defined in such a way so that any redundant constraints do not occur in the analyzed mechanical system. Bearing of the console of W -axis to the frame, ball screw bearing, ball screw nut and ball screw itself of both axes were considered as flexible. The damping of those elements was chosen as proportional to their stiffnesses in the simulation model. The deformation field of the flexible bodies was approximated with deformation modes, see [2]. It is a linear combination of static wave shapes of the body that respect the boundary conditions and the natural vibrations of the given flexible body. The modes of individual elements were established on the basis of the model of the particular body, created by using the FEM. Through those modes, there were determined further generalized mass matrix \mathbf{M} and stiffness matrix \mathbf{K} of the given flexible body whose dimension was acceptable for the purposes of subsequent calculations already. Damping matrix \mathbf{D} of the flexible body was defined on the basis of modal damping coefficients c_i . That one was introduced by means of damping ratio b_{ri} . The coefficients of proportional damping and damping ratio were verified with respect to the experimentally determined modal dampings of the natural wave shapes with the real mechanical system.

The resulting simulation model was characterized by 108 DOF.

5 Conclusions

It was selected such a procedure of the creation of the linked system of the cross slide when it is a composition of abstract dynamic subsystems with causal orientation input-output. This assembly is very simple because the outputs of one

model are the inputs of another model. Such a model of the related mechanical system can be solved in both time domain and frequency domain.

From the carried out computational simulations it is clear that the knowledge of the sub-model of damping in the given mechanical system and specific cutting resistance during machining process is crucial to determine the credible stability lobe diagrams and limit chip width b_{mez} .

Acknowledgments This paper was created within the work on the 2A-2TP1/038—Project supported by the Ministry of Industry and Trade—Ministerstvo průmyslu a obchodu.

References

1. Souček, P., Bubák, A.: Vybrané statě z kmitání v pohonech výrobních strojů. Česká technika—nakladatelství ČVUT (2008)
2. Slavík, J., Stejskal, V., Zeman, V.: Základy dynamiky strojů. Vydavatelství ČVUT (1997)
3. Souček, P.: Servomechanismy ve výrobních strojích. Vydavatelství ČVUT (2004)
4. Valášek, M., kolektiv: Mechatronika. Vydavatelství ČVUT (1995)

Impact of Thermal Stresses on Micro-Fabricated Devices Used for Optical Applications

K. Malinauskas, V. Ostasevicius and R. Dauksevicius

Abstract Thermal stresses induced during thin film deposition processes usually have important effects on the functionality and reliability of the microdevices used in optical applications. All surface-micromachined thin films are subject to thermal stresses that are usually observed on a substrate when thin film is evaporated on it and when it cools down to a room temperature. This paper presents a surface-micromachined membrane and its numerical model. Comsol Multiphysics is used for comparison of eigenfrequencies of the structure including and excluding thermal stresses.

Keywords MOEMS • Residual stresses • Thermal stresses • Surface micromachining • Finite element model • Micro-membrane

1 Introduction

Micro-opto-electromechanical systems (MOEMS) includes sensing, actuation mechanisms, signal processing, optical signal control, wireless and optical communication, and power generation on a single system [1]. There are numerous membrane-based MOEMS devices involved in various precise measurements such

K. Malinauskas (✉) · V. Ostasevicius · R. Dauksevicius
Kaunas University of Technology, Kaunas, Lithuania
e-mail: karolis.malinauskas@ktu.lt

V. Ostasevicius
e-mail: vytautas.ostasevicius@ktu.lt

R. Dauksevicius
e-mail: rolanas.dauksevicius@ktu.lt

as: pressure sensors, accelerometers, electrostatic RF switches, resonators, micro-motors and capacitive micro-machined ultrasonic transducers (CMUTs). In devices such as the CMUTs, the width of a membrane is typically 50–100 μm while the gap height is on the order of 0.1 μm to maximize the device efficiency. Hence, the aspect ratio of these devices is as high as 1:1000. Only 0.01 degrees initial membrane bow puts the membrane in contact with the bottom substrate, making the device inoperable. A principal source of contour errors in micro-machined structures is residual strain that results from thin-film fabrication and structural release. Surface micro-machined films are deposited at temperatures significantly above ambient. The relationship between stress and curvature in thin-film structures is an active area of research, both for the development of MOEMS technology and for the fundamental science of film growth [2, 3]. To summarize there are three main factors that cause a membrane-based structure to bow: (1) residual stress developed during the deposition, (2) the effect of atmospheric pressure on the membrane (constant ~ 0.1 MPa), and (3) thermal stress contribution during deposition.

2 Thin-Film Stress

The two main components that lead to internal or residual stresses in thin films are thermal stresses and intrinsic stresses. Thermal stresses are due to strain misfits as a result of differences in the temperature dependent coefficient of thermal expansion between the thin film and a substrate material such as silicon. Intrinsic stresses are due to strain misfits encountered during phase transformation in the formation of a solid layer of thin film [1]. Thus residual stress is defined as sum of both:

$$\sigma_R = \sigma_T + \sigma_I \quad (1)$$

where:

- σ_R is the residual thin film stress;
- σ_T is the thermal stress component;
- σ_I is the intrinsic stress component.

When the film/substrate composite is cooled to a room temperature, they contract by different amounts owing to differing coefficients of thermal expansion. The film is subsequently strained elastically to match the substrate and remain attached, causing the substrate to bend.

From Fig. 1 relationships between the biaxial stress in a plate and the bending moment M , is related to the stresses in the plate by:

Fig. 1 Free body diagram showing bending moment on a plate

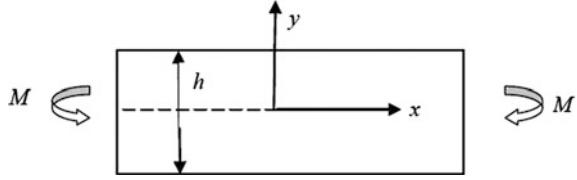
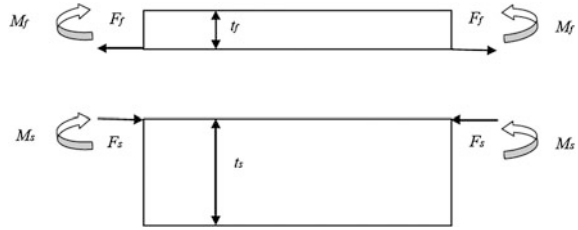


Fig. 2 Force and bending moment per unit length acting on thin film and substrate



$$M = \int_{-\frac{h}{2}}^{\frac{h}{2}} \sigma_{xx} y dy = y dy = \int_{-\frac{h}{2}}^{\frac{h}{2}} \alpha y^2 dy = \alpha \frac{h^3}{12} \quad (2)$$

where: y is the distance from the neutral axis; α is a constant and $\sigma_{xx} = \sigma_{zz} = \alpha y$

The stresses are given by:

$$\sigma_{xx} = \sigma_{zz} = \frac{12M}{h^3} y \quad (3)$$

The fundamental equation that calculates the residual stress experienced by a thin film can be derived from the Fig. 2 which depicts the force per unit length and the moment per unit length that are acting on the film (F_f and M_f), and substrate (F_s and M_s) respectively. The thickness of the film is t_f and the thickness of the substrate is t_s .

The stress that a single layer of thin film exerts on a substrate is:

$$\sigma_f = \left(\frac{E_s}{1 - \nu_s} \right) \frac{t_s^2}{6t_f} k = \left(\frac{E_s}{1 - \nu_s} \right) \frac{t_s^2}{6t_f R} \quad (4)$$

where: E_s is the Young's modulus of the substrate; ν_s is the Poisson ratio of the substrate; R is the radius of curvature of the film/substrate composite.

3 Eigenfrequency Comparison Evaluating Thermal Stresses

Using simulation software COMSOL three different dimension micro-membranes were modeled. Figure 3 represents scheme of the micro-membrane. Table 1 denotes exact dimensions, physical and mechanical properties.

Fig. 3 Schematic representation of micro-membrane that is used for numerical modeling

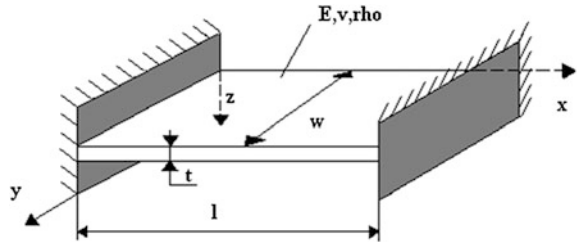


Table 1 Dimensions, physical and mechanical properties of micro-membrane

Description and symbol	Value	Unit
Length l	0.4–5	mm
Width w	0.4–5	mm
Thickness t	20	μm
Young's modulus E	155	GPa
Density ρ	2,330	kg/m^3
Poisson's ratio	0.23	–

Table 2 (a,b,c,d). 0.16 mm² area membrane

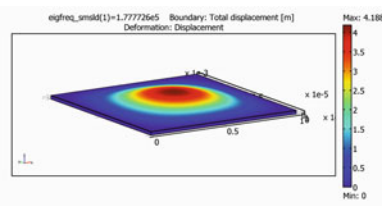
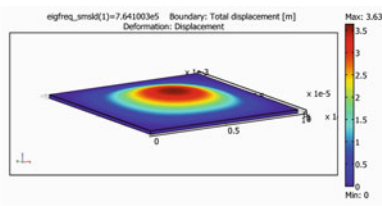
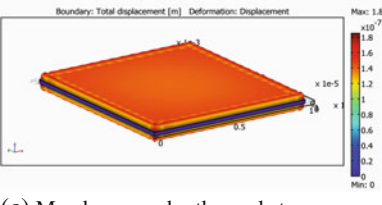
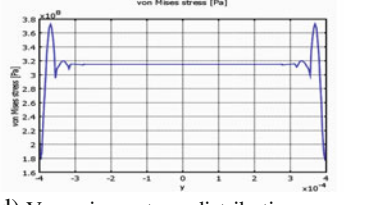
<i>Eigenfrequencies without thermal stresses</i>	<i>Eigenfrequencies with thermal stresses</i>
<div></div> <p>(a) Eigenfrequency is 177 kHz</p>	<div></div> <p>(b) Eigenfrequency is 764 kHz</p>
<i>Deformed shape of geometry of the membrane under thermal stresses</i>	<i>Von mises stress distribution going through the center of membrane</i>
<div></div> <p>(c) Membrane under thermal stresses</p>	<div></div> <p>(d) Von mises stress distribution</p>

Table 3 (a,b,c,d). 1 mm² area membrane

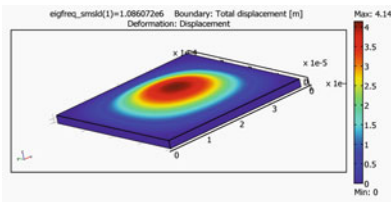
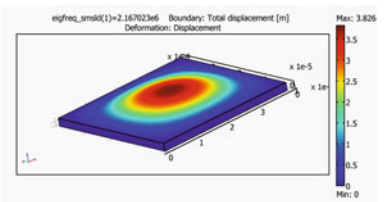
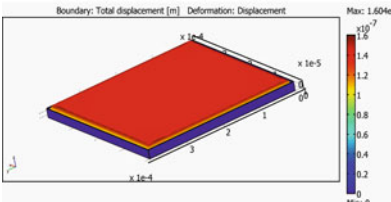
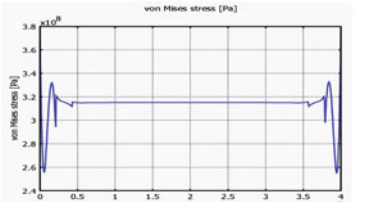
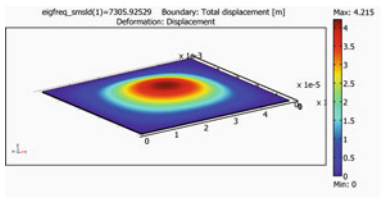
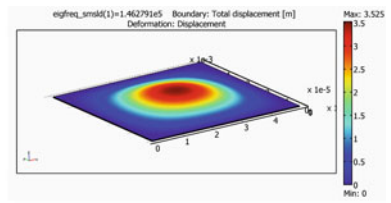
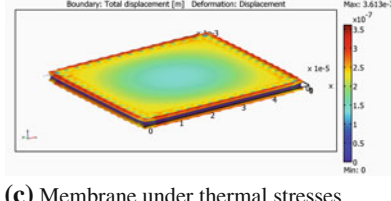
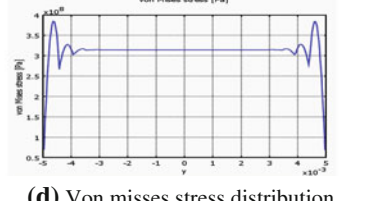
<i>Eigenfrequencies without thermal stresses</i>	<i>Eigenfrequencies with thermal stresses</i>
	
(a) Eigenfrequency is 1080 kHz	(b) Eigenfrequency is 2160 kHz
<i>Deformed shape of geometry of the membrane under thermal stresses</i>	<i>Von misses stress distribution going through the center of membrane</i>
	
(c) Membrane under thermal stresses	(d) Von misses stress distribution

Table 4 (a,b,c,d). 25 mm² area membrane

<i>Eigenfrequencies without thermal stresses</i>	<i>Eigenfrequencies with thermal stresses</i>
	
(a) Eigenfrequency is 7305 Hz	(b) Eigenfrequency is 146 kHz
<i>Deformed shape of geometry of the membrane under thermal stresses</i>	<i>Von misses stress distribution going through the center of membrane</i>
	
(c) Membrane under thermal stresses	(d) Von misses stress distribution

Mechanical model of micro-membrane was created using powerful finite element (FE) modeling software COMSOL. FE describes microstructure dynamics by the following classic equation of motion presented in general matrix form [4–14]:

$$[M]\{\ddot{U}\} + [C]\{\dot{U}\} + [K]\{U\} = \{Q(t, U, \dot{U})\} \quad (5)$$

where $[M]$, $[C]$, $[K]$ —mass, damping and stiffness matrices respectively, $\{\ddot{U}\}$, $\{\dot{U}\}$, $\{U\}$ —displacement, acceleration and velocity vectors respectively, $\{Q(t, U, \dot{U})\}$ is vector representing the sum of the forces acting on micro-membrane. For the evaluation of residual thermal stresses the temperature differences are between 620 °C, usually present in surface-micromachining processes, and ambient room temperature 25 °C Tables 2, 3, 4.

4 Conclusions

Micro-membranes of different dimensions were modeled and fabricated. Judging from the modeling results it can be easily observed that having smaller dimension, but the same thickness micro-membrane the influence of residual stresses is smaller as the dimensions of membrane decreases. Therefore, it is obvious that in order to properly fabricate operable micro-membrane area and width ratio of the microdevice needs to be as small as possible.

For further analysis fluid structure interaction models will be executed using the micro-membrane as basic sensing element in MOEMS biocompatible portable blood flow pulse and velocity sensor.

Acknowledgments This research was funded by a grant (No.MIP-060/2012) from the Research Council of Lithuania.

References

1. Vinci, R.P., Vlassak, J.J.: Mechanical behavior of thin films. *Annu. Rev. Mater. Sci.* **26**, 431–462 (1996)
2. Nix, W. D.: The mechanical properties of thin films. *Dept. Mater. Sci. Eng.* **353** (Jan 2005)
3. Stoney, G.G.: The tension of metallic films deposited by electrolysis. *Proc. Roy. Soc. London* **A82**, 172 (1909)
4. Fang, W., Wickert, J.A.: Determining mean and gradient residual stresses in thin films using micromachined cantilevers. *J. Micromechan. Microeng.* **6**(3), 301–309 (1996)
5. Yuan, F., Shih, Y., Knight, L.V., Perkins, R.T., Allred, D.D.: Using thin films to produce precision, figured X-ray optics. *Thin Solid Films*, **220**, 284–288 (1992)
6. Ostasevicius, V., Tamulevicius, S., Grigaliunas, V., Kopustinskas, V., Palevicius, S., Gudonyte, S., Dauksevicius R.: Design and fabrication of a microelectromechanical switch. *Mater. Sci.* **10**(4), 313–316 (2004)
7. Senturia, S.D.: *Microsystem Design*. Kluwer Academic Publishers, Norwell (2001)

8. Madou, M.: *Fundamentals of Microfabrication*, 2nd edn. CRC Press, Boca Raton (2002)
9. Wood, R. et al.: MEMS microrelays. *Mechatronics*, **8**, 535–547 (1998)
10. Judy, J.W.: Microelectromechanical systems (MEMS): fabrication, design and applications. *Smart Mater. Struct.* **10**, 1115–1134 (2000)
11. Yao, Z.J., Chen, S., Eshelman, S., Denniston, D., Goldsmith C.: Micromachined low-loss microwave switches. *J. Microelectromech. Syst.* **8**, 129–134 (1999)
12. Toshiyoshi, H., Fujita, H.: Electrostatic microtorsion mirrors for an optical switch matrix. *J. Microelectromech. Syst.* **5**, 231–237 (1996)
13. Ostasevicius, V., Gaidys, R., Dauksevicius, R.: Numerical analysis of dynamic effects of a nonlinear vibro-impact process for enhancing the reliability of contact-type MEMS devices. *Sensors* **9**(12), 10201–10216 (2009)
14. Ostasevicius, V., Dauksevicius, R., Gaidys, R., et al.: Numerical analysis of fluid-structure interaction effects on vibrations of cantilever microstructure. *J. Sound Vib.* **308**, 660–67 (2007)

Exponential Damping as an Approach to Internal Hysteretic Damping of Rotor Systems: FEM Model of Timoshenko Rotating Beam with Maxwell-Weichert Damping Model

Antonín Skarolek

Abstract Since material losses of many engineering materials are known to be independent on frequency, the viscous damping is not always appropriate model of damping. In the case of structures, the effect of damping is usually small far from the system resonance. Unlike the case of structures, the material damping of rotor can lead to system instability. Traditional concept of hysteretic damping introduced by complex modulus of elasticity has serious drawback of its inapplicability in the time domain. Also it is inconsistent when frequency of vibration tends to zero, what is the case of rotor undergoing synchronous forward precession. In this paper, the Maxwell-Weichert material model is used to approach hysteretic material damping of rotor systems. Presented finite element model of Timoshenko rotating beam with non-viscous internal damping with exponential kernel is suitable for time domain solutions as well as for calculation of decay rates and Campbell plots of rotor systems.

Keywords Maxwell-Weichert material model • Exponential damping • Internal damping of rotors • Hysteretic damping

1 Introduction

Exponential non-viscous damping is a generalization of classical viscous damping. For the case of structures, the equations of motion of N-degree-of-freedom linear system with exponential damping can be formulated in following manner [1, 2]:

A. Skarolek (✉)
VÚTS, a.s., u Jezu 525/4, 46001, Liberec Czech Republic
e-mail: antonin.skarolek@vuts.cz

$$\mathbf{M}\ddot{\mathbf{u}}(t) + \mathbf{K}\mathbf{u}(t) + \sum_{k=1}^n \mathbf{B}_k \int_0^t \mu_k e^{-\mu_k(t-\tau)} \dot{\mathbf{u}}(\tau) d\tau = \mathbf{f}(t) , \quad (1)$$

where $\mathbf{u}(t)$ is displacement vector, \mathbf{M} and \mathbf{K} are the mass matrix and the stiffness matrix respectively. $\mathbf{f}(t)$ is the time-dependent forcing vector. The non-negative constants μ_k are called the relaxation parameters, \mathbf{B}_k are known as the damping coefficient matrices, n is the number of relaxation parameters used to describe the damping of the system.

The convolutions of displacement vector time derivative $\dot{\mathbf{u}}(t)$ and exponential kernels are understood as new state variables

$$\mathbf{y}_k(t) = \int_0^t \mu_k e^{-\mu_k(t-\tau)} \dot{\mathbf{u}}(\tau) d\tau . \quad (2)$$

Laplace transform of Eq. (2) renders the relation between the newly introduced state variables and displacements in frequency domain

$$s\hat{\mathbf{y}}_k(s) + \mu_k \hat{\mathbf{y}}_k(s) = s\mu_k \hat{\mathbf{u}}_k(s) , \quad (3)$$

where

$$\hat{\mathbf{y}}_k(s) = \mathcal{L}(\mathbf{y}_k(t)) , \quad \hat{\mathbf{u}}_k(s) = \mathcal{L}(\mathbf{u}_k(t)) . \quad (4)$$

Equation (3) demonstrates that the system from the Eq. (1) can be treated in the time domain as following set of linear differential equations

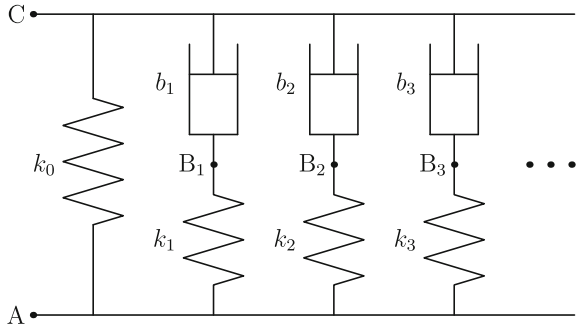
$$\mathbf{M}\ddot{\mathbf{u}}(t) + \mathbf{K}\mathbf{u}(t) + \sum_{k=1}^n \mathbf{B}_k \mathbf{y}_k(t) = \mathbf{f}(t), \quad \dot{\mathbf{y}}_k(t) + \mu_k \mathbf{y}_k(t) = \mu_k \dot{\mathbf{u}}(t). \quad (5)$$

2 Maxwell-Weichert Model and Hysteretic Material Damping

Relation to the Maxwell-Weichert model can be simply demonstrated by means of single-degree-of-freedom problem [3]. Considering harmonic deformation of the element on Fig. 1 (A–C distance) and the ratio between stiffness and damping of each branch of the element

$$\mu_k = \frac{k_k}{b_k}, \quad (6)$$

the complex dynamic stiffness of the element can be defined as

Fig. 1 The Maxwell-Weichert model

$$k_{AC}(\omega) = k_0 + \sum_{k=1}^n k_k \left(\frac{\omega^2}{\mu_k^2 + \omega^2} + j \frac{\mu_k \omega}{\mu_k^2 + \omega^2} \right). \quad (7)$$

It is trivial to show that single-degree-of-freedom case of Eq. (5) leads to the same dynamic stiffness as per (7). Contribution of k -th spring-damper branch to the imaginary part of dynamic stiffness $k_{AC}(\omega)$ has its maximum at the angular frequency $\omega = \mu_k$. It should be noticed that the real part of dynamic stiffness $k_{AC}(\omega)$ slightly increases with angular frequency ω and is no longer equal to k_0 . However, the effect is practically insignificant for small value of loss factor η typical for metal materials.

In order to obtain constant imaginary part of dynamic stiffness (7), thus getting the frequency-independent damping, the infinite number of branches n is needed. For practical use of this model, only limited number of branches can be taken into account. The imaginary part of dynamic stiffness $k_{AC}(\omega)$ can then only approximate constant ηk_0 in certain frequency range of interest, spanned with selected parameters μ_k . η is the energy loss factor for particular material in order to approach hysteretic damping. Stiffness coefficients k_k are obtained by following set of equations

$$\sum_{k=1}^n k_k \frac{\mu_k \mu_r}{\mu_k^2 + \mu_r^2} = \eta k_0, \quad \text{for } r = 1 \dots n. \quad (8)$$

The set of Eq. (8) means following condition

$$\Im(k_{AC}(\mu_k)) = \eta k_0, \quad \text{for } k = 1 \dots n. \quad (9)$$

Let us define proportional coefficients α_k for each damper branch by means of

$$b_k = \frac{k_k}{\mu_k} = \alpha_k k_0. \quad (10)$$

For the case of the N -degree-of-freedom systems, we can now rewrite the Eq. (5) to the

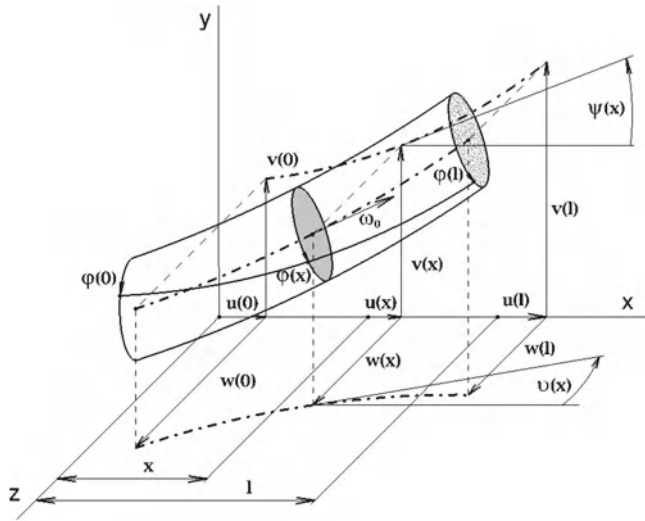


Fig. 2 Timoshenko shaft finite element configuration

$$\mathbf{M}\ddot{\mathbf{u}}(t) + \mathbf{K}\mathbf{u}(t) + \mathbf{K}_H \sum_{k=1}^n \alpha_k \mathbf{y}_k(t) = \mathbf{f}(t), \quad \dot{\mathbf{y}}_k(t) + \mu_k \mathbf{y}_k(t) = \mu_k \dot{\mathbf{u}}(t). \quad (11)$$

The imaginary part of dynamic stiffness matrix of this system approaches some constant matrix $\eta \mathbf{K}_H$.

3 Timoshenko Shaft FEM Element with Exponential Damping

In the paper [4], the use of exponential damping for the internal and external rotor damping in the modal space is demonstrated. Approach presented in this article incorporates both the internal and external damping in the configuration space of FEM model instead. Configuration of the Timoshenko shaft finite element used in this study is described by vector of 16 lateral degrees of freedom [5]

$$\tilde{\mathbf{q}}^e = \left(v(0) \frac{dv}{dx}(0) v(l) \frac{dv}{dx}(l) \psi(0) \frac{d\psi}{dx}(0) \psi(l) \frac{d\psi}{dx}(l) \right. \\ \left. w(0) \frac{dw}{dx}(0) w(l) \frac{dw}{dx}(l) \vartheta(0) \frac{d\vartheta}{dx}(0) \vartheta(l) \frac{d\vartheta}{dx}(l) \right)^T \quad (12)$$

Equations of motion of the single element for this configuration space is

$$\tilde{\mathbf{M}}^e \ddot{\mathbf{q}}^e + \omega_0 \tilde{\mathbf{G}}^e \dot{\mathbf{q}}^e + \tilde{\mathbf{K}}^e \mathbf{q}^e = \tilde{\mathbf{f}}^e, \quad (13)$$

where ω_0 is the angular frequency of shaft rotation. $\tilde{\mathbf{f}}^e$ is the forcing vector. $\tilde{\mathbf{M}}^e$, $\tilde{\mathbf{G}}^e$ and $\tilde{\mathbf{K}}^e$ are the local matrices of mass, gyroscopic effects and stiffness respectively:

$$\tilde{\mathbf{M}}^e = \begin{pmatrix} \mathbf{I}_1 & \mathbf{0} & \mathbf{0} & \mathbf{0} \\ \mathbf{0} & \mathbf{I}_2 & \mathbf{0} & \mathbf{0} \\ \mathbf{0} & \mathbf{0} & \mathbf{I}_1 & \mathbf{0} \\ \mathbf{0} & \mathbf{0} & \mathbf{0} & \mathbf{I}_2 \end{pmatrix}, \quad \tilde{\mathbf{G}}^e = \begin{pmatrix} \mathbf{0} & \mathbf{0} & \mathbf{0} & \mathbf{0} \\ \mathbf{0} & \mathbf{0} & \mathbf{0} & -2\mathbf{I}_2 \\ \mathbf{0} & \mathbf{0} & \mathbf{0} & \mathbf{0} \\ \mathbf{0} & 2\mathbf{I}_2^T & \mathbf{0} & \mathbf{0} \end{pmatrix}, \quad \tilde{\mathbf{K}}^e = \begin{pmatrix} \mathbf{I}_3 & -\mathbf{I}_4 & \mathbf{0} & \mathbf{0} \\ -\mathbf{I}_4^T & \mathbf{I}_5 + \mathbf{I}_6 & \mathbf{0} & \mathbf{0} \\ \mathbf{0} & \mathbf{0} & \mathbf{I}_3 & \mathbf{I}_4 \\ \mathbf{0} & \mathbf{0} & \mathbf{I}_4^T & \mathbf{I}_5 + \mathbf{I}_6 \end{pmatrix}, \quad (14)$$

$$\mathbf{I}_1 = \int_0^l \rho A \mathbf{S}^T \mathbf{S} dx, \quad \mathbf{I}_2 = \int_0^l \rho J \mathbf{S}^T \mathbf{S} dx, \quad \mathbf{I}_3 = \int_0^l \kappa G A \frac{\partial \mathbf{S}^T}{\partial x} \frac{\partial \mathbf{S}}{\partial x} dx, \quad (15)$$

$$\mathbf{I}_4 = \int_0^l \kappa G A \frac{\partial \mathbf{S}^T}{\partial x} \mathbf{S} dx, \quad \mathbf{I}_5 = \int_0^l E J \frac{\partial \mathbf{S}^T}{\partial x} \frac{\partial \mathbf{S}}{\partial x} dx, \quad \mathbf{I}_6 = \int_0^l \kappa G A \mathbf{S}^T \mathbf{S} dx.$$

Here \mathbf{S} is the vector of basis functions:

$$\mathbf{S} = (S_1 \ S_2 \ S_3 \ S_4)^T, \quad (16)$$

$$\begin{aligned} S_1 &= 1 - 3 \frac{x^2}{l^2} + 2 \frac{x^3}{l^3}, & S_2 &= x - 2 \frac{x^2}{l} + \frac{x^3}{l^2}, \\ S_3 &= 3 \frac{x^2}{l^2} - 2 \frac{x^3}{l^3}, & S_4 &= -\frac{x^2}{l} + \frac{x^3}{l^2}. \end{aligned} \quad (17)$$

Meanings of the other symbols are here: ρ material density, A shaft cross section area, J polar moment of inertia, E young modulus of elasticity, G shear modulus of elasticity and κ shear correction coefficient.

The external exponential damping can be added to the equations of motion (13) directly in the sense of Eq. (5), using relaxation parameters μ_k and additional degrees of freedom $\tilde{\mathbf{y}}_k^e(t)$. Internal damping must be added in the co-rotating coordinate system. Transformation of vector of nodal quantities from non-rotating to co-rotating coordinates

$$\tilde{\mathbf{q}}_R^e = \mathbf{R}(t) \tilde{\mathbf{q}}^e \quad (18)$$

is determined by unitary transformation matrix

$$\mathbf{R}(t) = \begin{pmatrix} \mathbf{C} & \mathbf{0} & \mathbf{S} & \mathbf{0} \\ \mathbf{0} & \mathbf{C} & \mathbf{0} & -\mathbf{S} \\ -\mathbf{S} & \mathbf{0} & \mathbf{C} & \mathbf{0} \\ \mathbf{0} & \mathbf{S} & \mathbf{0} & \mathbf{C} \end{pmatrix}, \quad \mathbf{C} = \mathbf{I}_7 \cos \omega_0 t, \quad \mathbf{S} = \mathbf{I}_7 \sin \omega_0 t, \quad \mathbf{I}_7 = \text{diag}(1 \ 1 \ 1 \ 1 \ 1 \ 1 \ 1). \quad (19)$$

In the co-rotating coordinates, the internal damping is formulated in identical way as per Eq. (5). After transformation back to the non-rotating coordinates and owing to the properties of unitary matrix $\mathbf{R}(t)$, the equations of motion of single element become

$$\begin{aligned} \tilde{\mathbf{M}}^e \ddot{\mathbf{q}}^e(t) + \omega_0 \tilde{\mathbf{G}}^e \dot{\mathbf{q}}^e(t) + \tilde{\mathbf{K}}^e \mathbf{q}^e(t) + \sum_{k=1}^n \tilde{\mathbf{B}}_k^e \tilde{\mathbf{y}}_k^e(t) + \sum_{l=1}^m \mathbf{R}^T(t) \tilde{\mathbf{C}}_l^e \mathbf{R}(t) \tilde{\mathbf{w}}_l^e(t) &= \tilde{\mathbf{f}}^e(t), \\ \dot{\tilde{\mathbf{y}}}_k^e(t) + \mu_k \tilde{\mathbf{y}}_k^e(t) - \mu_k \dot{\mathbf{q}}^e(t) &= \mathbf{0}, \\ \dot{\tilde{\mathbf{w}}}_l^e(t) + \gamma_l \tilde{\mathbf{w}}_l^e(t) + \omega_0 \tilde{\mathbf{D}}^e \tilde{\mathbf{w}}_l^e(t) - \gamma_l \omega_0 \tilde{\mathbf{D}}^e \mathbf{q}^e(t) - \gamma_l \dot{\mathbf{q}}^e(t) &= \mathbf{0}. \end{aligned} \quad (20)$$

where

$$\tilde{\mathbf{D}}^e = \begin{pmatrix} \mathbf{0} & \mathbf{I}_8 \\ -\mathbf{I}_8 & \mathbf{0} \end{pmatrix}, \quad \mathbf{I}_8 = \text{diag}(1 \ 1 \ 1 \ 1 \ -1 \ -1 \ -1 \ -1). \quad (21)$$

Number of m relaxation parameters γ_l is used to describe internal damping.

In the system (20), the $\tilde{\mathbf{w}}_l^e(t)$ are newly introduced additional degrees of freedom of internal damping. Let us call the matrices $\tilde{\mathbf{B}}_k^e$ and $\tilde{\mathbf{C}}_l^e$ the local coefficient matrices of external and internal damping. Correct determination of these matrices can be difficult task from the physical perspective and detailed analysis of this matter is beyond scope of this article.

For practical purposes, the hysteretic material damping can be implemented proportional to local stiffness matrix. Damping coefficient matrices will be then also proportional to the local stiffness matrix

$$\tilde{\mathbf{B}}_k^e = \alpha_k \tilde{\mathbf{K}}^e, \quad \tilde{\mathbf{C}}_l^e = \beta_l \tilde{\mathbf{K}}^e = \mathbf{R}^T(t) \tilde{\mathbf{C}}_l^e \mathbf{R}(t). \quad (22)$$

The damping coefficient matrices can for more complex analyses be implemented separately for normal and shear deformations, using different loss factors. In this case, the damping coefficient matrices will be proportional to parts of local stiffness matrix corresponding to normal and shear deformation energy.

After reordering the nodal quantities to global displacement coordinates

$$\begin{aligned} \mathbf{q}^e = & \left(v(0) \ \frac{dv}{dx}(0) \ \psi(0) \ \frac{d\psi}{dx}(0) \ w(0) \ \frac{dw}{dx}(0) \ \vartheta(0) \ \frac{d\vartheta}{dx}(0) \right. \\ & \left. v(l) \ \frac{dv}{dx}(l) \ \psi(l) \ \frac{d\psi}{dx}(l) \ w(l) \ \frac{dw}{dx}(l) \ \vartheta(l) \ \frac{d\vartheta}{dx}(l) \right)^T \end{aligned} \quad (23)$$

and assembly of local matrices, the global matrices of mass \mathbf{M} , gyroscopic effects \mathbf{G} , stiffness \mathbf{K} , circulatory matrix \mathbf{D} , as well as global forcing vector \mathbf{f} , are obtained. The model of rotor with internal and external exponential damping in the state space can be than constructed as follows:

$$\mathbf{N}\dot{\mathbf{z}} + \mathbf{P}\mathbf{z} = \mathbf{f}_G, \quad (24)$$

which expanded into blocks is

$$\begin{pmatrix} \mathbf{N}_1 & \mathbf{0} & \mathbf{0} \\ \mathbf{0} & \mathbf{N}_2 & \mathbf{0} \\ \mathbf{0} & \mathbf{0} & \mathbf{N}_3 \end{pmatrix} \begin{pmatrix} \dot{\mathbf{z}}_1 \\ \dot{\mathbf{z}}_2 \\ \dot{\mathbf{z}}_3 \end{pmatrix} + \begin{pmatrix} \mathbf{P}_1 & \mathbf{P}_2 & \mathbf{P}_3 \\ \mathbf{P}_4 & \mathbf{P}_5 & \mathbf{0} \\ \mathbf{P}_6 & \mathbf{0} & \mathbf{P}_7 \end{pmatrix} \begin{pmatrix} \mathbf{z}_1 \\ \mathbf{z}_2 \\ \mathbf{z}_3 \end{pmatrix} = \begin{pmatrix} \mathbf{f} \\ \mathbf{0} \\ \mathbf{0} \end{pmatrix}, \quad (25)$$

$$\mathbf{z}_1 = (\dot{\mathbf{q}}^T \quad \mathbf{q}^T)^T, \quad \mathbf{z}_2 = (\mathbf{y}_1^T \quad \mathbf{y}_2^T \quad \dots \quad \mathbf{y}_n^T)^T, \quad \mathbf{z}_3 = (\mathbf{w}_1^T \quad \mathbf{w}_2^T \quad \dots \quad \mathbf{w}_m^T)^T, \quad (26)$$

$$\mathbf{N}_1 = \begin{pmatrix} \mathbf{M} & \\ & \mathbf{M} \end{pmatrix}, \quad \mathbf{N}_2 = \begin{pmatrix} \mathbf{I} & & \\ & \mathbf{I} & \\ & & \ddots \\ & & & \mathbf{I} \end{pmatrix}, \quad \mathbf{N}_3 = \begin{pmatrix} \mathbf{I} & & \\ & \mathbf{I} & \\ & & \ddots \\ & & & \mathbf{I} \end{pmatrix} \quad (27)$$

$$\mathbf{P}_1 = \begin{pmatrix} \mathbf{B}_v + \mathbf{B}_b + \omega_0 \mathbf{G} & \mathbf{K}_b + \omega_0 \mathbf{K}_c + \mathbf{K} \\ -\mathbf{M} & \mathbf{0} \end{pmatrix}, \quad \mathbf{P}_2 = \begin{pmatrix} \alpha_1 \mathbf{K} & \alpha_2 \mathbf{K} & \dots & \alpha_n \mathbf{K} \\ \mathbf{0} & \mathbf{0} & \dots & \mathbf{0} \end{pmatrix} \quad (28)$$

$$\mathbf{P}_3 = \begin{pmatrix} \beta_1 \mathbf{K} & \beta_2 \mathbf{K} & \dots & \beta_m \mathbf{K} \\ \mathbf{0} & \mathbf{0} & \dots & \mathbf{0} \end{pmatrix}, \quad \mathbf{P}_4 = \begin{pmatrix} -\mu_1 \mathbf{I} & \mathbf{0} \\ -\mu_2 \mathbf{I} & \mathbf{0} \\ \vdots & \vdots \\ -\mu_n \mathbf{I} & \mathbf{0} \end{pmatrix}, \quad \mathbf{P}_5 = \begin{pmatrix} \mu_1 \mathbf{I} & & \\ & \mu_2 \mathbf{I} & \\ & & \ddots \\ & & & \mu_n \mathbf{I} \end{pmatrix} \quad (29)$$

$$\mathbf{P}_6 = \begin{pmatrix} -\gamma_1 \mathbf{I} & -\gamma_1 \omega_0 \mathbf{D} \\ -\gamma_2 \mathbf{I} & -\gamma_2 \omega_0 \mathbf{D} \\ \vdots & \vdots \\ -\gamma_m \mathbf{I} & -\gamma_m \omega_0 \mathbf{D} \end{pmatrix} \quad \mathbf{P}_7 = \begin{pmatrix} \omega_0 \mathbf{D} + \gamma_1 \mathbf{I} & & \\ & \omega_0 \mathbf{D} + \gamma_2 \mathbf{I} & \\ & & \ddots \\ & & & \omega_0 \mathbf{D} + \gamma_m \mathbf{I} \end{pmatrix}. \quad (30)$$

Matrices \mathbf{K}_b and \mathbf{B}_b are stiffness and damping matrices of bearings. In addition to exponential damping, the model can also incorporate classical viscous damping by means of standard approach using matrix of viscous damping \mathbf{B}_v and circulatory stiffness matrix \mathbf{K}_c , providing the opportunity to model various configurations of complex rotors.

4 Numerical Results

A simple numerical example is provided in order to demonstrate the proposed modelling technique in the frequency domain for obtaining the Campbell plot and decay rates plot of trial rotor. The eigenvalues of the system are obtained from eigenvalue problem established upon homogenous part of Eq. (24): $(\mathbf{N}s + \mathbf{P})\mathbf{u} = \mathbf{0}$. 300 mm long rotor of 15 mm in diameter has been chosen. There were two discs of parameters $m_d = 0.5$ kg (mass), $J_{d0} = 1.56 \cdot 10^{-4}$ kg m² (moment of inertia w.r.t. shaft rotation axis), $J_d = 7.81 \cdot 10^{-5}$ kg m² (moment of inertia w.r.t. axis perpendicular to the shaft rotation axis) at both the ends of the rotor. Rotor was supported by two identical linear isotropic bearings with stiffness 10^7 N m⁻¹ and damping 100 N s m⁻¹ at the third and two thirds of the shaft length. Exponential approach to internal hysteretic damping used following parameters: $\gamma_1 = 10$ s⁻¹, $\gamma_2 = 100$ s⁻¹, $\gamma_3 = 10^3$ s⁻¹, $\gamma_4 = 10^4$ s⁻¹. The material loss factor of $\eta = 10^{-3}$ led to parameters $\beta_1 = 1.7 \cdot 10^{-4}$, $\beta_2 = 1.36 \cdot 10^{-5}$, $\beta_3 = 1.36 \cdot 10^{-6}$, $\beta_4 = 1.7 \cdot 10^{-7}$. External exponential damping was neglected, instead small amount of external viscous damping was added to the model ($\zeta_{eq} = 10^{-4}$ with respect to the lowest whirl mode) in order to demonstrate the possibility of incorporating different types of damping.

5 Conclusions

Presented is a finite element model of Timoshenko rotating beam that allows for incorporating exponential damping in both the non-rotating and co-rotating coordinates. The exponential model of damping is more general than the classical viscous damping and can be used to approach the frequency-independent hysteretic damping in the frequency domain. The model is constructed in the state space and the time domain, what offers the possibility of direct numerical integration of created set of differential equations.

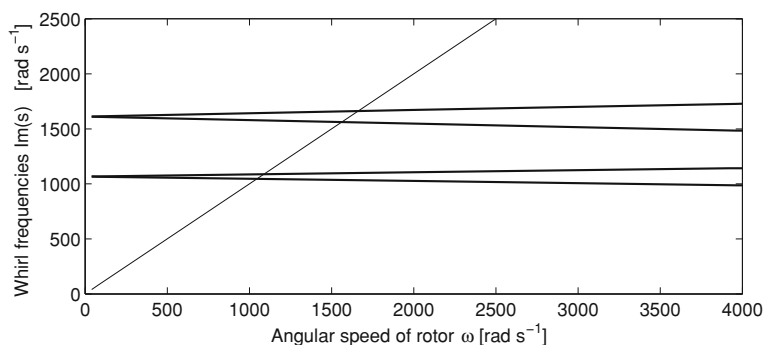


Fig. 3 Campbell plot of the trial rotor: the lowest 4 whirl frequencies

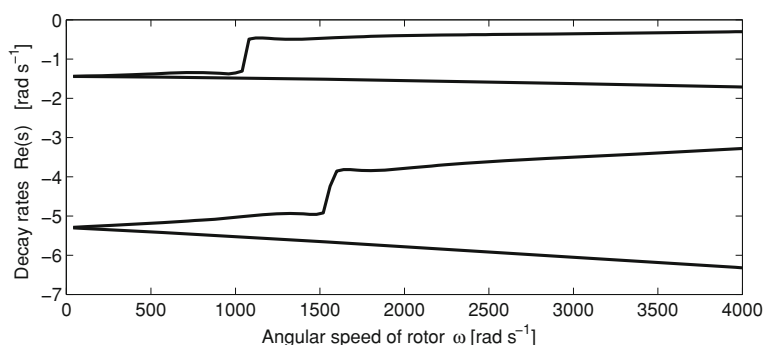


Fig. 4 Decay rates plot: real parts of eigenvalues corresponding to the lowest 4 whirl frequencies

References

1. Adhikari, S., Woodhouse, J.: Identification of damping: part 2, non-viscous damping. *J. Sound Vib.* **243**(1), 63–88 (2001)
2. Adhikari, S., Wagner, N.: Direct time-domain integration method for exponentially damped linear systems. *Comput. Struct.* **82**(29–30), 2453–2461 (2004)
3. Genta G, Amati N (2009) On the equivalent viscous damping for systems with hysteresis. *Atti dell'Accademia delle Scienze di Torino*.
4. Genta, G., Amati, N.: Hysteretic damping in rotordynamics: an equivalent formulation. *J. Sound Vib.* **329**(22), 4772–4784 (2010)
5. Skarolek, A.: Numerical analysis of rotor systems with aerostatic journal bearings. PhD Thesis, Technical University of Liberec, (2012).

Contribution to Numerical Analysis of Uncertain Mechanical Systems Using Probability and Possibility Theory

M. Vaško, M. Sága and V. Dekýš

Abstract The paper presents chosen traditional (based on probability theory) and non-traditional (based on possibility theory) computational tools for analysis of the uncertainties (geometric, material or loading uncertainties) in mechanical structures. Uncertainties are introduced as intervals or fuzzy numbers (bounded possible values), assuming possibility theory and as random parameters in the case of the probability theory. The objective is to propose numerical algorithms for interval modal and spectral FE computations suggested by authors and their additional implementation into interval and fuzzy analysis and Monte Carlo method.

Keywords Uncertain parameter • Interval number • Interval arithmetic • Fuzzy number • Fuzzy set • Random variable • Optimization • Possibility analysis

1 Introduction

In the last years there has been an increased interest in the modeling and analysis of engineering systems under uncertainties. To obtain reliable results for the solutions of engineering problems, exact values for the parameters of the model

M. Vaško (✉) · M. Sága · V. Dekýš
University of Žilina, Žilina, Slovakia
e-mail: milan.vasko@fstroj.uniza.sk

M. Sága
e-mail: milan.saga@fstroj.uniza.sk

V. Dekýš
e-mail: vladimir.dekys@fstroj.uniza.sk

Table 1 The first five eigenfrequencies are presented for constant, interval and fuzzy model

Frequencies	Constant model	Interval model	Fuzzy model
f_1	1.8606	<1.8419, 1.8791>	<1.8419, 1.8606, 1.8792>
f_2	2.1126	<2.0678, 2.1565>	<2.0914, 2.1126, 2.1337>
f_3	2.2508	<2.2282, 2.2732>	<2.2281, 2.2508, 2.2732>
f_4	2.5165	<2.4912, 2.5415>	<2.4911, 2.5165, 2.5416>
f_5	7.5494	<7.4735, 7.6245>	<7.4735, 7.5494, 7.6249>

Table 2 The first five eigenfrequencies are presented for triangular probability density function

Frequencies	Mean value	Confidence interval 99 %	Confidence interval 95 %
f_1	1.86057	(1.8486, 1.8726)	(1.8513, 1.8699)
f_2	2.11261	(2.1000, 2.1252)	(2.1029, 2.1223)
f_3	2.25046	(2.2320, 2.2694)	(2.2362, 2.2652)
f_4	2.51641	(2.4956, 2.5373)	(2.5002, 2.5326)
f_5	7.54933	(7.4862, 7.6127)	(7.5003, 7.5981)

equations should be available. In the reality, however, those values often can not be provided, and the models usually show a rather high degree of uncertainty. Computational mechanics encounters uncertainties in geometric, material and load parameters as well as in the model itself and in the analysis procedure too. For that reason, the responses, such as displacements, stresses, natural frequency, or other dynamic characteristics will usually show some degree of uncertainty. The obtained result using one most significant value for an uncertain parameter cannot be considered as representative for the whole spectrum of possible results.

It is generally known that probabilistic modeling and statistical analysis are well established for modeling of mechanical systems with uncertainties. In addition, a number of non-probabilistic computational techniques have been proposed, e.g. fuzzy set theory [1], interval approach [2], imprecise probabilities [3], etc.

2 Interval Finite Elements Analysis (IFEA)

Interval arithmetic was developed by Moore [2] while studying the propagation and control of truncation and rounding off the error, using floating point arithmetic on a digital computer. In this approach, an uncertain number is represented by an interval of real numbers. The interval numbers derived from the experimental data or expert knowledge can then take into account the uncertainties in the model parameters, model inputs etc.

The finite element method (FEM) [4] is a very popular tool for a complicated structural analysis. The ability to predict the behavior of a structure under static or dynamic loads is not only of a great scientific value, it is also very useful from an economical point of view.

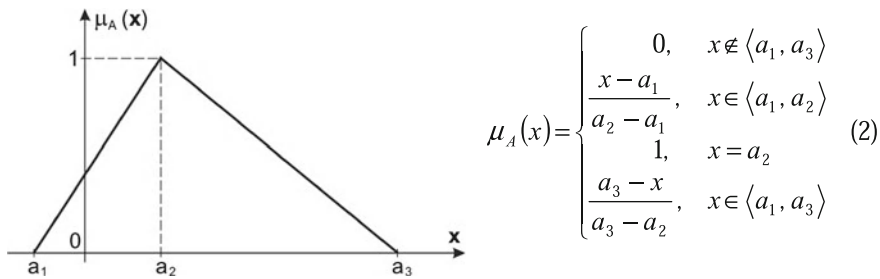


Fig. 1 MSF for a triangular fuzzy number

It is sometimes very difficult to define a reliable FE model for realistic mechanical structures when a number of its physical properties is uncertain. In the case of FE analysis the mechanical properties of the used materials are very hard to predict and therefore an important source of uncertainty. Reliable validation can only be based on an analysis which takes into account all uncertainties that could cause this variability. It is the aim of this part to incorporate the most important uncertainties in FE analysis.

According to the character of the uncertainty, we can define a structural uncertainty (geometrical and material parameters) and uncertainty in load (external forces, etc.) [5]. The structural uncertainty parameters are usually written into vector $\mathbf{x} = [\underline{\mathbf{x}}, \overline{\mathbf{x}}]$ and the interval modal FE analysis may be formulated as follows

$$[\mathbf{K}(\mathbf{x}) - \lambda_j \cdot \mathbf{M}(\mathbf{x})] \cdot \mathbf{V}_j = \mathbf{0}, \quad \text{or} \quad \left(\underline{\mathbf{K}}, \overline{\mathbf{K}} - [\underline{\lambda_j}, \overline{\lambda_j}] \cdot [\underline{\mathbf{M}}, \overline{\mathbf{M}}] \right) \cdot [\underline{\mathbf{V}_j}, \overline{\mathbf{V}_j}] = \mathbf{0}, \quad (1)$$

where $\underline{\lambda_j}$, $\overline{\lambda_j}$ and $\underline{\mathbf{V}_j}$, $\overline{\mathbf{V}_j}$ are the j -th eigenvalue with corresponding eigenvector, $\underline{\mathbf{K}}$, $\overline{\mathbf{K}}$, $\underline{\mathbf{M}}$, $\overline{\mathbf{M}}$ are of course the infimum and supremum of the mass and stiffness matrices. The application of the classic interval arithmetic for FE analysis is very limited. Its *overestimation* grows with the problem size (the dimension of the system matrices) and has not a physical foundation in the reality [6].

3 Fuzzy Set Approach

By Zadeh [1] was formulated the initial theory of fuzzy sets. A fuzzy set \mathbf{x} is the set with boundaries that are not sharply defined. A function, called membership function (MSF), signifies the degree to which each member of a domain \mathbf{X} belongs to the fuzzy set \mathbf{x} . For a fuzzy variable $x \in \langle x_1, x_2 \rangle$, (or $x \in \mathbf{x}$), the membership function is defined as $\mu(x)$. If $\mu(x) = 1$, x is definitely a member of the \mathbf{x} . If $\mu(x) = 0$, x is definitely not a member of the \mathbf{x} . For every x with $0 < \mu(x) < 1$, the membership is not certain. Typical membership functions of fuzzy sets are shown on Figs. 1 and 2.

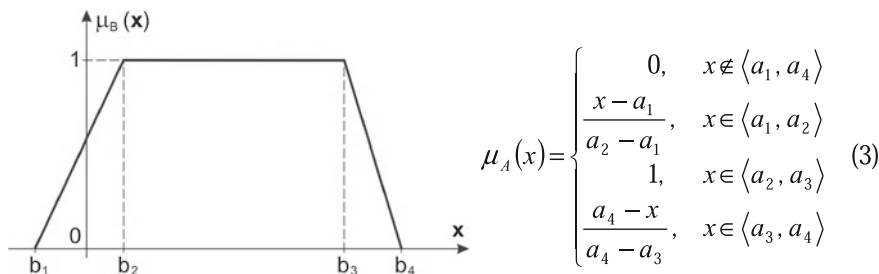


Fig. 2 MSF for a trapezoidal fuzzy number

4 Probabilistic Approach

Probabilistic approach is based on the transformation of random variables. Let $\mathbf{X} = (X_1, \dots, X_n)^T$ be a n -dimensional random variable with joint probability distribution function $f_{\mathbf{X}}(x_1, \dots, x_n)$. We find joint probability distribution function $g_{\mathbf{Y}}(y_1, \dots, y_n)$ of n -dimensional variable $\mathbf{Y} = (Y_1, \dots, Y_n)^T$, $Y_j = h_j(X_1, \dots, X_n)$, $j = 1, \dots, n$; $\mathbf{h} = (h_1, \dots, h_n)^T$ is 1:1 transformation of \mathbf{X} into \mathbf{Y} [3].

Lets inverse function $\mathbf{h}^{-1} : \mathbf{x} = \mathbf{h}^{-1}(\mathbf{y})$ is differentiable and Jacobian will be

$$J = \begin{vmatrix} \frac{\partial h_1^{-1}}{\partial y_1} & \dots & \frac{\partial h_1^{-1}}{\partial y_n} \\ \vdots & \ddots & \vdots \\ \frac{\partial h_n^{-1}}{\partial y_1} & \dots & \frac{\partial h_n^{-1}}{\partial y_n} \end{vmatrix}, \quad \frac{1}{J} = \begin{vmatrix} \frac{\partial h_1}{\partial x_1} & \dots & \frac{\partial h_1}{\partial x_n} \\ \vdots & \ddots & \vdots \\ \frac{\partial h_n}{\partial x_1} & \dots & \frac{\partial h_n}{\partial x_n} \end{vmatrix}, \quad \text{and } J \neq 0 \quad (4)$$

The joint probability distribution function $g_{\mathbf{Y}}$

$$\begin{aligned} g_{\mathbf{Y}}(\mathbf{y}) &= g_{\mathbf{Y}}(y_1, \dots, y_n) = f_{\mathbf{X}}[h_1^{-1}(y_1, \dots, y_n), \dots, h_n^{-1}(y_1, \dots, y_n)] \cdot J \\ &= f_{\mathbf{X}}[\mathbf{h}^{-1}(\mathbf{y})] \cdot J. \end{aligned} \quad (5)$$

Probability density function $f_X(x)$ is for uniform distribution of random variable X on the interval (a_1, a_3) , $X \sim \text{Unif}(a_1, a_3)$,

$$f_X(x) = \begin{cases} 0, & x \notin \langle a_1, a_3 \rangle \\ \frac{1}{a_3-a_1}, & x \in \langle a_1, a_3 \rangle \end{cases} \quad (6)$$

Probability density function $f_X(x)$ is for triangular distribution of random variable X on the interval (a_1, a_3) , $X \sim \text{Tri}(a_1, a_2, a_3)$,

$$f_X(x) = \begin{cases} 0, & x \notin \langle a_1, a_3 \rangle \\ \frac{2(x-a_1)}{(a_3-a_1)(a_2-a_1)}, & x \in \langle a_1, a_2 \rangle \\ \frac{2(a_3-x)}{(a_3-a_1)(a_3-a_2)}, & x \in \langle a_2, a_3 \rangle \end{cases} \quad (7)$$

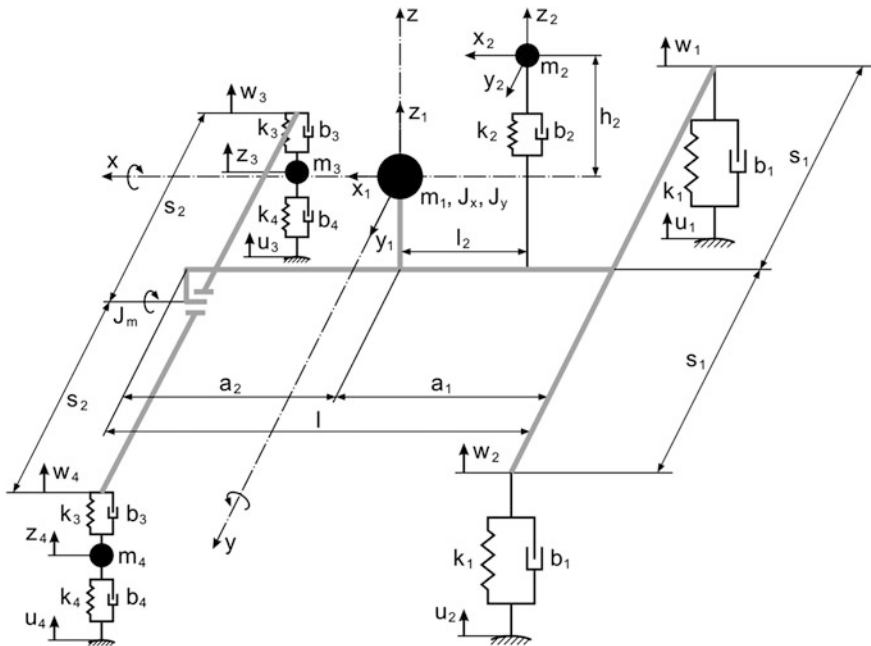


Fig. 3 The dynamic model of agricultural tractor

Calculation of the function g_Y can be very difficult. The increasing of dimension of independent random variable \mathbf{X} means generally increasing of difficult and time consuming too. We will use Monte Carlo method to create the random samples of variable \mathbf{Y} . We can use next process by determination these samples of \mathbf{Y} :

1. Generation of input vector $\mathbf{X} = (X_1, \dots, X_n)^T$ by using random number generator,
2. Obtain of output vector $\mathbf{Y} = (Y_1, \dots, Y_n)^T$ by using $\mathbf{h} = (h_1, \dots, h_n)^T$ transformation,
3. Saving file with \mathbf{Y} or processing this vector immediately,
4. Repeat step from 1st to 3rd, until the required number of vectors \mathbf{Y} is fulfilled.

5 Numerical Example

Vehicle dynamic models are often characterized by uncertain system parameters. The main goal will be to explain difference between three different approaches to the analysis influence of the uncertain parameters on the natural frequencies case of the model. Let's consider the 7-DOFs model of the agricultural tractor (Fig. 3).

All input parameters without stiffness will be constants. The stiffnesses are modeled as follows:

1. Deterministic values:

$$k_1 = 3 \cdot 10^5, \quad k_2 = 2 \cdot 10^4, \quad k_3 = 1 \cdot 10^5, \quad k_4 = 2 \cdot 10^5.$$

2. Interval numbers:

$$k_1 = \langle 2.9399 \cdot 10^5, 3.0601 \cdot 10^5 \rangle, \quad k_2 = \langle 1.9599 \cdot 10^4, 2.0401 \cdot 10^4 \rangle, \\ k_3 = \langle 0.9799 \cdot 10^5, 1.0201 \cdot 10^5 \rangle, \quad k_4 = \langle 1.9599 \cdot 10^5, 2.0401 \cdot 10^5 \rangle.$$

3. Triangular fuzzy numbers:

$$k_1 = \langle 2.9399 \cdot 10^5, 3 \cdot 10^5, 3.0601 \cdot 10^5 \rangle, \\ k_2 = \langle 1.9599 \cdot 10^4, 2 \cdot 10^4, 2.0401 \cdot 10^4 \rangle, \\ k_3 = \langle 0.9799 \cdot 10^5, 1 \cdot 10^5, 1.0201 \cdot 10^5 \rangle, \\ k_4 = \langle 1.9599 \cdot 10^5, 2 \cdot 10^5, 2.0401 \cdot 10^5 \rangle.$$

4. Random variables:

Uniform distribution Unif (a, b):

$$k_1 \sim \text{Unif}(2.9399 \cdot 10^5, 3.0601 \cdot 10^5), \\ k_2 \sim \text{Unif}(1.9599 \cdot 10^4, 2.0401 \cdot 10^4), \\ k_3 \sim \text{Unif}(0.9799 \cdot 10^5, 1.0201 \cdot 10^5), \\ k_4 \sim \text{Unif}(1.9599 \cdot 10^5, 2.0401 \cdot 10^5);$$

Triangular distribution Tri (a, c, b):

$$k_1 \sim \text{Tri}(2.9399 \cdot 10^5, 3 \cdot 10^5, 3.0601 \cdot 10^5), \\ k_2 \sim \text{Tri}(1.9599 \cdot 10^4, 2 \cdot 10^4, 2.0401 \cdot 10^4), \\ k_3 \sim \text{Tri}(0.9799 \cdot 10^5, 1 \cdot 10^5, 1.0201 \cdot 10^5), \\ k_4 \sim \text{Tri}(1.9599 \cdot 10^5, 2 \cdot 10^5, 2.0401 \cdot 10^5).$$

The first five natural frequencies (eigenfrequencies) for constant, interval and fuzzy model are presented in Table 1 and first five natural frequencies for triangular probability density function are presented in Table 2.

6 Conclusions

The paper deals with the possibilities of the interval, fuzzy and probability approaches in fundamental problems of the mechanics. The use of presented numerical approaches provides a new possibility of the quality and reliability appraisal of analyzed objects. Due to this numerical approach, we can analyze mechanical or technological properties of the investigated structures more authentically.

Acknowledgments This work has been supported by VEGA grant No. 1/0125/09.

References

1. Zadeh, L. A.: Fuzzy Sets and Their Applications to Pattern Classification and Cluster analysis. Classification and clustering. Academic, New York, (1977).
2. Moore, R. E.: Interval Analysis. Prentice Hall, Englewood Cliffs, New Jersey (1966).
3. Vaško, M., Sága, M.: Solution of mechanical systems with uncertainty parameters using IFEA, communications. ISSN 1335–4205, vol. 11, no. 2, pp. 19–27 (2009).
4. Kopas, P., Melicher, R., Handrik, M.: FE analysis of thermo-plastic material model using for bearing steels. Applied Mechanics 2008, Wisła, Poland, ISBN 978-83-60102-49-7, pp. 37–38 (2008).
5. Vaško, A.: Image analysis in materials engineering. In: Konferencje, ISSN 1234-9895, no. 61, pp. 667-670 (2007).
6. Neumaier, A.: Interval Methods for Systems of Equations, Cambridge University (1990).

Reducing the Steady State Vibrations of Flexible Rotors by Squeezing Thin Layers of Normal and Magneto Rheological Oils

J. Zapoměl and P. Ferfecki

Abstract The investigated semiactive damping element works on the principle of squeezing two lubricating layers formed by classical and magneto rheological oils. The damping effect is controlled by the change of intensity of magnetic field passing through the layer of magneto rheological lubricant. The developed mathematical model of the studied element, in which the oils are represented by Newtonian and Bingham materials, was implemented into the computational algorithm for determination of the frequency response characteristic of a flexible rotor and of the dependence of magnitude of the force transmitted between the rotor and its casing on angular speed of the rotor rotation. A trigonometric collocation method was applied to calculate the steady state response. Advantage of the proposed damping element is that it does not require an expensive and complicated control system for its operation.

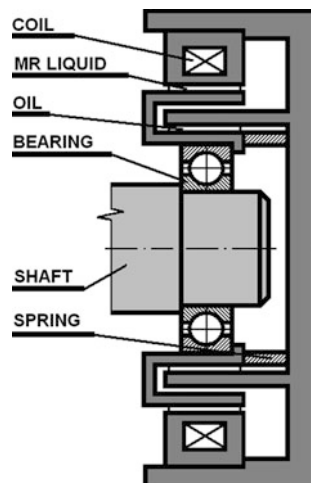
Keywords: Flexible rotors • Vibration reduction • Enhanced magneto rheological damping element • Computational simulations

1 Introduction

Lateral vibrations of rotating machines can be attenuated by adding the damping devices to the constraint elements placed between the rotor and its casing. To achieve their optimum performance, the damping effect must be controllable to be

J. Zapoměl (✉) · P. Ferfecki
VSB-Technical University of Ostrava, Ostrava, Czech Republic
e-mail: jaroslav.zapomel@vsb.cz

P. Ferfecki
e-mail: petr.ferfecki@vsb.cz

Fig. 1 The damping element

possible to adapt its magnitude to the current operating conditions. For this purpose several damping strategies have been developed and tested, among which there are those based on application of the controllable classical squeeze film dampers, electromagnetic dampers, hydrodynamic and magnetic bearings and magneto rheological semiactive damping devices.

A new concept of a magneto rheological damper intended for attenuation of lateral vibrations of rigid rotors is reported in [1]. In this paper there is analysed its effect on the steady state vibrations of a flexible rotor excited by unbalance forces. The studied damper works on the principle of squeezing two lubricating layers formed by classical and magneto rheological oils. Its main advantages are that the magneto rheological damping can be switched on only if the damping effect produced by the classical oil is insufficient and that it does not require an expensive and complicated control system for its operation.

2 Determination of the Damping Force Components

The main parts of the enhanced damping element are two fixed and two movable rings. The latter are coupled with the shaft through a rolling element bearing and with the damper's body by a squirrel spring, which enables their vibration in the radial direction and prevents their rotation (Fig. 1). The gaps between the fixed and movable rings are filled with classical (inner layer) and magneto rheological oils (outer layer). The damping device is equipped with an electric coil generating magnetic field passing through the film of the magneto rheological liquid. As its flow depends on magnetic induction, the change of the magnetic flux can be used to control the damping effect.

The developed mathematical model of the damping element is based on assumptions of the classical theory of lubrication adapted for short dampers. The normal and magneto rheological oils are represented by Newtonian and Bingham fluids. Then the pressure distribution in non cavitated parts of the lubricating layers is described by the Reynolds' equations

$$\frac{\partial^2 p_{CO}}{\partial Z^2} = \frac{12\eta_{CO}}{h_{CO}^3} \dot{h}_{CO}, \quad h_{MR}^3 p_{MR}^3 + 3(h_{MR}^2 \tau_y - 4\eta_{MR} \dot{h}_{MR} Z) p_{MR}^2 - 4\tau_y^3 = 0 \quad (1)$$

where

$$h_{CO} = c_{CO} - e_H \cos(\varphi - \gamma), \quad h_{MR} = c_{MR} - e_H \cos(\varphi - \gamma) \quad (2)$$

p_{CO} , p_{MR} denote the pressure in the layers of the classical and magnetorheological oils, η_{CO} , η_{MR} are their dynamic viscosities, Z is the axial coordinate, τ_y represents the yield shear stress, h_{CO} , h_{MR} are thicknesses of the normal and magnetorheological films, c_{CO} , c_{MR} are widths of the gaps filled with the normal and magnetorheological oils, e_H is the journal centre eccentricity, φ is the circumferential coordinate, γ is the angle of the line of centres [2] and (\cdot) , $(\cdot)'$ denote the first derivatives with respect to time and axial coordinate Z .

At locations where the thickness of the lubricating films rises with time ($\dot{h}_{CO} > 0$, $\dot{h}_{MR} > 0$) a cavitation is assumed. In these areas the pressure remains constant and equal to the pressure in the ambient space. Components of the damping force in the y and z directions F_{dy} , F_{dz} are then calculated by integration of the pressure distributions p_{DCO} , p_{DMR} in the layers of normal and magneto rheological oils taking into account the cavitation

$$F_{dy} = -2R_{CO} \int_0^{2\pi} \int_0^{\frac{L}{2}} p_{DCO} \cos \varphi dZ d\varphi - 2R_{MR} \int_0^{2\pi} \int_0^{\frac{L}{2}} p_{DMR} \cos \varphi dZ d\varphi, \quad (3)$$

$$F_{dz} = -2R_{CO} \int_0^{2\pi} \int_0^{\frac{L}{2}} p_{DCO} \sin \varphi dZ d\varphi - 2R_{MR} \int_0^{2\pi} \int_0^{\frac{L}{2}} p_{DMR} \sin \varphi dZ d\varphi. \quad (4)$$

R_{CO} and R_{MR} are the radii of the layers of the normal and magneto rheological lubricants and L is the length of the damping element.

For the simplest design of the damping device, the dependence of the yielding shear stress on magnetic intensity can be approximately expressed

$$\tau_y = k_y \left(\frac{N_C I}{2h_{MR}} \right)^{n_y}. \quad (5)$$

k_y and n_y are material constants of the magneto rheological liquid, N_C is the number the coil turns and I is the electric current. More details can be found in [3].

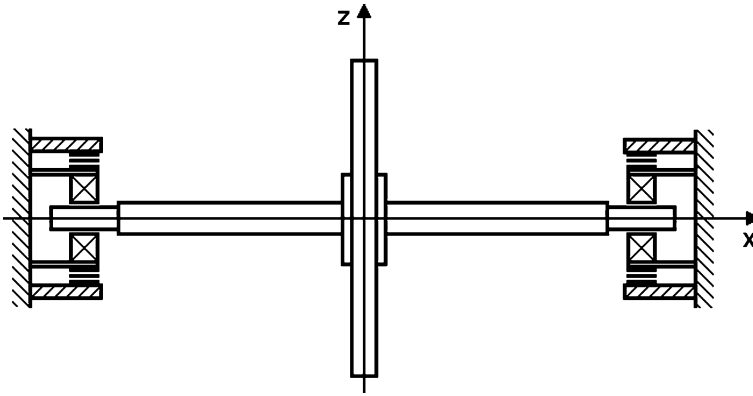


Fig. 2 Scheme of the rotor system

3 Steady State Vibration of a Flexible Rotor

The analysed rotor consists of a flexible shaft and of one disc (Fig. 2). The shaft is supported at its ends by the studied damping elements. The rotor turns at constant angular speed and is loaded by its weight and by the disc imbalance. The squirrel springs are prestressed to be eliminated their deflection caused by the weight of the rotor. In the mathematical model the damping devices are represented by the force couplings.

Taking into account the system symmetry relative to the disc middle plane perpendicular to the shaft axis, lateral vibration of the rotor is governed by a set of four differential equations of the first and second order

$$m\ddot{y} = -b_P\dot{y} - k_S y + k_S y_B + m e_T \omega^2 \cos(\omega t + \psi_T) \quad (6)$$

$$m\ddot{z} = -b_P\dot{z} - k_S z + k_S z_B + m e_T \omega^2 \sin(\omega t + \psi_T) - mg \quad (7)$$

$$0 = k_S y - (k_S + 2k_B)y_B + 2F_{dy} + 2F_{PSy} \quad (8)$$

$$0 = k_S z - (k_S + 2k_B)z_B + 2F_{dz} + 2F_{PSz} \quad (9)$$

m is the disc mass, k_S is the shaft stiffness, k_B is stiffness of each squirrel spring, b_P is the coefficient of the disc external damping, e_T is eccentricity of the disc centre of gravity, g is the gravity acceleration, y , z , y_B , z_B are displacements of the disc and shaft journal centres in the horizontal and vertical directions, ω is angular speed of the rotor rotation, t is the time, ψ_T is the phase shift of the unbalance excitation, F_{PSy} , F_{PSz} are the y- and z- components of the prestress force and $(\ddot{\cdot})$ denotes the second derivative with respect to time.

After some manipulations Eqs. (6, 7, 8, 9) can be rewritten in a matrix form

$$\mathbf{M}\ddot{\mathbf{x}} + \mathbf{B}\dot{\mathbf{x}} + \mathbf{K}\mathbf{x} = \mathbf{f}_0 + \mathbf{f}_C \cos \omega t + \mathbf{f}_S \sin \omega t + \mathbf{f}_H(\mathbf{x}, \dot{\mathbf{x}}). \quad (10)$$

\mathbf{M} , \mathbf{B} , \mathbf{K} are the mass, external damping and stiffness matrices of the rotor system, \mathbf{f}_0 , \mathbf{f}_C , \mathbf{f}_S are the vectors of applied forces, \mathbf{f}_H is the vector of damping forces in the rotor constraints and \mathbf{x} is the vector of the rotor generalized displacements.

To obtain the steady state solution of the governing Eq. (10) a trigonometric collocation method was applied. This requires to approximate the response by a finite number of terms of a Fourier series

$$\mathbf{x} = \mathbf{x}_0 + \sum_{j=1}^{N_{FS}} \mathbf{x}_{Cj} \cdot \cos\left(j \frac{2\pi}{T} t\right) + \mathbf{x}_{Sj} \cdot \sin\left(j \frac{2\pi}{T} t\right) \quad (11)$$

and to specify $2N_{FS} + 1$ collocation points of time t_k . \mathbf{x}_0 , \mathbf{x}_{Cj} , \mathbf{x}_{Sj} are the vectors of the Fourier coefficients and T is the estimated response period (period of the rotor rotation).

Inserting the assumed solution (11) and its first and second derivatives with respect to time in the governing Eq. (10) for all collocation points yields a set of nonlinear algebraic equations. The one for the k -th point takes the form

$$\begin{aligned} \mathbf{K}\mathbf{x}_0 + \sum_{j=1}^{N_{FS}} \left[\cos\left(j \frac{2\pi}{T} t_k\right) \left(\mathbf{K} - j^2 \frac{4\pi^2}{T^2} \mathbf{M} \right) - j \frac{2\pi}{T} \sin\left(j \frac{2\pi}{T} t_k\right) \mathbf{B} \right] \mathbf{x}_{Cj} \\ + \sum_{j=1}^{N_{FS}} \left[\sin\left(j \frac{2\pi}{T} t_k\right) \left(\mathbf{K} - j^2 \frac{4\pi^2}{T^2} \mathbf{M} \right) + j \frac{2\pi}{T} \cos\left(j \frac{2\pi}{T} t_k\right) \mathbf{B} \right] \mathbf{x}_{Sj} \\ = \mathbf{r}_k(\mathbf{y}_0, \mathbf{y}_{C1}, \mathbf{y}_{S1}, \mathbf{y}_{C2}, \mathbf{y}_{S2}, \dots, t_k) \end{aligned} \quad (12)$$

\mathbf{r}_k is the right-hand side vector corresponding to the k -th collocation time point.

Solving the set of nonlinear algebraic equations (12) gives the unknown values of the Fourier coefficients.

4 Results of the Simulations

The main parameters of the investigated rotor system are: mass of the disc 130 kg, stiffness of the shaft 7.0 MN/m, stiffness of one squirrel spring 3.0 MN/m, eccentricity of the disc centre of gravity 50 μm , length of the damping element 30 mm, the width and diameter of the damper clearances 0.2, 110 mm (normal oil), 1.0, 150 mm (magneto rheological oil), viscosity of the normal oil 0.004 Pas, viscosity and proportional and exponential material constants of the magneto rheological liquid 0.3 Pas, $4 \times 10^{-5} \text{ N/A}^2$, 2 and the number of coil turns 100. For these parameters the rotor natural frequencies are 158 rad/s for undamped and 232 rad/s for strongly over damped supports. The task was to analyse influence of the enhanced damping element on amplitude of the rotor vibration and of the force transmitted into the rotor casing.

Fig. 3 Response characteristic (disc)

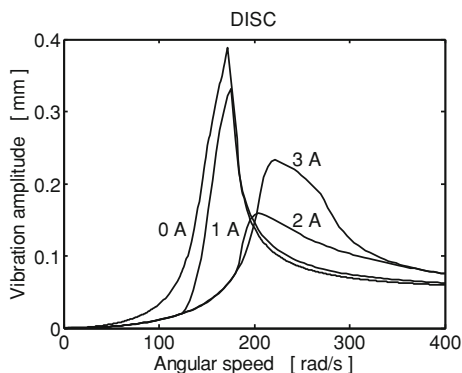


Fig. 4 Response characteristic (journal)

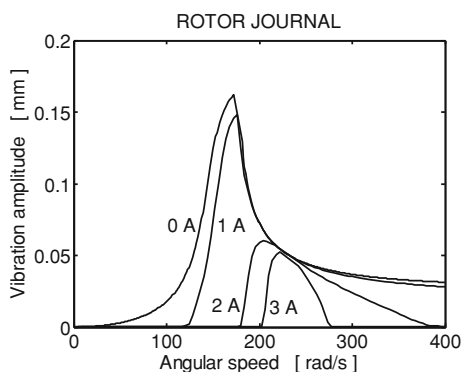
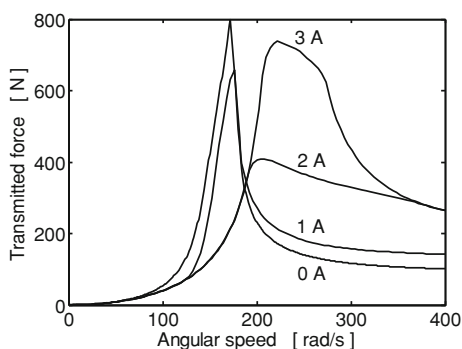
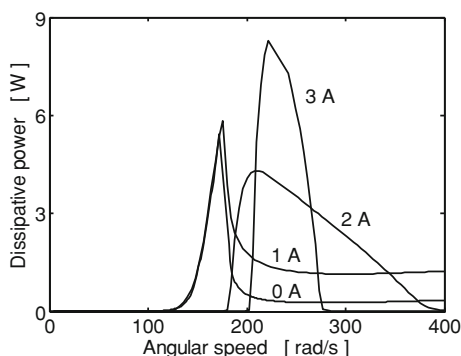


Fig. 5 Force-angular speed relation



In Figs. 3 and 4 there are drawn the frequency response characteristics of the disc and of the rotor journal centres. The results of the carried out computational simulations show that the rotor critical velocities are close to its natural angular frequencies and the rising current shifts the resonance peaks to higher velocities. The maximum vibration attenuation and transmitted force reduction can be achieved if the damping effect is maximum for velocities smaller than about 200 rad/s. In the region of higher speeds the damping should be as low as possible which can be achieved by switching the applied current off (Figs. 3, 4, 5). The thermal power due

Fig. 6 Dissipative power-speed relation



to transforming mechanical energy to the heat in both lubricating layers is small and reaches the value of order of units of watts or less (Fig. 6).

5 Conclusions

The investigated semiactive damping element works on the principle of squeezing two layers of normal and magneto rheological oils and its damping effect is controlled by the change of magnitude of the magnetic flux passing through the film of magneto rheological liquid. The computational simulations prove that adding this element to the rotor supports makes it possible to extend the velocity interval in which the rotor can be operated without exceeding the maximum allowable amplitude of its vibration and magnitude of the force transmitted between the rotor and the stationary part. Advantage of the proposed damping element is that it always produces some amount of damping, which can be increased or decreased if needed. It does not require an expensive and complicated control system for its operation and on the contrary to the classical magneto rheological dampers a lower consumption of magneto rheological liquid and a simpler design of the hydraulic circuit can be expected.

Acknowledgments The work reported here has been supported by the research projects P101/10/0209, MSM 6198910027 and CZ.1.05/1.1.00/02.0070. The support is gratefully acknowledged.

References

1. Zapoměl, J., Ferfecki, P.: Stability investigation of the steady state response of flexibly supported rigid rotors. *Springer Proc. Phys.*, **139**, 521 (2011).
2. Krämer, E.: *Dynamics of Rotors and Foundations*. Springer, New York (1993)
3. Zapoměl, J., Ferfecki, P.: A numerical procedure for investigation of efficiency of short magneto rheological dampers used for attenuation of lateral vibration of rotors passing the critical speeds. In: *Proceedings of the 8th IFToMM International Conference on rotor dynamics*, CD 1–8 (2010).

Part IV
Robots and Manipulators

Development of an Upper Limb Motorized Assistive-Rehabilitative Robot

Masoud Amiri and Federico Casolo

Abstract While the number of people requiring help for the activities of daily living are increasing, several studies have been shown the effectiveness of robot training for upper limb functionality recovery. The robotic system described in this paper is an active end-effector based robot which can be used for assisting and rehabilitating of human upper limb. The robot is able to take into account desire of the patient for the support that patient needs to complete the task.

Keywords Robot training • End-effector robot • Home-use therapy • Impedance control

1 Introduction

In recent years, many active upper-limb robot systems have been proposed for rehabilitation and power assist. The use of robot training are increasing since the number of people who are physically weak (aged, injured and post-stroke) are increasing. Arm Partial disability is a condition following stroke, that limits patient's autonomy in activities of daily living [1]. According to [2] in Italy 30 % of stroke patients suffer from activity of daily living (ADL). Positive effect of robot training has been proved in several studies [3]. Therefore, development of an effective robot for total or partial recovery of functionality of upper limb is fundamental.

M. Amiri (✉) · F. Casolo
Politecnico di Milano, Via La Masa 1,
e-mail: masoud.amiri@mail.polimi.it

F. Casolo
e-mail: federico.casolo@polimi.it

End-effector or exoskeleton robot type can be used to help patient to do ADL. End-effector robots are connected to the patient's hand or forearm at one point, they have simpler mechanical structure [4, 5]. Exoskeletons resemble the human arm anatomy and they are connected to human arm at several points [6–8]. In exoskeleton type robots every joint of human arm is actuated by corresponding joint of the robot. One of the difficult part of an exoskeleton is design of proper shoulder joint of robot in order not to over stress the shoulder joint of human arm.

There are two groups of robot training systems. First, the ones that are mainly used in a clinical environment and the second group are home-use systems [9, 10]. Assistive and rehabilitative robots can be also split into passive and active systems. In passive systems, no mechanical actuator is used to move patient limbs, instead limbs are passively supported [11, 12], while active systems are mainly equipped with electromechanical, pneumatic and hydraulic actuators to move patient limbs actively.

While most of the training robots are exoskeletons that are used in clinical environment, the aim of this research is to develop a low weight and simple end-effector based robot that can be used in home, due to light weight and simplicity it can be also mounted on wheelchair. The robot has two working modes the first one provides gravity compensation while the other mode helps patient to follow predefined movement.

2 Methods

2.1 Kinematics and Dynamics

The robot is mounted slightly behind the patient and support arm of the patient at forearm. Kinematic of human and robot is based on Denavit–Hartenberg (DH) Approach. Human arm has 7 DOF but since the robotic arm is connected to forearm, DOF of the wrist are not considered and human arm with 4 DOF has been taken into account.

There are several methods for obtaining a rigid dynamic model. The two most common approaches are the Lagrange formulation [13] and the Newton–Euler formulation [14]. A third method is Homogeneous matrix approach [15, 16] that can be considered as a powerful extension of the Denavit–Hartenberg kinematic approach. Dynamic simulation of robot and human arm is done using the third method.

Dynamic equation for robot and human arm is defined as:

$$\begin{aligned} M_1 \ddot{Q}_1 &= \mathfrak{S}_1 - J_R^T F \\ M_2 \ddot{Q}_2 &= \mathfrak{S}_2 - J_h^T F \end{aligned} \quad (1)$$

where M_1 is mass matrix of robot, M_2 is mass matrix of human arm, Q_1 is vector of robot joint coordinates, Q_2 is vector of human arm joint coordinates, \mathfrak{S} is vector of

generalized force, J'_R is robot jacobian, J'_h is human arm jacobian, F is the reaction force between human arm and robot at the connection point.

The robot and human arm are constrained at connection point, therefore they share the same position and linear velocity at that point. It is possible to write constrained dynamical equation as:

$$J_R \ddot{Q}_1 - J_h \ddot{Q}_2 = -\dot{J}_R \dot{Q}_1 + \dot{J}_h \dot{Q}_2 \quad (2)$$

From Eqs. (1) and (2) we can write the complete equation of motion in matrix form as:

$$\begin{bmatrix} [M_1] & [0] & J'_R \\ [0] & [M_2] & -J'_h \\ J_R & -J_h & [0] \end{bmatrix} \begin{bmatrix} \ddot{Q}_1 \\ \ddot{Q}_2 \\ F \end{bmatrix} = \begin{bmatrix} \mathfrak{S}_1 \\ \mathfrak{S}_2 \\ -\dot{J}_R \dot{Q}_1 + \dot{J}_h \dot{Q}_2 \end{bmatrix} \quad (3)$$

In order to solve above formula the Udwadia–Kalaba approach (K–U formulation) [17, 18] is used. According to K–U formulation the complete constrained dynamics can be written in matrix form as:

$$\begin{bmatrix} M & A^T \\ A & 0 \end{bmatrix} \begin{bmatrix} a_a \\ -\lambda \end{bmatrix} = \begin{bmatrix} f \\ b \end{bmatrix} \quad (4)$$

where a_a is actual acceleration, λ is Lagrange multiplier and A is constrained Jacobian matrix. It can be proved that a_a is:

$$a_a = a_f + M^{-1/2} D^+ (b - A a_f) \quad (5)$$

where $D = AM^{-1/2}$, D^+ is the Moore–Penrose generalized inverse of D and a_f is unconstrained acceleration. The validity of equation (5) was shown by Kalaba and Udwadia.

Returning to the complete constrained dynamic equation of robot and human arm (3) and comparing it to Eq. (4) it is easy to find following relations:

$$\begin{aligned} A &= [J_R - J_h] \\ F &= -\lambda \\ b &= -\dot{J}_R \dot{Q}_1 + \dot{J}_h \dot{Q}_2 \end{aligned}$$

In order to make sure that small numerical error does not accumulate during simulation process Baumgarte stabilization has been used [19]. Practically, instead of using an original constraint equation $\psi = 0$, Baumgarte proposes the use of a second order equation, $\ddot{\psi} + 2\alpha\dot{\psi} + \beta^2\psi = 0$. With this method equation (5) can be written as:

$$a_a = a_f + M^{-1/2} D^+ (b^* - A a_f) \quad (6)$$

where $b^* = b - 2\alpha\dot{\psi} + \beta^2\psi$, and α , β are Baumgarte parameters. Usually α and β are assumed to be equal and assigned a value between 1 and 10.

2.2 Cartesian Impedance Control

Impedance control is used for controlling the robotic arm [20, 21]. Dynamic equation of the robot in presence of external force is:

$$M(q)\ddot{q} + C(q, \dot{q})\dot{q} + g(q) = \tau + \tau_{ext} \quad (7)$$

where q is robot joint variable, τ is joint vector of the generalized torques, $M(q)$ is the inertia matrix, $C(q, \dot{q})$ is Coriolis/centrifugal matrix, $g(q)$ is the vector of gravity torques, τ_{ext} is the vector of external torques.

The aim of Impedance control is to put a mass-damper-spring between robot end-effector and target position.

$$M_d\ddot{\tilde{x}} + D_d\dot{\tilde{x}} + K_d\tilde{x} = F_{ext} \quad (8)$$

where K_d , D_d and M_d are the symmetric and positive definite matrices of the desired stiffness, damping and inertia respectively. $\tilde{x} = x - x_d$ is difference between end-effector position x and desired position x_d . The external torques τ_{ext} is related to the vector of generalize external forces F_{ext} via $\tau_{ext} = J(q)^T F_{ext}$.

Equation (6) is in joint coordinate, while in task space is in the form of:

$$M_x(q)\ddot{x} + C_x(q, \dot{q})\dot{x} + F_g(q) = J(q)^{-T} \tau + F_{ext} \quad (9)$$

where

$$\begin{aligned} M_x(q) &= J(q)^{-T} M(q) J(q)^{-1} \\ C_x(q, \dot{q}) &= J(q)^{-T} \left(C(q, \dot{q}) - M(q) J(q)^{-1} \dot{J}(q) \right) J(q)^{-1} \\ F_g(q) &= J(q)^{-T} g(q) \end{aligned}$$

Therefore the control input is given by:

$$\begin{aligned} \tau &= g(q) + J(q)^T (M_x(q)\ddot{x}_d + C_x(q, \dot{q})\dot{x}_d) \\ &\quad + J(q)^T M_x(q) M_d^{-1} (K_d(x_d - x) + D_d(\dot{x}_d - \dot{x})) \\ &\quad + J(q)^T (M_x(q) M_d^{-1} - I) F_{ext} \end{aligned} \quad (10)$$

The above equation can be simplified by choosing $M_x(q) = M_d = J^{-T}(q)M(q)J^{-1}(q)$, therefore control input becomes:

$$\tau = -M(q)J^{-1}(q)\ddot{J}(q)\dot{q} + C(q, \dot{q})\dot{q} + g(q) + J^T(q)(K_d(x_d - x) + D_d(\dot{x}_d - \dot{x})) \quad (11)$$

Considering slow motions typical in rehabilitation applications, the control law is:

$$\tau = g(q) + J^T(q)(K_d(x_d - x) + D_d(\dot{x}_d - \dot{x})) \quad (12)$$

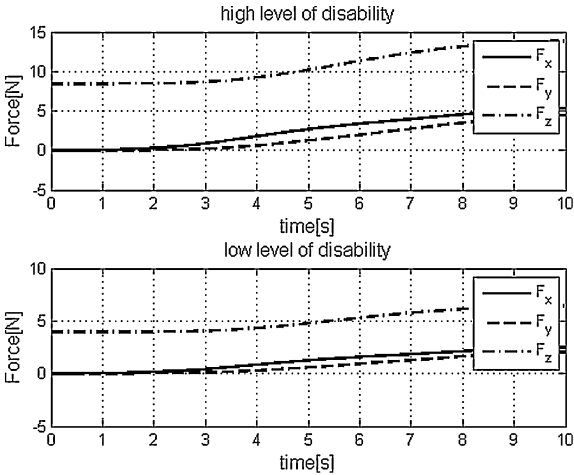
Table 1 Stiffness and damping parameters for the patient with high level of disability

Parameter	x	y	z
Stiffness	500 [N/m]	500 [N/m]	500 [N/m]
Damping	250 [Ns/m]	250 [Ns/m]	250 [Ns/m]

Table 2 Stiffness and Damping parameters for the patient with low level of disability

Parameter	x	y	z
Stiffness	300 [N/m]	300 [N/m]	300 [N/m]
Damping	160 [Ns/m]	160 [Ns/m]	160 [Ns/m]

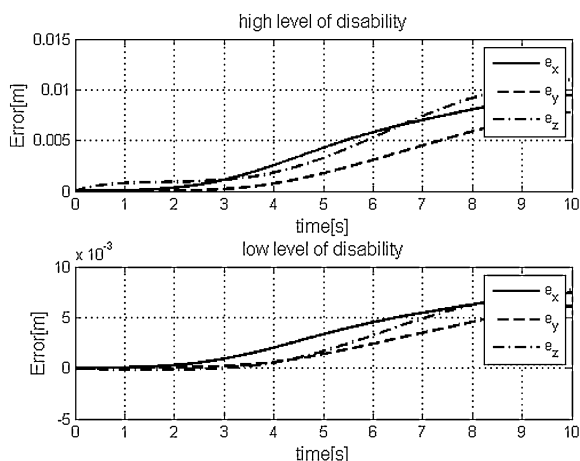
Fig. 1 Reaction force between robot end effector and human arm at connection point



3 Preliminary Results and Concluding Remarks

The function of the robot is to help patient to complete a predefined motion task while two different cases have been considered. The first case is when patient has high level of disability and requires more help from robot to follow predefined motion, therefore Impedance parameters must be enough high, for this case Impedance parameters are chosen as Table 1. The second case is when patient has low level of disability, with respect to first case patient needs less help from robot and smaller impedance parameters must be chosen (Table 2). It is clear that higher level of disability results in higher reaction force between human arm and robot at

Fig. 2 Error between hand position and desired position for the hand



connection point which is also observable from Fig. 1. Figure 2 shows position error between patient's hand and desired position, it is observable that in both cases robot is able to maintain minimum error to let patient to do ADL.

References

1. Olsen, T.S., Nakayama, H., Jorgensen, J.S., Raaschou, H.O.: Recovery of upper extremity function in stroke patients: the Copenhagen stroke study. *Arch. Phys. Med. Rehabil.* **75**(4), 394–398 (1994)
2. Inzitari, D.: The Italian guidelines for stroke prevention. The stroke prevention and educational awareness diffusion (spread) collaboration. *Neurol. Sci.* **21**(1), 5–12 (2000)
3. Shor, P. C., Majmundar, M., van der Loos, M., Lum, P.S., Burgar, C.G.: Robot-assisted movement training compared with conventional therapy techniques for the rehabilitation of upper-limb motor function after stroke. *Arch. Phys. Med. Rehabil.* **83**, 952–959 (2002)
4. Hesse, S., Schmidt, H., Werner, C.: Machines to support motor rehabilitation after stroke: 10 years of experience in Berlin. *J. Rehabil. Res. Dev.* **43**(5), 671–678 (2006).
5. Igo Krebs, H., Hogan, N., Aisen, M.L., Volpe, B.T.: Robot-aided neurorehabilitation. *IEEE Trans. Rehabil. Eng.* **6**(1), 75–87 (1998).
6. Frisoli, A., Borelli, L., Montagner, A., Marcheschi, S., Procopio, C., Salsedo, F., Bergamasco, M., Carboncini, M.C., Tolaini, M., Rossi, B.: Arm rehabilitation with a robotic exoskeleton in virtual reality. In: 2007 IEEE 10th International Conference on Rehabilitation Robotics, ICORR'07, pp 631–642 (2007).
7. Perry, J.C., Rosen, J., Burns, S.: Upper-limb powered exoskeleton design. *IEEE/ASME Trans. Mechatron.* **12**(4), 408–417 (2007)
8. Nef, T., Mihelj, M., Riener, R.: Armin: a robot for patient-cooperative arm therapy. *Med. Biol. Eng. Comp.* **45**(9), 887–900 (2007)
9. Riener, R., Nef, T., Colombo, G.: Robot-aided neurorehabilitation of the upper extremities. *Med. Biol. Eng. Comp.* **43**(1), 2–10 (2005)
10. Alqasemi, R.M., McCaffrey, E.J., Edwards, K.D., Dubey, R.V.: Wheelchair-mounted robotic arms: Analysis, evaluation and development. *IEEE/ASME Int. Conf. Adv. Intel. Mechatro. AIM*, **2**, 1164–1169 (2005)

11. Mastenbroek, B., De Haan, E., Van Den Berg, M., Herder, J.L.: Development of a mobile arm support (armon): design evolution and preliminary user experience. In: 2007 IEEE 10th international conference on rehabilitation robotics, ICORR'07, pp 1114–1120 (2007)
12. Herder, J.L.: Development of a statically balanced arm support: Armon. In: Proceedings of the 2005 IEEE 9th international conference on rehabilitation robotics, vol. 2005, pp. 281–286 (2005)
13. Hutchinson, S., Spong, M.W., Vidyasagar, M.: Robot modeling and control. Wiley, New York (2006)
14. Craig, J.J.: Introduction to robot mechanics and control. Addison-Wesley, (1989)
15. Legnani, G., Casolo, F., Righettini, P., Zappa, B.: A homogeneous matrix approach to 3D kinematics and dynamics part i. Theory. Mech. Mach. Theor. **31**, 573–587 (1996)
16. Legnani, G., Casolo, F., Righettini, P., Zappa, B.: A homogeneous matrix approach to 3D kinematics and dynamics part ii. Applications to chains of rigid bodies and serial manipulators. Mech. Mach. Theor. **31**, 589–605 (1996)
17. Udwadia, F.E., Kalaba, R.E.: A new perspective on constrained motion. In: Proceedings mathematical and physical sciences, **439**, 407–410 (1992)
18. Udwadia, F.E., Kalaba, R.E.: Analytical Dynamics: A New Approach. Cambridge University Press (1996)
19. Baumgarte, J.: Stabilization of constraints and integrals of motion in dynamical systems. Comp. Methods Appl. Mech. Eng. **1**, 1–66 (1972).
20. Hogan, N.: Impedance control: an approach to manipulation, Part i, ii, iii. ASME J. Dyn. Sys. Meas. Control, **107**, 1–24 (1985).
21. Villani, L., Oriolo, G., Siciliano, B., Sciacivco L.: Robotics Modelling, Planning and Control. Springer (2009).

Workspace Evaluation for Analysis and Synthesis of Manipulators

M. Ceccarelli

Abstract In this keynote lecture, manipulator workspace is presented by discussing its basic characteristics as fundamental for design and operation of mechanical systems in manipulation applications. Algorithms are explained for numerical evaluation of the workspace of serial and parallel manipulators. Formulations are introduced also for design purposes. Design problem for manipulators is formulated by using workspace characteristics. Experimental procedures for workspace determination are outlined both for model validations and performance evaluation.

Keywords Manipulators • Workspace • Analysis • Design • Characterization

1 Introduction

Manipulator workspace is a region of points that can be reached by a reference point on the manipulator extremity. This is usually referred as position workspace and it is widely used to characterize industrial robots and in general mechanical systems, Fig. 1. Similarly orientation workspace is a set of orientation that can be reached by the extremity or end-effector of a manipulator. It has been introduced to complete a workspace characterization of parallel manipulators, but it is used also for serial manipulators. An extension of workspace characterization is today used also for mechanical systems with general manipulation purposes.

M. Ceccarelli (✉)

LARM: Laboratory of Robotics and Mechatronics, DICIME, University of Cassino and South Latium, Via Di Biasio 43, 03043 Cassino (Fr), Italy
e-mail: ceccarelli@unicas.it

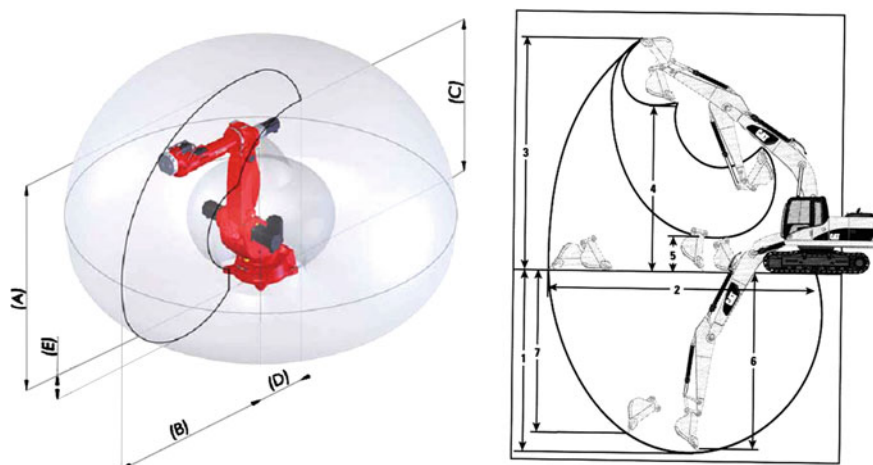


Fig. 1 Workspace indication in: **a** robot SMART Nj4; **b** excavator Cat 319D

Because of the above definitions, a numerical evaluation of the manipulator workspace has been considered fundamental since the early days of robotics both to evaluate the performance of a robot arm and to design/locate it properly in a manipulation process.

Thus, there is a very rich literature dealing with modeling, formulating, computing workspace characteristics mainly with numerical procedures (main sources can be found in the reference lists in [1–3]). Few attempts have been developed to derive closed-form formulation that nevertheless has been devoted to specific manipulator structures. Most of the works has been done for serial manipulators and only in the last decade attention has been addressed also to the workspace of parallel manipulators. Thus, in general different algorithms have been proposed and are used for a numerical characterization of workspace performance of parallel manipulators.

Design issues and algorithms have been developed by using results of workspace analysis but in general only few attempts have used the workspace formulations for design purposes by inverting them. Several design procedures have been elaborated by using optimization problems in which one or more objective functions have been considered from workspace characteristics.

In this paper, the reference list has been limited to the main works of the authors' team for space limits in which indeed a reader can easily find sources for further reading. At LARM (Laboratory of Robotics and Mechatronics, University of Cassino and South Latium), a research line has been specifically devoted to manipulator workspace since the early of 1990 s and results are reported in publications that are listed in the LARM webpage.

In this paper, a survey of the procedures for workspace analysis is discussed with the aim to stress open problems that still attract research interest and can give enhancement on the manipulator characterization and design. In addition, an

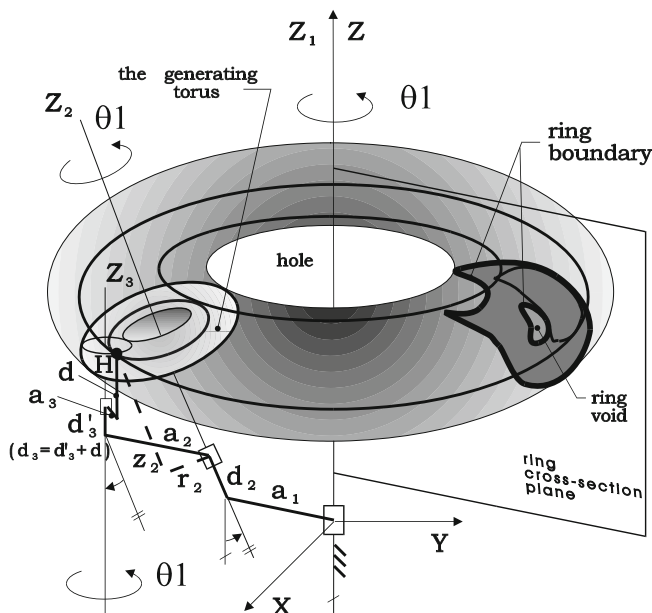


Fig. 2 Topology of the generation process of workspace of manipulators with revolute joints as function of design parameters, [4]

attempt is reported to formulate a unique approach to study the workspace of both serial and parallel manipulators. Open issues on workspace aspects can be considered in how to use workspace formulation in design algorithms, development of more efficient numerical determination of workspace boundary and workspace measures, formulation with direct indication of parameter influence on workspace characteristics for operation feasibility in given applications.

2 Workspace Generation and Algorithms

Workspace can be modeled and formulated by looking at the generation process. Thus, different views can be adopted to derive different approaches for numerical determination and characteristic evaluation, as reported in a rich literature.

The generation of a workspace can be modeled as in Fig. 2, [2, 4], when referring to serial manipulator with revolute joints. The basic features of the generation of the manipulator workspace can be used for an algebraic formulation.

This formulation can be derived, with the hypotheses $C_1 \neq 0$ and $E_1 \neq 0$, and expressed through the radial reach r and the axial reach z of the workspace boundary points with respect to reference frame attached to the base in the form, [4],

$$r = \left[A_1 - z^2 + \frac{(C_1 z + D_1)G_1 + F_1}{E_1} \right]^{1/2}; \quad z = \frac{-L_1 \pm Q_1^{1/2}}{K_1 C_1} - \frac{D_1}{C_1}; \quad (1)$$

where the so-called structural coefficients can be computed, after algebraic manipulations in deriving Eq. (1), as functions of Denavit and Hartenberg parameters

$$\begin{aligned} A_1 &= a_1^2 + r_2^2 + (z_2 + d_2)^2; \\ B_1 &= -4 a_1^2 r_2^2; \quad C_1 = 2 a_1 / s\alpha_1; \\ D_1 &= -2 a_1 (z_2 + d_2) c\alpha_1 / s\alpha_1; \\ E_1 &= -2 a_3 (d_2 s\alpha_2 c\theta_3 + a_2 s\theta_3); \\ F_1 &= 4a_1^2 a_3 (a_3 s\alpha_2^2 s\theta_3 c\theta_3 + a_2 s\theta_3 - d_3 s\alpha_2 c\alpha_2 c\theta_3); \\ G_1 &= 2a_1 a_3 c\alpha_1 s\alpha_2 c\theta_3 / s\alpha_1; \\ Q_1 &= -E_1^2 [F_1^2 + B_1 (G_1^2 + E_1^2)]; \end{aligned} \quad (2)$$

in which $c\alpha_i = \cos \alpha_i$, $s\alpha_i = \sin \alpha_i$, for any angle α_i ; $c\theta_3 = \cos \theta_3$ and $s\theta_3 = \sin \theta_3$

The reach distances r_2 and z_2 can be expressed from the link geometry as

$$\begin{aligned} r_2 &= \left[(a_3 c\theta_3 + a_2)^2 + (a_3 s\theta_3 c\alpha_2 + d_3 s\alpha_2)^2 \right]^{1/2}; \\ z_2 &= d_3 c\alpha_2 - a_3 s\theta_3 s\alpha_2; \end{aligned} \quad (3)$$

Thus the workspace boundary can be obtained from Eqs. (1)–(3) by scanning the angle θ_3 from 0 to 2π and plotting r and z . By using Eqs. (1)–(3) it is possible to analyze the cross section of workspace boundary of a general three-revolute manipulator [4]. It consists of an internal and an external branches. The external branch envelope represents the boundary of the bulk workspace ring and the internal one gives the boundary of a ring void [5].

The generation process of a hyper-ring for N -revolute manipulator is a consecutive revolving process of a circle, a torus, a ring, a 4R hyper-ring, and so on. This can be expressed for a general hyper-ring workspace through a revolution operator Rev in the form [2]

$$W_{(N-j+1)R}(H) = \underset{\vartheta_j=0}{\overset{2\pi}{\text{Rev}}} W_{(N-j)R}(H) \quad j = 1, \dots, N-1 \quad (4)$$

where $W_{(N-j+1)R}(H)$ represents reachable points, with respect to frame $X_j Y_j Z_j$ fixed on link j , due to $(N-j+1)$ last revolute joints in the chain; and $W_{(N-j)R}(H)$ is with respect to $X_{j+1} Y_{j+1} Z_{j+1}$ on link $j+1$ due to $N-j$ revolute pairs, Fig. 3.

Alternatively, $W_{(N-j+1)R}(H)$ can be considered as the union of a suitable torus family which is traced by the boundary points in revolving torus, ring, 4R hyper-ring and so on, when they are rotated completely about the first two revolute axes in the corresponding generating sub-chain, [2],

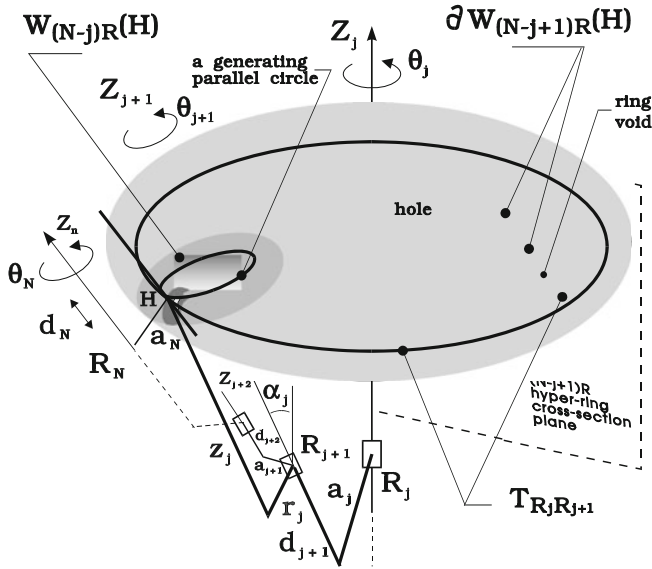


Fig. 3 Generation process of hyper-ring workspace [4]

$$W_{(N+1-j)R}(H) = \bigcup_{\vartheta_j, \vartheta_{j+1}=0}^{2\pi} T_{R_j R_{j+1}} [\partial W_{(N-j)R}(H)] \quad (5)$$

where $T_{R_j R_{j+1}}(H)$, represents a torus generated by revolutions θ_j and θ_{j+1} about the joints axes of R_j and R_{j+1} , Fig. 3. The revolution in θ_{j+1} generates a parallel circle in $W_{(N-j)R}(H)$ and together with θ_j generates the torus $T_{R_j R_{j+1}}(H)$. Hence, the boundary $\partial W_{(N-j+1)R}(H)$ of a $(N-j+1)R$ hyper-ring can be described as an envelope of the torus family traced by all the points on $\partial W_{(N-j)R}(H)$, Fig. 3, and it can be synthetically expressed as, [2].

$$\partial W_{(N-j+1)R}(H) = \text{env}_{\vartheta_j, \vartheta_{j+1}=0}^{2\pi} T_{R_j R_{j+1}} [\partial W_{(N-j)R}(H)]. \quad (6)$$

Thus, a workspace boundary $\partial W_{NR}(H)$ of a general N - R manipulator can be generated by using recursively Eq. (6), to determine the tori envelopes from the ring up to the NR hyper-ring in the chain from the extremity to the base of the manipulator chain. We have obtained an analytical formulation of Eq. (6) in a recursive way, which is based on the equation of ring workspace deduced by using the equation of torus. Details are reported in the papers of the reference list [2, 4, 6, 7].

An alternative approach is based on the use of matrices as for a problem of Direct Kinematics, [1].

A suitable procedure can be proposed by formulating specifically the Direct Kinematics for specific chains and a general evaluation of workspace performance

can be carried out as outlined in the following. A general numerical evaluation of the workspace can be deduced by formulating a suitable binary representation of a cross-section, [1, 3]. A cross-section can be obtained with a suitable scanning of the computed reachable positions and orientations, once the Direct kinematic problem has been solved to give the positions and orientations as functions of the kinematic input variables. A binary matrix P_{ij} can be defined for a cross-section of the workspace as follows: if the (i, j) grid pixel includes a reachable point, then $P_{ij} = 1$; otherwise $P_{ij} = 0$, as shown in Fig. 4 [1]. For example, one can consider a cross-section at a given value of Z-Coordinate, then a point in the grid is indicated as P_{ij} , with i along X axis and j along the Y axis, namely

$$i = \left\lfloor \frac{x + \Delta x}{x} \right\rfloor; \quad j = \left\lfloor \frac{y + \Delta y}{y} \right\rfloor \quad (7)$$

where i and j are computed as integer numbers. Therefore, the binary mapping for the workspace cross-section can be given as

$$P_{ij} = \begin{cases} 0 & \text{if } P_{ij} \notin W(H) \\ 1 & \text{if } P_{ij} \in W(H) \end{cases} \quad (8)$$

where $W(H)$ indicates workspace region; \in stands for “belong to” and \notin is for “not belonging to”. In addition, whilst scanning the vector of the computed reachable positions to build P_{ij} through Eq. (8), it is possible to evaluate the dexterity performance of a manipulator by counting the times that each P_{ij} is reached. Thus, a suitable reach frequency matrix f_{ij} can be defined during the scanning process for P_{ij} with the condition for each entry given by

$$f_{ij} = f_{ij} + 1 \quad (9)$$

to count each time the corresponding P_{ij} is reached. Thus, f_{ij} can be considered a measure for repeatability and dexterity of a manipulator. Indeed, a synthetic measure can be proposed as the average D_z over the sum of all the values of the entries f_{ij} for each cross-section.

In addition, the proposed formulation is useful for a numerical evaluation of the position workspace by computing the cross-sections areas A_z as

$$A_z = \sum_{i=1}^{i_{\max}} \sum_{j=1}^{j_{\max}} (P_{ij} \Delta x \Delta y) \quad (10)$$

and finally, the workspace volume V can be computed as

$$V = \sum_{Z=Z_{\min}}^{Z=Z_{\max}} A_z \Delta z \quad (11)$$

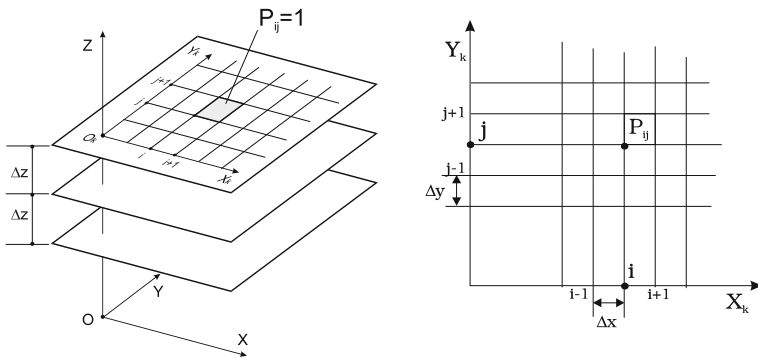


Fig. 4 A scheme for binary representation and evaluation of a cross-section of a computed workspace, [1]

An average D_{tot} over the sum of all the values of the D_z can give a synthetic measure for repeatability and dexterity capability of a given manipulator.

Similarly, a numerical evaluation of orientation workspace can be carried out by using the formulation of Eqs. (7)–(11) in order to compute the corresponding performance measures cross-sections areas A_ϕ , the orientation workspace volume V_ϕ , the average D_ϕ over the sum of all the values of the entries F_{ij} for each cross-section, and the average $D_{\phi\text{tot}}$ over the sum of all the values of the D_ϕ .

Of course, one can use Eqs. (7)–(11) in order to evaluate any cross-section by properly adapting the formulation to the scanning cross-section plane and intervals.

The proposed formulation can be implemented with no great efforts also in an experimental validation of the above-mentioned workspace performances.

Issues are still considered to improve computational efficiency both in terms of computing time and result accuracy for numerical based approaches, and to get extension of the formulation for algebraic approaches.

Thus, for example Fig. 5 shows an attempt to extend the algebraic approach of Fig. 3 to the workspace analysis of parallel manipulators.

Further numerical analysis can be elaborated by considering other operation aspects in conjunction with workspace determination as from the above kinematic viewpoint. Thus, for example when considering workspace mapping with static force transmission as for payload capability in W_S and with vibration response as for dynamic behavior in W_D , an operation workspace W_{OP} can be determined from the general workspace W_K as, [8],

$$W_{OP} = W_K \cap W_S \cap W_D \quad (12)$$

in which each workspace sub-set is determined with specific procedures for the considered aspect. The so-called Operation Workspace is the region of efficiently reachable points and can be considered a mapping for a practical user-oriented application of the corresponding manipulator.

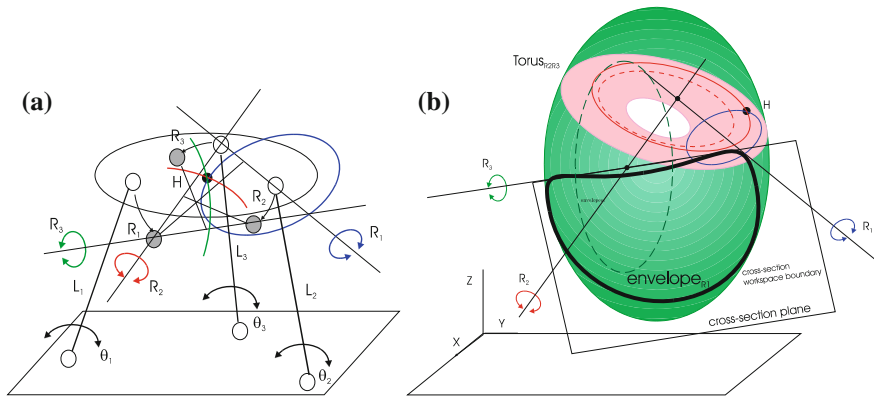


Fig. 5 A scheme for a rationale of the extending the algebraic algorithm to parallel manipulators: **a** the generation process; **b** the general topology

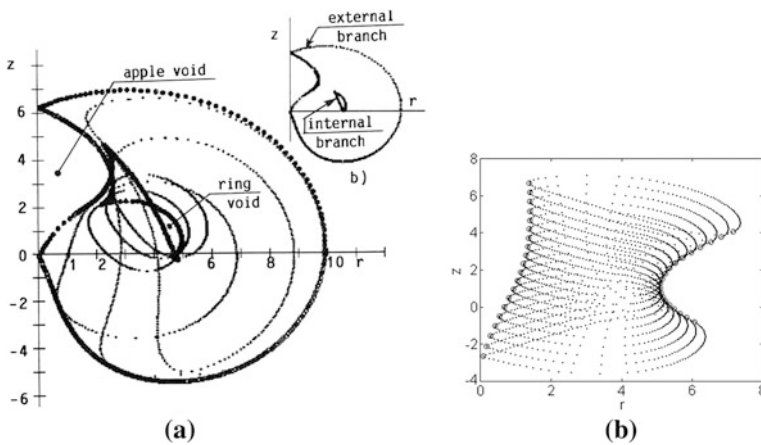


Fig. 6 Examples of computed workspace boundary by means of algebraic formulation for the case of: **a** a 4R manipulator with $a_1 = 3 \text{ u}$, $a_2 = 4 \text{ u}$, $a_3 = 2 \text{ u}$, $a_4 = 5 \text{ u}$, $\alpha_1 = \alpha_2 = \alpha_3 = 60 \text{ deg}$, $d_2 = d_3 = d_4 = 1 \text{ u}$; **b** a 2RP telescopic manipulator arm with $a_1 = 3 \text{ u}$, $a_2 = 2 \text{ u}$, $h_1 = 0 \text{ u}$, $h_2 = 2 \text{ u}$, $\alpha_1 = 30 \text{ deg}$, $\alpha_2 = 30 \text{ deg}$, $d_{\min} = -5 \text{ u}$, $d_{\max} = 5 \text{ u}$. (u is a unit length)

2.1 Numerical Examples

Illustrative examples are reported in Figs. 6, 7, 8 and 9 for the outputs of the presented algorithms to determine manipulator workspace. An example for a multi-operation aspects analysis is reported in Fig. 9 as related to the operation workspace.

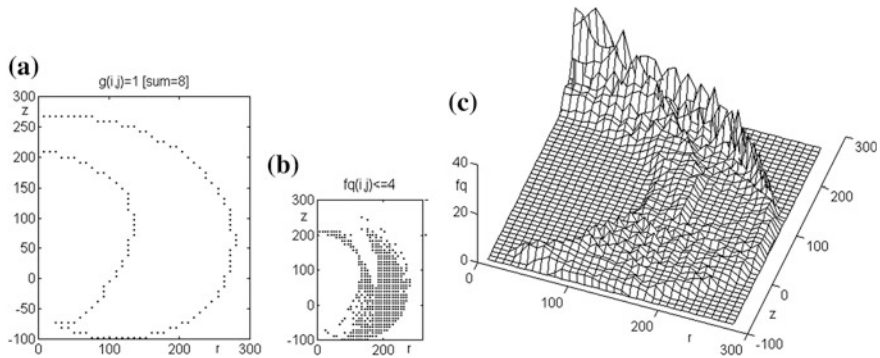


Fig. 7 Example of binary matrix representation of workspace volume for the case of an industrial robot COMAU SMART 6.100A with $a_1 = 300$ mm, $\alpha_1 = 90$ deg., $a_2 = 1,100$ mm, $\alpha_2 = \alpha_3 = 0$ deg., $a_3 = 1,625$ mm, and $b_1 = b_2 = b_3 = 0$: **a** cross-section workspace contour generated with $\text{sum} = 8$; **b** cross-section area of secondary workspace with $f_q(i,j) \leq 4$; **c** a map for the repeatability matrix $f_q(i,j)$

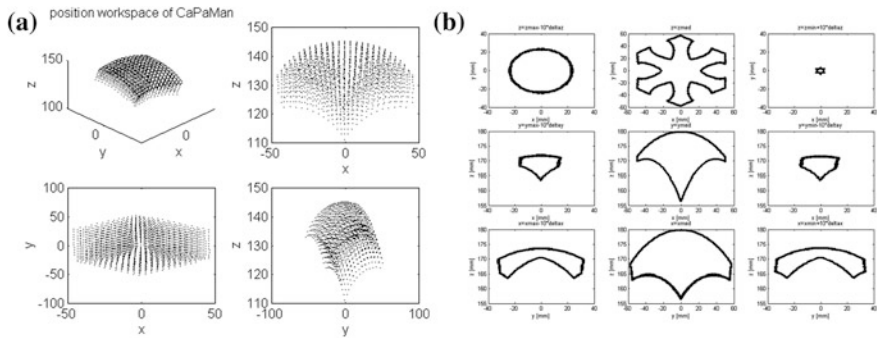


Fig. 8 Example of computed workspace of CAPMAN (Cassino Parallel Manipulator): **a** general shape; **b** cross-sections

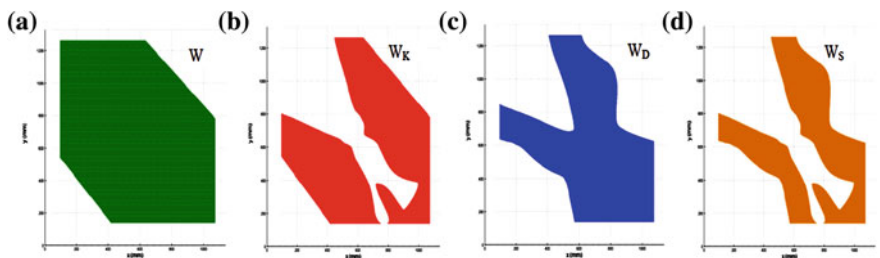


Fig. 9 Example of computed workspace of DAEDALUS I, parallel manipulator with, [8]: **a** general kinematic determination; **b** statics performance; **c** dynamic response; **d** the final operation workspace

3 Design Formulations

Workspace analysis can be conveniently used for design purposes by using algorithms in procedures with repeated computations or by inverting formulation to get synthesis.

The inversion of matrix expressions seem not to give the possibility of useful expressions for sizing the design parameters and for further manipulations in a direct insight of workspace dependency from design parameters.

Manipulations of algebraic expression of workspace formulation from different approaches (by using Screw Theory, Jacobian analysis, and Direct or Inverse Kinematics) can be used to formulate design algorithms for prescribed workspace areas though given points and/or for given workspace constraints. An extensive literature is available as related to those approaches, including discussions on their advantages. But more promising for a close-form formulation cab expected the algebraic representation of the workspace boundary.

For example, by using formulation in Eqs. (1)–(3) design parameters for 3R manipulators can be obtained once the inversion of the ring equation is solved the structural coefficients are expressed, [9]. Thus, for the case of unknown robot base location the unknown A_1 , E_1 , F_1 , G_1 , Q_1 and s can be solved from, [9],

$$E_1 K_1 (\mathbf{x} \cdot \mathbf{x} - 2\mathbf{s} \cdot \mathbf{x} + \mathbf{s} \cdot \mathbf{s} - A_1) - \left(-L_1 \pm Q_1^{1/2} \right) G_1 - F_1 K_1 = 0 \quad (13)$$

in which vector \mathbf{x} is the position vector of prescribed points in the workspace boundary. Additional four boundary points to give C_1 , D_1 and \mathbf{r}_3 from

$$\mathbf{r}_3 \cdot (\mathbf{x} - \mathbf{s}) = \frac{-L_1 \pm Q_1^{1/2}}{K_1 C_1} \frac{D_1}{C_1} \quad r_{31}^2 + r_{32}^2 + r_{33}^2 = 1 \quad (14)$$

Since we are interested in \mathbf{k} , \mathbf{r}_3 together with the orthonormal unit vector, constraints can be used to evaluate the R matrix, whose third column represents \mathbf{k} unit vector of base orientation with respect to XYZ.

An example of computed results is reported in Fig. 10, [9].

In addition, an analysis of the feasible domain for workspace results, [10], can give charts like in Fig. 11 that can be useful to forecast the feasibility of prescribed workspace conditions and workspace output with general characteristics.

Similarly, a level-set analysis of workspace generation, [11], can give better insight of the singularity characteristics of the boundary points like in the example in Fig. 12, [11] when considered also in a design algorithm with path planning feasibility of the full workspace area.

Design formulation can be also proposed as optimization problems by considering workspace characteristics such as shape, volume, voids, hole as main objective functions even in conjunction with other operation characteristics.

In particular algebraic formulation can be helpful to deduce procedures with great numerical efficiency and good converge possibility to feasible solutions, as for the experience case in [12].

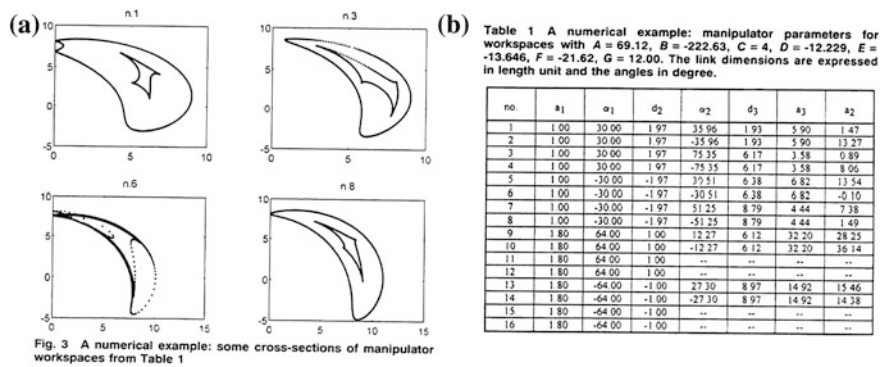


Fig. 10 An example of design result for 3R manipulators by inverting algebraic formulation for workspace analysis, [9]

Fig. 11 General geometry of feasible workspace regions for two-revolute manipulators depicted as grey area

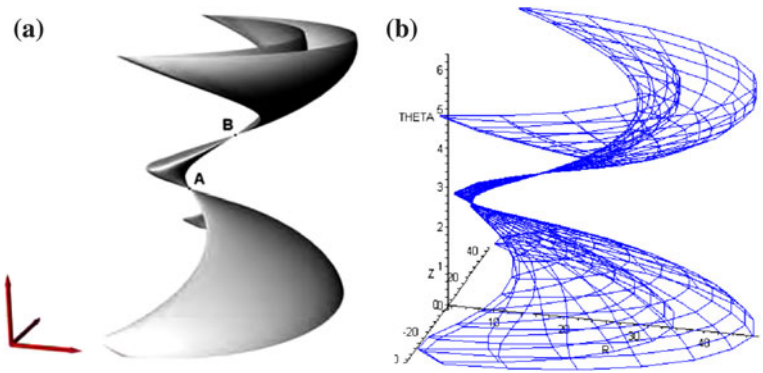
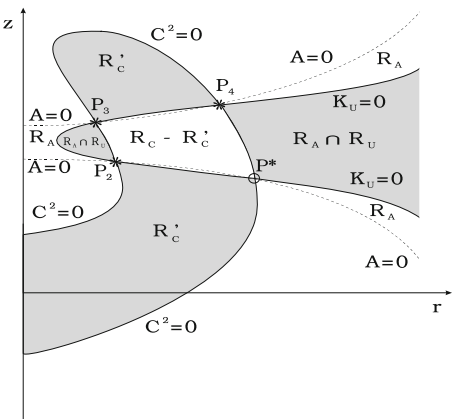


Fig. 12 An example of singularity characterization by means of level-set analysis of workspace generation of 3R manipulators, [11]: **a** a general topology; **b** a numerical example

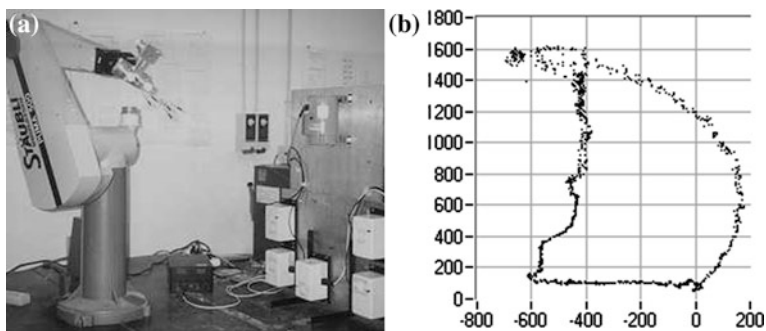


Fig. 13 Example of experimental determination of workspace cross-section boundary for the case of PUMA robot, [13]: **a** a phase of the operation with CATRASYS; **b** the determined contour

4 Experimental Characterizations

Although workspace determination is a topic that has been usually approached only with modeling and numerical computations, an experimental procedure can be conveniently used to validate the numerical results but even to characterize the determined workspace also with functionality issues.

Motion trackers can be used to follow end-effector when a manipulator moves along workspace borders, even for calibration purposes. Experimental characterizations can be determined for practical evaluation of workspace that very often differs from the numerically computed one mainly because of real constraints in mechanical design and actuation mobility.

In Fig. 13 an example is reported to show such an output from author's experience by using CATRASYS, a cable-based parallel manipulator system for monitoring large displacements of multi-body systems, [13]. An output of an experimental characterization can be an indication of motion resolution both along the workspace boundary and within the workspace regions. An example is shown in Fig. 13b). Indeed, an internal mapping and experimental calibration can be considered essential for a practical check of system behavior before sale or implementation, as in general done by producers of advanced mechanical systems.

5 Conclusions

Manipulator workspace is recognized as a basic performance characteristics both for design issues and rational use of mechanical systems. Numerical procedures are used for evaluating basic characteristics like workspace volume, hole existence, void extension and dexterity/repeatability mapping. Those procedures can be applied to specific architectures, even with generality characters, but they

can be still very laborious and time consuming. Approaches with algebraic formulation are also derived but they are very specific for specific architectures. In addition, serial and parallel manipulators are differentiated also in the numerical evaluation of the workspace. Design issues make use of workspace algorithms and numerical evaluations but they still are not general and only in very specific cases they are formulated to show direct effect of the design parameters. A better insight of workspace characteristics is required to deduce better formulations both for analysis and design purposes in terms of computational efficiency and generality of solutions and results.

References

1. Ceccarelli M., *Fundamentals of Mechanics of Robotic Manipulation*, Kluwer/Springer, Dordrecht, 2004. (ISBN 1-4020-1810-X).
2. Ceccarelli M., "A Formulation for the Workspace Boundary of General N-Revolute Manipulators", *Mechanism and Machine Theory*, Vol.31, 1996, pp.637-646.
3. Castelli, G., Ottaviano, E., Ceccarelli, M.: A fairly general algorithm to evaluate workspace characteristics of serial and parallel manipulators. *Int J Mechanics Based Design of Structures and Machines*. 36, 14-33 (2008)
4. Ceccarelli, M.: On the workspace of 3R robot arms. In: *Proceedings 5th IFToMM International Symposium in Theory and Practice of Mechanism*, Vol. II-1, Bucharest, pp. 37–46 (1989)
5. Ottaviano, E., Ceccarelli, M., Lanni, C.: A characterization of ring void in workspace of three-revolute manipulators. In: *Proceedings of the 10 IFToMM World Congress on the TMM*, Vol.3, Oulu, pp. 1039–1044 (1999)
6. Ottaviano E., Husty M., Ceccarelli M., "Identification of the Workspace Boundary of a General 3-R Manipulator", *ASME Journal of Mechanical Design*, 2006, Vol.128, No.1, pp.236-242.
7. Ottaviano E., Ceccarelli M., Husty M., "Workspace Topologies of Industrial 3R Manipulators", *Int. Journal of Advanced Robotic Systems*, 2007, Vol. 4, No. 3, pp. 355–364
8. Corral Ch. Pinto, J., Herrero, S., Altuzarra, O., Ceccarelli, M.: A characterization of workspace of parallel manipulators with dynamic and operation features, 10 Cong. Iberoamericano de Ingeniería Mecánica, Oporto., pp. 501–509 (2011)
9. Ceccarelli M., "A Synthesis Algorithm for Three-Revolute Manipulators by Using an Algebraic Formulation of Workspace Boundary", *ASME Journal of Mechanical Design*, Vol. 117, June 1995, pp.298-302.
10. Ceccarelli M., "Designing Two-Revolute Manipulators for Prescribed Feasible Workspace Regions", *ASME Journal of Mechanical Design*, 2002, Vol., 124, pp.427-434.
11. Husty M., Ottaviano E., Ceccarelli M., "A Geometrical Characterization of Workspace Singularities in 3R Manipulators", *Advances in Robot Kinematics ARK2008*, Springer, Wien, 2008, pp. 411-418.
12. Ceccarelli M., Lanni C., "Multi-Objective Optimum Design of General 3R Manipulators for Prescribed Workspace Limits", *Mechanism and Machine Theory*, Vol. 39, N.2, pp.119-132, 2004.
13. Ceccarelli, M., Historical development of CATRASYS – a cable system. In: *IFToMM International Symposium on History of Machines and Mechanisms*, Amsterdam, May 2012. in: *Explorations in the History of Machines and Mechanisms*, Springer, Dordrecht (2012) (in Print)

The Force Reaction Control of the Wheel-Legged Robot's Limb Prototype

A. Gronowicz, J. Szrek and S. Wudarczyk

Abstract The wheel-legged robot is a vehicle with many degrees of freedom. Thanks to its peculiar design, the vehicle will use one of its ways of moving (travelling on wheels or walking), depending on the actual need. The paper presents a solution of the wheel-legged robot equipped with special designed limb kinematic system and first test of the control algorithms. The investigation has been done on the prototype of wheel-legged robot's limb.

Keywords Control system • Control algorithms • Mobile robot

1 Introduction

The mobile robots can be divided into several categories such as: flying robots, amphibious robots and land robots, depending on the environment in which they operate. The land robot's locomotion systems are based on caterpillar, wheeled and walking undercarriages and sometimes on their combinations.

A mobile robot with a wheel-legged suspension system combines the merits of the two designs, which allows the robot to move as a wheeled vehicle or, if necessary, as a walking machine [1].

The robot can move on wheels on an even terrain and when it encounters an obstacle which it cannot bypass like stairs [2], it will surmount it by walking on it or over it. By changing the configuration of its limbs the robot also can keep the platform level.

A. Gronowicz (✉) · J. Szrek · S. Wudarczyk
Wrocław University of Technology, Wrocław, Poland
e-mail: Antoni.Gronowicz@pwr.wroc.pl

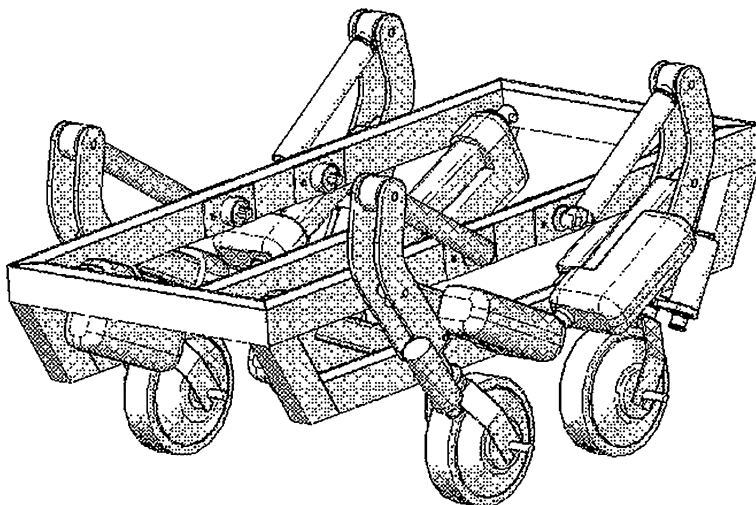


Fig. 1 3D model of wheel-legged robot being designed

The wheel-legged robots moving on wheels but also able to negotiate obstacles, known from the literature are: WorkPartner [3], Hylos [4], Roller-Walker [5]. Another idea of wheel-legged robot is LegVan [6–9]—robot built in the Division of Machine Theory and Mechatronical Systems at Wrocław University of Technology, Poland. Each of them has four wheels and is able to walk.

Controlling the wheel-legged robot is a complex task. The control system has many degrees of freedom and in order to function properly a considerable number of measurement data need to be acquired and processed and the motions of many drive motors need to be synchronized.

This paper presents single robot leg construction, whereby a series of preliminary control algorithm tests could be carried out. This is one of the stages in developing a prototype wheel-legged robot, which a 3D model of it is shown in Fig. 1.

2 Concept of the Robot's Limb Prototype

A view of the robot's limb is shown in Fig. 2. The limb comprises: a frame made from hollow sections, a set of servomotors with controllers, a supervising computer with communication interfaces, and a measuring system.

The supervising computer has a direct connection with a local control modules. Local modules are responsible for the execution of the desired motors movement and for taking all the measurements. All the calculations are made on supervising computer, which subsequently sends the proper parameters to the local controllers. The communication in the robot is fully controlled by the supervising computer.

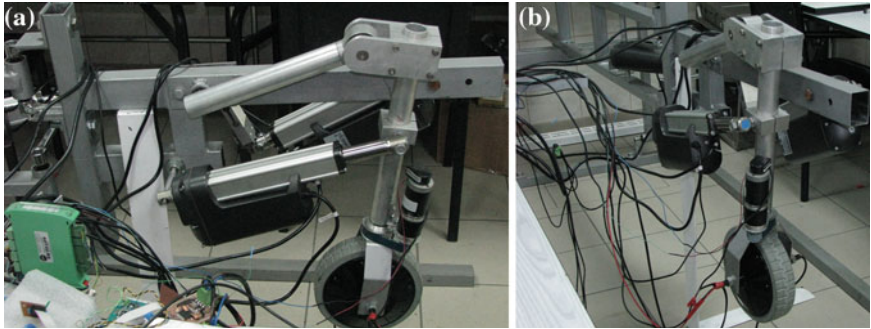


Fig. 2 View of the robot's limb

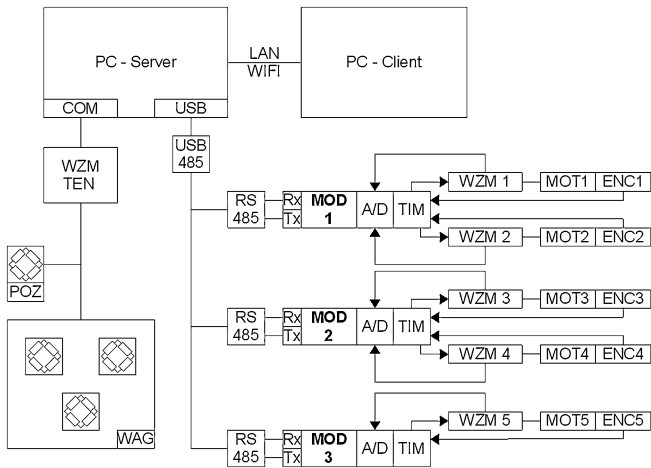


Fig. 3 Control system of the robot's limb prototype diagram

Having sent a request to a proper module, the supervising unit receives a specific amount of data (measurement data, motion parameters acceptance acknowledgement, etc.) dependent on the request sent. A diagram of the control system is shown in Fig. 3.

The local drive controller modules (MOD) are based on the STM32F103RbT6 microcontroller with the ARM Cortex core. The system has all the resources and peripherals necessary to control the motors (MOT) and take all the measurements (timer block (TIM), an analog to digital converter block (A/D)).

Position and speed are measured by incremental encoders (ENC) mounted on the axle of each of the drives. The position and rotational speed of the motor can be determined on the basis of pulse counts.

To measure wheel load (reaction of ground) a tensometric beam was employed. The beam also serves as a crank (Fig. 4) transforming servomotor elongation into

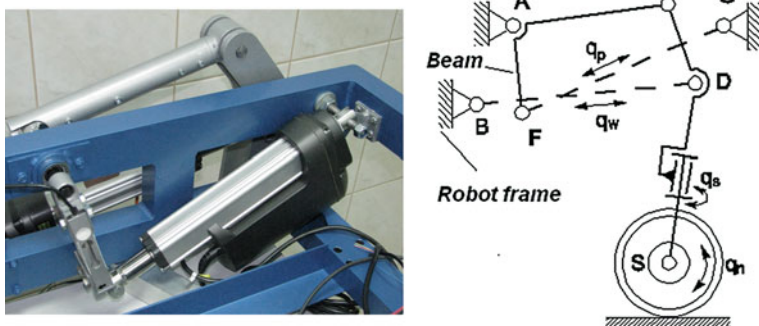


Fig. 4 Lifting drive with measuring beam and its kinematic scheme

the rotational motion of the leg for the lifting function. Owing to the fact that the sensor is part of the leg and is located on the crank it is possible to read the force directly connected with the pressure exerted by the leg on the ground and the force is not disturbed by any other components. The tensometric beam supplies information about wheel/ground contact loss instants, which is useful for negotiating obstacles by walking. Besides information about the deviation of the platform from the horizontal position is delivered by 2D digital accelerometer.

3 Force Reaction Control Algorithm

In order to verify the leg's mechanical part and its measuring, control and communication systems tests were carried out on the leg prototype. Among other things, the following were checked: the general and communication functionality the motor control algorithms parameters (PID), the measuring path and data interpretation. The tests showed the data readings to be correct and provided a basis for developing robot control algorithms.

The diagram in Fig. 5 shows the servomotor elongation and the force measured by the tensometric beam. A change in the sign of the force value represents an instant when the wheel loses contact with the ground. It appears from the data that the measuring system works correctly and the data can be used for the autonomous determination of the robot parameters.

The tensometric beam provides an information about ground force reaction. The robot, by changing the configuration of its limbs can change the pressure exerted by the limbs on the base, which should be constant (in a certain margin). The force reaction algorithm was tested by changing a current equilibrium, by activation of external pressure or elevation of the limb (simulation of uneven ground). At the current stage, the operation of this algorithm is based on a PD controller. The algorithm works as follows:

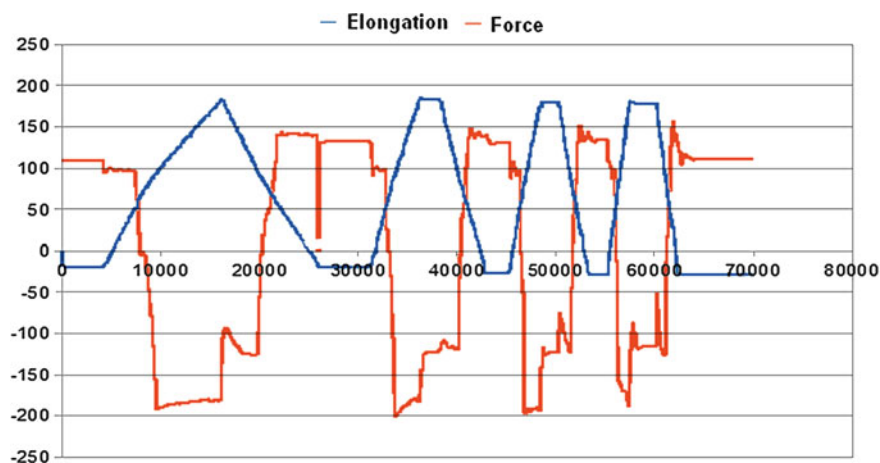


Fig. 5 The servomotor elongation and the force measured by the tensometric beam

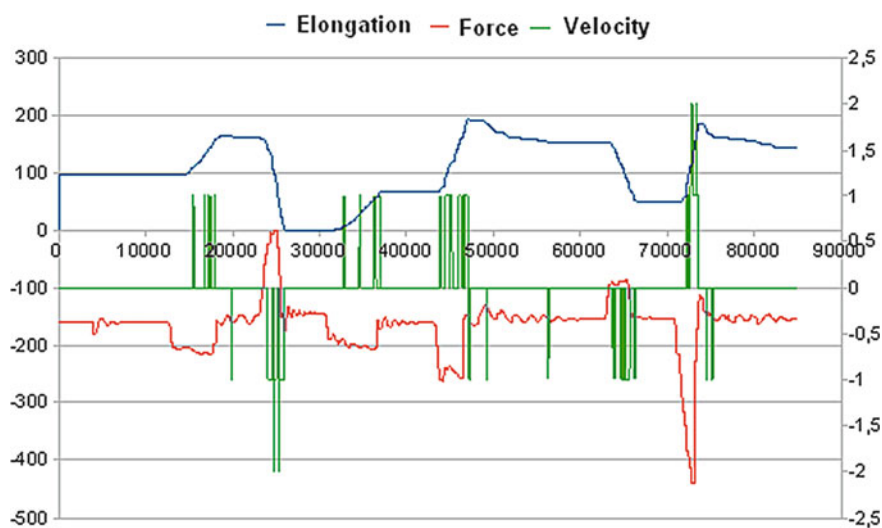


Fig. 6 The force reaction experiment measurement data

1. if the pressure $> \pm e$ (equilibrium), specify the drives and the direction of motion reducing deviation e ;
2. if $e > 0$, raise the limb; if $e < 0$, lower the limb;
3. if the pressure $< e$, stop the motion, return to 1.

The particular stages in the force reaction are shown in Fig. 6. Initially the limb is in equilibrium (wheel exerts stable pressure on the base). At some moment the sensors (beam) give information that current pressure is larger (14,000 ms).

If the pressure is larger, robot raises the limb to reduce the pressure. The opposite situation occurs in 24,000 ms—the pressure exerted on the base decreases and limb's position decreases. Figure 6 shows also the velocity of the actuator elongation.

4 Conclusions

The design and construction of the wheel-legged robot's limb with a complete control, communication and diagnosis system is the first step in research on wheel-legged robots. The presented experimental studies have proved the adopted mechanical structure and control system solutions to be correct. Further research should focus on application the force reaction system in each robot's limb and control it's stability. The two cases should be considered when the robot moves on four or three wheels—the negotiation of an obstacle.

Acknowledgments This research, under project no. N502 271037, was funded from the resources for science in the years 2009–2012 in Poland.

References

1. Bałchanowski, J., Gąsieniec, P.: Budowa i badania symulacyjne robota kroczącego. *Acta Mechanica et Automatica*. **4**(2), s. 9–16 (2010)
2. Gonzalez, A., Ottaviano, E., Ceccarelli, M.: On the kinematic functionality of a four-bar based mechanism for guiding wheels in climbing steps and obstacles. *Mech. Mach. Theor.* **44**, 1507–1523 (2009)
3. Grand, Ch., BenAmar, F., Plumet, F., Bidaud, Ph.: Stability control of a wheel-legged mini-rover. In: *Proceedings of the CLAWAR Conference*, 2004
4. Halme, A., Leppänen, I., Salmi, S., Ylönen, S.: Hybrid locomotion of wheel-legged machine. In: *Proceedings of the CLAWAR Conference*, 2000
5. Endo, G., Hirose, S.: Study on roller-walker (system integration and basic experiments). In: *Proceedings of the 1999 IEEE International Conference on Robotics and Automation*, Detroit, 1999
6. Gronowicz, A., Szrek, J.: Idea of a quadruped wheel-legged robot. *Arch. Mech. Eng.* **56**(3), 263–278 (2009)
7. Gronowicz, A., Szrek, J.: Design of LegVan wheel-legged robot's mechanical and control system, In: *Proceedings of the 10th IFToMM International Symposium on Science of Mechanisms and Machines, SYROM 2009*. Springer, Romania (2010)
8. Szrek, J.: Synteza układu kinematycznego i sterowania czworonożnego robota kołowo-kroczącego (Synthesis of the kinematic and control system of a quadruped wheel-legged robot), PhD Thesis, Wrocław (2009) (in Polish)
9. Szrek, J., Wójtowicz, P.: Idea of wheel-legged robot and its control system design, *Bull. Polish Acad. Sci. Tech. Sci.* **58**(1), s. 43–50 (2010)

Method for Planning the Finger's Movement in the Anthropomorphic Manipulator Hand-K3, Using a Tactile Sensors Network, with the Aim of Optimal Grasping

A. Handke and W. Twaróg

Abstract The work discusses the issue of planning movements in common plane of cooperating 4-DOF serial manipulators, of which the 28-DOF anthropomorphic manipulator Hand-K3 consists. On the basis of these studies are proposed guidelines in order to create algorithms for controlling the movements of each finger's segment. Based on the applied tactile sensors placed on all segments of the finger's modules, in order to obtain a reduction of computational time that is essential for planned movements during the grasping of an object of undetermined shape and in undefined position relative to manipulator's working space, the new criteria of control were determined.

Keywords Movement planning • Serial manipulator • Anthropomorphic • Tactile sensing

1 Introduction

Alongside with redundancy of degrees of freedom in finger modules of an anthropomorphic manipulators, the complexity of computing processes, controlling movements of the constrained joints are increasing. Therefore it has become necessary to minimize the amount of processed signals acquired from a tactile sensors network. In the developed model anthropomorphic Hand-K3 [1] manipulator there

A. Handke (✉) · W. Twaróg
Wrocław University of Technology, Wrocław, Poland
e-mail: artur.handke@pwr.wroc.pl

W. Twaróg
e-mail: wladyslaw.twarog@pwr.wroc.pl

are five finger modules each equipped with three joints capable of flexion and additional adductive joint. In order to achieve stable grasp of the manipulated object of unspecified shape and in unknown initial position relative to the manipulator's workspace, criteria for defining sufficient condition for optimal grasp were established.

2 Specifying Prehensile Criteria

To resolve this problem two approaches were determined: in planar and also in spatial system. In Hand-K3 manipulator four finger modules work in opposition to the fifth—thumb module, forming a four planes, hence the possibility to assume four pairs of cooperating 3 DOF planar manipulators. In spatial system finger modules in groups of 3 had to be allocated with fixed angles orientating planes, in which the last three bending joints are revolving. In each group a pair of modules was allocated to the fifth module, located opposite relatively to the metacarpus because the first four modules are characterized by their bending planes, which are by the limitation of the adductive joint almost parallel. By this procedure six tri-modular sets were distinguished.

2.1 Modules Operating in Common Plane

Considering two serial manipulators composed of three revolute pairs operating in opposition to each other, the arrangement of tactile sensors was applied according to Fig. 1a. In order to determine the minimum size of the transversal section of the manipulated objects a workspace had to be designated for the singled out pair of manipulators with uncoupled motions in the bending joints—Fig. 1b. Assuming that the object is in range of at least one of the modules—areas A or B, it is still possible to guide it to the common area of both modules—C area. Area D determines the minimum diameter of the circle circumscribed on the cross-section of the manipulated object, specifying practically the limitation parameters of grasped objects.

Specifying the minimal number of contact points between grasped object and sensory network of both finger modules, is crucial for designation of the full grasp criteria [2]. Considering manipulators cooperating in pair as a planar mechanism, the bending joints were assumed as class I kinematic pairs, and the points of contact with the object as class II pairs (point to surface constraint). It was possible to designate the number of contact points on the basis of the mobility of serial manipulators pair holding the object. Assuming that mobility of such mechanism is equal to the number of drives, as well as the number of revolute pairs and assuming that the number of links is greater by 1 than the quantity of both finger modules segments, the number of contacts is always 3. This is the optimal number

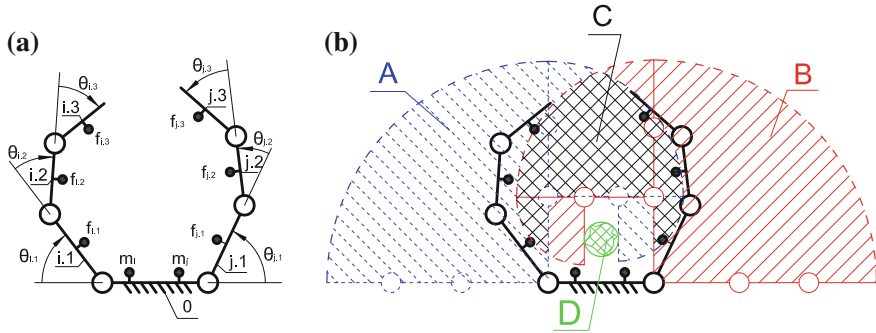


Fig. 1 **a** Kinematic structure 3DOF finger modules pair, **b** workspace of the finger modules pair

of detected signals in the distinguished pair of manipulators, allowing to determine the actual grasp of the object [3]. Moreover the number of contacts is independent from the number of revolute pairs. While distinguishing the general types of three-point contact variants between the object's surface and the sensory elements in established solutions, the two investigated finger modules have one sensor on each segment and additional sensor on the basis of each finger module (metacarpal sensor). To determine the optimal variant of the three-point grasp of the object, the full grasp probability parameter was assumed—Eq. (1), to determine the probability of obtaining optimal grasp of the object from among all the combinations of the three-point contacts registered by the sensory network.

$$P_v = \left(\frac{m}{v} \right) c_{n,1,v} \left(\frac{s}{n} \right)^{-1} 100 \% \quad (1)$$

where: $c_{n,1,v}$ —full grasp combinations, n —number of contacts, v —number of metacarpal sensors, m —all metacarpal sensors, s —all sensors.

During the estimation of all possible full grasp combinations for all grasping variants, a solution with a contact on only one finger module was excluded, due to the possibility of acquiring by the sensory network all three contacts on only one module, or between the metacarpal base, and one finger. This resulted from the necessity to use modules from both sides, in order to avoid the occurrence of passive constraints in case of double contact of the object with the metacarpus. Based on the results from the calculation of the situation with only one and without any contact with the metacarpal sensor, there is 64 % probability of a stable object grasp, assuming at least one contact on each of selected finger modules of the manipulator.

2.2 Three Modules Operating in Allocated Group

While analyzing the same problem in the spatial system, a group of three modules was assigned, forming two pairs analogically to the situation in a planar system. Again an optimal number of contact points between the assigned group and grasped object was designated, assuming similarly bending joints as class I kinematic pair and the points of contact with the object as class V pairs (point to surface constraint). The number of mobile links is still equal to the number of connections and active drives. Therefore, regardless of the configuration of the manipulator and the number of movable segments, six points of contact between the sensors and the object are required for the optimal grasp. The maximum number of combinations for the six-point grasp of the object in spatial system, was selected relative to twelve tactile sensors, including three located in the base of the group, one for each module. During the calculation of the probability parameter according to Eq. (1) one solutions was excluded, in which the object was located between only one finger module and the metacarpus. While detecting no metacarpal contacts, it was necessary to maintain the contact in at least one segment for all finger modules, analogically to planar problem. In spatial system study of the object grasping by the group of three modules, only 16 % of all six-point contact combination wasn't sufficient enough for a stable object grasp.

3 Movement Planning Method

While determining the movement planning method of Hand-K3 manipulator's finger modules, the main criterion was the minimization of the control units load. In the process of movement planning of individual revolute constraints, operating in the common plane, a priority was given for the closest joints to the metacarpus. This approach ensured the maximum use of modules' workspace and the increase in probability of guiding grasped object in range of greater number of fingers. A conditioning function (2) was designated for cease the movement of all drives, confirming as well the stable grasp of manipulated object. For this purpose, information were used acquired from sensory network, while determining the possible combinations of the three-point surface contact with the object, for at least two pairs of finger modules working in opposite orientation.

$$h(i,j) = \sum_{a=1}^3 f_{a,i} + \sum_{b=1}^3 f_{b,j} + H(m_i \cdot m_j) > 2 \quad (2)$$

where: $f_{a,i}$ —detected contact in a -segment of i - finger module, $f_{b,j}$ —detected contact in b -segment of j - finger module, m —detected contact in metacarpal sensor of a finger module, H —Heaviside step function.

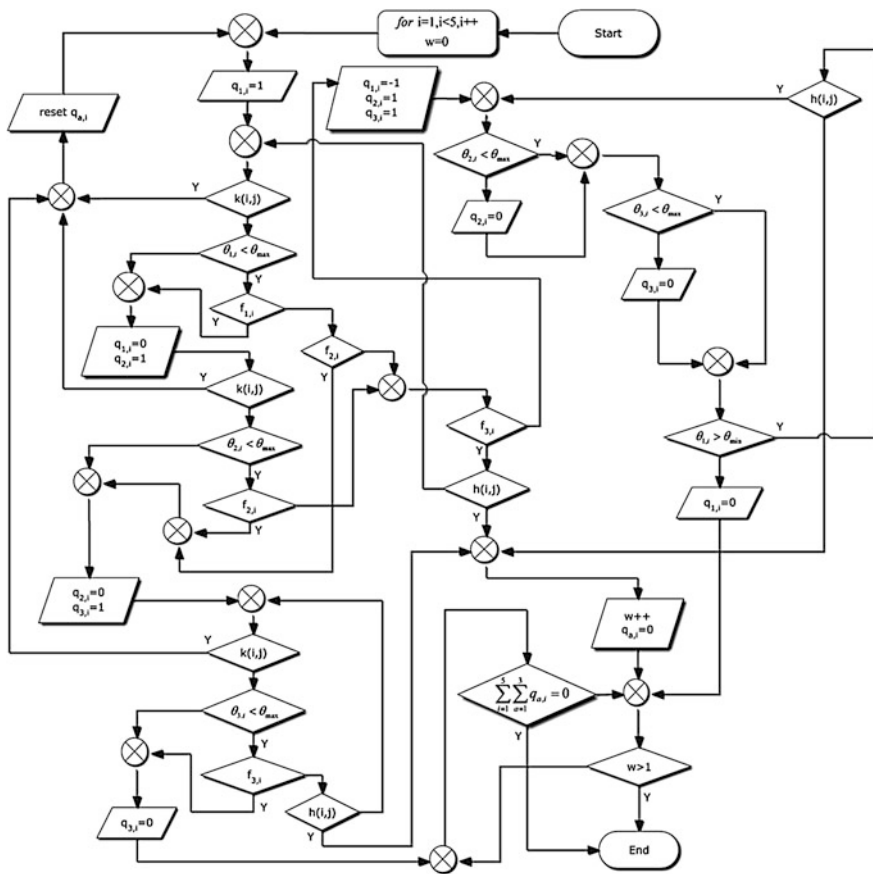


Fig. 2 Algorithm flowchart for finger module movement planning

This allowed to reduce the computational time necessary for verification of all possible contact combinations from 5,544 in spatial system (924 combination for each group) to only 224 (56 combinations for each pair). Referring to the criterion of grasp stability evaluation by two finger modules operating in a common plane, it was crucial to use the information from the middle segment and metacarpal sensors, which was included in KTH and manipulator [4], unlike in solutions limited to fingertip sensors [5]. The main algorithm operates interchangeably for the all fingers besides the thumb module, it stop all the drives after the fulfillment of a stable grasp condition, or exceeding the established time for finding the object. When the first pair of modules complies with the main stable grasp condition (2), only non-opposite module stops its drives, allowing the algorithm to find the second pair and satisfy the essential condition. The main movement planning algorithm scheme based on proposed criteria shows Fig. 2.

In addition to the basic processes assessing the interaction status of the tactile sensory network with the manipulated object, it was necessary to use a condition for movement priority of finger modules on the basis of the proposed criterion regarding the collision between the fingers (3). In the event of a collision, an algorithm for redeploying the finger modules is required [6].

$$k(i, j) = k_1(i, i + 1) + k_1(i, i - 1) + k_2(i, j) \quad (3)$$

where: k_1 —side collision of adjoining modules, k_2 —frontal collision of opposite modules.

4 Conclusions: Control Optimizing

While creating a movement planning algorithm for finger segments of the Hand-K3 manipulator, the main intention was above all to simplify the decision process, defining the further work of the manipulator. Because of the redundant nature of the multi-DOF and multi-finger anthropomorphic manipulators, there is increased risk of collision between the finger modules, in particular when they aren't working in parallel planes. Considering integrally such manipulators, makes it explicitly impossible to validate a proper and stable grasp. In addition, continuous monitoring of the collisions between finger segments and determining the movement priority of certain modules excessively overloads the control units. Striving to minimize the amount of acquired sensory measurements necessary to determine a stable grasp, enabled the energy consumption reduction of non driving components. Such an approach to control the movements of individual segments will find practical application for anthropomorphic manipulators in prosthetics.

Acknowledgments The research work reported here was developed within the research project: *Prehensile parameters and efficiency studies of the Hand-K3 manipulator prototype* (N N514 676740) founded by the National Science Center in Krakow.

References

1. Handke, A., Twaróg, W.: Correlation of the sensory parameters' mathematic models with the kinematic structure of the HAND-K3 hand type manipulator. *Acta Mechanica et Automatica* **4**(3), (2010)
2. Roa, A., Argus, M.J., Leidner, D., Borst, C., Hirzinger, G.: Power grasp planning for anthropomorphic robot hands. In: *Proceedings of International conference on Robotics and Automation*, 2012
3. Bicchi, A.: Hands for dexterous manipulation and robust grasping: a difficult road toward simplicity. *IEEE Trans. Robot. Autom.* **16**(6), 652–662 (2000)
4. Tegin, J., Iliev, B., Skoglund, A., Kragic, D., Wikander, J.: Real life grasping using an under-actuated robot hand—simulation and experiments. In: *IEEE 14th International Conference on Advanced Robotics*, vol 1–2, pp. 366–373, 2009

5. Borst, C., Fischer, M., Herzinger, G.: Calculating hand configurations for precision and pinch grasps. In: Proceedings of IEEE/RSJ International Conference on Intelligent Robots and Systems, pp. 1553–1559, 2002
6. Hasegawa, T., Murakami, K., Matsuoka, T.: Grasp planning for precision manipulation by multifingered robotic hand. In: Proceedings of IEEE International Conference on Systems, Man, and Cybernetics, vol. 6, p. 762–767, 1999

Part IV

Robots and Manipulators

Development of Spherical Ultrasonic Motor as a Camera Actuator for Pipe Inspection Robot

M. Hoshina and S. Toyama

Abstract In this paper we present a driving system and control method of newly developed spherical ultrasonic motor (SUSM) as a camera actuator for pipe inspection robot. The pipe inspection robot using SUSM that is very small actuator with three rotational degrees of freedom (DOF) can be inserted to the inside of pipe of 50 mm in diameter. The novel SUSM has improved the range of movement compared to previous SUSM. The robot can point a camera in any direction.

Keywords Ultrasonic motor • Pipe inspection • Robot • Actuator

1 Introduction

Many research groups have attempted the development the compact pipe inspection robot with new actuation to see a flaw and rust on the pipe directory [1–3]. Pipe inspection devices using a camera with fish-eye lens has a problem not to show a detail of condition. Pneumatic actuators [1–3], shaped memory alloy (SMA) [4], piezoelectric actuators [5, 6], giant magnetostrictive alloy, have been employed to incline the head with camera in the robots. Pneumatic wobble motor, compact and flexible actuator, rotates the camera and hands of the robot. Snake robots, the aim of which can be to move in a pipe, also has camera at the head of

M. Hoshina (✉) · S. Toyama

Tokyo University of Agriculture and Technology, Tokyo Noko Daigaku,
3-8-1 Harumi-cho, Fuchu-shi, Tokyo, 183-8538 Japan
e-mail: hoshina@cc.tuat.ac.jp

S. Toyama

e-mail: toyama@cc.tuat.ac.jp

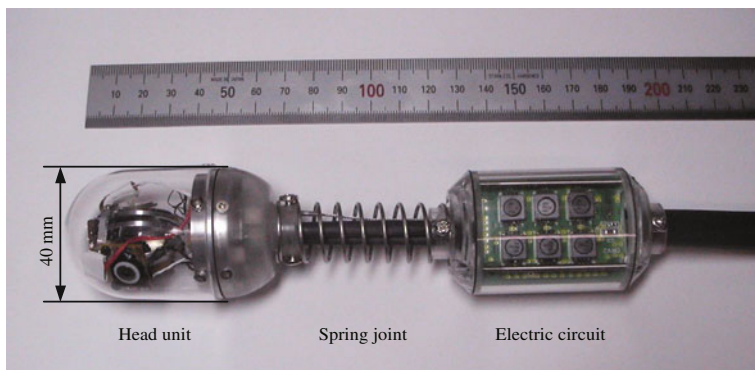


Fig. 1 Schematic of the pipe inspection robot, the *left side* includes camera actuator and position sensor, the *right side* includes driving circuit for the actuator and processing circuit for sensors

the robot and can incline the head. Dual drive actuators designed to allow for the deployment and retraction of three arms with wheels can push and pull the robot in a pipe.

We have developed a pipe inspection robot using a spherical ultrasonic motor (SUSM) [7–10] as the camera actuator, aimed to inspect a pipe of 50 mm in inner diameter. The robot has three rotational DOF and position sensing system compact enough to be inserted to a pipe. Because the robot is able to point a camera at any directions, the robot can directly observe flaws and corroding and enables us to accurately determine flaw's size and condition. Figure 1 shows the schematic of the pipe inspection robot. Left side of the robot includes the SUSM as a camera actuator and a three-dimensional sensing system using three rotary potentiometers. The right side includes the driving circuit for the SUSM and processing circuit for the sensing system.

2 Spherical Ultrasonic Motor

The motion of SUSM composed of three ring-shaped vibrators and one sphere are geometrically described. The vibrator consists of annular metallic elastic body, to which piezoelectric elements are glued. When an AC voltage is applied to piezoelectric elements, a standing-wave is generated on the elastic body. When two AC voltages with a time phase difference are applied to the positive and negative sections of piezoelectric elements, a traveling-wave is generated due to combination of the two standing-waves [7]. The vibrators provide vibration energy to the sphere by the elliptical motion generated by the traveling-wave. We can control the magnitude and direction of the torque by changing the phase difference. The relationship between the torque T and the phase difference ρ in a single vibrator is approximated by the following equation.

$$T = A \sin \rho \quad (1)$$

where A is the maximum value of the torque. The torque of the SUSM is determined by the resultant vector of the vibrators. Figure 2a and b show the locations of the vibrators and the sphere. The component of the resultant vector generated by each vibrator, S_1 , S_2 and S_3 are described by the following equations:

$$\begin{aligned} S_1 &= T_1 \begin{bmatrix} \cos \frac{3}{2} \pi \cos \phi & \sin \frac{3}{2} \pi \cos \phi & \sin \phi \end{bmatrix}^T \\ S_2 &= T_2 \begin{bmatrix} \cos \frac{5}{6} \pi \cos \phi & \sin \frac{5}{6} \pi \cos \phi & \sin \phi \end{bmatrix}^T \\ S_3 &= T_3 \begin{bmatrix} \cos \frac{1}{6} \pi \cos \phi & \sin \frac{1}{6} \pi \cos \phi & \sin \phi \end{bmatrix}^T \end{aligned} \quad (2)$$

where T_1 , T_2 and T_3 are scalar of each vibrator. ϕ is the angle with the X–Y plane as shown in Fig. 2b. The resultant vector that the torque generated by SUSM S is described as follows:

$$S = S_1 + S_2 + S_3 \quad (3)$$

Here, torque of the SUSM has three rotational degrees of freedom. By controlling the torque of each vibrator, the SUSM generate the torque between the outer case and the sphere.

3 Experiment of Spherical Ultrasonic Motor

We propose a new hybrid control method using the phase differences for the direction control, and using the frequencies for speed control. The input phase differences are obtained from Eqs. (1) and (3). The input frequencies of each vibrator are similarly varied from the resonant frequencies without varying the phase differences. The torque of the SUSM is varied with the ratio of torques of each vibrator kept. Therefore, we can vary the rotational speed without varying the rotational direction. In the experiment to evaluate this control method, the phase differences of three vibrators were 0, 60 and -60° to rotate the SUSM around only X axis. We varied the input frequencies by 0.55 kHz from the resonant frequencies, and measured the rotational speed and angle error from the desired angle. Figure 3 shows the results, which indicate that the rotational speed decreased gradually as the input frequencies increased from the resonant frequencies. In addition, the angle error did not increased at low speed. Consequently, this hybrid control method of frequencies and phase differences was effective.

The SUSM was returned to the default position using the hybrid control method. The rotational direction of SUSM is decided by the position sensing system. The input phase differences are determined by Eqs. (1) and (3). The rotational speed of SUSM is controlled using Proportional-Integrate (PI) controller. The control

Fig. 2 Location of the vibrators. **a** X–Y plane. **b** X–Z plane

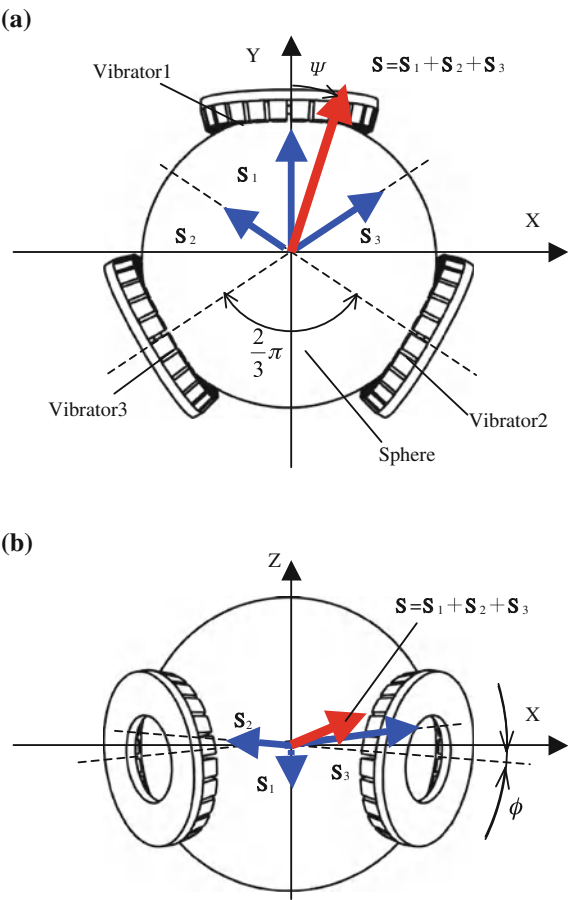
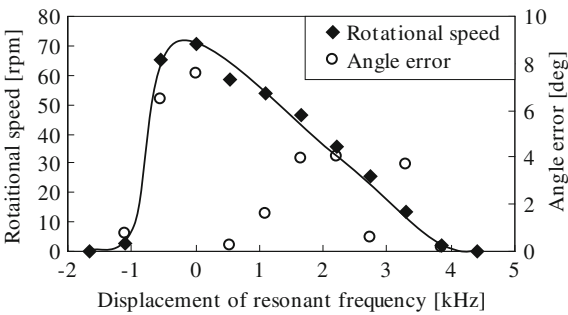
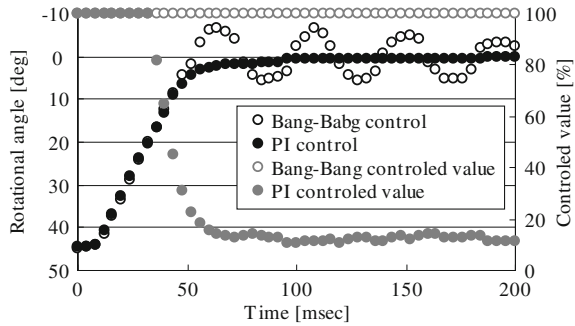


Fig. 3 Relationship between frequency and rotational speed



variable is the value of the frequency differed from the resonant frequency. The rotational speed becomes the maximum when the input frequencies are the resonant frequencies. It is changed in proportion to the frequency difference by Fig. 3.

Fig. 4 Results of return to default position using Bang–Bang control and PI control



Therefore, the controlled value is 100 % when the frequency difference is 0 kHz. The controlled value MV is described as follows:

$$MV_n = MV_{n-1} + K_P(e_n - e_{n-1}) + K_I e_n \quad (4)$$

Here, MV_n and MV_{n-1} mean the controlled variable of the n th times and $n - 1$ th times. e_n and e_{n-1} mean the angle errors from the default position of the n th times and $n - 1$ th times. K_P is proportional gain. K_I is integral gain.

We conducted the experiment of returnability of the SUSM from the position whose angle distance was 45° to the default position using the PI control and the Bang–Bang control whose controlled value is always 100 %, and measured the rotational angle and the controlled value. Figure 4 shows the results. These results show that the PI control reduced the overshoot and eliminated steady-state error.

4 Conclusions

In this study, we developed the motor driving system and the hybrid control strategy using the phase differences and frequencies of applied voltages to move to desired directions. The pipe inspection robot can be inserted to the interior of a 50 mm inner diameter pipe. Using the driving system with sensing system, the SUSM could return to default position within accuracy of 1° .

References

1. Fukuda, T., et al.: Rubber gas actuator driven by hydrogen storage alloy for in-pipe inspection mobile robot with flexible structure. In: Proceedings of the IEEE International Conference on Robotics and Automation (ICRA 1989), p. 1847 (1989)
2. Anthierens, C., et al.: Design of an electro pneumatic micro robot for in-pipe inspection. In: Proceedings of the IEEE International Symposium on Industrial Electronics (ISIE 1999), p. 968 (1999)

3. Chang-Hwan, C., et al.: Feeder pipe inspection robot using an inch-worm mechanism with pneumatic actuators, In: Proceedings of the IEEE International Conference on Robotics and Biomimetics (ROBIO 2004), p. 889 (2004)
4. Brunete, A., et al.: Modular multiconfigurible architecture for low diameter pipe inspection microrobots. In: Proceedings of the IEEE International Conference on Robotics and Automation (ICRA 2005), p. 490 (2005)
5. Matsuoka, T., et al.: A prototype model of micro mobile machine with piezoelectric driving force actuator. In: Proceedings of 5th International Symposium on Micro Machine and Human Science, p. 47 (1994)
6. Idogaki, T., et al.: Characteristics of piezoelectric locomotive mechanism for an in-pipe micro inspection machine. In: Proceedings of the Sixth International Symposium on Micro Machine and Human Science (MHS 1995), p. 193 (1995)
7. Toyama, S., et al.: Multi degree of freedom spherical ultrasonic motor. In: Proceedings. IEEE International Conference on Robotics and Automation (ICRA1995), p. 2935 (1995)
8. Purwanto, E., Toyama, S.: Control method of a spherical ultrasonic motor. In: Proceedings of IEEE/ASME International Conference on Advanced Intelligent Mechatronics (AIM 2003), p. 1321 (2003)
9. Mashimo, T., et al.: Development of a spherical ultrasonic motor with an attitude sensing system using optical fibers. In: Proceedings of the IEEE International Conference on Robotics and Automation (ICRA 2007), p. 4466 (2007)
10. Mashimo, T., et al.: Development of an MRI compatible surgical assist manipulator using spherical ultrasonic motor (1st report)-prototype of the spherical ultrasonic motor. J. Jpn. Soc. Precis. Eng. **73**(2), 275 (2007)

Research on Multi-Directional Pose Accuracy Variation to a Welding Robot

V. Vacarescu, E. Ch. Lovasz and C. F. Buciuman

Abstract Evaluation of functional characteristics of industrial robots is one aspect of their development. If one examines the many robotic applications, it is found that in most cases the performance characteristics involve aspects of positioning and orientation. Parameter analyzed in this paper refers precisely to this type of performance. In the robotics field, there are different methods and techniques in order to determine the performance characteristics of the industrial robots. In this paper the authors used a method for measuring and evaluating multi-directional pose accuracy variation performance for a welding robot, through 3D triangulation with two digital theodolite. For this purpose it uses a calibrated cube, mounted on the robot end—effector. The method allows the determination of the performances in concordance with the ISO 9283 recommendations and is validated of experimentally researches.

Keywords Robot • Theodolite • Accuracy • Triangulation • Performances

1 Introduction

Optimizing robotics processes needs an analysis of the performances of the robot involved in the process, in order to improve these performances by calibrating the robot. Analyzing the performance characteristics of industrial robots, it appears

V. Vacarescu (✉) · E. Ch. Lovasz · C. F. Buciuman
Politehnica University of Timisoara, Timisoara, Romania
e-mail: valeria.vacarescu@mec.upt.ro

E. Ch. Lovasz
e-mail: erwin.lovasz@mec.upt.ro

C. F. Buciuman
e-mail: cella_buciuman@yahoo.com

that most of them are reduced to matters of pose (positioning and orientation). In this paper, the authors present a theoretical and experimental research of the performance parameter “multi-directional pose accuracy variation”, which refers exactly to this category of performances. In the robotics field, there are different methods and techniques in order to determine the performance characteristics of the industrial robots. So, in [1] it is used a laser interferometer system for assessing the positioning performance of a six-axis industrial serial robot. In [2] is presented the performance characteristics of robots and the test methods. In [3], the authors propose an automatic partial pose measurement system with theodolite for robot calibration. The system is used only for positioning characteristics having a spherical illuminated target. This paper brings some additional clarifications regarding the definition of multi-directional pose accuracy variation. The experimental evaluation of this pose performance characteristic, was made for a welding robot type Cloos-Romat, using an optical method with two digital theodolite and a calibrated cube. The algorithm for this method was presented by the authors in [4]. Measurements were made in accordance to the ISO 9283-1998 standard, [5].

2 Multi-Directional Poses Accuracy Variation

Command pose is specified by teach programming. Multi-directional pose accuracy variation (vAP), define the maximum deviation between the different mean poses attained of the TCP point of robot (barycentre of the cluster of attained points), achieved for the same command pose, n times repeated, from three perpendicular direction, Fig. 1. The three perpendicular directions are parallel with the axes of base coordinate system. vAP expresses by:

– *Multi-directional positioning accuracy variation*(vAP), represents the maximum distance between barycentres of the cluster of points attained of the robot TCP, for the command TCP pose, after completion of n times of three different directions (usually perpendicular). vAP is determined by the relation (1):

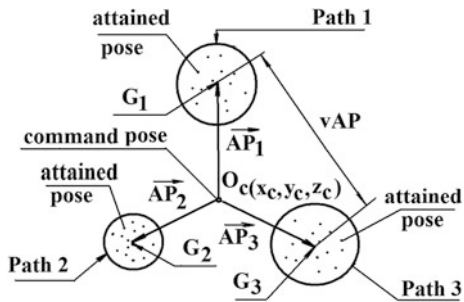
$$vAP = \max_{h,k=1}^3 \sqrt{(\bar{x}_h - \bar{x}_k)^2 + (\bar{y}_h - \bar{y}_k)^2 + (\bar{z}_h - \bar{z}_k)^2} \quad (1)$$

the points $\bar{x}_{h(k)}$ $\bar{y}_{h(k)}$ $\bar{z}_{h(k)}$ are the coordinates of the barycenter of the cluster of attained points, obtained at the extremity of the direction h or k ($h, k = 1, 2, 3$), n times repeated. Vectorial, vAP can be expressed by the relation (2):

$$vAP = \max_{h,k=1}^3 |\bar{A}\vec{P}_h - \bar{A}\vec{P}_k| \quad (2)$$

where: $\bar{A}\vec{P}_h$ ($\bar{A}\vec{P}_k$) is the pose vector of the barycenter G_h of the cluster of attained points at the extremity of the direction h (k), in relation with the commanded pose $O_C(x_C, y_C, z_C)$. $\bar{A}\vec{P}_h$ ($\bar{A}\vec{P}_k$) is calculated with the relation (3):

Fig. 1 Multi-directional positioning accuracy variation



$$\vec{AP} = (\bar{x} - x_c) \cdot \vec{u} + (\bar{y} - y_c) \cdot \vec{v} + (\bar{z} - z_c) \cdot \vec{w} \quad (3)$$

with \vec{u} , \vec{v} , \vec{w} —the unit vectors of the reference system axis attached to the commanded pose O_c .

– *Multi-directional orientation accuracy variation* (vAP_a , vAP_b , vAP_c) is expressed as the maximum angular deflection between the medium values of the angular orientations achieved, going through n times on different directions (usually 3), for the same commanded orientation, Fig 2. This is determined in the relations (4):

$$\begin{aligned} vAP_a &= \max_{h=1}^3 \left[\max_{k=1}^3 (\bar{a}_h - \bar{a}_k) \right] \\ vAP_b &= \max_{h=1}^3 \left[\max_{k=1}^3 (\bar{b}_h - \bar{b}_k) \right] \\ vAP_c &= \max_{h=1}^3 \left[\max_{k=1}^3 (\bar{c}_h - \bar{c}_k) \right] \end{aligned} \quad (4)$$

3 Method and Experiments

In order to perform measurements, the welding robot Cloos-Romat was equipped with a test body, a calibrated cube, having its side of 50 mm. To be easily spotted against the décor, the cube has white reflective sides, and the tip target is marked with 1. For measurements have been used two digital theodolite Rec-Elta, produced by Carl-Zeiss, Fig. 3.

The basic measurement principle is simple: the calibrated cube is being fixed on the robot end-effector. A cube's corner (characteristic point $TCP \equiv N1$) is targeted by both of the theodolite, T_1 and T_2 . The corner is located at the intersection of two sighting lines. Measuring the two sighting lines angles in horizontal plane ($\alpha_H \equiv H_z$) and in vertical plane ($\alpha_V \equiv V$), with the two theodolite, and then using the topographical triangulation method, are determined the coordinates of the targeting point. These coordinates are expressed in relation to an axis system

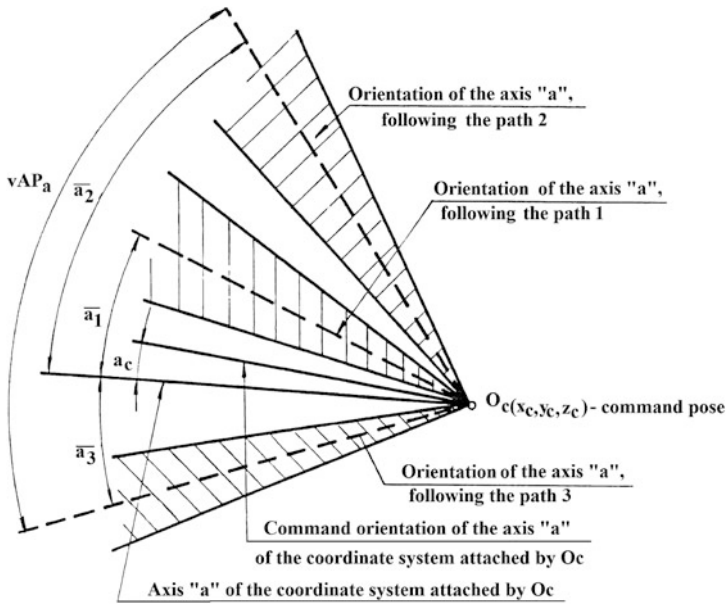


Fig. 2 Multi-directional orientation accuracy variation

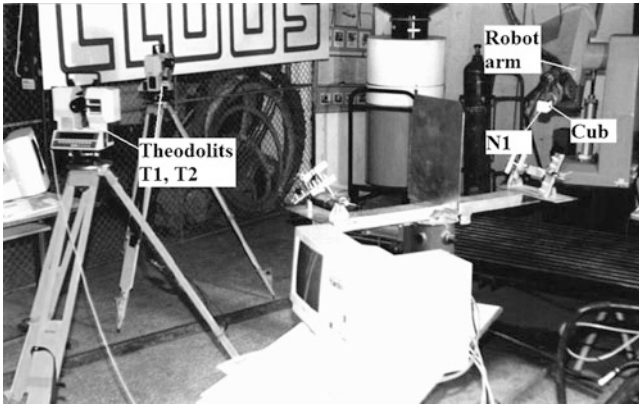


Fig. 3 Experimental stand

related to one of the theodolite, respectively T1. The origin of this axis system is the optical center of the theodolite T1. Because it is necessary to know the optical center position of the second device, in order to calculate the targeted points, this was determined through reciprocal sighting between the two theodolite. In this manner, are determined the optical center coordinates of theodolite T₂ (0; 5.98592; 0.02721) reported with T₁. It is noted that these coordinates are expressed in [m]. The measurement unit is selected from the initial menu of the program. In order to

Table 1 The coordinate x, y, z, of the attained positions for path1, path2, path3

Path 1			Path 2			Path 3		
x [m]	y [m]	z [m]	x [m]	y [m]	z [m]	x [m]	y [m]	z [m]
7.04939	1.82838	2.11029	7.04915	1.82821	2.11011	7.04968	1.82915	2.11055
7.04945	1.82859	2.11002	7.04961	1.82832	2.11048	7.04965	1.82872	2.11038
7.04942	1.82847	2.11021	7.04925	1.82805	2.11032	7.04928	1.82835	2.11025
7.04931	1.82853	2.11015	7.04915	1.82879	2.11048	7.04939	1.82842	2.11062
7.04928	1.82831	2.11049	7.04912	1.82835	2.11055	7.04958	1.82841	2.11041
7.04935	1.82825	2.11019	7.04925	1.82868	2.11024	7.04991	1.82905	2.11059
7.04936	1.82857	2.11035	7.04931	1.82848	2.11079	7.04948	1.82858	2.11078
7.04948	1.82865	2.11048	7.04935	1.82865	2.11071	7.04915	1.82855	2.11045
7.04924	1.82844	2.11045	7.04952	1.82871	2.11052	7.04955	1.82872	2.11062
7.04943	1.82829	2.11015	7.04035	1.82849	2.11055	7.04958	1.82861	2.11075

Table 2 Relationship calculation (ISO 9283:1998 and [4])

Characteristics	Relationship calculation
Command pose	$(x_{N1c}, y_{N1c}, z_{N1c})$
Attained pose	$(x_{kj}, y_{kj}, z_{kj}); \quad j = 1 \div 10 \quad k = 1 \div 3$
Mean of coordinates x attained	$\bar{x}_{kj} = \frac{1}{10} \sum_{j=1}^{10} x_{kj}$
Mean of coordinates y attained	$\bar{y}_{kj} = \frac{1}{10} \sum_{j=1}^{10} y_{kj}$
Mean of coordinates z attained	$\bar{z}_{kj} = \frac{1}{10} \sum_{j=1}^{10} z_{kj}$
Distance between mean positions attained (1-2)	$D_1 = \left[(\bar{x}_1 - \bar{x}_2)^2 + (\bar{y}_1 - \bar{y}_2)^2 + (\bar{z}_1 - \bar{z}_2)^2 \right]^{1/2}$
Distance between mean positions attained (1-3)	$D_2 = \left[(\bar{x}_1 - \bar{x}_3)^2 + (\bar{y}_1 - \bar{y}_3)^2 + (\bar{z}_1 - \bar{z}_3)^2 \right]^{1/2}$
Distance between mean positions attained (2-3)	$D_3 = \left[(\bar{x}_2 - \bar{x}_3)^2 + (\bar{y}_2 - \bar{y}_3)^2 + (\bar{z}_2 - \bar{z}_3)^2 \right]^{1/2}$
Multi-directional pose accuracy variation	$vAP = \max (D_1, D_2, D_3)$

determine the vAP characteristic, have been performed a set of measurements for a commanded pose. The proximity of this position is done on three different directions parallel to the axis of the reference system. It is mentioned that has been targeted only the tip 1 of the calibrated cube (robot TCP) because was considered only the aspect of pose. All tests were conducted as recommended by ISO 9283: 1998 [5]. The coordinates x, y, z, of the robot's TCP, respectively by the cube's N_1 tip, are given in Table 1.

The processing of the experimental results was performed using the presented algorithm in [4]. The calculations for this are systematized in Table 2. The commanded pose coordinates are: $x_{N1c} = 7.04935$ m; $y_{N1c} = 1.82844$ m; $z_{N1c} = 2.11058$ m. By processing data from Table 1 using the expressions in Table 2 the value of multi-directional pose accuracy variation for analyzed robot is: $vAP = 0.0004$ m.

4 Conclusions

In this paper the authors used a simple method for measuring and evaluating vAP for the robot Cloos—Romat, through 3D triangulation with two theodolite. There are two contributions in this paper: the first one is that it brings additional clarifications regarding the defining of the multi-directional pose accuracy variation; the second contribution is the validation of the method for determining the vAP characteristic using two digital theodolite by the results of the tests conducted. In the future, the authors propose the development of the method and algorithm also in medical applications (positioning system for HIFU, anthropometric measurements etc).The research work presented in this paper were made using a robot Cloos—Romat in the Robotics Laboratory of the University “Politehnica” of Timisoara. It is specified that the experiments presented in the paper is part of a protocol of several measurements of the robot’s performance characteristics.

References

1. Slamani, M., Nubiola, A., Bonev, I.: Assessment of the positioning performance of an industrial robot. *Ind. Rob.: An Int. J.*, **39**, 1, 57 (2012)
2. Dombre, E., Khalil, W.: *Robot manipulators: modeling, performance analysis and control*. ISTE Ltd., London (2007)
3. Morris, R., Uday, S. Robot calibration using an automatic theodolite. *Int. J. Adv. Manuf. Technol.* **9**, 114 (2005)
4. Vacarescu, V., Vacarescu, C.F., Argesanu, V., Draghici, A.: An optical method for the robot’s performances testing. *Proceedings of the 20th international DAAAM symposium*, **20**, 807 (2009)
5. ISO 9283: *Manipulating industrial robots. Performance criteria and related test methods*. ISO, Geneva (1998)

Part V

Biomechanics

Inverse Dynamics Model for the Ankle Joint with Applications in Tibia Malleolus Fracture

E. Budescu, E. Merticaru and M. Chirazi

Abstract The paper presents a biomechanical model of the ankle joint, in order to determine the force and the torque of reaction into the articulation, through inverse dynamic analysis, in various stages of the gait. Thus, knowing the acceleration of the foot and the reaction force between foot and ground during the gait, determined by experimental measurement, there was calculated, for five different positions of the foot, the joint reaction forces, on the basis of dynamic balance equations. The values numerically determined were compared with the admissible forces appearing in the technical systems of osteosynthesis of tibia malleolus fracture, in order to emphasize the motion restrictions during bone healing.

Keywords Biomechanics • Dynamic model • Ankle • Inverse dynamic analysis

1 Introduction

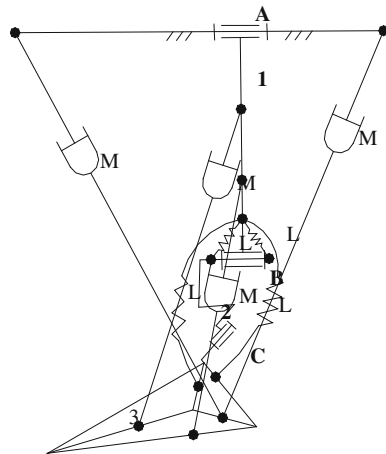
The biomechanics of articular prosthesis and implants for osteosynthesis of fractures uses inverse dynamic analysis aiming to determine the articular reaction forces, knowing the motion parameters of the analyzed segments. Due to the fact

E. Budescu (✉) · E. Merticaru
Technical University of Iasi, Iasi, Romania
e-mail: emil.budescu@gmail.com

E. Merticaru
e-mail: eugenmerti@yahoo.com

M. Chirazi
Al. I. Cuza University Iasi, Iasi, Romania
e-mail: chirazim@gmail.com

Fig. 1 Biomechanical structural model of the shank-foot



that muscular forces, ligaments stresses or viscous friction forces from the synovial liquid can not be marked out for any position of body motion, it is resorting to the method of reducing the internal forces to a unique resultant which is acting on a certain point. In this way there are determined the internal reaction forces and the muscular torque, similar to the motor torque from the theory of mechanisms, on the basis of neglecting the external forces excepting the gravity force and knowing the motion of each element and the reaction forces between the analyzed segments and the environment [1].

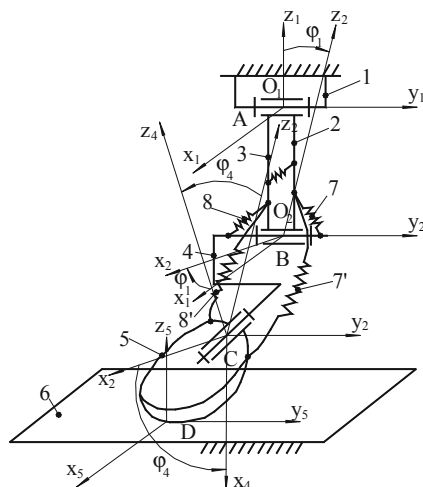
In the case of human lower limb, the dynamic model depends of the type of considered structural model, respectively the elements corresponding to body segments, the joints complexity, the number of muscles acting the body segments and the presence or absence of ligaments. Thus, starting from elementary structural models, such as the simple pendulum used for analysis of the orthostatic balance or locomotion [2, 3], there can come to complex structural models, planar or spatial, with or without muscular acting, with or without ligamentary links [4–8].

The goal of this paper is to present a dynamic model of the ankle joint, based on the dynamic balance equations of d'Alembert, with which the inverse dynamic analysis is performed to determine the articular reaction force, and that force is compared with the maximum force required to destroy an implant for osteosynthesis, in the case of tibial malleolus fracture.

2 Definition of the Structural Model of the Ankle Joint

The structural or physical model of the assembly shank-foot, used for the biomechanical analysis, is represented in Fig. 1. The notations used in Fig. 1 have the following signification:

Fig. 2 Definition of geometrical angular parameters

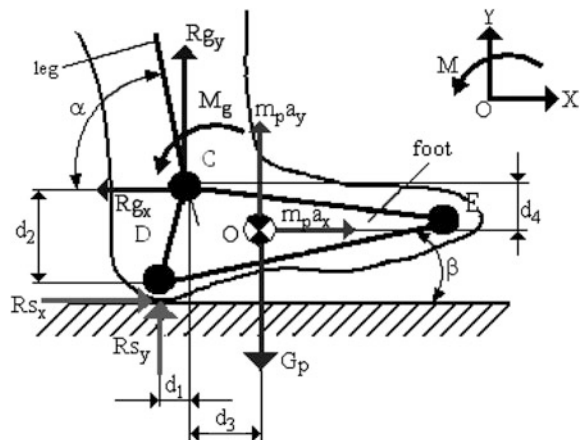


- 1, 2, 3—represent the shank, the talus and respectively the calcaneus together with the foot;
- A, B, C—represent the joints of the knee, talocrural joint and respectively the talocalcaneus joint;
- L, M—represent the main anterior, posterior and lateral ligaments and respectively the main muscular groups which realize the motions of dorsal-plantar flexion and eversion-inversion of the foot with respect to the shank.

The same structural model, but in which the shank is detailed represented by tibia and fibula, the foot is in contact with the ground and the muscular groups are not appearing, can be seen in Fig. 2. In this case were used the notations:

- 1—thigh; 2—tibia; 3—fibula; 4—talus; 5—calcaneus-foot assembly; 6—ground;
- 7, 7', 8, 8'—medial and external collateral ligaments;
- A—knee joint; B—talocrural joint; C—talocalcaneus joint; D—the contact between foot and ground (external link);
- $(x_1 O_1 y_1 z_1)$ —fix triorthogonal reference system with the origin in knee joint, with the medio-lateral axis $O_1 y_1$, vertical axis $O_1 z_1$ and the axis $O_1 x_1$ completes the right triorthogonal system (antero-posterior);
- $(x_2 O_2 y_2 z_2)$ —mobile triorthogonal system solidar with the shank (elements 2 and 3), with the origin in the talocrural joint and with the possibility to perform the flexion-extension motion of the shank with the angle ϕ_1 ; rotation of the shank is performed around the medio-lateral axis $O_1 y_1$, the axes $O_1 y_1$ and $O_2 y_2$ remaining parallel;
- $(x_4 O_4 y_4 z_4)$ —mobile triorthogonal system solidar with the talus (element 4), with the origin in the talocalcaneus joint (C), where the axis y_4 is perpendicular to the axis y_2 and around of which the foot can perform the motion of eversion-inversion; the angle of rotation of eversion-inversion was denoted with ϕ_4 ;

Fig. 3 The scheme of mechanical loading of the foot



- $(x_5O_5y_5z_5)$ —mobile triorthogonal system solidar with the assembly calus-foot, with the origin in the point of contact of the foot with the ground (D), respectively the external link between the foot and the ground.

The ankle joint was represented in this structural model by two kinematic joints of rotation, with perpendicular axes, denoted B and C, necessary to ensure the motion of plantar–dorsal flexion and eversion–inversion motion.

3 Articular Biomechanical Dynamic Model

In order to determine the reaction force in the ankle joint, the method of body isolation was used, the motion equations for the foot being written for different positions of that with respect to the ground, during the gait. Taking into account the notations in Figs. 3 and 4, for the position of initial contact of the heel on the ground, the components of the reaction forces in the ankle were determined:

$$\begin{cases} R_{gx} = R_{sx} - m_p \cdot a_x \\ R_{gy} = -R_{sy} + G_p + m_p \cdot a_y \\ M_g = R_{sx} \cdot y_D - R_{sy} \cdot x_D + G_p \cdot x_{O'} + J_p \cdot \varepsilon_p - m_p \cdot a_y \cdot x_{O'} + m_p \cdot a_x \cdot y_{O'} \end{cases} \quad (1)$$

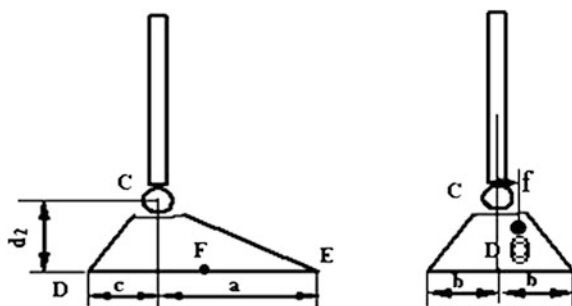
where:

a_x, a_y —represent the components along the axes (Ox) and (Oy) of the linear acceleration of the mass center of the foot;

J_p —the mass moment of inertia of the foot with respect to its mass center;

ε_p —angular acceleration of the foot;

Fig. 4 Dimensional parameters of the foot



$R_{s_{x,y}}$ is the reaction force of the ground on the foot, acting along the directions O_x , O_y ;

G_p the weight force of the foot;

M_g the torque acting in the ankle joint.

The geometric position of points C, D, E and O' were determined from the structural model described above, these positions being dependent by angular variables φ_1 and φ_4 .

The reaction forces R_{gx} and R_{gy} were calculated for five positions of dynamic balance of the foot. For the numerical application, the following values of the anthropometric amounts were used: $M = 88.6$ kg—the total mass of the body; $H = 1.76$ m—the total height of the body; $m_p = 1.20$ kg—the foot mass; $L_p = 0.27$ m—length of the foot, which is denoted with DE; $CD = 0.087$ m—the distance between the rotation center of the ankle joint and the heel; $CE = 0.206$ m—the distance between the rotation center of the ankle joint and the end of the second metatarsian, $J_p = 0.04$ kg m²—the mass moment of inertia of the foot.

Following the numerical results, were drawn the graphs of variation of joint reaction components, R_{gx} și R_{gy} , in different phases of gait, represented in Fig. 5.

Linear accelerations, required numerical calculations in Eq. (1), were determined experimentally, using an accelerometer. To determine the reaction force between foot and ground was used a Kistler force platform.

4 Discussion and Conclusions

Analyzing the graphs in Fig. 5, can be seen that between the two components of the ankle reaction force, vertical force is predominant, with a horizontal component with a variation less than 10 % of vertical component. The share of horizontal component in value of the resultant reaction force of the ankle, R_g is insignificant, so only the vertical component has influence regarding the mechanical load which acting on ankle.

It can observe, also, that the reaction force is smaller than weight, regardless of the leg support phase on the ground. The lower reaction force can be an advantage

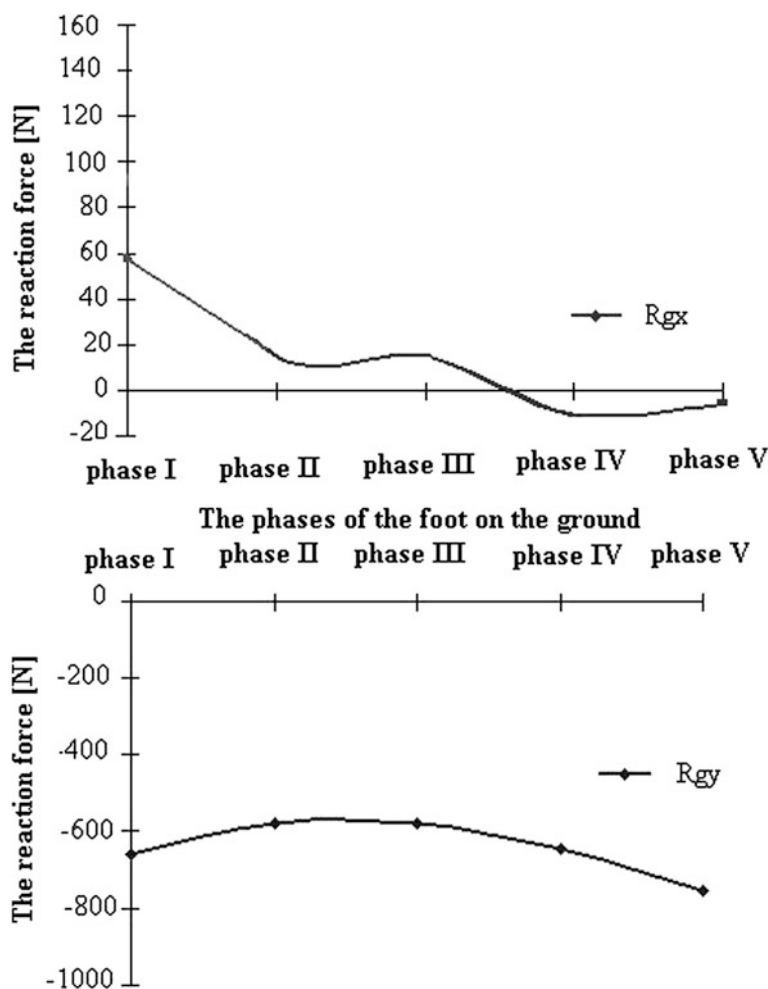


Fig. 5 The diagrams of the components of the reaction force

in case of an implant fixation in the ankle. In the same time, the reaction force is greater than the force necessary to unlink the connection by fixation with implant, determined experimentally for three orthopedic surgical techniques. From this point of view, it is necessary to be immobilized the foot to a fracture of the ankle or the possibility of using a crutch to take most part of the mechanical loading which acting in articulation.

References

1. Hatze, H.: The fundamental problem of myoskeletal inverse dynamics and its implications. *J. Biomech.* **35**(1), 109–115 (2002)
2. Hurmuzlu, Y.: Dynamics of bipedal gait: part 1—objective functions and the contact event of a planar five link biped. *ASME J. Appl. Mech.* **60**(2), 331–336 (1993)
3. Kuo, A.N.D.: The relative roles of feed forward and feedback in the control of rhythmic movements. *Motor Control* **6**, 129–145 (2002)
4. Mc Mahon, T.A.: Mechanics of locomotion. *Int. J. Rob. Res.* **3**(2), 4–28 (1984)
5. Vukobratovic, M., Borovac, B., Surla, D., Storkic, D.: *Biped locomotion*. vol. 7 Springer, Berlin (1990)
6. Blazer, W., Schiehlen, W.: Walking without impacts as a motion/force control problem. *Trans. ASME* **114**, 660–664 (1992)
7. Eberhard, P., Spagele, Th., Gollhofer, A.: Investigations for the dynamical analysis of human motion. *Multibody Sys. Dyn.* **3**(1), 1–20 (1999)
8. Bauby, C.E., Kuo, A.D.: Active control of lateral balance in human walking. *J. Biomech.* **33**, 1433–1440 (2000)

Dynamic Characteristics of Prosthetic Feet: A Comparison Between Modal Parameters of Walking, Running and Sprinting Foot

S. Noroozi, A. G. A. Rahman, M. Dupac and J. E. Vinney

Abstract Current methods of evaluating the performance of Energy Storing and Returning (ESR) prosthesis are subjective and rely on VO₂ consumption. Current prosthetic feet are designed for specific applications and the majority are designed for walking and moderate running. These mechanical feet have fixed mechanical and dynamic characteristics. They have to be selected to meet the requirement of the task and any use outside the domain of the task can result in extreme/severe lack of gait symmetry and loss of energy. Poor gait symmetry results in excess consumption of energy, back pain or fatigue. To investigate if a multipurpose foot can be designed to passively adapt to the walking or running condition one must first understand the different dynamics that are involved and are required from the task specific foot. Static tests have shown these feet to have non-linear stiffness, making the prediction of their dynamic response difficult. The most reliable method to test for dynamic characteristics is drop and modal testing. A method approach has been developed as part of this research to test and compare the dynamic characteristics of three different types of foot (natural frequency, mode shapes and damping). This is needed to explore the differences in the responses of these feet that allow one to be used for walking, one to be used for running and one to be used for sprinting with ease.

S. Noroozi · M. Dupac (✉) · J. E. Vinney
Bournemouth University, Bournemouth, UK
e-mail: mdupac@bournemouth.ac.uk

S. Noroozi
e-mail: snoroozi@bournemouth.ac.uk

J. E. Vinney
e-mail: jevinney@bournemouth.ac.uk

A. G. A. Rahman
University Malaysia Pahang, Kuantan, Malaysia
e-mail: agar@um.edu.my

Keywords Energy return • Dynamics • Amputee • Prosthesis • Lower-limb • Foot

1 Introduction

To understand the requirement of a prosthetic foot during walking, jogging and sprinting [1, 2, 9] one needs to understand the differences in the responses of these feet during such activities. Initial work on the prosthetic design focused on restoring walking ability [5]. The advance in composite materials has made possible to have passive adaptive feet as well as the ability to store and release energy (ESR), as originally presented in [15]. Recent developments of ESR's prosthesis have enabled individuals with a lower-limb amputation to participate in sports [13], other design have been developed later [6].

The kinematic and kinetic of a prosthetic foot have been studied in [6] but little attention to date has been given to its dynamic characteristics such as natural frequencies of oscillation, damping and mode shapes [7, 8]. It was observed in [3] that a reduction in stiffness can increase energy storage and energy return, and minimize asymmetries. A parametric study relating effect of force, stiffness and damping on the dynamics of the impact during running was introduced in [16].

A comprehensive literature reviews of human walking dynamic forces identification and their associated mathematical models used in vibration assessments, i.e., “how excessive structural vibrations modifies walking” have been mentioned in [14]. The structural behaviour of a prosthetic foot—for transtibial amputees—subject to ground reaction forces has been studied in [12]. It was confirmed that ambulation with a Flex Foot at higher speeds tended to conserve energy resulting in enhanced gait efficiency [10], while modification to the prosthetic foot mass or stiffness has altered their dynamic characteristics [4].

In this paper the dynamic characteristics of three different composite energy storing and returning (ESR) prosthetic feet attached to a mass are compared for their distinct modal differences. The mode shapes and frequencies obtained using experimental modal analysis are compared and their differences discussed to identify key requirement of the foot during, walking, jogging and sprinting. Other key issues such nonlinearities due anisotropy, variable thickness and changing boundary conditions are also discussed in order to better understand and exploit their effect on the dynamic characteristics to aid the design of an optimum foot.

2 Mechanical Modeling and Results

In the absence of any damping and harmonic excitation force, a mechanical system whose mass is displaced and released from equilibrium will oscillate about its equilibrium position. Different masses with the same spring or different springs

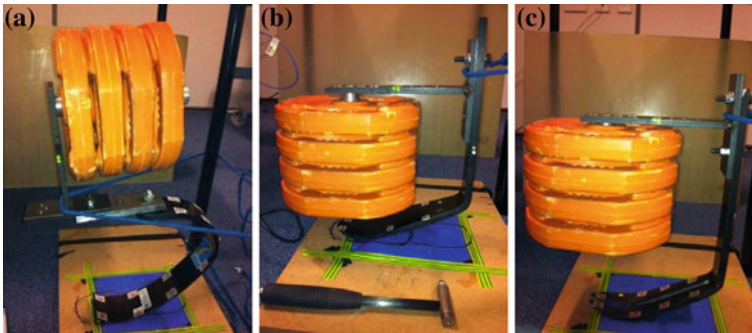


Fig. 1 Experimental foot/mass arrangements. **a** Sprinting foot, **b** jogging foot and **c** walking foot with heel

with the same mass produce different natural frequencies and mode shapes. Therefore, both mass and stiffness play an important role in controlling the vibration of the system. All modes of vibration are usually excited due to impact or impulse to a system. This happens naturally due to running action or superficially introduced due to action of an impact hammer. Most of these modes will damp out due to the high damping factor of the composite, but low frequency bending mode will remain in the system, while the foot is in contact with the ground.

Experimental modal analysis is one method of measuring the dynamic characteristics of mass and foot system. This was done using a combination of DasyLab virtual instrumentation environment, MeScope modal analysis software, a tri-axial accelerometers, a 4 channel NI DAQ system and IPC impact hammer with soft tip. The set up of the experimental MA of three ESR prosthetic feet is shown in Fig. 1.

Each leg was attached to a 9 kg mass as shown in Fig. 1 using a steel angle bracket. Depending on the foot anything between 14 and 18 roving points was selected on each foot and marked as measurement point. Impact hammer was used to apply energy to the system in X, Y, Z directions. This was repeated five times at each roving points. These impacts excited all modes of vibration in the system. The majority of these natural modes of vibrations damped out quickly due to high damping factor of these feet. The captured data was then transferred to MEScope where damping factors and mode shapes were calculated and animated respectively as shown in Figs. 2 and 3 and listed in Table 1.

Four low frequency mode shapes for each foot and mass arrangements were created but only the two most relevant to either walking or running or sprinting are shown in Figs. 2 and 3. It was observed that both bending and torsional oscillations exists on all the feet, however, the damping and the frequency difference between each system was quite obvious.

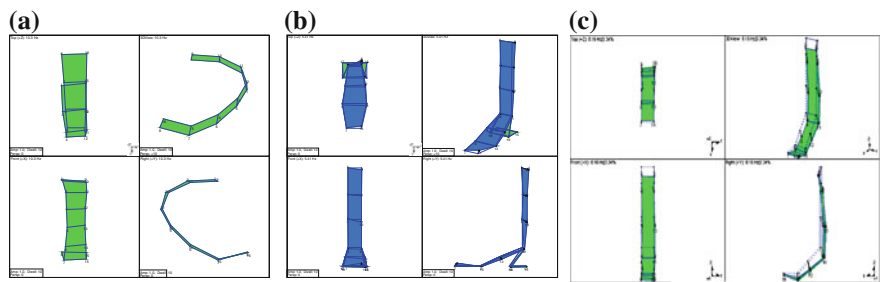


Fig. 2 1st bending mode shapes obtained using experimental technique, foot/mass arrangements. **a** Sprinting foot, **b** walking foot with heel and **c** jogging foot

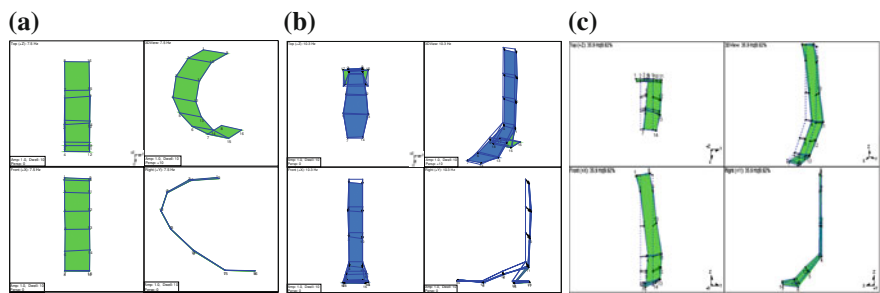


Fig. 3 1st twisting mode shapes obtained using experimental technique, foot/mass arrangements. **a** Sprinting foot, **b** walking foot with heel and **c** jogging foot

Table 1 Natural frequencies for foot/mass arrangements, (a) Sprinting foot, (b) walking foot with heel and (c) jogging foot

Sprinting foot		Walking foot with heel		Jogging foot	
Mode 1	Mode 2	Mode 1	Mode 2	Mode 1	Mode 2
6.15	9.73	4.29	8.16	5.15	8.41
4.70	7.11	4.20	5.74	4.33	5.63

3 Discussions

The experimental modal analysis done in [11], show that by controlling the mass or the stiffness similar natural frequency of around 4 Hz for Elite Blades can be achieved. From the above investigation it can be seen that the same argument is also true for these three different classes of feet. This indicates that the running frequency can be matched with the natural frequency by simple control of the mass or stiffness of the foot or both. However, it can be seen that twisting mode also creeps in for the elite feet and the feet with heels, and only the heaving mode appears for the flex run blade. This further reinforces the initial guess that

excessive anisotropy in the Elite blade design may be responsible for twisting mode of vibration which can be a design feature that can either bring modes of vibration close to the same frequency or move them far apart from each other. It can be noted that the flex run appears to be balanced and to experience more flexure due to larger deflection hence giving the system more time to absorb the impulse, and to transfer the strain energy due to bending into the system.

The Elite Blade has a complex, non-uniform geometry and due to its high stiffness it has a high natural frequencies and damping. Therefore, it is expected that the running specific prosthetic feet (such as the Flex-Run) will have lower stiffness due to the nature of their symmetric layup and shape make them easier to tune for running as compared to the geometrically more complex Elite Blades studied in this investigation. Also the Elite blades have high levels of unidirectional anisotropy that gives higher shear coupling causing twisting while bending.

The full effect of twisting mode on the system is yet to be fully investigated and understood. However, early indication is that it is possible to bring the key modes (twisting and bending) closer in order to take advantage of both phenomena. The twisting, can be achieved either mechanically—using novel section properties—or as a result of the non-symmetrical and unbalanced properties of composite. Twisting can have an impact on the alignment of the foot during the loading phase. Currently, FEA analysis cannot predict damping nor it can adequately model transverse shear in thick composite, which was also suggested by [6] and states that more knowledge is needed to understand the influence of carbon layup variations and shape alterations.

4 Conclusions

A better understanding of the link between the laminate layup, levels of anisotropy and non linear structure and their effect on the performance of prosthetic feet is fundamental if fair inclusion of technology in disability sports is to be achieved.

Model design and materials can influence the characteristics of such feet and as a result it can have an impact on how multi tasking passive adaptive composite foot should be designed in the future to provide: (1) better gait symmetry for uni and bilateral amputees, (2) better performance during walking, (3) better performance during jogging and (4) better performance during sprinting. A better understanding can inform designers on how they can minimise amputee energy consumption. Such information can be translated into a tool that can assist prosthetics to better match the amputee's walking/running/sprinting frequency with the dominant resonant frequency and the dynamics elastic response of their prosthetic foot.

Acknowledgments The authors would like to thank Chas A Blatchford and Sons Ltd and Endolite for their kind donation of the Elite Blades used for this investigation.

References

1. Blickhan, R.: The spring mass model for running and hopping. *J. Biomech.* **22**(11–12), 1217–1227 (1989)
2. Buckley, J.: Sprint kinematics of athletes with lower limb amputations. *Arch. Phys. Med. Rehabil.* **80**, 501–508 (1999)
3. Fey, N.P., Klute, G.K., Neptune, R.R.: The influence of energy storage and return foot stiffness on walking mechanics and muscle activity in below-knee amputees. *Clin. Biomech.* **26**, 1025–1032 (2011)
4. Gailey, R.: Optimizing prosthetic running performance of the transtibial amputee. Proceedings of the AOPA annual meeting (2003)
5. Hafner, B., Sanders, J., Czerniecki, J., Fergason, J.: Trans-tibial energy-storage-and-return prosthetic devices: a review of energy concepts and a proposed nomenclature. *J. Rehabil. Res. Dev.* **39**(1), 1–11 (2002)
6. Lechler, K.: Lower-limb prosthetics—design improvements of a prosthetic spring foot. *Am. Acad. Orthotists and Prosthetists—J. Proc.* (2005)
7. Lehmann, J.F., Price, R., Boswell-Bessette, S., Dralle, A., Questad, K., deLateur, B.: Comprehensive analysis of energy storing prosthetic feet: flex foot and seattle foot versus standard SACH foot. *Arch. Phys. Med. Rehabil.* **74**(11), 1225–1233 (1993b)
8. Lehmann, J.F., Price, R., Boswell-Bessette, S., Dralle, A., Questad, K.: Comprehensive analysis of dynamic elastic response feet: seattle ankle/lite foot versus SACH foot. *Arch. Phys. Med. Rehabil.* **74**(8), 853–861 (1993)
9. Lewis, J., Buckley, J., Zahedi, S.: An insight into paralympic amputee sprinting. *Br. J. Therapy Rehabil.* **3**(8), 440–444 (1996)
10. Macfarlane, P., Nielsen, D., Shurr, D., Meier, K.: Gait comparisons for below-knee amputees using a flex-foot versus a conventional prosthetic foot. *J. Prosthetics and Orthotics* **3**, 150–161 (1991)
11. Noroozi, S., Sewell, P., Vinney, J., Dyer, B. T.J., Rahman, A. G. A., Zhi Chao, O.: Modal analysis of composite prosthetic energy-storing-and-returning feet: an initial investigation, Proceedings of the institution of mechanical engineers part P: J. Sports Eng. Technol. (2012, in press)
12. Omasta, M., Palousek, D., Návrát, T., Rosicky, J.: Finite element analysis for the evaluation of the structural behaviour, of a prosthesis for trans-tibial amputees. *Medical engineering and physics* (2011, in press)
13. Paillet, D., Sautreuil, P., Piera, J.B., Genty, M., Goujon, H.: Evolution in prostheses for sprinters with lower-limb amputation [Evolution des protheses des sprinters amputes de membre inferieur], *Annales de Réadaptation et de Médecine Physique* **47**(6), 374–81 (2004)
14. Racic, V., Pavic, A., Brownjohn, J.M.W.: Experimental identification and analytical modelling of human walking forces: literature review. *J. Sound Vibr.* **326**, 1–49 (2009)
15. Versluys, R., Beyl, P., Van Damme, M., Desomer, A., Van Ham, R., Lefeber, D.: Prosthetic feet: state-of-the-art review and the importance of mimicking human ankle-foot biomechanics. *Disability Rehabil.: Assistive Technol.* **4**(2), 65–75 (2009)
16. Zadpoor, A.A., Nikooyan, A.A., Arshi, A.R.: A model-based parametric study of impact force during running. *J. Biomech.* **40**, 2012–2021 (2007)

Biomechanical Solutions in Tibial Malleolus Fracture

C. Oprisan, E. Budescu and V. Cotoros

Abstract This paper presents a biomechanical analysis of three solutions with implants in fracture fixation of tibial malleolus, on the mechanical strength testing. Samples were tested in mechanical traction, the forces revealed the minimum threshold from which start the phenomenon of bone destruction and maximum forces that destroyed the fractured fragments achieved by fixation elements. Experimental tests showed the best technical solution of the three, namely that consists of two Kirschner pins, cortical screws and wire tightening.

Keywords Biomechanics • Tibial fracture • Traction • Implants • Osteo-synthesis

1 Introduction

The negative effect of human body motion on a bone is represented by the lesion which, in the worst condition for bone, is the fracture. A fracture may be produced by various causes such as:

- application of a mechanical load that produces structural break of the bone;

C. Oprisan (✉) · E. Budescu
Gh. Asachi Technical University of Iasi, Iasi, Romania
e-mail: coprisan@yahoo.com

E. Budescu
e-mail: budescu@gmail.com

V. Cotoros
Municipal Hospital Medgidia, Medgidia, Romania
e-mail: victorcotoros@yahoo.ca

- external factors like a random traumatism, produced by a direct force (due to an exterior impact), an indirect force (indirectly transmitted along one or more segments) and/or an abnormal muscular force;
- internal factors like change of the bone's strength (due to a tumour, osteoporosis, infection, hormonal change, modification of calcium concentration in blood etc.) to normal mechanical loads.

In the lesions occurring at the level of the ankle, the malleolus fractures (the articular bone protuberances of the tibia or fibula) constitutes 20–22 % from skeleton lesions and, for this reason, it yields the importance of the analysis of surgical techniques. These techniques ensure, after healing, a functional recovering of the bone, with minimum secondary effects (Davila [1]; Sturz [2].

The use of mechanical systems of fixing the fracture with plates, screws, Kirschner broaches or metallic wires, was developed and standardized in orthopedic surgery in the last 30 years (Wissing [3]; Thordarson [4]. In the case of bigger fragments of malleolus fracture there can be used screws (one or two) or broaches and metallic wires and in the other cases only broaches and metallic wires (Schatzker [5]. In the case of bi-malleolus fractures at the ankle level, respectively the fracture both of the tibia malleolus and the fibula malleolus, the surgical technique approaches the continuity recovering first at the level of lateral malleolus (fibula) and, immediately there is established the articular continuity at the medial malleolus (tibia).

Into the place of metallic elements of fixing there were proposed bioabsorbable materials, with the same role of mechanical fixing, but which are auto-degrading into the organism, their elimination following a biological natural way (Bostman [6]; Ahl [7]; Arva [8]; Benz [9]; Bucholz [10]. But due to fragility of the elements made by these bio-polymers, respectively the low strength to mechanical stresses occurring at the level of separation surfaces of fracture, the fixing of malleolus fractures is done now with metallic elements of osteo-synthesis.

2 Method and Materials

Malleolar areas of tibia and fibula form at interior the inferior articular surface of shank, respectively the higher ankle joint. Fractures that may occur at the level of the two malleolus, have specific surgical techniques with metallic elements of osteo-synthesis. Thus, depending on the lesions produced at the ankle level, there are the following surgical techniques:

fracture of the tibia malleolus and lesion of the external colateral ligament—use of two screws;

posterior fracture of tibia malleolus and fracture by pulling of fibula malleolus—use of two broaches and link with metallic wire for fibula and two screws for tibia; posterior fracture of tibia malleolus and transversal fracture of fibula malleolus—use of two broaches and link with metallic wire both for fibula and tibia;

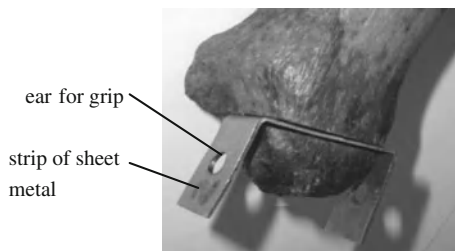


Fig. 1 View of the separation plane



Fig. 2 The bone ready for testing

fracture of fibula malleolus and fracture of tibia malleolus with anterior lesion of articular surface—use of a plate with screws for fibula and a screw for tibia; simple fracture of fibula diaphysis and fracture of tibia malleolus—fibula osteo-synthesis using a plate with screws and a fibula-tibia cortical screw, and for tibia osteo-synthesis using two Kirschner broaches and a link with metallic wire; fracture of fibula diaphysis and lesion of medial colateral ligament—use a plate with screws for fibula and fibula-tibia cortical screw.

In terms of biomechanics, the mechanical stress which acting on the two fragments of the fracture and the implant of osteo-synthesis is traction. Thus, to verify experimentally the mechanical resistance to traction for the ensemble of osteo-synthesis, first we made a separation between the fractured fragments, as seen in Fig. 1.

An ensemble of osteo-synthesis, with metallic wire, in this case, before testing to traction, can see in Fig. 2.

The implant elements, such as the malleolar screws or the cortical screws, such as Kirschner broaches or such as the metallic wires, used in osteo-synthesis, are made of stainless steel.

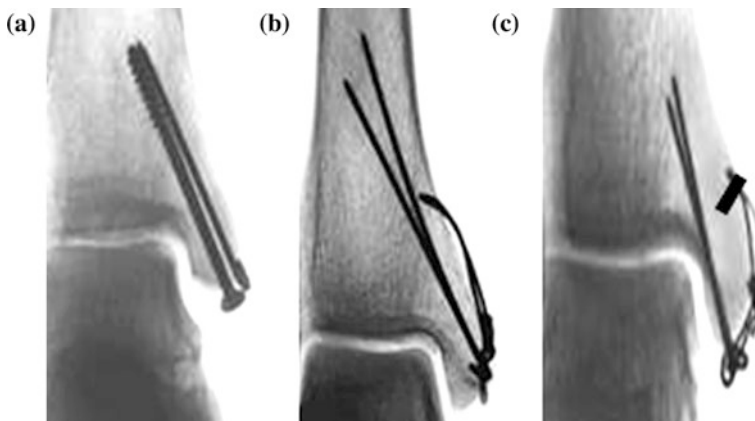


Fig. 3 Implants for osteo-synthesis: malleolus screw (a); Kirschner pins and metallic wire (b); Kirschner pins, cortical screw and metallic wire (c)

3 Experimental Analysis of the Break Limit for Surgical Techniques of Osteo-Synthesis

For the experimental analysis at traction of few surgical techniques used at present for osteo-synthesis of the fracture of tibia malleolus, there was simulated the fracture by cutting the tibia malleolus and after that by putting together the fragments using the following surgical techniques:

use of a malleolus screw introduced into the fractured fragments (Fig. 3a);
 use of two Kirschner broaches and link with metallic wire introduced through two upper holes in bone (Fig. 3b);
 use of two Kirschner pins and link with metallic wire fixed at the upper side with a cortical screw transversally introduced in bone (Fig. 3c).

The three radiographs from Fig. 3 correspond to male patients, aged between 40 and 55, these conditions being same for the three sets of osteo-synthesis tensile tested.

The variation curve of the force function of time was recorded on paper, the speed of the roll being of 60 [mm/min]. Also, for testing there was chosen a speed for the heads of testing machine of 1.4995 [mm/min], so that to be observed the threshold at which occurs the destruction of the bone. In Figs. 4, 5 and 6 there are represented the variation curves of the stretching force function of time, for the three analyzed surgical techniques. In the surgical techniques with fixation with wire, the experimental testing were stopped when begins to crush the bone.

The maximum force recorded corresponds to the time when the wire started to crush bone. In these cases, the entire mechanical system has maintained its integrity. In the surgical technique with fixation with screw, experimental testing was conducted until when the screw started to leave the fractured bone fragments.

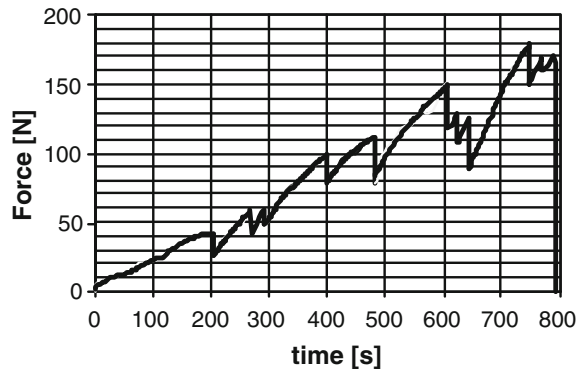


Fig. 4 Stretching force for malleolus screw

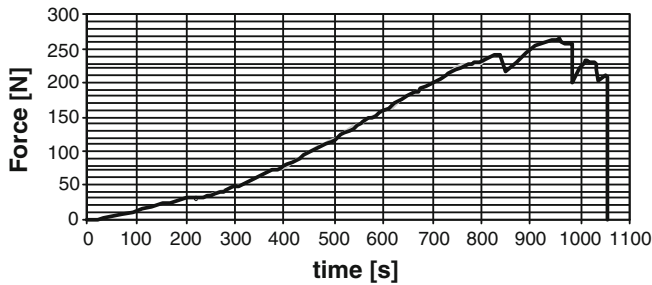


Fig. 5 Stretching force for broaches and metallic wire

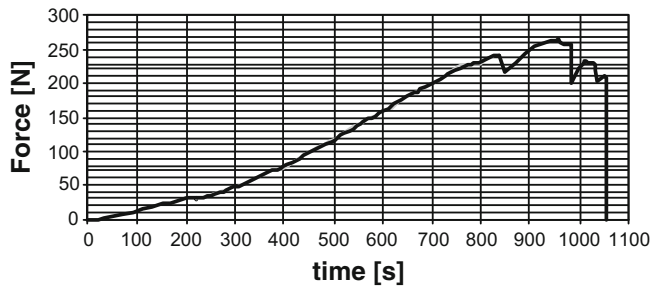


Fig. 6 Stretching force for broaches, screw and metallic wire

4 Discussion and Conclusions

In Fig. 4 is observed a discontinuous variations of the curve force—time; they are caused by forced displacements between two strips of spongy bone tissue. The screw has a tendency to “escape”, to move between two strips bone spongy tissue. At each such displacement, the contact surfaces of the fractured bone fragments

become smaller. In this mode, gradually get to interrupt the contact between the surfaces of osteo-synthesis.

For the second surgical technique analyzed, the curve of variation force–time (Fig. 5) is continues in the first 800 s, after which appear some discontinuities. The force at which appear this discontinuity is greater than the critical force of the first case analyzed. It can be said therefore that the surgical technique is superior comparative with the first technique. In the third case analyzed, the curve of variation force–time (Fig. 6) is continuous, almost 1600 s. This technique has the best variation, respectively a continuous variation, the best critical force and the most time for maintaining the contact between the surfaces of the fractured bone fragments. The difference between the second and third surgical technique, from biomechanical point of view, is evident regarding the appearance of crushing of bone phenomenon. Thus, the second surgical technique leads to the crushing phenomenon to approximatively 850 s of starting tractive force action, while the third solution increases this time up close to 1600 s.

As can be seen in Figs. 4, 5 and 6, the best surgical technique is one that uses two Kirschner broaches, a wire for fixation and a transversal screw for anchorage (Fig. 3c).

References

1. Davila, S., et al.: Analysis of results of surgical treatment of malleolar fractures. *Lijec Vjesn.* **123**(3–4), 59–63 (2001)
2. Sturz, H., et al.: Bedeutung der osteosynthese und funktionellen weiterbehandlung fur die knochenbruchheilung. *Op. J.* **8**(1), 69–73 (1992)
3. Wissing, J.C., Van Laarhoven, C.J., Van der Werken, C.: The posterior antiglide plate for fixation of fractures of the lateral malleolus. *Injury.* **23**(2) 94–96 (1992)
4. Thordarson, D.B.: Complications after treatment of tibial pilon fractures: prevention and management strategies. *J. Am. Acad. Orthop. Surg.* **8**(4), 253–265 (2000)
5. Schatzker, J., Tile M.: The Rationale of Operative Fracture Care. *J. Margo Anterior* (1999) (2, 4), 12–16, 8–10.
6. Bostman, O., Partio, E., Hirvensalo, E., et al.: Foreign-body reactions to polyglycolide screws. Observations in 24/216 malleolar fracture cases. *Acta Orthopaedica Scand.* **63**(2), 173–176 (1992)
7. Ahl, T., Dalen, N., Lundberg, A., Wykman, A.: Biodegradable fixation of ankle fractures. A roentgen stereophotogrammetric study of 32 cases.—*Acta Orthopaedica Scand.* **65**(2), 166–170 (1994)
8. Arva, G., Frohlich, P.: Osteo-synthesis using absorbable implants.—*Magyar traumatologia ortopedia kezebeszet Plasztikai Sebeszet.* **37**(1), 85–88 (1994)
9. Benz, G., Kallieris, D., Seebock, T.: Bioresorbable pins and screws in paediatric traumatology. *Eur. J. Pediatric Surgery.* **4**(2), 103–107 (1994)
10. Bucholz, R.W., Henry, S., Henley, M.B.: Fixation with bioabsorbable screws for the treatment of fractures of the ankle. *J. Bone Joint Surgery—Am. Volume.* **76**(3), 319–324 (1994)

Validation of Human Body Model VIRTHUMAN and its Implementation in Crash Scenarios

Ing. Jaroslav Mañas, Ing. Luděk Kovář, Ing. Jan Petřík, Ing. Hana Čechová and Ing. Stanislav Špírk

Abstract Standard virtual prototyping approach of passive safety field is based on virtual models of dummies, but human body models become to be more and more important for specific crash scenarios. VIRTHUMAN is human body model based on MBS (Multi-Body Structure) approach. The model consists of movable rigid segments, which represent proper mass of each human part and enables to evaluate injury criteria describing safety risks during crash scenarios. There is evident advantage of the MBS approach in simple preparation of crash configuration—human body positioning, reasonable calculation times and mainly its applicability for robust designs development respecting variety of human population. The project VIRTHUMAN is directed on development of scaling technique enabling to generate human model based on the standard anthropometric inputs. The contribution describes status of the VIRTHUMAN model, procedures of its validation and results in standard crash scenarios.

Keywords Safety • Crash • Human body • Multi-body structure

Ing. Jaroslav Mañas (✉) · Ing. Luděk Kovář
MECAS ESI s.r.o, Plzen, Czech Republic
e-mail: jaroslav.manas@mecasesi.cz

Ing. Luděk Kovář
e-mail: ludek.kovar@mecasesi.cz

Ing. Jan Petřík
Technical University of Liberec, Liberec, Czech Republic
e-mail: jan.petrík@tul.cz

Ing. Hana Čechová · Ing. Stanislav Špírk
University of West Bohemia, Plzen, Czech Republic
e-mail: hcechov@ntc.zcu.cz

Ing. Stanislav Špírk
e-mail: spirks@kks.zcu.cz

1 Introduction

The present transportation standards define safety requirements for European traffic as frontal and side impact (ECE-R94, 96/79/EC and ECE-R95, 96/27/EC) with specific dummies (Hybrid III 50 % and Eurosid II). Design and included sensors of each dummy are developed for the specific test scenario. There are strict limits of these dummies, for example pedestrian protection is now current issue of using the standardized dummies. It is possible to use group of virtual human FE models for simulations like H-Model, THUMS or JAMA model. There models developed in academic environment by support of European projects (HUMOS, APROSYS). There is problem of implementation of these models is their complexity—positioning and setting test configuration for these models is very difficult and require help of the development team.

The main aim of the project is to create model of a general individual of the human population, which can be used for virtual prototyping in area of traffic safety (not limited to automotive industry), prepare a methodology for testing the safety of vehicles in general crash scenarios and to enable evaluation of injury criteria describing safety risk. In the project VIRTHUMAN there is created virtual model of human body on the basis of MBS (Multi Body System). There has been already created model, which represents average representative of European population, so called 50 % model. Methodology of automatic creation of virtual human body is planned to be created with corresponding age and weight of any European on the basis of scaling. Large group of models can be used for robust design of vehicle, eventually general transport infrastructure.

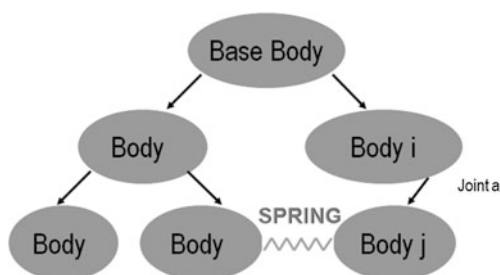
2 MBS Model of Human Body

The whole model is created as Multi Body System (MBS). The main advantages of MBS method are to reduce computation time and it also allows to include deformation of each component. MBS consist of rigid bodies, that are connected with joints (or springs) of specific type. This system has to be as open tree structure (Fig. 1) starts in base body.

The candidate for average European was chosen from Europe database CAE-SAR based on requested statistically average mass and size (Fig. 2) close to dummies Hybrid III 50 % or Eurosid II.

This external shape was meshed with special approach, because model can be placed in sitting position (front, side crash test) or standing position (pedestrian test) or other general configurations. Some parts of VIRTHUMAN were developed

Fig. 1 MBS tree structure connected by joints



with regard to using sensors and measured injury criterions, which corresponds to methodologies used in automotive industry.

3 Validation of VIRTUMAN Model

For a good behavior of model had to be performed its validation according existing measurements with human body/cadavers. Validation was performed on component level and based on test for whole body. There were used several data sources for the validation. There are presented two different approaches. The thorax was validated based on the official sources and pelvis based on material data validated during creation of FE model.

Validation test for chest is described on Fig. 3. The test sample (PMHS) is established on a horizontal surface, arms are forward and easily fixed to the ground so that the torso held upright.

Cylindrical impactor (mass of 23.4 kg and 150 mm diameter) is placed in front of torso and impact into chest with prescribed velocity. The impactor is positioned in the center of sternum, which corresponds to the height between the fourth and fifth rib. Tests were performed for different impact speeds as follows: 4.9, 6.7 and 9.9 m/s.

In case of sitting model, pelvis and femur segments represents the deflection of the sitting human body. Characteristics of translational joints, which are coupled with base structure, are validated via reference FE solid model (Fig. 4). The reference model is created based on the outer skin of the seated VIRTUMAN. Pelvis and femur bones respect joints location of the MBS model. Space between skin and bones is modeled via solid elements. The characteristics of solid material are used from specific human models for comfort evaluations created in ESI Group. Force–deflection curve from virtual static loading test of FE pelvis is directly used as characteristics for surface MBS segment coupling with the body representing upper leg/pelvis.

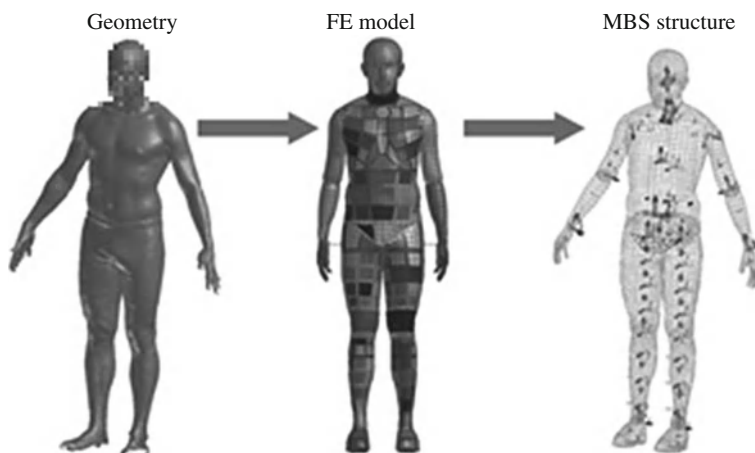


Fig. 2 MBS structure of reference virtual human body model

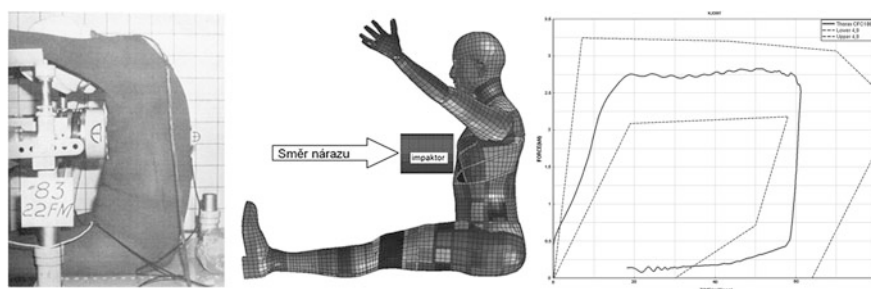


Fig. 3 Configuration of Kroell (14 PMHS) test with reference MBS model and result of chest deflection in corridors

4 Crash Scenarios

Great potential of the model is expected with emerging legislation, for example in the field of interior of rail vehicles. VIRTHUMAN can be used in railway transportation for evaluation of several types of collision scenarios. In the railway vehicle occupant body is loaded only by acceleration generated by crash of a train unit. For injury of human are the most important orientation of human body in the vehicle and orientation against acceleration direction. The final impact is caused by contact of occupant with interior features like handle, seat and floor. Different types of collision scenarios were performed—impact into wall (Fig. 5), crash with the seat and fall to the ground.

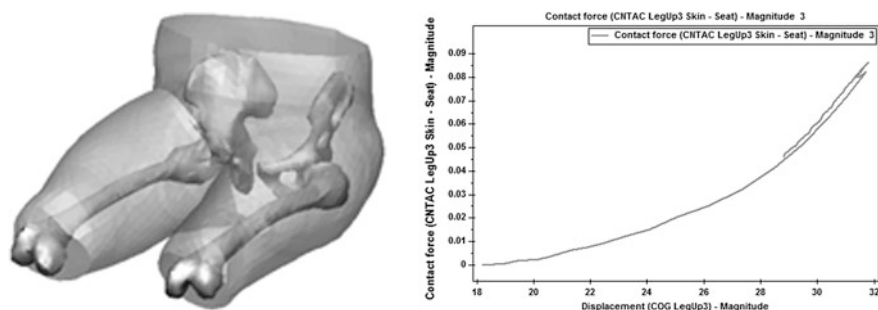


Fig. 4 Used skin of sitting VIRTUMAN, reference FE solid model of pelvis and femur, results of one segment loading

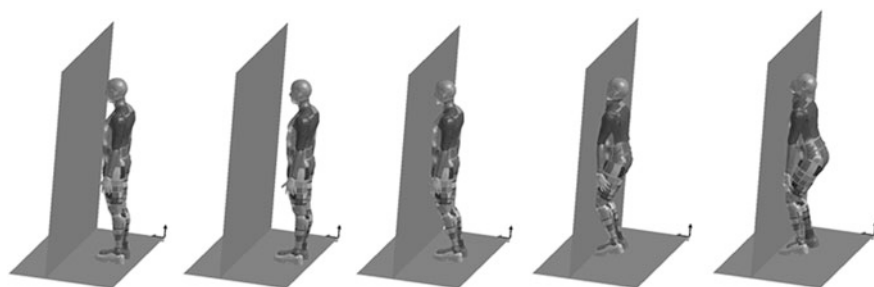


Fig. 5 Impact into wall

5 Conclusions

Thanks to Multi-Body Structure of VIRTUMAN (simple positioning, calculation times) it is possible to get result of safety risks during crash scenarios in a short time. The contribution results show principal validation techniques used in the model for validation of thorax and pelvis. The big advantage of the model built based on the MBS approach is its modularity, which will be with advantage used for development of scaling technique based on [1]. Temporary results with presented 50 % individual give very promising feedback for creation of general model of any individual of human population with proper mass distribution according general anthropometric parameters age, height, weight, ... for robust design of vehicles and transportation infrastructure. The work is supported by the project TA01031628 of Technology Agency of the Czech Republic.

Reference

1. Hynčák, L., Nováček, V., Bláha, P., Chvojka, O., Krejčí, P.: On scaling of human body models. Applied and computational mechanics, pp. 63–74, University of West Bohemia, Pilsen, vol. 1, no.1 (2007)

Numerical Simulation of the Self-Oscillations of the Vocal Folds and of the Resulting Acoustic Phenomena in the Vocal Tract

P. Švancara, J. Horáček and J. G. Švec

Abstract The study presents a three-dimensional (3D) finite element (FE) model of the flow-induced self-oscillation of the human vocal folds in interaction with acoustics of simplified vocal tract models. The 3D vocal tract models of the acoustic spaces shaped for simulation of phonation of Czech vowels [a:], [i:] and [u:] were created by converting the data from the magnetic resonance images (MRI). For modelling of the fluid–structure interaction, explicit coupling scheme with separated solvers for fluid and structure domain was utilized. The FE model comprises vocal folds pretension before starting phonation, large deformations of the vocal fold tissue, vocal-fold collisions, fluid–structure interaction, morphing the fluid mesh according to the vocal-fold motion (Arbitrary Lagrangian–Eulerian approach), unsteady viscous compressible airflow described by the Navier–Stokes equations and airflow separation. The developed FE model enables to study the relationship between flow-induced vibrations of the vocal folds and acoustic wave propagation in the vocal tract and can also be used to simulate for example pathological changes in the vocal fold tissue and their influence on the voice production.

P. Švancara (✉)

Institute of Solid Mechanics Mechatronics and Biomechanics, Brno University of
Technology, Brno, Czech Republic
e-mail: svancara@fme.vutbr.cz

P. Švancara · J. Horáček

Institute of Thermomechanics, Academy of Sciences of the Czech Republic, Prague, Czech
Republic
e-mail: jaromirh@it.cas.cz

P. Švancara · J. G. Švec

Department of Biophysics, Faculty of Science, Palacky University Olomouc, Olomouc,
Czech Republic
e-mail: SvecJanG@gmail.com

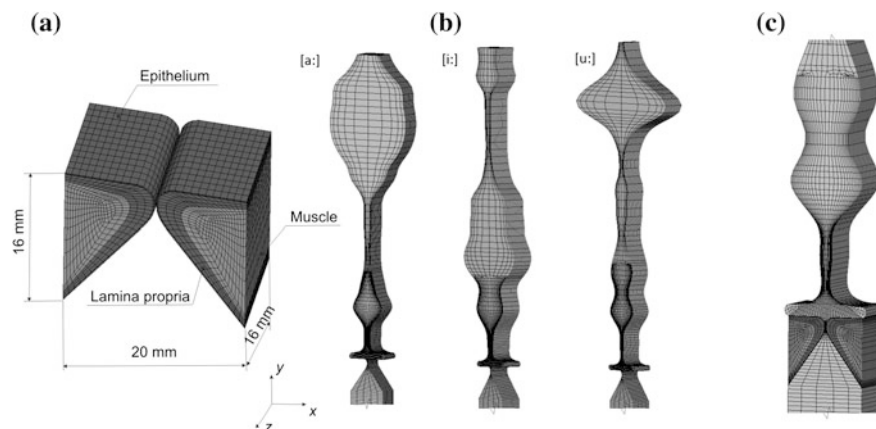


Fig. 1 **a** FE model of the three layered tissue of the vocal folds, **b** FE models of the acoustic spaces of the trachea and the vocal tract for vowels [a:], [i:], [u:], **c** detail of the complete FE model of the vocal folds together with a part of the model of the vocal tract for vowel [u:]

Keywords Biomechanics of voice • Fluid–structure-acoustic interaction • Finite element model • Simulation of phonation • Videokymography

1 Introduction

Voice production is a result of flow-induced vibrations of the vocal folds which generate acoustic waves propagating through the vocal tract. The phonation process can be considered as a fluid–structure-acoustic interaction problem. One of the main restrictions in experimental studies published on solution of this problem in literature [1, 2] is the difficulty with obtaining a more detailed spatial and temporal information on measured quantities such as the subglottal pressure, impact stress etc. The computational models published in literature include low degrees of freedom structural models [3], models of fluid flow [4] and FE models [5, 6]. These are able to solve the fluid–structure-acoustic interaction combining the tissue elasticity with aerodynamics and to deal with a complex material structure and 3D geometry of the vocal folds and the vocal tract.

In recent works of these authors [7, 8] a 3D FE model was developed which covered the flow-induced oscillations of the vocal folds in interaction with acoustic spaces of a simplified vocal tract modelled as a straight prismatic rectangular channel and shaped for vowel [a:]. This paper presents newly developed FE models of phonation with a 3D shaped vocal tract for vowels [a:], [i:] and [u:] and simulation of videokymographic (VKG) images constructed from the FE model of vibrating vocal folds. VKG is a high-speed imaging technique for investigation of vocal folds vibrations commonly used in clinical practise [9, 10].

2 Finite Element Model of Phonation

The program system ANSYS 13.0 was used for developing the FE models. The FE models of the trachea and the simplified acoustic spaces of the human vocal tract shaped for simulation of phonation of vowels [a:], [i:] and [u:] are shown in Fig. 1, together with the FE model of the three layered tissue of the vocal folds.

The models of the vocal tracts for the Czech vowels were created by converting data from magnetic resonance images (MRI) described previously [11]. The tissue of the vocal folds is modelled using three layers—epithelium, lamina propria and muscle. Each layer is considered to be homogenous and isotropic material with the Young modulus of 25 kPa for epithelium, 3 kPa for the lamina propria and 65 kPa for the muscle, based on literature data [1]. The material density of 1040 kg.m^{-3} was used for all three layers. Poisson ratio of 0.49 was used for the epithelium and lamina propria and 0.40 for the muscle. Vocal-fold contact during phonation was modelled by a symmetric surface-to-surface contact pair elements on faces of the vocal folds. An unsteady viscous laminar airflow was modelled by compressible Navier–Stokes equations which enabled modelling of acoustic wave propagation phenomena in fluid using ANSYS/Flotran code with the material properties of the air: speed of sound 343 m/s, fluid viscosity $1.8135 \times 10^{-5} \text{ kg.m}^{-1}.\text{s}^{-1}$ and the density of 1.205 kg.m^{-3} . Zero acoustic pressure was prescribed at the upper end of the vocal tract at the position of the lips and constant airflow velocity 0.4 m/s was prescribed at the entrance to the subglottal space. This airflow velocity was the only driving parameter of the model. The motion of the vocal folds was computed in the ANSYS/Structure code by a transient analysis with a time step $\Delta t = 1.5 \times 10^{-4} \text{ s}$, taking into account the large strain of the vocal fold tissue and vocal fold collisions.

Before the phonation simulation starts, the vocal folds are prolonged in the longitudinal direction by one quarter of original length and pushed slightly into contact. Explicit coupling scheme is used for modelling the fluid–structure interaction. The results of the flow solution are transferred as loads on the vocal fold surface, then the vocal-fold motion is computed, then the fluid mesh is morphed according to the new vocal fold position and then the fluid flow is solved in the next time step. The Arbitrary Lagrangian–Eulerian ALE approach implemented in ANSYS is utilized to represent moving boundaries in fluid domains. During the solution the distance between the faces of the vocal folds is monitored and if a defined minimal distance between two colliding nodes is reached, the mesh morphing is stopped at these nodes and the flow velocity is set to zero (vocal folds closure).

3 Results and Discussion

Figure 2 shows an example of numerically simulated displacements in x , y and z directions of two selected nodes in the middle cross-section of the vocal folds.

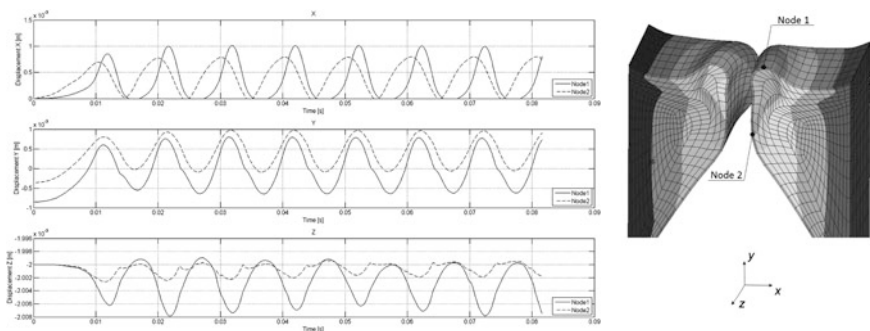


Fig. 2 Computed displacements of two selected nodes in x , y and z directions in the mid-membranous part of the vocal folds

The first node was located on the top margin of the vocal folds and the second one on the bottom margin. The simulated results showed that a prescribed constant airflow velocity at the entrance to the trachea produced vocal fold self-oscillations that get stabilized after first few periods of the transient regime. Dominant movement of the selected nodes was in x and y direction. Deformations in z direction were much smaller. We could also observe a phase delay in displacement in x direction between the node on the top and bottom margins of the vocal folds as a result of upward-propagating mucosal wave.

Figure 3 shows the numerically simulated displacement of the middle part of the vocal folds demonstrating the change of vocal folds from convergent to divergent shape during one oscillation period.

Example of a VKG image created from the results of FE modelling is shown in Fig. 4. The program for creating the VKG images was developed in Matlab using emission cosine law for computation of light intensity reflected from visible vocal folds surface depending on the surface normal.

The acoustic pressure and the corresponding power spectral densities computed at two selected nodes above the vocal folds and near the lips for vowel [u:] are shown in Fig. 5. The spectrum shows a peak at the fundamental frequency and many higher harmonics. Some of these are enhanced by formant frequencies of the vocal tract typical for the modelled vowel [u:]. Similar results were obtained for the vowels [a:] and [i:]. The computed results show very close similarities with real human voice production: the fundamental vocal-fold oscillation frequency was 98 Hz, the maximum intra-glottal fluid velocity was about 30 m/s and the maximum intraglottal pressure was about 700 Pa.

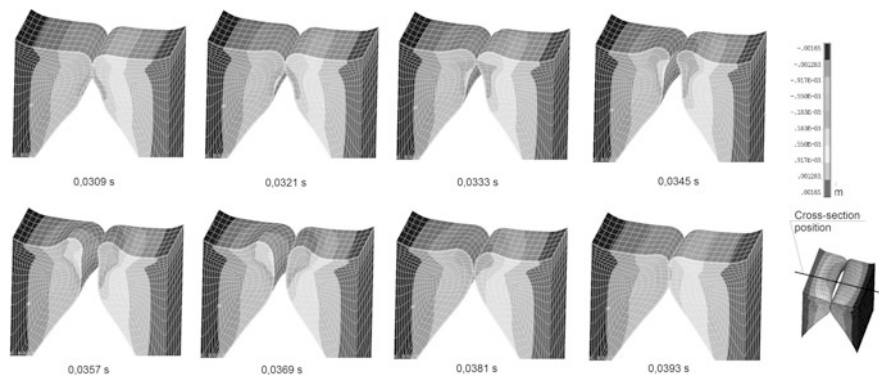


Fig. 3 Numerically simulated displacement of the tissue in the middle of the vocal folds at eight time steps during one oscillation period ($t = 0.0309\text{-}0.0393$ s)

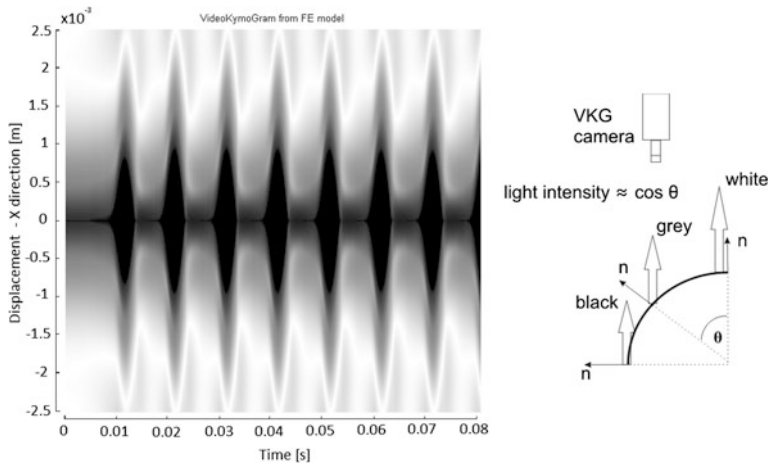


Fig. 4 Example of a VKG image created from the FE modelling results with a schematic of the reflected light intensity using a cosine emission law

4 Conclusions

A three-dimensional FE model of the flow-induced vocal fold self-oscillations in interaction with the vocal tract acoustics was created. Compressible Navier–Stokes equations were used which enabled modelling of the propagation of the acoustic waves in the vocal tract and therefore modelling of a complete fluid–structure-acoustic interaction. So far only homogenous and isotropic material of each layer of the vocal folds tissue was considered. The computed results showed regular vocal folds oscillations after a few periods of the transient regime. The numerical simulations showed close similarities of the developed model with a real

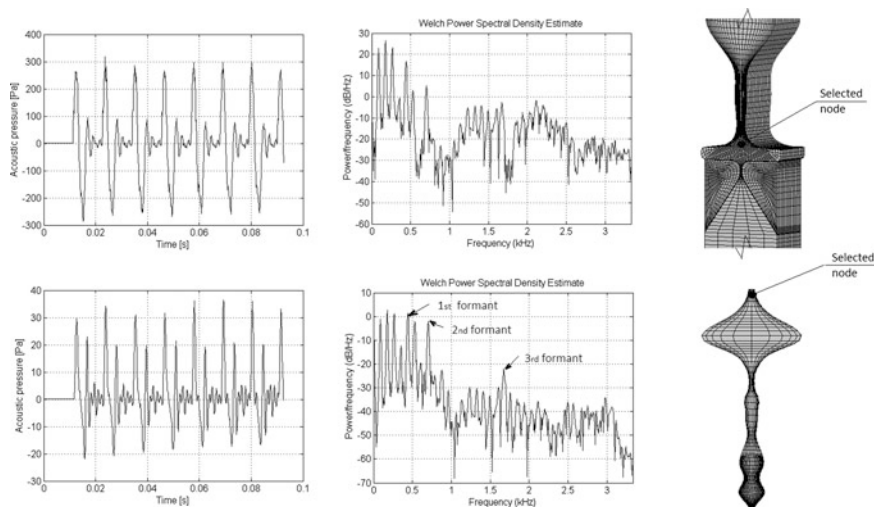


Fig. 5 Acoustic pressure (*left graphs*) and the corresponding power spectral densities (*right graphs*) computed in the selected nodes above the vocal folds (*upper panel*) and near the lips (*lower panel*) for the vowel [u:]

production of voice in humans. The simulated VKG images can be related to those observed laryngoscopically *in vivo*.

Acknowledgments This research is supported by the Grant Agency of the Czech Republic by the project No P101/12/1306 and by the European Social Fund Projects OP VK C.1.07/2.3.00/20.0057 and CZ.1.07/2.4.00/17.0009.

References

1. Titze, I.R.: The myoelastic aerodynamic theory of phonation, National centre for voice and speech, Denver and Iowa City, (2006)
2. Šidlof, P., Švec, J.G., Horáček, J., Veselý, J., Klepáček, I., Havlík, R.: Geometry of human vocal folds and glottal channel for mathematical and biomechanical modelling of voice production. *J. Biomech.* **41**, 985–995 (2009)
3. Horáček, J., Šidlof, P., Švec, J.G.: Numerical simulation of self-oscillations of human vocal folds with Hertz model of impact forces. *J. Fluids Struct.* **20**, 853–869 (2005)
4. Zhao, W., Zhang, C., Frankel, S.H., Mongeau, L.: Computational aeroacoustic of phonation, part I: numerical methods, acoustic analogy validation, and effects of glottal geometry. *J. Acoust. Soc. Am.* **112**, 2134–2146 (2002)
5. Alipour, F., Berry, D.A., Titze, I.R.: A finite element model of vocal-folds vibration. *J. Acoust. Soc. Am.* **108**, 3003–3012 (2000)
6. Thomson, S.L., Mongeau, L., Frankel, S.H.: Aerodynamic transfer of energy to the vocal folds. *J. Acoust. Soc. Am.* **118**, 1689–1700 (2005)
7. Švancara, P., Horáček, J., Hrůza, V.: Development of FE model of interaction between oscillating vocal folds and acoustic space of the vocal tract. *Proceedings of The 6th*

- International Conference on Voice Physiology and Biomechanics, University of Tampere, Tampere, Finland, 163–167 (2008)
8. Švancara, P., Horáček, J., Hruza, V.: FE modelling of the fluid-structure-acoustic interaction for the vocal folds self-oscillation, *Vibration Problems ICOVP 2011*, pp. 801-807. Springer, Berlin (2011)
 9. Švec, J.G., Schutte H.K.: Videokymography: high-speed line scanning of vocal fold vibration, *J. Voice*. **10**, 201–205 (1996)
 10. Švec, J.G., Šram, F., Schutte, H.K.: Videokymography in voice disorders: What to look for? *Annals of Otology Rhinology and Laryngology* **116**(3), 172–180 (2007)
 11. Radolf, V.: Direct and inverse task in acoustics of the human vocal tract, PhD. thesis, Faculty of Mechanical Engineering, Czech Technical University, Prague, p. 95(2010)

Part VI
Optimization of Mechanisms
and Machines, The Mechanisms
of Textile Machines

Analysis of Heald Motion During of Weaving Process

M. Bilek

Abstract The paper is concerned with description of the mathematical model meant for an analysis of the movement of healds during the weaving cycle. The referred model consists of mathematical description of shedding motion, coupled with the solution of the model of the heald of weaving loom. The effected calculations show a high value of acceleration of the heald produced after its drop upon the supporting wire. The referred model allows analysing a considerable part of designs of heald shaft that are employed in weaving looms nowadays.

Keywords Weaving loom • Heald • Mathematical model • Analysis

1 Introduction

The paper is concerned with the assessment of the existing structural design of fastening the heald into the heald shaft. The present state is characterised by an increased loading of the heald produced at its drop upon the supporting wire, bringing about a reduced service life of healds, their wear and an increased noise level of the whole machine. The means for realisation of the objective of this paper has been a complex description of the system shedding motion—heald—warp, employing a verified mathematical model (Fig. 1). Because of an ample spectrum of possible variants of arrangement of individual parts of the system, the paper does not pretend to devise definite parameters of the structural design, but it intends to specify possible ways how to reach its optimisation.

M. Bilek (✉)

Technical University of Liberec, Liberec, Czech Republic
e-mail: martin.bilek@tul.cz

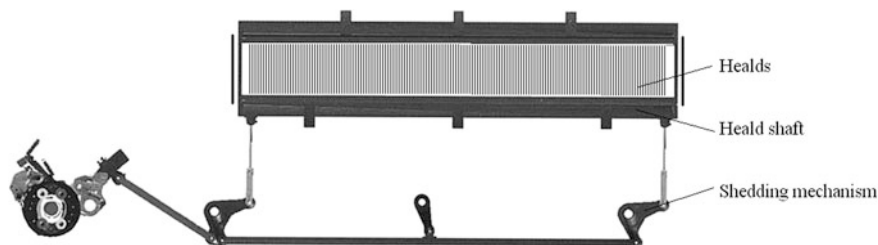


Fig. 1 Shedding mechanism

2 Mathematical Model of the System Shedding Mechanism: Heald—Warp

The heald shaft is the frame in which there are fastened the healds governing warp threads. The healds are fastened in this frame with a necessary designing play. Because of textile technology reasons, this play must allow axial displacement of the heald along the support wire. As the heald shaft performs feed reverse movement, the system of healds gets transferred during the weaving cycle. This transfer produces a load on the supporting wire upon which the healds drop down, bringing as a consequence an increased stressing of the whole shedding mechanism [1].

In view of the fact that the lifting section of the shedding motion is a joint mechanism, a number of procedures and methods can be employed for the modelling of the above structure. It is possible to apply successfully the description of a mechanism based upon the method of devising motion equations by means of Lagrangian equations of the 2nd type according to [2, 3]. The concerned mathematical model is described with more details in [4]. The referred universal mathematical model of the shedding motion can be modified in a simple manner by introducing the time-dependent lift dependence on the driving element, defining the course of its angular displacement. For example, it is possible to realise in this manner a calculation of the movement of a rotational dobby.

The studies realised up to now have shown that the heald is one of the most important parts of the shedding motion and it exerts an important effect upon its dynamic loading. Because of this reason, it also constitutes one of the limiting elements impeding to increase its operational revolutions. The heald is influenced by a number of forces, which determine with which supporting wire it will be coupled. The most important ones are the dynamic force of the heald, the component of the warp force in the direction of movement of the shaft and the weight of the heald.

The analysis of behaviour of the heald during the operating cycle has been realised by means of devised models of the heald. The motion equations describing the movement of the heald during the weaving process are complemented with motion equations of the shedding motion. In all compiled models, the mass of the

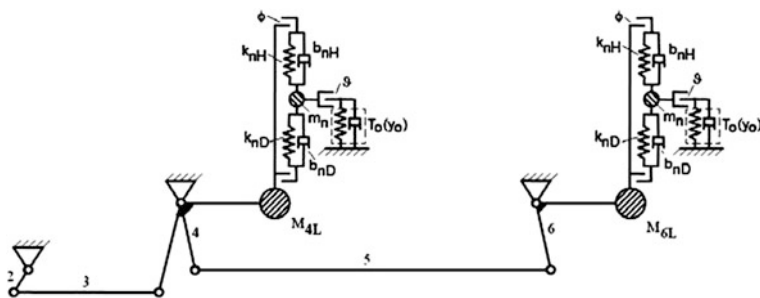


Fig. 2 Schematic model of the system shedding motion–heald (model 1)

heald m_n is concentrated in one mass point. The force T_o from the warp operates in the position of the thread eyelet. The point of action of this force is located in one mass point. It is possible to disregard the bowing of the heald due to its lateral loading. The devised models proceed from the assumption that the movement of the mass point substituting the heald is carried out on a straight line.

An important designing element influencing the behaviour of the heald is the play in its fastening in the heald shaft frame. Thanks to this play, the forces in the warp threads are transmitted upon one of the couple of rods of the heald shaft only in the majority of cases. In the mathematical model, this play can be defined by means of the difference of positions of the upper and lower support wires. The extent of the play in the fastening of the heald on the supporting wire is determined by the parameter ϕ . The devised models of the heald consider also the effect of the size of the thread eyelet 9 upon the course of the force in the warp. At present, there are used flat healds made of a flat steel band by pressing process. The healds are contoured in the positions of their suspension eyes; however, it reduces their rigidity. Because of this reason, mathematical models have considered different rigidities of the upper and lower sections of the heald.

2.1 Mathematical Model of the Elastic Heald

The preceding model of the heald can be complemented with elasticity of its end sections. The whole system which is being solved can be represented schematically according to the Fig. 2. The body of the heald is modelled by means of the Kelvin-Voigt visco-elastic rheologic model with the rigidity k_{nH} and co-efficient of viscous damping b_{nH} in the upper part, and the rigidity k_{nD} and co-efficient of viscous damping b_{nD} in the lower part of the heald. A general motion equation of this model can be written in the form (1).

$$m_n \cdot \ddot{y}_n = T_o - m_n \cdot g + H \cdot k_{nH} \cdot (y_h - y_n) + H \cdot b_{nH} \cdot (\dot{y}_h - \dot{y}_n) - D \cdot k_{nD} \cdot (y_n - y_d) - D \cdot b_{nD} \cdot (\dot{y}_n - \dot{y}_d) \quad (1)$$

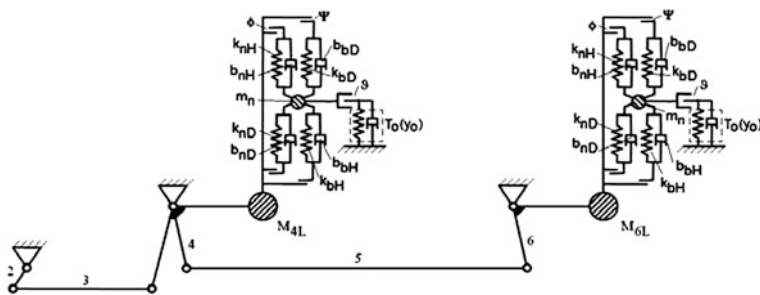


Fig. 3 Schematic model of the system shedding motion-heald (model 2)

The control constants H and D assume the values 0 and 1, and they determine which members of the equation will be employed in the calculation. In the following text, this mathematical model is referred to as the model 1.

2.2 Mathematical Model of Elastic Heald with Damping Element

With the products intended for high-speed weaving looms, some firms begin to employ a damping system of the drop of the heald upon the supporting wire. This system makes use of a damping element (band), fitted in the profile of the rod at an optimum distance from heald eye. This element provides for a reduction of the heald velocity before its drop upon the supporting wire, because the opposite section of the heald is pressed into the rubber element.

The mathematical model of the heald with a damping system is obtained by a modification of the model of the elastic heald. This model is complemented with the effect of the damping element. The whole solved system can be shown schematically according to the Fig. 3. The general motion Eq. (2) describing the behaviour of the heald during a revolution of the weaving loom is complemented with further terms describing the rigidity and the effect of the damping element. The rigidity k_{bH} and the co-efficient of viscous damping b_{bH} characterise the properties of the element in the upper section, meanwhile the rigidity k_{nD} and the co-efficient of viscous damping b_{nD} the properties of the element in the lower section of the heald. The parameter Ψ determines the depth of heald nesting into the damping element before its drop upon the supporting wire. The constants H , H_1 , D and D_1 determine which members of the equation will be employed in the calculation. In the following text, this mathematical model is referred to as the model 2.

The general equation of this case can be written in the following form:

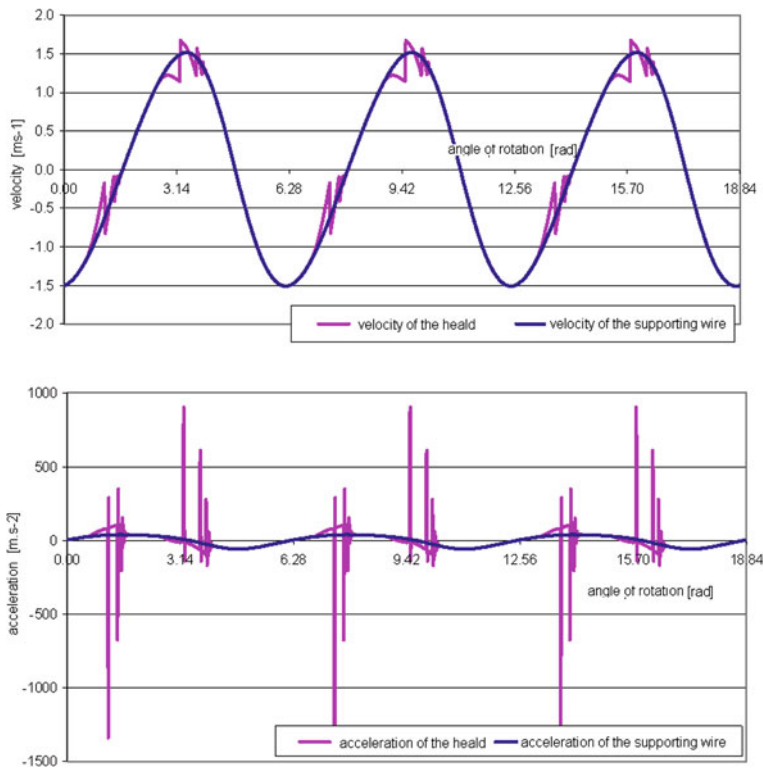


Fig. 4 The courses of velocity and acceleration of the heald shaft and of the heald for the operating velocity of the shedding motion 300 rpm (model 1)

$$\begin{aligned}
 m_n \cdot \ddot{y}_{in} = & T_o - m_n \cdot g + H \cdot k_{nH} \cdot (y_h - y_n) + H \cdot b_{nH} \cdot (\dot{y}_h - \dot{y}_n) \\
 & - D \cdot k_{nD} \cdot (y_n - y_d) - D \cdot b_{nD} \cdot (\dot{y}_n - \dot{y}_d) + H_1 \cdot k_{bD} \cdot (y_d - y_n - \varphi + \Psi) \\
 & + H_1 \cdot b_{bD} \cdot (\dot{y}_d - \dot{y}_n) - D_1 \cdot k_{bH} \cdot (y_n - y_h - \varphi + \Psi) - D_1 \cdot b_{bH} \cdot (\dot{y}_n - \dot{y}_h)
 \end{aligned} \quad (2)$$

3 Conclusions

The first model (the model 1) is the simplest case of heald modelling, solving its behaviour during the weaving process. However, this model is suitable for realisation of a basic analysis of behaviour of the system, precisely because of its simplicity. The basic outputs of the model 1 are the moment of separation of the heald from the support wire, the time characterising the duration of the heald

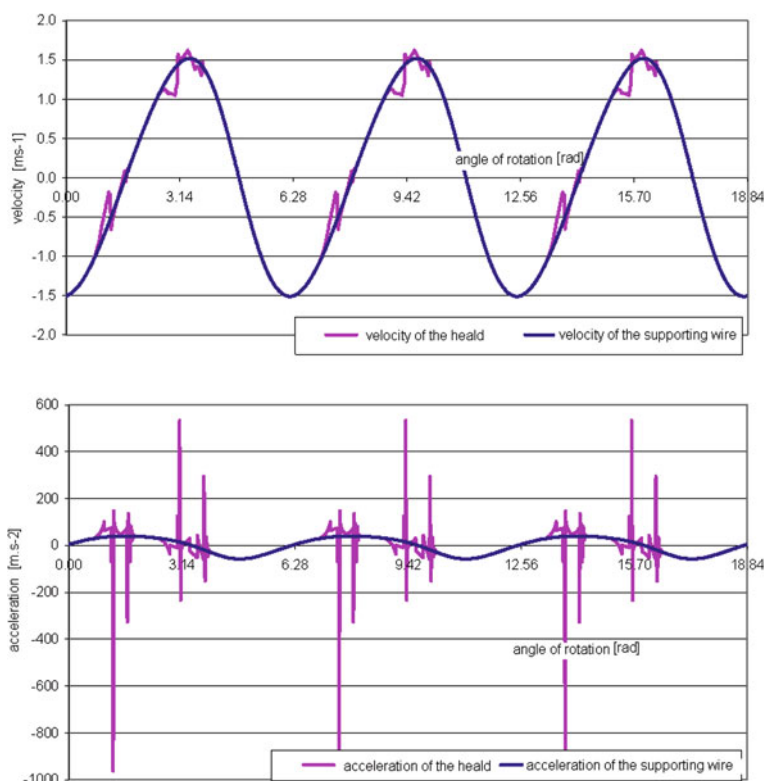


Fig. 5 The courses of velocity and acceleration of the heald shaft and of the heald for the operating velocity of the shedding motion 300 rpm (model 2)

transfer between the rods of the heald shaft, the difference between the velocity of the heald and that of the supporting wire etc.

The mathematical model 1 describing the behaviour of the heald during the weaving cycle simplified in this way can be used conveniently e.g. for an analysis of principal parts of the shedding motion. It allows analysing the load distribution between the rods of the heald shaft during the weaving cycle (Fig. 4). The said model allows determining principal areas of operating states of the heald and a simple analysis of the character of the heald transfer between rods of the heald shaft. Should the analysis be concerned with the behaviour of the heald during the weaving cycle directly, the mathematical model must be still extended and elaborated. In particular, the said extension allows determining the number and size of heald bounces from supporting wire after its transfer between individual supporting wires. In this mathematical model, both the moment of separation of the heald from supporting wire and the duration of its transfer between the rods of the heald shaft is the same as in case of the model 1. The referred model allows for determining of the force load upon individual end eyelets of the heald. The

performed calculations show a high value of the heald acceleration generated after its drop upon the supporting wire. By means of this model, it is possible to analyse a large part of the cases of fastening of healds into the heald shaft frame, employed in weaving looms nowadays.

The model 2 permits to solve the structural design of fastening of healds into the heald shaft frame, intended for high revolution weaving looms. The courses obtained from this model show a reduction of the number of heald bounces after its transfer between individual supporting wires, compared with a system without a damping element. The use of a damping element brings a considerable reduction of the maximum value of heald acceleration (Fig. 5). From the performed analysis there follows that in case of application of a damping system, the equilibrium of forces on the heald occurs in another moment than in case of preceding models. An important aspect of this solution is the transfer of a part of the load upon the lower supporting wire; due to this fact, the loading of the rods of the heald shaft frame is made more equal.

Acknowledgments The paper has been elaborated in the frame of the solution of the grant project: MSM:4674788501

References

1. Recep, E., Gülcan, Ö., Yildiray, T.: Kinematics of rotary dobby and analysis of heald frame motion in weaving process. *Text. Res. J.* **78**(12), 1070–1079 (2008)
2. Mrázek, J.: Theoretical analysis of dynamics four-bar beat up mechanisms of a loom. In: *Mechanism and machine theory*, Pergamon Press, USA, pp. 125–136 (1992)
3. Bílek, M., Mrázek, J.: Dynamic stress of heald shaft of weaving looms. *Vlákna a textil*, č. 3, pp. 131–134, Slovakia (1998)
4. Mrázek, J., Bílek, M.: Heald dynamics analysis of weaving looms. *Zeszyty naukowe*, č. 39, s. 231–236, Polsko. ISSN 0867-3128, (2001)

Kinematic Design and Ideal Dimensioning of New Highly Dynamic Drive Assemblies for Knitting and Braiding Machines

D. Denninger, M. Berger and A. Heine

Abstract The paper deals with the kinematic design and the ideal dimensioning of highly dynamic drive assemblies using MCAD strategies. The procedure is explained step by step by the example of a round braider construction. The analysis of the general mechanical principle and the definition of boundary conditions and objective criteria is our top priority. Innovative potential to increase performance and improve meshwork quality lies in the highly dynamic drive assembly to lay the threads. For a newly developed, non-linear mechanical drive concept, feasibility studies up to dimensional synthesis and draft analysis are demonstrated.

Keywords Round braiding • Mechanism analysis and synthesis • coupling and cam gear • Virtual transmission design

1 Round Braiding

Cable armors are usually generated by round braiding with the fast braiding system “horn”. With the so-called lever arm braiders the chaining thread is guided along a special laying curve to realize the braid patterns. To generate this layer curve a cam gear with a solid track cam ring and the therein guided lever arm are used. Typical products are cables with copper network as outer conductor.

D. Denninger (✉) • M. Berger • A. Heine
Chemnitz University of Technology, Chemnitz, Germany
e-mail: daniel.denninger@mb.tu-chemnitz.de

M. Berger
e-mail: maik.berger@mb.tu-chemnitz.de

The braiding takes place in an imaginary hollow sphere. Center of this sphere is the point of braiding. The yarn store circle on a latitude of the sphere around the point of braiding. Each thread has got the same distance from the start point of the coil support to the braiding point. This leads to a constant and continuous filament process. To generate a meshwork, for example, the filling threads revolve clockwise around the braiding point and the chaining thread threads revolve in opposite directions. The filling threads are at one latitude, while the chaining threads jump from a higher to a lower degree of latitude to the filling longitude. For the crossing of the chaining thread a sinusoidal web is necessary. A braid pattern of 2 over 2 is generated by lever arm braiders. [3, 4]

2 Analysis of the Existing Mechanism Principle

Round braiders, which are available on the market nowadays, are at their technological limit regarding the operating speed. Two counter rotating carriers on which coils for filling or chaining threads are attached, are rotating around the stationary cam ring. The laying device (thread take-up lever), for realizing the required path of motions of the chaining thread, is mounted in the cam-guide (control curve) of the stationary cam ring on the one hand, and movably at the chaining thread rotor on the other hand. The cam-guide causes the raising and lowering of the thread take-up lever, which passes the thread either above or below the filling thread [2]. This sort of thread guide entails a vibration excitation at a higher rate, that can cause a flaw of the thread. The guide of the thread take-up lever is an example for reasonable impressing of the abnormal oscillations. Small irregularities, in the form of a control curve, abate themselves on the laying of the thread take-up lever, which confers it upon the thread.

To implement a novel drive concept for the laying device, one has to desist from the principle of circular enclosure of the machine by the cam ring. For the processing of the new, nonlinear transmitting device for the laying of the chaining thread, kinematic initial values arise out of the analysis and interpretation of existing general mechanical principle. Based on these initial values, the braiding technology as well as the subsequent specific standards were defined. The ideal laying curve for the braiding of a lever arm braider derives itself from the following criteria: the fast braiding system “Horn”, the machine specific geometrical boundary conditions and the specific standards of the meshwork and its bonding. The twisting of the thread is prohibited for a lot of braiding. These specific standards of the meshwork have to be considered during the structuring of the laying curve [4].

The aforesaid machine specific geometrical boundary conditions result from the constructive conversion of the filling thread rotor as well as the rotation of the yarn store. In the machine concept, cavities for the chaining thread laying are created, by using deflector plates and notch. These cavities are however, according to the rotational velocity, available and passable in a specific time frame. If the chaining

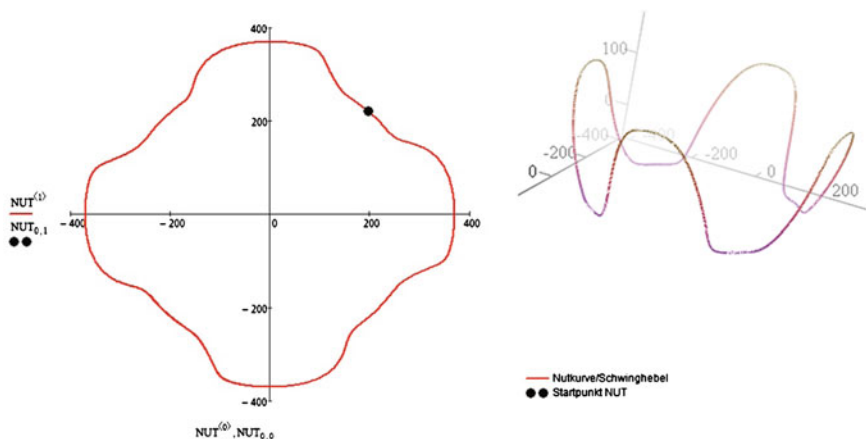


Fig. 1 Laying curve (cam gear with solid track cam ring/lever arm)

thread doesn't perform the required raising and lowering regarding the filling thread in the "Shed", it leads to thread breakage. The path of motions is inflicted by additional time specifications. These mathematically defined specifications have to be observed by a nonlinear motion. Therefore, the ideal laying curve is a track way which can be realized by the perfect laying of the chaining thread under the vibration excitation as low as possible. The processing of the ideal laying curve is realizable with the dimensional synthesis of each feasibility studies. Inalienable tools are the different functionalities of syntheses and analysis of MathCad and Creo. By using the available port, simulation results can be analyzed and used directly. Important insights for the processing of an ideal laying curve were gained from explicit analysis of existing machine concepts. Therefore the existing mathematical specification of the controlling- and laying curve offer reference values and clues, and give indications for the optimization potential as well. The trajectory of the common laying curve is shown in Fig. 1.

The projected power enhancement as well as the enhancement of the meshwork quality implies a novel laying of thread with mathematically defined irregular motion of the laying device. For the specification of the required laying curve of the laying device, a braid pattern of 2 over 2 were exemplarily selected, to generate an approximated ideal laying curve out of the given boundary conditions. The desired motion of the laying device originates by a mechanical superposed lifting and rotatory motion in combination with a nonlinear drive.

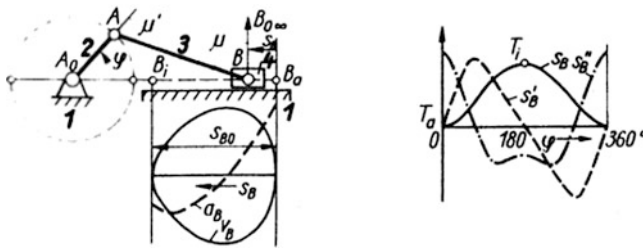


Fig. 2 Plan (*left*) and trajectories (*right*) of a slider-crank

3 Integrated Mechanism Dimensioning with MCAD Strategies

The aim of the integrated mechanism dimensioning was the deflection from ideas and drafts via MCAD strategies and feasibility studies to get to the stages of development, based on a detailed virtual prototype and which are required for the dimension synthesis and the concept analysis. Another aim was the modification for practical application.

3.1 Structural Classification

Creating the horizontal path difference, only an option with a prismatic joint comes into consideration to lay the chaining thread, Fig. 2. The defined specifications correspond with the benefits, having consequently space-saving construction in addition to a guidance of the laying device over the whole path of motions. To realize the required transmission of this linkage on the output side a mechanical primary gear unit is favored. From the analytical and constructional point of view, it is possible to generate a continuous irregular action with approximated or rather exact indexing with a multitude of options.

Initially, the concept question of the action partition comes to the fore. In principle, the possibility to create a primary gear unit per laying device or a primary gear unit for the whole construction of the chaining thread exists. The potential options result from the mentioned structure concepts.

The variation of a slider-crank is regulated by the length of the crank without any further ado. Indeed, the variation alternatives of the transfer function over the eccentricity doesn't suffice to create the required transmission. In addition, the geometrical boundary conditions on the chaining thread rotor, carrying in total of eight laying devices of a braid pattern of 2 over 2 are inappropriate. The realization of the drive of the slider-crank is supplied by a frame fixed bevel pinion. On this, a gear per laying device rolls off to the drive of the slider-crank. The unrolling is enforced by the rotary motion of the chaining thread-rotor.

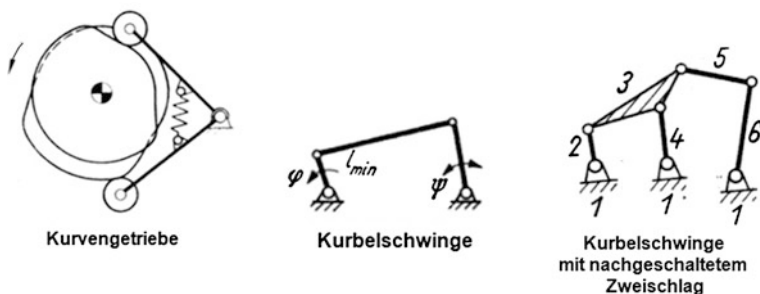


Fig. 3 Mechanism structures for generating oscillations

3.2 Comparison of Variants of Possible Primary Gear Units

Two approaches open up to transform the revolving driving. A continuous irregular movement with rather exact indexing has to be originated via the superposition of the drive with an oscillatory motion with two reverse positions. There is on the one hand a possibility due to the systematization, to grip a constant number of revolutions and to transmit it nonlinear for each laying device by a cascade gearbox. The second option would be the generation of a defined oscillatory motion before gripping. Both possibilities have pros and cons and have to be considered separately for the concrete conversion of the cascade gearbox.

The structure selection for the generation of the nonlinear drive function of the slider-crank before the gripping of the number of revolutions at the rocking bevel gear produces the illustrated options in Fig. 3. All performed mechanism structures were analyzed, simulated and optimized.

To put the nonlinear drive function of the slider-crank after the gripping of the number of revolutions at the stationary bevel gear into effect, multiple options exist. A great nonlinear transmission is producible via the antiparallel-crank that is shown in Fig. 4. Due to the required auxiliary gear, a constructive conversion in the highly dynamic range can be eliminated. Therefore the replacement transmission, a elliptic gear pair is chosen as primary gear unit. In the following, the drive concept to lay the chaining thread via a slider-crank and a upstream elliptic gear pairing with the required transmission to pass the “Shed” is dimensioned and designed.

3.3 Dimensional Synthesis and Concept Analysis of a Laying Device

The analysis of the existing machine principle, especially the structuring of the ideal laying curve, gives the required conditions for the synthesis of the drive concept. In this connection the height to lay the chaining thread is directly derived

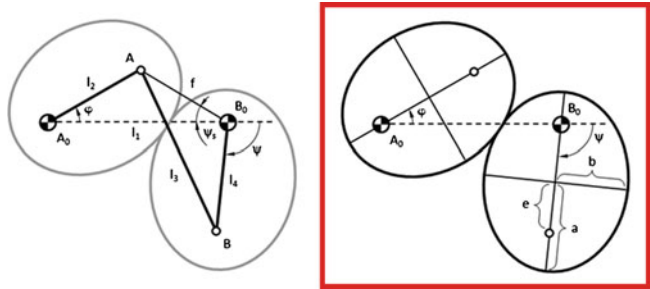


Fig. 4 Antiparallel crank and elliptical gear pair (see red box) for direct generation of continuous non-uniform motion

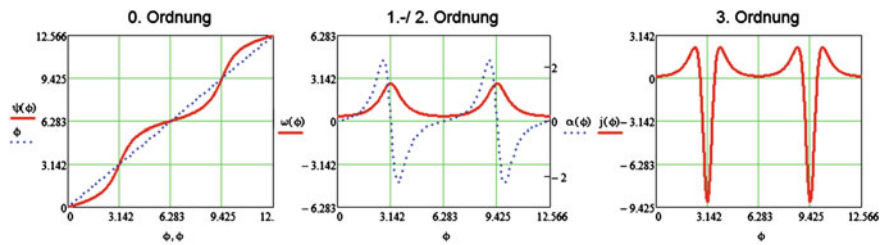


Fig. 5 Transmission function 0. to 3. order

from the laying curve. The geometrical conditions result from the fast braiding system “Horn”. An eccentric slider-crank to originate the requested lifting is dimensioned considering the drive corresponding to VDI 2130 [6].

The elliptic gear pair can easily be calculated using a replacement transmission structure. The linkage is described by trigonometric relations [5], Fig. 4. In this case, the necessity of the analytic calculation of the wanted transfer function exists, because today the direct simulation of non-circular gears in Creo is not possible. The constructive realization of the replacement transmission structure proves to be not qualified, due to needed auxiliary gear to assure against turnovers.

The approach to calculate the output function $\psi(\varphi)$ like described in [5] is realized in MathCad [1] and processed up to 3rd order, Fig. 5. For further models to verify the requested path of motions, a nonlinear driving was defined in the simulation by a servo drive. Examples are the passing of the shed as well as the detection of the kinematic, kinetostatic and kinetic parameters. The required maximum transmission of the elliptic gear pairing is $\text{imax} = 2.9$.

4 Virtual Model of the Fast braiding System

A virtual simulation model is used for all further design analysis. The slider-crank on the chaining thread-rotor is powered by a servo drive. The chaining thread-rotor is carrying eight laying devices each offset by 45° . This optimized virtual model was subsequently adopted as a module in the machine design. With the help of dynamic analyzes it was efficient to find the necessary parameters for the dimensioning and design issues. The relationships of the kinetic energy of a system, considered as a rigid machine, the speed and the reduced mass moment of inertia are described [7]. The reduced mass moment of inertia is necessary for the analytical calculation of the required driving torque. Creo is a quick and effective way to determine the interrogation of the kinetic energy in the provided system.

5 Results and Conclusion

The kinematic design and the ideal dimensioning of new highly dynamic drive assemblies for knitting and braiding were exemplified for round braider constructions. Therefore, the comprehensive transmission design via MathCad und CreoTM Elements/ProTM was focused on. The problem with the fastbraiders was implemented by the detailed analysis of the existing machine concept considering the boundary conditions on the braid patterns and physical requirements for this particular gear. The structural selection was the basis for a comparison of options and the synthesis of the most promising structures. Virtual prototypes were created in order to implement the selected options. For the effective generation of solutions, MathCad-Tools and motion-skeletons were used. The following steps, such as the design and dimensioning, were based on the implementation of the options. The result is a comprehensive virtual model of the new fastbraider.

Acknowledgments The research work reported here was made possible by the AiF.

References

1. Berger, M., Matthes, J.: MATTOOL—Eine Sammlung modularer Algorithmen zur rechnerunterstützten Antriebs- und Getriebeauslegung, VDI Berichte , ISBN : 3-18-091966-3 (2006)
2. Berger, M., Jakel, R.: Ganzheitliche Getriebeauslegung. PTC, Darmstadt (2008)
3. Denninger, D.: Einsatz von Pro/E-MCAD-Strategien zur integrativen Entwicklung des “Kettfaden”- Antriebssystems einer Rundflechtmaschine, ISBN: 978-3-00-031136-9 (2010)
4. Denninger, D., Berger, M.: Entwurf und Auslegung eines neuen nichtlinearen Antriebskonzeptes mittels Creo Elements/Pro, ISBN: 978-3-941003-31-6 (2011)
5. Dittrich, G.: IGM-Getriebeauslegung Ellipsenrädergetriebe, RWTH Aachen (2000)

6. VDI-Richtlinie, : Getriebe für Hub- und Schwingbewegungen; Konstruktion und Berechnung viergliedriger ebener Gelenkgetriebe für gegebene Totlagen. VDI Verlag (2130)
7. Ullmann, M.: Mathematische Auslegung sowie steuerungs- und regelungstechnische Modellierung eines Force-Feedback-Simulators zur haptischen Analyse ebener Mechanismen, Projektarbeit TU-Chemnitz (2011)

Analysis of the Loop Spinning System

J. Beran and M. Hejnova

Abstract The loop spinning system ranks among systems where centrifugal forces, friction shear forces and resistance of air play an important role. The process of yarn formation is related with the rotation of yarn round a fixed axis, generating a phenomenon which is called yarn ballooning. The mathematical model of ballooning yarn is employed for analysis of the loop spinning system. The effect of the radius of the package on the value of the maximum radius of rotating loop and on the value of maximum tensile force in the rotating yarn is studied in this article.

Keywords Loop spinning system • Balloon • Balloon separator

1 Introduction

The system of loop spinning ranks among new spindle systems of formation of yarn with permanent twist which achieve high spinning velocities. In these systems, the yarn twisting and the winding of yarn upon the bobbin constitute an inseparable process. Important roles there play centrifugal forces, friction shear forces and resistance of air. The process of yarn formation is related with the rotation of yarn round a fixed axis, generating a phenomenon which is called yarn ballooning. This phenomenon has been studied in relation with a number of

J. Beran (✉) · M. Hejnova
Technical University of Liberec, Liberec, Czech Republic
e-mail: jaroslav.beran@tul.cz

M. Hejnova
e-mail: monika.hejnova@tul.cz

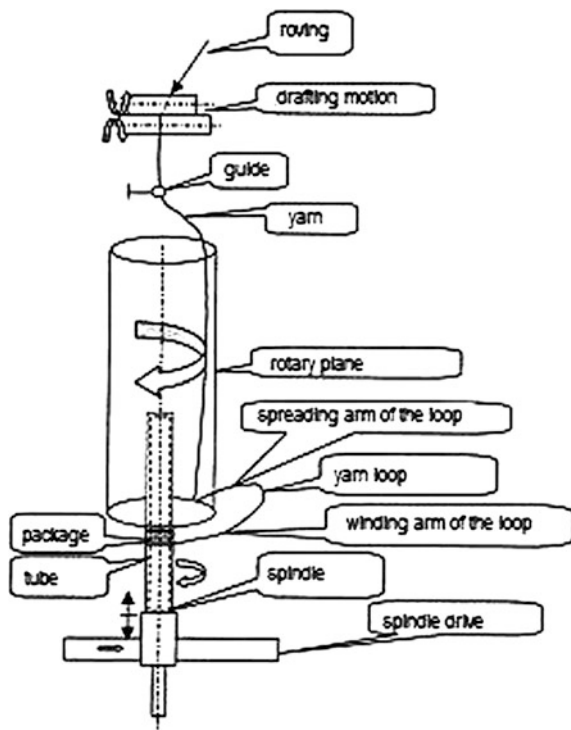
applications in textile industry, e.g. in the papers [1–3]. The mathematical model of ballooning yarn compiled in the paper [4] will be employed for simulation of the complete process of yarn winding under determined boundary conditions as well as for analysis and optimisation of the loop winding system. The examined process is described by a system of non-linear differential equations of 2nd order [1–3]. Since an analytic solution can be obtained under a series of very simplifying assumptions only, instruments of numerical simulation are used for determination of the shape of curve of rotating yarn in the section between the yarn guide behind the drafting motion and the place where the yarn is wound on a tube, as well as for determination of tensile forces in the spinning system.

2 System of Loop Spinning

The twisting of yarn is provided by means of a rotating hollow body (carrier), through the hollow of which the produced yarn is passing, lying on its inner wall (see Fig. 1). The rotating inner wall carries the yarn, and at the same time, it functions as separator of the yarn balloon, which would be generated by the rotating yarn. The angular velocity of carrying rotational movement of the yarn (yarn loop) with respect to the carrier changes in dependence on the winding diameter, and the yarn is dragged along the inner wall of the carrier. After leaving the hollow of the carrier, the yarn passes into a loose balloon, it creates a loop and it is wound upon a bobbin. The loop spinning ranks among the systems of yarn formation with a constant balloon height. The simplified diagram in the Fig. 1 consists of the following components: drafting motion, yarn guide, carrier, spindle, tube with package.

3 Assumptions Defining the Mathematical Model

An exact solution of the shape of the yarn curve in general three-dimensional case results very difficult. It is practically impossible to get a simple analytic expression. Under certain simplifying assumptions, it is possible to obtain the result by numerical solution of the given task, see e.g. the papers [1–3]. During the loop spinning process, there changes the boundary condition produced by the change of winding radius during formation of the package. We shall consider this change to be quasi-stationary, which will allow us to employ a stationary mathematical model for the solution. The high-frequency processes which bring about vibrations of the yarn round the quasi-stationary position and constitute a response to existing manufacturing and assembling irregularities are not taken into account in the model. Assumptions defining a simplified model of the ballooning yarn:

Fig. 1 Loop spinning system

- the yarn is elastic ideally and uniform in mass,
- the deformation of the yarn is not influenced either by relaxation or creeping phenomena, and it does not depend upon temperature,
- the carrying angular velocity of the yarn is constant,
- the relative velocity of the yarn feeding is constant,
- the boundary conditions are independent on time,
- the effect of air resistance in the direction of a tangent to the curve of ballooning yarn is disregarded.

4 Mathematical Model of Ballooning Yarn

For the case of ballooning yarn according to Fig. 2, we shall introduce a system of cylindrical co-ordinates $O r \varphi z$, revolving round the co-ordinate axis z at an angular velocity ω . The beginning of the co-ordinate system is in the centre of the guide eye and the axis z is identical with the axis of the spindle. The angular velocity of rotating loop is ω and the relative velocity of yarn is w . The component equations

acceleration. The resistance of air F_o in the direction of a normal to the curve of ballooning yarn can be expressed by the relation:

$$\mathbf{F}_o = -\frac{1}{2} C_n \rho D |\mathbf{v}_n| \mathbf{v}_n \quad (2)$$

where C_n is non-dimensional co-efficient of the air resistance, \mathbf{v}_n is the vector of the normal component of yarn velocity, ρ is specific gravity of air, D is effective diameter of yarn. The co-efficient of air resistance C_n depends on the Reynolds' number. For the by-passing of air round the yarn, these dependences have been established experimentally for varied yarns.

5 Mathematical Model of Movement of the Yarn on Balloon Separator

During its movement on the separator, the yarn is influenced—in addition to forces produced in loose ballooning—by the reaction from the separator. The same can be broken into the normal component and into the shear one

$$\mathbf{N} = R \mathbf{n}_0 \cdot \mathbf{F}_s = -R f_1 \frac{\mathbf{v}}{v}, \quad (3)$$

where R is the reaction on the yarn from the separator, referred to the unit of yarn length, \mathbf{n}_0 is the vector of the normal to the plane constituting the surface of the separator, given by the equation $P(r, \varphi, z) = 0$, f_1 is the co-efficient of shear friction between the yarn and the separator. For balloon separators that are symmetrical axially with respect to the axis of rotation z there holds that the normal component of the reaction lies in the meridian plane. The equations of motion of the yarn in loose balloon (1) can therefore be adapted for the movement of yarn on balloon separator into the following general form:

$$\begin{aligned} \frac{d}{ds} \left(T_a \frac{dr}{ds} \right) - T_a r \left(\frac{d\varphi}{ds} \right)^2 + \frac{\mu_0}{f(T)} \omega^2 + \omega^2 r + 2 \frac{\mu_0}{f(T)} \omega \omega r \frac{d\varphi}{ds} + F_{or} + N_r + F_{sr} &= 0 \\ \frac{1}{r} \frac{d}{ds} \left(T_a r^2 \frac{d\varphi}{ds} \right) - 2 \frac{\mu_0}{f(T)} \omega \omega \frac{dr}{ds} + F_{o\varphi} + F_{s\varphi} &= 0 \\ \frac{d}{ds} \left(T_a \frac{dz}{ds} \right) + \frac{\mu_0}{f(T)} g + F_{oz} + N_z + F_{sz} &= 0 \end{aligned} \quad (4)$$

$$\begin{aligned} T_a &= T - \frac{\mu_0}{f(T)} \omega^2, \quad \frac{ds}{dl} = f(T), \quad \left(\frac{dr}{ds} \right)^2 + r^2 \left(\frac{d\varphi}{ds} \right)^2 + \left(\frac{dz}{ds} \right)^2 = 1 \\ P(r, \varphi, z) &= 0, \end{aligned}$$

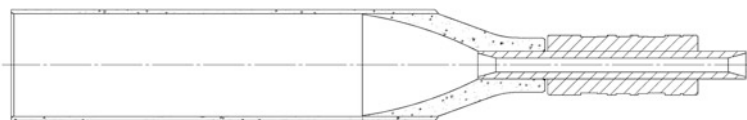


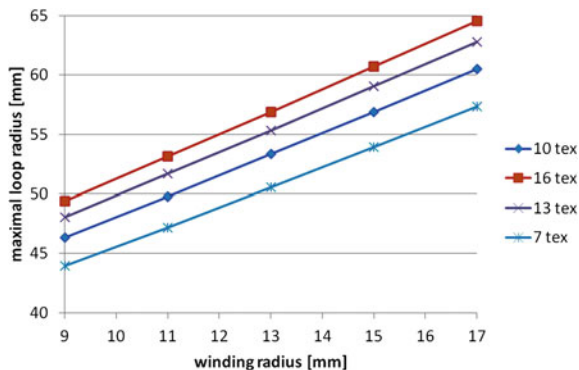
Fig. 3 Selected carrier (separator)

where N_r and N_z are components of normal reaction, F_{Sr} , $F_{S\phi}$, F_{Sz} are components of shear reaction. The general Eq. (4) is specified in the model for the particular surface of the balloon separator, i.e. the cylindrical, conical and toric planes.

6 Boundary Conditions

From the point of view of acting forces, the curve of the twisting yarn in the spinning system can be divided into several sections, depending whether the yarn balloons loosely in the concerned section or the yarn balloon is limited in some manner. The proposed mathematical model simulates the process of yarn formation in the section between the guide eye and the winding of the yarn upon the tube. The model includes the angle of embracement of the yarn on the guide eye and the increase of tensile force determined by the Euler's relation. As has been stated already, during its formation in the spinning system the yarn passes through several sections, differing in particular by their geometric shapes and different forces acting upon the yarn. For the selected structure of the carrier, Fig. 3, they are the following six sections:

- first section of loosely ballooning yarn between the guide eye and the input of the carrier tube, including the transfer of yarn upon its inner wall; the small cone on the input section is not considered,
- the section of yarn movement on the inner wall of the cylindrical part of the carrier tube, including the transfer upon its conical end section, considering the Euler's relation for the increase of tensile force,
- the section of yarn movement on the inner wall of the conical section of the carrier including the transfer of yarn upon inner toric plane, considering the Euler's relation for the increase of tensile force,
- the section of yarn movement on the toric plane including the transfer of the yarn upon the inner cylindrical wall of the carrier,
- the section of yarn movement on the inner wall of the cylindrical part of the carrier, including the transition into loose balloon, considering the Euler's relation for the increase of tensile force,
- the section of loosely ballooning yarn between the bottom edge of the separator and the place of winding on the bobbin.

Fig. 4 Results of analysis

In the last section of loosely ballooning yarn, the compiled model considers the movement of the rotating loop in the plane perpendicular to the spindle axis only, i.e. the distributing motion of the spindle board has been disregarded.

In the quality of an example, there are indicated here the boundary conditions for the first section of yarn in loose balloon. In the place of the guide eye, the following conditions can be set:

$$s = 0 : r(0) = r_0, \varphi(0) = 0, z(0) = 0, \varphi'(0) = 0.$$

where r_0 is the radius of the guide eye. If s_1 is the length of yarn in the balloon between the guide eye and the tube of the carrier, then the boundary conditions in the place of transfer of loosely ballooning yarn to the cylindrical area of the carrier tube are:

$$s = s_1 : r(s_1) = r_1, r'(s_1) = 0,$$

where r_1 is the radius of the carrier tube. On the opposite end of the spinning system, in the place where the yarn is wound on a bobbin, the following condition must be complied with:

$$s = s_6 : r(s_6) = r_n, z(s_6) = h,$$

where r_n is the radius of winding on the bobbin, h is the distance between the guiding eye and the bottom edge of the separator.

7 Numerical Solution of the Mathematical Model

The solution of the model of the yarn moving in the system of loop spinning leads to a boundary task for a system of non-linear differential equations of 2nd order, where the sought functions are $r(s)$, $\varphi(s)$, $z(s)$, $T(s)$, and their first or second derivatives. The arc length of the curve s figures as an independent variable here. The system of Eqs. (1) or (4) can be resolved with respect to the highest

Fig. 5 Results of analysis

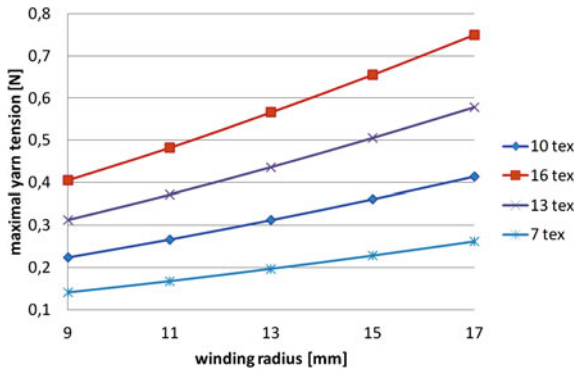


Fig. 6 Results of analysis

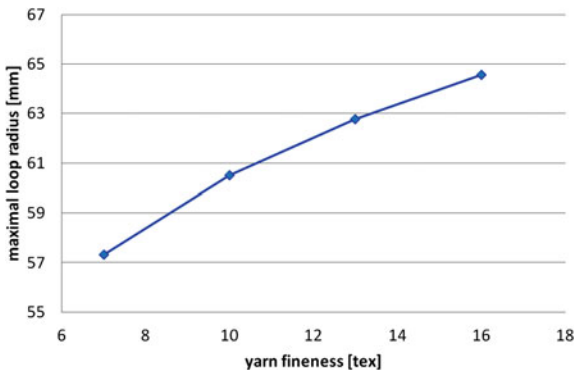
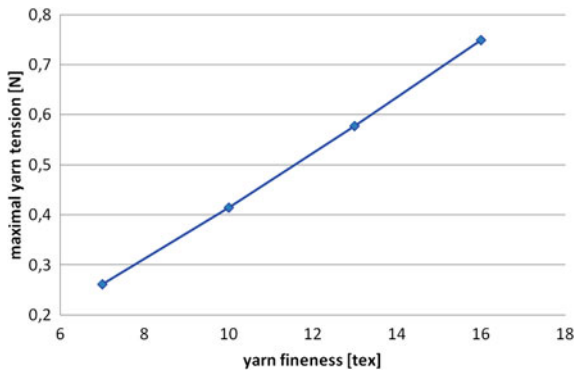


Fig. 7 Results of analysis



derivatives of sought functions, and converted into a system of equations of 1st order. The boundary task is resolved by the shooting method, where the character of the boundary conditions allows converting the solution into a problem with initial conditions [3]. The calculation of the yarn curve is carried out for each section of the spinning system separately, with some sections leading to boundary tasks. The system of differential equations is resolved by the Runge–Kutta method.

For determining the approximations of the missing initial values, the iteration method of secants has been employed. As the basis of the calculation, there serves the outer iteration cycle for determination of the initial value $T(0)$, and the iteration is ended if the boundary condition in the place where yarn is wound on the bobbin is fulfilled. The missing initial values of individual sections are determined by means of inner iteration cycles; for example, for the first section there is resolved the progression of initial tasks with varied values $r'(0)$, and the iteration is ended if the boundary conditions in the place of transfer of loosely ballooning yarn upon the cylindrical plane of the carrier tube are fulfilled. For the resolution of the problem there has been compiled a program in the environment MATLAB.

8 Analyses of the System of Loop Spinning

For analysis of the system of loop spinning, two principal parameters have been chosen, namely the maximum radius of the loop and the maximum value of tensile force in the yarn. The first one influences the structure of the system, the other one the yarn breakage rate. Therefore, there is examined the effect of the radius of the package on the value of the maximum radius of rotating loop and on the value of maximum tensile force in the rotating yarn at constant velocity of spindles 44,000 rpm and at constant twist factor 55. Furthermore, there has been analysed the dependence of both chosen parameters on the yarn counts under the same conditions. The results of the analysis are indicated in form of charts in the Figs. 4, 5, 6, and 7.

9 Conclusions

From the performed analysis there can be deduced the following conclusions for the new system of loop spinning. The dependence of maximum value of radius of the loop depends on the winding radius linearly, with different slopes for concerned yarn counts. Moreover, it is possible to state that this value increases with increasing yarn fineness, but the increment of the value decreases gradually. This dependence can for example be approximated very precisely by a polynomial of 3rd degree. The dimension of the rotating loop influences the pitch of spindles, and consequently, the structure of the spinning machine. The maximum value of the tensile force in the yarn increases quadratically with the winding radius, because the velocity of the loop during the winding process increases at the same time. The quadratic dependence of the tensile force on the velocity of the rotating yarn is known from the physical phenomenon of yarn ballooning. The maximum value of the tensile force increases with the increasing yarn count markedly. For example, for yarn of the fineness 16 tex it increases nearly to a triple, compared with the yarn of the fineness 7 tex. The loop spinning has a certain disadvantage in

comparison to ring spinning, where the value of the tensile force can be influenced—at a given velocity of spindles—by the choice of the traveller. With the loop spinning system, the tensile force is determined by the rpm of spindles directly, and can be regulated by a change of this velocity only.

Acknowledgments The paper was supported by the subvention from Ministry of Education CZ under contract code MSM 4674788501 and in part by the Project OP VaVPl Centre for Nano materials, Advanced Technologies and Innovation CZ.1.05/2.1.00/01.0005.

References

1. Batra, S.K., Ghosh, T.K., Ziedman, M.I.: An integrated approach to dynamic analysis of the ring spinning process. *Text. Res. J.* **59**, 309–317, (1989)
2. Fraser, W.B.: Air drag and friction in the two-for-one twister: results from theory. *J. Tex. Inst.* **84**(3), 364–375 (1993)
3. Beran, J.: Dynamic analysis of the ring spinning process. *Eng. Mech.* **12**(6), 393–401 (2005)
4. Beran, J., Smolková, M.: Mathematical model of loop spinning system. In: *Proceedings of 10th international conference on the theory of machines and mechanisms*. TUL, Liberec 2008, pp. 55–62.
5. Migušov, I.I.: *Mechanika tekstilnoj niti i tkani*, Moskva (1980)

Adjusting the Chain Gear

Z. Koloc, J. Korf and P. Kavan

Abstract The adjustment (modification) deals with gear chains intermediating (transmitting) motion transfer between the sprocket wheels on parallel shafts. The purpose of the adjustments of chain gear is to remove the unwanted effects by using the chain guide on the links (sliding guide rail) ensuring a smooth fit of the chain rollers into the wheel tooth gap.

Keywords Vibrations · Impact · Sliding guide rail · Drive chain

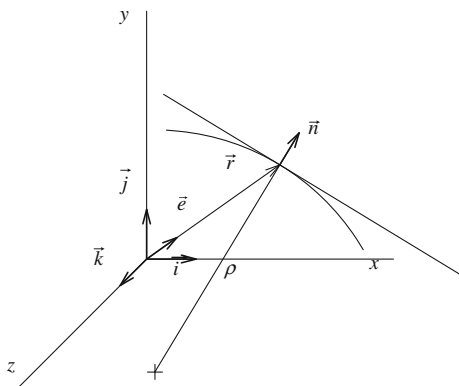
1 Introduction

The adjustment (modification) deals with gear chains intermediating (transmitting) motion transfer between the sprocket wheels on parallel shafts. When another tooth of the driven wheel engages into the chain roller, the non-adjusted chain gear always shows impact between those links. Furthermore, the periodic lifting and lowering of the chain excites the transverse vibrations of the chain, gear ratio unevenness and chain wear.

Z. Koloc · J. Korf · P. Kavan (✉)
VÚTS, a. s. Liberec, Czech Republic
e-mail: pavel.kavan@vuts.cz

Z. Koloc
e-mail: zdenek.koloc@vuts.cz

J. Korf
e-mail: jaroslav.korf@vuts.cz

Fig. 1 Chain guide curve

The purpose of the adjustment is to remove those unwanted effects by using the chain guide on the links (sliding guide rail) ensuring a smooth fit of the chain rollers into the wheel tooth gap.

1.1 The curvature of the guide curve

Suppose the chain guide curve shown in Fig. 1. If $\vec{i}, \vec{j}, \vec{k}, \vec{e}$ are unit vectors and τ the parameter, then position vector $\vec{r}(\tau)$, its first and second derivatives and normal vector \vec{n} can be expressed by following relationships:

$$\begin{aligned}\vec{r}(\tau) &= r(\tau) \vec{e}(\tau) \\ \frac{d\vec{r}}{d\tau} &= r'\vec{e} + r\vec{k} \times \vec{e}, \quad \left| \frac{d\vec{r}}{d\tau} \right| = \sqrt{r'^2 + r^2} \\ \frac{d^2\vec{r}}{d\tau^2} &= (r'' - r)\vec{e} + 2r'\vec{k} \times \vec{e} \\ \vec{n} &= \frac{\frac{d\vec{r}}{d\tau} \times \vec{k}}{\left| \frac{d\vec{r}}{d\tau} \times \vec{k} \right|} = (r'\vec{e} \times \vec{k} + r\vec{e}) \frac{1}{\sqrt{r'^2 + r^2}}.\end{aligned}$$

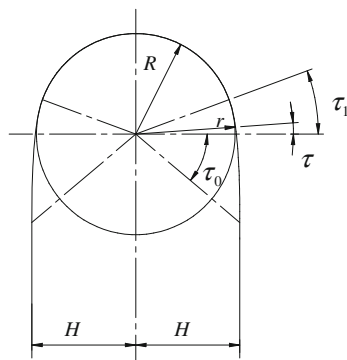
(Fig. 2).

A component of the second derivative of vector \vec{r} in the direction of normal \vec{n} is equal to the negative curvature multiplied by the power of the arc length

$$\left[(r'' - r)\vec{e} + 2r'\vec{k} \times \vec{e} \right] \cdot (r'\vec{e} \times \vec{k} + r\vec{e}) \frac{1}{\sqrt{r'^2 + r^2}} = -\frac{1}{\rho} (r'^2 + r^2), \quad (1)$$

from where after transformation it follows an equation expressing the curvature of the guide curve

Fig. 2 Choosing the type of guiding curve



$$\frac{1}{\rho} = \frac{r(r - r'') + 2r'^2}{(r^2 + r'^2)^{\frac{3}{2}}}. \quad (2)$$

1.2 Choosing the Type of Guide Curve

The guide curve is axially symmetric in such a way so that the axis of symmetry is parallel to the straight parts of the chain. The distance of the roller axes from the axis of symmetry is denoted by degree (rate) H and the pitch radius of the wheel is R .

Due to the axial symmetry of the guide curve it will be sufficient to solve radius vector $r(\tau)$ in angular interval $\langle \tau_0, \tau_1 \rangle$ between the linear and circular parts. The boundary values and the first three derivatives of the radius vector by angle τ are

$$r(\tau_0) = \frac{H}{\cos \tau_0}; \quad (3)$$

$$r'(\tau_0) = H \frac{\sin \tau_0}{\cos^2 \tau_0}, \quad (4)$$

$$r''(\tau_0) = H \frac{1 + \sin^2 \tau_0}{\cos^3 \tau_0}, \quad (5)$$

$$r'''(\tau_0) = H \frac{(5 + \sin^2 \tau_0) \sin \tau_0}{\cos^4 \tau_0}, \quad (6)$$

$$r(\tau_1) = R, \quad (7)$$

$$r'(\tau_1) = r''(\tau_1) = r'''(\tau_1) = 0 \quad (8)$$

Conditions (3)–(8) can be fulfilled by the seventh degree polynomial.

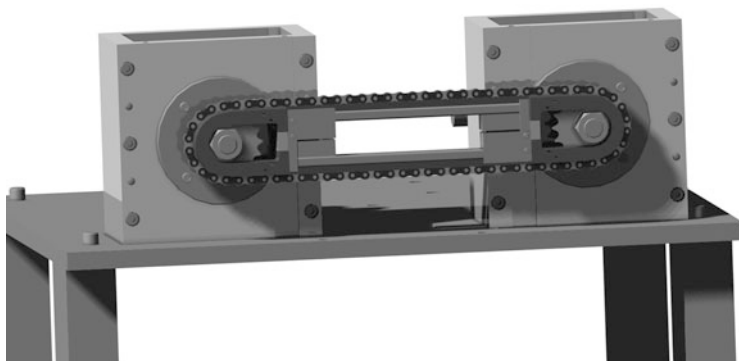


Fig. 3 The test stand for checking the properties of the adjusted chain gear

$$r(\tau) = \sum_{i=0}^7 C_i (\tau - \tau_0)^i, \quad \tau \in \langle \tau_0, \tau_1 \rangle \quad (9)$$

By quantifying coefficients C_i based on conditions (3)–(8), we obtain an expression for the guiding curve.

1.3 Optimizing the Parameters

The parameters of the guiding curve are lengths R , H and angles τ_0 , τ_1 . The optimization condition is the monotonically increasing curvature $\frac{1}{\rho}$ in interval $\langle 1, \frac{1}{R} \rangle$. The expression for radius vector $r(\tau, R, H, \tau_0, \tau_1)$ is linear in relation to R and H , therefore ratio H/R can be optimized in the chosen range $\langle 1.01; 1.06 \rangle$.

For the chosen boundary values of angles $\tau_0 = -40^\circ$ and $\tau_1 = 20^\circ$, there is the optimal ratio in interval $H/R \in \langle 1.02; 1.04 \rangle$. In interval $H/R > 1.04$, the optimized curvature is no longer monotonically increasing and at higher values H/R it also takes negatives. These properties were found also in curvature $\frac{1}{\rho}$ for angles $\tau_0 \in \langle -40^\circ; -30^\circ \rangle$ and $\tau_1 \in \langle 20^\circ; 30^\circ \rangle$.

2 Test Stand

For the purposes of an experimental verifying the properties of the adjusted chain gear, a test stand was designed and manufactured. A CAD model of the stand is presented in Fig. 3, the parameters of the chain gear are given in Table 1. Both sprocket wheels are provided with chain guide links, the sprocket wheel in the

Table 1 Parameters of the chain gear

Quantity	Value
Pitch circle radius of driving wheel R_1	36.57 mm
Pitch circle radius of driven wheel R_2	36.57 mm
Number of teeth of driving wheel z_1	18
Number of teeth of driven wheel z_2	18
Chain pitch t	12.7 mm
Roller diameter	7.75 mm
Gear ratio	1:1

right part of the Fig. 3 is driven by a servo drive, the wheel in the left part of the Fig. 3 is broken by the identical servo drive.

3 The Results of the Carried Out Measurements

On the test stand, there were carried out measurements of noise, the course of rotational speed during one revolution (or revolutions) of the shafts of the driven and braked sprocket wheel and the course of the accelerations (vibrations) of the bearing of both sprocket wheels, i.e., for a total of 3 different arrangements of the stand: (1) stand with non-adjusted chain gear, i.e., without guide links, (2) stand with adjusted chain gear provided with non-lubricated chain guide links, (3) stand with adjusted chain gear provided with lubricated chain guide links. Measurements were carried out totally for 3 nominal rotational speeds of the driven sprocket wheel (300, 600 and 900 rev/min) and two different values of the torque of the braked sprocket wheel (0.2695 and 0.539 Nm).

3.1 Noise Measurement

At the given revolutions and load, the sound pressure level was the lowest without the guide links, when using the lubricated guide links, the sound pressure level increased by about 1–2 dB and when using the non-lubricated guide links, then, this level rose by approximately another 2 dB. The given fact can be explained by an increased friction between the chain and the guide links in comparison to the gear without the guides. It is obvious that the lubricated (greased) guide links cause less noise in comparison to the non-lubricated guide links.

3.2 Measurements of the Revolutions and Accelerations (i.e. Vibrations) of Sprocket Wheels in the Sprocket Wheel Bearings

The time courses of the revolutions of sprocket wheels were measured using incremental encoders (sensors) located on the axes of the driving and braking shafts, the time courses of vibrations were captured simultaneously by means of accelerometers mounted on the stand frame above the axes of the driving and braking shafts. From the records of 3 revolutions of the sprocket wheel between two impacts of the chain coupling, there were quantified the differences of the maximum and minimum values of those quantities. If we consider the values of those differences for the non-adjusted chain gear as referential, it is clear that at 300 rev/min, the guide links cause an increase of those values whereas at 600 and 900 rev/min they cause their decrease by up to 15 %. It is likely that at low speeds, the negative influence of friction between the chain and the guides will outweigh the positive effect of the guides. At higher speeds, the positive influence of the guides will be applied more then.

3.3 Evaluation of Spectral Analysis

Through the spectral analysis, velocity and acceleration maxima for the 18th and 36th harmonic frequencies were found. They are caused by the number of 18 teeth on the driven and braking sprocket wheel so that at the non-adjusted chain gear during 1 revolution of the sprocket wheel, it occurs 18 times impact between the roller and the sprocket wheel tooth. From the evaluation it was found out that at 300 rev/min the guide links caused speed and acceleration increase for the 18th and 36th harmonic frequency compared to the non-adjusted gear whereas at 600 and 900 rev/min, a decrease of those quantities by up to 55 % occurred due to the guide links. Again, there is obvious the positive influence of the guides at higher rotational speeds.

4 Conclusions

According to the mathematical models, which, however, did not include passive resistances, the adjustment of the chain gear was supposed to lead to removing impact between the chain roller and sprocket wheel. The measurement however showed that the noise decrease of the gear as a whole would not occur just due to friction between the chain and the guide links. Furthermore, it appeared that vibrations decreased only at higher speeds. It can be concluded from the measurements that the proposed chain guide is more suitable for high-speed machines.

For the proposed adjustment of chain gear, PV 2011-330 patent application and PUV 2011-24421 utility model applications were filed. Acknowledgments

The topic was investigated within the project No. 1M0553 Výzkumné centrum “Textil II” (“Textil II” - Research Centre).

References

1. Korf, J.: Vedení řetězu pomocí vačky. *Výzkumná zpráva č. MAF-III-K/2009*, VÚTS, a.s., Liberec, 2009, in Czech, (Guiding the chain by means of a cam), Research Report.
2. Koloc, Z.-Korf, J.-Kavan, P.: Optimalizace řetězového převodu. *Průběžná zpráva o realizaci projektu č. 1M0553 za rok 2011*, Technická univerzita v Liberci, 2011, in Czech, (Chain gear optimization), (Operating statement on the implementation of the project No. č. 1M0553 for 2011), Technical University of Liberec.
3. Koloc, Z.-Korf, J.-Kavan, P.: Způsob navádění hnacího řetězu na řetězové kolo a naváděcí prostředek. *Příhláška vynálezu PV 2011-330*, in Czech, (Method of guiding the driving chain on the sprocket wheel and sliding guide rail—PV 2011-330 Patent application).

Modification of Upper Thread Tensioner of Sewing Machine

P. Klouček and P. Škop

Abstract Standard mechanical upper thread tensioner of sewing machines is more and more limited in use for industrial sewing machines due to increasing requests for quality and raising velocity of machines. If we omit mostly manual settings of force made only by sense, the most problematic things are influence of different friction coefficient of the different batch of threads and strong relation between thread tension and sewing machine velocity. The article describes the development focused to the elimination of the most significant disadvantages of a standard tensioner and mainly finding of new conception of the tensioner with electromagnetic brake, development and testing of its prototype.

Keywords Thread · Tensioner · Sewing machines · Electromagnetic tensioner · Upper thread

1 Introduction

The standard device for tensioning of upper thread is built up from disc tensioners with spring and friction parts as pins etc. This system has been used for more than 100 years and it is still workable, but due to increasing requests for quality and machine velocity more and more disadvantages are found. If we omit mostly manual setting of force made only by sense, the most problematic things are the

P. Klouček (✉) · P. Škop
VUTS Liberec, a.s., Measuring Department, Liberec, Czech Rep
e-mail: pavel.kloucek@vuts.cz

P. Škop
e-mail: petr.skop@vuts.cz

influence of different friction coefficient of different threads batch and strong relation between thread tension and sewing machine velocity. These uncertainties should affect not only the visual quality of the seam, but also functional properties of parts for example used as airbag covers etc.

2 Improving of Standard Tensioner

The first step was the measuring of properties of standard upper thread tensioner system [1]. Figure 1 shows position of two strain gauge sensors measuring input and output force and geometry of thread going through the tensioner system. There were also measurements of separate parts, it means only disc brake and only friction pins. For pins stands theoretical formula $F_{OUT} = F_{IN} e^{\mu\alpha}$, where μ is friction coefficient and α is wrapping angle. It means that these friction parts amplify force irregularity with factor $e^{\mu\alpha}$, so it means that input force should be utmost stable and number of friction parts reduced to necessarily quantity. For disc brakes stands theoretical formula $F_{OUT} = F_{IN} + N\mu$, where N is adherence pressure of brake discs. Both pins and disc brakes forces are strongly dependant on thread velocity, tension force is higher with rising velocity. All measurements were made with 100 % PES threads.

One of the problems is non-definable part of flat and smooth surface of friction parts. Surface of pins and brake discs was modified by welds made by laser welding machine for making defined points of contact with thread (see Fig. 2). For pins there were linear welds made perpendicular to thread movement direction, welds on brake discs were made as concentric circles.

These roughened surfaces don't increase friction coefficient, but make it more stable. The most distinctive are results from the pins shown in Fig. 3.

3 Electromagnetic Tensioner

The upper mentioned solution can improve the relation between the tension force and thread velocity, better results were received for thinner threads. But problems with different friction for different sets of threads and repetitious setting of thread tensioner still remained together with life-time of grooved surfaces. The way to solve this problem is the elimination of friction between thread and tensioner. It can be realized as disc brake with defined braking disc and roller connected. Braking force can be controlled by the electromagnet. Figure 4 shows a prototype of upper thread tensioner with electromagnet designed in VUTS Liberec, a.s. [2] Roller is standard purchased material used in different thread applications and works perfectly for holding thread without slippage with wrapping angle 360° . The only requirement for non-slippage holding is some small input force of thread around 50 cN, which is made by small disc brake.

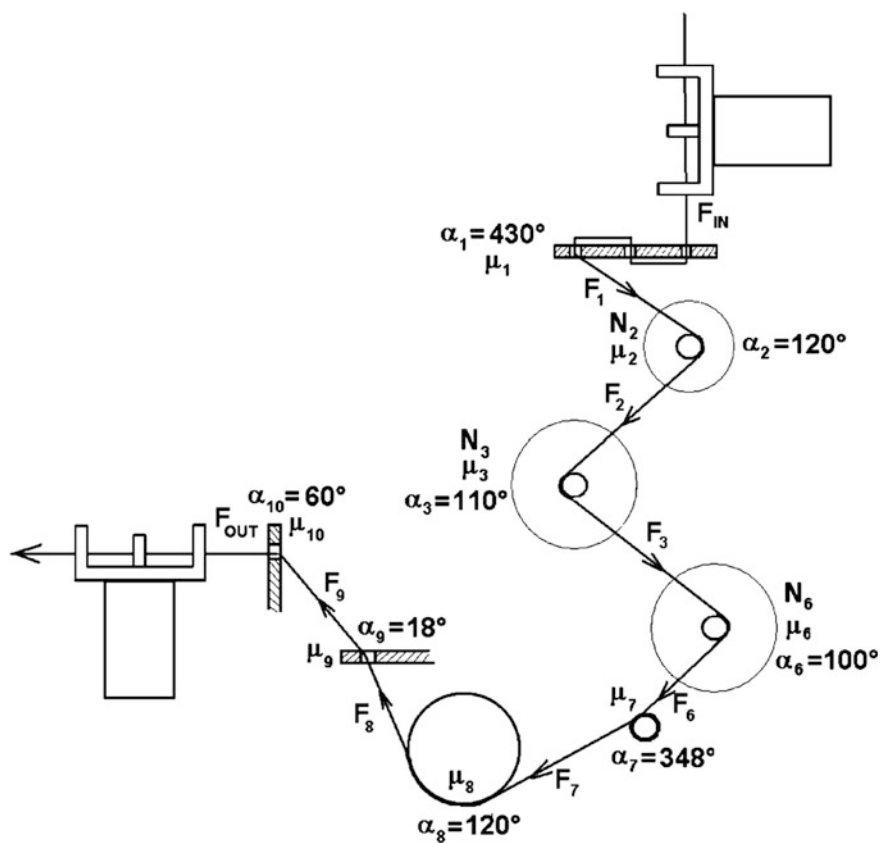


Fig. 1 Scheme of standard upper thread tensioner

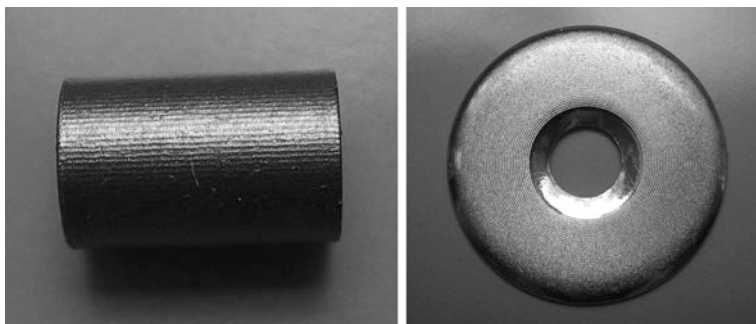


Fig. 2 Grooved surfaces of modified pin and brake disc

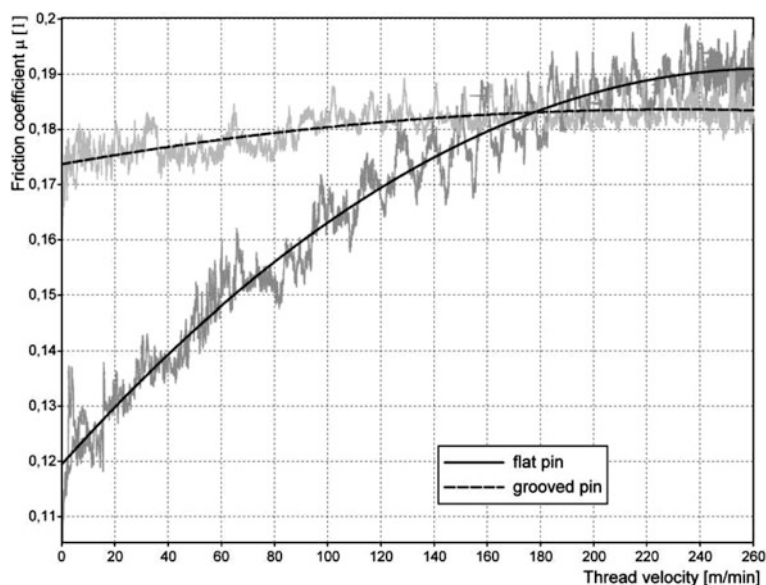


Fig. 3 Relation between friction coefficient and thread velocity for flat and grooved pins

Fig. 4 The first prototype of upper thread tensioner with electromagnet during tests



The roller is firmly connected to a friction brake disc. For production of friction force the holding electromagnet is used, it can produce much bigger force for short distances than standard control electromagnets and has a lower size of body and a lower current consumption, so it means the temperature of the metallic case is lower (it is safer in textile industry).

A schematic lay-out of the thread tensioner prototype is shown in Fig. 5. Holding electromagnet 1, connected to basic frame 2, controls pressure plates 4 and 5 with defined air gap. The air gap is adjustable and its size gives force range of tensioner. The roller 9 is connected to friction brake disc 8, there were several materials tested for friction brake disc (FAG-M, bronze, stainless steel and vulcanized fibre). When the thread has to be moved freely (during thread trimming, threading etc.), the brake disc is released by planchet spring 5.2.

Fig. 5 Schematic layout of thread tensioner with electromagnet

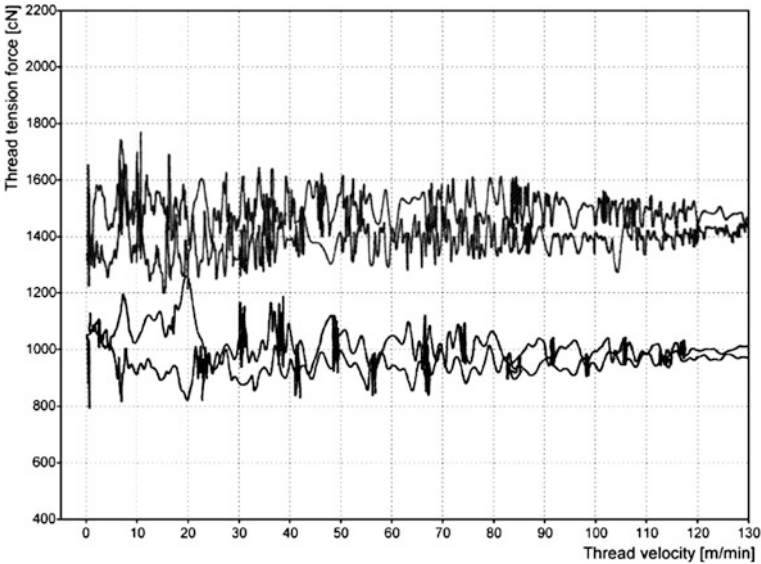
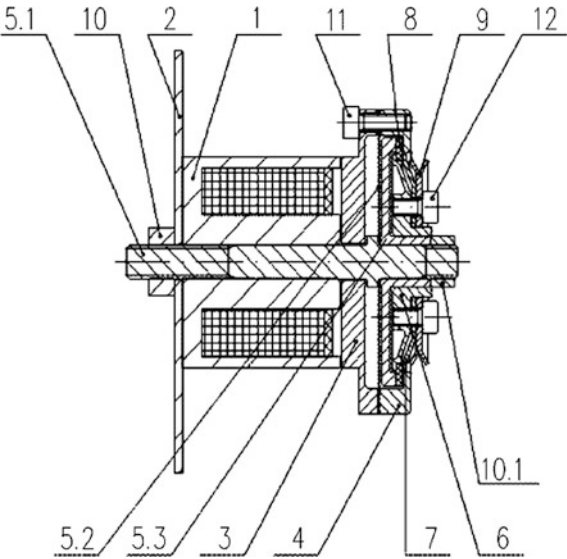


Fig. 6 Relation between tension force and thread velocity for two different desired values of force measured on thread tensioner with bronze brake disc

For all tests pressure plates were made from steel and the only material of friction brake disc was changed. Tested materials showed significantly different results. Material FAG-M, normally used for car brake-pad plates, had so sharp rising of force that it was impossible to set force to requested value by electric

current. The best results were made with bronze. Due to the lowest friction coefficient of this material, electric current resolution for force setting is the highest. Good friction properties of bronze lead to very small relation between thread tension force and thread velocity (see Fig. 6).

The bronze disadvantage is a small abrasive resistance, it means the lifetime of these parts is much shorter than the other parts of sewing machine. There were other plastic materials tested for friction brake disc with good abrasive resistance [3]. For the lifetime aspect Tecamid with MoS₂ addition was chosen as the best material. This material is able to work properly during full planned lifetime of thread tensioner, it means 1000 h of sewing with tension force 1000 cN, recalculated to number of roller rotations it means 3,5 millions cycles. But these plastic materials have a worse relation between thread tension force and thread velocity compare to bronze. So the next step will be the finding of material with bronze addition or some different type of bronze with higher abrasive resistance.

The electronic control unit with microprocessor was built for the thread tensioner. It can set desired value of the tension force due to the PWM modulation control signal and the power unit with feedback loop. There are also compensation functions for the sewing machine velocity and the thickness of sewn material with adjustable compensation factor up to 25 % of the tension force.

4 Conclusion

Change of mechanical parts surface of standard upper thread tensioner can improve the force stability for velocity changes. More complex solution is new thread tensioner with electromagnetic brake and roller, which eliminate more disadvantages. The prototype of the electromagnetic upper thread tensioner was developed and tested in VÚTS, a.s. The prototype series of these thread tensioners was produced by known producer of industrial sewing machines and now is tested in normal conditions by customers during standard industrial produce.

References

1. Klouček, P., Škop, P.: Měření vlastností nitových napínačů, MER-12/2007, VÚTS internal report (2007)
2. Klouček, P., Škop, P., Bandouch, M.: Vývoj napínače horní nitě šicího stroje s elektronickým nastavením tahové síly (napětí) nitě, MER-13/2008, VÚTS internal report (2008)
3. Klouček, P.: Ověření funkčních vlastností prototypu elektronického napínače horní šicí nitě při použití plastových brzdových kotoučů, MER-05/2010, VÚTS internal report (2010)

Optimization of Car Seats in the Interaction of Sitting Man on the Size of the Contact Pressure

R. Martonka and V. Fliegel

Abstract The crew vehicle, the driver and passengers are in a car in direct interaction with the car seat while driving, which affects a sitting person in many areas such as safety, comfort, a feeling of comfort and customization to individual requirements, ergonomics and variability. All these effects are caused by one or a group of elements used in the construction of the seat. Objective assessment of the requirements for the construction of car seats, regardless of the characteristics of the occupant is not possible to provide a subjective feeling of comfort for any seated person. Therefore, we include in the design of automotive seat occupant's subjective feelings. It is clear that car seats must "adapt" individual characteristics of a seated man (weight, corpulence, age, gender,...). One of the subjective feelings of a man sitting in the seat is comfortable for any seated person defined differently. Correlation was found between comfort seats and contact pressure distribution depending on the weight of a seated man. It is understandable that every sitting person has a different distribution of contact pressure. This has resulted in the same seat each person differently seems comfortable-hard. The research objective is always to ensure maximum contact area for any seated person. Parameter that must be optimized is the hardness of butt pads sitting person (usually polyurethane pad coated fabric cover). In the conventional design seat cushion hardness is fixed, without the possibility of adaptability by the individuality sitting man. This article deals with the assessment, definition and optimization of hardness of pad in the automobile seat, the contact pressure distribution and determining the regulatory range of hardness depending on the weight of a seated man.

R. Martonka (✉) · V. Fliegel
Technical University of Liberec, Liberec, Czech Republic
e-mail: rudolf.martonka@tul.cz

V. Fliegel
e-mail: vitezslav.fliegel@tul.cz

Keywords Optimization • Contact pressure • Distribution • Car seat

1 Introduction

Each person perceives comfort while sitting in another way. Some suits sit on a hard seat. Someone likes the contrary very soft cushion. It is not easy for everyone to make a single seat in the conventional way, which would all sit comfortably. In the first steps is necessary to define a seat element is essential to comfortable sitting. Of the many observations and experiments it was found that the major impact has the size and distribution of contact pressure between a man seated and seat.

When comparing the set of seats by the same sitting people It is appeared correlation between subjective evaluation and the results simultaneously measured maps of contact pressures. This trend has been shown both in the short test lasting several minutes, and in a few hour long test.

From previous tests we found that the best man sitting and he is most comfortable seat that can evenly distribute contact pressure to the largest possible contact area. And this map contact pressure distribution over time does not worsen. This means that there are not a dangerous area with high values of contact pressures.

On this basis it is possible to objectively define the basic criterion for assessing the comfort of the seat using a map contact pressures.

The following experiment compares the two materials used in automotive seat cushion.

2 Experiment

The experimental work (Fig. 1) was performed simulating the measurement of man sitting on the seat. During the experiment was carried measurement maps of contact pressures and fall through indenter into the sample material in time. To measure the contact pressure maps were used gauge Xsenzor 48.48.01 [1]. To measure the decline was used gauge BOD 26 K [2]. Indentor Fig. 2 in the shape of the buttocks has been added to the total mass of weight 64 kg, which simulate the weight of a seated man. This indenter loaded samples of material Fig. 3.

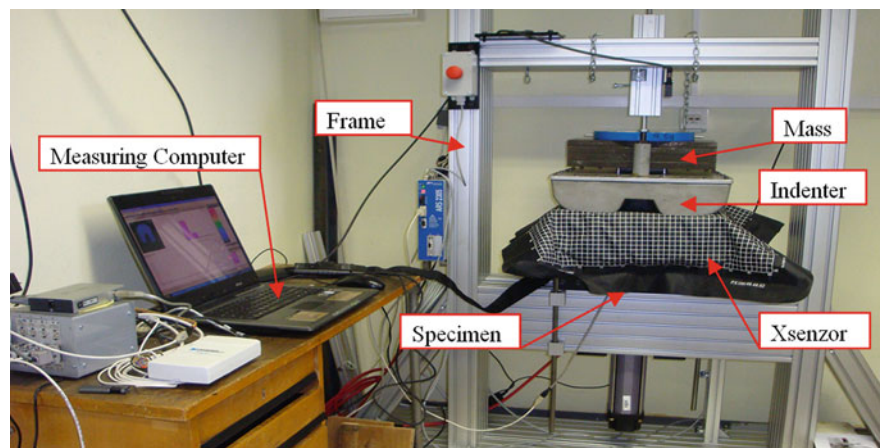


Fig. 1 Experimental workplace



Fig. 2 Indenter

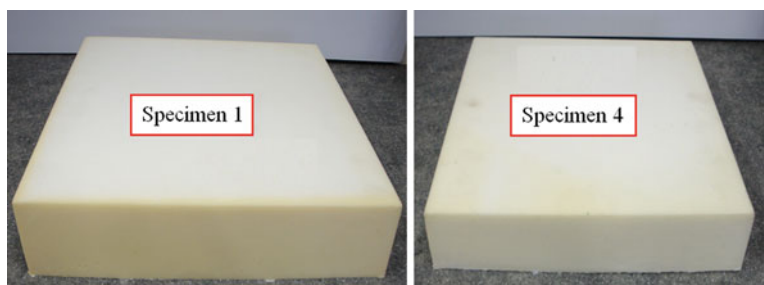


Fig. 3 Specimen 1 and specimen 4 of PU foam

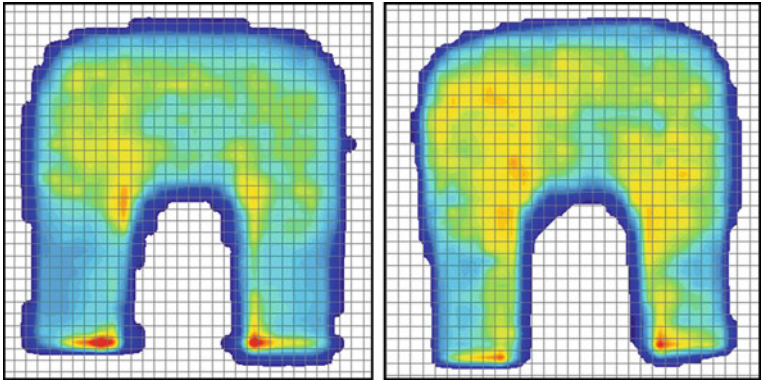


Fig. 4 Map contact pressure specimen 1 and specimen 4 in 1st minute

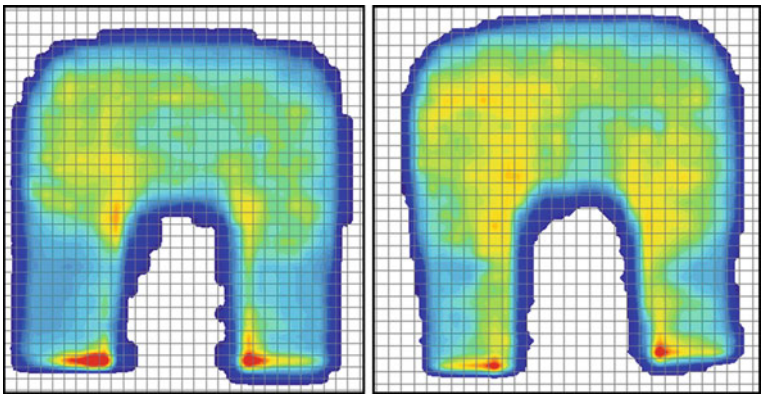


Fig. 5 Map contact pressure specimen 1 and specimen 4 in 10th minute

3 Measuring

The Fig. 4 shows the contact pressure maps of sample 1 and sample 4 load for one minute. The following Fig. 5 are also maps of both the contact pressure patterns loaded for 10 min. Of the four maps are not only apparent differences between the two samples, but variability in time.

The Table 1 summarizes the measured values of deformation, contact areas and peak and average pressure. Fig. 6 and 7 shows deformation in time.

Table 1 Table of measured value

Measured value (min)	Specimen 1	Specimen 2
Deformation 1	16,9 mm	16 mm
Deformation 10	19,1 mm	20,1 mm
Contact area 1	1005 cm ²	971 cm ²
Contact area 10	1061 cm ²	1021 cm ²
Average pressure 1	0,69 kPa	0,81 kPa
Average pressure 10	0,68 kPa	0,78 kPa
Peak pressure 1	1,88 kPa	1,52 kPa
Peak pressure 10	2,15 kPa	1,74 kPa

Fig. 6 Deformation in time—sample 1

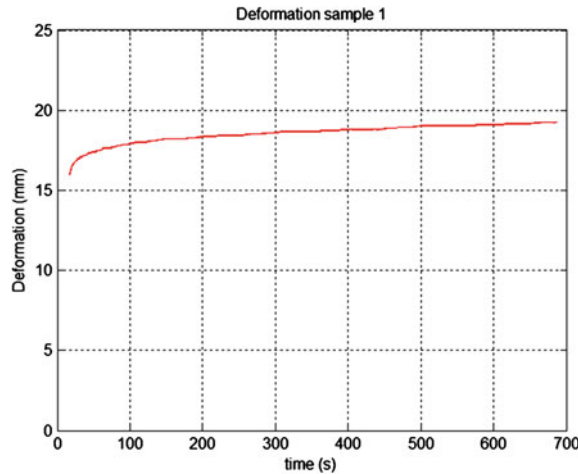
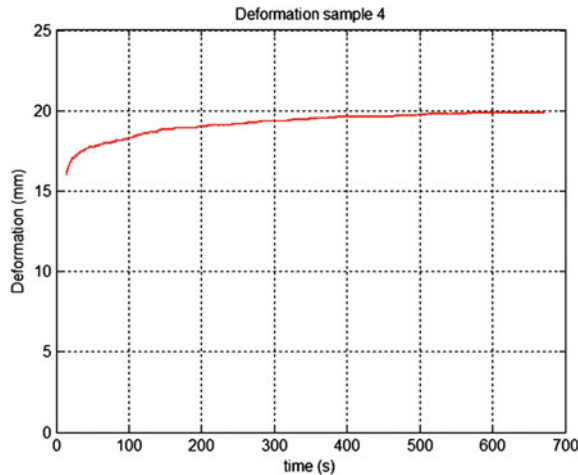


Fig. 7 Deformation in time—sample 4



4 Results

By comparing maps of contact pressures between the two samples in Fig. 4 shows that sample 4 has a more evenly distributed pressure—area is more than one color sample first. However, the yellow hue color map indicates the higher contact pressure. In Figs. 4 and 5 shows that sample 4 also better distributes the contact pressure in time. The total contact area is increased and simultaneously increases the area affected by high pressure. In contrast, sample 1 shows only a slight increase in contact area, but a large increase in the maximum surface pressure (red area). At the same time, the sample 4 is dropped more than the sample 1 after the 10 min. This is also evidence of better adaptation to stress. These results are documented in the summary table.

5 Discussion

Laboratory measurements has been shown that the measurement of contact pressure maps is objective and is suitable for assessing the basic material for use in the car seat. It was further demonstrated need for adjustable seating material properties over time, depending on load.

References

1. Xsensor Technology Corporation. [online]. [cit. 2012-04-29]. WebPage: <http://www.xsensor.com>
2. Balluff GmbH. [online]. [cit. 2012-04-29]. <http://www.balluff.com>

Trajectories of Dop Points on a Machining Wheel During Grinding of High Quality Plane Surfaces

I. Petrikova, R. Vrzala and J. Kafka

Abstract The basic requirement for plane grinding synthetic monocrystals is uniform wear of the grinding tool. This article deals with the case where the grinding process is carried out by relative motion between the front faces of rotating wheels with parallel axes. The dop is attached by the end of the pendulous arm, which movement is controlled by a cam. Kinematic relations have been drawn for the relative motion of the dop points in the reference to the abrasive wheel. The aim of the work is set the methodology for finding out of uniformity respectively nonuniformity of the motion of dop points on the abrasive wheel. The computational program was compiled in MATLAB. The sums of the number of passes were performed in the transmission range of 0.4–1. The number of passes of selected points on the dop passed over areas of the square mash was computed. The density of trajectory passes depends on four factors: the speed of both wheels, the number of arm operating cycles, the angle of the arm swings and the cam shape. All these dependencies were investigated. The uniformity the density of passes is one of the criteria for setting the grinding machine.

Keywords Grinding machine · Monocrystals · Kinematics · Trajectory · Dop

I. Petrikova (✉) · R. Vrzala · J. Kafka
Technical University of Liberec, Liberec, Czech Republic
e-mail: iva.petrikova@tul.cz

R. Vrzala
e-mail: rudolf.vrzala@tul.cz

J. Kafka
e-mail: jiri.kafka@tul.cz

1 Introduction

The paper deals with a detailed analysis of tool movement during grinding of plane surfaces of crystalline materials such as synthetic single crystals of Yttrium Aluminum Garnet (YAG) or Yttrium Aluminum Perovskite (YAP). It is necessary to maintain the planeness of the grinding tools as perfect as possible in order to achieve high-quality products. It leads to requirement that trajectories of points of the work piece are distributed uniformly over the working field of grinding wheel. The mathematical modeling of kinematics of this process in comparison with the actual wear of the grinding tool is used to obtain suitable input parameters of the grinding process.

2 Basic Information on Grinding Process

The investigated grinding device in Fig. 1 generates a contact and a relative motion of the fronts of two rotating discs with parallel axes. A schematic description of the mechanism is shown on the left in Fig. 2. The grinding wheel 2 is mounted on the frame 1 and rotates at a constant angular velocity ω_{21} . The machined crystals are bonded on the disc 3 so called “dop” which is mounted on a swinging arm 4. The dop rotates also with constant angular velocity ω_{34} . The both angular velocities are controlled and the swiveling movement of the arm 4 is controlled by an electronic cam. A grinding medium is introduced between the active surfaces.

Parameters of the grinding device:

$D_2 = 380$ mm, $d_2 = 100$ mm, $D_3 = 140$ mm, $l = 210$ mm, revolutions of grinding wheel $n_{21} = (60 \text{ or } 70)$ rpm, revolutions of the dop $n_{34} = \mu \cdot n_{21}$, ratio μ is chosen in the range 0.3–1.0; the arm operates with 5 resp. 6 cycles per minute.

The initial and final angles of the swing arm 4 determine the uniformity of density of passes of points of the work piece over the working field of grinding wheel. These boundary angles characterize the overlap of the dop beyond the inner and outer circumferences of the grinding wheel.

3 Coordinates of a Point of Dop and Positions of Arm

The dop 3 performs a relative motion 32 with respect to the grinding wheel. The relative motion is composed of three sub-motions: the motion of the dop with respect to the arm 4, the motion of the arm 4 with respect to the frame 1 and the motion of frame with respect to the grinding wheel 2, which express the symbolic equation $32 = 34 + 41 + 12$. To derive the transformation relations we use the kinematics scheme on the right in Fig. 2, in detail see [1].

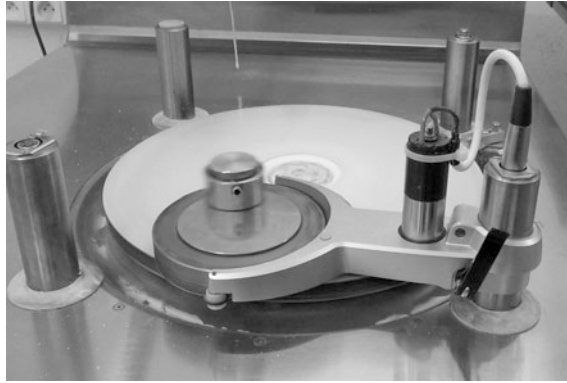


Fig. 1 Grinding machine

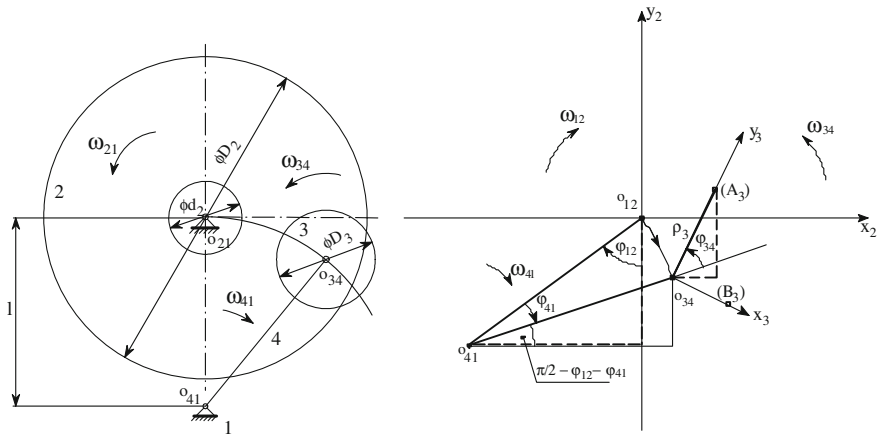


Fig. 2 Schematic mechanism of grinding machine and kinematics motion

We select first a point A_3 on the axis y_3 , i.e. point lying on the vertical when the arm 4 is in the vertical position (i.e. $\varphi_{41} = 0$). The coordinates of the image of the point A_3 in the space of the body 2 are:

$$x_2 = -l \sin \varphi_{12} + l \sin(\varphi_{41} + \varphi_{12}) - \rho_3 \sin(\varphi_{34} - \varphi_{41} - \varphi_{12}), \quad (1)$$

$$y_2 = -l \cos \varphi_{12} + l \cos(\varphi_{41} + \varphi_{12}) + \rho_3 \cos(\varphi_{34} - \varphi_{41} - \varphi_{12}). \quad (2)$$

Similarly, for the point B_3 lying on the axis x_3 reads:

$$x_2 = -l \sin \varphi_{12} + l \sin(\varphi_{41} + \varphi_{12}) + \rho_3 \cos(\varphi_{34} - \varphi_{41} - \varphi_{12}), \quad (3)$$

$$y_2 = -l \cos \varphi_{12} + l \cos(\varphi_{41} + \varphi_{12}) + \rho_3 \sin(\varphi_{34} - \varphi_{41} - \varphi_{12}). \quad (4)$$

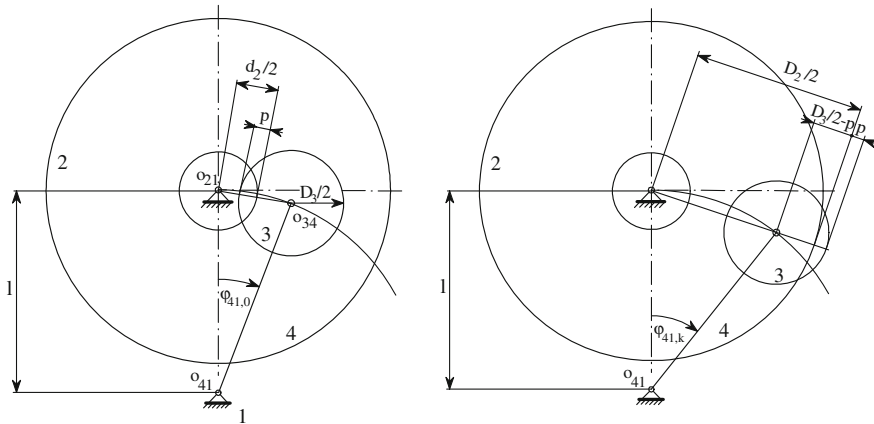


Fig. 3 The inner and outer limit position of the arm ($p = p_i$, $p = p_e$)

The radial distance of the image of the point A on the body 3 from the centre of the body 2 is expressed:

$$\rho_2^2 = x_2^2 + y_2^2 = 2l\{l(1 - \cos \varphi_{41}) - \rho_3[\cos \varphi_{34} - \cos(\varphi_{34} - \varphi_{41})]\} \quad (5)$$

This expression reflects the influence of the particular parameters on the radial distance. For a chosen value of ρ_2 , the influence of the value ρ_3 and the relative position of the bodies 3 and 4 (characterized by the angles φ_{34} and φ_{41}) on a radial filling of the working field of the grinding wheel were investigated.

The inner boundary angle $\varphi_{41,o}$ for inner overlap p_i , as shown in Fig. 3 on the left, and the outer boundary angle $\varphi_{41,k}$ for outer overlap p_e , as shown in Fig. 3 on the right, are calculated from Eqs. (6 and 7):

$$\varphi_{41,o} = \arccos \left[1 - \frac{(d_2 - 2p_i + D_3)^2}{8l^2} \right] \quad (6)$$

$$\varphi_{41,k} = \arccos \left[1 - \frac{(D_2 - D_3 + 2p_e)^2}{8l^2} \right] \quad (7)$$

4 Computational Model

By the mathematical modelling, the working field of the grinding disk was divided by the perpendicular grid to 60×60 individual small squares with dimension 6×6 mm. The distance ρ_3 on the dop was chosen for 6 points on the axis y_3 ($\rho_3 = 20, 30, \dots, 70$ mm). For each of those points was calculated the trajectory of motion 32, i.e. coordinates x_2, y_2 from Eqs. (1, 2) and calculated the sum of passes

Table 1 Parameters for numerical solution

Revolution of body 2	Transmission	Revolution of body 3	Angular velocity	Number of cycles	Angle of overlap
n_{21}	μ	$n_{34} = \mu \cdot n_{21}$	$\omega_{34} = (\pi/30) \cdot n_{34}$	6 sw/min = 0.1 sw/s	$\varphi_{41o}/\varphi_{41k}$
70 rpm	0.4	28	2.93 s^{-1}	1swing = 10 s	$27^\circ/40^\circ$

from all those trajectories through the control squares of the grinding disk. The passes of the trajectories was monitored during the working cycles (cycles of arm 4). For all numerical simulation and results visualization was used the software MATLAB [2].

Input parameters are dimensions, revolutions of the grinding wheel, the transmission between the grinding disk and the dop, number of cycles of the arm, overlaps of the dop in boundary positions, step, total calculation time and cam displacement law. The chosen displacement law was modeled by Cam Designer software and was transferred using spline functions to software MATLAB.

Pendulous motion of the arm 4 is given by electronic cam.

The results of numerical solution were displayed in the plane of the grinding wheel with resolution of the numbers of passes using the color scale from yellow to red. Some from input parameters cause the formation of “star-like patterns”, i.e. repeating of trajectories in short cycle time, resp. periodic repeating of passes during the same squares.

5 Specifics of the Investigated Mechanism

Let us consider some other features of the investigated motion. The motion 31 i.e. the motion of the body 3 (the dop 3 mounted on the arm 4) with respect to the frame 1 is the final motion composed of two forced motion, i.e. $31 = 34 + 41$, then $\omega_{31} = \omega_{34} + \omega_{41}(t)$.

Let us assume real parameter of grinding machine, as listed in Table 1.

The angular velocity ω_{41} is dependent on the time and the value will be double, i.e. $\omega_{41} = 0.09 \text{ s}^{-1}$.

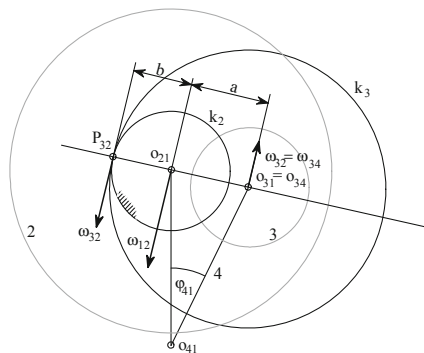
We see from the results that the ratio $\omega_{34}/\omega_{41} = 32.5$, i.e. the angular velocity of the swing motion of arm $\omega_{41} = 2.93 \text{ s}^{-1}$, i.e. is much smaller than the angular velocity ω_{34} of rotation of the body 3 around the axis o_{34} . The pole P_{31} lies close to the axis o_{34} , i.e. close to the centre of the dop 3.

On the basis of the above considerations, it can be written approximately $\omega_{31} \cong \omega_{43}$. The relative angular speed of the motion 32 follows from the relation $\omega_{32} = \omega_{31} + \omega_{12}$.

The schema in Fig. 4 shows the circular polodes k_2, k_3 of the pericycloidal motion 32, which tangent in the pole P_{32} . Circle k_2 is the fixed polode and the circle k_3 is the moving polode. Each point of the body 3 runs over a cycloid in the

Fig. 4 Position of the pole of motion in the case

$$\omega_{31} \cong \omega_{43}$$



space of the body 2. The ratio of the radii of the polodes is equal to the ratio of the number p of closed branches of the resulting curve of the relative motion and number q of revolutions of the moving polode [3]

$$\frac{b}{a+b} = \frac{p}{q}, \quad (8)$$

where p and q are relatively prime numbers. The configuration in Fig. 4 corresponds to the input parameters $n_{21} = 70$ rpm, $\mu = 0.4$, $\varphi_{41} = 25^\circ$ and for $\omega_{41} \cong 0$. In such case: $a = 91$ mm, $b = 61$ mm and $p/q = \mu$ and the ratio p/q does not depend on the choice of the position of the swing arm (the distance a), it depends only of the ratio μ (for $\omega_{41} \cong 0$).

Results of a numerical example with the input parameters $\mu = 0.4 = 8/q \rightarrow q = 20$ are shown on the left in Fig. 5.

In this example, the body 3 rotates 20 times with the angular velocity ω_{32} around the pole P_{32} , which corresponds to 20 full revolutions of the circle k_2 over the circle k_3 with the angular velocity $\omega_{31} (\cong \omega_{43})$ around the axis of $o_{31} (\cong o_{43})$. Each point of the body 3 orbits over a star with 8 vertices. It is clear that the position of the pole P_{32} changes according to the position of the swing arm (angle φ_{41}). The formation of star-like patterns depends on the value of the ratio μ .

If we choose the ratio e.g. $\mu = 0.84$ the star-like patterns do not appear, see on the right in Fig. 5. The pictures draws areas with different numbers of passes in scale from yellow to red color in ascending order.

The detailed input parameters of the grinding device for pictures list in Table 2. The passes were summarize for the total number cycles 100.

As we can see in Figures uniformity of grinding is given mainly by values of transmission μ . If we choose the numbers as 0.4, 0.5, 0.6, ..., 1.0 the star-like patterns appear. Next important parameters are inner and outer overlaps and type of the electronic cam and course of angular velocity. As shown in Fig. 5, the overlaps $p_i = 40$ mm and $p_e = 60$ mm cause higher number of passes near the boundary areas of the wheel than for e.g. $p = 25$ mm. Parameters as number of cycles of the arm and revolutions of the grinding wheel n_{21} are less important. All mentioned parameters are adjustable on control panel on grinding machine.

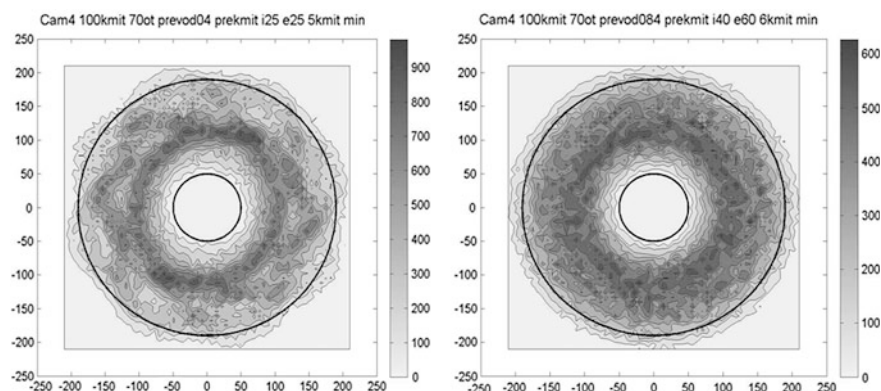


Fig. 5 Number of passes for $n_{21} = 70$ rpm, $\mu = 0.4$ (*star patterns*) and 0.84

Table 2 Parameters for numerical solution

Revolution of body2 n_{21} (rpm)	Transmission μ	Number of cycles	Overlap (mm)
70	0.4	6	25/25
70	0.84	6	40/60

6 Conclusion

For grinding process it is important to set up right combination of input parameters on the basis of presented results. The influence of nonuniform distribution of the velocity in the range of arm swing was investigated. It turned out that the trajectory passes uniformity in the boundary parts is dependent on the size of the overlaps very much. It is preferable to choose a larger value of those overlaps. Significant influence on the result has the choice of transmission between the grinding wheel and the dop, especially in case of formation “star-like” patterns on the grinding wheel. The conditions and parameters of this described phenomenon were derived.

Acknowledgments This work was supported by a grant from Ministry of Industry and Trade of the Czech Republic under contract code MPO FR-TI 1/320.

References

1. Vrzala, R., Petrikova, I., Kafka, J.: Grinding of friction discs front faces—transmitted torque. *Fine Mech. Opt.* **53**, 245–247 (2008)
2. Vrzala, R., Petrikova, I., Kafka, J.: The trajectories of dop points on a machining wheel during grinding of high quality flat surfaces. *Fine Mech. Opt.* **56**, 150–152 (2011)
3. Rektorys, K. et al.: Overview of Applied Mathematics I, II, Prometheus, Prague (2000)

A Design and Optimization of the Fully Automatic Shunting Mechanism

A. Sapietova and V. Dekys

Abstract In this paper, the design of the fully automatic mechanism for shunting of cylindrical parts is presented. The virtual prototype (VP) of the design was modeled in Pro/Engineer program and selected members of the mechanism were modeled in ANSYS program as the flexible bodies. The VP was imported into MSC. ADAMS, where particular structural and dynamic parameters will be optimized. At this solution, the MATLAB program will be also utilized.

Keywords Mechanism • Optimization • Virtual prototype • ADAMS

1 Introduction

The primary goal of manufacturing concerns is to increase the salability of their product which consequently has to fulfill strict criteria. In order to fulfilling all imposed requirements it is necessary to optimize not only the product, but also mechanism used in the process of its manufacturing. Employing the technology of simulation is progressive and unthinkable option of solving optimal properties of machines.

Commonly used mechanisms for conveying, shunting and shifting of cylindrical components do not ensure sufficient stability of components by their mutual

A. Sapietova (✉) · V. Dekys
University of Žilina, Žilina, Slovakia
e-mail: alzbeta.sapietova@fstroj.uniza.sk

V. Dekys
e-mail: vladimir.dekys@fstroj.uniza.sk

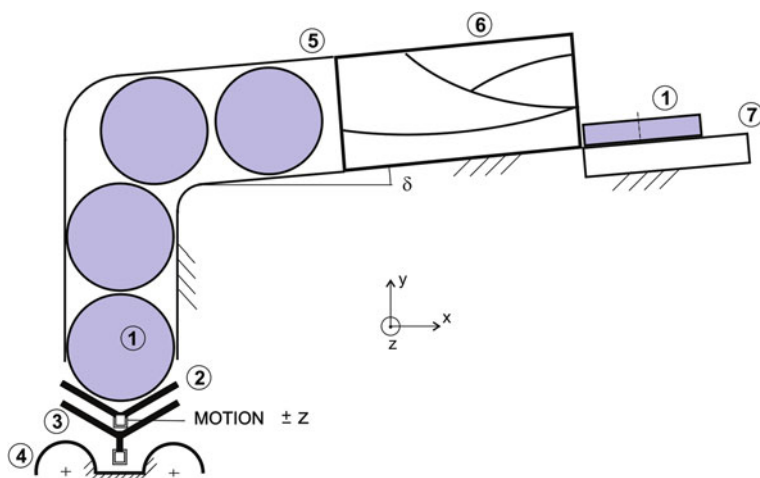


Fig. 1 Kinematic scheme of dosing mechanism

arrangement. In addition, separate mechanism is used for their shifting which increases overall dimensions of a machine.

In this paper, the virtual prototype of the mechanism which enables to orient, convey cylindrical parts. Then the equipment creates the set of parts and shifts they on given position.

The environment of MSC. ADAMS program includes tools of parametric analysis which will be used for refining of properties of the model of VP. In this paper, optimization in ADAMS/Insight environment is presented. Structural parameters which have an influence not only on failure-free operation of a machine but also on achieving its higher power and increasing the lifetime of conveyed components will be optimized.

2 Kinematic Scheme of the VP of Dosing Mechanism

Figure 1 illustrates the kinematic scheme of dosing mechanism which conveys and doses cylindrical components after the desired number of pieces. This mechanism has two degrees of freedom, i.e. displacement of the members 2 and 3 in z -direction (Fig. 1). The motion of mechanism is regulated by hydraulic drive.

The mechanism is composed of the following members:

1. cylindrical components
2. blankholder
3. carrier
4. sliding surface
5. trench

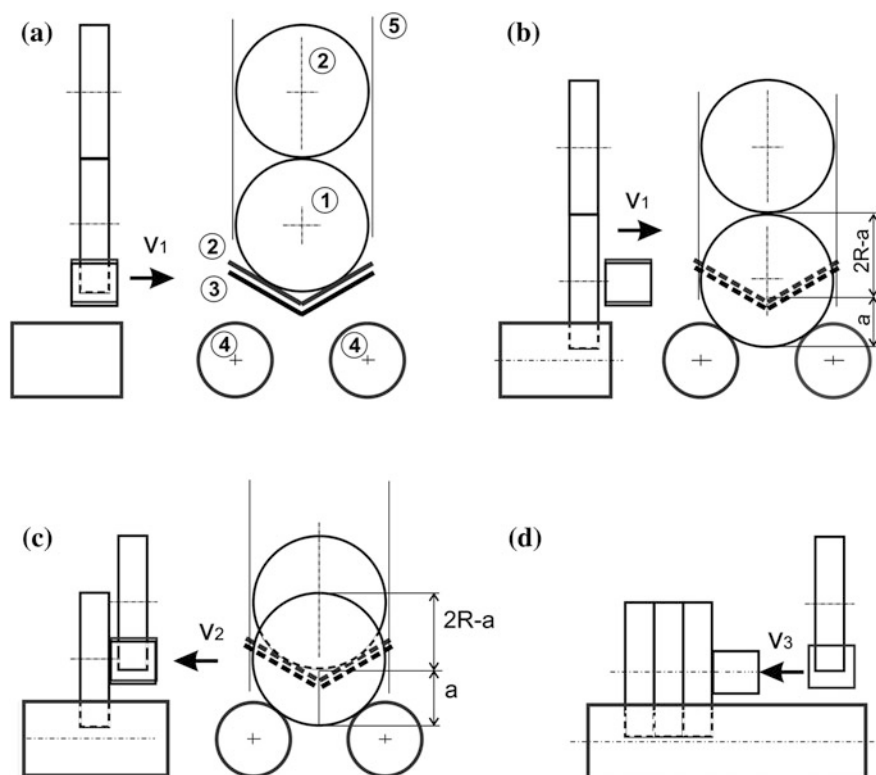


Fig. 2 Kinematic scheme of working cycle of the mechanism

6. worm

7. vibrating conveyor

The mechanism work as follows (Fig. 2): Cylindrical components are conveyed from the vibrating conveyor 7 to the worm 6, where they are oriented to required position. Cylindrical components then cross into vertical part of the trench and then they fall out on the member 2 (Figs. 1 and 2a). The members 2 and 3 execute translational motion in z -direction (Fig. 2b). The members 2 and 3 push out from under components and these components fall out on the member 4 (Fig. 2b). By the simultaneous motions of the members 2 and 3 in $+z$ -direction the bottom component is pushed out on the sliding surface 4 and the component above it will fall out on the member 2 (Fig. 2c). This procedure repeats unless there is required number of components on the sliding surface 4. When this condition is fulfilled, the member 3 will push out in $+z$ -direction (further than member 2) and shift the set to the next technological operation.

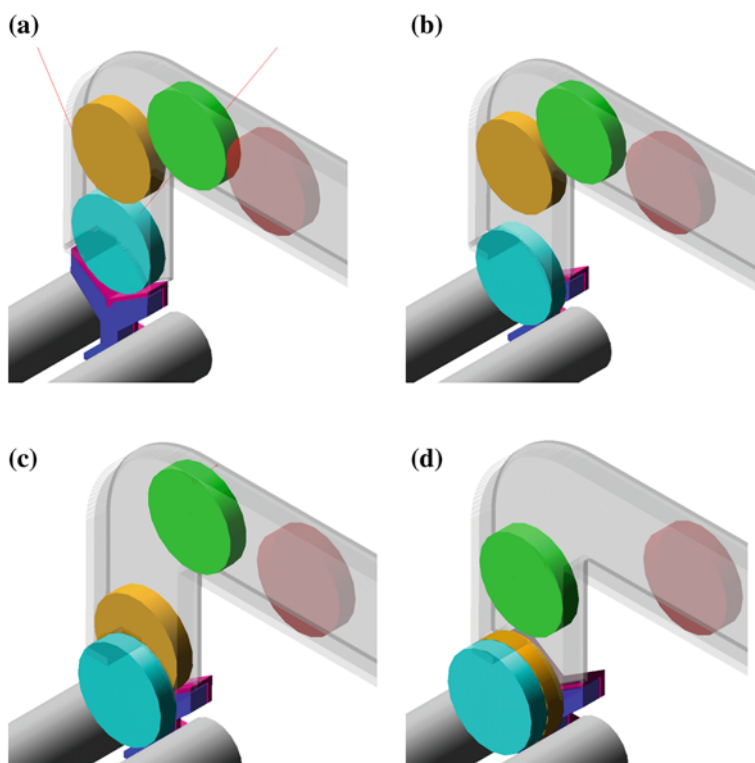


Fig. 3 VP in A/View environment a, b, c, d. Fig 2a corresponds to the Fig. 3a, ... and Fig. 2d corresponds to Fig. 3d

3 Optimization of Structural Parameters in ADAMS/Insight Environment

By the impact of cylindrical component on the blank holder and sliding surface, there are impact forces which can damage the component. The VP is modeled in ADAMS/View environment (Fig. 3). The optimization is performed in ADAMS/Insight environment. The conveyed components are cylinders modeled in ANSYS environment.

Structural parameters which have an influence on magnitudes of the contact forces are optimized in the process of solution. These variables represent the angle of the blank holder $\alpha_n = DV_1$ and position $p_n = DV_2$ from which the height of impact of the component on the sliding surface is calculated (Fig. 4). The objective functions are contact force in the impact of the cylinder on the sliding surface $4-F_v - OBJECTIVE_1$ and contact force in the impact of the cylinder on the blankholder $2-F_p - OBJECTIVE_2$. Optimal values of the structural parameters respond to minimal values of the mentioned contact forces.

Fig. 4 Structural parameters of the VP

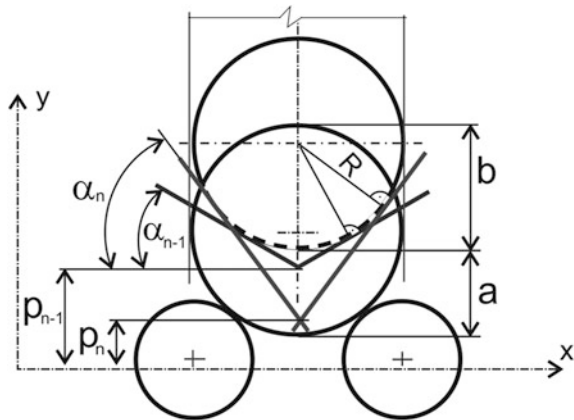


Table 1 The result block design of experiment summary

Trial	Objective_1	Objective_2	DV_1	DV_2
1	5573.7	3363.4	20.0	88.0
2	5940.6	3921.0	20.0	93.0
3	6580.0	7688.0	25.0	88.0
4	6168.1	7480.0	25.0	93.0
5	6564.1	4661.1	30.0	83.0
6	6151.5	3963.7	30.0	79.0
7	5666.0	8297.3	30.0	74.0
8	4200.6	4373.4	30.0	70.0
9	4906.1	4641.9	35.0	83.0
10	4584.1	6358.7	35.0	79.0

After performing analyses with solver settings, [1]: GSTIFF, SI2 and performing of post processing in A/Insight environment, the result block Design of Experiment Summary will be displayed (Table 1). We can assess the influence of combinations of the optimizing variables on the objective functions and choose the most suitable combinations of the optimizing variables.

As we can see, the objective function OBJECTIVE_1 reaches minimal values for trial 8: OBJECTIVE_1 = 4200.6 N, DV_1 = 30° and DV_2 = 70 mm. The second objective function reaches the minimum in trial 1 in angle of DV_1 = 20° and position of DV_2 = 88 mm.

As we can see, the minimum of both objective functions will not be achieved by the same values of the variables. So we get into the field of multi-criterion optimization where the optimal result is assessed as an acceptable compromise between both objective function.

The results from particular trials are loaded in A/Insight environment. These results are prepared for regression analysis (fitting quadratic surface through the results of experiments in terms of least squares) (Fig. 5).

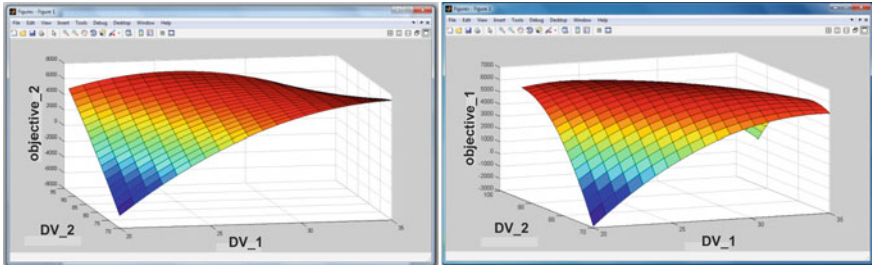


Fig. 5 Response of the objective functions OBJECTIVE_1 and OBJECTIVE_2

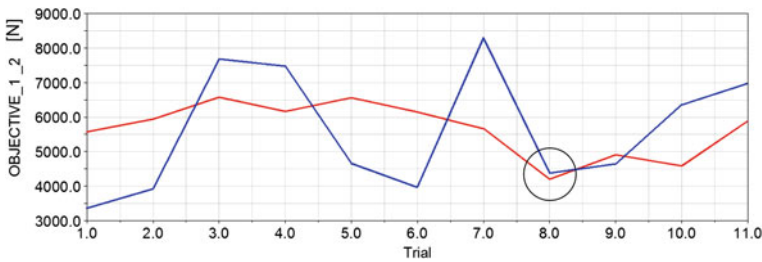


Fig. 6 Response of the objective functions OBJECTIVE_1 and OBJECTIVE_2

4 Conclusions

The goal of the optimizing analysis was to find the angle of blank holder and its position so that the load onto the sliding surface and carrier was minimal and was equally large if possible. Table 1 and Fig. 5 were combined into Fig. 6 for that reason. Y-axis represents the value of impact force and x-axis represents the number of combination of parameters. Parameters responding to combination 8 marked by circle are considered as an optimal values. Corresponding structural parameters for this combination were mentioned as a recommendation for future structural design.

It should be noted that solution with more refined distribution of structural variables would refine the given results. The solution revealed stress concentrations on the blank holder by the impact of the component. So the next solution will be an optimization of the shape of blank holder or use of damping materials on its surface. It is also notable to consider uncertainties of geometrical and material parameters of the device. Then the next step will be the formulation of this problem as a task with uncertainty parameters, [2, 3].

Acknowledgments The work has been supported by the grant project VEGA 1/1000/12 and 1/1259/12.

References

1. Palcak, F.: Program MSC ADAMS. V authorized training center for MSC. ADAMS [online]. [cit. 2012-25-4]. http://atc.sjf.stuba.sk/msc_adams.html (2009)
2. Vasko, M., Saga, M.: Solution of mechanical systems with uncertainty parameters using IFEA. *Commun. Sci. Lett. Univ. Zilina*. **11**(2), 19–27 (2009)
3. Zmindak, M., Saga, M.: Structural optimization of truss structures for deterministic and nondeterministic loads using MATLAB, In: *Proceedings of the 7th international conference on numerical methods in continuum mechanics*, pp. 368–373. High Tatras (1998)

Modelling and Optimization of the Half Model of a Passenger Car with Magnetorheological Suspension System

S. Segla

Abstract The paper deals with modelling and optimization of the half model of a passenger car with an ideal semi-active suspension, semi-active suspension equipped with magnetorheological dampers, passive suspension equipped with hydraulic dampers without control and compares their dynamic characteristics. The conventional skyhook control is used to control semi-active dampers taking into account the time delay. Selected parameters of the suspension systems are optimized for given road profiles using genetic algorithms. The results show that implementation of the magnetorheological dampers can lead to a significant improvement of the ride comfort and handling properties of passenger cars provided that the time delay is low enough.

Keywords Magnetorheological damper • Semi-active suspension • Skyhook control • Random vibration • Optimization

1 Introduction

The fundamental purpose of suspension systems in various kinds of vehicles is the improvement of the ride comfort, reduction or restriction of the dynamic road-tire forces and working space [1, 2]. Most suspension units are still passive ones which do not require any external source of power. By using various kinds of controllers, sensors and actuators controlled by feedback signals, it is possible to create active suspensions that can produce ideal vibration control for different running

S. Segla (✉)

Technical University of Liberec, Liberec, Czech Republic
e-mail: stefan.segla@tul.cz

Fig. 1 Passive suspension system

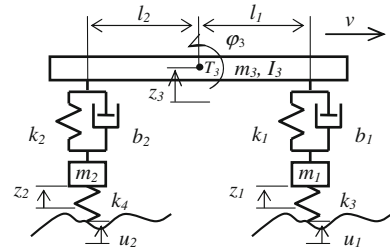
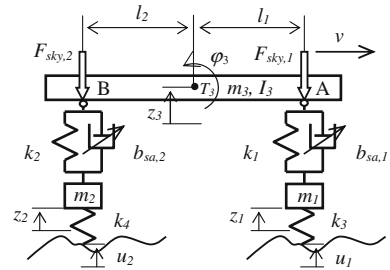


Fig. 2 Semi-active suspension system



conditions [3]. A compromise between passive and active suspensions are semi-active suspensions. Especially magnetorheological (MR) dampers have attracted interest in automotive engineering for their quick time response and low energy consumption.

In the paper the dynamic characteristics of three suspension systems are optimized and compared. Further, the time delay is analyzed and also the influence of the nonzero damping force of MR dampers in their off states is judged.

2 Dynamic and Mathematical Models

Figures 1 and 2 show the half dynamic models of a passenger car with passive and semiactive suspensions. Basic mass and geometric parameters of the passenger car of segment D (corresponding to e.g. Audi A4 or Renault Laguna) are used in the paper.

The equations of motion of the passive suspension, assuming permanent wheel-road contact, have the following form

$$\begin{aligned}
 m_1 \ddot{z}_1 - b_1(\dot{z}_3 + l_1 \dot{\varphi}_3 - \dot{z}_1) - k_1(z_3 + l_1 \varphi_3 - z_1) + k_3(z_1 - u_1) &= 0, \\
 m_2 \ddot{z}_2 - b_2(\dot{z}_3 - l_2 \dot{\varphi}_3 - \dot{z}_2) - k_2(z_3 + l_2 \varphi_3 - z_2) + k_4(z_2 - u_2) &= 0, \\
 m_3 \ddot{z}_3 + b_1(\dot{z}_3 + l_1 \dot{\varphi}_3 - \dot{z}_1) + b_2(\dot{z}_3 - l_2 \dot{\varphi}_3 - \dot{z}_2) + k_1(z_3 + l_1 \varphi_3 - z_1) \\
 - k_2(z_3 - l_2 \varphi_3 - z_2) &= 0, \\
 I_3 \ddot{\varphi}_3 + b_1 l_1(\dot{z}_3 + l_1 \dot{\varphi}_3 - \dot{z}_1) - b_2 l_2(\dot{z}_3 - l_2 \dot{\varphi}_3 - \dot{z}_2) + k_1 l_1(z_3 + l_1 \varphi_3 - z_1) \\
 - k_2 l_2(z_3 - l_2 \varphi_3 - z_2) &= 0,
 \end{aligned} \tag{1}$$

where m_3 is the body mass, T_3 is the body mass centroid, I_3 is the body mass moment of inertia (about T_3), m_1 and m_2 are the wheel masses, k_1 and k_2 are the spring stiffnesses in the main suspension, k_3 and k_4 are the tyre stiffnesses.

The equations of motion of the ideal semi-active suspension have the same form, but instead of the damping coefficients of the conventional hydraulic dampers b_1 and b_2 , the variable coefficients $b_{sa,1}$ and $b_{sa,2}$ are used. The forces exerted by fictitious skyhook dampers acting at points A and B (Fig. 2) are as follows

$$F_{sky,1} = b_{sky,1}(\dot{z}_3 + l_1\dot{\varphi}_3), \quad F_{sky,2} = b_{sky,2}(\dot{z}_3 - l_2\dot{\varphi}_3). \quad (2)$$

The damping forces exerted by the front and rear couples of the semi-active dampers are as follows

$$F_{sa,1} = 2b_{sa,1}(\dot{z}_3 + l_1\dot{\varphi}_3 - \dot{z}_1), \quad F_{sa,2} = 2b_{sa,2}(\dot{z}_3 - l_2\dot{\varphi}_3 - \dot{z}_2). \quad (3)$$

From the equalities $F_{sa,1} = F_{sky,1}$, $F_{sa,2} = F_{sky,2}$ (as we want the semi-active dampers to exert the same damping force as the fictitious skyhook dampers do) the following equations for the variable damping coefficients of the semi-active dampers hold

$$b_{sa,1} = \frac{b_{sky,1}(\dot{z}_3 + l_1\dot{\varphi}_3)}{2(\dot{z}_3 + l_1\dot{\varphi}_3 - \dot{z}_1)}, \quad b_{sa,2} = \frac{b_{sky,2}(\dot{z}_3 - l_2\dot{\varphi}_3)}{2(\dot{z}_3 - l_2\dot{\varphi}_3 - \dot{z}_2)}. \quad (4)$$

The on-off conditions of the front dampers are as follows: if $(\dot{z}_3 + l_1\dot{\varphi}_3)(\dot{z}_3 + l_1\dot{\varphi}_3 - \dot{z}_1) > 0$ then the dampers are on, otherwise off. If $(\dot{z}_3 - l_2\dot{\varphi}_3)(\dot{z}_3 - l_2\dot{\varphi}_3 - \dot{z}_2) > 0$ then the rear dampers are on, otherwise off.

The effect of the time delay on the performance of the semi-active dampers is taken into account by the following equations

$$T_d \dot{b}_{sa,1} + b_{sa,1} = b_{sadem,1}, \quad T_d \dot{b}_{sa,2} + b_{sa,2} = b_{sadem,2}, \quad (5)$$

where $b_{sadem,1}$ and $b_{sadem,2}$ are the demand damping coefficients, $b_{sa,1}$ and $b_{sa,2}$ are the actual damping coefficients and T_d is the time delay.

In semi-active suspensions with MR dampers (Lord RD—105—3, [4]) the following equation for the damping force hold

$$F_{sa} = F_{sa}(\dot{x}_{rel}, I) = c_f k_3 \dot{x}_{rel} + F_y(I) \tanh[\beta k_3 \dot{x}_{rel}], \quad (6)$$

where the inertia effects of the MR fluid flowing through the piston channels are neglected. In this equation I is the electric current, \dot{x}_{rel} is the relative velocity between the unsprung mass m_1 and m_2 and points A and B (Fig. 2), respectively, c_f expresses viscous damping of the MR fluid, β expresses influence of the friction force rate in the vicinity of zero relative velocity \dot{x}_{rel} , $k_3 = -k_2/k_1$, where k_1 and k_2 describe compressibility of the hydraulic and pneumatic parts of the MR damper. The parameters of the MR damper described above were experimentally identified [4] and the following approximation functions hold

Table 1 Optimization results for stochastically uneven road

Optimization variable	Units	Passive system	Ideal semi-active dampers	Semi-active lord dampers
k_1, k_2	N.m	70,000	70,000	70,000
b_1, b_2	kg m.s ⁻²	1,007	–	–
b_{sky1}, b_{sky2}	kg m.s ⁻²	–	13,728	8,049
f_{op}	m s ⁻²	$3.770.10^{-2}$	$2.540.10^{-2}$	$2.543.10^{-2}$

Table 2 Optimization results for deterministic “hat” bump

Optimization variable	Units	Passive system	Ideal semi-active dampers	Semi-active lord dampers
k_1, k_2	N.m	70,000	70,001	70,000
b_1, b_2	kg m.s ⁻²	1192,6	–	–
b_{sky1}, b_{sky2}	kg m.s ⁻²	–	12,194	6,002
f_{op}	m.s ⁻²	$3.62.10^{-2}$	$1.60.10^{-2}$	$1.84.10^{-2}$

$$\begin{aligned} c_f(I) &= c_1 I + d_1, & F_y(I) &= a_2 I^3 + b_2 I^2 + c_2 I + d_2, \\ k_1(I) &= b_3 I^2 + c_3 I + d_3, & k_2(I) &= b_4 I^2 + c_4 I + d_4. \end{aligned} \quad (7)$$

Based on the experimental data, a least-square method was employed to determine the numerical values of all parameters in above equations [5]. The on-off conditions are the same as for the ideal semi-active suspension.

The passengers cars with the three different suspensions described above are subjected to the deterministic “hat” bump of the form

$$u(x) = \frac{h_m}{2} \left(1 - \cos \frac{2\pi}{d} x \right), \quad \text{for } 0 \leq x, \quad \text{otherwise } u(x) = 0, \quad (8)$$

where h_m is the bump height and d is the bump length. The stochastically uneven road is characterized by its power spectral density $S_u(\Omega_0)$ [6].

3 Optimization and Results

The dynamic behaviour of the semi-active system is optimized using genetic algorithms [5, 7, 8]. The objective function expressing the effective value of the vertical sprung mass centroid acceleration has the following form

$$f_{op} = \sqrt{\frac{1}{T} \int_0^T \ddot{z}_3^2(t) dt}. \quad (9)$$

Further, the following constraints are taken into account

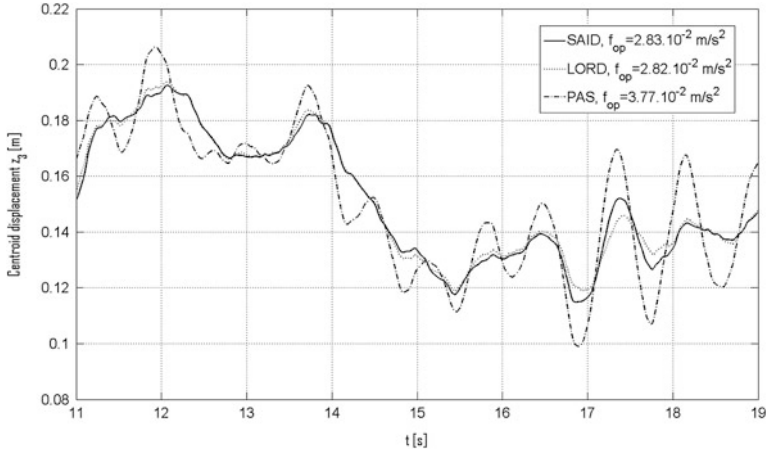


Fig. 3 Vertical displacements of the centroid T_3 (stochastically uneven road)

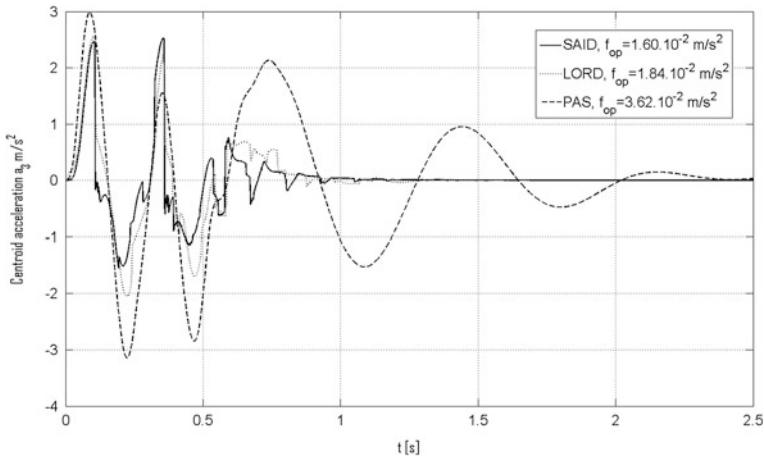


Fig. 4 Vertical accelerations of the centroid T_3 (deterministic “hat” bump)

1. Constraints on the relative motions between the sprung and unsprung masses

$$(z_3 + l_1 \varphi_3 - z_1) \leq z_{r1,\max}, \quad (z_3 - l_2 \dot{\varphi}_3 - z_2) \leq z_{r2,\max}. \quad (10)$$

2. Constraints on the dynamic road-tyre force

$$k_3(z_1 - u_1) \leq f_{dyn1,\max}, \quad k_4(z_2 - u_2) \leq f_{dyn2,\max}. \quad (11)$$

In the inequalities above $z_{r1,\max}$ and $z_{r2,\max}$ mean the permissible allowances of the relative motions between the sprung and unsprung masses, $f_{dyn1,\max}$ and $f_{dyn2,\max}$ mean the permissible allowances of the dynamic road-tyre forces.

Table 3 Dependence of the objective function on the time delay for stochastically uneven road

Time delay T_D	f_{op} for ideal dampers	f_{op} for lord dampers	Time delay T_D	f_{op} for ideal dampers	f_{op} for lord dampers
0.0	$2.540 \cdot 10^{-2}$	$2.543 \cdot 10^{-2}$	0.011	$3.019 \cdot 10^{-2}$	$3.145 \cdot 10^{-2}$
0.001	$2.579 \cdot 10^{-2}$	$2.672 \cdot 10^{-2}$	0.012	$3.052 \cdot 10^{-2}$	$3.217 \cdot 10^{-2}$
0.003	$2.666 \cdot 10^{-2}$	$2.722 \cdot 10^{-2}$	0.013	$3.082 \cdot 10^{-2}$	$3.287 \cdot 10^{-2}$
0.006	$2.820 \cdot 10^{-2}$	$2.835 \cdot 10^{-2}$	0.014	$3.110 \cdot 10^{-2}$	$3.367 \cdot 10^{-2}$
0.01	$2.985 \cdot 10^{-2}$	$3.070 \cdot 10^{-2}$	0.015	$3.135 \cdot 10^{-2}$	$3.456 \cdot 10^{-2}$

The following variables are specified: the velocity of the ride $v = 20$ m/s, the road power spectral density $S_u(\Omega_0) = 22.3 \cdot 10^{-6}$ m³ (stochastic road), $v = 11$ m/s (“hat” bump), the bump height $h_m = 0.06$ m, the bump length $d_m = 2.68$ m, $m_1 = 110$ kg, $m_2 = 118$ kg, $m_3 = 1,370$ kg, $I_3 = 4,192$ kg m², $k_3 = k_4 = 4,00,000$ N/m (common tyre stiffness coefficient of the whole axle), $z_{r1,max} = 0.08$ m, $z_{r2,max} = 0.08$ m.

Tables 1 and 2 show the results of optimization for the stochastically uneven road and deterministic “hat” bump, respectively, for zero time delay.

Figure 3 shows the centroid T_3 vertical displacements for stochastically uneven road and zero time delay. Figure 4 presents the centroid T_3 vertical accelerations for the deterministic bump and zero time delay. Table 3 presents dependence of the objective function f_{op} on the time delay T_D for stochastically uneven road.

4 Conclusions

The results showed that MR dampers with nonzero damping force in their off states are able to reduce the effective acceleration of the sprung mass significantly (compared with passive suspensions with conventional hydraulic dampers) only if the time delay is low enough—less than approx. 10–12 s.

References

1. Guglielmino, E. et al.: Semi-active suspension control, improved vehicle ride and road friendliness, Springer, Berlin (2008)
2. Segla, S., Reich, S.: Optimization and comparison of passive, active, and semi-active vehicle suspension systems. Proceedings of the 12th IFToMM World congress on mechanism science, Besancon (2007)
3. He, Y., McPhee J.: Multidisciplinary design optimization of mechatronic vehicles with active suspensions. J. Sound Vib. **283**, 217 (2005)
4. Úradníček, J.: Multidisciplinary optimization of a vehicle suspension model with semi-active magnetorheological damper (in Slovak), PhD thesis, Slovak technical university in Bratislava, Bratislava, (2008)

5. Genetic Algorithm and Direct Search Toolbox—User's Guide. The Mathworks Inc., Natick (2004)
6. Nigam, N.C., Narayanan, S.: Appl. Random Vib. Springer, Berlin (1994)
7. Sága, M. et al.: Selected methods of analysis and synthesis of mechanical systems (in Slovak), VTS ŽU in Žilina (2009)
8. Zmindak M., Sága M., Tvaruzek J., Husar S.: Optim. Mech. Syst. (in Slovak), VTS ŽU in Žilina (2000)

Optimization of Industrial Sewing Machine Balancing Using Adams and Mathematica Software

P. Šidlof and J. Ondrášek

Abstract This paper deals with method of balancing optimization of a very complex set of sewing machine mechanisms. Dynamic forces and moments generated in the mechanisms are evaluated by powerful Adams software, but balancing optimization and the project of additional balancing mechanism are realized in Mathematica software, which is more suitable for this purpose and is cheaper. Results are verified in Adams once again.

Keywords Sewing machine • Balancing • Adams • Mathematica

1 Introduction

For industrial sewing machines, vibration is one of the important parameters affecting the utility value. The main sources of vibrations are inertia forces and moments generated in the mechanisms of the machine. For most industrial sewing machines, inertia forces and moments are reduced or affected only by rotational counterweights on the shafts. Rarely auxiliary balancing mechanisms are used. Adams software [1] that allows simulations of very complex set of mechanisms is used to perform qualified dynamic calculations and to verify the design of a new machine. One of the outputs is the total inertia force and moment. But optimization of rotational unbalance and possible balancing mechanism is time-consuming and

P. Šidlof (✉) · J. Ondrášek
VÚTS, a.s., Liberec, Czech Republic
e-mail: pavel.sidlof@vuts.cz

J. Ondrášek
e-mail: jiri.ondrasek@vuts.cz

expensive in the Adams. The paper provides a method and example of balancing optimization performed in the Mathematica software [2] using results taken from the Adams.

2 Modelling Mechanisms of the Machine and Calculation of Balancing

Simpler mechanisms can be solved directly in the own programme in the Mathematica software, where the bodies are replaced by point masses. The discussed sewing machine for sewing of heavy materials, however, is relatively complicated and calculations of stress on particular components of the mechanisms were needed. The solution was thus calculated in the Adams software.

The primary part of the model of mechanisms is a model of a fixed body, which has assigned geometric-weight characteristics when solving dynamic tasks. In complicated cases such as this one, geometric models were derived from the design documentation in the NX I-DEAS system along with setting weights, matrix of inertia and location of centres of gravity. Then the parts were assembled into operational sub-assembly. In the Adams programme environment kinematic constraints, external forces, etc. were defined and numerical solution of the equations of motion derived from Lagrange equations.

The resulting model is formed of a spacial set of 50 bodies (Fig. 1) between which ideal kinematic constraints are defined (without backlash and passive resistance). The bodies are considered rigid (however, in calculations of stress and vibrations in the mechanism some bodies are considered flexible) and the calculation is carried out for constant angular speed of 1,500 RPM of the upper main shaft. Zero of the main shaft angle is in the upper dead point of the needle bar. From inertia forces of all elements of mechanism the resulting inertia force F (F_x , F_y , F_z) and the resulting moment to the centre of gravity of the entire machine M (M_x , M_y , M_z) are derived. Behaviour of this force and its components (component F_z is zero) and of the moment is depicted in Figs. 2 and 3.

The calculated components of the inertia force and moment were transferred into the Mathematica software. The basic balancing of the machine was carried out here by use of two rotational counterweights on the main shaft. One was close to the crank of the needle bar mechanism and the second was close to the fly-wheel. Their inertia forces and moments were added to the overall force and the moment obtained from the Adams. Weights and angle positions of the counterweights were optimised (4 parameters). For optimisation various criteria are used. Decisive are overall vibrations of the machine suspended on silent-blocks in the working desk, which has a relatively flexible frame. From this point of view with respect to comfort of the seamstress the most important are usually vibrations in direction of the x axis, which are most influenced by the F_x force and M_z moment. Thus we tried to find the parameters of the counterweights so that absolute maxima of these

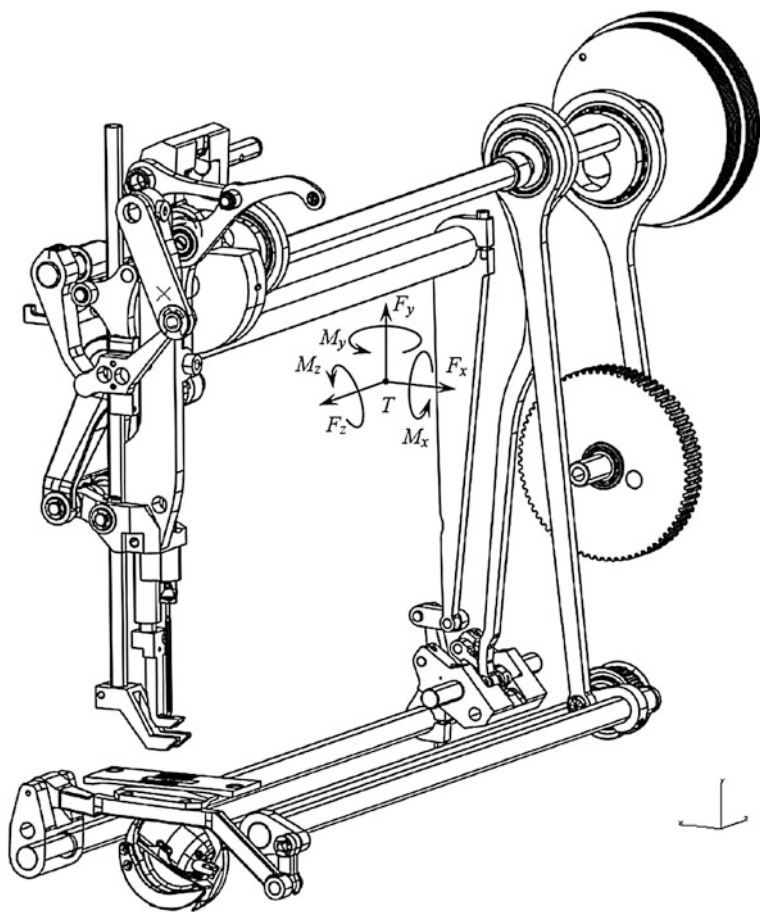


Fig. 1 Mathematical model of mechanisms of the machine in the Adams programme (pulleys on the *right hand side* of the picture are connected by a toothed belt)

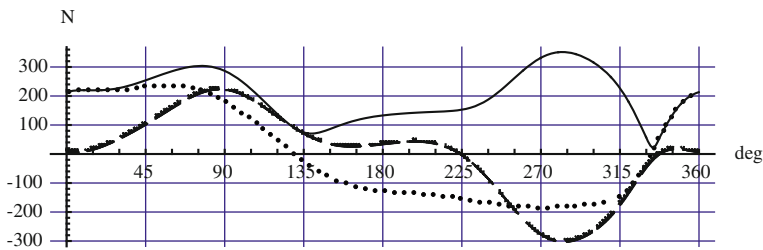


Fig. 2 Resulting inertia force of all mechanisms before balancing: F_x (*dashed*), F_y (*dotted*) and overall force F (*solid line*) (max. of absolute values: F_x : 302, F_y : 239, F : 352 (N))

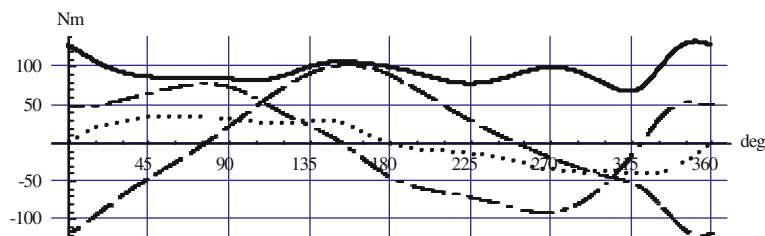


Fig. 3 Resulting inertia moment of all mechanisms before balancing: M_x (dashed), M_y (dot-dash), M_z (dotted) and overall moment M (solid line) (max. of absolute values: M_x : 121, M_y : 91, M_z : 41.4, M : 133 (Nm))

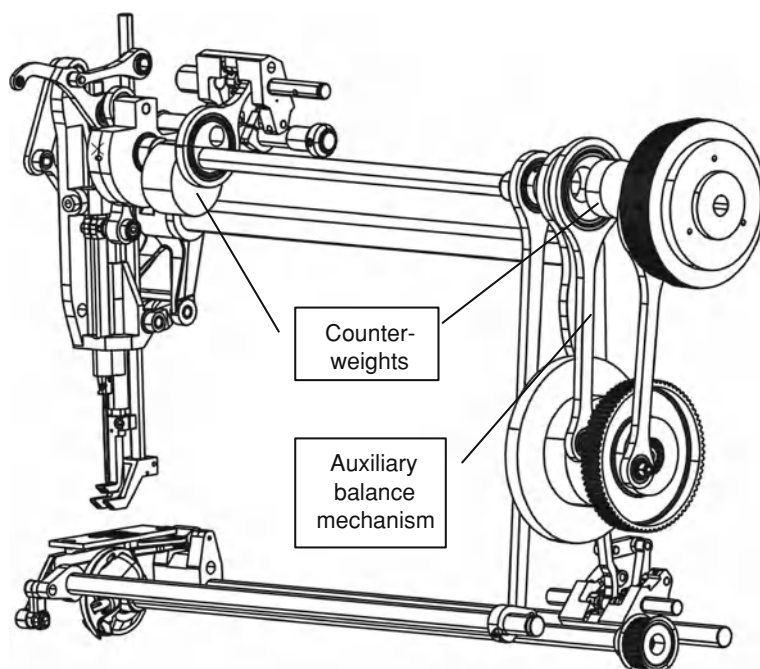


Fig. 4 Counterweights on the main shaft and the auxiliary mechanism to balance the M_z moment (fly-wheel placed in the axis of the pulley is driven by an eccentric and a connecting rod)

components and absolute maxima of the overall force and moment were minimal. It appeared that when lowering the F_x the M_z is growing and vice versa. Thus we proposed an auxiliary balancing mechanism to balance the moment M_z depicted in Fig. 4. It is a four-bar mechanism driven by an eccentric on the main shaft. The balancing element is a fly-wheel placed close to the pulley of the shuttle drive. Calculations with this mechanism were then performed in this way: First employing the iterative method we found a suitable position angle of eccentric and eccentricity of the pivot on the fly-wheel. Then for zero moment of inertia of the

Table 1 Balancing by rotational counterweights and idem with use of the balancing mechanism

	<i>max</i> <i>F_x</i> (N)	<i>max</i> <i>F_y</i> (N)	<i>max</i> <i>F</i> (N)	<i>max M_x</i> (Nm)	<i>max M_y</i> (Nm)	<i>max M_z</i> (Nm)	<i>max M</i> (Nm)
Original	302	239	352	121	91	41.4	133
Rotational balancing	155	170	181	48.2	37.9	58.4	66.1
%	51.3	71.4	51.6	39.8	41.6	141	49.7
Final balancing	167	164	167	40.3	36.1	23.4	41.3
%	55.2	68.7	47.3	33.3	39.7	56.7	31

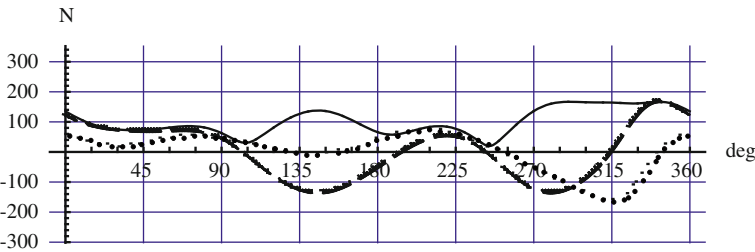


Fig. 5 Inertia force of all mechanisms after balancing by use of rotational counterweights and auxiliary balancing mechanism (*F_x* dashed, *F_y* dotted, overall force *F* solid line)

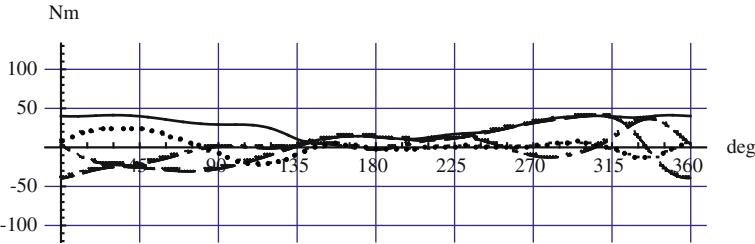


Fig. 6 Inertia moment of all mechanisms after balancing by use of rotational counterweights and with the auxiliary balancing mechanism (*M_x* dashed, *M_y* dash-dot, *M_z* dotted, *M* solid line)

fly-wheel we optimised rotational counterweights on the main shaft to minimize F_x (regardless of M_z). Lastly we optimized the moment of inertia of the fly-wheel so that the M_z moment was minimal (the fly-wheel moment of inertia does not influence the inertia forces). For the obtained result the iterative process was refined and calculation of the counterweights and moment of inertia was repeated.

In the upper part of Table 1 are depicted maximums of absolute values of the overall inertia force and moment before balancing and after it by use of rotational counterweights only. We picked a compromise balancing, which lowers the F_x force but does not increase the M_z moment much. In the lower part we present balancing by use of the auxiliary balancing mechanism. The F_x force is by 4 % greater than in the previous case, but the M_z moment dropped 2.5 times. The resulting graphs are on Figs. 5 and 6.

Fig. 7 Amplitude spectra of inertia moment M_z before balancing. (1. harmonic: 37.3 (Nm), 2. harmonic: 8.5 (Nm), 3. harmonic: 6.7 (Nm))

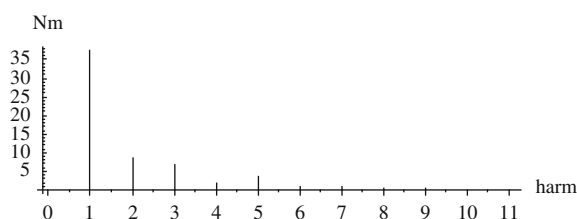
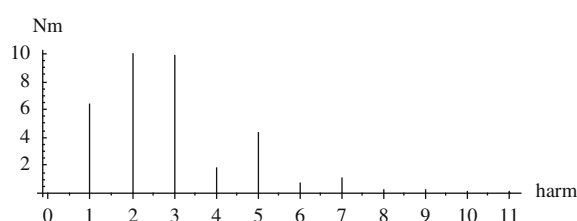


Fig. 8 Amplitude spectra of the overall inertia moment M_z (Nm) after balancing. (1. harmonic: 6.4 (Nm), 2. harmonic: 10 (Nm), 3. harmonic: 9.9 (Nm))



Greater importance than reduction of maximum values of inertia forces and moments has the change of their harmonic response because the lowest harmonic components are decisive for appearance of resonance vibration of the whole machine. Rotational balancing lowers only the first harmonic, while the balancing mechanism influences also higher harmonics. To give an example, the Figs. 7 and 8 show the amplitude spectra of the M_z moment before and after balancing. The proposed balancing lowers the amplitude of the first harmonic almost six times, the relatively low second and third harmonics grew somewhat. In the F_x force the first harmonic dropped 2.4 times, the second harmonic grew slightly, third harmonic did not change.

3 Conclusions

The article presents the process of calculation of dynamic balancing on an industrial sewing machine with a relatively complex system of mechanisms. The overall inertia force and moment of the mechanisms calculated in the Adams programme are transferred into the Mathematica programme, where first balancing by use of only rotational counterweights is proposed and then derived also with use of a balancing four-bar mechanism. We managed to lower the components of the resulting inertia force and moment significantly, but mainly the first harmonic of the M_z moment and F_x force were lowered, being the main source of vibration of the machine with the work desk.

Acknowledgments The research work reported here was made possible by project FR-TI3/320 sponsored by MPO.

References

1. MSC-ADAMS: User's Reference Manual, Mechanical Dynamics.
2. <http://www.wolfram.com/products/>

Application of the Impact-Free Lift Dependence in Small-Diameter Knitting Machines

J. Skřivánek and M. Bilek

Abstract The article is concerned with evaluation of the existing and new concepts of the drive of small-diameter knitting machines. The present arrangement of the drive provides for coupled movement of the needle cylinder and of the dial, realised by one driving unit. The new solution employs three unit drives, governing the principal construction assemblies. The result of the analysis is a comparison of courses of kinematic quantities of the motion of principal parts of the driving system.

Keywords Knitting machine • Drive • Mathematical model • Analysis

1 Introduction

The present small-diameter knitting machines are in overwhelming majority equipped with one brushless servomotor, driving the needle cylinder, the dial and the cutting disk by means of mechanical transmissions. In the endeavour to make the production as economic as possible, there appear a number of problems related with dynamic behaviour of the machine [1], due to a considerable number of transmissions driving these elements. With the intense development of electronics there appears a possibility to employ electronically controlled drives in the knitting machines, thus reducing the number of mechanical transmissions. The present

J. Skřivánek (✉) · M. Bilek
Technical University of Liberec, Liberec, Czech Republic
e-mail: josef.skrivanek@tul.cz

M. Bilek
e-mail: martin.bilek@tul.cz

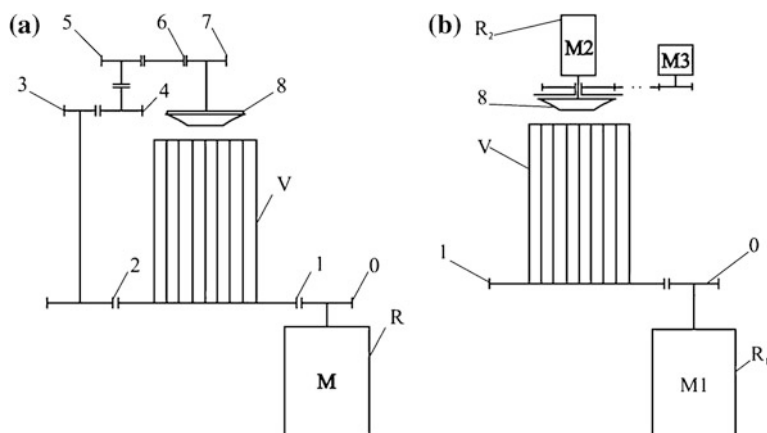


Fig. 1 The original structure of the drive of a knitting machine and the newly proposed one

arrangement of the drive cannot—owing to the joint driving unit—provide for effective movement of individual assemblies that realise the knitting process.

The aim of this article is to assess the structures of the drive employed presently and newly devised ones [2], which allow for reducing the power demands of the knitting process, as well as for a more favourable dynamic behaviour with higher positional precision. The suggested state can be achieved by utilising modern, electronically governed drives for individual operating elements. Another important criterion for assessing the suitability of its use are the demands on dynamics of the machine, as the acceleration of production and minimisation of production times sets limitations for mechanical transmissions, and they encounter bounds of their use in dependence on their applications.

2 Mathematical Model of the System

In order to be able to describe the behaviour of the examined system, it is necessary to compile a suitable mathematical model, which will describe its behaviour during an operation cycle with the maximum possible precision. For the purpose of comparison of the present structure of the drive (Fig. 1a) and the newly proposed one (Fig. 1b), there have been compiled mathematical models of both the systems. In the mathematical model, the drive is substituted with a discrete chain of concentrated masses connected by flexible and damping links with defined rigidities and internal damping. The proper mathematical model of the driving system of knitting machines has been devised under the following conditions:

the masses of individual elements of the mechanism including the corresponding part of shafts and seating are substituted by mass points. With the mass points, their moments of inertia are established

the shafts that connect the gear wheels transmitting the driving moment are considered to be flexible elements, and their torsional rigidities have been included. the mass of the needle cylinder is considered including needles, sinkers and its other parts. It is divided into two mass points, interconnected by a torsional spring. elastic elements are damped by viscous damping, with the damping co-efficient b . in the calculation, there are considered plays in kinematic couples. These plays are substituted with angular deflections of gear wheels of the mechanism,

The motion equations have been compiled employing the Lagrange equation of the second kind, using the method indicated in [2]

$$\frac{d}{dt} \left(\frac{\partial E_K}{\partial \dot{q}_i} \right) - \frac{\partial E_K}{\partial q_i} + \frac{\partial E_P}{\partial q_i} = Q_j - \frac{\partial R_d}{\partial \dot{q}_i} \quad (1)$$

Motion equations of the present structure

$$\ddot{\varphi}_0(I_0 + I_1\eta_{01}^2 + I_2\eta_{02}^2) + b_{0R}(\dot{\varphi}_0 - \dot{\varphi}_R) - b_V(\dot{\varphi}_V - \dot{\varphi}_1)\eta_{01} - b_{23}(\dot{\varphi}_3 - \dot{\varphi}_2)\eta_{02} + k_{0R}(\varphi_0 - \varphi_R) - k_V(\varphi_V - \varphi_1)\eta_{01} - k_{23}(\varphi_3 - \varphi_2) = 0 \quad (2)$$

$$I_V\ddot{\varphi}_V + b_V(\dot{\varphi}_V - \dot{\varphi}_1) + k_V(\varphi_V - \varphi_1) = 0 \quad (3)$$

$$\ddot{\varphi}_3(I_3 + I_4\eta_{34}^2) + b_{23}(\dot{\varphi}_3 - \dot{\varphi}_2) - b_{45}(\dot{\varphi}_5 - \dot{\varphi}_4)\eta_{34} + k_{23}(\varphi_3 - \varphi_2) - k_{45}(\varphi_5 - \varphi_4)\eta_{34} = 0 \quad (4)$$

$$\ddot{\varphi}_5(I_5 + I_6\eta_{56}^2 + I_7\eta_{57}^2) + b_{45}(\dot{\varphi}_5 - \dot{\varphi}_4) - b_{78}(\dot{\varphi}_5 - \dot{\varphi}_4)\eta_{57} + k_{45}(\varphi_5 - \varphi_4) - k_{78}(\varphi_8 - \varphi_7)\eta_{57} = 0 \quad (5)$$

$$I_8\ddot{\varphi}_8 + b_{78}(\dot{\varphi}_8 - \dot{\varphi}_7) + k_{78}(\varphi_8 - \varphi_7) = 0 \quad (6)$$

Motion equations of the optimised structure

$$I_0\ddot{\varphi}_0 + b_{0R}(\dot{\varphi}_0 - \dot{\varphi}_{R1}) - b_{10}\eta_{01}(\dot{\varphi}_1 - \dot{\varphi}_0\eta_{01}) + k_{0R}(\varphi_0 - \varphi_{R1}) + k_{10}\eta_{01}(\varphi_1 - \varphi_0\eta_{01}) = 0 \quad (7)$$

$$I_1\ddot{\varphi}_1 + b_{10}(\dot{\varphi}_1 - \dot{\varphi}_0\eta_{01}) - b_V(\dot{\varphi}_V - \dot{\varphi}_1) + k_{10}(\varphi_1 - \varphi_0\eta_{01}) - k_V(\varphi_V - \varphi_1) = 0 \quad (8)$$

$$I_V\ddot{\varphi}_V + b_V(\dot{\varphi}_V - \dot{\varphi}_1) + k_V(\varphi_V - \varphi_1) = 0 \quad (9)$$

$$I_8\ddot{\varphi}_8 + b_{R8}(\dot{\varphi}_8 - \dot{\varphi}_{R2}) + k_{R8}(\varphi_8 - \varphi_{R2}) = 0 \quad (10)$$

Variables appearing in the equations: E_K —kinetic energy, E_P —potential energy, R_d —dissipative function, q_i —generalised co-ordinate, b_i —co-efficient of viscous damping [N.m.s/rad⁻¹], k_i —co-efficient of rigidity [N.m.rad⁻¹], η_i —transmission, I —moment of inertia [kg.m²], ϕ —position [rad]

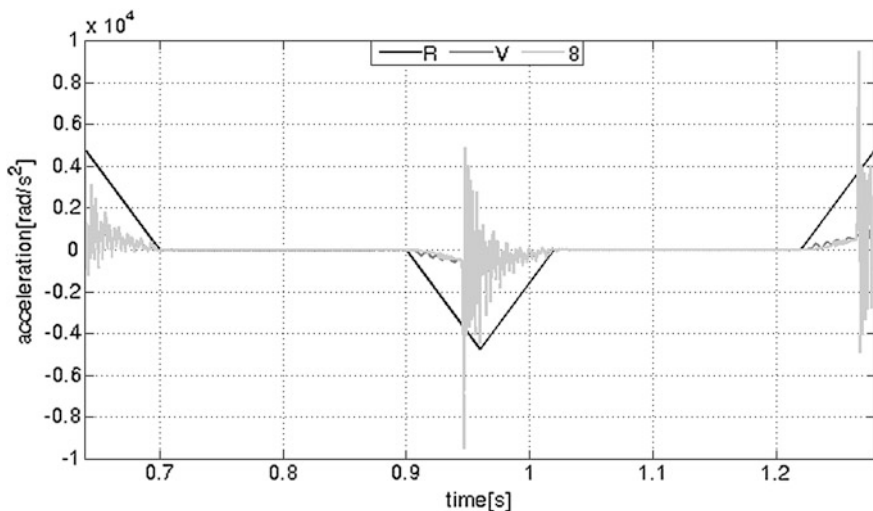


Fig. 2 Courses of accelerations of individual elements of the present drive

The least favourable loading of the system occurs during cyclical rotary reverse motion when knitting the heel and toe of sock goods. In order to reduce the force loading of the structure, for this case of motion of the knitting cylinder it is suitable to employ an impact-free course of the lift dependence. This condition is fulfilled e.g., by the polynomial 4-5-6-7, where the angle of slewing of the needle cylinder (Fig. 2) is a function of displacement of a fictitious cam within one period of time, when the cylinder performs a symmetric motion from the rest position with return to the same position.

$$\begin{aligned} \gamma(\psi) = & C_0 + C_1\psi + C_2\psi^2 + C_3\psi^3 + \\ & + C_4\psi^4 + C_5\psi^5 + C_6\psi^6 + C_7\psi^7 \end{aligned} \quad (11)$$

ψ —angle of slewing of fictitious cam [rad], γ —angle of slewing of the mechanism [rad], C_n —constants

In the Eq. (12) there figure eight constants, for the establishment of which eight boundary conditions must be found. By calculating successive derivatives of this relation, we obtain four equations more. Another precondition is the fact the cam revolves at constant velocity.

Equations of the polynomial 4-5-6-7

$$\begin{aligned} \Omega(\psi) = & C_1\omega + 2C_2\omega\psi + 3C_3\omega\psi^2 + 4C_4\omega\psi^3 + \\ & + 5C_5\omega\psi^4 + 6C_6\omega\psi^5 + 7C_7\omega\psi^6 \end{aligned} \quad (12)$$

$$\begin{aligned} \varepsilon(\psi) = & 2C_2\omega^2 + 6C_3\omega^2\psi + 12C_4\omega^2\psi^2 + \\ & + 20C_5\omega^2\psi^3 + 30C_6\omega^2\psi^4 + 42C_7\omega^2\psi^5 \end{aligned} \quad (13)$$

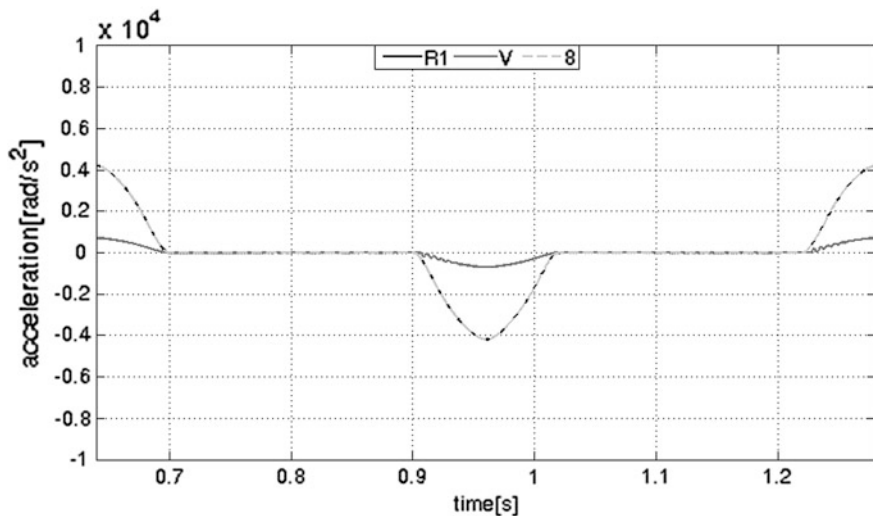


Fig. 3 Courses of accelerations of individual elements of the optimised drive

$$\delta(\psi) = 6C_3\omega^3 + 24C_4\omega^3\psi + 60C_5\omega^3\psi^2 + 120C_6\omega^3\psi^3 + 210C_7\omega^3\psi^4 \quad (14)$$

Equations of the linear function

$$\gamma(\psi) = C_{10} + C_{11}\psi \quad (15)$$

$$\Omega(\psi) = C_{11}\omega \quad (16)$$

$$\varepsilon(\psi), \delta(\psi) = 0 \quad (17)$$

For the present system there is employed a polynomial of 3rd degree in combination with linear function in the points where a zero acceleration of the system is required.

$$\gamma(\psi) = C_1\omega + 2C_2\omega\psi + 3C_3\omega\psi^2 + 4C_4\omega\psi^3 \quad (18)$$

$$\Omega(\psi) = 2C_2\omega^2 + 6C_3\omega^2\psi + 12C_4\omega^2\psi^2 \quad (19)$$

$$\varepsilon(\psi) = 6C_3\omega^3 + 24C_4\omega^3\psi \quad (20)$$

3 Conclusions

For the derived motion equations there has been compiled a mathematical model in the software MATLAB. The individual equations have been written in matrix form, and subsequently solved by gradual integration by means of the solver in the software Simulink. There has been utilised a solver employing the standard method Dormand-Prince termed ode45. The outputs of the analyses are the courses of principal kinematic quantities of the system, which enable studying the changes of behaviour of the new structure of the drive, including the deviation of the positions of the knitting cylinder and the dial.

The courses of acceleration of selected elements of the drive of the present structure are shown in the Fig. 2. In this figure there can be seen significant peaks of the acceleration, generated namely by existing plays and subsequent mutual collision of individual teeth during their meshing. An impact in a gear set generates a temporary oscillating effect, which is then damped gradually due to viscous damping. These values are as much as three times higher in comparison with the concept of a system without plays. For the start-up of the system there has been employed a polynomial of 3rd degree, see the Eqs. (18–20).

The courses of acceleration of selected elements of the drive of the new structure are shown in the Fig. 3. In this case, there has been employed the lift dependence 4-5-6-7, see the equations (11–17). When comparing both the above figures it is evident that in case of the new structure the peak values of acceleration have been suppressed.

Another very important factor serving for evaluation of both concepts is the value of the deviation of positions of the knitting cylinder and the dial. In case of the new structure, it is lower in the level of orders, due to the reduction of the number of elastic mechanical elements which during the reverse motion of the cylinder, together with the plays, were causing an increase of the resultant value of the deviation. The performed analysis proves that the application of the new structure of the drive in small-diameter knitting machines is advisable.

Acknowledgments The paper has been elaborated with financial support of TUL in the framework of specific university research competition.

References

1. Skřivánek, J., Bílek, M.: Dynamics of the frame of small-diameter knitting machine. Acc. J. XVI, Liberec, pp. 60–66, ISSN 1803-9782 (2010)
2. Mrázek, J.: Theoretical analysis of dynamics four-bar beat up mechanisms of a loom. In: Mechanism and Machine Theory, Pergamon Press, USA, 27(3), pp. 125–136 (1992)

The Optimal Design of an Auxiliary Switch for an Internal Combustion Engine Starter

J. Stropnik

Abstract An auxiliary switch is part of a mechanism—the starter motor—that starts an internal combustion engine. While starting the engine, a part of direct current runs from the accumulator through the ignition switch in the driver's cabin. Since this current is relatively large, this leads to a substantial power load on the ignition switch, which can be prevented by building in an auxiliary switch—a starter relay. The auxiliary switch must comply with certain electrical and mechanical requirements. Particularly important are the current intensity through the relay under operating voltage and the voltage required to switch over contacts. The excess of current intensity can be very small, which is conditioned by accurate dimensioning of the coil. When the current runs through the coil, a force is created that moves the core into the final position and, hence, a switchover of contacts. The force created must be large enough to overcome the force in the spring and provide a quality switchover. All this requires an optimal configuration of relay components. The article provides an analysis of magnetic states in the relay and, based on this, proposes a final structural design of the relay.

Keywords Starter motor • Auxiliary switch • Optimisation

1 Introduction

We use the starter that is actually a one-way electric motor powered by an accumulator battery, to start the internal combustion engine [1]. The main components of the starter are (Fig. 1a): 1—cowling, 2—stator winding, 3—front lid, 4—back lid,

J. Stropnik (✉)
University of Ljubljana, FME, Ljubljana, Slovenia
e-mail: joze.stropnik@fs.uni-lj.si

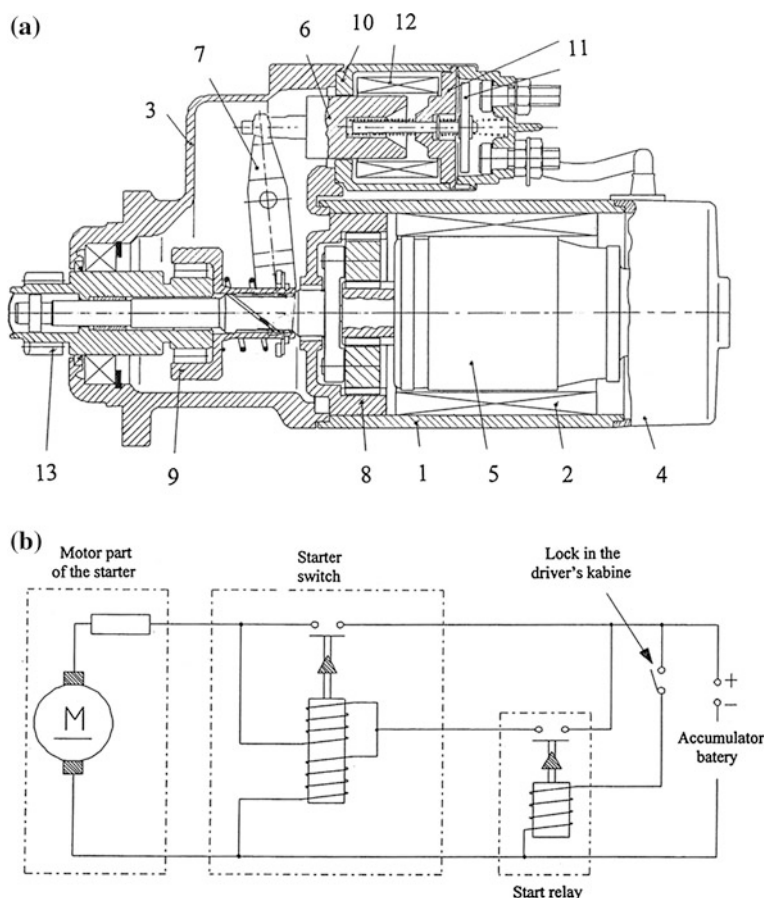


Fig. 1 a Starter, b Connection diagram of starter with a start relay

5—rotor, 6—core, 7—fork, 8—reductor, 9—clutch, 10—switch, 11—contact plate, 12—winding 13—pinion. In the vehicle's lifespan, the starter performs around 30,000 startups. Because startup time is very short (around 1 s), the starter is inactive for the most part of engine operation. By turning the key in the driver's cabin, electric current first flows from the accumulator battery to the switch (10). When the cur and a force that moves the core (6) in the axial direction and joins the contact plates (11). Motion of the core also causes the fork (7) to spin and move the pinion (13), which connects with the engine sprocket. Because the core is in its end position at this point, a powerful magnetic field is created in the cowling of the starter, rent flows through the winding in the switch, it creates a powerful magnetic field which causes the starter's main rotation and the engine starts running.

At this point, the starter has to be stopped, which is done by the driver, by returning the key to its original position. The time between engine startup and starter shutdown must be as short as possible. As the starter is turned off, the

magnetic force in the switch is reduced, and the spring pushes the core of the switch back to its original position. The contact plate moves away from the contact screws and the flow of electric current to the motor part of the starter is interrupted.

When the switch is activated, there is a large electric current flowing between the lock and the switch. Because other consumers of electric current can be active during engine startup, the electric current flowing through the lock is even higher. Because of this, manufacturers tend to install another smaller switch, mainly into industrial vehicles—a start relay. A small current is required to activate the start relay (around 2 A). This switch is electrically connected in such way that it serves as the intermediate link between the lock and the winding inside the starter's switch (Fig. 1b). The electric current flows directly from the accumulator battery and past the lock, reducing the current through the lock by a large amount.

The start relay must be constructed for the nominal voltage of accumulator battery 24 V and must be capable of switching at a voltage of 14 ± 1.5 V and switching off at 3.5 ± 1.5 V. The maximum current through the relay can be 1.4 ± 0.1 A. The relay must be capable of operating for 3 min continuously. For the relay to function correctly, we must find components of such shapes, dimensions and materials that will create the best conditions for its reliable operation [2, 3].

2 Start Relay

In function and appearance, the start relay resembles the starter switch (Fig. 2a), except that it is smaller. The start relay consists of: 1—core, 2—mandrel, 3—bottom side, 4—coil, 5—casing, 6—top side, 7—contact plate, 8—lid, 9—contact screw, 10—return spring, 11—auxiliary spring. When the electric current flows through the coil (4), a magnetic field is created and with it the attractive force between the core (1) and the top side (6). The core starts moving to connect with the contact plate (7) and the contact screws (9). Here the attractive force must overcome the force of tensioning of the springs (10). When the start relay stops operating, the spring must return the core to its original position. The start relay construction must feature a strong enough spring and other elements, as well as a large enough coil.

The magnetic field is provided by a coil with sufficient excitation (magnetic voltage) Θ (A), which is dependent on current I (A) through the coil and number of turns n [4, 5] and is given by the equation $\Theta = I \cdot n$. The number of turns n is dependent on wire diameter and space available for the winding inside the relay. Electrical resistance of the wire inside the winding is dependent on specific resistance of the wire ρ ($\Omega \text{ mm}^2/\text{m}$), length of the wire L (m), cross-section of the wire A (mm^2) and is $R = \rho \cdot L/a$. Intensity of electric current through the coil I (A) is specified by Ohm's law $I = U/R$, where $U = 24$ V for operating voltage and $U = 15$ V for ignition voltage. All described electrical quantities are calculated for a coil of certain selected proportions for different diameters of wires in the winding.

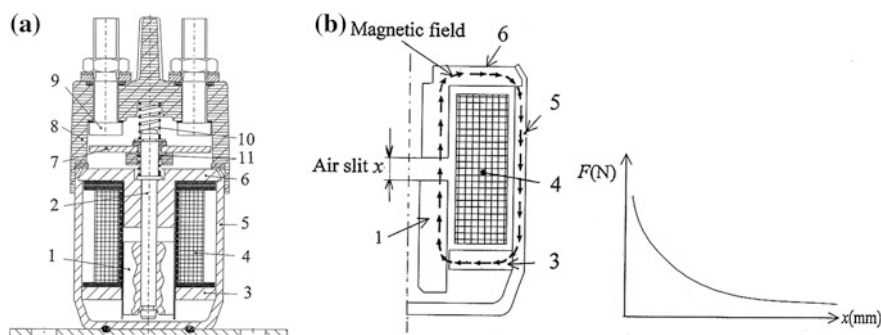


Fig. 2 a Start relay, b Magnetic field current, attractive force in relation to air slit size

Magnetic current Φ (Wb) is dependent on magnetic current density B (T) and section A (m²) and is given by the equation $\Phi = \int B \cdot dA$. Magnetic current density B is dependent on magnetic field strength H (A/m) and material permeability μ (Wb/A m) and is $B = \mu \cdot H$. Magnetic field strength is $H = I \cdot n / L$, where I (A) is the intensity of electric current through the coil, n the number of wire turns in the coil and L (m) the length of magnetic lines of force.

Attractive force is dependent on the size of magnetic field, which is dependent on dimensions of elements composing the relay. The initial air slit represents a large magnetic resistance. When the core begins to move towards the side, the slit decreases, which causes the attractive force to increase (Fig. 2b).

The magnetic field must be such that the attractive force will be as large as possible, so the components of the relay must be of optimal dimensions. The computer program MAXWELL 2D which is based on the FEM method was used to calculate the magnetic field and attractive force. Components of the relay have to be appropriately divided into final elements and material attributes have to be specified for this calculation.

The optimal form of the start relay components was chosen based on results of computer processing of several variations [6]. The continuation only shows results for two forms, namely from the start of optimisation and for the final solution. The differences between the initial and the final form include increasing the bottom side thickness from 2 to 3 mm, shortening the core for 2 mm, decreasing the top side keyway, increasing core diameter by 1 mm and thinning the core in the central part.

3 Results of Numerical Analysis of the Start Relay

Displayed are the results of magnetic current Φ , magnetic current density B in the relay, and the diagram of attractive force F in relation to air slit width x .

Figure 3a shows magnetic current Φ for (a) initial and (b) final version. In Fig. 3a we can see an unwanted spread of magnetic current through the bottom

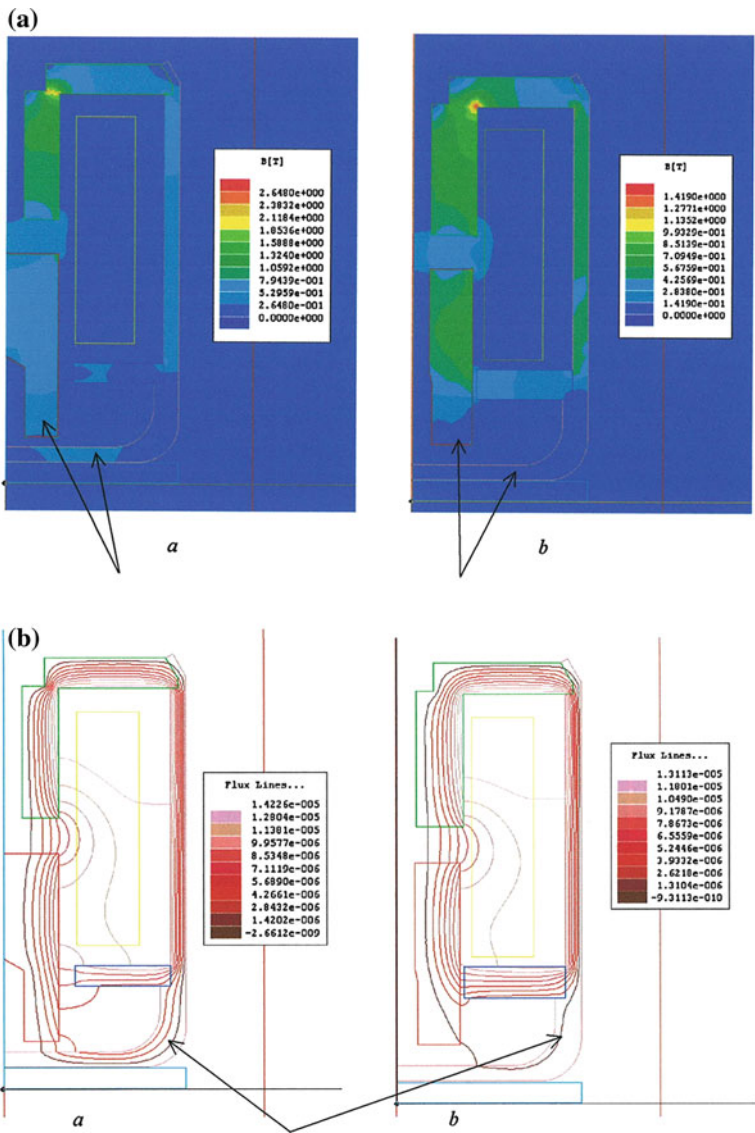


Fig. 3 a Magnetic current Φ in start relay, b Magnetic current density B in start relay

side of the casing. Shown in Fig. 3b at the initial form is additional magnetisation in the bottom side of the casing and the lower part of the core. Figure 4a shows the course of attractive force F in relation to slit width x for both versions of the relay. The diagram indicates that the results of the initial form are up to 50 % worse compared to the final form of the relay.

The magnetic conditions in the relay are also affected by the form of contact surfaces between the core and the top side. Examples of straight contact surface,

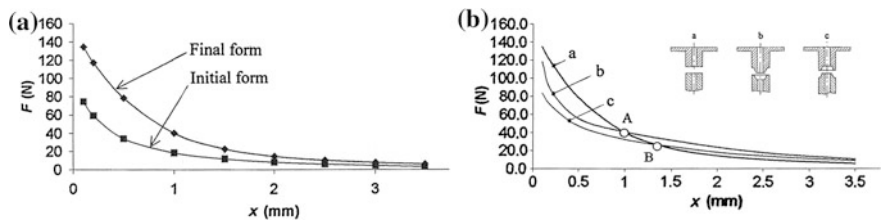
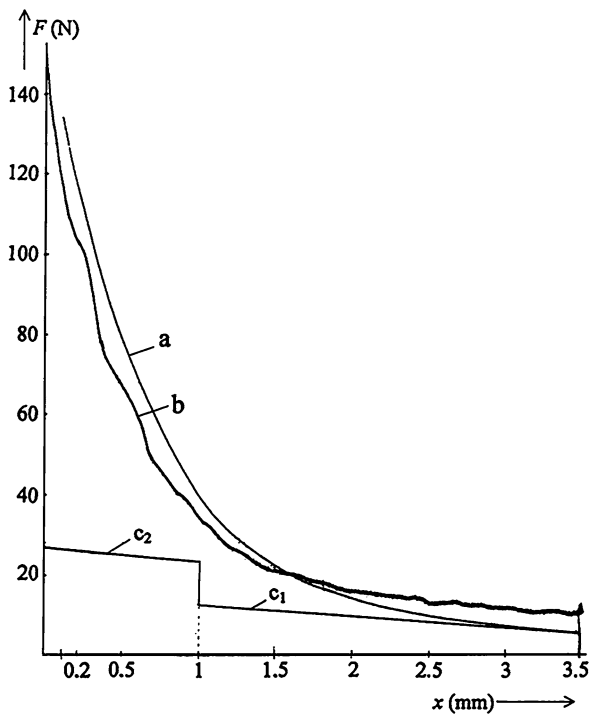


Fig. 4 a F - x diagram, b F - x diagram for different forms of contact surfaces

Fig. 5 Attractive force F in relation to slit width x (a—calculated, b—measured)



conical concave and convex surface were analysed. Figure 4b shows results for attractive force of all three variations.

4 Comparison of Calculated and Measured Attractive Force, Return and Contact Spring

Attractive force F was measured for the optimal chosen and completed form of the start relay. Measurements were performed without a return spring installed. Figure 5 shows measured and calculated force in relation to air slit width x and as it can be seen, the calculated values match the measured ones quite well.

A return spring (10) and a contact spring (11) are installed into the start relay (Fig. 2a). The return spring is tensioned and pressures the core (1) and the mandrel (2) with a certain force. This force ensures that the relay core is separated from the side (6) during inactivity. If the spring is too soft, the core could move in the axial direction in the event of strong shock and in extreme cases the relay would activate. Engine startup during its operation could occur, which could cause breaking of cogs on the pinion or the engine sprocket. Neither can the spring be too hard, because then the magnetic attractive force would be too weak, the core would not move, and contacts would not connect. The contact spring is installed between the mandrel (2) and the contact plate (7). This spring is tensioned with a certain force. When the core (1) contacts the side (6), the contact spring compresses even further. The return and contact springs of correct dimensions that are tensioned correctly must ensure a force smaller than the magnetic attractive force [4, 6]. The characteristics of properly chosen springs are displayed in Fig. 5, where line c_1 illustrates the force in the return spring and line c_2 the collective force of return and contact springs.

5 Conclusion

The article shows an example of picking the optimal dimensions of start relay components. Key factors are the size of attractive force and properly chosen return spring and contact spring. The attractive force is affected by magnetic current and magnetic field density, which are dependent on winding in the coil and the size of relay parts. Many numerical calculations had to be performed for different relay configurations to reach the final, most favourable construction of the relay. The performed tests have shown good matching between measured and calculated values of attractive force.

References

1. Frane, J.T.: Magnetic Starter. Craftsman Book Company, California (1994)
2. Furlani, E.P.: Permanent magnet and Electromechanical Devices: Material, Analyses and Applications. A P (2001)
3. Smeaton, R.W., Ubert William, H.: Switchgear and Control Handbook. Mc Graw Hill, New York (1998)
4. Decker/Kabus: Maschienen-elemente. Funktion, Gestaltung und Berechnung. 15.Aufl., Hanser (2006)
5. Kenda, M., Zajc, B.: Elektrotehnika. TZS, Ljubljana (1995)
6. Bratuš, T.: Diplomsko delo. FS, Ljubljana (2003)

Construction for High Pressure Application on 3D Nanofibers

L. Ševčík and D. Vejrych

Abstract This article discusses the construction of new facilities, which is based on influencing the final structure of the nanofibers. The device operates with high pressure on the arrangement of fibers in the process of spinning wire electrode. Testing was made for polyamide (PA6) and polycaprolacton (PCL) at a concentration of 12 %. The device is designed for lab NS 500 with the highest value of high voltage to 75 kV. The flow of gaseous medium is verified by measurements together with simulations, which confirms the theory of constant output pressure without turbolency. The following is a description of facilities with photographs and records of tests of strength and permeability of the new 3D material. The resulting structure is composed of open spaces with dimensions from 10 to 30 nm.

Keywords Nanofibers · Construction · High voltage · Permeability · Atmospheric pressure

1 Introduction

Today's technological procedures in nanotechnology production must be constantly evolve. Due to requirements for new structures of materials, arise construction for adjusting nanofiber structures. Based on the demand for nanofibers with greater porosity was constructed facilities which transporting gas into the

L. Ševčík (✉) · D. Vejrych
Technická univerzita v Liberci, Liberec, Czech republic
e-mail: ladislav.sevcik@tul.cz

D. Vejrych
e-mail: david.vejrych@tul.cz

Fig. 1 Real box in nanospider

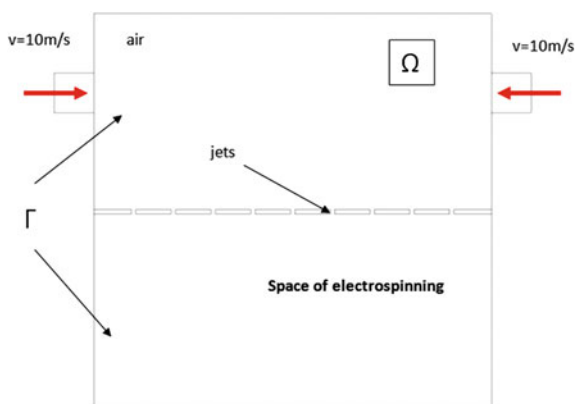
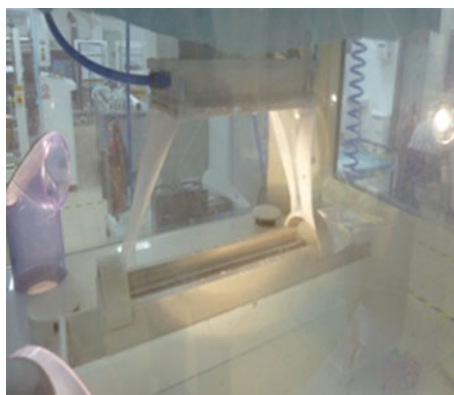


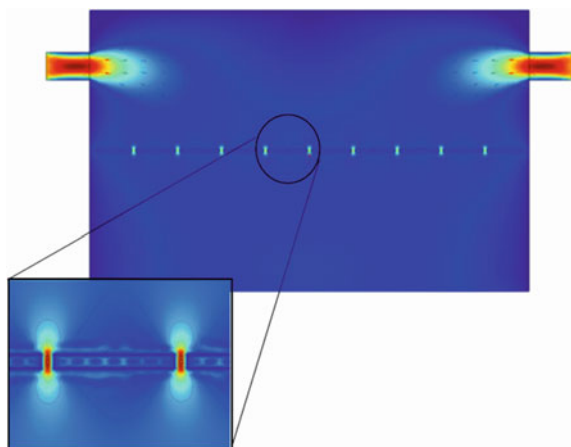
Fig. 2 The simulation box (100 × 100 × 100 mm)



space of electro-spinning. Equipment must withstand aggressive environments acids, high voltage and its control is always provided outside Nano-lab space.

2 Theory

For correct function of nanospider is necessary to keep a safe distance at the basic construction for safety, depending on the intensity of electric field and at the same prescribed distance between the electrodes. High voltage range is from 60 to 85 kV. Surface directional nozzle operates simultaneously as an electrode nanospider that uses high pressure gas creates a space between the nanostructure. The resulting product creates spaces between the fibers of the value of 5–30 nm. Features new materials were measured at the measuring device METEFEM permeability values. Together with permeability was material tested for analyzer of resilience.

Fig. 3 PA6 with SF6 995

3 Experiment

Custom testing equipment was carried out on the NS-LAB 500, which is fitted with an output of 85 kV transformer. This device includes a wire electrode with a speed of 5/min. Type of polymers: Polyamid 6 12 % and Polycaprolacton 12 %. Polymer solution at a concentration of 12 % has been spinning for 10 and 5 min without added gas samples for PA6 and PCL. These samples are named as the base. The second test is divided into 4 categories of pressure derived from the atmospheric pressure, which was measured 978 hPa. Increasing the pressure acting was done after each of these values 980–995 hPa using of the reducing valve SMC. Fine increases of pressure is applied due to determine characteristics of surface directional jets. The air was used from pressure distribution of company without special additives. The same procedure is applied to SF6 gas about the values 980–995 hPa. A total of 20 samples drawn for testing: 4 samples of basic material without blowing 10 and 5 min, 8 samples with air pressures 980–995 hPa 5 min, 8 samples with SF6 and pressure 980–995 hPa 5 min.

3.1 Measurement of Permeability of Samples

Drawn samples were subjected to permeability measurements on the device type Metefem FF-12/A. The device can be seen in Fig. 1. The test is measuring the amount of intake air rotameter, tube in a well-defined diameter, which is located in the float. According to the heights of floater in a tube the amount of air flowing in Pascal, which passes between the opposing surfaces of articles related to time-tested and standardized in the area measured pressure drop to be 196 Pa (20 mm H₂O) in the jaw area of 1 cm². The jaw is circular in shape, in which the sample is clamped nanowires, through which the intake air flow of rotameter.

Fig. 4 The resulting progression

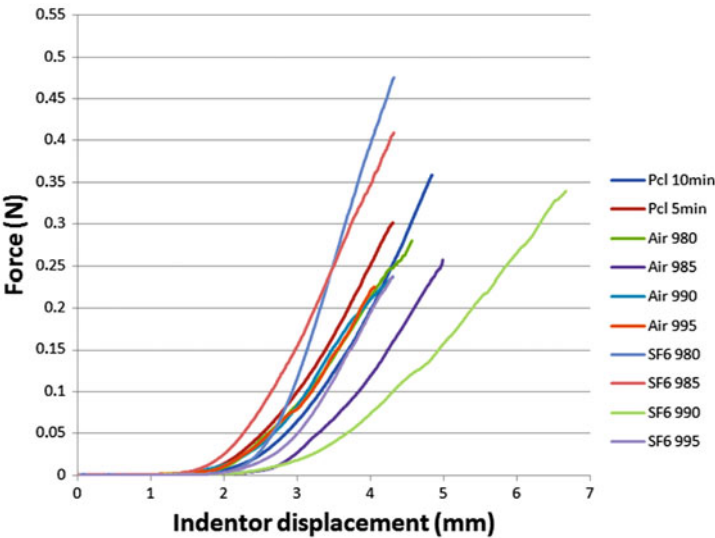
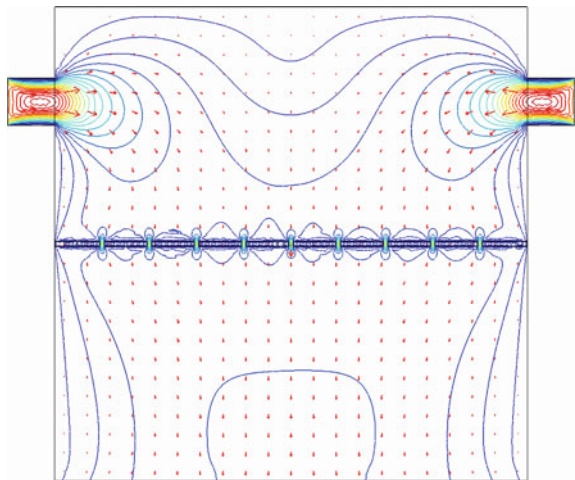


Fig. 5 The vector progression

3.2 Measurement of Mechanical Properties

Measurements were performed on the device LABTEST 4050 in combination with the force sensor 5 N and indenter diameter of 5 mm. Punch is provided with a flat end, his speed was 150 mm/min which was recorded in a data series with the active force. Based on evaluation of samples is apparent increased strength of samples with SF6 gas, which because of its physical properties of the dielectric directly influences the efficiency of the process of spinning Fig. 2.

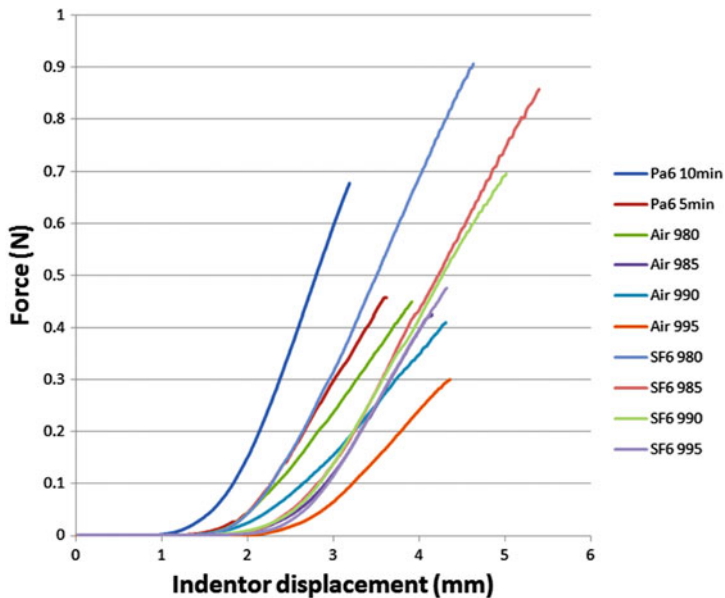


Fig. 6 PCL with SF6 995

4 Simulation of Flow in a Linear Directional Nozzle

4.1 Mathematics and Physical Description of the Simulation

Fluid flow (gas/liquid) in a general anisotropic media can be described with non-linear Navier-Stokes Eq. (2) [1].

$$\frac{\partial u_i}{\partial t} + (\mathbf{u}, \nabla) u_i = -\rho^{-1} \frac{\partial p}{\partial x_i} + \nu \Delta u_i + f_i \quad (1)$$

$$\text{div } \mathbf{u} = 0 \quad (2)$$

Equation (1) primarily involves the fundamental principle of inertia and external balance, i.e the volume and surface forces (used Einstein's summation convention), which can be expressed as integral for deformable region $\Omega(t)$.

$$\int_{\Omega(t)} \rho \frac{d\mathbf{u}}{dt} dV = \int_{\Omega(t)} \rho \mathbf{a} dV + \int_{\partial\Omega(t)} n_j \tau_{ji} ds \quad (3)$$

Equation (3) expresses the argument in a local coordinate system with the onset of naturally situated in the center of the considered area (volume of element).

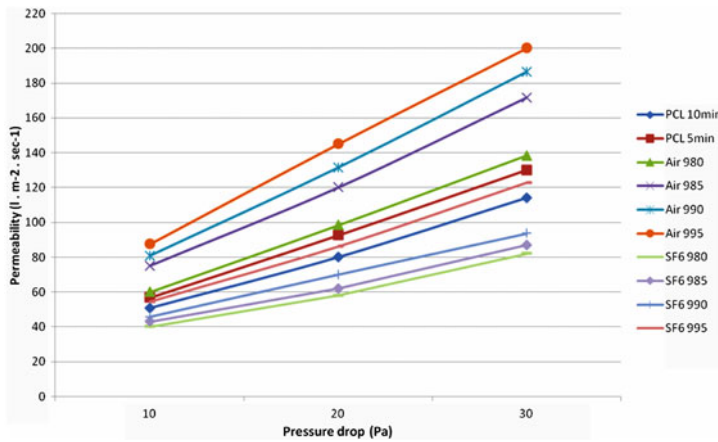


Fig. 7 Increased strength of samples PCL

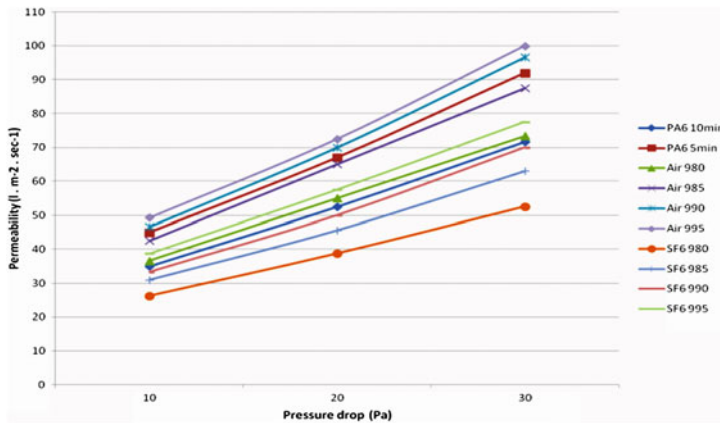


Fig. 8 Increased strength of samples PA6

$$\frac{d}{dt} \int_{\Omega(t)} \alpha dV = \int_{\Omega(t)} \left(\frac{\partial \alpha}{\partial t} + \text{div}(\alpha \mathbf{u}) \right) dV \quad (4)$$

Initial formulation gives rise to that Eq. (4) expresses the difference considered integral state area (volume element) and α variables over time $t + \delta t$ a t which is related to time step of infinitesimal δt .

Fig. 9 PCL with AIR 995

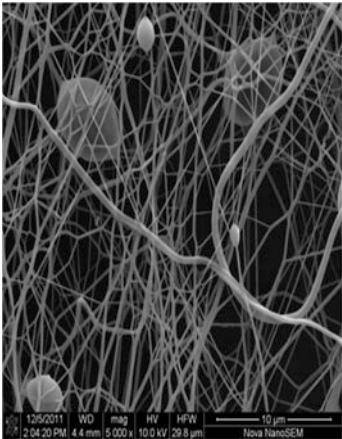


Fig. 10 PA6 with AIR 995

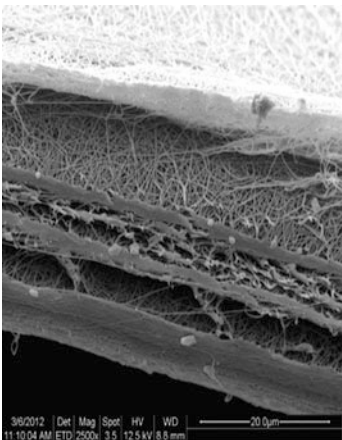


Fig. 11 PCL normal 5 min

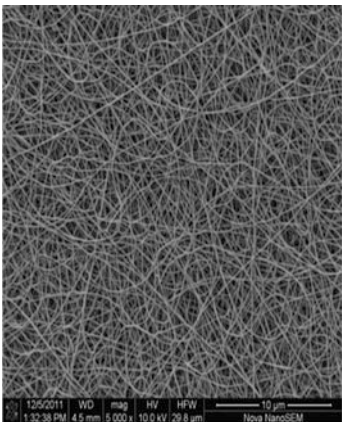
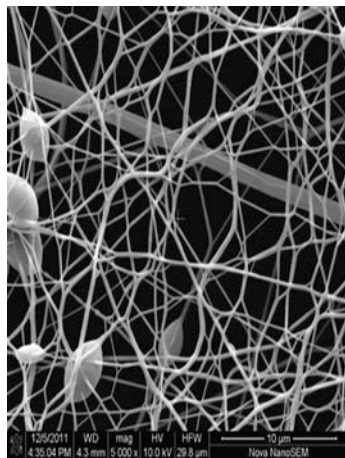
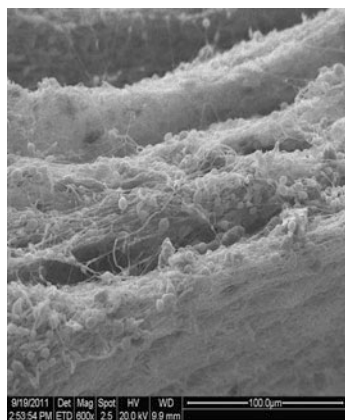
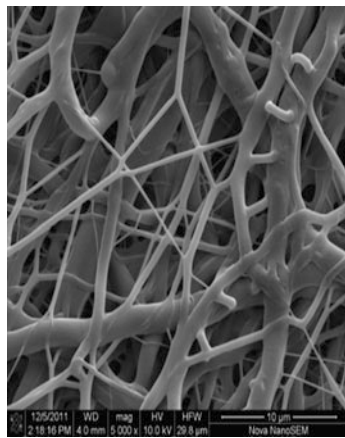


Fig. 12 PA6 normal 5 min**Fig. 13** Test of permeability
PCL**Fig. 14** Test of permeability
PA6

$$\frac{d}{dt} \int_{\Omega(t)} \alpha dV = \lim_{\delta t \rightarrow 0} \left[\frac{1}{\delta t} \left(\int_{\Omega(t+\delta t)} \alpha(t+\delta t) dV - \int_{\Omega(t)} \alpha(t) dV \right) \right] \quad (5)$$

After crediting the member representing the area integral in the time variable α at time $t + \delta t$ at the positive and negative sense, it is available form:

$$\begin{aligned} \frac{d}{dt} \int_{\Omega(t)} \alpha dV = & \lim_{\delta t \rightarrow 0} \left[\frac{1}{\delta t} \left(\int_{\Omega(t+\delta t)} \alpha(t+\delta t) dV - \int_{\Omega(t)} \alpha(t+\delta t) dV \right) \right. \\ & \left. + \frac{1}{\delta t} \left(\int_{\Omega(t)} \alpha(t+\delta t) dV - \int_{\Omega(t)} \alpha(t) dV \right) \right] \quad (6) \end{aligned}$$

5 FEM Simulation

For optimal flow extending from the linear nozzle that is new design model i.e. velocity flowing were developed in the COMSOL Multiphysics FEM simulations. This program allows you to simulate very complex physical phenomena e.g. study and compare deformation of nonlinear material structures in the electrostatic field, where deformation causes bring flow of inert gas. The basic FEM model represent basic linear flow from the nozzle into the space nanolab. The side inputs are connected to an external compressed air to linear of nozzle, which is constantly pressurized. The lower part of the construction is provided with a set of nozzles, which are involved in the transformation of nanolayers (Figs. 3). Model jets and the space is divided into FEM computational grid (axisymetrické cubic elements), which is adapted to the complexity of the calculations. The resulting process flow with respect to the input pressure, output and size of inlets is shown in detail (Fig. 4) that shows the exact direction of the applied force in the area of the nozzle shown in more detail vector field (Fig. 5).

6 Results

Samples drawn measured on equipment LABTEST 4050 are recorded in the graph of force and displacement, which recorded the strength of each sample to rupture. This measurement pointed to the increased strength of samples when using SF₆ gas, which is known as dielectric and therefore strongly influenced by the strength

of the electrical space of the nanolab. This effect can be seen to increase the efficiency of both the spinning material PA6 and PCL (Figs. 6 and 3) confirmed the increased strength in the resulting graphs (Figs. 7 and 8). At the same time it is possible to observe a decrease in strength when using compressed air with improve of material properties in the form of free spaces in the blown structure, where are produce the desired spaces 10-30 nm (Figs. 9 and 10). To compare changes in the structure is assigned file of no-blowing structure without the use of gas (Figs. 11 and 12). The same samples were subjected to measurement of permeability depending on the surface of the water column to show the effect of air blowing on the permeability of the material and the intensity of cross-linking using SF6 (Figs. 13 and 14).

7 Conclusions

Planar directional jet structure clearly affects the resulting nanofibers using compressed gas. These properties have been demonstrated in experimental samples by measuring permeability and stress analysis. The new material is suitable for application of the basic cell size of less than 30 nm from the use of biodegradable polymer as the building structure. When using SF6 gas is to increase process efficiency and strength of nanomaterials.

Acknowledgments The article originated with the subvention MPO 13/2011/FR-TII/451.

Reference

1. Teman, R.: Navier-Stokes Equations: Theory and Numerical Analysis ISBN 978-0821827376 Am. Math. Soc., 340–345 (2001)

Part VI
Optimization of Mechanisms
and Machines, The Mechanisms
of Textile Machines

Dynamic Properties of Traversing Rod

P. Žabka, J. Valtera and J. Beran

Abstract The paper deals with an analysis of traversing rod dynamic properties. The traversing rod is a part of winding mechanisms on rotor spinning machines, and transmits periodical linear traversing motion from motor to yarn guides. The rod is specific by its very thin and long shape where the ratio between length and diameter reaches almost 4,000:1. Due to a demanding exciting motion it is subject of high dynamic load resulting in mainly longitudinal vibrations. In order to better understand the behaviour of the system, several measurements of material and dynamic properties of the rod were carried out. Moreover a mathematical model of the rod was created and loaded by the requested motion. The performed analysis disclosed new information about the dynamic behaviour of the rod. However, the results confirmed the assumptions that the rod poses limiting factor in reaching high speeds.

Keywords Traversing rod · Winding · Rotor spinning · Vibration

1 Introduction

The aim of research is to analyse a traversing rod and its behaviour under dynamic load. The traversing rod is a common part of traversing mechanisms on rotor spinning machines, which ensure rectilinear reversible traversing of yarn and

P. Žabka · J. Valtera (✉) · J. Beran
Technical University of Liberec, Liberec, Czech Republic
e-mail: jan.valtera@tul.cz

J. Beran
e-mail: jaroslav.beran@tul.cz

together with bobbin rotation produce cross-wound bobbins. It is common to use only one motor on one side of the machine and therefore the traversing rod is used to transmit the requested motion from motor to yarn guides.

The rotor spinning is together with ring spinning one of leader technologies in the yarn production. The speed of traversing mechanism poses one of the limiting factors in the production productivity. Therefore, several new structural designs were projected [1].

The traversing rod reaches almost 50 m—the same length as the machine itself. For practical reasons it is composed from sections that are joined together. Due to a high dynamic load it can not be made of heavy steel. Instead a combination of duralumin and carbon composite materials is used. The assembly is designed in a way that the difference between thermal expansion of the rod and the machine is minimal.

1.1 Requested Motion

In order to obtain a quality bobbin, the guide should follow the demanded motion as close as possible. The requested motion consists of sections with uniform linear motion that are reversed near dead centres. Graphs of basic kinematic courses: stroke, velocity and acceleration relative to the virtual cam rotation are shown in Fig. 1. The fourth graph displays the spectrum of acceleration. On the basis of the graph it can be noted that frequencies higher than thirteen times the basic excitation frequency are negligible. Provided that the maximum basic frequency is 5 Hz, the maximal important exciting frequency is about 65 Hz.

2 Mathematical Models

Two mathematical models were assembled so as to predict the system behaviour. First in MSC Adams utilizes discrete flexible link [2]. The second model was assembled in Matlab [3]. Thanks to the thin shape the rod could be treated as one dimensional object. Both mathematical models use discretisation of the rod as it is schematically displayed in Fig. 2.

In order to be able to build the mathematical models, mechanical properties of the rod was measured, namely mass, Young's modulus and damping [4, 5]. Especially the measurement of dumping poses complex task and the results are obtained with high uncertainty.

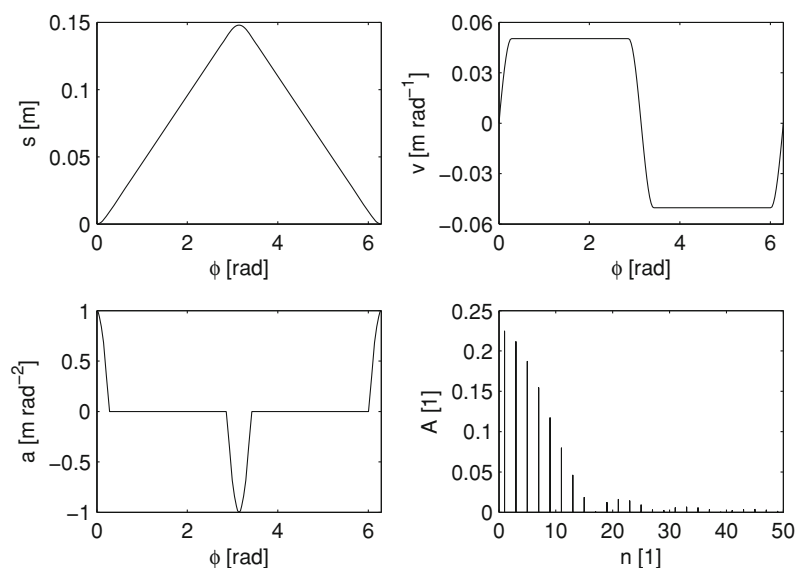


Fig. 1 Graphs of kinematic properties of requested motion

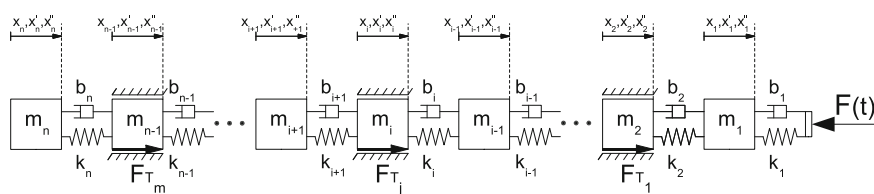


Fig. 2 Structure of the mathematical models of the traversing rod

3 Measurement

Measurement of the rod behaviour was performed for 20 section and 10 section assembly under working conditions. It was measured position, acceleration and force in selected places along the rod for several speeds expressed in double-strokes per minute (dspm). Figure 3 shows maximum force in dependence on the speed. Unsurprisingly the force rises with higher speed while the force in the longer rod is approximately two times the force in the shorter one. A remarkable phenomenon is the existence of local peaks marked with circles. These local increases in force were noticeably accompanied with increased noise especially at high speeds [6].

The reason for this behaviour could be disclosed if we have a closer look on the course of kinematic quantities, for example velocity. In the Fig. 4 it is shown the measured velocity at speed 230 dspm—the speed when the increased noise appears. The areas with constant requested speed include noticeable additional

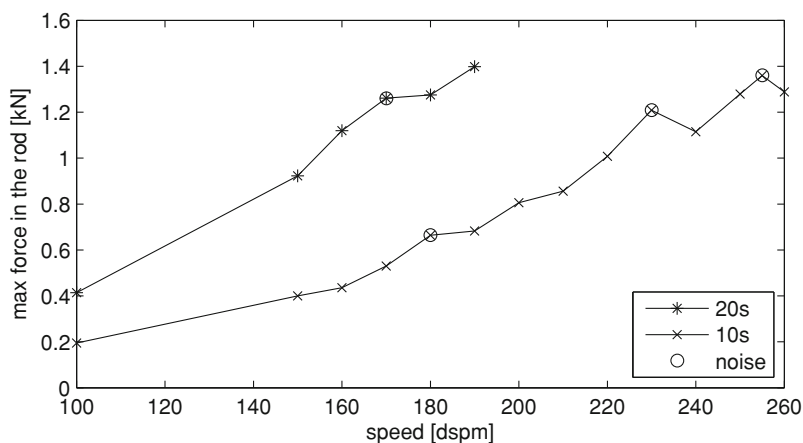


Fig. 3 Maximum force versus speed

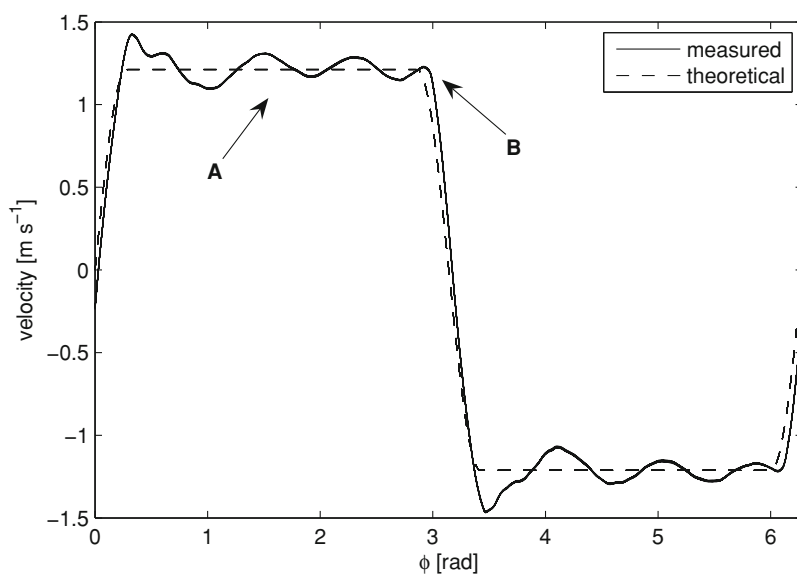


Fig. 4 Course of velocity at speed 230 dspm

vibration (A) caused by the jerk from the reversion of motion. This additional vibration is present at other speeds as well; however, at the critical speed the beginning of reversion meets an anti-phase of vibration (B). So with increasing speed at this moment the additional vibration changes from four periods to three periods shape.

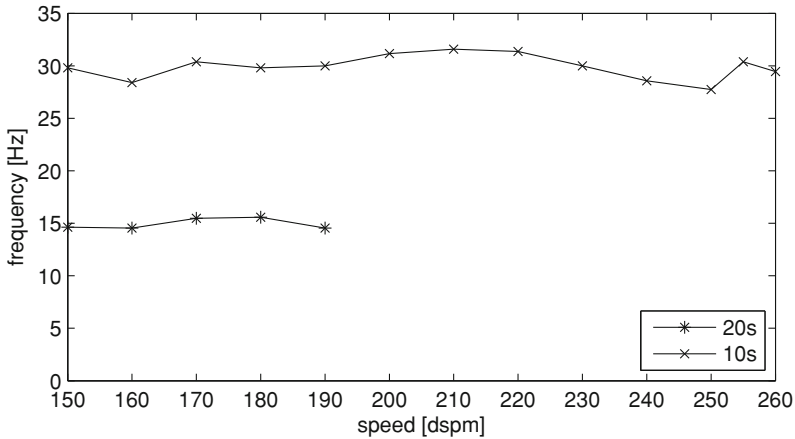


Fig. 5 Frequency of additional vibration versus speed

3.1 Additional Vibration

The next step was determination of the frequency and source of the additional vibration. In order to enumerate the period of the vibration it was employed the autocorrelation of selected areas and the results was manually checked by comparison of measured curve with harmonic curve. Even though the method achieved a good match, the error could reach several per cent because of short analysed areas available.

The results of the analysis are shown in Fig. 5. It discloses that the frequency of additional vibration is independent on the speed, and the frequency of the long rod is two times the frequency of the shorter rod. If we compare this frequency with the natural frequency of the rod, the results show us that the additional frequency is actually a bit smaller than the natural frequency of the rod with one free end. This is probably caused by the servomotor that is not absolutely rigid.

4 Conclusion

The experimental measurement disclosed that the traversing rod is exposed to significant additional vibrations. It is highly probable that this vibration corresponds to the first natural frequency of the whole system of the rod and driving mechanism. At some speed the additional vibration gets into an anti-phase with the exciting motion and causes locally increased load and noise.

The experiment confirmed that the usage of very long traversing rod at high speeds results in problems. The rod is clearly a limiting factor in the effort to

increase the overall productivity of rotor spinning machines. Therefore, the future research should be focused mainly on systems without the traversing rod.

Acknowledgments The research work reported here was made possible by the project for promotion of Specific University Research by Czech Ministry of Education.

References

1. Beran, J., Valtera, J., Žabka, P.: New trends in yarn distribution systems on spinning machines. *Structural Mechanics of Textile Fabrics (STRUTEX 2008)*, pp. 579 (2008)
2. Valtera, J., Beran, J.: Mathematical model of the long traversing rod with a discrete flexible link utilization. In: *Proceedings of Transfer 2011*, pp. 26 (2011)
3. Žabka, P., Beran, J.: Mathematical model of the yarn traversing mechatronic system. *Structural Mechanics of Textile Fabrics (STRUTEX 2009)*, pp. 125 (2009)
4. Valtera, J., Beran, J.: Analysis of vibration of the traversing rod on the rotor spinning machine. In: *1st International Summer School on Mechatronic Systems: Transfer of Innovation to the Interdisciplinary Teaching of Mechatronics for the Advanced Technology Needs*, Wisla Poland, pp. 389 (2009)
5. Beran, J., Valtera, J.: Dynamics analysis of the distribution rod on the rotor spinning Machine. In: *The XIII-th Romanian Textile and Leather Conference (CORTEP)*, pp. 367 (2007)
6. Žabka, P., Valtera, J., Procházka, V.: Výzkumná zpráva z měření provozních veličin klikového rozváděcího systému rotorového doprácího stroje, Výzkumné centrum Textil II (2011)

Flexible Elements in the Mechanisms of Weaving Machines

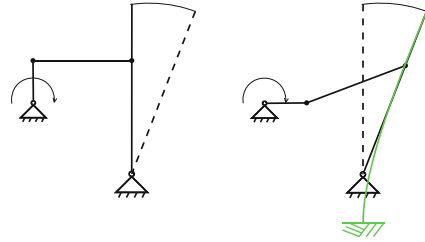
J. Žák

Abstract Weaving machines use several mechanisms to produce a fabric; their relative (mutual) position is exactly defined at any point of working cycle and must be maintained as accurately as possible. From that, it results some requirements on their design, such as stiffness of the joint frame, synchronization of their drives, accuracy and stiffness of particular links of those mechanisms and minimization of the clearances between them. In this paper, we have attempted to outline the possibility of replacing the binary links by using the flexible mechanism elements. In this step, we always removed one rotary constraint at least which is necessary when using a binary link, i.e., a rod, pitman or connecting rod. In practice, it means reducing the number of bearings which have a limited service life, require maintenance and when using them we cannot avoid the formation of clearances. In the case of a slay of the CAMEL weaving machine, it was furthermore possible to use the deformation energy to a relief of the drive, its better regulation and an overall reduction of energy consumption. Although this procedure is not subject to the use of special materials, there can be advantageously used fiber composites whose certain features make the design of such mechanisms easy to a great extent.

Keywords Weaving machines • Mechanisms • Composite materials • Energy saving

J. Žák (✉)
VÚTS a.s., Liberec, Czech Republic
e-mail: josef.zak@vuts.cz

Fig. 1 Flexible element—a beam—replacing an articulated arm in a four-bar mechanism



1 Functional Description of Weaving Machine

Weaving machines use several mechanisms to produce fabrics: a slay for beating-up the inserted weft, a shedding motion for creating a space for this picking between the warp threads (creating a shed), a proper mechanism for weft insertion and other mechanisms, such as scissors (cutter), waste removal, weft repairing, etc. Some of these devices can be implemented using the “massless” means, such as air picking or weft repairing, in most cases, however, there are classical mechanisms, consisting of several links. The functional links of those mechanisms, i.e., those which are in direct contact with the woven yarn, warp or weft yarn, must follow the desired trajectory as closely as possible and moreover, they must be synchronized with each other. The particular links of those mechanisms are connected mutually by rotary or sliding structure (constraint), commonly designed as a rolling or sliding bearing or as a link roller—cam. These mechanisms perform periodic motion, generally spatial, but usually only planar. The relative position of individual members and their position against the frame change during the cycle, i.e., from the full rotation to a relatively—to the dimensions of the mechanism—small shift or rotation. Two major problems result from the above mentioned:

The individual links must meet the requirements on stiffness and strength in such a way so that the fabric quality is attained or so that no collision between two mechanisms occurs in the extreme case.

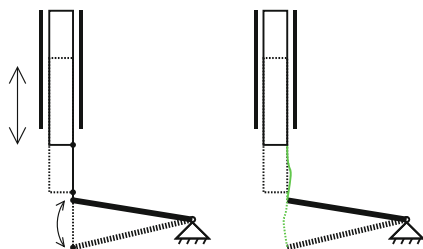
The connections between the particular mechanism links are the source of complications; they require maintenance such as lubrication and adjustment and simultaneously clearance, which influences the operation as a whole, arises in them.

2 The Principle of Mechanism Flexible Links

The principle of using a flexible link can be easily illustrated on an example of a four-bar mechanism (Fig. 1) [1].

In this case, one rotational constraint is removed (typically a rolling bearing) while maintaining the sufficient accuracy of the trajectory of a functional element.

Fig. 2 Use of a flexible link in the leno shedding mechanism of the loom BETA



The disadvantage is an increased load of the drive and the whole mechanism with internal forces. Thus, it is obvious that the use of flexible link must be adequately justified by eliminating the problematic constraint or, as we shall see further, just by using the stiffness of the flexible link to “save” elastic energy in a certain part of the operating cycle.

3 Flexible Links on VÚTS’s Weaving Machines

3.1 BETA Weaving Machine

On the BETA air-jet weaving machine, a flexible link appeared in the shed motion for leno weave. It took the form of a steel foil; its low bending stiffness replaced two rotational bearings at once whereas high stiffness in its plane then provided the sufficient lateral guiding of a shed forming beam (Fig. 2).

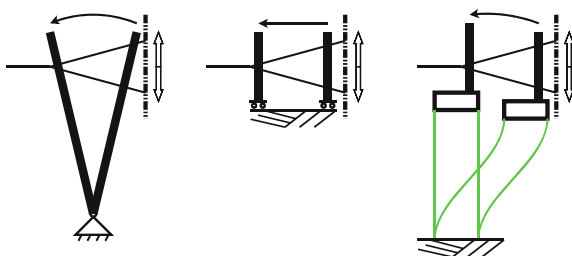
With this machine, we have not used the finite (and controllable) stiffness of the elements for influencing the operation of the mechanism in any way; we were focused primarily on simplifying and lightening the harness (frame) design.

3.2 CAMEL Weaving Machine

At this weaving machine, we used the flexible links of the mechanism in two units. In both cases, in addition to simplifying the design, we succeeded in using the compliance of the element to improve the machine running. It is the flexible slay and the needle bar guiding. The slay is part of every weaving machine of a “classic” conception, the needle bar is specific for healdless weaving of leno fabric.

The slay performs swinging or sliding motion, or a combination of both, with the frequency of machine running, as the case may be. Thus, it is loaded with dynamic forces and the forces from the fabric forming, of course. It must be sufficiently rigid and its structure is also limited with built-in relations with other units. The displacement law must allow a safe insertion of the weft for the applied type of picking and the given weaving width. The Fig. 3 gives an idea on the different possible slay versions including the CAMEL slay.

Fig. 3 Various types of slay with the CAMEL slay furthestmost at right



It is clear that by using the flexible links with the CAMEL slay, it was succeeded in eliminating several roller bearings at once. Should be required the lifetime of weaving machine in the order of 10^9 cycles, in the event of such bearings, it would be necessary either to dimension those bearings adequately or to proceed to their regular replacement. Moreover, with the CAMEL loom slay we also succeeded in achieving savings of energy needed for the slay drive by a suitable choice of the stiffness of the slay springs. During the working cycle, this is to say, a fluctuation of the driving motor speed occurs. This phenomenon, which is basically unwanted with the loom of a conventional conception, was modified by contrast with the help of a slay flexible bearing in such a way so that it could help in itself to create a displacement law. In practice, it means that in the picking position, where the slay should remain a relatively longer time for the reasons of the time reserve as long as possible for inserting the weft, the springs are deformed and thus they accumulate a substantial part of the energy of the whole mechanism. In contrast, when moving into the beat-up position, these springs are straightening and elastic energy changes into kinetic energy, needed for beating-up the weft to the fabric front. This solution obviously has its disadvantages: the weaving machine works only in a certain range of speeds optimally, at lower speeds, there is an increase of drive load from the deformation of the springs not compensated by inertia effects, the enhanced demands are placed on the life service of the material of the springs, the size of the slay stroke is limited by the strength of the springs.

The second unit where flexible elements in the mechanism were applied in the CAMEL loom is the needle bar. It's part of the shed motion which creates the lateral (transversal) motion of one warp branch in the leno weave. It works with the half frequency of the machine and its stroke is given by the pitch of one pair of warp threads, typically in the range from 1 up to 5 mm (Fig. 4).

In this case, by means of applying the flexible links, we avoided using the linear guiding or alternatively a multiple parallelogram. The path of the needle bar can be considered as a straight line due to the sufficiently large ratio between the spring length and the required lift (stroke) (here, approximately 50:1). Also here, we used the above described phenomenon using the accumulation of elastic energy in the extreme positions by means of the selected stiffness of the springs.

Fig. 4 Schema of the needle bar lateral motion

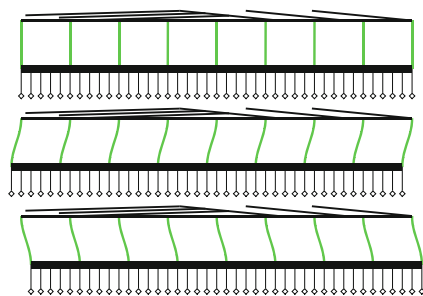
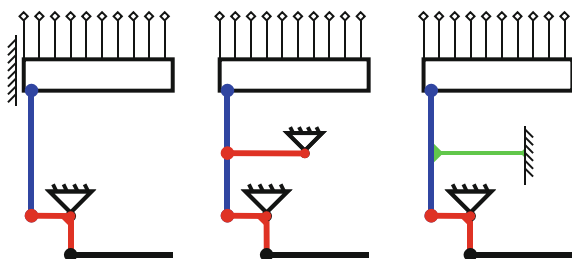


Fig. 5 The guiding of the heald shafts of various types



3.3 The Guiding of the Heald Shafts on the CAMEL2 Weaving Machine

At present, the development of a new version of the CAMEL weaving machine is under way, using a harness shed motion with its own drive. With regard to the specifics of weaving leno fabrics it is necessary to investigate the guiding of the heald rod in a different way. After experience with sliding lateral support (left on Fig. 5), we tried to solve this problem using the so-called direct linkage (middle on Fig. 5).

When the ratio of the upper and lower horizontal arm is 2:1, the motion of the upper end of the vertical rod will be in a certain range of strokes very close to a straight line. A similar solution has already appeared on the VÚTS loom, namely as a heald shaft lateral support on the BETA machine. By applying the direct linkage we indeed avoid the lateral guiding which causes problems especially when weaving aggressive materials such as glass, but on the other hand, it is necessary to use two rotation bearings more. With the CAMEL2 loom, we tried to replace the upper horizontal arm by using a flexible link (right on Fig. 5). In practice, it will be probably possible to produce a vertical drawing rod and this horizontal arm as one piece, without having to deal with their connecting. Also here, it is possible to use elastic energy to lighten the BPZ drive, although not to such extent as in the above given applications.

4 The Use of Composite Materials for the Flexible Links of the Mechanism

As already mentioned, it is commonly calculated with a life service of 10^9 cycles with weaving machines. A priori, there is not necessary to count with the use of sophisticated technologies and materials, in some cases, however, they cannot be avoided. From the above mentioned examples we applied composites in the manufacture of the slay for the CAMEL weaving machine. Here, we were forced to reduce the length of the springs with regard to the built-in spaces and a too large deformation resulted for the application of even very high-quality spring steel. If heald shaft guiding by means of direct linkage with flexible link is used on the CAMEL2 loom, we assume to use composites also here.

5 Conclusions

Flexible links in the mechanisms of weaving machines are one of the possible ways to increase the efficiency of weaving as textile technology. The specifics of the weaving process determine the shape of particular devices; the periodicity of binding and the dimensions of the binding point determine the character of the displacement laws of mechanisms involved in their creation. All functional links then perform periodic reciprocating motion, with greater or lesser amplitude. In pneumatic and hydraulic looms, there is no mechanism with the largest stroke that is weft insertion. The stroke size of other mechanisms is smaller by an order then. By applying flexible links, we will remove roller or sliding bearings which are a source of problems. This is particularly effective in the cases where the positive qualities of such bearings are not fully exploited; for example, roller bearings allow full rotational movement, but the desired range of motion is in several degrees (which in itself is not favorable for the operation of roller bearings). Similarly, sliding bearings are prone to increased wear and generation of clearances even with a minimum mutual stroke of components. In those cases, it is worth considering the use of a deformation link in the mechanism.

Acknowledgments The presented work is due to the whole team of VÚTS Tkalcovny department under the leadership of Mr.Dvořák.

Reference

1. Karel, P., Dvořák, J., Leinhaupel, R., Žák, J.: A weaving machine and a batten of the weaving machine. European Patent EP20040762314 20041007

Part VII
Mechatronics, Control and Monitoring
Systems of Machines

New Conception of Waving Machine CamEl Drive

A. Bílkovský, O. Marek, P. Jirásko and Z. Volanský

Abstract New mechatronic conception of waving machine CamEl drive is realized by two electronic cams Yaskawa and planetary gears. The first servo motor is used to slay and shedding motion in position mode and the second servo motor is used in automatic weaving mode. Moment of inertia of kinematic chain was reduced that it was possible used a smaller servo motor of electronic cam Yaskawa.

Keywords Electronic cam • Servo drive • Waving machine

1 Introduction

The waving machine CamEl is a complex machine with several servomotors. These servomotors mostly represent the electronic cams. The most critical is the main servo drive which is supposed to ensure the major movement of the machine. The major movement consists of slay motion and shedding motion. The reciprocating motion is ensured by the crank mechanism. The mechanism uses the accumulation of energy using the flexible link between the slay and the frame. The flexible link works like a spring and helps the reversing of the slay at the dead center position. The springs accumulate the energy during the deceleration of the slay and release the energy during the accelerating. The kinematic schema of the

A. Bílkovský (✉) • O. Marek • P. Jirásko • Z. Volanský
VÚTS a.s., Liberec, Czech Republic
e-mail: ales.bilkovsky@vuts.cz

O. Marek
e-mail: Ondrej.marek@vuts.cz

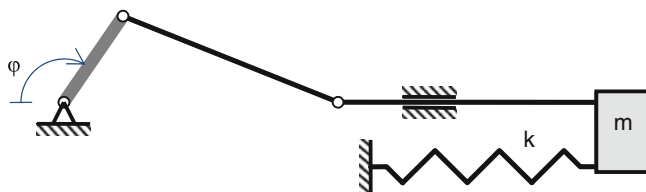


Fig. 1 The kinematic schema of chain between the servomotor and moving slay

chain between the servomotor and the moving elements is in Fig. 1. The gear ratios of the belt drives equal one.

The required driving torque M_{Hel} of the existing servomotor (the existing conception) is displayed in Fig. 2. The parameters are: speed 600 rpm, picking angle 210° , moment of inertia of the mechanism reduced to the servomotor shaft 0.026851 kgm^2 , inertia of the servomotor rotor 0.009048 kgm^2 , the cycloid displacement law is used. The maximum value of the required torque M_{Hel} is 55.5 Nm and effective torque (EKM) is 36.38 Nm. Minimum and maximum values of the servomotor speed are 150/1,050 rpm. Based on these values the catalogue list has to be checked. If the dynamic load causes the effective value of the required torque is higher than the catalogue value the servomotor will be overheated. The existing solution requires 8 kW servomotor.

2 New Conception of the Main Drive

The new prototype of the control system with servomotors Yaskawa was built. The test waving machine is in Fig. 3

New conception is characterized by:

1. The drive is considered in two modes, low speed mode and waving mode. Each mode has different requirements for the servo drive. The low-speed mode requires high values of torque because in the low dynamics the accumulation of the energy is not effective and the servo drive forces against strong springs. The waving mode requires the minimal inertia of the rotor and the minimal power because of the energy consumption. Each mode is driven by different motor. The control system ensures their collaboration by changing the position of the drive shaft with a spline. This shaft switches the motors by changing its position. In the low-speed mode there are two options of collaboration. First, the helping motor (SGMGV-09D, 0.85 kW) works in the torque mode and adds torque to the main servomotor. These servomotors are coupled and work together. Second, the helping motor works alone in the position mode. There are low speed requirements in the low speed mode therefore the gearbox can be used. The beginning of the waving is complicated and the right collaboration has to work. The first half-turn of the machine uses the low speed mode to get

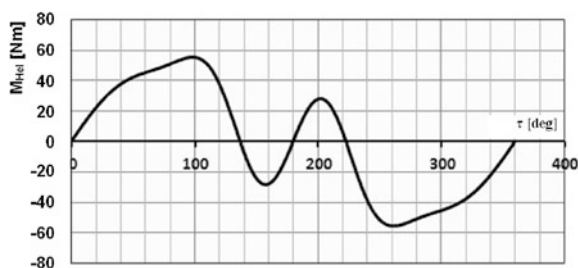


Fig. 2 Driving torque of the electronic cam applied to the main drive

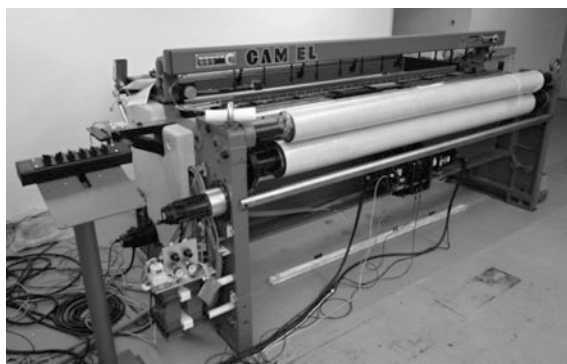


Fig. 3 The testing waving machine Camel

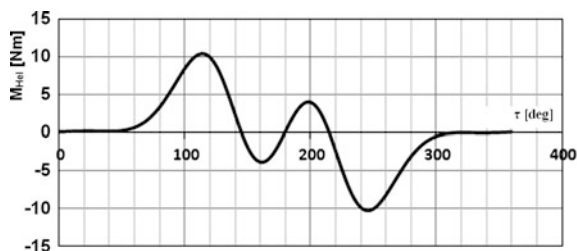


Fig. 4 New conception of the main drive using Yaskawa servomotors

the slay into the labile dead center position. This is the time to change the mode to the waving mode. The servomotor is able to reach the full speed within the next half-turn of the machine. Then the waving mode works and the accumulation of the energy helps to reduce the power requirements (Fig. 4).

2. The optimization of the reduced moment of inertia was performed by removing the break which was replaced by the break in the low-speed mode. The break is not needful in the waving mode and it has relatively high inertia (0.008 kgm^2).

Fig. 5 The driving torque of the new main drive conception



The optimization of gearbox ratio led to use the planetary gearbox with ratio 4 then the reduced momentum of inertia was 0.00121 kgm^2 .

3. Cycloid displacement law was replaced by inclined sinus line [1] and modified by VDI 2143 [2]. The modified displacement law is adjusted so that the driving torque was approximately zero in the labile dead center position ($\pm 40^\circ$).

The theoretical driving torque (after kinematics and dynamics optimizations) is displayed in Fig. 5. The parameters are: speed 600 rpm, picking angle 210° , moment of inertia of the mechanism reduced to the servomotor shaft 0.00121 kgm^2 , moment of inertia of the servomotor rotor 0.0007 kgm^2 [3], planetary gearbox with ration 4 and the moment of inertia relates to the input shaft 0.000032 kgm^2 [4], rigidity of composite slay spring 200 kN/m, inclined sinus line as displacement law. The maximum value of required driving torque M_{Hel} is 10.34 Nm and effective torque (EKM) is 4.7 Nm. Minimum and maximum values of servomotor speed are 808/4,325 rpm. The values of drive torque M_{Hel} and EKM (incl. selection of gearbox) are results of kinetostatic analyses of drive and selection of servomotor Yaskawa Sigma 5 SGMSV type (low inertia, medium capacity) [3]. Selected servomotor is SGMSV-30D (3 kW capacity, rated torque 9.8 Nm, peak torque 29.4 Nm, rated speed 3000 rpm, max. speed 5000 rpm). The efficiency of transmission is not included in results therefore it is selected this servomotor with higher torque capacity.

3 Verification of Theoretical Results on the Waving Machine

Theoretical result was applied to the test machine Camel. Unfortunately several elements with different mechanical parameters then theoretical optimized elements were used. The main differences are different rigidity of composite slay spring and different moment of inertia relates to the input shaft of main servomotor. Therefore new kinetostatic analyses were built. The results are demonstrated in Fig. 6. The different parameters are: speed 300/350/400/470 rpm, planetary gearbox with ration 4 and the moment of inertia relates to the input shaft 0.00032 kgm^2 [4], rigidity of composite slay spring 140 kN/m.

The efficiency was considered for the new simulation model. The efficiency of belt drives, planetary gearboxes and bearings were found of 90 %. The theoretical

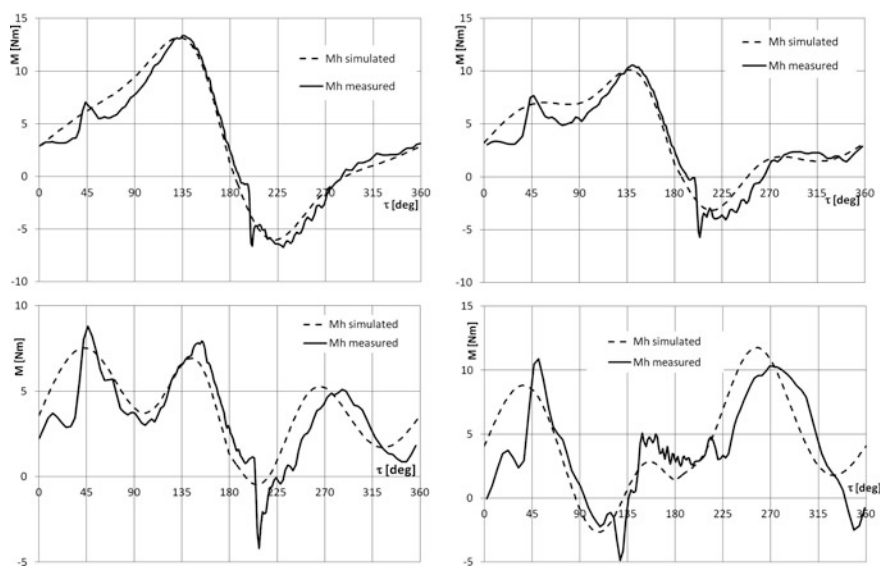
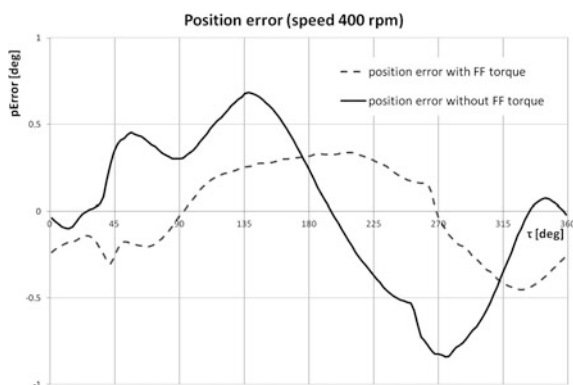


Fig. 6 Comparison of simulated and measured drive torque for several speeds

Fig. 7 Positive decrease of position error using simulated feed forward torque



results of main servomotor were compared with the measured values for several speeds. Peaks of torque which were not in simulation were appeared in measured values. These peaks are caused by changing forces in belts. The forces caused by springs act in the opposite direction of move in the first half of period (cause deceleration). In the second half the forces are in the positive direction (they cause the acceleration). Changes of the tension sign cause the peaks.

This simulation model was built in order to predict the drive torque for this machine. It is possible to use this drive torque from simulation as a feed forward torque to decrease position error. The position error is decreased to the half value than before (Fig. 7).

4 Conclusions

The importance of the optimal design of kinematic chain was shown especially when the electronic cams are used in the production machines. The new conception of the main drive brings high reduction of energy consumption. For future it is important the simulation model that was built.

References

1. Koloc, Z., Václavík, M.: Vačkové mechanismy. Praha: SNTL, 379s (1988)
2. VDI 2153 Bewegungsgesetze für Kurvengetriebe. Düsseldorf: VDI-Verlag GmbH (1980)
3. YASKAWA corp: AC Servo Drives Σ -V Series Product Catalog.[online]. Available: http://www.e-mechatronics.com/support/catalog/servo/kaeps80000042/data/kaeps80000042i_9_0.pdf (2012). Accessed 26 Apr 2012
4. NEUGART GmbH: Precision gearboxes—Catalogue [online]. Available: http://www.neugart.de/download/us/PLN/Katalog_PLN.pdf (2012). Accessed 26 Apr 2012

Application of Motion API for Input Production Data in a Single-Purpose Machine Tool with Control System by YASKAWA

P. Bureš

Abstract The issue of input of production data refers to many areas in the development of machine tool. The concept of input data must take into account many aspects—machining technology, computing possibilities of the control system, the amount of production data, performance of communication between user interface and control system, difficulty of input for operation and price of control system with user interface. The objective is a description of the possibilities of motion API and to identify possible use for the input of production data in single-purpose machine tools.

Keywords CNC control system • Motion API • Production data

1 Introduction

Present production of universal machine tools using universal CNC control systems (Siemens, Heidenhain, Fanuc). These control systems may be unsuitable for use in single-purpose machine tools. One reason is the price/functionality used by the control system, another reason may be follow adjustment of the basic SW equipment according to specifications for a particular purpose of machine.

Development of a custom control system is a complex matter. Development of control system for a specific single purpose machine allows to take into account the requirements of machinery, manufacturing technology, communication with

P. Bureš (✉)
VÚTS a.s, Liberec, Czech republic
e-mail: pavel.bures@vuts.cz

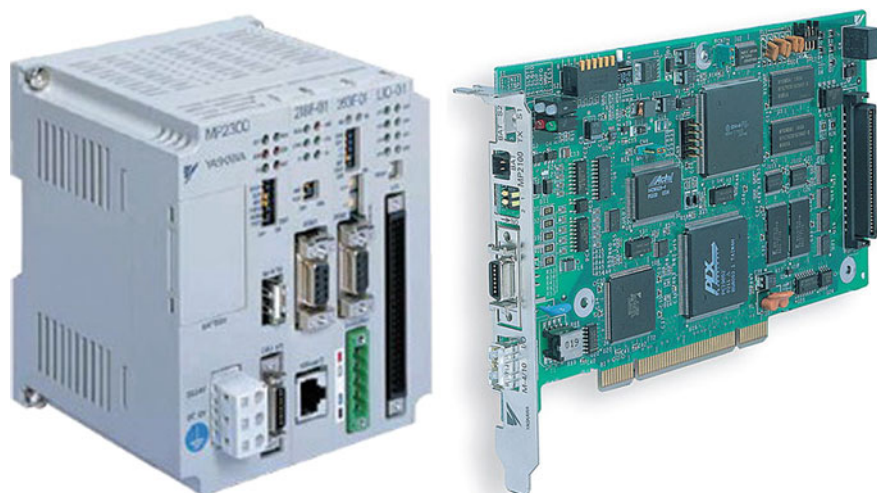


Fig. 1 Separate PLC MP2300 on the *left*, PCI card PLC MP2100 on the *right*

the user-machine interface according to customer specifications while maintaining low cost to functionality ratio.

Entering production data is meant to ensure the transferring data to control system from the user interface and ensuring single purpose machine movements.

Simple applications, such as 2D grinding of radial cams, that are not capacity-consuming manufacturing data (potentially thousands of values) and the computational complexity can be realized using the touch screen. More demanding applications such as 3D machining, in which it is entitlement to large amount of production data, it is necessary to ensure sufficient storage capacity for data.

2 Control System YASKAWA

YASKAWA offers control system in multiple versions, one as a separate device, the second platform is in the form of PCI expansion card into the PC. Both variants have the same possibilities for expansion I/O modules and the same software (Fig. 1).

The control system allows sequential and motion control, which together run synchronously and can communicate with each other via the global address space Fig. 2 [1, 2].

Sequential control is designed to control the logic of digital inputs and outputs, motion control is designed for continuous control of drives with an emphasis on maximum accuracy and continuity of movement without interruption. The basic control commands in the motion are linear, circular and helical interpolation.

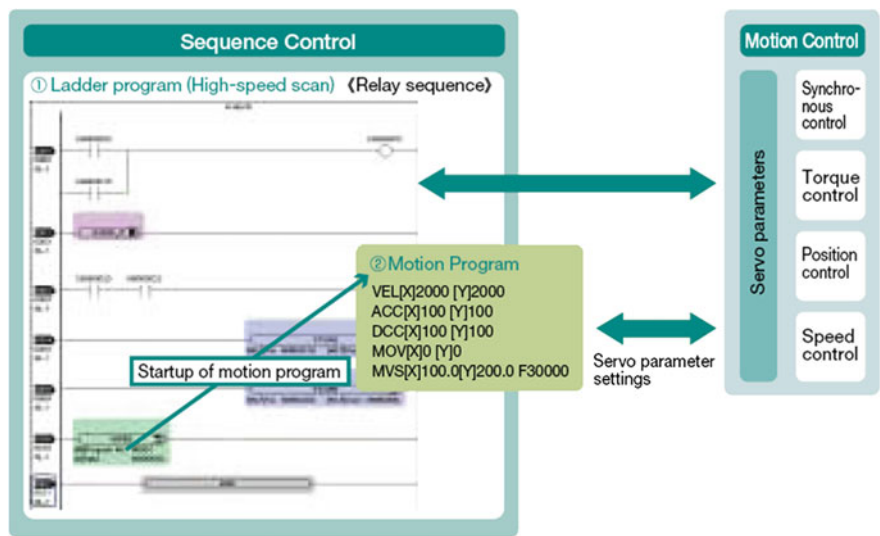


Fig. 2 Synchronous running of sequential and motion control

3 Motion API

Motion API is a library of functions that are used to communicate between the controller and the application running on the PC in Fig. 3.

The library contains 53 functions that can be divided into three branches according to the application. Control functions are used to control communications, error detection and their removal. Motion function is used to control individual actuators and mutual interpolation between multiple drives. Data function is used to transfer values between memory PC and PLC, functions can transfer up to 499 values in a continuous block of data (16 or 32 bits). Data and motion functions allow two different principles to enter production data into the control system. The first principle is the transfer of production entering data into the PLC memory, motion program reads data from the memory and controls the movement of individual axis. The second principle is to call the input motion features in the PC.

3.1 Transfer of Production Data to a Control System

This principle of production data entry is divided into two parts programmatically. One part governing the transmission of data between the PC and the PLC memory realized in the sequential control. PLC memory is limited in size in the tens of KB and the production amount of data can exceed the amount of memory several times in the PLC, because the transmission is realized by blocks. Blocks of data in the

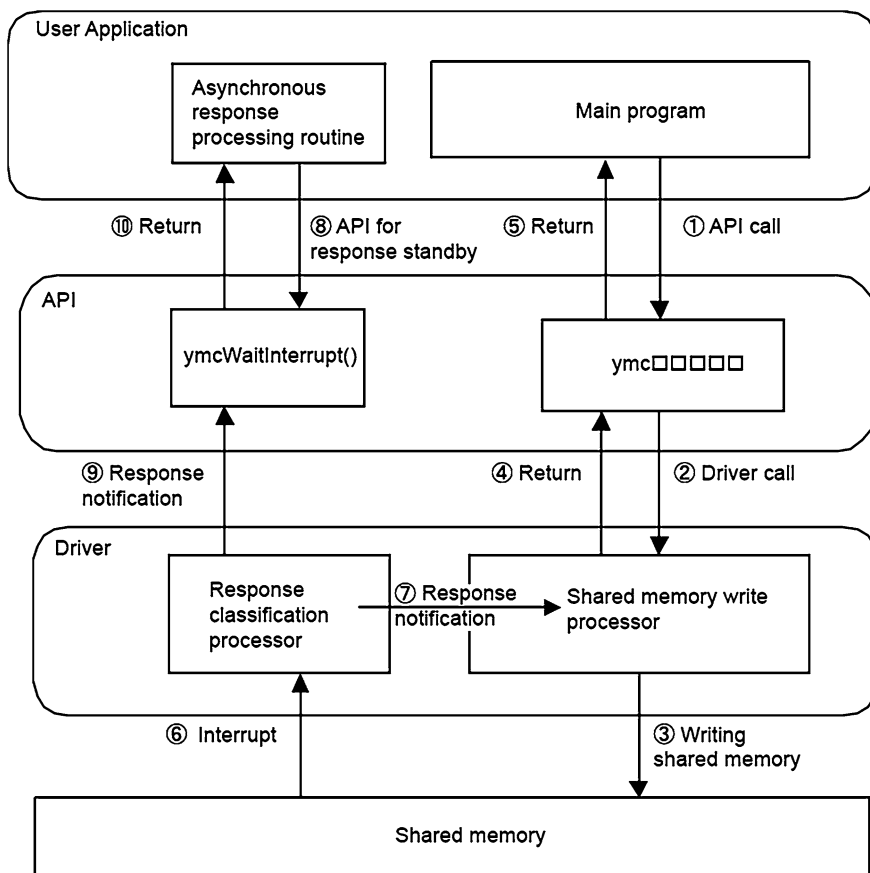


Fig. 3 The principle of communication between the PC and PLC

PLC are divided in half, which alternate between modes write from PC and read into the motion program. The principle is shown in Fig. 4, example of PLC and motion program is shown in Fig. 5.

3.2 Calling of Motion Function in the PC Application

This principle of entering production data using motion functions of Motion API. Declaring axes and equipment (cooperation more axes) must be performed before calling the function that implements the actual movement. Example is shown in Fig. 6 of the procedure function calls to implement the motion.

Motion API functions return a value that determines the function execution. Motion function returns the value after the move. The function returns an error

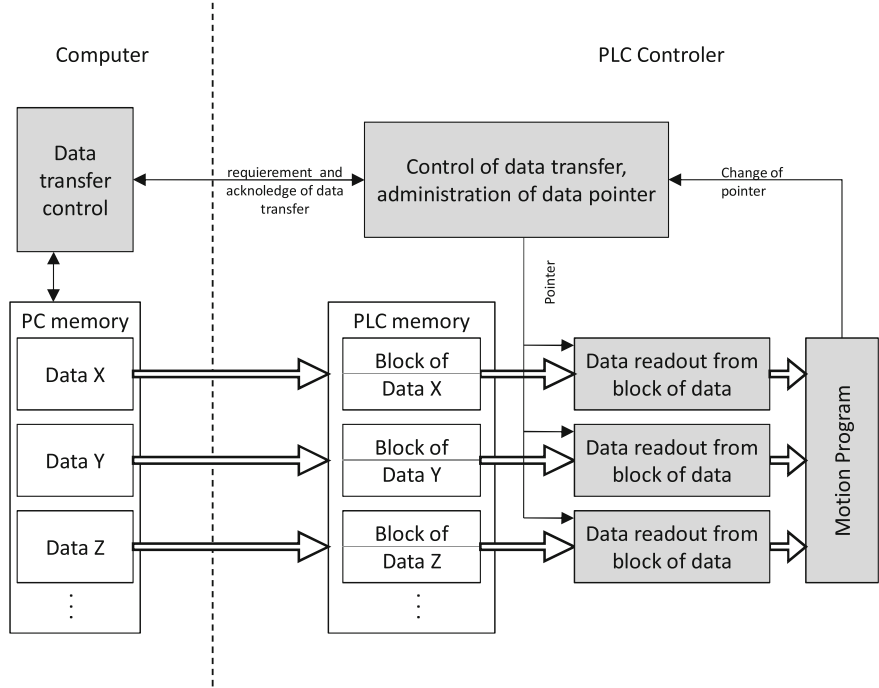


Fig. 4 The principle of the block data transfer

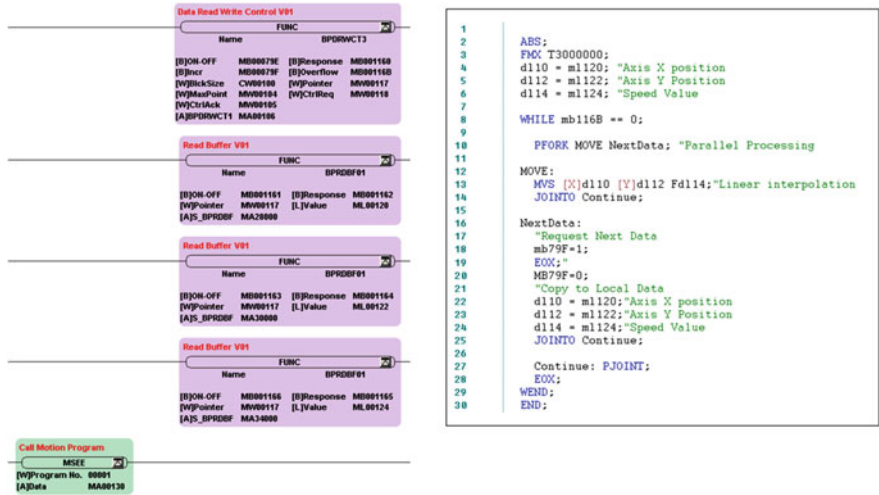


Fig. 5 PC-PLC communication functions on the left, reading data and interpolation in Motion program on the right

The Conception of the Control System of Radial Cam Grinder

P. Jirásko, V. Crhák and P. Bureš

Abstract VÚTS, a.s., has developed a single-purpose machine for grinding radial cams. The control system is built on Yaskawa's components with MP2310 controller. The paper deals with an entirely new concept of the control system of this single-purpose machine built in variants on the program area of controlled continuous movements and on the PLC program. Furthermore, the specific features of the system and the options of its other variants and industrial applications are declared.

Keywords Control system • PLC • Electronic cam • Radial cam grinder

1 Introduction

CNC control systems of machine tools are programmable complex and extensive systems. The Department of Mechatronics, VÚTS, a.s., focused on the development of control systems for single-purpose machines within the TIP project. One of the single-purpose machine tools is just the radial cam grinder (BRV). The limited extent of the paper does not allow us a broader description of the system, so we will talk only about the structure of the program and its unified modules

P. Jirásko · V. Crhák (✉) · P. Bureš
VÚTS, a.s, Liberec, Czech Republic
e-mail: vladislav.crhak@vuts.cz

P. Jirásko
e-mail: petr.jirasko@vuts.cz

P. Bureš
e-mail: pavel.bures@vuts.cz

("objects") that enable the collective development and maintenance of the system. In principle, it is such a building of the system that allows a team work of programmers and a simple usability of debugged objects in other applications. This is the same target (the economics and prosperity of the company making software [1]) which led to the creation of object-oriented programming languages. Thus, we will focus on the description, usability and diagnostics of user functions in the PLC field of the Yaskawa MPE720v.6 development environment.

2 Structure of the BRV Control System

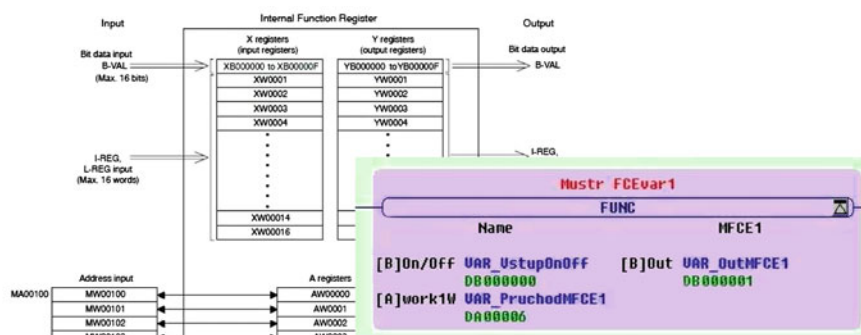
The BRV system is programmed in the PLC area and in the area of continuous motions (*Motion*). We will be dealing with the PLC area. Here, there are programmed all the functions of manual mode or machine states. The list of modes is (in the brackets the name of the user function): connecting power supply (Servo-ON), running references (REFR), defined incremental step (POSI-INK), running on a defined absolute position (POSI-ABS), stepping by selected step 1, 10, and 100 thousandth of a mm (STEP), stepping by selected step 1, 10, and 100 thousandth of a mm by a hand wheel (HW) and linear motion (JOG).

The first phase of the control system development was the processing of manual modes in the conventional structure of *Ladder* diagram with calls to subroutines [2] without the use of user functions. The user function was applied only to control the servo drive in the mode of electronic cam. The newly developed BRV control system consequently uses user functions for all machine states with its inputs, outputs, communication interface and internal closed (enclosed) code with internal variables.

3 User Functions

The user function is shown graphically in Fig. 1 with its inputs, outputs, and bi-directional addressing communication from the manufacturer's documentation and in the form of the MFCE1 general function in the PLC *Ladder* diagram. The productivity of programming work and cooperation of more programmers in one project of the control system sought unification or *template* of user function that will remain all the same or it will be modified according to the agreed rules. Thus, orientation and creation of the documentation of developed programs and user functions is facilitated. The template structure of the MFCE1 general user function as to Fig. 1 is in Fig. 2.

According to Fig. 1, each function has *always* one input (*[B]On/Off*) plus other possible specific inputs and outputs and *always* one mutually (bilaterally) communicating interface which is defined by address (*[A]work1 W*). The convention in the name of address 1 *W* symbolizes that only one 16 bit local register *D* is used



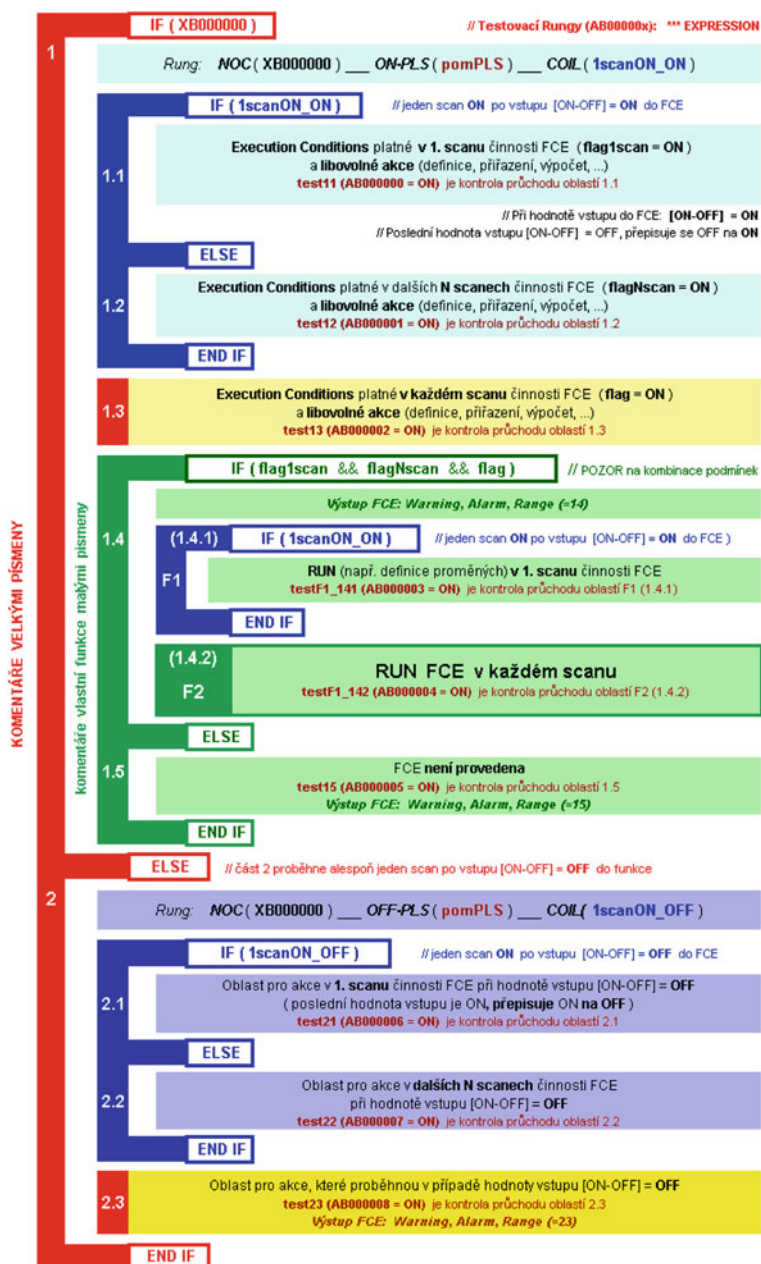


Fig. 2 Template of the MFCE1 unified general user function

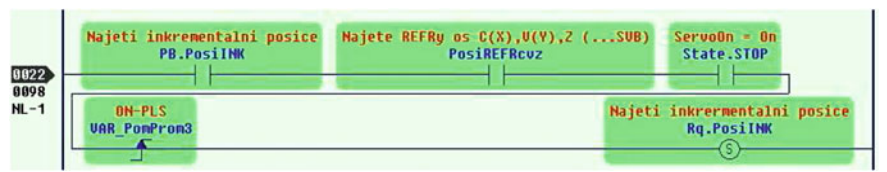
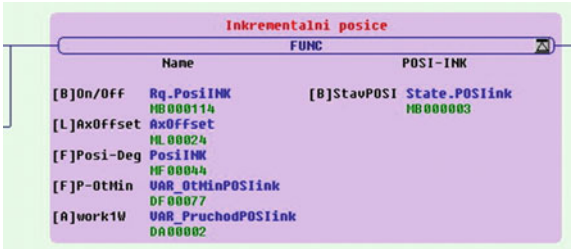


Fig. 3 Definition of input variable [B]On/Off of the POSI-INK function

Fig. 4 Function POSI-INK



machine is activated. After termination or interruption (*Abort*) of the chosen mode, return to the state *State.STOP* will occur.

5 Own Activity of the User Function (Exemplified POSI-INK)

Based of an example of successive parts of *Ladder* diagram, the logic of the inclusion of the POSI-INK user function is graphically illustrated. From Fig. 3, information as follows is obvious:

- Button status on the HMI (*PB.PosiINK*)
- The conditions of the run-up axis references and the basic machine state (*PosiREFRcvz*, *State.STOP*)
- Definition of application for activating the function POSI-INK (*Rq.PosiINK ... SET*)

After *Rung* 22, definitions of the remaining inputs (axis choice, the size of incremental step, axis motion speed) into the function as to Fig. 4 follow. When performing an incremental step, the machine is in a state *State.POSiInk = On* (function output *[B]stavPOSI*).

After completing the incremental step (*State.POSiInk = Off*), it follows the logics of resetting bit variables of the button pressing (*PB.PosiINK*) and function activation (*Rq.PosiINK*) in the *Ladder* diagram. Furthermore, through the communication address *[A]work1 W*, there are monitored variables in the function code structure (according to Fig. 2, there are variables *test11* up to *test23*). Those variables are monitored in the *Ladder* diagram clearly with introduced bit

variables. On this basis of monitored variables, various events can be programmed in the logics of the control system.

6 Function of the Electronic Cam in the BRV Control System

The electronic cam with a defined displacement diagram can be implemented by the user function. The contour of the radial cam is created standardly by two interpolating axes (rotational and sliding) programmed in the field of continuous motions (*Motion*) in the production. This interpolation of two axes in the field of *Motion* can be replaced with two user functions of electronic cams programmed in the PLC which have one common independent variable (*Master*).

7 Conclusions

In the same way as the POSI-INK function, there are programmed and integrated in the *Ladder* diagram all the above mentioned functions of the manual and automatic modes of grinding the contour of a radial cam on the basis of two synchronously implemented functions of the electronic cams of production axes. The same structure of user functions and their integration into the logics of the system makes clear the code of control system and thus increases the productivity of programmers' work. The control system, built in such a way, can be arbitrarily expanded to other controlled axes and applied to various manufacturing machines and devices with controlled servo drives or electronic cams.

References

1. Kraval, I.: Základy objektově orientovaného programování (Computer Press, ISBN 80-7226-047-2), in Czech, (Introduction to object-oriented programming)
2. Jirásko, P.: Methodology of electronic cam applications in drives of working links of mechanisms of processing machines. Dissertation, TU Liberec CZ (2010)

An Analysis of Planetary Gearboxes for Their use With Electronic Cam

P. Dostrašil, P. Jirásko and M. Bušek

Abstract For a reliable and optimal operation of electronic cams it is necessary to reduce the speed of own servomotor of electronic cam with various backlash-free types of step-down gears. The paper focuses on the analysis of gears by means of Neugart planetary gearboxes. On a dynamic stand, gearboxes with different tooth backlashes according to the classification of the manufacturer are tested and working inertial mass is kinematically excited by various types of displacement laws that differ in the continuity of their second derivatives.

Keywords Planetary gearing · Electronic cam · Displacement law · Tooth backlash

1 Introduction

The Department of Mechatronics, VÚTS, a.s., has been engaged in the applications of electronic cams of Yaskawa, a Japanese company, for many years. The electronic cams implement the kinematic excitation of a mechanical system with the required displacement law of its end working link on the servomotor output shaft. According to the nature of the application, we deal with the two implements of electronic cams. The one is the aforementioned motion function kinematic excitation, the other is the application of electronic cams designed as rotary tables

P. Dostrašil (✉) · P. Jirásko · M. Bušek
VÚTS, a.s, Liberec, Czech Republic
e-mail: petr.jirasko@vuts.cz

M. Bušek
e-mail: martin.busek@vuts.cz

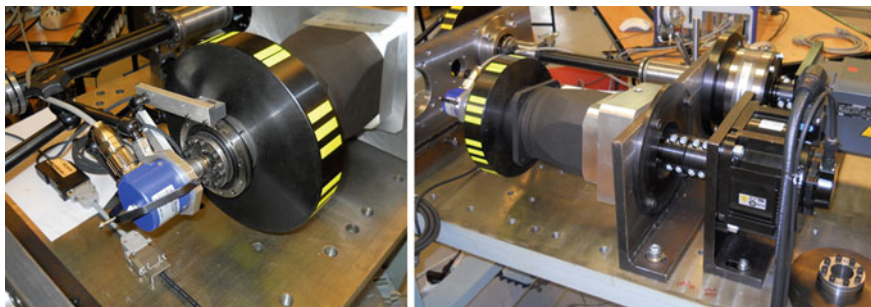


Fig. 1 Test stand (configuration I)

or NC interpolation axes in the machining process of milling and grinding. The speeds of servomotors are reduced with standard planetary gearboxes. Based on the anticipated applications, the impacts of tooth backlashes, running smoothness at the requirement on constant speed, and furthermore, the connections with the use of direct and indirect measurement are observed.

2 Test Stands und Measurement Methodology

The test stand (configuration I) as to Fig. 1 is used to test the influence of direct and indirect drive measurement in the mode of electronic cams. The used servomotor is Yaskawa SGMGV-30D [1] with 20-bit encoder, Neugart PLN72 [2] ($i = 20$) planetary gearbox and load inertia $0,1 \text{ kgm}^2$. Motion functions of the angle of stroke and stroke of 270 and 180° .

Specification of sensors and measurement:

The encoders

1x Sensor Renishaw Signum SR—head resolution $1 \mu\text{m}$, ring's diameter 75 mm , 59200 imp . [3]

1x Sensor Baumer IVO G0356—shaft type sensor, 80000 imp

Measurement analyzer Dewe 5000, software FlexPRO 7

Sampling: 50 kS/s .

DMU plug in PCI:

1x sensor Renishaw Signum SR

1x sensor Baumer IVO G0356

The test stand (configuration II) according to Fig. 2 is used for testing the effect of the tooth backlash size of planetary gearboxes in the mode of electronic cams. The measurement outcome is the input displacement compared to the output

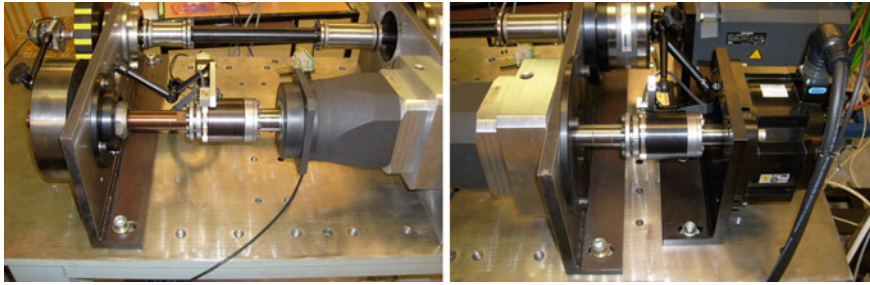


Fig. 2 Test stand (configuration II)

displacement. Then, a clear effect of the tooth backlash and the compliance of the gearbox depending on the exciting motion function can be seen in the results. The used servomotor is Yaskawa SGMGV-30D with 20 bit encoder, Neugart PLN72 planetary gearbox ($i = 20$ with a reduced and standard backlash) and inertial load $0,1 \text{ kgm}^2$. Motion functions with the angle of stroke and stroke 270 and 180° .

Specification of sensors and measurements:

The encoders

2x Sensor Renishaw Signum SR—head resolution $1\mu\text{m}$, ring's diameter 75 mm , 59200imp

Measurement analyzer Dewe 5000, software FlexPRO 7

sampling: 50kS/s .

DMU plug in PCI:

2x sensor *Renishaw Signum SR*

3 Applications of Gearboxes in the System of Electronic Cams

The working inertial mass is kinematically excited by various types of displacement laws which differ in the continuity of their second derivatives [4, 5]. There are polynomial, harmonic and parabolic displacement laws. There were tested gearboxes with different tooth backlashes according to the manufacturer's specifications with a reduced ($<1 \text{ arcmin}$) and standard ($<5 \text{ arcmin}$) tooth backlash in direct and indirect measurement according to Fig. 1. In this stand configuration, positional error (perr) to the theoretical position is evaluated on the basis of the drive direct control by a sensor as to Fig. 1 left. In the mode of indirect measurement, the position is then controlled on the basis of the servomotor encoder. From the large number of combinations and the measured data, we mention the

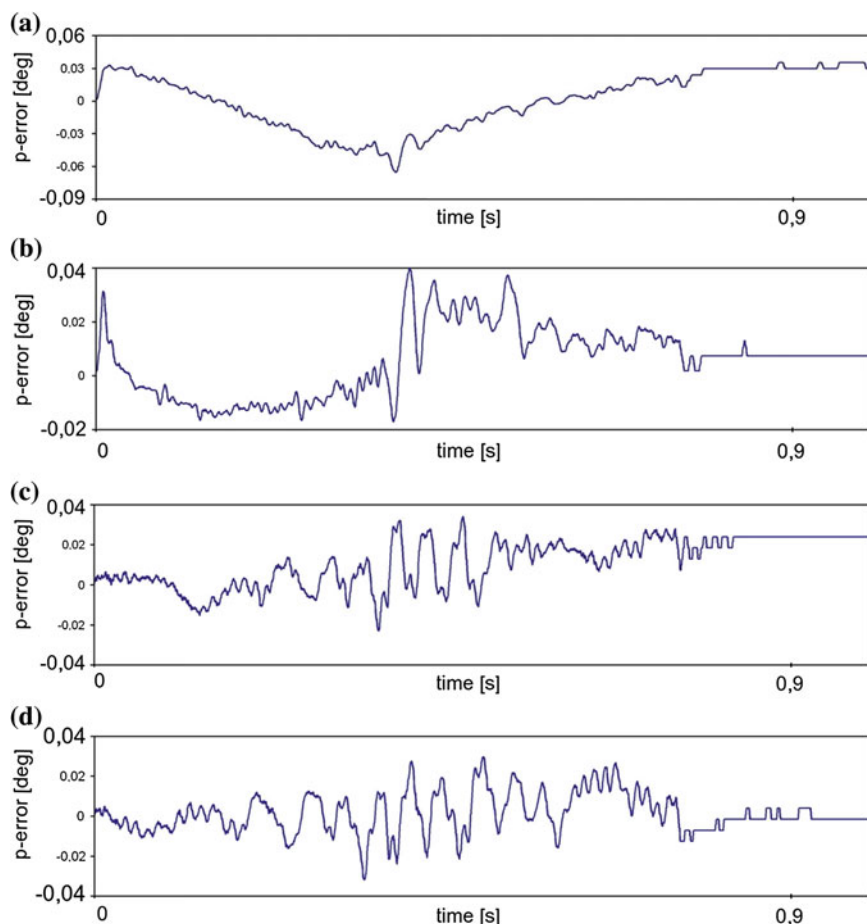


Fig. 3 **a** Indirect measurement, standard backlash. **b** Direct measurement, standard backlash. **c** Indirect measurement, reduced backlash. **d** Direct measurement, reduced backlash

results of direct and indirect position control for a parabolic motion exciting function with a gearbox with the reduced and standard backlash in Fig. 3a up to Fig. 3d.

The results in Fig. 4a up to Fig. 4b from the test stand as to Fig. 2 (configuration II) are given for the parabolic motion function only due to the limited extent of the paper.

The effect of the tooth backlash size in the mode of electronic cams with the dominant influence of dynamic inertia masses is obvious from the mentioned selected tests. Direct measurement decreases the positional error at the gearboxes with standard tooth backlash several times. For gearboxes with reduced tooth backlash, the influence of direct measurement is no longer so distinct. The similar character can be also observed with *harmonic* and *polynomial* displacement laws.

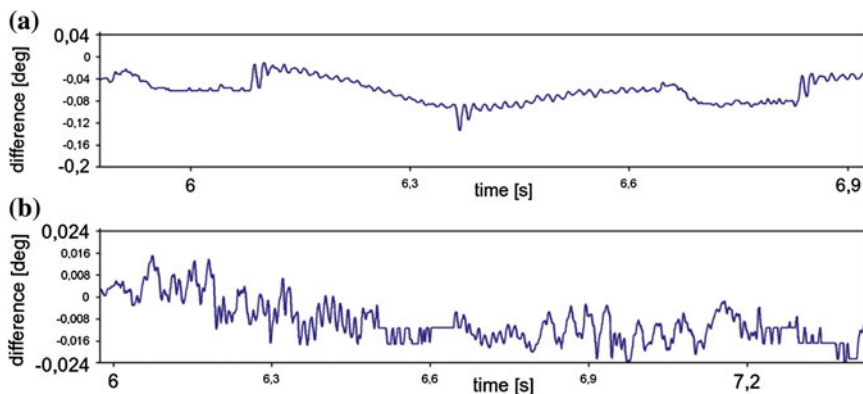


Fig. 4 **a** The difference of the angular position of input and output (standard backlash). **b** The difference of the angular position of input and output (reduced backlash)

4 The Application of Gearboxes in the Mode of Constant Speeds

The mode of constant speeds is the basic controlled motion to which another synchronous motion of a manufacturing mechanism or NC interpolating axis of any machine tool can be bound. The constant speed was observed in the range of 10 up to 500 min^{-1} for direct and indirect measurement with gearboxes with standard and reduced backlash. The typical results (positional deviation perr) are given in Fig. 5a up to 5d. In the range of measured speed, direct measurement reduces the positional error at the gearbox with standard backlash and at the gearbox with reduced backlash, the situation is reversed.

5 Conclusions

The limited extent of the paper does not allow us a detailed analysis of the measured data from the test stands. From the given examples, however, the influence of the control and quality of planetary gearboxes with regard to applications are obvious. Control with direct measurement achieves significantly better results using standard gearboxes. In contrast, influence of type of measurement is almost negligible for the gearboxes with a reduced backlash. The Department of Mechatronics is currently focused on the development of grinding machines for cams (radial and globoid) where the method of speed reduction from the servomotor onto the NC axis is crucial and influences the quality of the product. The control system of those machines uses the mode of electronic cams programmed in the PLC system and the mode with the requirement of constant speed to control the NC axes motion. One of the possible and economically advantageous methods of

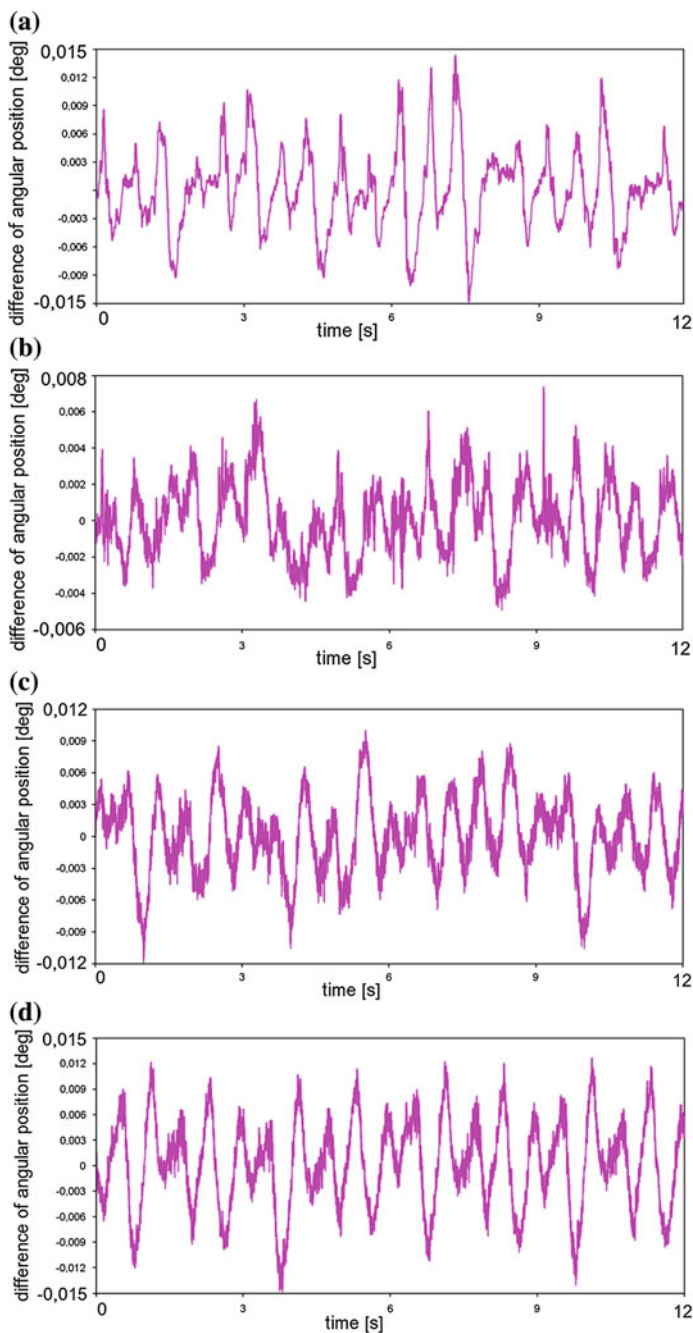


Fig. 5 **a** A gearbox with standard backlash, indirect measurement, 100 min^{-1} . **b** A gearbox with standard backlash, direct measurement, 100 min^{-1} . **c** A gearbox with reduced backlash, indirect measurement, 100 min^{-1} . **d** A gearbox with reduced backlash, direct measurement, 100 min^{-1}

reducing speed is just using the planetary gearboxes in the mode of direct measurement. Our application requires gearbox with a high efficiency and low gear ratio which excludes the use of cycloid and harmonic gearboxes.

References

1. Yaskawa corp: AC servo drives Σ -V series product catalog.[online]. [cit. 2012-04-26] Available: http://www.e-mechatronics.com/support/catalog/servo/kaeps80000042/data/kaeps80000042i_9_0.pdf (2012)
2. Neugart GmbH: Precision gearboxes—Catalogue [online]. [cit. 2012-04-26] Available: http://www.neugart.de/download/us/PLN/Katalog_PLN.pdf (2012)
3. Renishaw: Signum encoder system—datasheet [online]. [cit. 2012-05-22] Available: [http://resources.renishaw.com/en/Data+sheet%3a+SiGNUM%e2%84%a2+encoder+system\(34304\)?direct=true](http://resources.renishaw.com/en/Data+sheet%3a+SiGNUM%e2%84%a2+encoder+system(34304)?direct=true) (2012)
4. Koloc, Z., Václavík, M.,: Vačkové mechanismy. Praha: SNTL (1988)
5. Volmer, Johannes. Kurvengetriebe. Berlin: Verl. Technik, (1989). ISBN 3-341-00474-2

DC/DC Power Converter for Super-Capacitor Supplied by Electric Power Splitter

T. Haubert and P. Mindl

Abstract The aim of the article is design of DC/DC converter and discussing of problematic supply using electric power splitter. The electric power splitter with AC/DC converter is source for the DC/DC converter, which is dedicated for charging and discharging of hybrid car drive super-capacitor energy storage. The electric power splitter is synchronous machine with two rotating parts. First rotor contains permanent magnet and the second rotor contains three-phase windings. The amplitude of output voltage depends on difference between first and second rotor speed. The main role of the DC/DC converter is to optimize energy content in super-capacitor storage used to acceleration and deceleration driving period of the passenger car with hybrid electric vehicle (HEV) drive system using electric power splitter.

Keywords Hybrid electric vehicle · Electric power splitter · DC/DC power converter · Driving period

1 Introduction

Increasing of living standards increased needs for people transport. Gas emission and fuel consumption are actual problems for global environment quality on the Earth. Gas emission of car internal combustion engines brings many ecological

T. Haubert (✉) · P. Mindl
Czech Technical University, Prague, Czech Republic
e-mail: tomas.haubert@fel.cvut.cz

P. Mindl
e-mail: mindl@fel.cvut.cz

problems in big cities specially. Electric vehicles avoid this problem, because they do not rely on gas emission. Electric energy can be stored in batteries, but the disadvantages are limited capacity and inconvenient capacity/mass ratio. The compromise between vehicles with combustion engine and electric vehicles (EV) are hybrid electric vehicles (HEV). HEV combines the combustion engine and electric motor for motion [1].

The drive for HEV can be serial hybrid drive, parallel hybrid drive and combined hybrid drive. All of them have many advantages and disadvantages. In serial hybrid drive, the combustion engine works with high efficiency and it is connected to an electric generator. The electric generator produces electric energy for batteries, which supplies the electric motor, which drives the car wheels. In parallel hybrid drive, the combustion engine is connected to the cars wheels by the clutch. The electric motor is also parallel connected to the car's wheels. When the car brakes, the electric motor works like a generator, which supplies the batteries or super-capacitor. When the car accelerates, the electric motor actuates the cars wheels with combustion engine.

Both above mentioned systems have lower efficiency to compare with combined systems using power splitting. Therefore hybrid drive with electric power splitter is studied at CTU-FEE in Prague. Theoretical analysis of this system has been published in [2].

2 Experimental Stand of Hybrid Drive

As a part of Josef Bozek Competence Centre of Automotive Industry, the experimental stand of hybrid drive has been created. This stand can change the configuration of hybrid drives to serial hybrid drive, parallel hybrid drive and combined hybrid drive. The actual configuration is combined hybrid drive with electric power splitter. The schematic of this stand is shown on Fig. 1. The internal combustion engine (ICE) is simulated by asynchronous motor supplied by frequency converter and it works with speed close-loop. The traction load (BRAKE) is simulated by the asynchronous motor supplied by the frequency converter and it works with torque close-loop. Electric power splitter (EPS) has two rotating parts. The first rotor contains permanent magnet and the second rotor contains three coils, which are connected by brushes to the AC/DC converter. The ICE is mechanically connected to the first rotor of EPS. The second rotor is mechanically connected to the traction motor (TM) and BRAKE.

The source for hybrid drive is ICE, which produces the torque T_{ICE} and speed n_{ICE} . This mechanical energy is connected to the first rotor EPS. The EPS divides the input mechanical energy to the electrical energy and to the output mechanical energy by the second rotor. The second rotor is mechanically connected to the TM and to the BRAKE. BRAKE produces the braking torque T_{BRAKE} and speed n_{BRAKE} . The AC output voltage depends on different between n_{ICE} and n_{BRAKE} . The AC/DC converter transforms the AC output voltage from EPS to DC voltage

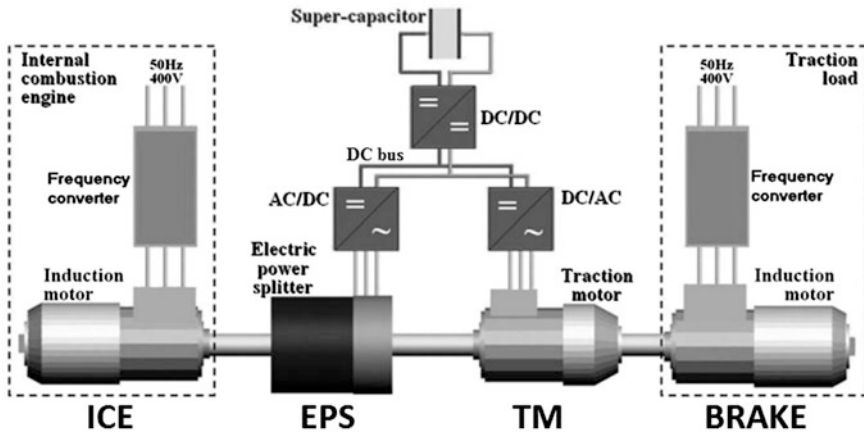


Fig. 1 Schematic of experimental stand of hybrid drive

Table 1 Parameters of electric power splitter

Parameter	Value
Power	$P = 5 \text{ kW}$
Rotor revolutions	$n = 4000, n_{\text{MAX}} = 6000 \text{ min}^{-1}$
Voltage	$U = 400 \text{ V}$
Frequency	$f = 267 \text{ Hz}$

on DC bus. More information about experimental stand of hybrid drive is presented in [3, 4].

3 Electric Power Splitter

The electric power splitter is a double rotor synchronous generator. First rotor and second rotor can rotate independently. The parameters of EPS are included in Table 1 and the cross section is shown on Fig. 2. The theory of this synchronous generator is presented in [4].

For working of experimental stand is important the electrical power on the DC bus. In this article the losses in EPS and in AC/DC converter are not considered.

The relative speed ω_{rel} is

$$\omega_{\text{rel}} = \omega_{\text{ICE}} - \omega_{\text{BRAKE}} \quad (1)$$

If the electromagnetic clutch is turn on, the $\omega_{\text{rel}} = 0$ and EPS does not produce the electrical power. If $\omega_{\text{rel}} \neq 0$, the electrical power from EPS is

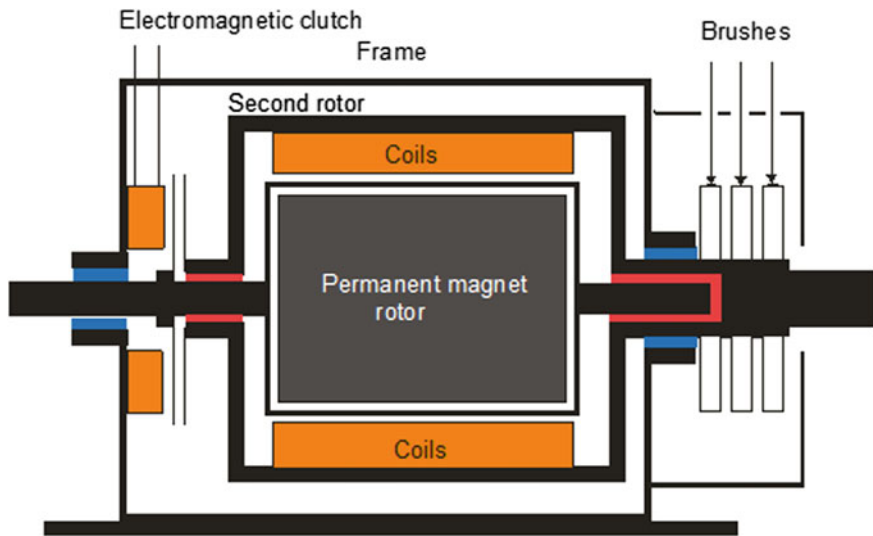


Fig. 2 Cross section of electric power splitter

$$P_{EPS} = T_{EPS} \cdot \omega_{rel} = (T_{ICE} - T_{BRAKE}) \cdot (\omega_{ICE} - \omega_{BRAKE}) \quad (2)$$

The ICE works with speed close loop, therefore the speed ω_{ICE} is constant and the torque T_{ICE} depends on traction load. In ideal case if $T_{BRAKE} = 0$ and $P_{EPS} > 0$, then $\omega_{BRAKE} \rightarrow \omega_{ICE}$ and $P_{EPS} \rightarrow 0$. For $P_{EPS} > 0$ it is necessary to produce the braking torque T_{BRAKE} . In theory of synchronous machines (synchronous generators) is confirmed rotor and fixed stator. The output power depends on rotor mechanical power (torque and speed). EPS has two rotating parts and the output power depends on the first and second rotor mechanical energy ratio.

The measured data from EPS are shown on Fig. 3. The n_{ICE} has constant value $n_{ICE} = 1480 \text{ min}^{-1}$ and the $T_{BRAKE} = 0$. At the time 42 s the load $R = 100 \Omega$ was connected. With increasing of n_{BRAKE} , the power P_{EPS} decreases to the zero. At the time 118 s the $T_{BRAKE} = 6 \text{ Nm}$ was connected and with increasing of ω_{rel} , also increase the output voltage U_{DC} and the output power P_{EPS} .

4 DC/DC Power Converter

The DC/DC converter for HEV we have chosen is the bidirectional type. This has been done because so that the converter is able to transfer the energy from higher voltage level to lower voltage level and second direction this converter lower voltage level on super-capacitor to higher voltage level on DC bus. The higher voltage (primary side) is presented at the DC circuit, which is connected to the

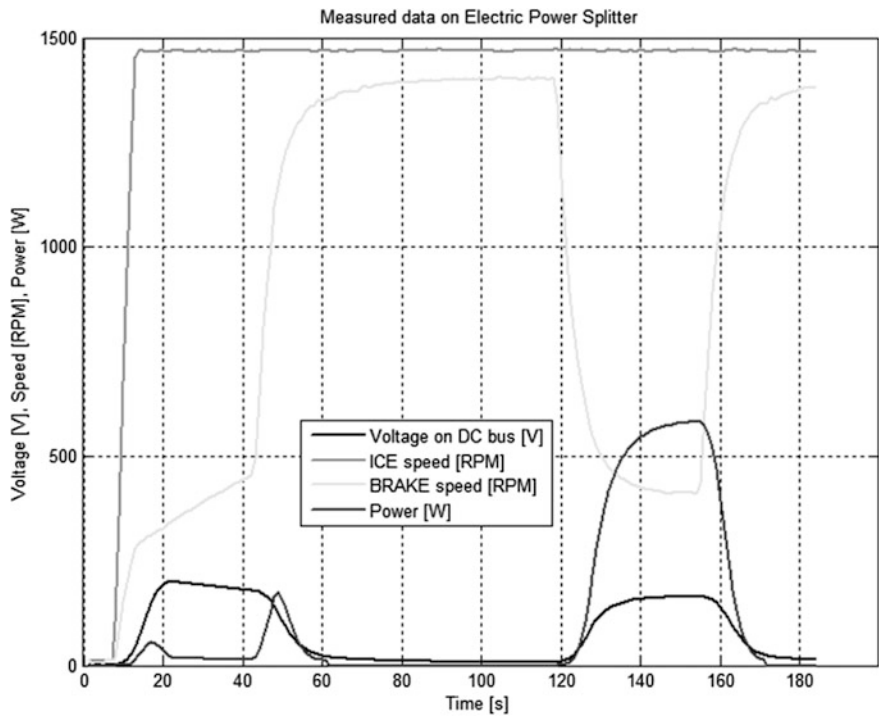
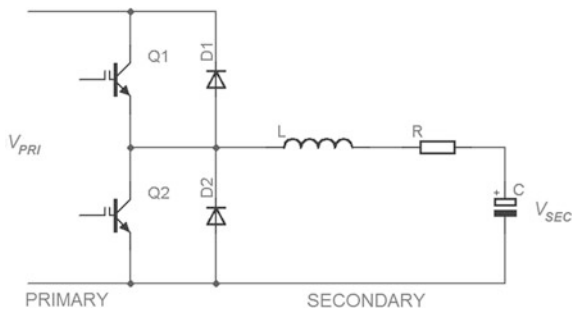


Fig. 3 Measured data on electric power splitter

Fig. 4 Schema of bidirectional DC/DC converter



converters (this converter, AC/DC converter for EPS and DC/AC converter for TM). The lower voltage (secondary side) is presented by super-capacitor, which is used instead of a battery. It is needed to transfer energy from the high side to the low side (buck mode) and on the opposite direction (boost mode). The schema is shown on Fig. 4.

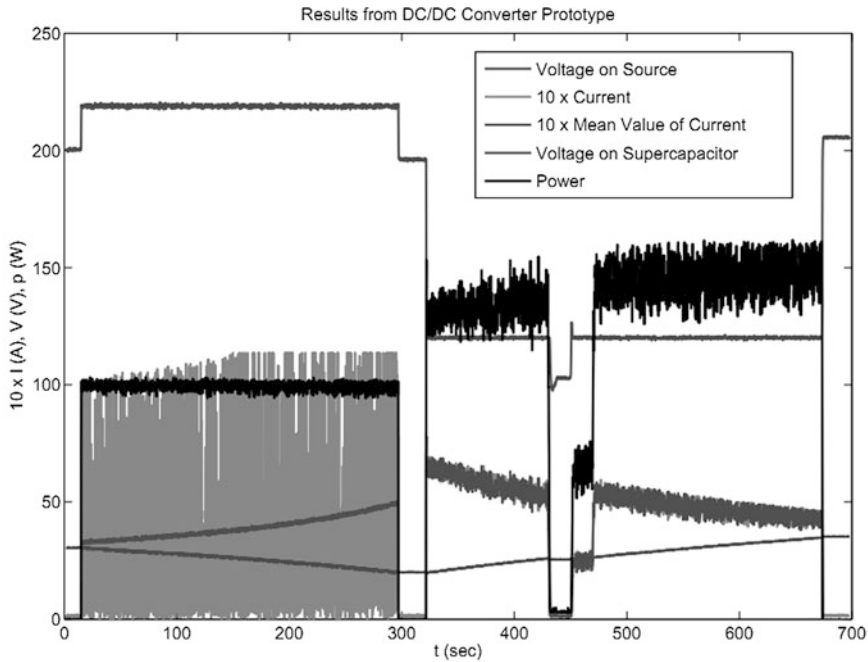


Fig. 5 Experimental results from DC/DC power converter supplied by electric power splitter

4.1 Control Strategy of DC/DC Converter

For control algorithm is designed a linear-quadratic regulator (LQR) [5]. Another control strategies based on polynomial method are presented in [6]. The reference value is power and output is PWM signal for IGBT transistors. The control algorithm is implemented to the Freescale 56F8257 processor and the laboratory model of this converter was created.

The control algorithm must control voltage value on DC bus in range 120–250 V, because the DC/AC converter for TM cannot operate if the voltage is lower than 100 V and greater than 300 V. The experimental results are presented on Fig. 5. The power in buck mode (10–280 s) is regulated to 100 W and power in boost mode (320–680 s) is regulated to 140 W.

5 Conclusions

It was presented the problematic of supplying DC/DC converter using electric power splitter. Electric power splitter and super-capacitor energy storage are perspective for using in hybrid electric vehicles.

Acknowledgments This work was supported by the Grant Agency of the Czech Technical University in Prague, grant No. SGS12/066/OHK3/1T/13 and it is supported by the Josef Bozek Competence Centre of Automotive Industry.

References

1. Cerovsky, Z., Mindl, P.: Hybrid electric cars, combustion engine driven cars and their impact on environment. In: Proceeding of SPEECAM 2008, Italy (2008)
2. Cerovsky, Z., Mindl, P.: Properties of hybrid electric drive with electric power splitter. Optimization of Electrical and Electronic Equipment—OPTIM 2008, Brasov, Romania (2006)
3. Cundev, D., Cerovsky, Z., Mindl, P.: Modelling of the hybrid electric drive with an electric power splitter and simulation of the fuel efficiency. EPE'09, Barcelona, Spain (2009)
4. Cerovsky, Z., Mindl, P.: Electric power divider in hybrid electric vehicle powertrain. In: 12-th International Power Electronic and Motion Control Conference EPE-PEMC 2006, pp. 1361–1365 (2006)
5. Olalla, C., Leyva, R., Aroudi, A. E., Queinnec I.: Robust LQR control for PWM converters: an LMI approach. IEEE Transactions on Industrial Electronics (2009)
6. Camara, M.B., Cualous, H., Gustin, F., Berthon, A., Dakyo, B.: DC/DC converter design for supercapacitor and battery power management in hybrid vehicle—polynomial control strategy, pp. 587–597 (2009)

Traction Control System for Formula Student Electric

Z. Houf, Z. Čerovský and V. Hlinovský

Abstract This paper deals with design of traction control of Formula Student Electric Car. There will introduced new conception of formula traction system and its application to the Formula car. In next season we would like to use 2 motors, each of them will be directly connected to its wheel. This solution needs precise control of them to provide high dynamics and great ability to ride curves in high speeds. Using the same torque on each wheel brings problem when one of wheel loss the traction ability. Some slip could happen and the unexpected lateral movement becomes. There will described the mathematic model of formula car. To reduce slips etc. we will publish the theoretical algorithm that reduces or increases torques on rear wheels to stabilize the car. There will be described what states have to be measured and evaluated. Also places where the sensors will be placed will be shown.

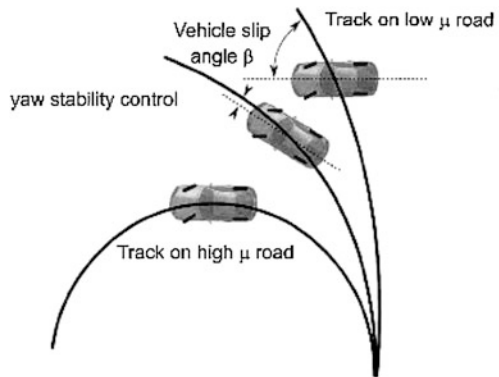
Keywords Formula • Traction Control • Electric Drives

Z. Houf (✉) · Z. Čerovský · V. Hlinovský
Department of Electrical Drives and Traction, Faculty of Electrical Engineering,
Czech Technical University in Prague, Prague, Czech Republic
e-mail: houfzden@fel.cvut.cz

Z. Čerovský
e-mail: cerovsky@fel.cvut.cz

V. Hlinovský
e-mail: hlinovsk@fel.cvut.cz

Fig. 1 Function of the yaw control system



1 Introduction

The concept behind Formula SAE is that a fictional manufacturing company has contracted a student design team to develop a small Formula-style racecar. The prototype racecar is to be evaluated for its potential as a production item. The target-marketing group for the racecar is the non-professional weekend autocross racer. Each student team designs, builds and tests a prototype based on a series of rules, whose purpose is both ensuring on-track safety (the cars are driven by the students themselves) and promoting clever problem solving. It is a great challenge to develop vehicles that can satisfy these diverse and often conflicting requirements. To meet this challenge, automobiles are increasingly relying on electro-mechanical sub-systems that employ sensors, actuators and feedback control.

2 Electronic Stability Control

2.1 Function of Stability Control System

Vehicle stability control systems prevent vehicles from spinning and drifting out. It has been developed and recently commercialized by several automotive manufacturers. Such stability control systems are also often referred to as yaw stability control systems or electronic stability control systems.

Figure 1 shows the function of a yaw stability control system. In this figure, the lower curve shows the trajectory that the vehicle would follow in response to a steering input from the driver if the road were dry and had a high tire-road friction coefficient.

In this case the high friction coefficient is able to provide the lateral force required by the vehicle to negotiate the curved road. If the coefficient of friction were small or if the vehicle speed were too high, then the vehicle would not follow the nominal motion expected by the driver—it would instead travel on a trajectory

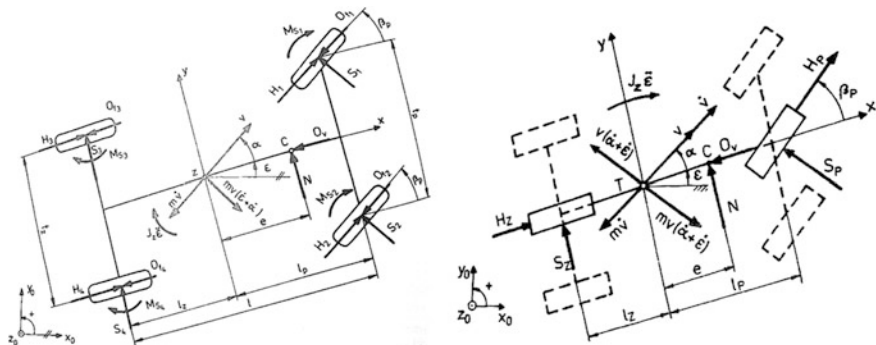


Fig. 2 Planar and bicycle model of vehicle

of larger radius (smaller curvature), as shown in the upper curve of Fig 1. The function of the yaw control system is to restore the yaw velocity of the vehicle as much as possible to the nominal motion expected by the driver. If the friction coefficient is very small, it might not be possible to entirely achieve the nominal yaw rate motion that would be achieved by the driver on a high friction coefficient road surface. In this case, the yaw control system might only partially succeed by making the vehicle's yaw rate closer to the expected nominal yaw rate, as shown by the middle curve in Fig 1.

2.2 Types of Stability Control Systems

1. Differential Braking systems, which utilize the ABS, brake system on the vehicle to apply differential braking between the right and left wheels to control yaw moment.
2. Steer-by-Wire systems, which modify the driver's steering angle, input and add a correction steering angle to the wheels
3. Active Torque Distribution systems which utilize active differentials and all wheel drive technology to independently control the drive torque distributed to each wheel and thus provide active control of both traction and yaw moment.

3 Dynamic Model of Yaw Rate and Slip

3.1 Linear Bicycle Dynamics Model of Vehicle

Vehicle maneuverability and stability is tested with the advantage of using a dynamic model of planar two-wheeled vehicle according to Fig. 2.

If we compare this model with the last used model we see that the lateral guiding force on the front axle $S_p = S1 + S2$ and $S_z = S3 + S4$ on the rear axle, Circumferential (Driving) Forces $H_p = H1 + H2$, $H_z = H3 + H4$. Rolling Forces are neglected. Also we can neglect Reversible Tires Torque because $lp \gg ns$, $lz \gg ns$ where ns is tire trail.

As in the last model we can write down 3 motion equations:

Equilibrium of the forces in the direction of the x-axis (longitudinal movement):

$$-m\dot{v}\cos\alpha + mv(\dot{\alpha} + \dot{\epsilon}) + S_p\sin\beta_p + H_p\cos\beta_p + H_z - O_v = 0 \quad (1)$$

Equilibrium of the forces in the direction of the y-axis (transverse motion):

$$-mv\sin\alpha - mv(\dot{\alpha} + \dot{\epsilon})\cos\alpha + S_p\cos\beta_p + S_{zz} + H_p\sin\beta_p + N = 0 \quad (2)$$

The balance of moments about an axis (yaw motion):

$$-J_z\ddot{\epsilon} + S_p l_p \cos\beta_p - S_z l_z + H_p l_p \sin\beta_p + Ne = 0 \quad (3)$$

If we linearize these three equations by substitution $\sin(x) \approx 0$, $\cos(x) \approx 1$, we will get 3 linear differential equations:

$$-m\dot{v}\cos\alpha + H_p + H_z - O_v = 0 \quad (4)$$

$$-mv(\dot{\alpha} + \dot{\epsilon}) + S_p + S_{zz} + N = 0 \quad (5)$$

$$-J_z\ddot{\epsilon} + S_p l_p - S_z l_z + Ne = 0 \quad (6)$$

Lateral Guiding Forces can be calculated as:

$$S_p = C_{xp}(-\alpha - \frac{l_p}{v}\dot{\epsilon} + \beta_p) \quad (7)$$

$$S_z = C_{xz}(-\alpha - \frac{l_z}{v}\dot{\epsilon} + \beta_z) \quad (8)$$

Where C_{xp} and C_{xz} are cornering stiffness of tires. These equations are used to make the model in Simulink.

4 Simulation of Correcting Yaw Angle to Correct Trajectory of Vehicle

4.1 Parameters and Constants of the Formula Student Car

See Table 1.

Table 1 Vehicle constants and parameters

Model parameter	Value	Unit	Description 4
m	350	kg	Mass of the car
g	9.81	m/s ²	Gravity constant
lz	0.816	m	
lp	0.884	m	Distances CG of axes
tz	1.264	m	Rear
tp	1.250	m	Front track
ro	1.28	kg/m ³	Density of air
Syz	1.1	m ²	Projection of car to yz plane
cx	0.8	(-)	Coefficient of aerodynamic forces
fk	0.015	(-)	Coefficient of rolling resistance on wheels (asphalt)
Calfap	75,000	N/rad	Directional stiffness of both front tires
Calfaz	75,000	N/rad	Directional stiffness of both rear tires
e	0.2	m	Distance of action of air forces from the center of gravity
J	150	kg m ²	Moment of inertia in vertical axis passing the center of gravity
Cr	6,000	Nm/ rad	Steering stiffness
r0	0.05	m	Radius of the lock

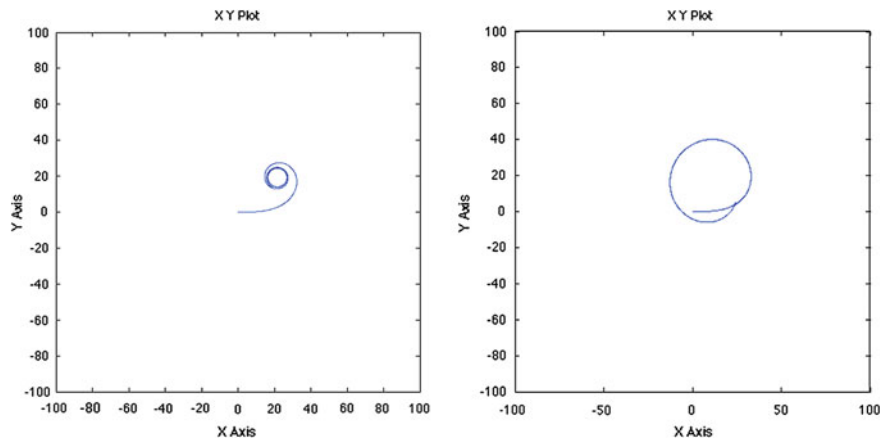


Fig. 3 Position of center of gravity with and without correction of traction

4.2 Simulation of Reducing Yawing Vehicle with Constant Steering Angle

Both rear-driving forces are 70 N; ideal radius of curve is 25 m; initial speed 20 m/s. As you can see the radius of curve has changed. Lets try when α reaches the 0.1 rad increase the H_3 to 470 N. All other conditions are the same as in the experiment before (Fig. 3).

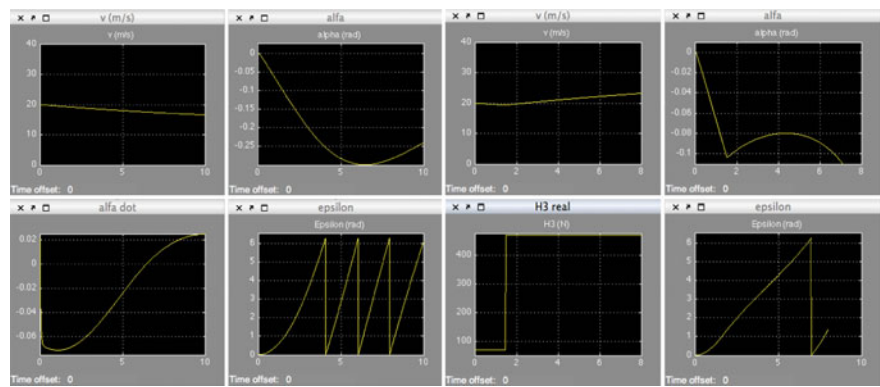


Fig. 4 Charts of speed of CG, epsilon, alpha, alpha dot and H3

5 Conclusions

One of the easy way how to control the stability of vehicle seems to be direct control of rear wheels. As it is shown on Fig. 4 this gives us great ability to control traction in sharp curves if we want to ride it in fast way.

Acknowledgments Research described in the paper was supervised by Prof. Z. Čerovský, FEE CTU in Prague and Ing. R. Tichánek, FME CTU in Prague.

Electro Dermal Quantification of Some Dental Treatment's Efficiency

M. Mateas and E. Ianosi

Abstract The evaluation of soft tissue laser treatment efficiency is usually achieved by means of tactile and thermal stimulation. As a measure of the laser treatment efficiency the absence of pain during and after stimulation is considered. The authors propose as reference indicator for the pain level the electro dermal reaction of the patient. In this paper the correlation between the level of pain and the patient's electro dermal reaction and also the statistical inference is underlined.

Keywords Pain evaluation • Electro dermal • Pain level

1 Introduction

It is known that dental specialists are using extensively the pain level to investigate the state of the patient before, during and after a treatment [1].

This paper presents the continuous effort of the authors to measure the pain level during the above mentioned situations in order to evaluate the efficiency of some laser dental treatments focused on reducing the constant pain claimed by the patient.

The authors believe that the skin electrical resistance modification illustrates the presence of acute pain and it is able to take different forms being able to dissociate emotional state from pain. The skin electrical resistance modification it is called

M. Mateas · E. Ianosi (✉)

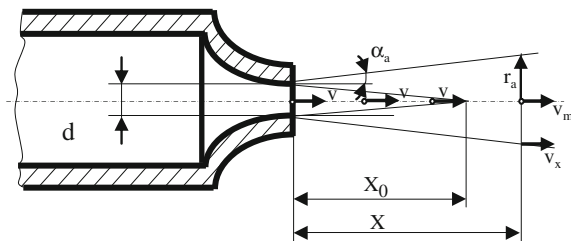
POLITEHNICA University of Timisoara, Timisoara, Romania

e-mail: endre.ianosi@mec.upt.ro

M. Mateas

e-mail: marius.mateas@mec.upt.ro

Fig. 1 The free spurt and the velocity configuration



psycho galvanic reflex, electro dermal response, skin conductance response or galvanic skin response (GSR).

The GSR reflects sweat gland activity and changes in the sympathetic nervous system due to emotional states or stress, including pain presence.

In order to induce the pain reaction or to verify the sensibility of certain areas to pain the dental specialist uses the air/water spray from the dental unit. Eriksson M, Storm H, Fremming A, Schollin J., 2008, underlines that there is a clear difference between the electro dermal reaction to tactile stimulation and the reaction to pain [2].

Also Karin Hani, Keenan Eng, Marie-Claude Hepp-Reymond, Lisa Holper, Birgit Keisker, Ewa Siekierka, and Daniel C. Kiper, 2008, showed that the electro dermal reaction is a clear indication of pain sensation [3].

The evaluation of soft tissue laser treatment efficiency is usually achieved by means of tactile and thermal stimulation. The authors propose the use of the air/water syringe in order to obtain tactile and thermic stimulation of the targeted tissue. The air/water syringe produces a stream of air, water or a combination of air and water. The dynamic pressure gives the tactile stimulation and the temperature of the stream gives the hot or cold stimuli. This set of parameters is identical to those currently involved in the mastication process.

Due to the importance of the fluid temperature, impact area and force of impact, it is necessary to establish mathematically the fluid jet configuration, distance of action, speed spectrum and dynamic pressure as follows.

2 Determination of the Stimulus Parameters

In Fig. 1 the situation of a free spurt/jet is presented [3] which are quitting the evacuation diuze with diameter d .

We can observe the two distinguished zones of the spurt, a conical nucleus with length x_0 and an outside zone of the nucleus, with length x , where the velocity are variable. The height of the conical nucleus, where the velocities are constant, is:

$$x_0 = \frac{d}{m} \quad (1)$$

where:

d diuze diameter;

m low coefficient; $m = 0,1$ for laminar flow; $m = 0,3$ for turbulent flow

For $d = 1,5$ mm and $m = 0,2$ the height of the conic nucleus will be:

$$x_0 = \frac{1,5}{0,2} = 7,5 \text{ mm}$$

The fluid velocity:

$$v = \frac{Q}{A} = \frac{4Q}{\pi d^2} \quad (2)$$

The medium velocity outside of the conic nucleus in center of the spurt is:

$$v_m = v \frac{x_0}{x} \quad (3)$$

The velocity at the spurt periphery:

$$v_x = \frac{v_m}{2} \quad (4)$$

The radius and the dispersion angle of the spurt:

$$r_a = m \sqrt{\frac{\ln 2}{2}} \cdot x = 0.5887mx \quad (5)$$

$$\alpha_a = a \tan \left[0.707m \sqrt{\ln \left(\frac{v_m}{v_x} \right)} \right]$$

For water at turbulent flow ($m = 0.3$) the dispersion angle of the spurt will be:

$$\alpha_a \approx 10^0$$

The volumic flow rate at the distance x is:

$$Q_x = 2mQ \frac{x}{d} \quad (6)$$

The force of the spurt of a frontal wall can be determinate with the relationship:

$$F = \rho Qv = \rho A v^2 \quad (7)$$

where: A—the transversal area of the spurt with parallel lines
In case of dental probes the pressure values for the two vehiculated fluids (air and water) are: $p_A = 4$ bar (air), $p_v = 2$ bar (water). The usual flow rate of the water used in the analyzed device is: $Q = 0.15$ l/min.

In case of air flow measurement with diaphragm ($d = 1$ mm, $D = 10$ mm), the values of the flow can be determinate with the relationship:

$$Q = \left(\alpha A_2 \sqrt{\frac{2}{\rho(1 - \Phi^2)}} \right) \Delta p \quad (8)$$

where: $\alpha = 1$ form coefficient, ρ —air density: 1.2 kg/m^3 , Φ —surfaces ratio:

$$\Phi = \frac{A_2}{A_1} = \left(\frac{d}{D} \right)^2 \quad (9)$$

The surface area for the strangulated zone:

$$A_2 = \frac{\pi d^2}{4} = \frac{\pi 1^2}{4} = 0.8 \text{ mm}^2$$

The surfaces ratio:

$$\frac{A_2}{A_1} = \left(\frac{d}{D} \right)^2 = \Phi = \left(\frac{1}{10} \right)^2 = 10^{-2}$$

With the air flow and the constructive parameters of the diaphragm we can determinate the pressure loss on the diaphragm: $\Delta p = 30 \cdot 10^3 \text{ Pa}$

For the nozzle with $d = 3$ mm the flow rate value and the pressure loss is: $Q = 2.1 \text{ l/min}$ and $\Delta p = 1.6 \cdot 10^3 \text{ Pa}$.

2.1 Study of the Free Water Spurt, Results

For a turbulent flow ($m = 0.3$) for an orifice with diameter of 0,4 mm the height of the conic nucleus is: $x_0 = \frac{d}{m} = \frac{0.4}{0.3} \approx 1.4 \text{ mm}$ With the crossing section:

$$A = \frac{\pi d^2}{4} = \frac{\pi}{4} 0.16 = 0.125 \text{ mm}^2$$

The velocity of the water at the output and in the conic nucleus (at a slight distance as x_0):

$$v = \frac{Q}{A} = \frac{2.5 \cdot 10^{-6}}{0.125 \cdot 10^{-6}} = 20 \text{ m/s}$$

The medium velocity of water at the current distance x (in the center of the spurt):

$$v_m = v \frac{x_0}{x} = 20 \frac{1.4}{x} \quad (10)$$

Table 1 Tactile stimulation for different distances of action

x [mm]	2	4	6	8	10	12	15
v_m [m/s]	14	7	4.7	3.5	2.8	2.33	1.87
$p_d = \rho \frac{v^2}{2}$ [bar]	0.98	0.25	0.11	0.061	0.04	0.027	0.017

For different values of the distance of action x the obtained values for the medium velocity’s and the dynamic pressure (tactile stimulation) are presented in Table 1. The velocity at the periphery of the spurt is given by relationship (4). The dynamic pressure in the center of the spurt is:

$$p_d = \rho \frac{v_m^2}{2} = 500 \cdot v_m^2 \cdot 10^{-5} = \frac{10^{-2}}{2} v_m^2 \text{ bar}$$

According with Fig. 1 the spurt diameter is:

$$d_j = d + 2x \cdot tg\alpha_a = 0.4 + 0.352 \cdot x \tag{11}$$

For $x = 10 \text{ mm}$ we have: $d_j = 0.4 + 3.52 \approx 4 \text{ mm}$. The force of a wall at 10 mm of the diuze:

$$F_{10} = p_d \frac{\pi d_j^2}{4} = 0.04 \frac{\pi \cdot 0.4^2}{4} = 0.05N$$

Considering the relationship (7) the value of the force is: $F = \rho Qv = \rho Av^2 = 0.1N$ from the obtained values we consider the maximum value.

3 Electro Dermal Reaction for Laser Dental Treatment Efficiency Evaluation

The method proposed by the authors is the utilisation of an electro dermal measurement device on the arm support of the dental unit. The patient can be connected to two electrodes placed on his fingers, the arm resting on the arm support of the chair. The variation of the skin electrical resistance can be graphically visualized on a display only for the specialist and not for the patient.

During the mechanical stimulation via the air/water spray the specialist can track the evolution of the skin electrical resistance and by this being able to appreciate the installation of pain and to differentiate the pain from tactile stimulation and emotional states.

Table 2 Measurement results

The state	Heart rate mean < bpm >	EDR mean < kΩ >	Degree of freedom
Relaxation	70.14	787.21	13
Stimulation (pain)	84.79	588.07	13

Table 3 Statistical evaluation

The state	Mean	95 % Confidence interval (C.I.)	Sig. (2-tailed)
Heart rate difference < bpm >	14.643	(−20.179; -9.107)	0.000
EDR difference < kΩ >	199.143	(142.783; 255.503)	0.000

3.1 The Experiment, Materials and Results

In order to validate the proposed method the authors designed the following experiment: a group of 14 volunteers, males and females, all young (20–25 years old) was submitted to electrical skin resistance and heart rate measurements, first after 30 min of reposing in the hospital environment and second sitting on the chair of the dental unit during mechanical stimulation via the air/water spray of the self-indicated potentially painful areas.

The authors included the heart rate as a pain indicator due to the fact that this is a generally recognised indicator for pain presence [4]. If the variation of the electrical skin resistance is associated with the increase of the heart rate and also with the installation of pain, then there is strong evidence that the electro dermal response can be used for the purpose of this paper.

In order to measure the electro dermal response (EDR), the digital multimeter UT-70B and the appropriate interface and software were used. Also, a pulse-oximeter was employed for the heart rate acquirement. For each volunteer and each situation, the average values for the electrical skin resistance and heart rate was collected. The data was processed via the SPSS software. The null hypothesis according to the research aim was that there is no difference between the electro dermal response and the heart rate variation due to the presence of pain. In order to verify if they can reject the null hypothesis, the authors applied the Paired Sample Test. The results are shown in Table 2 and Table 3.

The results of the first measurement set and from the second set were compared. The research hypothesis was that there is a correlation between the pain presence and the reduction of the electrical skin resistance and the increase of the heart rate.

In conclusion, due to the fact that Sig. < 0.05 and the 95 % C.I. did not included zero, the null hypothesis was rejected. Therefore, the electro dermal reaction is a statistically significant indicator for the presence of pain caused by mechanical stimulation of potentially painful areas envisaged by the dental intervention, because there is a statistical difference of the skin electrical resistance in the presence of pain and can be used to evaluate the efficiency of the laser dental treatment focused on pain reduction.

4 Conclusions

The authors underlined that if the physical parameters of the mechanical pain stimulus (air/water spray) are constant, then the dental specialist can use the spray to test the pain reaction of the patient. The authors showed that the pain level can be assessed by other means than the verbal or gestural indicators from the patient towards the dentist because due to the specificity of the dental treatments the patient cannot communicate in good conditions with the specialist in order to evoke the pain level using verbal or gestural indicators.

The electro dermal reaction can be employed as a statistically significant indicator for pain during dental treatment or interventions, with a large perspective of opportunities such as treatment efficiency evaluation, anesthesia control, diagnosis and other medical activities.

References

1. Ahuja, N.D., Agarwal, A.K., Mahajan, N.M., Mehta, N.H., Kapadia, H.N.: GSR and HRV: Its application in clinical diagnosis. In: Computer-Based Medical Systems, IEEE Symposium, 16th IEEE Symposium on Computer-Based Medical Systems (CBMS'03), pp. 279 (2003)
2. Eriksson, M., Storm, H., Fremming, A., Schollin, J.: Skin conductance compared to a combined behavioural and physiological pain measure in newborn infants. *Acta Paediatr.* **97**(1), 27–30 (2008)
3. Mateas, M., Ianosi, E.: Consideration about dental laser treatment evaluation methodologies. In: Proceedings of the X. International Conference TMM 2008, Liberec, pp. 393–398 (2008)
4. Mateas, M., Ianosi, E.: Proposal for a multifunctional stand for determination of some behavior indicators of human subjects in specific conditions—COMEFIM 8, Cluj-Napoca, pp. 343–348 (2006)

Servo Control Using Wave-Based Method

O. Marek

Abstract The wave-based control of flexible mechanical systems has been developed. It is based on the idea of sending waves into the mechanical system, measuring of the incoming waves and avoiding the re-sending of these waves into the continuum again. This approach actually absorbs the energy coming from the system. It has been successfully applied for the number of simulations. This paper deals with the implementation of the wave-based control for experiments using servomotor. It particularly describes the implementation on Yaskawa servo-motor and its PLC system.

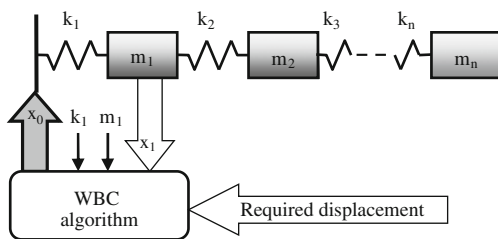
Keywords Wave-based control • WBC • Wave-based control implementation • Residual vibrations • Yaskawa

1 Introduction

The wave-based control of flexible mechanical systems is based on the idea of sending waves into the mechanical system, measuring the incoming waves and avoiding the re-sending of these waves into the continuum again. Many simulations were formerly performed [1, 2] and the stability was proven too [3]. This paper describes the possible wave-based control implementation to the real motor which moves the flexible mechanical system. The knowledge of the natural frequencies is not important at all.

O. Marek (✉)
VÚTS a.s., Liberec, Czech Republic
e-mail: ondrej.marek@vuts.cz

Fig. 1 Wave-based control applied on lumped mass system



2 Wave-Based Control

Wave-based control (WBC) is the new and breakthrough control method. It allows controlling the mechanical systems without full knowledge of the system models. This method requires only the partial knowledge of the system. The range of the system description is the same as for the simple systems so for the complex systems. The number of required measured signals for feedback is the same too. The basic idea is shown in Fig. 1. The wave-based algorithm and the number of measured signals do not depend on the number of masses in the chain [4, 5].

The dynamics of the system from Fig. 1 can be described by n differential equations of motion, or alternatively by wave model. The mechanical system in Fig. 1 is artificially described by a block diagram in Fig. 2. The positions of particular masses are defined by the equation

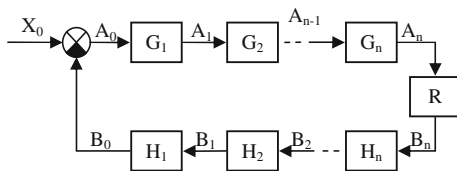
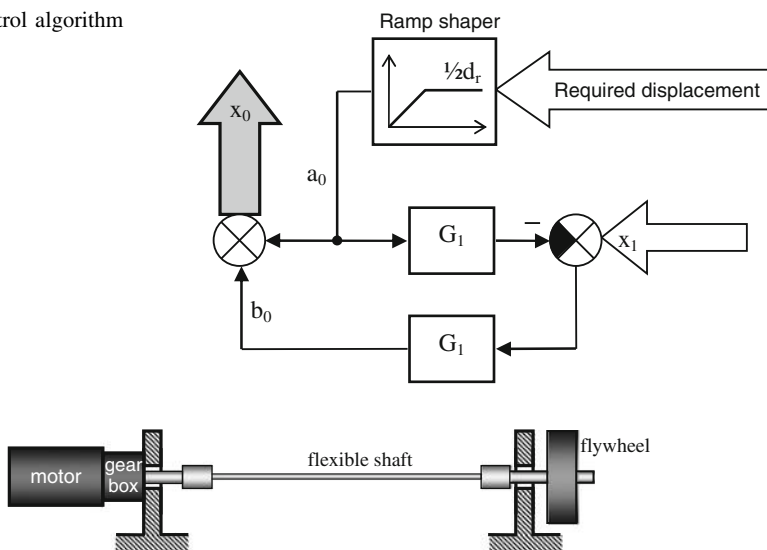
$$X_i(s) = A_i(s) + B_i(s) \quad (1)$$

where A_i respectively B_i are the variables between the blocks G_i respectively H_i . The values of $a_i(t)$ and $b_i(t)$ do not exist physically. Only the sum $a_i(t) + b_i(t)$ exists and equals the certain position $x_i(t)$ of the certain mass m_i . The transfer functions between the particular masses are given by the nature of the mechanical system.

Only values of $a_0(t)$ and $b_0(t)$ are used in the control algorithm. The launch wave $a_0(t)$ acts as the input variable. The reflected wave $b_0(t)$ is computed. The most important value for the control is $x_0(t)$ which is the position of the actuator. The speed limits of the actuator have to be taken into account too and therefore the required displacement value goes through the shaper first. The shaper builds the shape of a_0 in time. The simplest shapers use ramps as in Fig. 3. The final output value of the shaper equals the half of the desired displacement and is constant. The reflected wave b_0 reaches the same value as a_0 and using formula (1) it becomes obvious. This comes from the theory in [4, 5]. Figure 3 shows the scheme of the control algorithm which needs the block representing $G_I(s)$ only. The transfer function $G_I(s)$ can be arbitrary chosen using proposed formula (2) [3].

$$G_I(s) = \frac{\kappa \omega^2}{s^2 + 2\xi s + \omega^2} \quad (2)$$

The parameters ξ , ω , κ are chosen and positive.

Fig. 2 Wave model of lumped mass system**Fig. 3** Control algorithm schema**Fig. 4** The scheme of the experiment with the servomotor

3 Description of the Experiment

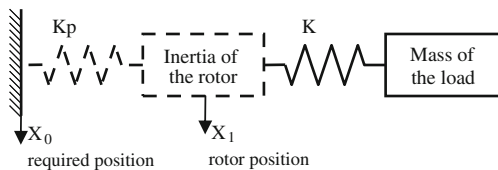
The simple flexible (1 DOF) mechanism has been selected. It is one spring one mass chain. The whole mechanical system contains of the actuator (motor), flexible element and the load (mass). The flexible shaft links the motor and the load as shown in Fig. 4.

The Yaskawa motor SGMSV 5 kW and the gearbox Neugart with the gear ratio $i = 5$ have been used. The minimum computing period 0.001s has been set. The software MPE720 ver. 6 was used for programming.

4 Wave-Based Control Implementation

The Yaskawa motor SGMSH uses 20-bit encoder. This encoder specifically measures the position of the rotor. The necessary feedback used by wave-based control is supposed to use this value in order to avoid installing extra sensors.

Fig. 5 The lumped mass system analogy



The control tactic is following. Firstly basic P regulation in the position loop has to be set. In the Sect. 2 the WBC is described for the mass-spring chain case. The analogy of this chain has been used (Fig. 5). The gain of P regulation Kp represents the first stiffness in the mass-spring chain actually. The same coefficient Kp is used in the wave-based control algorithm. The torque applied on the rotor is computed using formula (3).

$$\mathbf{M} = \mathbf{Kp}(X_1 - X_0) \quad (3)$$

X_1 represents the position of the rotor and X_0 represents the required position generated by WBC. The inertia of the rotor is known and it represents the first mass in the mass-spring chain. This value also affects the wave-based control computing.

The blocks G_I used in the control algorithm (Fig. 3) use the values Kp and I_{rotor} too. The already performed simulations were mostly simulated in Matlab-Simulink because of the simple implementation of the control loops. The Yaskawa's MPE720 does not offer anything similar to Simulink. The ladder programming is mostly performed. Therefore the control algorithm has to be converted to the state description first. The computing procedure will be briefly shown. Let us define: $m = I_{rotor}$; $k = Kp$; $c = 2\sqrt{(Kp \cdot I_{rotor})}$; g_{in} = input position; g = output position. Using formula (2) the parameters κ , ω and ζ are $\kappa = 1$, $\omega^2 = k/m$, $\zeta = 1$. G block is described by differential Eq. (4).

$$m\ddot{g} + c\dot{g} + k(g - g_{in}) = 0 \quad (4)$$

The state vector is defined (5).

$$G = \begin{bmatrix} g \\ \dot{g} \end{bmatrix} \quad (5)$$

The state description (6) is derived by combining Eqs. (4) and (5).

$$\dot{G} = \begin{bmatrix} 0 & 1 \\ -\frac{k}{m} & -\frac{c}{m} \end{bmatrix} G + \begin{bmatrix} 0 \\ \frac{k}{m} \end{bmatrix} g_{in} \quad (6)$$

Let us call the upper block G_I as G_a and the lower block G_I as G_b . The input of the block G_a is the value of the launch wave called a_0 . It is the output of the shaper (Fig. 3). Let us call the output value of the block G_a as g_{a1} . It is computed first. The value $(x_I - g_{a1})$ is the input value of the block G_b (Fig. 3). The computed output g_{b1} equals directly the reflected wave called b_0 . The sum of a_0 and b_0 gives x_0

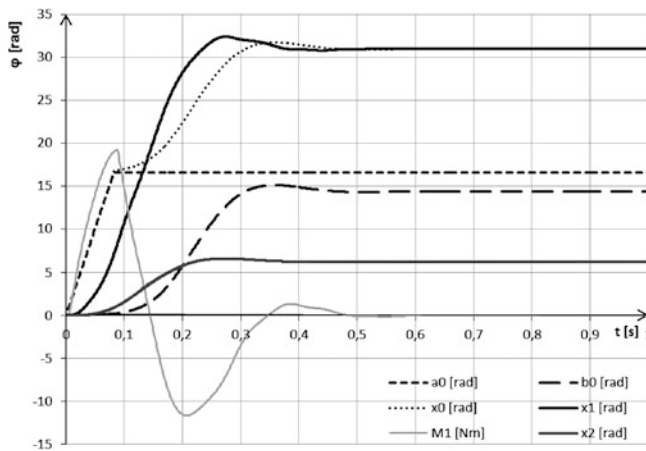


Fig. 6 The response of the system to the displacement command

which is the required position value coming into the P controller. Then the P controller computes the applied torque.

$$\mathbf{M} = \mathbf{Kp}(x_1 - x_0) = \mathbf{Kp}(x_1 - a_0 - b_0) \quad (7)$$

The servomotor is set in the torque mode and its drive is supposed to ensure the required torque. The real experiments run in real-time and they always use the fixed step solvers. The constant integration period is used. Then the simple numeric integration can be performed (8).

$$G(t + dt) = G(t) + \dot{G}(t)dt \quad (8)$$

5 Results

The displacement (rotation) commands were applied on the mechanical system described in the Sect. 4. The responses of two of them are plotted in Fig. 6. The position of the rotor x_1 , the launch wave a_0 , the reflected wave b_0 , x_0 and the position of the load x_2 are displayed.

The shaper produces a_0 in the ramp profile. The final value is the half of 10π rad thus 5π rad. Some error can occur because of the friction and other passive resistances. The position of the load (x_2) is five times smaller because of the used gearbox.

6 Conclusions

The paper describes the possibility of wave-based control implementation using the rotor position measuring only. It verifies the formerly performed simulations [1, 2]. The friction can negatively affect the strength of the wave-based control method. The friction can cause that the system does not reach the required position. It is difficult to predict the error. It could be reduced by performing of additional motions [1].

References

1. Marek, O., Valášek, M.: Wave-based control of motion of flexible bodies. In: Proceedings of Multibody Dynamics 2009, ECCOMAS Thematic Conference, 2009
2. Marek, O., Valášek, M.: Control of translational motion of flexible bodies by “wave method”. Bull. Appl. Mech. **4**(15), 104–108 (2008)
3. Valášek, M., Marek, O.: Stability analysis of wave-based control of flexible systems, In: Proceedings of Multibody Dynamics 2010, ECCOMAS Thematic Conference, 2010
4. O'Connor, W.J.: Wave-based Modeling and Control of Lumped, Multibody Flexible Systems. In: Proceedings of Multibody Dynamics 2005, ECCOMAS Thematic Conference, 2005
5. O'Connor, W.J.: Slewing Control of Space Structures with Flexible Joints: A Wave-based Approach. In: Proceedings of Multibody Dynamics 2007, ECCOMAS Thematic Conference, 2007

Drives Dynamic Models Implementation with Regard to Real-Time Simulation

J. Opálka

Abstract The paper deals with the problematic of drives dynamic models implementation into the hardware simulator. The hardware simulator will be used for the control system debug with advantage that the real device is not needed. The simulator works in real-time mode and therefore it is necessary to reduce computation demands and maintain sufficient accuracy. Each case can mean a different requirement for accuracy and therefore it is suitable to choose the appropriate drive model. The implementation of drives models considers the variable load. The models of particular drive power control units are implemented too, because it is not aim of hardware simulator to debug the power control settings of drives.

Keywords Hardware simulator • Real-time • Drive model

1 Introduction

Companies whose main subject of business is development, construction and control design of machines in industry would like to make the time of machine design shorter. The procedure of machine development usually begins with the machine construction (hardware part) and after that the control unit debugging is made. The control unit debugging is not usually possible to do during the construction of the hardware part. Therefore it could be profitable to have a real-time hardware simulator which can simulate the behaviour of the real machine. In this case the hardware simulator is connected with the control unit and it is possible to

J. Opálka (✉)
VÚTS, a.s, Liberec, Czech Republic
e-mail: jan.opalka@email.cz

make basic debugging of control unit and construct the hardware part of machine in the same time. This makes the machine design process shorter.

The most of machines are powered by some electric drive or by the set of electric drives. And for this reason it is necessary to implement sufficiently accurate drives dynamic models into the hardware simulator. The hardware simulator works in real-time and it is required to run it on common PC. Therefore it is needed to focus on the short computation time too.

The main aim of the hardware simulator is to debug the correct behaviour of the control unit in terms of the logic and time dependencies on machines with many digital and analog inputs and outputs. Therefore it is not important to simulate very detailed electromagnetic behaviour of drives. This is not neither possible, because the assumed sample time of the hardware simulator is 1 ms. However it is necessary to observe the rise times and the deceleration times. Further it is necessary to consider the variable moment of inertia and variable load torque because of the possible variable load.

The main (debugged) control unit usually controls the drive by setting the set-point of the drive power control unit. Therefore the models of the drives power control units have to be included in the hardware simulator too and they are shortly described with the drives models together.

The paper deals with the models discretization and with the sample time choice too. The optimal sample time choice is connected with the stability ensuring.

2 Drives Models

2.1 DC Drive

The DC drive model is based on the common DC drive model with the separate excitation [1]. Since the excitation is usually made by permanent magnet (it is constant) we can neglect the dynamics of excitation. We get following state space model:

$$\frac{d}{dt} \cdot \begin{pmatrix} i_a \\ \omega_r \end{pmatrix} = \begin{pmatrix} -\frac{R_a}{L_a} & -\frac{K_v}{L_a} \\ \frac{K_m}{J} & 0 \end{pmatrix} \cdot \begin{pmatrix} i_a \\ \omega_r \end{pmatrix} + \begin{pmatrix} \frac{1}{L_a} & 0 \\ 0 & -\frac{1}{J} \end{pmatrix} \cdot \begin{pmatrix} u_a \\ m_L \end{pmatrix} \quad (1)$$

Where i_a is armature current; ω_r rotor speed; u_a armature voltage; m_L load torque; R_a armature resistance; L_a armature induction; K_v , K_m voltage and torque constant; J moment of inertia.

The DC drives are usually controlled by cascade control structure [2] based on the PI controllers, where the current, speed and position feedback is closed (depends on the controlled value). This basic control structure is implemented in the hardware simulator. Particular controllers are equipped by the wind-up effect elimination and by the value and ramp saturation of the action value. In the

hardware simulator it is also possible to control the DC drive by simple PI controller or directly by armature voltage—e.g. from some analog input.

For less demanding application with DC drive it is possible to make a simplification of the drive model which reduces the computation time. It is possible to do this simplification only in case, where the DC drive is controlled by cascade control structure. In this case the dynamics of current control is neglected and it is replaced by static gain. The resulting simple DC drive model of the 1st order, which includes the current control feedback, is as follows:

$$\frac{d}{dt} \cdot (\omega_r) = \left(\frac{P_i K_m}{K_m K_v T_i + P_i J} - \frac{1}{J} \right) \cdot \begin{pmatrix} i_d \\ m_L \end{pmatrix} \quad (2)$$

Where P_i , T_i are parameters of PI current controller, other values see (1).

It is advantageous to do this simplification when the load moment of inertia is variable, because the modification of the model (parameter J) in discrete form is easy and fast.

2.2 Synchronous Servo

The synchronous servo with permanent magnets is usually used in dynamically demanding application (e.g. in electronics cams systems). These servos are usually controlled by vector control algorithm. Therefore it is suitable to use a nonlinear model, which works in rotating coordinates of rotor and where the stator current phasor is separated into the torque part and the magnetic flux part [3].

$$\frac{d}{dt} \cdot \begin{pmatrix} i_d \\ i_q \\ \omega_{el} \end{pmatrix} = \begin{pmatrix} (u_d - R i_d + \omega_{el} L_q i_q) / L_d \\ (u_q - R i_q - \omega_{el} (L_d i_d + \phi_B)) / L_q \\ p_p / J (1.5 p_p (\phi_B i_q + (L_d - L_q) i_d i_q) - m_L) \end{pmatrix} \quad (3)$$

Where i_d , i_q is magnetic flux and torque part of the stator current; u_d , u_q parts of the stator voltage; p_p number of pole pairs; ϕ_B magnetic flux from the permanent magnets; ω_{el} angular frequency of stator current phasor ($\omega_{el} = p_p \omega_r$).

Since the excitation is provided by permanent magnets, it is required to set the magnetic flux part of stator current i_d to zero. If we consider that current i_d is still zero, we can make a simplification where the dynamics of magnetic flux part is neglected. We obtain a linear model of the 2nd order which is similar to (1). Further since the synchronous servo is usually controlled by cascade control structure (similar to DC drive) it is also possible to do a simplification, where the dynamics of current control is neglected and we obtain the simple model similar to (2).

The nonlinear model gives almost the same results as the linear model of the 2nd order, because the current i_d is almost always closed to zero. The nonlinear model and the simplest linear model of the 1st order are easy to modify in their discrete form, when the load moment of inertia is variable (see 3). The model of

the 1st order is not suitable to use for torque servos or for application with high frequency changes of controlled values (current, speed), because the frequency response deviation between the model of the 1st and the 2nd order is larger in higher frequencies. The model of the 1st order is also not suitable for application with a high load torque.

2.3 Asynchronous Drive

The dynamics of the asynchronous drive can be described by relatively complicated three-phase nonlinear model which considers all mutual inductances between drive windings [1, 3]. But in reality it is very difficult to get or measure all necessary values which this model needs. Further the asynchronous drive usually works in the constant speed mode with fewer demands on the dynamics. Therefore the easy model based on the Kloss equation, which approximates the torque characteristic, was used.

The model (4) works in two modes. The mode with the constant maximal torque^{*} M_{\max} is valid when the power supply frequency from the frequency converter ω is smaller than synchronous frequency ω_s . In the opposite case the mode with the constant maximal power^{**} P_{\max} is valid.

$$s = \frac{\omega - p_p \omega_r}{\omega_s}; \quad {}^* m_{\max} = M_{\max}; \quad {}^{**} m_{\max} = \frac{P_{\max}}{\omega - s_{\max} \omega_s} \quad (4)$$

$$m_{asm} = \frac{2m_{\max}}{\frac{s}{s_{\max}} - \frac{s_{\max}}{s}}; \quad \frac{d}{dt} \cdot (\omega_r) = \frac{1}{J} (m_{asm} - m_L)$$

Where ω_r rotor speed; p_p number of pole pairs; s drive slip; s_{\max} slip in the maximal torque; m_{asm} actual drive torque; m_L actual load torque.

The model considers that the frequency convertor is set to the scalar control mode. In the scalar control mode, the torque characteristic is shifted with the power supply frequency because the U/ω value is constant. Therefore the calculating of slip s in (4) is except the synchronous frequency based on the power supply frequency too.

The frequency convertor model easily transfers the required speed into the power supply frequency. But it is very important to observe the startup time because of keeping the appropriate drive torque. Start up time is realized by the ramp saturation of the power supply frequency. This parameter is possible to set on each frequency convertor. The frequency convertor works in open loop mode without any feedback (the most often variant), but the close loop mode is implemented too.

3 Discretization

During the simulation it is necessary to solve the differential equations of the model. It is not suitable to directly solve the continuous equations using e.g. the Runge–Kutta methods. This approach is not effective for the real-time simulation. Since we exactly know the sample time of the hardware simulator, it is better to solve the difference equations of the discrete state space models. Therefore it is necessary to make a discretization of the continuous models.

According the [4] we can obtain the discrete state space model from the continuous one using the following formulas:

$$\mathbf{M} = e^{\mathbf{A}T_s} \quad \mathbf{N} = \mathbf{A}^{-1}(\mathbf{M} - \mathbf{E})\mathbf{B} \quad (5)$$

Where \mathbf{A} , \mathbf{M} is continuous and discrete system matrix; \mathbf{B} , \mathbf{N} continuous and discrete input matrix; T_s sample time. The \mathbf{A} is always regular in drive models.

In case of variable moment of inertia of load it is necessary to change appropriate parameter in the drive model and after that to make a new discretization during the real-time simulation. For this reason the discretization has to be fast and effective.

The most demanding it is the computation of the matrix exponential function in (5). There are more possibilities how to solve this. One of them could be using the eigen values and the spectral decomposition of the matrix \mathbf{A} . But this way is not so effective. Therefore the Taylor expansion of the exponential function is used. For the sufficient accuracy achievement the first seven terms are used.

The formulas (5) are valid only for the linear systems. In case of the nonlinear synchronous servo model (3) we cannot simply make the discretization. But we can separate this nonlinear model into two linear models (6) which we discretize according the (5). After that we obtain the discrete time nonlinear model.

$$\begin{aligned} \frac{d}{dt} \begin{pmatrix} i_d \\ i_q \end{pmatrix} &= \begin{pmatrix} -\frac{1}{L_d} & 0 \\ 0 & -\frac{1}{L_q} \end{pmatrix} \begin{pmatrix} i_d \\ i_q \end{pmatrix} + \begin{pmatrix} \frac{1}{L_d} & 0 & \frac{L_q}{L_d} & 0 \\ 0 & \frac{1}{L_q} & 0 & -\frac{1}{L_q} \end{pmatrix} \begin{pmatrix} u_d \\ u_q \\ \omega_{el} i_q \\ \omega_{el} (L_d i_d + \phi_B) \end{pmatrix} \\ \frac{d}{dt} (\omega_{el}) &= \frac{p_p}{J} (1.5 p_p \quad -1) \begin{pmatrix} \phi_B i_q + (L_d - L_q) i_d i_q \\ m_L \end{pmatrix} \end{aligned} \quad (6)$$

The control unit models have to be discretized in different way. When we discretize the drive model, the zero order hold is considered before the model. But it is not valid for PID controller equations. Therefore the Tustin discretization algorithm is used [5].

4 Stability Ensuring

Let us assume that the continuous model is stable. When we make a discretization of a stable continuous model we also get a stable discrete model. Therefore it would be profitable to make a one resulting model from the drive model and the control unit model and after that make the discretization. The stability is ensured naturally. But using of this approach it is not possible to implement nonlinearities as the wind up effect elimination, the saturation of the non state variables, etc.

Therefore it is necessary to make a discretization and solve these models separately, but stability is not ensured in this case. We have to make a test of stability of the resulting model which is created from the discrete drive and the control unit model. The Jury criterion of the discrete systems stability is used. If the model is not stable with the sample time 1 ms, it is decreased until the model is stable. Now we are on the bound of stability. Therefore we have to make next decrease of the sample time (e.g. 5 times lesser). In case that the sample time is less than 1 ms, appropriate number of steps have to be computed in one hardware simulator step.

5 Conclusion

The aim was to implement easy and sufficiently accurate drive models whose parameters are possible to measure or find them in a catalog. All models were verified on the real drives. The necessary computation time of one step of all models is much lesser than 1 ms (depends on particular PC). Therefore it is possible to implement a machine model into the hardware simulator with more drives.

In case that the drive load is connected, the drive gives information about the angular position and the load gives information about the load torque and the actual moment of inertia. Load can be stiff or its dynamics can be implemented.

Acknowledgments The paper was supported by grant of Ministry of Industry and Trade FR-TII/594.

References

1. De Doncker, R., Pulle, D.W.J., Veltman, A.: Advanced electrical drives: analysis, modeling, control. Series: Power Systems. Springer, Berlin (2011)
2. Souček, P.: Servomechanizmy ve výrobních strojích, ČVUT Praha, 2004
3. Rydlo, P.: Řízení elektrických střídavých pohonů, TU Liberec, 2007
4. Hendricks, E., Jannerup, O.E., Sorensen, P.H.: Linear Systems Control: Deterministic and Stochastic Methods. Springer, Berlin 2008
5. Macia, N.F., Thaler, G.J.: Modeling and control of dynamic systems. Thomson Delmar Learning, 2005

High Performance Real-Time Simulation for Control Systems Development on Fast but Ordinary PC

J. Rameš

Abstract In this paper we will describe methods that can be used to simulate hardware in order to enable control systems programmers to debug their code without the need of having the device already constructed. We will discuss several key parts of the simulator in detail regarding communication with the control system either by direct I/O connection or by a field-bus. Since most control systems work in short time-frame steps we will describe how the simulator handles the need for high performance approach of the simulation and which simplifications need to be used in order to maintain this functionality over extended period of time and complexity of the machine being simulated. We will also discuss our method used for creating schematics that are later loaded to the simulator engine.

Keywords Simulation • Control system • Real-time

1 Introduction

Nowadays typical approach of programming control systems' is by first acquiring a hardware that is then connected to control system and the software is tested in real conditions, prior development is possible with use of software emulators and rather simple debugging tools usually bundled with control systems' programming IDE.

We are presenting a different approach. After designing the machine needed to be controlled, system engineers may transform the machine into simulation

J. Rameš (✉)
VÚTS, a.s, Liberec, Czech Republic
e-mail: ramejan@gmail.com

schematic that simulates behavior of the hardware as if it was a real machine connected to the control system(s). The control systems' inputs and outputs (and possibly other expansion modules) are directly connected to the simulation PC and thus the control system will never know it is connected to virtual hardware rather than real machine. This is called Hardware-in-the-loop (HIL) simulation.

Problems with HIL simulation is that it often simulates a very complex hardware and thus needs a very powerful machine to handle the load the simulator generates. Our approach is to simplify the machine as much as possible (in terms of keeping the outputs of the simulation consistent with real hardware while stripping away all unnecessary blocks of the machine) and simulate it on ordinary PC with few pieces of extra hardware that is used to handle input/output operations and prepare some data for the CPU to make simulation even more efficient.

2 Schematic Creation

In order for the simulation to run as fast as possible a schematic needs to be created in a specific way (and stored in our proprietary format). It is best if all non-essential parts of the machine are omitted this allows the simulator to only focus on what's really important. Also we use a subset of mechanical, electrical and pneumatic elements that the schematic needs to be comprised of. If more complex elements are needed, they can be custom made for specified application. But the designer (as we call the schematic creation tool) should be familiar to other designing tools and thus should be easy to learn and use for any engineer.

As said before the schematic consist of electric, pneumatic and mechanic elements all with concrete positions and dimensions (as expected from other designing software) although some elements' (like amplifiers or pneumatic valves) position may be considered non-vital and can placed randomly (in order to make the schematic easier to read) rather than strictly follow the machine's design.

In future versions we also plan to add import functionality from applications like Solid Works to speed-up the process of schematic creation.

3 Schematic Simplification

Before the schematic is loaded to the simulation engine it goes through process we call pre-processing (or compilation). In this stage electric routes are examined to determine current direction, this should allow us (most of the time) to also determine direction of event triggering and pinpoint which elements can cause some event and which consume such event this will create an event graph that we can use to parallelize the calculation and speed-up simulation process.

Pneumatic elements do not need to be examined in such a difficult way as the air direction is somewhat obvious and unchangeable.

Also all mechanic elements are examined and divided into groups which has no or very small interactions between each other (mostly by just transferring a product, which is what we call an object the machine is producing or shaping like paper in the printer). These groups can mostly be simulated independently as well which also speeds-up the simulation.

There are some areas of the simulation that pose more dramatic impact on simulation performance or accuracy and I will describe them in the next chapter.

3.1 Major Performance Issues

The first issue the simulator has to handle is mechanics of bodies and collision detection. In real-life situations all elements should be evaluated and equations of motion should be calculated for all of them which, for large machines, have huge performance impact. In our approach, only certain elements evaluate collisions (determined in preprocessing phase described in previous chapter) these elements mostly handle the product or detect presence of other elements (sensors). Most elements don't need so precise movement evaluation so equations of movement aren't really needed since most machines don't actually want the product to move on its own and its movement is constrained by movers (cylinders, conveyors etc.). If more complex movement of elements is needed, another approach needs to be taken, see next chapter.

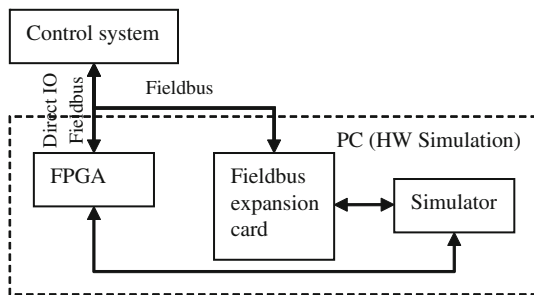
Another big performance hit is taken if more complex differential equations (or series of differential equations) need to be solved. Our simulator implementation tries to avoid solving them wherever possible but some dynamic systems need to have strict dynamic responses based on its actuation in this case special elements need to be created or some other approaches need to be chosen (again see next chapter).

A special (and rather complex) differential equations need to be used while simulation (electric) drives that are essential for most machines so more precise simulation need to be done. See paper by Jan Opálka—Drives dynamic models implementation with regard to real-time simulation.

3.2 Solutions of Performance Issues

Most of the problems with both differential equations solving and mechanics of bodies (which in the end is differential equations solving) can be simplified by method we call **delay event triggering**. For example if cylinder outstrokes the path of the end of the shaft could be complex but is not essential for the control system as it only measures (detects) it dead points. So in these cases the simulator will schedule an event that will trigger and event after a period of time in which some detection is needed and not simulating the whole path of the shaft.

Fig. 1 System/communication block diagram



If some elements need more specific behavior they can either be custom made for given application or they can be simulated as black-boxes with predefined behavior. This behavior can either be defined by premeasured values from real-world testing and measurement or defined by a function.

4 Simulation/Communication with HW/Real-Time Execution

As we are dealing with systems operating at time frame of about 1 ms, we need to ensure that the simulator runs at same speeds and is synchronized with this time frame which is needed to give the control system the response it expects in given time. Also responses (and operation) of the simulator need to be deterministic (not interruptible by other processes an ordinary PC is running). For this reason we're using real-time operating system, it is then synchronized by a FPGA card with very precise timer module. Simulator also executes the computation in multiple threads as predetermined by the compiler in order to perform one simulation step as fast as possible (Fig. 1).

The FPGA card (or cards if needed based on control systems' input/output count) is also used for signal preprocessing. It detects changes on digital input lines so the simulator doesn't have to evaluate previous states on its own, it also handles digital outputs to the control system and series of analog inputs and outputs and can be used to simulate simple functions on the digital outputs. The FPGA can also handle series of tasks that further enhance performance of the simulation like PWN encoding/decoding or encoder simulation.

Most of the control systems are using fieldbuses to communicate with external hardware. This external hardware should either be connectable to the FPGA (like encoder modules or input/output expansion modules) or they have to be emulated by the simulator itself or in combination with the FPGA card or other proprietary hardware (devices like drive controllers).

5 Conclusions

We hope that this approach will help end-users to speed up their development with relatively low-cost hardware (compared to other HIL simulators used primarily in automotive or avionic industry).

Function Properties of Electronic Cam with Great Unevenness of Angular Speed

P. Šidlof and P. Klouček

Abstract This paper deals with mechanical and electrical measurements on the electronic cam with great angular speed unevenness of the servomotor. This electronic cam was used on the special slay and shedding mechanisms of the CAM-EL loom. The drive parameters and quality of outputs from the inverter are evaluated and assessed.

Keywords Measurement • Electronic cam • Slay mechanism • Inverter

1 Introduction

Controlled electrical drives are being still wider applied in the industry. In cases where they replace or simplify the so far used cam mechanisms they are called electronic cams. The main problem when employing controlled electrical drives is to achieve the same dynamic properties and the same reliability as with cam mechanisms. Therefore, it is essential for developers and designers to understand their properties. With this intention detailed measurements were carried out on the driving slay and shading mechanisms of the CAM-EL loom where the standard cam mechanisms were replaced with a simplified mechanisms with a controlled servomotor. The angular speed of the motor during a single revolution is altering by $\pm 75\%$ from the mean value.

P. Šidlof (✉) · P. Klouček
VÚTS, a.s, Liberec, Czech Republic
e-mail: pavel.sidlof@vuts.cz

P. Klouček
e-mail: pavel.kloucek@vuts.cz

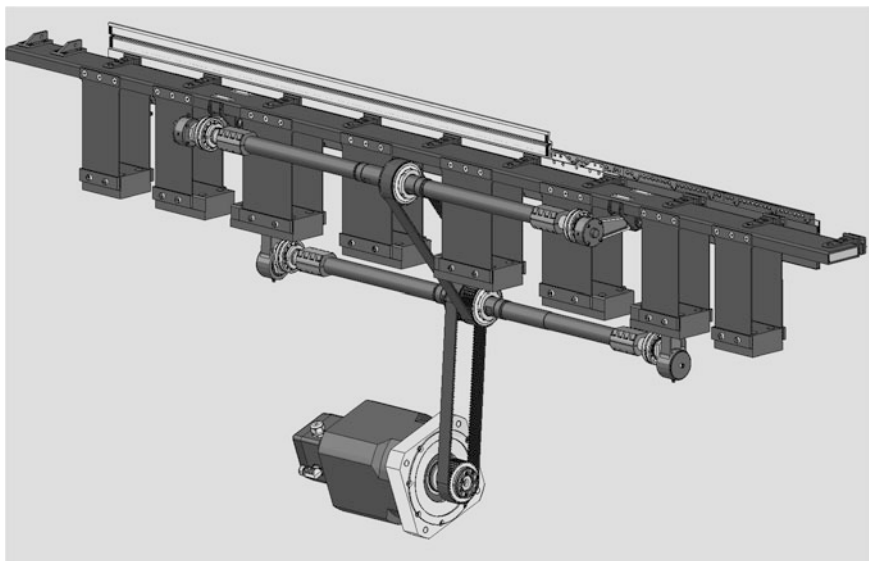


Fig. 1 Servomotor driven slay and shed mechanisms of CAM-EL loom

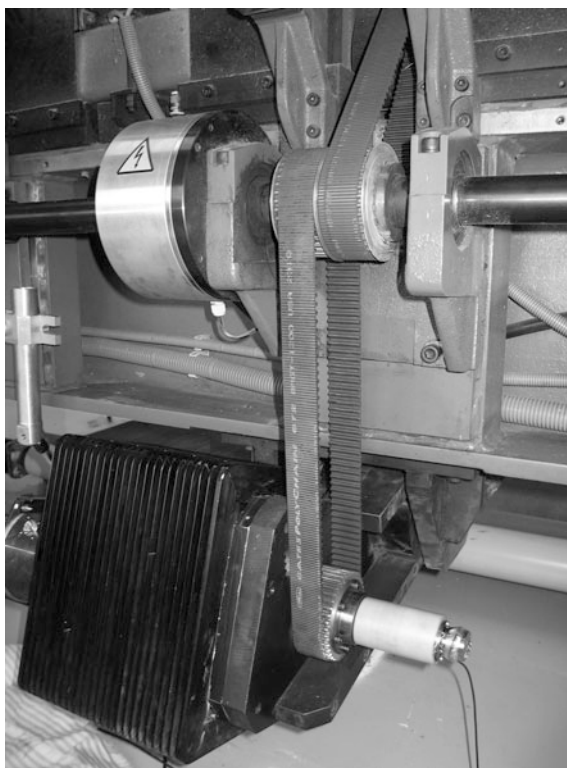
2 The CAM-EL Loom

As long as possible the slay shall remain around the back dead center, and provide sufficient time for the weft insertion. Then as quickly as possible the slay must move to the front dead center (beat-up) and return. The common drive slay mechanism is therefore double-cam and the slay performs a reversing rotary motion. The CAM-EL loom uses a simple linkage and sufficient time to achieve the weft insertion is accomplished by uneven angular speed of the servo drive. The slay is mounted on guide flat springs (Fig. 1) is powered by two connecting rods and eccentrics on the upper shaft and performs translation deforming the flat springs. The springs accumulate kinetic energy and reduce the required driving torque at operating speed. This enables high unevenness of angular speed of the servomotor. The lower shaft drives a not depicted heald frame placed behind the slay (the loom produces leno fabric).

Servomotor angular speed has been programmed into servo control system in sine wave form with a mean value equal to the virtual (constant) angular speed of the control system. In the measurements reported here the rate was 600 RPM. Unevenness of the servomotor angular speed is entered as a percentage of mean angular speed and was 75 %. The desired servomotor angular speed should therefore alter in one cycle (360° of servomotor, 0.1 s) from 150 to 1,050 RPM.

The control program is designed for given parameters of the mechanism and for projected rigidity of flat springs. Flat springs are made of carbon composite and their rigidity is not always strictly upheld. In this case unevenness of angular speed is not met accurately as well, but average speed remains accurate.

Fig. 2 The servomotor, torque sensor and slip ring assembly



The servomotor is wye-connected, has a rated torque of 40 Nm and is powered by the inverter (frequency converter) with a rated output of 18.5 kVA.

3 Brief Description of Measurements

Every phase conductor voltages of servomotor are measured against neutral. The phase currents coming up from the inverter to the servomotor and neutral current from the servomotor to the inverter are positive. Currents are measured with AC/DC current clamp probes with up to 100 kHz frequency range. Voltage differential probes have a frequency range up to 10 MHz. Besides the electrical parameters also angular speed, acceleration and angle of rotation of the servomotor shaft were measured. The torque on the shaft was measured by an especially manufactured strain gage transducer (Fig. 2). The slay and the heald frame acceleration were measured by piezoelectric accelerometers. On the inverter voltage terminals, voltages of the desired speed, angle and torque of the servomotor were measured and servomotor speed was scanned as well. Recording was made by of use two coupled waveform analyzers with a total of 20 recorded channels. Sampling

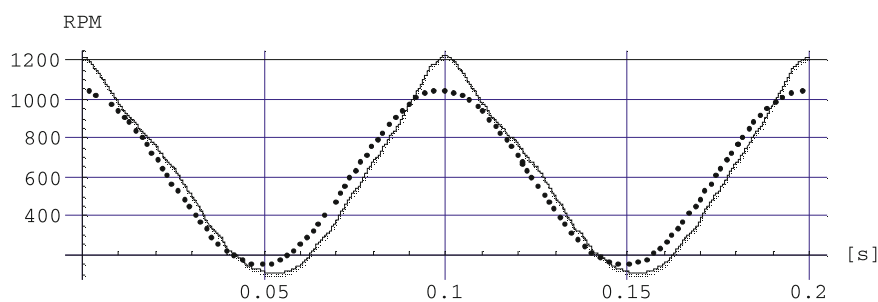


Fig. 3 Measured angular speed of the servomotor (*solid line*) and programmed speed (*dotted*) in two machine cycles (solid line: mean 600 RPM, max. 1,226 RPM, min. 103.4 RPM, unevenness +104.3, -82.8 %, dotted: mean 600 RPM, max. 1,050 RPM, min. 150.4 RPM, unevenness +75, -74.9 %)

frequency was 300 kHz and the length of records was at about 10^6 samples. The measurements are processed using the software Mathematica.

4 Measurement Results

Measured angular speed of the servomotor and programmed speed (set via the control system of the inverter) are drawn in Fig. 3. Due to the lower stiffness of slay flat springs actual speed has greater variation, but average speeds are the same.

One of the purposes of the measurement was to compare absorbed power of the measured servomotor and mechanic power and torque on its output shaft. Servomotor absorbed power is transmitted through a magnetic field to the rotor. In order to compare it with the power of the shaft, we subtract from it the power necessary to accelerate the rotor and part of the torque sensor. Thus converted power and the derived moment will be referred to as electro power and electro moment respectively on the shaft.

Inverter enables control of AC motors. Its main elements are 3 switch-mode power suppliers for 3 phases of the servomotor. They switch the rectified three-phase supply. Figure 4 shows an example of a short section (0.67 ms) voltage of phase W and its average value. Voltage has an approximately square shape with a frequency of 8 kHz and the average value is regulated by the pulse ratio. Current waveform is in comparison with the voltage smooth (Fig. 5) because it is filtered due to large inductance of servomotor coils. In Fig. 6, the filtered course of the voltage and current during a single revolution of the servomotor are presented. It can be seen that the waveforms are quite different and some sections have opposite phases.

Absorbed servomotor power of one phase is calculated as the product of corresponding voltage and current and total power is the sum of all three phases. The filtered servomotor absorbed power, electro power on the shaft and the mechanical

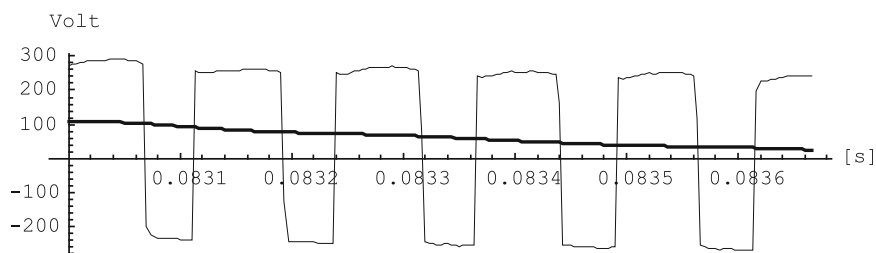


Fig. 4 Example of W-phase servomotor voltage and its average (smoothed) value

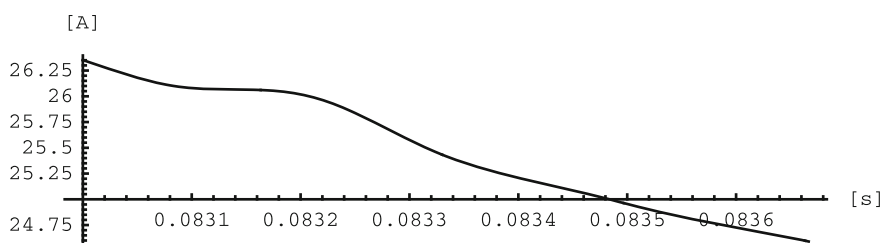


Fig. 5 Corresponding W-phase servomotor current

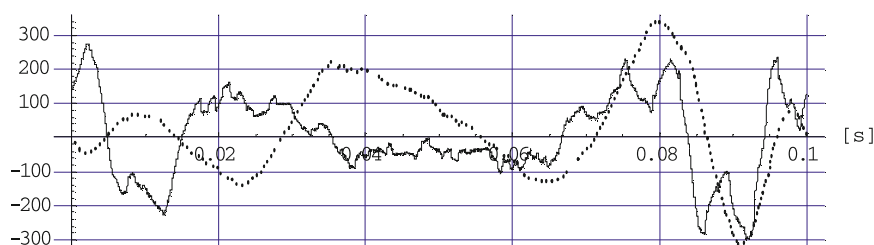


Fig. 6 Filtered W-phase voltage [V] (solid line) and $10 \times$ current [A] (dotted) during a single revolution of the servomotor

power on the shaft calculated from the measured torque and angular speed are shown in Fig. 7. Electrical powers are smoothed for lucidity. Interesting is the power needed to accelerate the rotor (difference of waveforms), which reaches up to 30 % of the absorbed power. In the positive part of electro power, electro power leads mechanical power. Servomotor efficiency can be calculated from the ratio of mechanical power and electro power and amounts to 64 %. The low value is caused by considerable big part of the cycle where servomotor brakes. The efficiency of the positive part of power is 83 %. The maximum absorbed power exceeds 10 kW, but the mean power is only 1.4 kW. However, required inverter power is greater, because the energy during braking is lost in resistances of the inverter. By comparing electro power and mechanical power it can be assessed with what accuracy mechanical power and torque can be determined from electro power. The torque is usually very difficult to measure on complete machine.

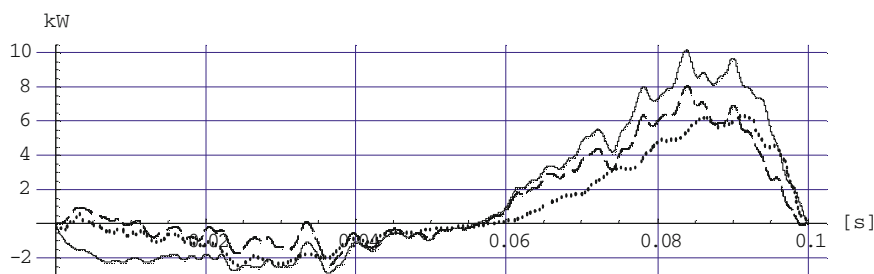


Fig. 7 Servomotor absorbed power (*solid line*), electro power on the shaft (*dash line*) and mechanic power (*dotted*) at one cycle

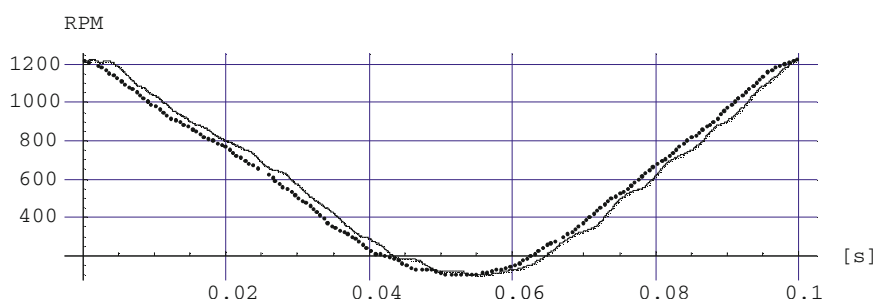


Fig. 8 Measured angular speed of servomotor (*dotted*) and speed measured by inverter (*solid line*) in one cycle

Required speed (Fig. 3), the angle of the servomotor, speed measured by the inverter, the desired torque and the additional torque were measured on the inverter terminals. An inverter function can be assessed from these variables. The servomotor angular speed measured by inverter is important because regulation action is often derived from it. In Fig. 8 is this inverter measured speed compared to the actual speed. The speed of the inverter has a staircase waveform because it is sampled with low frequency of 1 kHz. The mean phase delay to the actual speed is equal to two sampling periods. In virtual angular scale of the machine it corresponds to a significant angle of 7.2° . For serious regulation actions inverter speed signal is thus not appropriate.

5 Conclusions

On the CAM-EL loom equipped with electronic-cam with great unevenness of the angular speed, the measurement of electrical and mechanical quantities of servomotor and drive mechanisms was realized. Control of the inverter was hard-coded. Unevenness of angular speed did not correspond exactly to specifically

given speed, because the stiffness of recovery springs was lower than projected. From the measured current and voltage input of the servomotor the absorbed power was calculated and has been recalculated to the power on output shaft. This was compared to the real mechanical power calculated from the measured torque and angular speed. From these powers efficiency of the servomotor was derived. The measurement of electrical parameters on the inverter serves to assess its functionality and accuracy of the angular speed measured by the inverter. It has a phase delay and is affected by low sampling rate. The measurement results are used to improve the function of the machine drive, as shown in some other papers.

Author Index

A

Amiri, M., [281](#)
Arakelian, V., [159](#)

B

Balchanowski, J., [3](#), [89](#)
Bauer, J., [13](#), [193](#)
Belovodskiy, V., [167](#)
Beran, J., [383](#), [469](#)
Berger, M., [21](#), [129](#), [375](#)
Bílek, M., [367](#), [445](#)
Bílkovský, A., [483](#)
Bradna, J., [13](#)
Briot, S., [159](#)
Buciuman, C.F., [323](#)
Budescu, E., [331](#), [345](#)
Bukin, S.L., [167](#)
Bureš, P., [489](#), [495](#)
Bušek M., [501](#)

C

Cărbăș I., [35](#), [143](#)
Casolo, F., [281](#)
Ceccarelli, M., [289](#)
Čechová, H., [351](#)
Čeřovský, Z., [517](#)
Chichvarin, A., [57](#)
Chirazi, M., [331](#)
Ciupe, V., [35](#)
Corves, B., [27](#)
Cotoros, V., [345](#)
Crhák, V., [97](#), [495](#)

D

Dauksevicus, R., [245](#)
Dehelean, N., [35](#)
Dekys, V., [421](#)
Denninger, D., [375](#)
Dostrašil, P., [105](#), [501](#)
Drewniak, J., [81](#)
Dupac, M., [175](#), [339](#)

E

Ebert, F., [21](#)

F

Fan, Y., [121](#)
Ferfecki, P., [271](#)
Fischer, C., [113](#)
Fliegel, V., [407](#)
Fligl, S., [13](#)

G

Gronowicz, A., [303](#)
Gruescu, C.M., [35](#), [143](#)

H

Hajžman, M., [181](#)
Handke, A., [309](#)
Hanke, U., [113](#), [121](#)
Hartig, F., [105](#)
Haubert, T., [509](#)
Heine, A., [129](#), [375](#)

H (*cont.*)

Hejnová, M., 383
 Hlinovsky, V., 23, 517
 Horáček, J., 357
 Horiguchi, K., 65
 Hortel, M., 187
 Hoshina, M., 317
 Houf, Z., 187, 517
 Houfek, M., 187

I

Ianosi, E., 525
 Ivanov, I., 49

J

Jirásko, P., 105, 483, 495, 501

K

Kafka, J., 413
 Kavan, P., 393
 Kern, D., 193
 Khajiyeva, L., 201
 Klouček, P., 401, 551
 Klouček, V., 137
 Koloc, Z., 393
 Konečný, M., 209
 Kopeć, J., 81
 Korf, J., 393
 Kovář, L., 351
 Kozánek J., 217
 Kratochvíl, C., 187
 Kydyrbekuly, A., 223

L

Le Baron, J.-P., 159
 Lin, S., 121
 Lonij, G., 27
 Loufek, J., 231
 Lovasz, E., 35, 143, 323

M

Malinauskas, K., 245
 Mañas, J., 351
 Maniu, I., 35
 Marek, O., 483, 533
 Margineanu, D., 35
 Martonka, R., 407
 Mateas, M., 525
 Merticaru, E., 331

Mindl, P., 509
 Modler, K.-H., 113, 143
 Nakamura, M., 65

N

Neumann, R., 113
 Noroozi, S., 175, 339

O

Ondrášek, J., 237, 437
 Opálka, J., 539
 Oprisan, C., 345
 Ostasevicius, V., 245

P

Palčák, F., 43
 Perju, D., 143
 Petřík, J., 351
 Petrikova, I., 413
 Petrovic, T., 49

R

Rahman, A.G.A., 339
 Rameš, J., 545
 Razum, M., 27
 Reeßing, M., 27
 Ren, Z., 121
 Russell, K., 151
 Rybak, L., 57
 Rychecký, D., 181

S

Sága, M., 263
 Sapietová, A., 421
 Seemann, W., 193
 Segla, S., 429
 Ševčík, L., 459
 Shen, Q., 151
 Šidlof, P., 437, 551
 Sidorenko, R., 57
 Skarolek, A., 253
 Šklíba, J., 57
 Škop, P., 401
 Skřivánek, J., 445
 Škuderová, A., 187
 Slavík, J., 209
 Sodhi, R. S., 151
 Špirk, S., 351
 Stropnik, J., 451

Sukhorukov, M.Y., [167](#)
Švancara, P., [357](#)
Švec, J. G., [357](#)
Szrek, J., [303](#)

T

Takahashi, R., [65](#)
Terada, H., [65](#)
Thöndel, E., [73](#)
Toyama, S., [317](#)
Twaróg, W., [309](#)

V

Vacarescu, V., [323](#)
Václavík, M., [105](#)
Valtera, J., [469](#)
Vaško, M., [263](#)
Vejrych, D., [459](#)

Vinney, J. E., [339](#)
Vlček, V., [217](#)
Volanský, Z., [483](#)
Vondrich, J., [73](#)
Vrzala, R., [413](#)

W

Wudarczyk, S., [303](#)

Z

Zábavá, E.S., [143](#)
Žabka, P., [469](#)
Žák, J., [475](#)
Zapoměl, J., [271](#)
Zawiślak, S., [81](#)
Zhu, Y., [65](#)
Zolotarev, I., [217](#)